International CLIMATE CHANGE ADAPTATION Initiative

Pacific Climate Change Science Program

Climate Change in the Pacific: Scientific Assessment and New Research

Volume 1: Regional Overview

Australian Government

Australian AID

National Library of Australia Cataloguing-in-Publication entry

Climate change in the Pacific: scientific assessment and new research. Volume 1. Regional overview / Australian Bureau of Meteorology, Commonwealth Scientific and Industrial Research Organisation.

ISBN: 9781921826733 (pbk.)
ISBN: 9781921826740 (ebook)

Includes index.

Climatic changes--Pacific Region.
Climate change mitigation--Pacific Region.

551.691823

This publication should be cited as:

Australian Bureau of Meteorology and CSIRO, 2011. Climate Change in the Pacific: Scientific Assessment and New Research. Volume 1: Regional Overview. Volume 2: Country Reports.

Foreword

This report is a first in many ways. To date our understanding of how the climate of the Pacific is changing, and is likely to change in the future, has been limited. Lack of scientific knowledge is a major challenge to effective adaptation planning for Pacific Island countries. In 2007, the Fourth Assessment Report of the Intergovernmental Panel on Climate Change identified key information gaps in the Pacific. *Climate Change in the Pacific: Scientific Assessment and New Research* is a significant step forward in our understanding of climate drivers in the Pacific region.

Climate Change in the Pacific is the final report of Australia's Pacific Climate Change Science Program, a landmark investment in climate science for the region. It is the result of three years' scientific research. This report is an invaluable reference for climate scientists, communities and decision-makers in the Pacific.

Climate Change in the Pacific also tells the climate change story - for the first time - for individual countries. It includes the first-ever country scale projections for the region, along with more detailed information for 15 small island developing states including East Timor. Enhanced understanding of climate change impacts is critical to building the capacity of countries to plan appropriate adaptation responses.

The Pacific Climate Change Science Program is one element of Australia's five-year, $328.2 million International Climate Change Adaptation Initiative. The Initiative assists countries to identify and implement priority adaptation measures, assess their vulnerability and develop evidence-based adaptation strategies. As part of this, *Climate Change in the Pacific* will be an essential tool for Pacific Island countries and their development partners in progressing adaptation and building resilience to future climate change.

Climate Change in the Pacific finds that during this century the Pacific will continue to see increasing temperatures and sea level rise, changes to rainfall variability, further ocean acidification and more extreme weather events. Pacific Island countries will face increasing impacts on human health, fresh water availability, agriculture, fisheries, marine ecosystems and tourism – with flow-on effects to livelihoods, culture and custom.

Australia is committed to working with developing countries to develop effective adaptation responses to the unavoidable impacts of climate change. Australia's adaptation support focuses on least developed countries and small island developing states – because these countries need it most urgently. Australia is committed to building on the achievements of the Pacific Climate Change Science Program and supporting further research and investment to increase the resilience of the Pacific. Australia will continue to support our neighbours in the Pacific and East Timor to respond to the challenges identified in the *Climate Change in the Pacific* report – and work together towards a sustainable future for the region.

The Hon Greg Combet AM MP

Minister for Climate Change and
Energy Efficiency

The Hon Kevin Rudd MP

Minister for Foreign Affairs

Contents

Abbreviations

CCAM	Conformal Cubic Atmospheric Model
CliCom	CLImate COMputing Project (of the World Meteorological Organization)
CliDE	Climate Data for the Environment
CMAP	Climate Prediction Centre Merged Analysis of Precipitation
CMIP3	Coupled Model Intercomparison Project (Phase 3)
CSIRO	Commonwealth Scientific and Industrial Research Organisation
ECMWF	European Centre for Medium-Range Weather Forecasts
EMI	ENSO Modoki Index
ENSO	El Niño-Southern Oscillation
GCM	Global Climate Model
GPCP	Global Precipitation Climatology Project
IOD	Indian Ocean Dipole
IPCC	Intergovernmental Panel on Climate Change
IPO	Interdecadal Pacific Oscillation
ITCZ	Intertropical Convergence Zone
MJO	Madden Julian Oscillation
NMS	National Meteorological Services
PCCSP	Pacific Climate Change Science Program
PDO	Pacific Decadal Oscillation
SAM	Southern Annular Mode
SPCZ	South Pacific Convergence Zone
SRES	Special Report on Emission Scenarios
TCLV	Tropical cyclone-like vortices
TRMM	Tropical Rainfall Measuring Mission
UNFCCC	United Nations Framework Convention on Climate Change
WMO	World Meteorological Organization
WPM	West Pacific Monsoon

Acknowledgements

This scientific assessment and new research has benefitted from the high degree of cooperation that exists between the implementing agencies: Australian Bureau of Meteorology and the Commonwealth Scientific and Industrial Research Organisation, other contributors from the region and beyond, and colleagues from our Partner Countries and regional/international organisations.

Chapter 1

Coordinating Lead Author: Gillian Cambers

Contributing Authors: Stephanie Baldwin, Jillian Rischbieth

Chapter 2

Coordinating Lead Author: Brad Murphy

Lead Authors: Alexander Sen Gupta, Simon McGree

Contributing Authors: Jaclyn Brown, Josephine Brown, John Church, Rob Colman, Andrew Dowdy, Ron Hoeke, Rod Hutchinson, Yuri Kuleshov, Kathleen McInnes, Aurel Moise, Skye Platten, Scott Power, Ian Smith, Xuebin Zhang

Acknowledging the essential contribution by the following representatives in our Partner Countries particularly to Section 2.5: Riibeta Abeta, David Aranug, Douglas Audoa, Nitoro Bates, Johannes Berdon, Kilateli Epu, Ofa Fa'anunu, Tumau Faasaoina, Lino Fiapati, David Hiriasia, Kasis Inape, Lee Z. Jacklick, Andrew Kaierua, Salesa Kaniaha, Tareti Kireuna, Ravind Kumar, Errol Lewthwaite, Mele Lakai, Ned Lobwij, David Maihia, Philip Malsale, Adorra Misikea, Rossylynn Pulehetoa-Mitiepo, Terencio F. Moniz, Maria Ngemaes, Dirutelchii Ngirengkoi, Fata Lagornauitumua Sunny K. Seuseu, Sebastião da Silva, Godwin Sisior, Eden Skilling, Lloyd Tahani, Felicia Pihigia Talagi, Franklin Teimitsi, Tebwaau Tetabo, Ueneta Toorua, Maarametua Vaiimene, Hilia Vavae, Maino Virobo, Varanisese Vuniyayawa, Reginald White

Chapter 3

Coordinating Lead Author: Dean Collins

Lead Authors: Alexander Sen Gupta and Scott Power

Contributing Authors: Karl Braganza, Jaclyn Brown, Josephine Brown, Wenju Cai, John Church, Robert Colman, Andrew Dowdy, Paul Durack, David Jones, Mareva Kuchinke, Yuriy Kuleshov, Andrew Lorrey, Chris Lucas, Simon McGree, Kathleen McInnes, Aurel Moise, Les Muir, Brad Murphy, Steven Phipps, Ian Smith, Bronte Tilbrook, Neil White

Acknowledging the essential contribution by the following representatives from our Partner Countries and our Program Partners: Akapo Akapo, David Aranug, Douglas Audoa, Nitoro Bates, Johannes Berdon, Howard Diamond, Kilateli Epu, Ofa Fa'anunu, Tumau Faasaoina, Lino Fiapati, Georgina Griffiths, David Hiriasia, Sebastien Hugony, Kasis Inape, Lee Z. Jacklick, Andrew Kaierua, Salesa Kaniaha, Ravind Kumar, Mele Lakai, Ned Lobwij, David Maihia, Philip Malsale, Adorra Misikea, Rossylynn Pulehetoa-Mitiepo, Terencio F. Moniz, Maria Ngemaes, Dirutelchii Ngirengkoi, Hans Malala, Alexandre Peltier, Alan Porteous, Jim Salinger, Fata Lagornauitumua Sunny K. Seuseu, Sebastião da Silva, Godwin Sisior, Eden Skilling, Lloyd Tahani, Felicia Pihigia Talagi, Franklin Teimitsi, Tebwaau Tetabo, Ueneta Toorua, Maarametua Vaiimene, Hilia Vavae, Maino Virobo, Varanisese Vuniyayawa, Reginald White, Xiaolan Wang

Chapter 4

Coordinating Lead Author: Damien Irving

Lead Authors: Kevin Hennessy, Jack Katzfey, Philip Kokic, Deborah Abbs

Contributing Authors: Josephine Brown, Savin Chand, Andrew Lenton, Alexander Sen Gupta, Nicholas Summons, Kevin Tory

Chapter 5

Coordinating Lead Authors: Josephine Brown, Robert Colman, Jack Katzfey

Lead authors: Damien Irving, Alexander Sen Gupta, Deborah Abbs, Sarah Perkins

Contributing Authors: Craig Arthur, Jaclyn Brown, Savin Chand, Mohar Chattopadhyay, John Church, François Delage, Paul Durack, Philip Kokic, John McGregor, Aurel Moise, Les Muir, Brad Murphy, Kim Nguyen, Skye Platten, Scott Power, Ian Smith, Nicholas Summons, Kevin Tory, Susan Wijffels, Xuebin Zhang

Chapter 6

Coordinating Lead Author: Kevin Hennessy

Lead authors: Damien Irving, Sarah Perkins, Brad Murphy, Josephine Brown, Aurel Moise, Robert Colman, Alexander Sen Gupta, John Church, Bronte Tilbrook, Xuebin Zhang

Contributing authors: Jaclyn Brown, Wenju Cai, Mareva Kuchinke, Andrew Lenton, Les Muir, Skye Platten, Scott Power, Ian Smith, Neil White

Chapter 7

Coordinating Lead Authors: Jack Katzfey and Philip Kokic

Lead authors: Sarah Perkins, Deborah Abbs

Contributing authors: Craig Arthur, Savin Chand, Mohar Chattopadhyay, Steven Crimp, Damien Irving, John McBride, John McGregor, Kim Nguyen, Nicholas Summons, Marcus Thatcher, Kevin Tory

Chapter 8

Coordinating Lead Authors: Stephanie Baldwin, Scott Power, Gillian Cambers

Contributing Authors: Deborah Abbs, Josephine Brown, John Church, Dean Collins, Robert Colman, Kevin Hennessy, Damien Irving, Jack Katzfey, Philip Kokic, Brad Murphy

Other Contributors

Cook Islands: Cook Islands Meteorological Service, National Environment Service

East Timor: National Directorate of Meteorology and Geophysics, Ministry of Infrastructure

Federated States of Micronesia: National Weather Service, Office of Environment and Emergency Management

Fiji: Fiji Meteorological Service, Department of Environment

Kiribati: Kiribati Meteorological Service, Ministry of Environment, Land and Agriculture Development, Office of the President

Marshall Islands: National Weather Service, Office of Environmental Planning and Policy Coordination

Nauru: Tropical Western Pacific Climate Research Station, Department of Commerce Industry and Environment

Niue: Department of Meteorology and Climate Change

Palau: National Weather Service Office, Office of Environmental Response and Coordination

Papua New Guinea: Papua New Guinea National Weather Service, Department of Environment and Conservation, Office of Climate Change and Development

Samoa: Samoa Meteorology Division, Ministry of Natural Resources and Environment

Solomon Islands: Solomon Islands Meteorological Service, Ministry of Environment, Climate Change, Disaster Management and Meteorology

Tonga: Tonga Meteorological Service, Ministry of Environment and Climate Change

Tuvalu: Tuvalu Meteorological Service, Ministry of Communications and Transport

Vanuatu: Vanuatu Meteorology and Geo-hazard Department

All staff involved in the Pacific Climate Change Science Program

Software design and development: John Clarke, Timothy Erwin, Andrew Howard

Sub-contractors: Geoscience Australia, Iowa State University, National Institute of Water and Atmospheric Research (New Zealand), University of Melbourne, University of New South Wales

The modelling groups; the Program for Climate Model Diagnosis and Intercomparison and the World Climate Research Programme's Working Group on Coupled Modelling for their roles in making available the World Climate Research Programme's CMIP3 multi-model dataset. Support of this dataset is provided by the Office of Science, U.S. Department of Energy

Regional and International Organisations: National Institute of Water and Atmospheric Research (New Zealand), National Oceanic and Atmospheric Administration (NOAA), Secretariat of the Pacific Regional Environment Programme (SPREP), Secretariat of the Pacific Community (SPC), United Nations Development Programme (UNDP), University of the South Pacific (USP)

Peer Review

Anthony Chen, University of the West Indies, Graeme Pearman, Graeme Pearman Consulting Pty Ltd

Other Reviewers

Australian Agency for International Development, Department of Climate Change and Energy Efficiency, Johann Bell, Ian Cresswell, Janice Lough, Peter May, Netatua Pelesikoti

Scientific Editors

Kevin Hennessy, Scott Power, Gillian Cambers

Volume Editors

Volume 1: Stephanie Baldwin

Volume 2: Jillian Rischbieth

Other Editors

Karen Pearce (Bloom Communication); Whitehorne Communication and Design

Coordination

Stephanie Baldwin, Bernadette Barlow, Gillian Cambers, Gillian Cook, Dev Capey, Lily Frencham, Mandy Hopkins, Lucy Manne, Zarif Raman, Jillian Rischbieth

Design and Layout

Siobhan Duffy, Lea Crosswell, Carl Davies, Soussanith Nokham, Louise Bell

Funafuti Atoll, Tuvalu

Executive Summary

Introduction and Background

Islanders, especially in the Pacific region, have a strong relationship with the land and ocean so changes in climate can represent a threat not only to the physical environment but also to their culture and customs. Already, people living in Pacific Islands and East Timor are experiencing changes in their climate such as higher temperatures, shifts in rainfall patterns, changing frequencies of extreme events and rising sea levels. These changes are affecting peoples' lives and livelihoods, as well as important industries such as agriculture and tourism. In recognition of this, leaders of the Pacific Island Countries and Territories developed the Pacific Islands Framework for Action on Climate Change 2006–2015 to guide the building of resilience to the risks and impacts of climate change.

In 2008, the Australian Government launched the International Climate Change Adaptation Initiative to meet high priority adaptation needs of vulnerable countries within the Asia-Pacific region. Improved understanding of the physical climate system is required to inform effective adaptation and this is being addressed through a component of the International Climate Change Adaptation Initiative called the Pacific Climate Change Science Program (PCCSP). The PCCSP is a collaborative research partnership between Australian Government agencies, East Timor and 14 Pacific Island countries (Cook Islands, Federated States of Micronesia, Fiji, Kiribati, Marshall Islands, Nauru, Niue, Palau, Papua New Guinea, Samoa, Solomon Islands, Tonga, Tuvalu and Vanuatu), carried out in collaboration with regional and international organisations (Figure ES.1).

The Fourth Assessment Report of the Intergovernmental Panel on Climate Change (IPCC, 2007) identified significant research gaps which needed to be filled to better inform climate change adaptation and resilience building in small-island developing States. The report identified a number of information gaps and research priorities, noting in particular that many small islands lacked adequate observational data, and that output from global climate models was not of sufficiently fine resolution to provide specific information for islands. These regional and Partner Country climate change science needs formed the basis for the development of the research of the PCCSP.

The 15 Partner Countries are immensely diverse in terms of their history, geography, climate, natural resource base and culture. As part of the group of small island developing States, they share many similar sustainable development challenges such as small populations, limited resources, remoteness, susceptibility to natural disasters, vulnerability to external shocks and dependence on international trade.

Guided by the Australian Agency for International Development and the Australian Department of Climate Change and Energy Efficiency, the PCCSP is delivered by the Australian Bureau of Meteorology and the Commonwealth Scientific and Industrial Research Organisation, through their research partnership in the Centre for Australian Weather and Climate Research. The PCCSP's objectives are to:

- Conduct a comprehensive climate change science research program aimed at providing in-depth information about past, present and future climate in Partner Countries.
- Build the capacity of Partner Countries' national meteorological services and scientific organisations to undertake scientific research.
- Disseminate the information to Partner Countries' stakeholders and other parties.

Climate is defined as the average weather over 30 years or more. In different chapters in this publication, different averaging periods, such as 20 years, are also used. Climate change is defined as a change in the state of the climate, identified by changes in the mean and/or the variability of its properties, and that persists for an extended period, typically decades or longer (IPCC, 2007).

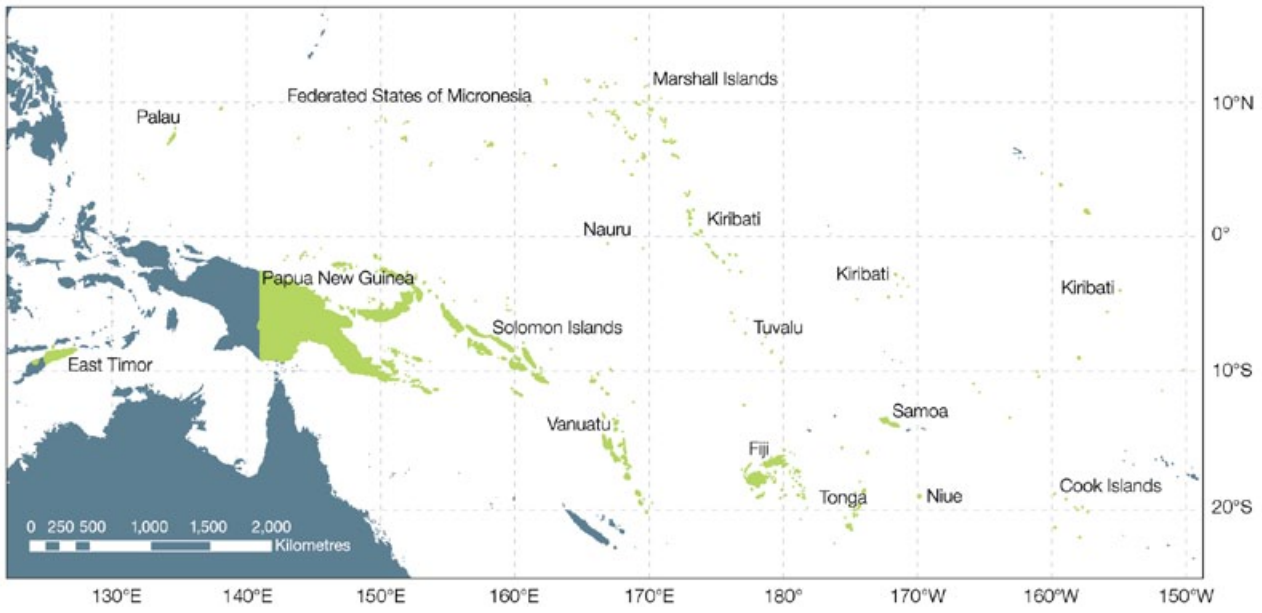

Figure ES.1: PCCSP region, defined by the coordinates: 25°S–20°N and 120°E–150°W (excluding the Australian region south of 10°S and west of 155°E), and Partner Countries: Cook Islands, East Timor, Federated States of Micronesia, Fiji, Kiribati, Marshall Islands, Nauru, Niue, Palau, Papua New Guinea, Samoa, Solomon Islands, Tonga, Tuvalu and Vanuatu

About this Publication

Building on the Fourth Assessment Report of the Intergovernmental Panel on Climate Change (IPCC, 2007), this publication draws on recent research conducted by the PCCSP as well as other research, such as the recently published 'Vulnerability of Tropical Pacific Fisheries and Aquaculture to Climate Change' (Bell et al., 2011). It is anticipated that this PCCSP publication and associated products and capacity-building activities will provide senior decision makers and other stakeholders in the Partner Countries, as well as the wider scientific community, with up-to-date, robust, climate change science information for the region and the individual countries.

This publication has two volumes. The first volume presents a detailed assessment and analysis of the PCCSP region encompassing latitudes 25°S–20°N and longitudes 120°E–150°W, excluding the Australian region south of 10°S and west of 155°E. Climate change reports for each Partner Country are presented in the second volume. Each of the 15 reports has four main sections which present and discuss (1) seasonal cycles, (2) climate variability, (3) observed annual trends, and (4) projections for atmospheric and oceanic variables. Projections are provided for temperature, rainfall, extreme events, (including tropical cyclones, extreme hot days and heavy rainfall days), sea-surface temperature, ocean acidification, and sea-level rise for three future 20-year periods centred on 2030, 2055 and 2090, and for three different scenarios of greenhouse gas and aerosol emissions: B1 (low), A1B (medium) and A2 (high).

Current Climate of the PCCSP Region

The PCCSP region is characterised by three extensive bands of large-scale wind convergence and associated rainfall: the Intertropical Convergence Zone (ITCZ), the South Pacific Convergence Zone (SPCZ) and the West Pacific Monsoon (WPM) (Figure ES.2).

The ITCZ lies just north of the equator and influences climate in the Federated States of Micronesia, Kiribati, Marshall Islands, Nauru, Palau and Papua New Guinea. These same countries, together with East Timor, also experience very high seasonal rainfall variations associated with the WPM, although in Nauru and the Marshall Islands this only occurs in some years.

The SPCZ has a significant impact on most of the Partner Countries in the South Pacific: Cook Islands, Fiji, Nauru, Niue, Samoa, Solomon Islands, Tonga, Tuvalu and Vanuatu; and Kiribati in some years.

Many of the Partner Countries experience marked seasonal rainfall variations, but little variation in temperature. However, they may experience extreme events including tropical cyclones, storm surges, heat waves, drought and heavy rainfall. Tropical cyclones produce damaging winds, heavy rainfall and storm surges which can have devastating impacts.

Large-scale atmospheric circulation patterns influence ocean currents and sea-surface temperature patterns, while the ocean in turn also affects atmospheric winds, temperatures and rainfall. For example, the equatorial trade winds push warm water to the west, giving rise to the Warm Pool, and drive the upwelling of cooler water in the eastern Pacific; while the warmer water near the equator and the Warm Pool in particular, drive strong convection in the overlying atmosphere which helps to draw the trade winds across the Pacific Ocean.

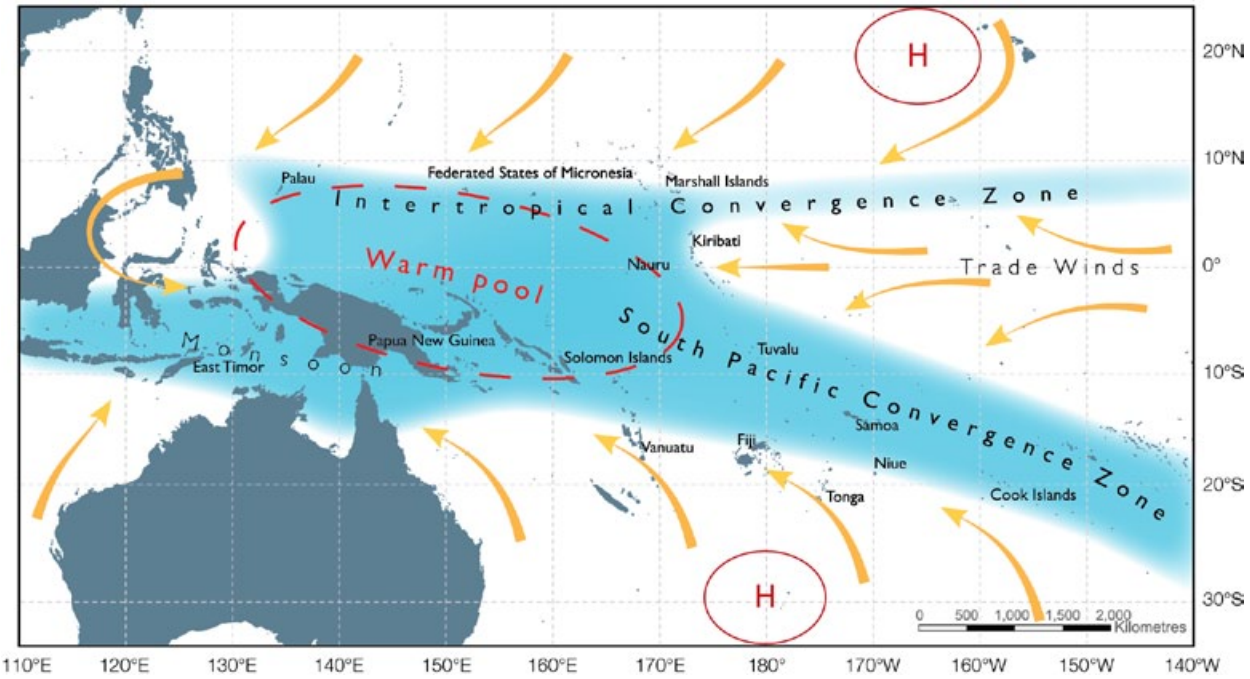

Figure ES.2: The average positions of the major climate features of the PCCSP region in November to April. The yellow arrows show near surface winds, the blue shading represents the bands of rainfall (convergence zones with relatively low pressure), and the red dashed oval indicates the West Pacific Warm Pool. H represents the typical positions of moving high pressure systems.

Climate Variability and Trends

Climate variability in the PCCSP region occurs on a wide range of time scales. Palaeoclimatic records indicate that during the millennia before the Industrial Revolution (around 1750), the climate of the Pacific underwent large variations, primarily associated with changes in the intensity and frequency of the El Niño-Southern Oscillation (ENSO). These climate shifts were driven by natural mechanisms, whereas some of the changes observed over the past decades are also partially driven by human influences. Consequently, it is important to understand the range of climate variability experienced in the past in order to provide a context in which to interpret projections of future climate change.

The major pattern of climate variability in the PCCSP region is ENSO. This is a coupled atmosphere-ocean phenomenon, with time scales of about two to seven years. The term El Niño is identified with a basin-wide warming of the tropical Pacific Ocean east of the dateline. The term La Niña is a basin-wide cooling of the tropical Pacific Ocean east of the dateline. This event is associated with a fluctuation of a global-scale tropical and sub-tropical pressure pattern called the Southern Oscillation.

ENSO is strongly linked with variations in climatic features such as the ITCZ, the SPCZ and the WPM. During El Niño events the SPCZ tends to shift towards the north-east, while the ITCZ tends to shift closer to the equator. These shifts have a profound influence on rainfall, sea level and the risk of tropical cyclones in the region. All PCCSP Partner Countries are affected by ENSO in some way, although the magnitude and timing of this influence varies.

As well as ENSO there are other natural patterns of climate variability that influence the region, including the Interdecadal Pacific Oscillation and the closely related Pacific Decadal Oscillation.

The climate trends for the PCCSP region that are presented in this publication are based on updated and improved climate datasets. This work has involved significant collaboration with Partner Country meteorological services and has resulted in improved data access and security, and enhanced scientific and technical capacity in the region.

All updated temperature records from Pacific Island observation stations show warming over the past 50 years, with trends mostly between 0.08 to 0.20°C per decade, consistent with global warming over this time. Unlike temperature, rainfall across the Pacific Islands displays large year-to-year and decade-to-decade changes in response to natural climate variability. Over the past 50 years, rainfall has increased north-east of the SPCZ, and declined to the south.

Over the 1981–2007 period of satellite measurement there are no significant trends in the overall number of tropical cyclones, or in the number of intense tropical cyclones, in the South Pacific Ocean. However, this is a short period of time for the analysis of infrequent extreme events such as tropical cyclones. Determining trends over longer periods is difficult due to the lack of adequate data prior to satellite measurements.

Sea-surface temperatures of the Pacific Ocean have generally increased since 1950. In addition, the western tropical Pacific Ocean has become significantly less salty, while regions to the east have generally become saltier. In combination, these changes have driven an increase in the stratification of the upper ocean in this region.

A distinctive pattern of intensified warming of surface waters and cooling of sub-surface equatorial waters centred near a depth of 200 m is also apparent over the past 50 years in the Pacific Ocean. These patterns of observed change in the ocean are reproduced in climate model simulations that include increased atmospheric greenhouse gases.

Sea level has been rising globally including in the PCCSP region over recent decades. Extreme high sea levels are also increasing, primarily as a result of increases in mean sea level. There is significant interannual variability of sea level in the region related to ENSO and other natural variability.

As a consequence of higher carbon dioxide (CO_2) concentrations in the atmosphere, the oceans are absorbing more CO_2. The CO_2 taken up by the ocean reacts in water and causes a decrease in the pH of the seawater that is referred to as ocean acidification. Acidification is accompanied by a decrease in the seawater saturation state of carbonate minerals that are secreted as shells and skeletal material by many key species in reef ecosystems. Aragonite is the form of calcium carbonate precipitated by reef building corals and studies have shown that coral growth declines as the aragonite saturation state of seawater decreases.

Aragonite saturation states above a value of 4 are considered optimal for coral growth and for the development of healthy reef ecosystems. Throughout most of the sub-tropical and tropical Pacific Island region, the saturation state in pre-industrial times exceeded 4. By the mid 1990s, the uptake of anthropogenic CO_2 had resulted in a widespread decline in the aragonite saturation state.

Climate Modelling

The complexity of the climate system means that past trends cannot be simply extrapolated to forecast future conditions. Instead, mathematical representations of the Earth's climate system, based on the laws of physics, are used to simulate the fundamental processes affecting weather and climate. Global climate models calculate variables such as temperature and rainfall at points over the globe spaced 100–400 km apart, with about 30 layers in the ocean and 30 layers in the atmosphere. They are run on supercomputers and have been used extensively over recent decades to not only estimate future climate change, but also to help better understand the present and past climate.

Emissions of greenhouse gases and aerosols have played a major role in the climate of the past century. In order to make future climate projections, it is necessary to make plausible estimates of how these emissions will evolve into the future. To assist in modelling the future climate, the IPCC has prepared 40 greenhouse gas and sulphate aerosol emissions scenarios for the 21st century that combine a variety of plausible assumptions about demographic, economic and technological factors likely to influence future emissions. Such estimates can then be put into climate models to provide projections of future climate change. Climate model projections in this publication are based on three of the most widely used emissions scenarios, B1 (low), A1B (medium) and A2 (high).

Performance of Climate Models

To make projections of future climate, it first has to be demonstrated that climate models are sufficiently realistic in simulating the observed climate. This depends on the model's ability to represent several different aspects of climate, including:

- The long-term average pattern of various atmospheric and oceanic characteristics, e.g. temperature, rainfall, wind, salinity and sea level.
- Important regional climate features, e.g. ITCZ, SPCZ and WPM.
- Major patterns of climate variability on various timescales, e.g. ENSO.
- Extreme weather events, e.g. heat waves, tropical cyclones.
- Long-term trends.

How well the models agree with the observed present climate is used to assess model reliability, with the underlying assumption that a model which adequately simulates the present climate will provide more reliable projections of the future. No single model is the 'best' in representing all aspects of climate so a range of models should be considered when making projections of future climate.

After analysing data from 24 global climate models from around the world, the PCCSP identified a set of 18 models which provide a reasonable representation of observed climate over the PCCSP region. These 18 models were used to construct projections of future climate for the PCCSP region and the individual Partner Countries.

These 18 global climate models can simulate many aspects of climate, and generally give a reasonable representation of climate in the Pacific region. Most models, however, show biases, such as a tendency to underestimate sea-surface temperatures and rainfall along the equator. The representation of ENSO in climate models has improved over the years but remains a challenge at the regional scale. For example, sea-surface temperature variability associated with ENSO tends to be too narrowly focused on the equator and extends too far to the west.

Global climate models do not have sufficiently fine resolution to represent small islands and important small-scale climate processes. Downscaling techniques are used to represent important small island effects, however, these techniques are very computer intensive.

Global Climate Model Projections

The IPCC Fourth Assessment Report (2007) presents broad-scale projections for the Pacific. Annual-mean temperature and rainfall projections are averaged over two large Pacific regions (the North Pacific and the South Pacific), for three 30-year periods (2010–2039, 2040–2069 and 2070–2099), based on results from seven global climate models and four emissions scenarios.

The PCCSP provides a more detailed set of climate change projections, building on the IPCC assessment. The projections for the PCCSP region are based on simulations from up to 18 global climate models for three emissions scenarios; B1 (low), A1B (medium) and A2 (high), and three future 20-year periods centred on 2030, 2055 and 2090, relative to a 20-year period centred on 1990. The selection of years and emissions scenarios is limited by data availability.

A summary of the key climate projections for the PCCSP region is outlined on the following pages. Volume 2 of this publication provides detailed discussion on the range of possible futures simulated for each country.

Projected Changes in Major Climate Features and Patterns of Variability

South Pacific Convergence Zone

In the wet season (November-April), the SPCZ is not expected to shift position, but there is some evidence for a projected equatorward shift in the dry season (May-October). Increased rainfall is projected within the SPCZ in the wet season in particular, due to increased atmospheric moisture content in a warmer climate. Many models also suggest that islands located near the eastern edge of the SPCZ will become drier in the wet season as the trade winds in the south-east Pacific become stronger.

Intertropical Convergence Zone

Changes in rainfall averaged over the ITCZ show a general increase in June-August, with little change in December-February, thereby amplifying the current seasonal cycle. There is an increase in the area of the ITCZ in all models in June-August, and in all but three in December-February. Models suggest the ITCZ may shift equatorward in March-May and June-August, although displacement is small.

West Pacific Monsoon

There is a general tendency for rainfall to increase in the WPM region throughout the year, but with an amplification of the seasonal cycle of rainfall. There is no significant projected change in the east-west winds over the region.

El Niño-Southern Oscillation

Year-to-year variability in the region will continue to be strongly affected by ENSO. However, climate models do not provide consistent projections of changes in the frequency, intensity and patterns of future El Niño and La Niña events. As climate changes, however, aspects of climate experienced in some regions during El Niño and La Niña events may differ from the past. For example, if El Niño tends to warm a particular region now, then temperatures experienced during future El Niño events may tend to be higher than those experienced during past El Niño events.

Indian Ocean Dipole

The IOD influences climate both locally and in remote regions, mainly affecting East Timor. It also affects the Indian and Australian monsoons, however, the IOD is a much weaker source of climate variability for the Pacific region than ENSO. Climate models suggest that a more positive IOD mean state will exist with easterly wind trends and a shallowing thermocline (a zone in the ocean separating warm surface waters from cold deep waters) over the eastern Indian Ocean, associated with a weakening of the Walker Circulation.

Atmospheric Projections

Temperature

The magnitude of the projected warming over the PCCSP region is about 70% as large as the magnitude of global average warming for all emissions scenarios. This is linked to the fact that the oceans have been warming, and are projected to warm into the future at a lower rate than land areas. As the PCCSP region is dominated by the ocean, it follows that temperature increases in the region will be less than those seen globally. The projections centred on the three 20-year periods (relative to 1990 baseline temperatures) show that:

- By **2030**, the projected regional warming is around +0.5 to 1.0°C, regardless of the emissions scenario.
- By **2055**, the warming is generally +1.0 to 1.5°C with regional differences depending on the emissions scenario.
- By **2090**, the warming is around:
  - +1.5 to 2.0°C for B1 (low emissions scenario).
  - +2.0 to 2.5°C for A1B (medium emissions scenario).
  - +2.5 to 3.0°C for A2 (high emissions scenario) (Figure ES.3).

Large increases in the incidence of extremely hot days and warm nights are also projected.

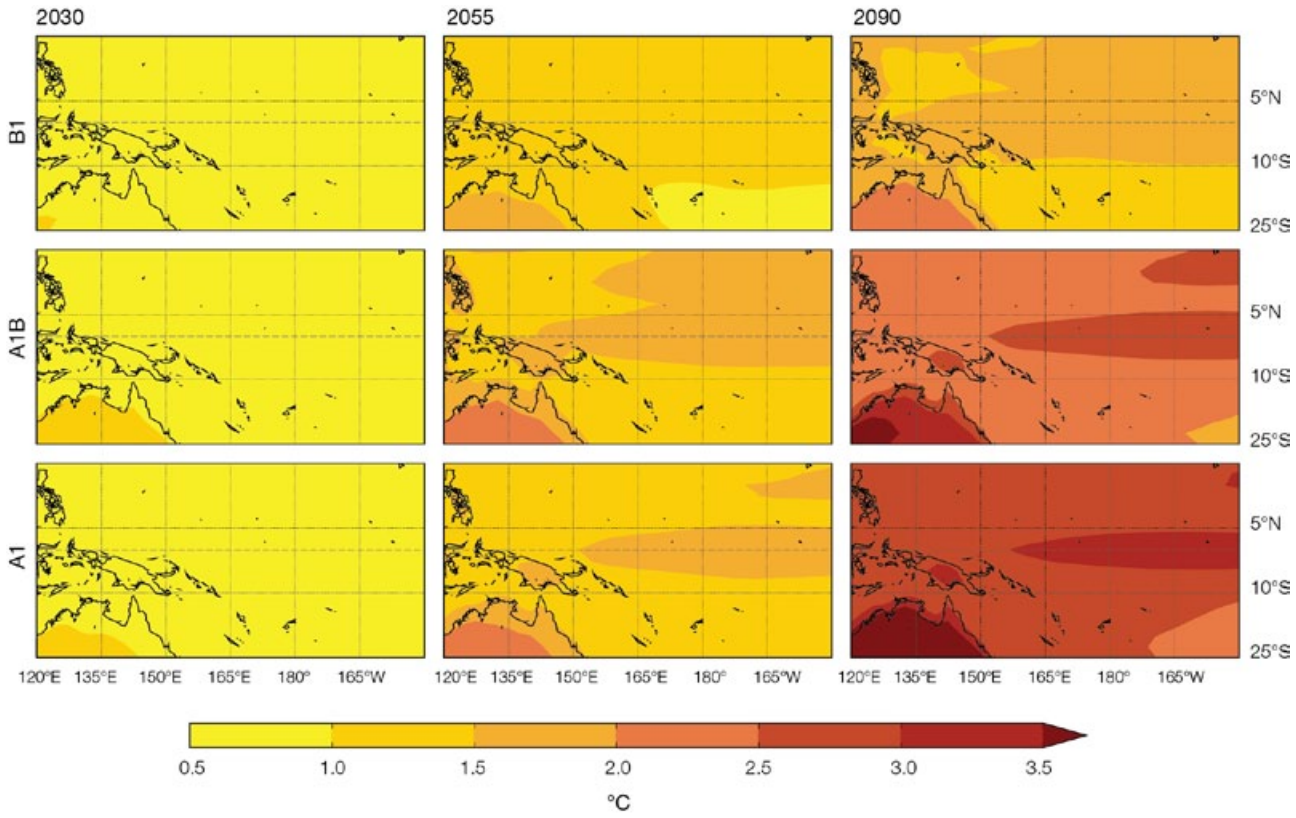

Figure ES.3: Projected multi-model mean changes in annual mean surface air temperature for 2030, 2055 and 2090, relative to 1990, under the A2 (high), A1B (medium) and B1 (low) emissions scenarios. All models agree on warming in all locations.

Rainfall

In the PCCSP region, increases in annual mean rainfall are projected to be most prominent near the SPCZ and ITCZ, with little change in the remainder of the region (Figure ES.4). The annual numbers of rain days (over 1 mm), light rain days (10–10 mm) and moderate rain days (10–20 mm) are projected to increase near the equator, with little change elsewhere in the region. There is a widespread increase in the number of heavy rain days (20–50 mm). Extreme rainfall events that currently occur once every 20 years on average are generally simulated to occur four times per 20-year period, on average, by 2055 and seven times per 20-year period, on average, by 2090 under the A2 (high) scenario. Droughts are projected to occur less often.

Potential Evapotranspiration

Evapotranspiration is the sum of evaporation and plant transpiration from the Earth's land surface to the atmosphere. Potential evapotranspiration is a reflection of the energy available to evaporate water, and of the wind available to transport the water vapour from the ground up into the lower atmosphere. Potential evapotranspiration is highest in hot, sunny, dry (arid), and windy conditions. Increases in potential evapotranspiration are expected in the PCCSP region.

The ratio of annual average rainfall to potential evapotranspiration is a measure of aridity. Aridity increases in most, but not all, of the PCCSP region (i.e. the projected increase in potential evapotranspiration is not being matched by sufficient increases in rainfall).

Humidity and Solar Radiation

Projected changes in humidity and solar radiation are relatively small in the PCCSP region, i.e. less than 5% by 2090.

Wind

Surface wind speed is generally expected to decrease in the equatorial and northern parts of the PCCSP region, while increases are indicated in the south. However these changes are projected to be relatively small in most locations.

Ocean Projections

Salinity and Stratification

Sea-surface salinity is expected to decrease, with regional differences closely matching projected changes in net rainfall (rainfall minus evaporation). The intensified warming and freshening at the surface is projected to make the surface ocean less dense compared to the deep ocean, so the ocean becomes more stratified. This increase in stratification acts to inhibit mixing, thereby reducing the supply of nutrients from the deep to the surface ocean. This has consequences for biological productivity, particularly fisheries.

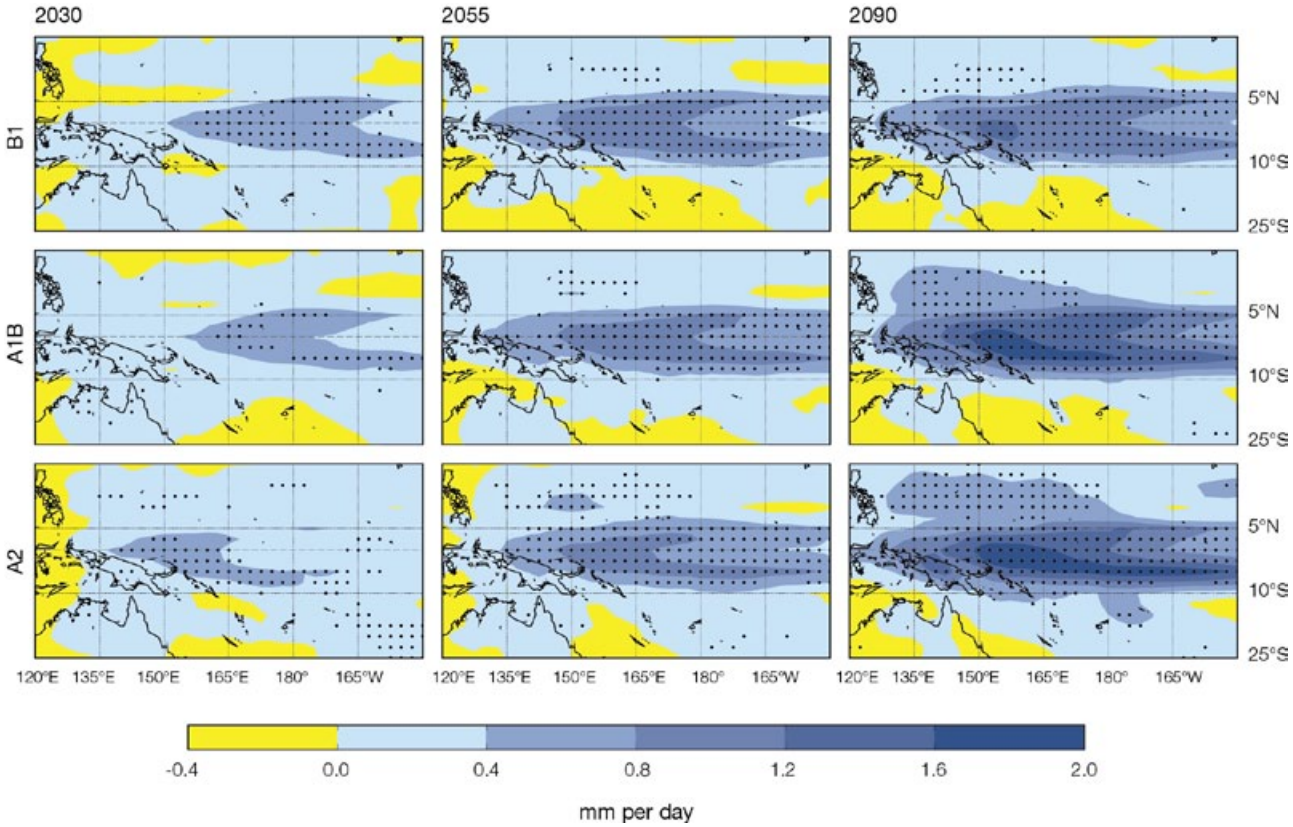

Figure ES.4: Projected multi-model mean changes in annual rainfall (mm/day) for 2030, 2055 and 2090, relative to 1990, under the A2 (high), A1B (medium) and B1 (low) emissions scenarios. Regions where at least 80% of models agree on the direction of change are stippled.

Sea Level

Global climate models reproduce the observed pattern of the regional distribution of sea level reasonably well. Models indicate that the rise will not be geographically uniform. However, deviations between models make regional estimates uncertain (Figure ES.5). In current projections, the sea-level rise in the PCCSP region is similar to the global average.

Projections of sea-level rise require consideration of ocean thermal expansion, the melting of glaciers and ice caps, the surface mass balance and dynamic response of the ice sheets of Antarctica and Greenland, and changes in terrestrial water storage. Current projections indicate sea levels are expected to continue to rise, on average, during this century. The Fourth Assessment Report of the IPCC (IPCC, 2007) states that global average sea level is projected to rise by 0.18 to 0.59 m by 2080–2099, relative to 1980–1999, with an additional potential contribution from the dynamic response of the ice sheets. By scaling to global temperature changes this additional rise was estimated to be 10 to 20 cm but larger increases could not be ruled out. Observations indicate sea level is currently rising at near the upper end of the projected range. Larger rises than in the IPCC projections have been argued by some but one recent study suggests that global-mean sea-level rise greater than 2 m by 2100 is physically untenable and that a more plausible estimate is about 80 cm, consistent with the upper end of the IPCC estimates and the present rate of rise. However, improved understanding of the processes responsible for ice sheet changes are urgently required to improve estimates of the rate and timing of 21st century and longer-term sea-level rise.

Ocean Acidification

The projected growth in atmospheric CO_2 concentration is expected to cause further ocean acidification. Aragonite saturation values below 3.5 are projected to become more widespread and have the potential to disrupt the health and sustainability of reef ecosystems. The lowest values of aragonite saturation in the region of the Partner Countries are projected to occur in the eastern equatorial Pacific, to the east of longitude 160°W, affecting the easternmost islands of Kiribati, with the highest values in the region of the South Equatorial Current, affecting the islands of Cook Islands, Samoa and Tuvalu.

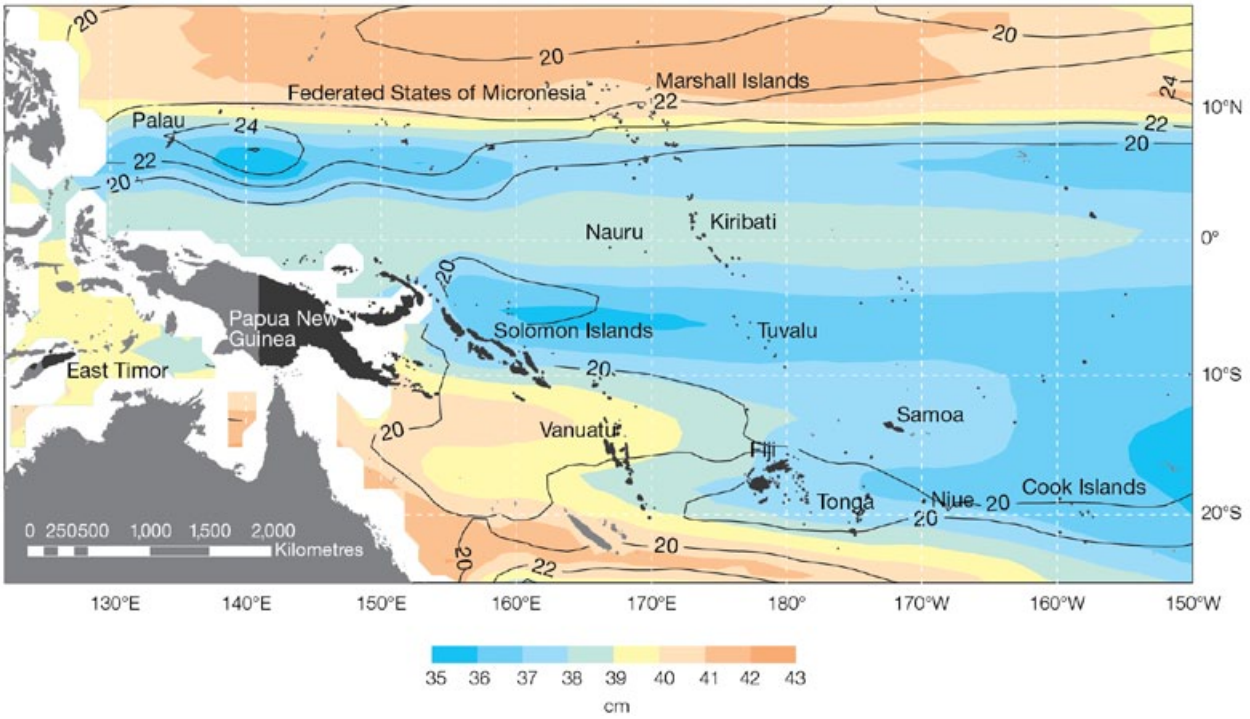

Figure ES.5: Sea-level rise projections for the A1B (medium) emissions scenario in the PCCSP region for 2081–2100 relative to 1981–2000 are indicated by the shading with the uncertainty indicated by the contours (in centimetres). The distribution of the projections of sea-level change is estimated by combining the global average sea-level projections, the dynamic ocean departure from the global average and the regional changes associated with the changing ice-mass distribution. Note that white areas indicate no model data are available for that area.

Downscaled Projections

Dynamical and statistical downscaling techniques were used to provide small-scale (i.e. country-scale and/or individual island-scale) climate projections. The output from six global climate models was downscaled to 60 km over the PCCSP region, and to 8 km for selected islands. The 60 km downscaled projections are broadly consistent with those of the global climate models, however, some differences are noted such as bands of rainfall decrease around latitudes 8°N and 8°S.

The 8 km downscaled projections complement the projections from the global climate models and show regional variations of the climate change signal, largely related to the topography of the islands where significant changes in elevation exist.

Tropical Cyclone Projections

It is difficult to make projections of tropical cyclone activity for two reasons. First, the features of a tropical cyclone occur at a smaller spatial scale than can be represented by most climate models. Second, climate models vary in their ability to simulate large-scale environmental conditions that are known to influence tropical cyclones including patterns of variability such as ENSO and large-scale climate features such as the SPCZ.

Three methods were used by the PCCSP to diagnose tropical cyclones from global climate models. While large uncertainty still remains, the results from this study indicate that the frequency of tropical cyclones in the PCCSP region is projected to decrease by the late 21st century. There is a moderate level of confidence in this direction of change, however, there is little consistency in the magnitude of changes between either the models or the analysis methods.

For the Partner Countries in the south Pacific sub-basins (latitudes 0–35ºS; longitudes 130°E–130ºW), most models indicate a decrease in the frequency of tropical cyclones by the late 21st century and an increase in the proportion of more intense storms. For the Partner Countries in the North Pacific sub-basin (latitudes 0–15ºN; longitudes 130º-180ºE), there is a decrease in the frequency of tropical cyclones and a decrease in the proportion of more intense storms. This decrease in occurrence is more robust in the Southern Hemisphere than in the Northern Hemisphere, and may be due to a combination of increased vertical wind shear in the Southern Hemisphere, and changes in the thermodynamic characteristics of the atmosphere which are associated with tropical storm activity and intensity.

Uncertainties in Climate Model Projections

While climate models are all based on the same physical laws, they are not perfect representations of the real world. As such, there will always be a range of uncertainty in climate projections. The existence of uncertainty is common to all areas of science and does not negate the usefulness of model projections. Uncertainty exists in the projections provided in this publication and it is expected to exist for future projections, so reducing and achieving greater clarity on the uncertainties is still required. It is important that this uncertainty is understood and incorporated into any future impact assessments based on climate model projections. Box ES.1 summarises key uncertainties associated with climate projections (IPCC, 2007).

Box ES.1: Climate Projection Uncertainties

- Since it is uncertain how society will evolve over this century, it is not possible to know exactly how anthropogenic emissions of greenhouse gases and aerosols will change. Each of the 40 emissions scenarios produced by the IPCC is considered plausible, with the range of uncertainty increasing over the 21st century. Subtle differences between models associated with the representation of key physical processes result in a range of climate projections for a given emissions scenario.
- Models differ in their estimates of the strength of different feedbacks in the climate system, particularly cloud feedbacks, oceanic heat uptake and carbon cycle feedbacks.
- Direct and indirect aerosol impacts on the magnitude of the temperature response, on clouds and on precipitation remain uncertain.
- Future changes in the Greenland and Antarctic ice sheet mass are a major source of uncertainty that affect sea-level rise projections.
- Confidence in projections is higher for some variables (e.g. temperature) than for others (e.g. precipitation), and it is higher for larger spatial scales and longer averaging periods. Conversely, confidence is lower for smaller spatial scales, which represents a particular challenge for projections for Partner Countries in the PCCSP region.
- Some of the most difficult aspects of understanding and projecting changes in regional climate relate to possible changes in the circulation of the atmosphere and oceans, and their patterns of variability.
- When interpreting projected changes in the mean climate, it is important to remember that natural climate variability (e.g. the state of ENSO) will be superimposed and can cause conditions to vary substantially from the long-term mean from one year to the next, and sometimes from one decade to the next.
- It is not currently possible to determine if downscaled projections provide more reliable future climate projections than those from the coarser resolution global models. For this reason, dynamically downscaled projections can provide complementary information, but should be interpreted in conjunction with global climate models over the same region.

Future Research to Advance Climate Science in the PCCSP Region

Better understanding the past climate helps to inform more robust projections of future climate which are essential for underpinning climate change adaptation strategies and contributing to the sustainable development of the Partner Countries.

While there has been excellent progress on many fronts to monitor, document, understand and project climate change relevant to Partner Countries, there are still many challenges. Further work to strengthen the scientific understanding of climate change is required to inform adaptation and mitigation. The following areas have been identified as priorities.

The geographical spread of Partner Countries means that the land- and ocean-based climate observation network in the PCCSP region is sparse. Expanding atmospheric data measurements in the PCCSP region will strengthen the ability of Partner Countries to monitor climate. Enhancing and, in some cases, creating oceanic observation networks is equally important. The rescue and rehabilitation of historical climate data is also needed to extend the climate data record in the PCCSP region. Further analysis of palaeoclimate data will enhance the understanding of climate variability on a wide variety of time scales.

A better understanding of the state of climate features in the PCCSP region, including the SPCZ, ITCZ and WPM, and patterns of variability in the climate, including ENSO, is needed to advance climate science. Determining the extent to which climate trends are attributable to natural variability and to human activities is also a priority. Greater clarity on these issues and more reliable estimates of past variability in the atmosphere and the ocean, including extreme events, will help strengthen the credibility and communication of climate projections.

Analysing the ability of the next generation of climate models to simulate climate in the PCCSP region is essential. This will provide for improved projections for rainfall, extreme weather events, ENSO, sea level and ocean acidification, among other variables. Work needs to continue to improve the global climate models and to rigorously verify downscaling methods so as to provide finer resolution projections over smaller areas.

United Nations Development Program: Millenium Development Goals, Samoa

Chapter 1
Introduction

Summary

- People living in small tropical islands are experiencing changes and variability in their climate that are affecting their environment, culture and livelihoods.
- Focusing on the western Pacific region, and especially the independent Pacific countries and East Timor, this scientific assessment and new research builds on the Fourth Assessment Report of the Intergovernmental Panel on Climate Change (IPCC, 2007). Detailed analyses and new research relating to the current climate, observed variability and trends, and climate change projections are presented.
- Extensive analysis of the performance of 24 global climate models identified a set of 18 models which provide a reasonable representation of climate over the Pacific Islands and East Timor. These 18 models were used to construct climate change projections for three emissions scenarios: A2 (high), A1B (medium) and B1 (low); and three future 20-year periods centred on 2030, 2055 and 2090, relative to a 20-year period centred on 1990. Downscaling techniques were used to provide more detail for selected regions.
- This scientific assessment and new research has been undertaken as part of the Pacific Climate Change Science Program (PCCSP), a component of the Australian Government's International Climate Change Adaptation Initiative.
- The PCCSP is a collaborative research partnership between Australian Government agencies, 14 Pacific Island countries and East Timor, and regional and international organisations. The 14 Pacific countries are: Cook Islands, Federated States of Micronesia, Fiji, Kiribati, Marshall Islands, Nauru, Niue, Palau, Papua New Guinea, Samoa, Solomon Islands, Tonga, Tuvalu and Vanuatu. The 15 Partner Countries are immensely diverse in terms of their history, geography, climate, natural resource base and culture.
- The PCCSP addresses two of the key principles of the Pacific Islands Framework for Action on Climate Change 2006–2015 (Secretariat of the Pacific Regional Environment Programme, 2005): improving the understanding of climate change; and provision of education, training and awareness.
- This publication is designed to provide decision makers and other stakeholders within the Pacific Island countries and East Timor, as well as the wider scientific community, with up-to-date, robust climate change science information for the PCCSP region (Volume 1) and for individual PCCSP Partner Countries (Volume 2).

1.1 Background

This chapter sets the contextual background and outlines the framework for the science presented in this publication.

People living in small tropical islands are experiencing changes and variability in their climate such as shifts in rainfall patterns, increasing frequency of some extreme weather events and rising sea levels. These changes are affecting peoples' environment, culture and livelihoods, as well as important economic sectors such as agriculture and tourism.

Scientists are working to understand these changes and how they reflect natural climate variability and changes due directly or indirectly to human activity that alters the composition of the global atmosphere.

Distinguishing between natural variability and climate change due to human activity is extremely difficult. Throughout these two volumes the definition of climate change in the Fourth Assessment Report of the Intergovernmental Panel on Climate Change (IPCC, 2007) is used (Box 1.1). A more detailed definition is presented in the Glossary. This definition includes changes due to natural variability and changes resulting from human activity. Climate is defined as the average weather over 30 years or more. In different chapters in this publication, different averaging periods, such as 20 years, are also used.

Box1.1: Definition of Climate and Climate Change

Climate change refers to a change in the state of the climate that can be identified (e.g. by using statistical tests) by changes in the mean and/or the variability of its properties and that persists for an extended period, typically decades or longer (IPCC, 2007).

Climate is usually defined as the average weather over 30 years or more. In different chapters in this publication, different averaging periods, such as 20 years, are also used.

Focusing on the western Pacific region, and especially the independent Pacific countries and East Timor, the scientific assessment and the new research presented in these two volumes builds on the Fourth Assessment Report of the IPCC (IPCC, 2007) and other research undertaken since 2007, e.g. the recently published research on climate change and fisheries (Bell et al., 2011). These volumes analyse the current climate, observed variability and climate trends, and further develop climate change projections for the region and individual countries. The research was been undertaken between 2009 and 2011 as part of the Pacific Climate Change Science Program (PCCSP), a key component of the Australian Government's International Climate Change Adaptation Initiative. The information presented here will provide decision makers, other stakeholders in the Partner Countries and the wider scientific community, with up-to-date, robust, climate change science information. Volume 1 presents a regional overview and Volume 2 presents individual country reports. A Glossary of terms is presented at the end of each volume.

1.2 Contextual Setting

Building on a foundation of regional and international agreements, and in recognition of the seriousness of the adverse effects of climate change, the Pacific Island Countries and Territories developed the Pacific Islands Framework for Action on Climate Change 2006–2015, which was released in June 2006.

The goal of this Framework is to "ensure that Pacific Island people build their capacity to be resilient to the risks and impacts of climate change" with the key objective to deliver on the expected outcomes under the following principles:

- Implementing adaptation measures.
- Governance and decision making.
- Improving understanding of climate change.
- Education, training and awareness.
- Contributing to global greenhouse gas reduction.
- Partnerships and cooperation.

The Intergovernmental Panel on Climate Change's Fourth Assessment Report (IPCC, 2007) found significant research gaps which needed to be filled to better inform climate change adaptation and resilience building in small island developing States. The report identified a number of information gaps and research priorities, noting in particular that many small islands lacked adequate observational data, and that output from global climate models was not of sufficiently fine resolution to provide specific information for islands.

In 2008, the Australian Government launched the International Climate Change Adaptation Initiative to meet high-priority adaptation needs of vulnerable countries within the Asia-Pacific region.

The objectives of the International Climate Change Adaptation Initiative are to:

- Establish a sound policy, scientific and analytical basis for long-term Australian action to help Partner Countries adapt to the impacts of climate change.
- Increase Partner Country understanding of the impacts of climate change on their natural and socio-economic systems.
- Enhance Partner Country capacity to assess key climate vulnerabilities and risks, formulate appropriate adaptation strategies and plans, and mainstream adaptation into decision making.
- Identify and finance priority adaptation measures that can immediately increase the resilience of Partner Countries to the impacts of climate change.

The PCCSP is contributing to the International Climate Change Adaptation Initiative by providing scientific information and improved understanding so the Partner Countries can better prepare for the future.

1.2.1 Pacific Climate Change Science Program

The PCCSP is a collaborative research partnership between Australian Government agencies and 14 Pacific Island countries and East Timor, carried out in collaboration with regional and international organisations.

Guided by the Australian Agency for International Development and the Australian Department of Climate Change and Energy Efficiency, the PCCSP is delivered by the Australian Bureau of Meteorology and the Commonwealth Scientific and Industrial Research Organisation (CSIRO) through their research partnership in the Centre for Australian Weather and Climate Research.

The PCCSP addresses two of the key principles of the Pacific Islands Framework for Action on Climate Change 2006–2015: improving the understanding of climate change (principle 3); and the provision of education, training and awareness (principle 4).

The PCCSP's primary objective is to conduct a comprehensive climate change science research program aimed at providing in-depth information about past, current and future climates in Partner Countries. Specific objectives are to:

- Undertake meteorological, climatological and oceanographic research, particularly in areas where there are identified gaps in Partner Country knowledge.

- Build the capacity of each Partner Country's national meteorological service and scientific organisations, where feasible, to undertake scientific research.
- Disseminate the information to Partner Country stakeholders and other parties.

Box 1.2 shows how these three objectives are interlinked.

The PCCSP recognises that this research must be delivered to Partner Countries in practical and relevant ways to be useful to decision makers. Partner Country engagement, information sharing and capacity building have been undertaken in a coordinated way across all areas of research. Besides this publication, other PCCSP products include:

- Two regional brochures, one focusing on the PCCSP and the second on climate variability and change.
- Fifteen country-specific brochures outlining past, current and future climate, targeted towards a general audience and produced in English and local languages.
- Fifteen country-specific posters.
- A database management system and three web-based tools for improved analysis of past, current and future climate and supplemented by user manuals and fact sheets. These products provide for information sharing among different levels of users.
- An extensive program of training, capacity building and engagement with island stakeholders, especially representatives of the respective national meteorological services.

1.2.2 Partner Country Diversity

The Pacific Islands are immensely diverse in terms of their history, geography, climate, natural resource base and culture. The Pacific Islands may be divided culturally into three main groups: Melanesia, Polynesia and Micronesia. East Timor is one of the Sunda Islands at the eastern end of the Indonesian Archipelago.

Historically, the 15 Partner Countries belong to the group of small-island developing States (SIDS), a group of low-lying coastal countries that share many similar sustainable development challenges such as small populations, limited resources, remoteness, susceptibility to natural disasters, vulnerability to external shocks and dependence on international trade (www.un.org/esa/dsd/dsd_aofw_sids/sids_members.shtml). SIDS were first recognised as a distinct group of developing countries at the United Nations Conference on Environment and Development in June 1992.

Table 1.1 provides a summary of selected characteristics for the 15 Partner Countries and illustrates their diversity.

Box 1.2: Description of the Pacific Climate Change Science Program

Retrieving, managing and analysing climate data, and understanding major climate phenomena such as the El Niño-Southern Oscillation

Analysing and downscaling global climate models to prepare projections of how the atmosphere and oceans may change around 2030, 2055 and 2090

Partner Country engagement to build local capacity in climate science, and atmosphere and oceans projections; and the preparation of a scientific assessment, country reports, brochures and posters

Table 1.1: Characteristics of the PCCSP Partner Countries

Country	Capital	Land area (km^2)	Exclusive economic zone area (million km^2)	Maximum height above sea level (m)	Population (2010 estimate except Vanuatu)	Languages	Government
Cook Islands	Avarua	237	1.8	652	11 500	English, Maori	Semi-independent country in free association with New Zealand
East Timor	Dili	15 007	Under determination	2 963	1 066 582	Portuguese and Tétum + 15 local dialects. (Working languages: English and Bahasa Indonesian)	Republic
Federated States of Micronesia	Palikir	702	2.98	791	111 364	English, Chuukese, Pohnpeian, Yapese	Independent with free association arrangements with USA until 2023
Fiji	Suva	18 333	1.3	1 300	844 420	English, Fijian, Hindi	Independent state
Kiribati	South Tarawa	811	3.6	87	100 835	I-Kiribati, English	Democratic republic
Marshall Islands	Majuro	181	1.81	3	54 439	Marshallese, English	Republic in free association with the USA
Nauru	No official capital. Yaren District (largest settlement)	21	0.32	70	9 976	Nauruan, English	Republic with parliamentary system
Niue	Alofi	259	0.39	69	1 470	Niuean, English	Free association with New Zealand
Palau	Melekeok	535	0.63	214	20 518	Palauan, English	Independent nation in free association with the USA
Papua New Guinea	Port Moresby	462 243	3.12	4 697	6 744 955	Tok Pisin, English + more than 700 other languages	Independent state
Samoa	Apia	2 934	0.12	1 860	183 123	Samoan, English	Independent state
Solomon Islands	Honiara	28 785	1.34	2 447	549 574	English, Pidgin + 87 other languages	Independent state
Tonga	Nuku'alofa	748	0.72	1 030	103 365	Tongan, English	Independent kingdom
Tuvalu	Funafuti	26	0.9	5	11 149	Tuvaluan, English	Independent state
Vanuatu	Port Vila	12 281	0.71	1 877	234 023 (2009)	Bislama, French, English + 105 other languages	Republic

Sources for Table 1.1 data:

- List of individual country statistics, Secretariat of the Pacific Community Applied Geoscience and Technology Division (SOPAC); http://www.sopac.org/index.php/member-countries
- List of individual countries' First National Communication under the United Nations Framework Convention on Climate Change (UNFCCC); http://unfccc.int/national_reports/non-annex_i_natcom/items/2979.php
- Country statistics for East Timor; http://timor-leste.gov.tl/?p=547&lang=e; and http://www.dfat.gov.au/geo/east_timor/east_timor_brief.html

1.3 Building on the Fourth Assessment Report of the IPCC

Key findings relating to the Pacific, as defined by the region between 20°N and 30°S and 120°E to 120°W, from the Fourth Assessment Report (IPCC, 2007) include the following:

- The main climatic processes that play a role in the climate of this region are the easterly trade winds, the Southern Hemisphere high pressure belt, the Intertropical Convergence Zone (ITCZ) and the South Pacific Convergence Zone (SPCZ).
- Year-to-year climatic variability is very strongly affected by the El Niño-Southern Oscillation (ENSO).
- Global climate models do not have sufficiently fine resolution to represent the small islands and very little work has been done to represent important island effects resulting from island shape and topography using techniques such as downscaling. Some climatic processes are still not well understood.
- The ability of the multi-model dataset models to simulate present climate in the Pacific is satisfactory for temperature simulations, however, there are large spreads in precipitation simulations. There are systematic errors in simulating mean climate and natural variability.
- All North and South Pacific Islands are very likely to warm during this century. The warming is likely to be somewhat smaller than the global annual mean warming in all seasons.
- Annual rainfall is likely to increase in the equatorial Pacific, while most models project decreases just east of French Polynesia in December-February.
- There is much less certainty about changes in frequency and intensity of tropical cyclones on a regional basis than for temperature and precipitation changes. There is no clear picture with respect to regional changes in frequency and movement, but increases in intensity are indicated. ENSO fluctuations have a strong impact on patterns of tropical cyclone occurrence in the South Pacific, and uncertainty with respect to future ENSO behaviour contributes to uncertainty with respect to tropical cyclone behaviour.
- Sea levels are likely to continue to rise, on average, during the 21st century. Models indicate that the rise will not be geographically uniform. Large deviations among models make regional estimates across the Pacific Ocean uncertain.

1.4 Major New Contributions to Pacific Climate Change Science

Building on the findings of the IPCC (2007) Fourth Assessment Report, the PCCSP has assessed recent literature and conducted new research. Attention is primarily focused on the region defined by the coordinates 25°S–20°N and 120°E–150°W (excluding the Australian region south of 10°S and west of 155°E). This region is referred to in this publication as the PCCSP region and differs slightly from the region defined in the IPCC Fourth Assessment Report (2007). The PCCSP region includes the 14 independent Pacific Islands labelled in Figure 1.1 and East Timor.

The research and new findings presented in these two volumes represent the first comprehensive climate change science research program for the independent Pacific Islands and East Timor and complements other research such as the recently published, 'Vulnerability of Tropical Pacific Fisheries and Aquaculture to Climate Change', (Bell et al., 2011). As such it covers new ground for the PCCSP region as a whole (Volume 1) and especially for the individual island countries (Volume 2). Recognising the diversity among the islands, the second volume of this publication presents reports for each of the 15 Partner Countries. Each report details their seasonal and annual climate cycles including extreme events, observed trends and climate variability. The reports also include projections for several atmospheric and ocean variables (temperature, rainfall, wind speed, extreme events, sea-surface temperature, ocean acidification and sea-level rise) for three future 20-year periods centred on 2030, 2055 and 2090, and for three emissions scenarios from the IPCC Special Report on Emissions Scenarios (SRES): B1 (low), A1B (medium) and A2 (high).

The findings are, to a large extent, based on data from weather and ocean-observing stations together with regional and global gridded data based on in-situ and satellite data. In collaboration with Partner Country meteorological services, extensive work has been done to retrieve and analyse these data and ensure that they are of the highest possible quality.

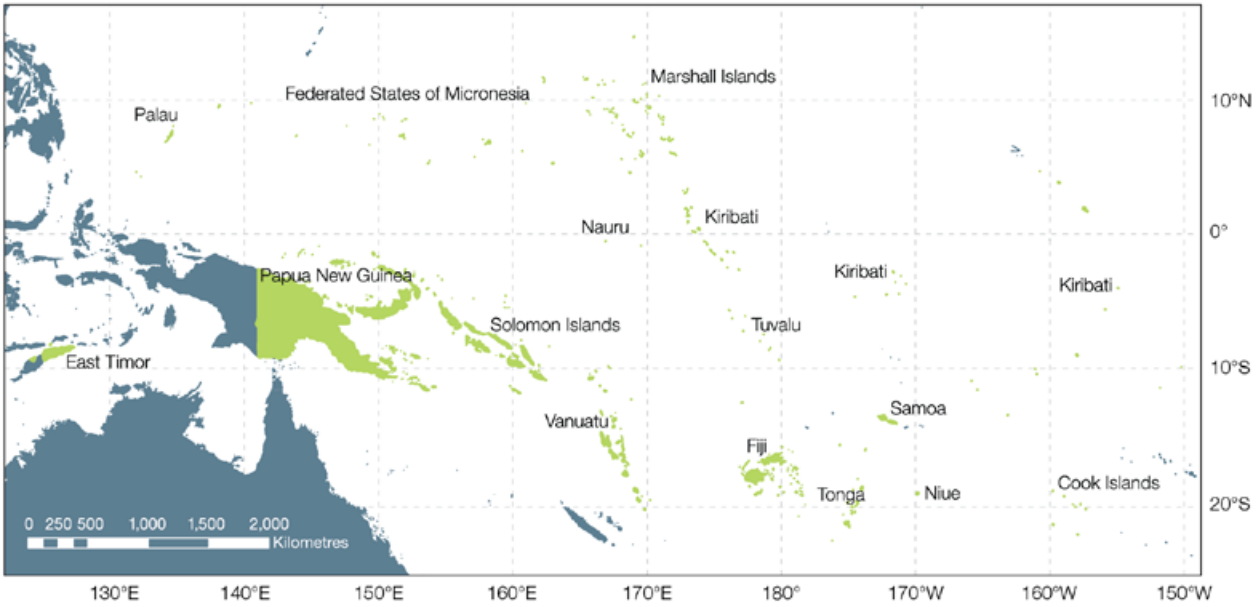

Figure 1.1: PCCSP region and Partner Countries: Cook Islands, East Timor, Federated States of Micronesia, Fiji, Kiribati, Marshall Islands, Nauru, Niue, Palau, Papua New Guinea, Samoa, Solomon Islands, Tonga, Tuvalu and Vanuatu

A number of major advances have been made over the course of the PCCSP, making this publication the most comprehensive assessment of Pacific climate change science to date. Advances include:

- A detailed assessment of observed changes in Partner Country climate showing a climate in constant transition over the past 50 years with fluctuations in patterns of variability, such as ENSO, and in large-scale climatological features, such as SPCZ, driving the variability on seasonal to decadal time scales (Chapters 2 and 3).
- Extensive analysis of the performance of 24 global climate models identified a set of 18 models which provide a reasonable representation of climate over the PCCSP region (Chapters 4 and 5).
- Projections for six atmospheric variables: air temperature, rainfall, relative humidity, potential evapotranspiration, solar radiation and wind; and four ocean variables: sea-surface temperature, sea-surface salinity, sea level and ocean acidification, based on up to 18 models and three emissions scenarios, as well as projected changes in key large-scale climate features and patterns of variability (Chapter 6).
- Enhanced resolution of model output using both dynamical and statistical downscaling methods to complement the projections from the global climate models (Chapter 7).
- Projected changes in the frequency and intensity of tropical cyclones based on model downscaling (Chapter 7).

While the PCCSP has sought to address some of the key gaps identified in the IPCC Fourth Assessment Report (IPCC, 2007), there still remain several areas requiring further work (Chapter 8). These include:

- Expansion of the land and ocean-based climate observational networks and the rescue and rehabilitation of historical climate data.
- Enhanced understanding of large-scale climate features, patterns of variability and the detection and attribution of climate change.
- Continual improvement and assessment of climate models so as to provide progressively more robust projections of atmospheric and ocean variables.

Taking rainfall observations, Niue Department of Meteorology and Climate Change

Chapter 2
Climate of the Western Tropical Pacific and East Timor

Summary

- The main features of the climate of the Pacific and East Timor are detailed using climate data from weather and ocean observing stations in the PCCSP region, together with regional and global gridded data based on in-situ and satellite data. In some instances observational data have been used in conjunction with computer models to produce spatially and temporally complete datasets.
- Many high-quality, multi-decadal observations have been recorded at sites across the region. However, many data have not yet been digitised and there are significant gaps in coverage. The quality of the digitised data has been carefully controlled and these data have been made accessible through new tools developed by the PCCSP. There are few multi-decadal sea-level records in the region.
- In broad terms, there are significant regional variations in mean climate, with different temperature and rainfall regimes in the eastern and western PCCSP region, with further differences between countries near the equator and those closer to the sub-tropics.
- Regions of strong convective rainfall exist in the equatorial Pacific in two bands: the Intertropical Convergence Zone (ITCZ), just north of the equator and the South Pacific Convergence Zone (SPCZ) from near the Solomon Islands to east of the Cook Islands.
- The ocean and atmosphere interact strongly in the region. Large-scale atmospheric circulation patterns drive both the ocean currents and temperature patterns; the ocean in turn also affects atmospheric winds, temperatures and rainfall.
- Most Partner Countries have weak seasonal variations in temperature but strong seasonal cycles in rainfall, with pronounced wet and dry seasons. Many are also affected by tropical cyclones, storm surges and other extreme events which can have devastating impacts on coasts and low lying regions.
- Typical seasonal variations of each country are described in terms of the main large-scale climate features of the region that exist throughout the year (e.g. the SPCZ and the ITCZ) or re-occur in certain seasons each year (West Pacific Monsoon), as well as other influences, such as sub-tropical weather systems and local effects on islands that are related to topographic features.
- Ocean currents driven by atmospheric circulation result in significantly warmer waters in the western Pacific than in the eastern Pacific.
- Regional differences in the mean sea-level distribution in the PCCSP region is largely a result of surface winds, with higher sea level in the western Pacific, particularly at latitudes 20–30°N and 20–30°S.

2.1 Introduction

This chapter describes the main features of the climate of the atmosphere and ocean of the region covering all PCCSP Partner Countries (Figure 1.1). Firstly, available observational data that are used throughout this publication to describe the climate of the region are summarised. The large-scale features of the atmospheric circulation and the ocean are then presented. The seasonal cycles of the climate in Partner Countries are discussed, as well as the climate features that determine this seasonality (e.g. the West Pacific Monsoon). Extreme events affecting the region are also described (e.g. tropical cyclones).

The Pacific Ocean is the largest ocean in the world, covering almost one third of the Earth's surface. It plays a dominant role in shaping the climate of not just the PCCSP region but also the entire planet. There are regional variations due to the presence of:

- Large land masses (e.g. the Maritime Continent, consisting of parts of Southeast Asia and the islands of Indonesia and the Philippines on the western equatorial edge of the Pacific) affecting climate on the regional scale.
- Mountainous regions in some countries that have large influences on their local climate.

Also, because some Partner Countries consist of small islands scattered across huge areas of ocean, very different climate conditions may exist within the one country.

The Pacific and the Maritime Continent are at the heart of some of the most prominent phenomena of the global climate system. The region is also characterised by extensive bands of large-scale wind convergence and associated rainfall features, such as the Intertropical Convergence Zone. Some regions experience very high seasonal rainfall variations associated with the West Pacific Monsoon. The waters in the western tropical Pacific are the world's warmest, and this and other unique features give rise to tropical cyclones that can produce storm surges and flooding. As is typical in tropical regions, many countries experience prominent and marked seasonal rainfall variations but little seasonal variation in temperature, and they are at significant risk of extreme events.

2.2 Data Record

Analysis of observed climate relies on long, complete, spatially extensive observational records of meteorological and oceanographic data. In the PCCSP region, land-based monitoring sites are sparse due to the small size of islands and the large distances between them. The Pacific Ocean covers a huge area. However only a small portion of it is routinely monitored. To overcome this, a significant effort has been made to collect all land and ocean observational records and, in the case of land-based records, digitise and homogenise them (apply quality control checks, Section 2.2.1.2). These records have been supplemented with satellite observations and combined with computer models of the climate system to provide a more complete spatial coverage over the region.

2.2.1 Atmospheric Data

2.2.1.1 Data from Observing Stations in the Pacific and East Timor Region

Many observed surface meteorological data (such as maximum and minimum air temperatures, rainfall, wind, air pressure, and sunshine measurements) from PCCSP Partner Countries are now available for analysis. These data have been recorded over long periods and significant efforts have been made to source, digitise, and quality-control these records. In the region, there are no station data available in the large ocean areas between most islands, and this represents a significant limitation to the data coverage. This gap can be filled with data from non-station data sources and such data are described in Section 2.2.2.

The earliest known observations began in 1851 at Malua, Samoa (Turner, 1861) and 1861 at Levuka, Fiji (Smythe, 1864). These observations were taken by European settlers, initially out of meteorological interest, but also to understand the weather and climate of the islands for the purposes of economic development. Over the next few decades, there was gradual growth in the numbers of observation stations as industry expanded in the new colonies.

The 1937 International Meteorological Conference in Wellington, New Zealand established the 'South-West Pacific' as the Fifth International Meteorological Organization region. Subsequent World War II developments provided the catalyst for rapid development of meteorological services in the region. Civil aviation, weather forecasting, tropical cyclone warnings and further industry development (e.g. agriculture, forestry, and mining) provided the main impetus for sustained meteorological services development in the region (Krishna, 2009). In the former British colonies, formal meteorological practices were established by the New Zealand Meteorological Service and the Australian Bureau of Meteorology.

Summaries of observation records were generally sent to the home country of previous administrations, however many of the original paper records and books were retained in the country of origin. A key present-day issue for the Partner Countries is determining how many historical data remain in colonial archives in paper form. Recovering and digitising all available data is critical for understanding the past climate in the Partner Countries.

Many of the electronic records sourced by PCCSP scientists have been obtained from five datasets (see below). These include the Australian Bureau of Meteorology's ADAM, New Zealand's National Institute of Water and Atmospheric Research (NIWA) CLIDB database, the National Oceanographic and Atmospheric Agency (NOAA) Global Summary of the Day, and Partner Country CliCom databases. Data have also been collected from Partner Country spreadsheets.

Australian and New Zealand datasets containing Partner Country data are sourced from original observation registers designed in those countries. In some cases monthly summaries, which have been transcribed by hand, have been used in lieu of the original registers. Office procedures in place at the time ensured that the summaries provide a reliable facsimile of the original record. In most Partner Countries these office procedures have continued to this day. NOAA datasets are captured from the World Meteorological Organization Global Telecommunications Network. This network transmits meteorological reports worldwide immediately after the observation is made.

Pre-independence paper records from Papua New Guinea, Nauru and the Solomon Islands, which were transferred to Australia, have been entered into the Australian Bureau of Meteorology ADAM database. These observation booklets and rainfall registers are kept in the National Archives of Australia in Victoria. ADAM contains the most complete pre-independence archive for Papua New Guinea, Nauru and the Solomon Islands. Likewise, the NIWA CLIDB database is the most extensive pre-independence archive for the Cook Islands, Fiji, Kiribati, Niue, Samoa, Tonga, Tuvalu and Vanuatu. These countries were formerly part of the New Zealand region of responsibility. Pre-independence data stored in CLIDB have been observed and recorded under New Zealand meteorological practices. An exception to this is where more recent Partner Country data have been captured from the Global Telecommunications Network and have not passed through a quality control process. NOAA datasets have been sourced from Network message formats and have only passed a coarse level of quality control. The PCCSP has sourced NOAA data for Palau, Federated States of Micronesia, Marshall Islands and East Timor.

In the 1990s, Fiji, Solomon Islands, Papua New Guinea and Vanuatu began digitising records into their CliCom databases. The Fijian and Papua New Guinean Meteorological Services have excellent paper archives which contain all known observation booklets and registers which remained in-country.

The CliCom Climate Data Management System[1] was introduced in 1985 by the World Meteorological Organization (WMO), with the assistance of NOAA to assist small countries with climate data management. Over many decades CliCom began to lose reliability as hardware improved and operating systems changed. Many backup files were damaged and the loss of historical electronic data was notable in a number of Partner Countries. Only Solomon Islands and Fiji still maintain operational CliCom systems.

Following the breakdown of the CliCom database, many Partner Countries began using electronic spreadsheets. Spreadsheets are a user-friendly application to record data and produce reports and graphs; however they are poor data storage systems. The variety of spreadsheet designs across and within countries makes retrieval and transfer of data difficult as does the fact that spreadsheets are normally held on individual computers. They have little or no data validation tools, a high probability of data duplication, and are normally accessed by a single user. Databases, on the other hand, have built in data validation and checking, can be accessed by multiple users and modifications are made using proper programming techniques. In addition, many different reports can be generated from the same data.

The PCCSP has developed a climate database management system known as CliDE (Climate Data for the Environment). During 2010 and 2011, CliDE was offered to Partner Country national meteorological services and installed in all the Partner Countries except Nauru (which does not have a national meteorological service). CliDE provides quality controlled data and reports. The Partner Country national meteorological services now have a robust, secure and structured climate database management system to assist in the provision of services to government, researchers and consumers.

For most Partner Countries, there remains a large volume of non-electronic records of observations stored in-country. In addition there are a number of overseas repositories containing images of records. Online repositories include the British Atmospheric Data Centre[2] and NOAA[3]. Repositories holding paper records include the Portuguese archives in Lisbon, East Timor archives in Dili and the Noel Butlin Archives in Australia[4]. Many of the Partner Countries would benefit from a digitising program to rescue the paper records. Table 2.1 shows the known extent of digitised and non-digitised data.

Table 2.1: Meteorological station data available in PCCSP Partner Countries for digitised climate data and rainfall only stations, and known data in manuscript form not yet digitised (climate and rainfall only). For each country the total number of available stations is given, as is the range of record length (in years) at these stations, and the total number of years of data available is in parentheses. For example, the Cook Islands has digitised climate data from 17 stations with record lengths from 1 to 71 years, with 471 total years of data.

Country	Climate digitised[5]		Climate paper		Rainfall digitised[6]		Rainfall paper	
	Stations	Range of years (total years)	Stations	Range of years (total years)	Stations	Range of years (total years)	Stations	Range of years (total years)
Cook Islands	17	1 - 71 (471)	43	1 - 11 (103)	42	1 - 89 (988)	13	1 - 22 (211)
East Timor	21	1 - 53 (139)	48	2 - 28 (770)	22	1 - 53 (236)	73	2 - 26 (963)
Fiji	72	1 - 80 (1959)	276	1 - 103 (2936)	163	1 - 80 (5276)	146	1 - 80 (5015)
Federated States of Micronesia	10	31 - 65 (375)			11	1 - 65 (396)		
Kiribati	23	1 - 61 (710)	65	1 - 6 (93)	68	1 - 62 (1555)	92	1 - 32 (265)
Nauru	3	6 - 26 (39)			3	1 - 37 (64)		
Niue	5	5 - 92 (147)	31	1 - 1 (31)	10	2 - 92 (194)		
Palau	1	31 - 31 (31)			2	1 - 63 (64)		
Papua New Guinea	98	1 - 34 (818)	402	1 - 32 (934)	677	1 - 75 (8767)	2636	1 - 37 (3425)
Marshall Islands	7	34 - 66 (325)			7	34 - 37 (254)		
Samoa	3	1 - 58 (83)	119	1 - 35 (460)	28	1 - 60 (508)	150	1 - 59 (1823)
Solomon Islands	36	1 - 36 (512)	64	1 - 36 (420)	80	1 - 53 (994)	51	1 - 42 (460)
Tonga	14	3 - 76 (464)	106	1 - 2 (107)	19	2 - 78 (538)	1	89 - 89 (89)
Tuvalu	5	4 - 60 (217)	39	1 - 33 (353)	10	4 - 83 (525)	11	8 - 38 (272)
Vanuatu	15	6 - 29 (309)	22	1 - 38 (265)	31	2 - 61 (703)	68	1 - 66 (908)

[1] http://www.wmo.int/pages/prog/wcp/wcdmp/clicom/index_en.html

[2] http://badc.nerc.ac.uk/browse/badc/corral/images/metobs/pacific

[3] http://docs.lib.noaa.gov/rescue/data_rescue_portuguese.html

[4] http://www.archives.anu.edu.au/nbac/html/index.php

[5] 'Climate' means those weather stations which record temperature and rainfall observations. Note: the definition of 'Climate' differs within the Partner Countries. In the former New Zealand region of responsibility 'Climate' refers to stations where one observation within a 24-hour period, normally at 0900 hrs local time is conducted. Stations where multiple observations are conducted are referred to as 'Synoptic-climate' or 'Synoptic'. In Australia and in the former Australian region of responsibility 'Climate' refers to both single and multiple observation stations.

[6] 'Rainfall' means those weather stations that record rainfall only.

2.2.1.2 Homogenised Observed Station Data

Observed climate variables sometimes show sudden shifts in the average values or variability. Not all of these shifts are caused by real changes in climate. Non-climate related shifts can be due to changes in instrumentation, observation site, surrounding environment and observation practices, or other factors. The aim of climate data homogenisation is to adjust data if necessary, so that all variations in the data series are caused by real changes in the climate, and not due to changes in the way the data have been recorded.

The most recent effort at homogenising Partner Country records was undertaken by the PCCSP and respective national meteorological services who received training in data homogenisation at a PCCSP workshop in June 2010. The homogenisation methodology employed followed practices of the Australian Bureau of Meteorology for Australian data. The software included RHtest (Wang et al., 2007; Wang, 2008a; Wang, 2008b; Wang et al., 2010). RHtest is an application run in 'R', a programming language and environment for statistical computing and graphics. R is freely available via the Internet, therefore ideal for use in developing countries. RHtest includes functions to detect potential shifts in a candidate (or base) climate series. Further information on RHtest is available at http://cccma.seos.uvic.ca/ETCCDMI/software.shtml.

Approximately 60 monthly rainfall, 30 maximum and minimum air temperature and six mean sea-level pressure station records were homogenised between 2010 and 2011 by the PCCSP.

2.2.1.3 Pacific Climate Change Data Portal

A data portal (http://www.bom.gov.au/climate/pccsp/) has been developed to present historical raw and homogenised data at the monthly time scale for rainfall, maximum and minimum air temperature and mean sea-level pressure. PCCSP Partner Country data are presented in the portal along with data from neighbouring Australian, New Zealand, Tokelau, Pitcairn Islands, French and US Territories to provide as detailed coverage as possible for the region.

Within the portal (Figure 2.1), users are able to view trends in historical climate data on annual and seasonal time scales over any period of interest where data are available. Users are also able to view data averages and running averages over three to 15 year periods.

2.2.1.4 Datasets on Global or Regional Grids

While data from individual observing stations can be used for detailed studies on local climate, the spatial inconsistency and the relatively small number of stations across the huge PCCSP region pose significant problems for many types of analysis. Many spatially and temporally uniform datasets have been created to complement the in-situ observations. These gridded data are easier to analyse and display, and overcome many of these problems. However, these gridded data usually lose much of the small-scale local information available from individual station data. Outputs from global climate models are similarly gridded and as a result they can be more easily compared to gridded observational datasets.

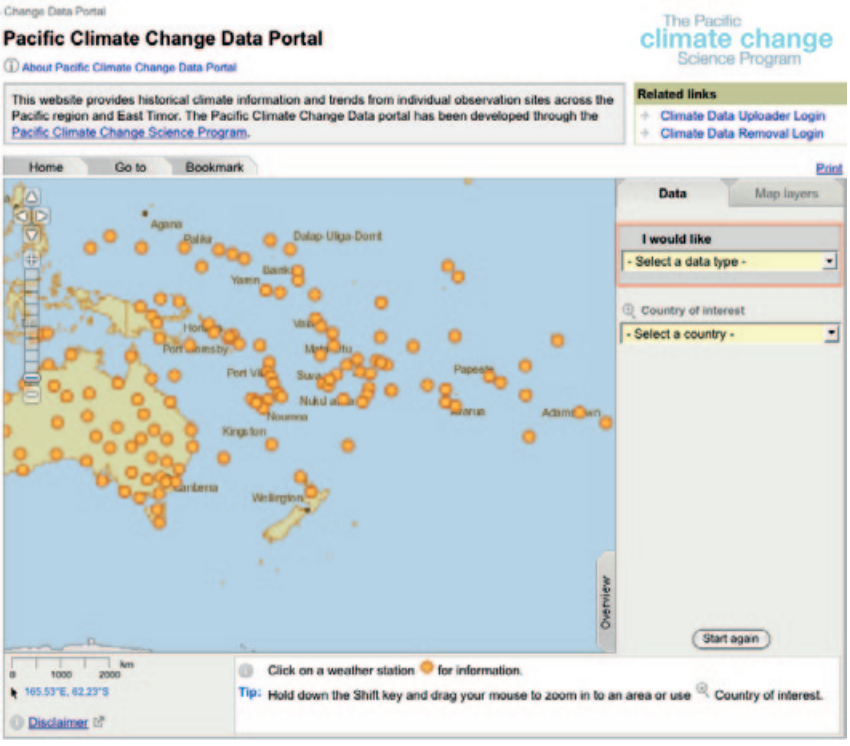

Figure 2.1: Locations of surface observed data stations in the Pacific Climate Change Data Portal http://www.bom.gov.au/climate/pccsp/.

A variety of gridded data products (Table 2.2) have been used for the analysis of past and present climate in the PCCSP region. It is important to distinguish between two types of gridded data products. The first type statistically interpolate the available in-situ observations to provide a dataset that has no gaps in space and time. Examples of this are the precipitation datasets described below. The second type, is a hybrid of numerical weather prediction model and observations known as reanalysis datasets.

Reanalysis products are produced by numerical weather prediction models that are constrained by available observations and where the interpolation is a result of the physical and dynamical processes embedded within the model. For surface air temperature, mean sea-level pressure and the surface winds the following reanalysis products were used:

- European Centre for Median-Range Weather Forecast (ECMWF) 40-year reanalysis (ERA-40; Uppala et al., 2005)
- Joint National Centres for Environmental Prediction and Department of Energy reanalysis (NCEP/DOE R-2; Kanamitsu et al., 2002)
- Japanese 25-year reanalysis (JRA25; Onogi et al., 2007).

The ERA-40, NCEP/DOE R-2 and JRA25 projects use state-of-the-art analysis/forecast systems to perform data assimilation using past data.

ERA-40 consists of a set of global analyses describing the state of the atmosphere and land and ocean-wave conditions from mid-1957 to mid-2002. ERA-Interim is an interim reanalysis of the period 1989–present in preparation for the next-generation extended reanalysis to replace ERA-40. The ERA-Interim archive is more extensive than that for ERA-40, e.g. the number of pressure levels in the atmosphere is increased from 23 to 37 and additional cloud parameters are included. ERA-Interim products are also available, including several products that were not available for ERA-40. It is therefore particularly useful for more high resolution applications.

The Global Precipitation Climatology Project (GPCP; Adler et al., 2003) and Climate Prediction Centre Merged Analysis of Precipitation (CMAP; Xie and Arkin, 1997) are generally considered to provide a more accurate representation of global rainfall than current reanalysis products (Beranger et al., 2006; Bosilovich et al., 2008), and these were used to represent the observational precipitation record.

Both GPCP and CMAP datasets merge satellite data from a number of satellite sources, and use rain gauge data over land. Details on the component datasets as well as the method used to merge these data are provided by Huffman et al. (1997) and Adler et al. (2003) for GPCP, and Xie and Arkin (1997) for CMAP.

Table 2.2: Overview of the gridded atmospheric datasets used in the PCCSP climate analysis

Climatological fields	Gridded dataset		Source	Reference
	Name	Origin		
Precipitation	CMAP version 0802	CPC Merged Analysis of Precipitation	http://www.cpc.ncep.noaa.gov/products/global_precip/html/wpage.cmap.html	Xie and Arkin (1997)
	GPCP version 2	Global Precipitation Climatology Project	http://precip.gsfc.nasa.gov	Adler et al. (2003) and Huffman et al. (1997)
	TRMM	Tropical Rainfall Measuring Mission	http://trmm.gsfc.nasa.gov/	Kummerow et al. (1998 and 2000)
	CRU	Climate Research Unit Rainfall Climatology	http://www.cru.uea.ac.uk/cru/data/	New et al. (1999)
Winds, mean sea-level pressure and surface air temperature	ERA-40	ECMWF 40-year reanalysis	http://www.ecmwf.int/products/data/archive/description/e4/index.html	Uppala et al. (2005)
	NCEP-DOE version 2	National Centre for Environmental Prediction and Department of Energy Reanalysis	http://www.esrl.noaa.gov/psd/data/gridded/data.ncep.reanalysis2.html	Kanamitsu et al. (2002)
	JRA25	Japanese 25-year Reanalysis	http://www.jreap.org/indexe.html	Onogi et al. (2007)
	ERA-Interim	ECMWF interim Reanalysis	http://www.ecmwf.int/research/era/do/get/era-interim	Dee et al. (2011)

Differences between GPCP and CMAP datasets are primarily due to differences in the input data and in the methodologies by which the various input data are merged. Over large land areas, these differences are negligible.

There are large-scale regional differences over the oceans. Over many of the oceanic tropical areas, CMAP has 20–50% more rain when compared to GPCP. Possible explanations are:

1. Differences in the use and manipulation of input data between CMAP and GPCP. Both CMAP and GPCP estimate rainfall over the oceans using microwave emissions calculated from brightness temperature measurements in various frequencies. CMAP also uses the Special Sensor Microwave Imager (SSM/I) scattering-based estimates over oceans while GPCP does not.
2. GPCP adjusts the Geostationary Operational Environmental Satellite precipitation index to the SSM/I, while CMAP does not.
3. The satellite estimates throughout the tropical oceans are adjusted by the atoll rain gauge reports in CMAP, while no such adjustment is made in GPCP.

Different analysis methods attempt to produce the most accurate precipitation data possible. However, there are still errors in all products, and the differences between their values reflect the uncertainties in each. Despite the differences in the means as discussed, CMAP and GPCP have considerably better agreement in departures from the climatological monthly means (anomalies), and temporal correlations between the two datasets are high.

Two other rainfall gridded datasets are used. The Tropical Rainfall Measuring Mission (TRMM) is a joint satellite mission between the National Aeronautics and Space Administration (NASA) and the Japan Aerospace Exploration Agency (JAXA) designed to monitor and study tropical rainfall. TRMM, during its mission and broad sampling footprint between latitudes 35°N and 35°S, is providing some of the first detailed and comprehensive data on the distribution of rainfall over vastly under-sampled oceanic and tropical continental regimes. It produces maps and gridded rainfall products on fairly fine spatial resolution (0.25° x 0.25°) and frequency (near-real-time; 1 to 3 hourly snapshots). Version 6 of the TRMM product used in this report covers a time period from 1998 until 2011.

The Climate Research Unit of the University of East Anglia, UK, has assembled a number of global gridded datasets for rainfall and temperature. All of these are land-only since they are based on station observations. One of their most recent products is the CRU TS2.1 dataset which includes a global land-only precipitation dataset on fairly fine spatial resolution (0.5° x 0.5°) covering the time period 1901–2006 in monthly time steps. This dataset is often used in the validation of global climate models and downscaling simulations.

2.2.2 Ocean Data

2.2.2.1 Datasets on Global or Regional Grids

Similar to atmospheric data from observing stations, ocean data are generally measured at irregularly spaced points in space and time. In order to create a more consistent coverage and to make these data easier to analyse, several systems have been used to generate datasets on regular grids and at regular time intervals.

The World Ocean Atlas 2005 (Locarnini et al., 2006; Antonov et al., 2006; Garcia et al., 2006) provides objectively analysed (i.e. based on the synthesis of multiple data sources) monthly, seasonally or annually averaged ocean climatologies displayed on a 1° x 1° geographic grid (Table 2.3). Variables include temperature, salinity, oxygen and nutrients at various depths. The CARS2006 from CSIRO (Ridgeway et al., 2002) provides surface and sub-surface temperature and salinity data for the tropical Pacific and Southern Hemisphere regions. The dataset uses all available historical sub-surface ocean property measurements (pre 2006) from ships and autonomous floats to provide climatology of various ocean properties.

Several sea-surface temperature (SST) datasets are used in this report (Table 2.3). Using different datasets allows the robustness of trends and variability to be evaluated. The UK Met Office Hadley Centre's dataset HadISST (Rayner et al., 2003) provides a 1° x 1° SST and sea-ice reconstruction (i.e. where modern measurements are used to extend sparse historical observations over a global domain) from 1870 to the present. Source data for SST come from the UK Met Office Marine Data Bank and the Comprehensive Ocean-Atmosphere Data Set (ICOADS). Interpolation provides a spatially continuous dataset. The related dataset HadSST2 (Rayner et al., 2006) product provides SST averaged in 5° x 5° grid cells. Unlike HadISST, HadSST2 does not perform any spatial interpolation, thus no SST estimates are provided in areas with poor data coverage. Also, based on the ICOADS dataset, the ERSST provides 2° x 2° resolution interpolated gridded output (Smith et al., 2008). The Kaplan et al. (1998) SST dataset is based on slightly different base datasets to the previously noted reconstructions with spatially interpolated data available at a 5° x 5° resolution.

QuikSCAT (NASA Quick Scatterometer, 2000) uses satellite scatterometer data to produce a high resolution database of ocean winds at 10m height. The NOAA Climate Forecast System Reanalysis (Wang et al., 2010) provides hourly surface wind and atmospheric pressure fields for 1979–2010. The NOAA Wave Watch III model (Tolman, 2002) provides surface wave field information from 1997 to the present.

Two new datasets using historical and Argo float data provide information on the temporal evolution of ocean temperature (1960–2007), and salinity (1950–2008), (Durack and Wijffels, 2010) down to about 2000 m depth. The multi-parametric analysis technique provides an estimate of the long-term trend, seasonal cycle and components of the temporal evolution related to the El Niño-Southern Oscillation and other patterns of climate variability.

The LDEOv2009 CO_2 partial pressure (pCO_2) dataset includes almost five million measurements of in-situ pCO_2, SST and sea-surface salinity spanning from 1957 to 2009. Data are available at 4° x 5° resolution (Takahashi et al., 2010).

2.2.2.2 Sea Level

Sea level varies on a wide range of time and space scales. While comprehensive sea-level observations to fully characterise this variability are not available, there has been a significant improvement in sea-level data from in situ and satellite observations over recent decades.

High quality satellite altimeter observations (from the TOPEX/Poseidon, Jason-1 and OSTM/Jason-2 satellites) of sea level between latitudes 66°S and 66°N are available from late 1992 to the present. The data are readily available (Table 2.3).

In situ sea-level observations made with tide gauges are also available at a number of locations in the PCCSP region. During the 1970s and 1980s, the number of gauges installed in the Pacific increased as part of efforts to understand the evolution of El Niño-Southern Oscillation events. With an increasing focus on sea-level rise in the late 1980s, projects like the South Pacific Sea Level and Climate Monitoring Project (http://www.bom.gov.au/pacificsealevel/) have resulted in an improved quality of individual gauges and of the network as a whole, using modern instrumentation with rigorous datum control (most recently with continuous global positioning system instruments). The publicly available in-situ sea-level datasets are detailed in Table 2.3.

The near global coverage of the altimeter data sets available since 1993 has provided information about the large-scale spatial distributions of sea level over the oceans. This information has been combined with coastal and island measurements of sea level over a longer time period using statistical techniques to estimate pre-altimeter period sea level from tide-gauge measurements alone on a 1° x 1° grid since 1950 (Church et al., 2004, 2006; called reconstructed sea level) and global averaged sea level since the late 19th century (Church and White, 2006, in press).

2.2.3 Climatological Periods

A period of 30 years is recommended for calculating climatological averages (Guttman, 1989; WMO, 1984), and the WMO's reference period is 1961–1990. This period is generally used here for calculating climate averages from Partner Country sites. However, 1971–2000 is used for many gridded analysis products, as there is greater availability of satellite data after the late 1970s, and this period is covered by most of the datasets listed in Tables 2.2 and 2.3. This period also closely matches the period used in Chapter 5 for evaluating climate models. It is important to note that in some instances the shorter time span of 1980–1999 had to be used when the data (e.g. the CMAP rainfall analysis) did not cover the full 30 years.

For some variables with small seasonal variations, only the annual averages are shown. In other instances, different seasonal averages are given, most often the four seasons (defined as December to February, March to May, June to August and September to November), as well as the tropical wet and dry seasons (November to April and May to October, the respective season depending on the hemisphere).

Table 2.3: Overview of the ocean datasets used in this publication (see text for details).

Climatological fields	Gridded dataset		Source	Reference
Sea-surface temperature, sea-surface salinity, nitrate concentration	WOA05	World Ocean Atlas 2005	http://www.nodc.noaa.gov/OC5/WOA05/pubwoa05.html	Locarnini et al. (2006), Antonov et al. (2006), Garcia et al. (2006)
Wind stress	QuikSCAT		ftp.ifremer.fr/products/gridded/mwf_quiskcat/data	NASA Quick Scatterometer (2000)
Wind stress, surface pressure	NOAA Climate Forecast System Reanalysis (CFSR)		http://cfs.ncep.noaa.gov/cfsr/	Wang et al. (2010)
Surface gravity wave height, direction, period	NOAA Wave Watch III		http://polar.ncep.noaa.gov/waves/	Tolman (2002)
Sea-surface temperature	HadISST	Hadley Centre SST dataset	http://badc.nerc.ac.uk/data/hadisst/	Rayner et al. (2003)
	HadSST2		http://hadobs.metoffice.com/hadsst2/	Rayner et al. (2006)
	ERSST	NOAA Extended Reconstructed SST	http://www.esrl.noaa.gov/psd/data/gridded/data.noaa.ersst.html	Smith et al. (2008)
	Kaplan Extended SST V2		http://www.esrl.noaa.gov/psd/data/gridded/data.kaplan_sst.html	Kaplan et al. (1998)
Temperature, salinity	CARS2006	CSIRO Atlas of Regional Seas	http://www.marine.csiro.au/~dunn/cars2006/	Ridgeway et al. (2002), Dunn and Ridgeway (2002)
			Contact authors for data availability	Durack and Wijffels (2010)
pCO_2	LDEOv2009	Lamont-Doherty Earth Observatory (LDEO) database	http://cdiac.ornl.gov/oceans/LDEO_Underway_Database/	Takahashi et al. (2010)
	Description/Institution		**Source/Reference**	
Sea-level altimetry	Measured along satellite ground tracks, from NASA		http://podaac.jpl.nasa.gov/DATA_CATALOG/topexPoseidoninfo.html; http://podaac.jpl.nasa.gov/DATA_CATALOG/jason1info.html; http://www.nodc.noaa.gov/SatelliteData/Jason2 or ftp://avisoftp.cnes.fr/AVISO/pub/jason-2/gdr_t/	
	Processed versions of this dataset		http://www.cmar.csiro.au/sealevel/sl_data_cmar_alt.html	
	Gridded products of this and other data		ftp://ftp.aviso.oceanobs.com; http://www.cmar.csiro.au/sealevel/sl_data_cmar_alt.html	
In situ sea-level data	Australian National Centre Facility		http://www.bom.gov.au/oceanography/projects/spslcmp/spslcmp.shtml	
	Permanent Service for Mean Sea Level		http://www.psmsl.org/; Woodworth and Player, (2003)	
	University of Hawaii Sea-level Centre		http://uhslc.soest.hawaii.edu/uhslc/	

2.3 Current Climate in the Region: Atmosphere

This section describes the features of the average climate in the region. One aspect that clearly emerges is the close connection between patterns in temperature, the atmospheric circulation and rainfall. The oceans play a vital role in these interactions, as described in Section 2.6.

2.3.1 Surface Air Temperature

Surface air temperatures observed in the PCCSP region are dominated by several important geographical features. Firstly, in many Partner Countries air temperatures are largely determined by the surface temperatures of the surrounding Pacific Ocean because the relatively small land areas of most islands have little influence on the local energy budget. Secondly, seasonal temperature variations can be driven by the large land masses on the western edge of the Pacific (Australia, Asia and the Maritime Continent) that heat and cool at different rates to the oceans. The resulting land-ocean temperature contrasts drive the West Pacific Monsoon and other atmospheric and ocean circulations.

In the tropics, with the sun being almost directly overhead, the amount of incoming solar radiation (heat) is high and changes only very slightly throughout the year. As a result, air temperatures remain high and relatively constant throughout the year. Temperature variations between the seasons increase with distance from the equator, as does the impact of extra-tropical air masses on temperatures.

Whilst the sun is the main driver of temperatures in the PCCSP region, interactions between the atmospheric circulation and the ocean result in regional variations in air temperatures. These temperature variations affect the patterns of rainfall across the region and closely match the ocean temperatures. Air temperatures in the western tropical Pacific and Maritime Continent are on average several degrees warmer than in the eastern tropical Pacific due to winds affecting ocean temperatures (Section 2.6). The warm waters in the west are known as the West Pacific Warm Pool, and the cool waters in the east are called the Equatorial Cold Tongue (Figure 2.2). Over the West Pacific Warm Pool there is virtually no seasonal variation in air temperature and over much of the tropics temperatures in the coldest months are only a few degrees lower than the warmest months (Figure 2.3). Along the equator, year-to-year variations in temperature can be larger than the average variations between the seasons (Chapter 3).

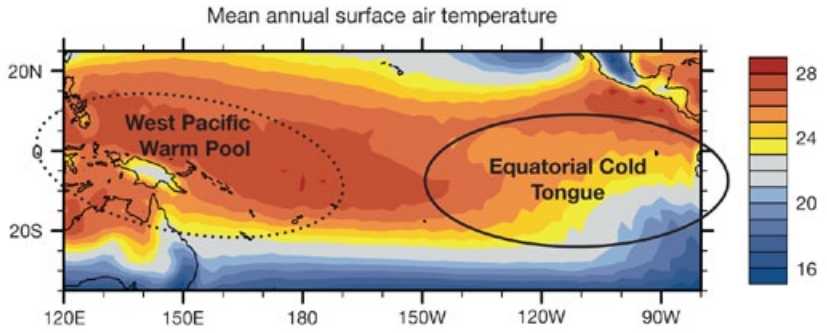

Figure 2.2: Annual average surface air temperature (°C) in the equatorial Pacific. Approximate positions of two important features are indicated: the West Pacific Warm Pool and the Equatorial Cold Tongue in the east. Data from the NCEP2 reanalysis for the period 1971–2000.

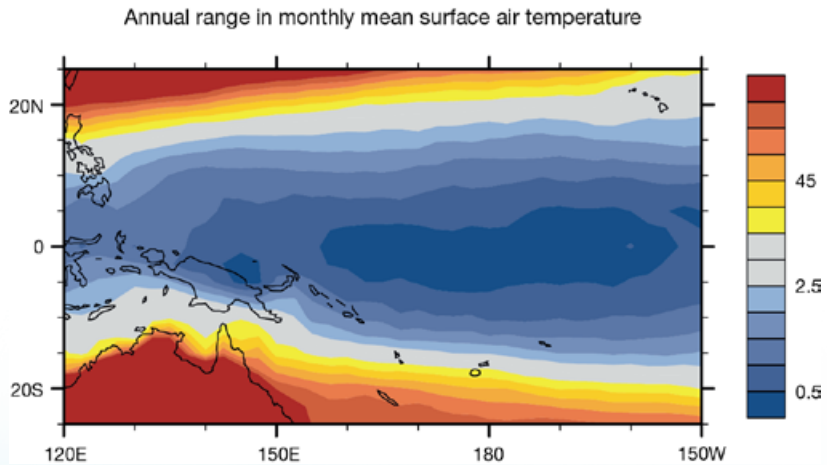

Figure 2.3: Range in surface air temperature (°C) between average hottest and coldest months. Data from the NCEP2 reanalysis for the period 1971–2000.

2.3.2 Atmospheric Circulation

The imbalance of higher amounts of incoming solar radiation (heat) in tropical regions, compared to higher latitudes, results in the Earth's atmosphere and ocean circulations transporting heat toward the poles. The Earth's rotation causes changes in the direction of the air movement (the Coriolis effect), giving rise to complex atmospheric circulation patterns. Large land masses and topographic features also modify regional and local circulations. In the tropics, the major features of this atmospheric circulation include the Hadley Circulation (the major vertical movement of heated equatorial air and its north-south transfer into the mid latitudes), the Walker Circulation (the east-west circulation of air across the Pacific region), the trade winds, large-scale convection over the West Pacific Warm Pool and convergence zones, the West Pacific Monsoon, tropical cyclones and sub-tropical high pressure systems. Some of these can be seen in Figure 2.4. Others are shown in Figure 2.5 and Box 2.2.

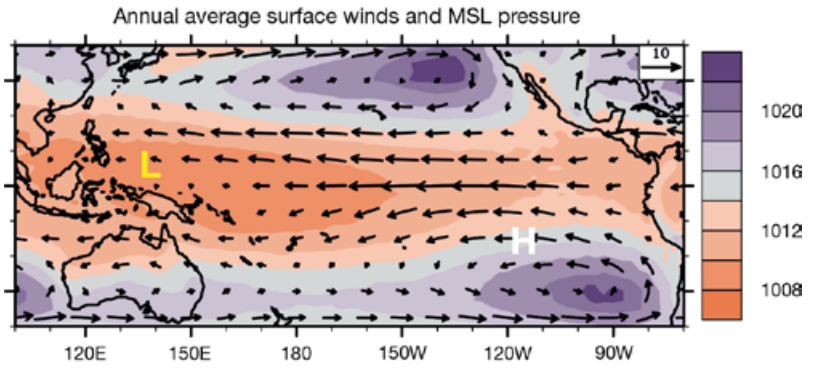

Figure 2.4: Annual average mean sea-level pressure (in hPa, purple=high pressure, red=low pressure), with semi-permanent pressure systems (H=high, L=low) and surface winds (in metres per second) indicated by the length of the arrows (the 10 metres per second reference arrow is shown in the top-right corner). Data from the NCEP2 reanalysis for 1971–2000.

Over areas where the ocean is relatively warm, rising air (convection) leads to the formation of clouds and produces rainfall. Surface winds tend to converge towards and feed into these convection areas. Strong convection occurs over the West Pacific Warm Pool so the surface trade winds blow from east to west across the Pacific along the equator, feeding into this large region of convection. Air rises high in the atmosphere over the Warm Pool and flows back from west to east in the upper atmosphere (the upper troposphere). This air descends in the eastern Pacific and over the Equatorial Cold Tongue, feeding the surface trade winds, thus completing the circulation. This is known as the Walker Circulation (Figure 2.5), and is one of the most prominent and important of the atmospheric circulations (Gill, 1982; Power and Smith, 2007).

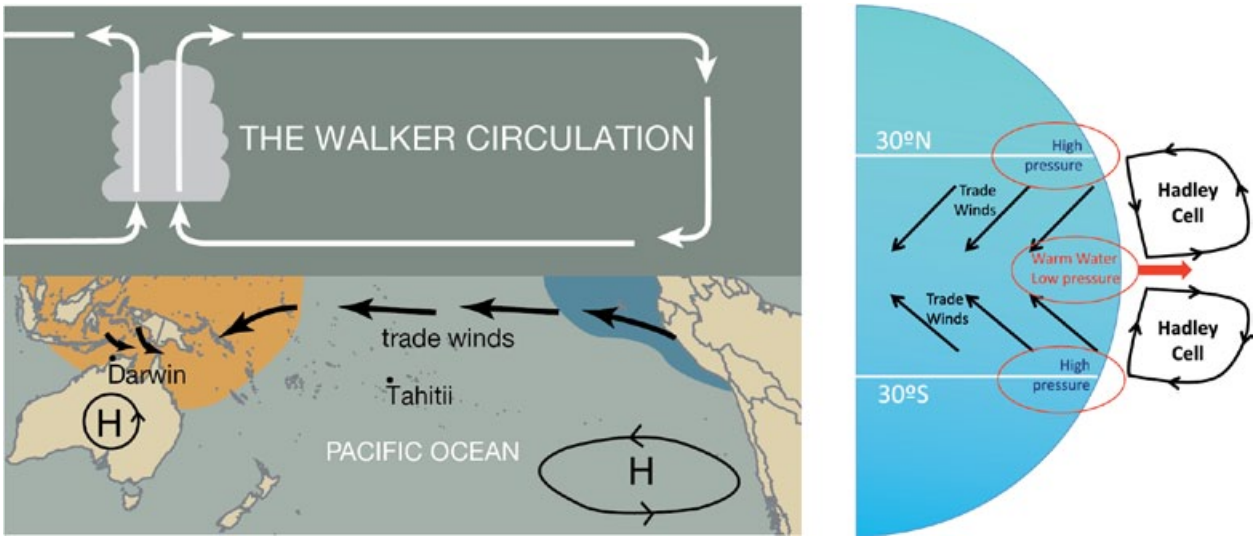

Figure 2.5: (Left) A schematic of the atmospheric Walker Circulation. Surface trade winds from the cold waters of the Equatorial Cold Tongue (blue) in the east blow across the Pacific, feeding into convection over the West Pacific Warm Pool (orange). Air rises and flows back to the east in the upper atmosphere to complete the circulation (Source: Australian Bureau of Meteorology). (Right) A schematic of the Hadley Circulation, with rising air at the equator, flowing poleward in the upper atmosphere, descending over the sub-tropics and flowing back to the equator as trade winds.

The Walker Circulation weakens during El Niño events and strengthens during La Niña events (Chapter 3), but in normal situations the equatorial trade winds are quite constant in both direction and strength. The Walker Circulation's rising air over the West Pacific Warm Pool creates a region of low pressure, while the descending air over the eastern Pacific (east of about 150°W) creates a region of higher pressure (Figure 2.4). When the Walker Circulation and equatorial trade winds change strength, the pressure in both regions usually changes at the same time. For example, if the Walker Circulation slows down, convection over the West Pacific Warm Pool decreases and so pressure increases, and subsidence over the eastern Pacific weakens and so pressure there tends to fall. This oscillation in air pressure across the region is known as the Southern Oscillation.

In addition to the Walker Circulation, rising convective air also feeds a north-south circulation, known as the Hadley Circulation. When the Walker Circulation strengthens, the Hadley Circulation tends to weaken and vice versa (Oort and Yienger, 1996). In the Hadley Circulation, the air that rises near the equator flows towards both poles in the upper troposphere, descending over the sub-tropics. The mean positions of this descending, dry air in both hemispheres determine the location of the more arid regions of the Earth.

This descending air leads to regions of high pressure around latitudes 30ºS and 30ºN (Figures 2.4 and 2.5). Within these regions lie the permanent South-east Pacific High and North-west Pacific High. These high pressure systems drive surface winds towards the equator and from the east, producing the predominantly south-east trade winds in the Southern Hemisphere, and north-east trade winds in the Northern Hemisphere. To the west of these permanent highs, high pressure systems migrate from west to east, modifying the local wind direction as they pass (Steiner, 1980). The intensity of these semi-permanent and migrating high-pressure systems determines the strength and direction of the predominantly north-east and south-east trade winds. Cold fronts and extra-tropical low pressure systems lie south of the high pressure zone and they can influence local weather when they approach.

The north and south descending branches of the Hadley Circulation and the resulting high-pressure systems generally move equatorward during the winter and spring and poleward during summer and autumn in response to changes in north-south temperature gradients with the seasons (Barry and Chorley, 1992). When the high-pressure systems move closer to the equator they can bring cooler conditions to a country as the more north-south winds bring cooler, extra-tropical air. They also bring drier conditions as the descending air associated with them is dry.

2.3.3 Rainfall

Many tropical areas receive very high annual rainfall as a result of moisture-laden winds. Evaporation and convection occur where the ocean surface is warm, and when the winds converge this convection is enhanced. In the Pacific and around the Maritime Continent there are several regions where these factors act together.

Patterns of average rainfall show that there are some differences between the December to February and June to August periods (Figure 2.6). However, some large-scale features remain year round where ocean temperatures remain warm and winds converge throughout the year. For example, over the West Pacific Warm Pool rainfall persists throughout the year. This warm reservoir of water provides the energy source for the extensive convective activity that drives the Walker Circulation and much of the Hadley Circulation in this region. This is a major moisture source for the heavy rainfall in the region, which averages more than 2–3 m per year (Delcroix et al., 1996). The South Pacific Convergence Zone (SPCZ) in the south-west Pacific, (Section 2.4.1) and Intertropical Convergence Zone (ITCZ) just north of the equator, (Section 2.4.2) are two other prominent features associated with high rainfall.

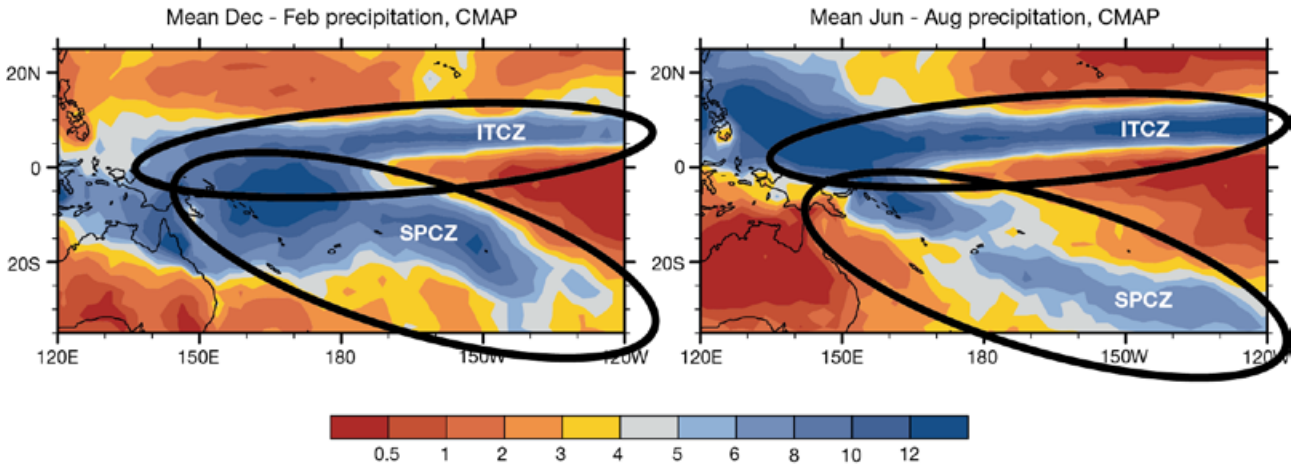

Figure 2.6: Average rainfall over the PCCSP region for December to February (left) and June to August (right), in mm per day (blue = wet and red = dry). Data from the Climate Prediction Center Merged Analysis of Precipitation dataset for years 1980–1999. The average ITCZ and SPCZ positions are indicated.

In the tropics, significant rainfall also comes from tropical cyclones and storms. Tropical cyclones are mostly confined to the latitudes 10º-25º in both hemispheres, where the ocean is warm enough to provide the energy for them to form and the Coriolis effect (related to the Earth's rotation) is large enough for them to spin-up. The contribution of tropical cyclones to Partner Country annual rainfall is generally around 5–10% in those countries affected by tropical cyclones, and up to around 15% in Vanuatu (Jiang and Zipser, 2010).

On some islands (including quite small ones) with significant topography the moist winds (such as the trade winds) are forced upwards, leading to condensation and enhanced rainfall. This can lead to very different local climates, depending on the location relative to the prevailing winds and the topography. In the sub-tropics, rainfall also comes from cold fronts that traverse the region, usually in the winter months.

The largest seasonal variations in rainfall are seen in regions strongly affected by the West Pacific Monsoon (Box 2.2 and Section 2.4.3) in the far west of the PCCSP region. In these countries the difference in rainfall between the wet season (during the monsoon) and the dry season is significant. For example, in Dili in East Timor, almost 80% of the total annual rainfall falls during the wet season of November to April.

In other countries there are some seasonal variations in rainfall, but smaller than in the region affected by the West Pacific Monsoon. Rainfall seasonality is associated with variations in the tropical cyclone seasons, the strength and position of the ITCZ and SPCZ, the position and strength of sub-tropical high pressure systems and cold fronts, and variations in the amount of available moisture as ocean temperatures vary. In those countries that have significant topography, rainfall will vary during the year depending on the strength and direction of winds, particularly the trade winds.

In all countries in the PCCSP region there is a significant difference in the regular rainfall that comes in the wet and dry seasons. The regularity of these seasons has a large impact on life in the region. This has led to long-held traditional knowledge of the seasons, reflected in the language of each of the peoples of the Pacific and East Timor. Each group has one or several names for the two seasons (Box 2.1), which usually refer to the wet and dry periods, the time of planting and harvesting crops, or the changes in the prevailing winds between the seasons.

Box 2.1: Indigenous Weather and Climate Terminology

Having lived with the extremes of weather and climate for many generations, the indigenous peoples of the Pacific and East Timor have intimate knowledge of climate phenomena. Most indigenous languages have terms for these climate phenomena that affect their everyday lives. This has led to terminology for the wet and dry seasons in local languages of the peoples in the Pacific and East Timor.

Country		Wet season	Dry season
Cook Islands		Tuatau Mauu	Tuatau Maro
East Timor		Udanben	Bailoron
Federated States of Micronesia	Chuuk	Nukuchochun	Pwas
	Yap	Nuw	Yal
Fiji		Suasua	Mamaca
Kiribati		Ameang	Aumaiaki
Marshall Islands		Mejleb	Anŕeńeaṕń
Nauru		Luai	Aré
Niue		Vahä Mafana	Vaha Mokomoko
Palau		Kemtimt	Sechal El Ongos
Papua New Guinea	Pidgin	Taim Bilong Ren	Taim bilong San
	Motu	Medu Ena Nega	Dina Ena Nega
Samoa		Vaipalolo / Taū Sūsū	Vaitoelau / Tau Mugalā
Solomon Islands		Komburu	Ara
Tonga		Fa'ahita'u 'Uha	Fa'ahita'u La'ala'a
Tuvalu		'Tau 'Moko	Tau Yela
Vanuatu (based on planting season)		Nowa mate (Harvesting)	Nowa Mourii (Planting)

2.4 Large-Scale Climate Features

As discussed in preceeding sections, there are several very important features of the climate system in the Pacific and East Timor region that influence the mean climate and seasonal climate variations in Partner Countries (Box 2.2). Some of these features exist throughout the year while others have pronounced and regular seasonal cycles. They are described here, and the average seasonal cycles of the climate in each Partner Country are briefly described and explained in terms of these climate features.

Box 2.2: Main features influencing the climate of the PCCSP region

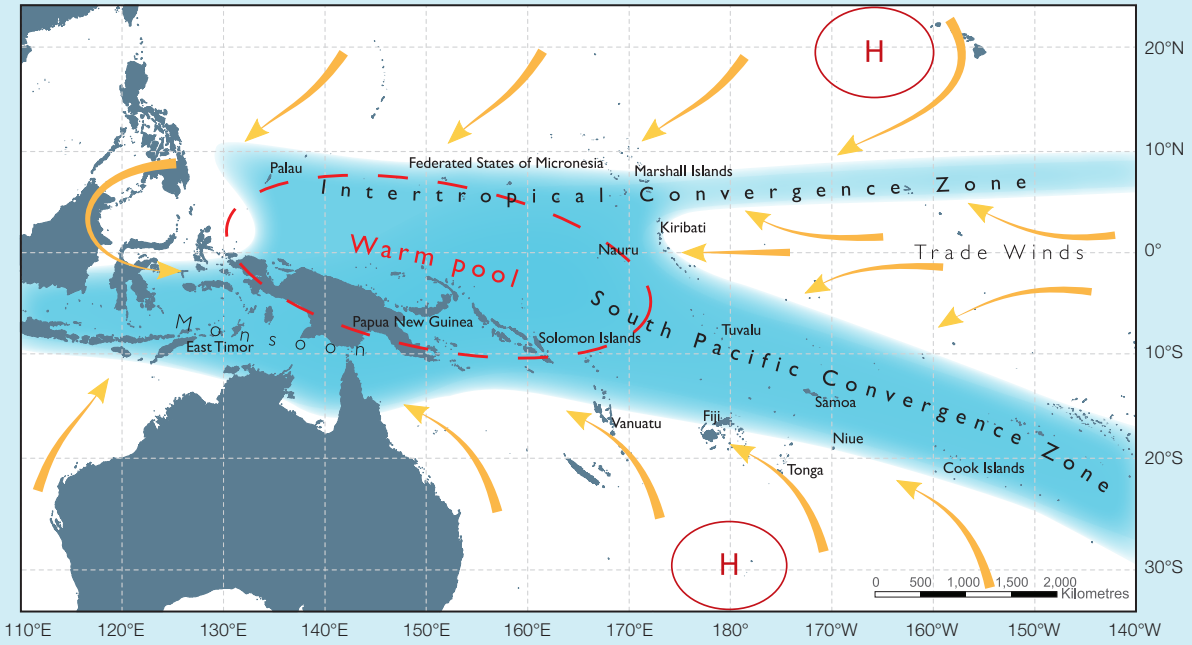

The average positions of the climate features in November to April. The yellow arrows show near-surface winds, the blue shading represents the bands of rainfall (convergence zones with relatively low pressure), and the red dashed oval indicates the West Pacific Warm Pool. H represents the typical positions of moving high pressure systems.

West Pacific Monsoon

This moves north to mainland Asia during the Northern Hemisphere summer and south to Australia in the Southern Hemisphere summer. The seasonal arrival of the monsoon usually brings a switch from very dry to very wet conditions. It affects countries in the far western Pacific and the Maritime Continent.

Intertropical Convergence Zone

This band of high rainfall stretches across the Pacific just north of the equator and is strongest in the Northern Hemisphere summer. It affects most countries on, or north of, the equator.

South Pacific Convergence Zone

This band of high rainfall stretches approximately from the Solomon Islands to east of the Cook Islands. It is strongest in the Southern Hemisphere summer and affects most countries in the South Pacific.

Sub-Tropical and High Latitude Influences

These include sub-tropical high pressure systems and associated south-east and north-east trade winds, and cold fronts.

2.4.1 South Pacific Convergence Zone

The SPCZ extends northwest-southeast in a diagonal line from near the Solomon Islands (0°, 150°E) to the south-eastern Pacific (around 30°S, 120°W) (Figure 2.6). It is composed of two parts (Trenberth, 1976; Kiladis et al., 1989; Vincent, 1994): the west-east-oriented western part attached to the West Pacific Warm Pool, which interacts with the West Pacific Monsoon; and the diagonally-oriented portion further to the east that extends into the sub-tropics. The Partner Countries affected by the SPCZ are the Solomon Islands, Tuvalu, Vanuatu, Fiji, Tonga, Samoa, Niue and the Cook Islands, and in some years Nauru and Kiribati. See Table 2.4 for further details.

The SPCZ forms in the region of convergence between the north-east trade winds and the south-easterly circulation ahead of anticyclones from the Australian region (Trenberth, 1976; Streten and Zillman, 1984). The western, tropical portion of the SPCZ lies over the warmest sea-surface temperatures of the West Pacific Warm Pool, while the eastern portion is dominated by interactions with troughs in the mid-latitude circulation, which contributes to its diagonal orientation (Kiladis et al., 1989; Vincent, 1994).

The seasonal cycle of rainfall in the SPCZ region can be seen in time-latitude plots of zonal mean (i.e. east-west) rainfall across the region (Figure 2.7). The SPCZ is most clearly defined with strongest rainfall in December-February when the monsoon trough (Section 2.4.3) is closest to the SPCZ region and winds feed more moisture into the SPCZ. It is weaker and less well defined in June-August (Vincent, 1994) as the monsoon trough moves north and the drier zone on the equator expands as the ITCZ (Section 2.4.2) moves north, feeding less moisture into the SPCZ.

Cloudiness and rainfall in the SPCZ region vary on a daily basis with the passage and merging of mid-latitude fronts and low-pressure systems. Tropical troughs and surface low-pressure systems also develop in the SPCZ region and influence rainfall, particularly in the dry season (Thompson, 1986). Therefore, the image of a continuous SPCZ with a line of high rainfall and strong convection represents the seasonal or long-term average conditions, rather than the conditions on any single day. There is evidence that the Madden-Julian Oscillation (Section 2.4.4) influences the SPCZ on intra-seasonal time scales (Vincent et al., 1994; Matthews et al., 1996). The interannual variability of the SPCZ is dominated by the impact of El Nino Southern Osclillation (ENSO) events, with the SPCZ moving north and east during El Niño events and south and west during La Niña events (Trenberth, 1976; Vincent, 1994; Folland et al., 2002; Vincent et al., 2011. See Chapter 3 for more information about ENSO.

2.4.2 Intertropical Convergence Zone

The ITCZ is a persistent east-west band of low-level wind convergence, cloudiness, and rainfall, located close to the equator and extending across the tropical North Pacific (Figure 2.6). These features are also co-located with high-level wind divergence and maxima in upward motion at an altitude equivalent to 500 hPa. The ITCZ is one of the major features determining the climate of the tropical North Pacific, marked by the presence of a surface pressure trough, and formed by the convergence of moisture and heat-laden Northern and Southern Hemisphere trade winds. The upward branch of the Hadley Circulation cell in the Pacific sits over the ITCZ. In the eastern Pacific its north-south position is located where sea-surface temperatures are warmest – to the north of the equator. In the west, in the region of the West Pacific Warm Pool, sea-surface temperature gradients are weaker, and the ITCZ is not necessarily located over the very warmest waters. The Partner Countries affected by the ITCZ are Papua New Guinea, Palau, Federated States of Micronesia, Marshall Islands, Nauru and Kiribati. See Table 2.4 for further details.

In the central and eastern Pacific, the ITCZ is narrow, whereas in the western Pacific the ITCZ becomes broad, due to strong monsoon flows, and the breadth of the West Pacific Warm Pool to the north and south. Seasonal variation in the position of the ITCZ in the central and eastern Pacific shows an amplitude of approximately 5° of latitude (Figure 2.7). The ITCZ is closest to the equator in March-May, and furthest north during September-November, when it becomes broader, expanding

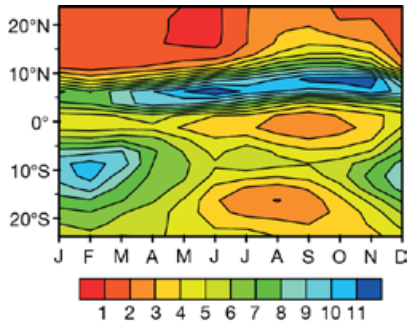

Figure 2.7: Variation of average rainfall with month (horizontal axis) and latitude (vertical axis) averaged over longitude band 155°E–140°W in mm per day. Data from the Climate Prediction Center Merged Analysis of Precipitation dataset for years 1979–1999. The regions of strong rainfall (blue/green) to the south and north of the equator indicate positions of the SPCZ and ITCZ respectively.

both to the north and south (Waliser and Gautier, 1993). Rainfall totals in the ITCZ region (defined here as 160°E–120°W, 0°-15°N) peak in September-November at values around 50% higher than those of the (late) southern summer, January-March. These results are based on CMAP precipitation analysis, with a smaller seasonality indicated by GPCP analysis.

A weak ITCZ-type feature, distinct from the SPCZ, forms in the eastern South Pacific at around latitude 5°S during March-May when northern rainfall is at its weakest with the rainfall pattern in the region symmetric across the equator (De Szoeke and Xie, 2008). As this South Pacific feature of the ITCZ is weak and only appears for a few months each year, the term ITCZ is almost always used to refer to the much more prominent Northern Hemisphere ITCZ. The same convention is used in this publication.

2.4.3 West Pacific Monsoon

The WPM is the eastern edge of the Maritime Continent Monsoon, and is the southern extension of the larger Asian-Australian Monsoon system. This system moves seasonally from the Northern Hemisphere across the equator into the tropical regions of the Southern Hemisphere during December-February. The WPM therefore extends into the transition region of both the SPCZ and the ITCZ.

The WPM can be characterised by the seasonal reversal of the prevailing winds (Figure 2.8; Kim et al., 2008). This reversal of the cross-equatorial low-level wind originates from a reversal in the cross-equatorial atmospheric pressure that results from changes in the land-sea temperature contrast (Wang, 2006). The timing of the onset of the monsoon is often tied to the arrival of the Madden-Julian Oscillation (Section 2.4.4; Hendon and Liebmann, 1990a, b) and intrusion of mid-latitude troughs (Davidson et al., 1983).

The right panel of Figure 2.8 indicates regions which experience a reversal in the east-west wind component between December-February and June-August and therefore receive rainfall from the WPM. In the Southern Hemisphere, these include East Timor, Papua New Guinea, Solomon Islands and, on the outer edges, Tuvalu and Vanuatu. In the Northern Hemisphere, a seasonal wind reversal is experienced in Palau and parts of the Federated States of Micronesia, and in some years as far east as the Marshall Islands.

Along with the reversal in low-level winds comes the typical intra-seasonal variability in monsoon rainfall (Figure 2.9). Monsoonal rainfall has significant daily to weekly variability, with a monsoon season having several burst (wet) and break (dry) periods between initial onset and final end of the monsoon season.

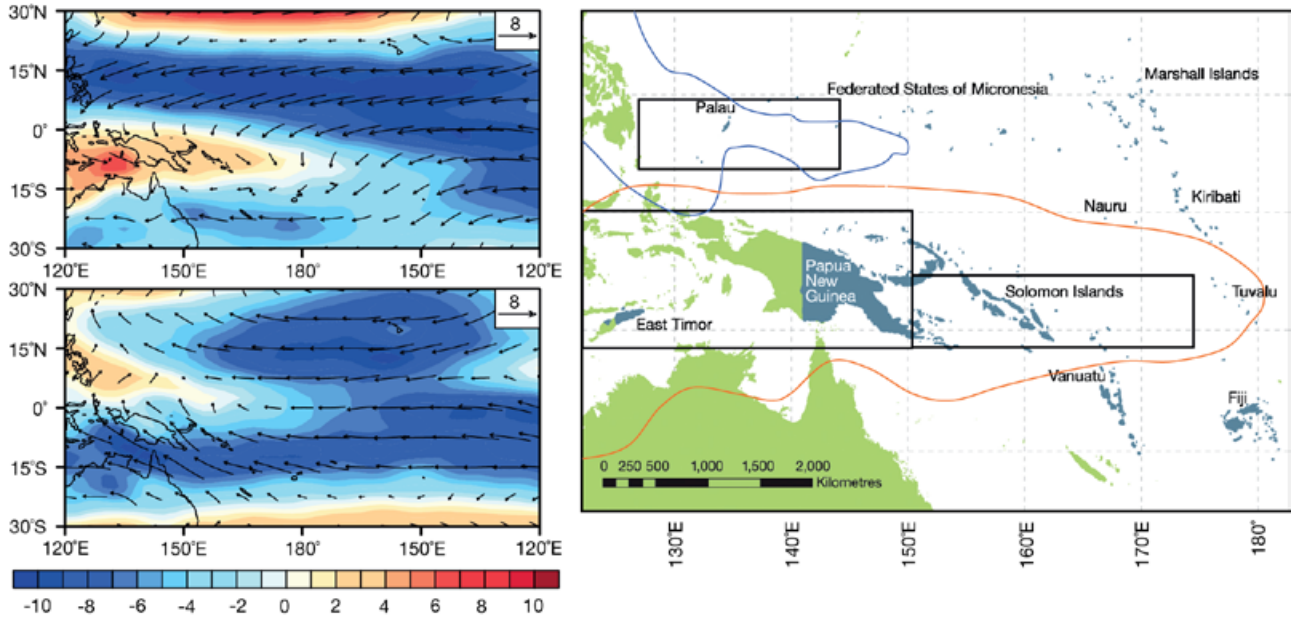

Figure 2.8: (Left) The magnitude of the low level (925 hPa) zonal wind components for the months of January (upper panel) and July (lower panel). The white shading indicates the transition from westerly (yellow to red) to easterly (blue) components. (Right) Regions affected by westerly wind components are found within (to the left of) the orange contour line during December-February and the blue contour line during June-August. Area averages have been calculated for the boxed regions Northern Hemisphere box (125–145°E; 5–10°N), Southern Hemisphere box-1 (120–150°E; 0–10°S), and Southern Hemisphere box-2 (150–175°E, 5°S–10°S). (Source: NCEP reanalysis data (Kalnay et al., 1996)).

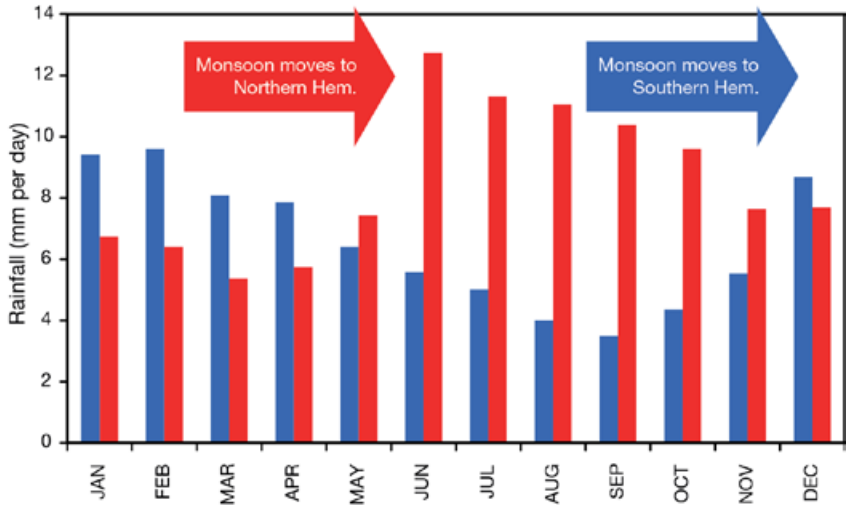

Figure 2.9: Annual cycle of monthly rainfall (in mm per day) for the Southern Hemisphere monsoon westerly region (Southern Hemisphere box-1, blue bars) and the Northern Hemisphere monsoon westerly region (Northern Hemisphere box, red bars) as indicated in Figure 2.8. Arrows show the build up to onset of the Northern (red) and Southern (blue) Hemisphere monsoons.

The onset of the monsoon in the Northern Hemisphere in May-June is much more sudden than its retreat in October-November. The reason for this lies in the different thermal inertia of land compared with ocean, which facilitates the south-eastward move but hinders the north-westward move during the retreat (Wang and Chang, 2008), leaving large monsoon convective regimes, mainly south of latitude 5°N, until the end May. For the Southern Hemisphere this feature is not present, showing a smoother transition for monsoon onset and retreat.

2.4.4 Other Climate Features

Whilst the large-scale climate features described previously are largely responsible for setting the mean state and seasonal variations in the climate of most PCCSP countries, there are other phenomena that affect the climate on shorter time scales. The Madden-Julian Oscillation (MJO) mentioned earlier is a tropical circulation feature moving west to east along the equator with a frequency of 40–60 days (Madden and Julian, 1994). The MJO brings significant variations in convection and is one of the dominant drivers of intra-seasonal rainfall variations in the tropics. It is most active in December-February, often resulting in short wet and dry periods within a single monsoon season (Wheeler and McBride, 2005). Active phases of the MJO usually develop in the western Indian Ocean and move eastward into the western Pacific Ocean. In the PCCSP region they can influence the climate variability within a season particularly in East Timor, Papua New Guinea and the Solomon Islands.

The Southern Annular Mode is another important feature of extra-tropical climate variability which varies on short, synoptic time scales (up to 10 days), as well as longer periods. It influences the sub-tropical high pressure systems that affect the climate of many countries in the South Pacific sub-tropics. It is described in more detail in Section 3.4.7.

2.5 Mean Climate at Key Locations Across the Region

Average seasonal climate variations are given here for one site in every Partner Country (Figure 2.10) to demonstrate climatic conditions across the region. More detailed descriptions for each country are given in the individual country reports in Volume 2.

Islands between latitudes 15°N and 15°S experience a relatively weak seasonal variation in air and sea-surface temperature (between 1–2°C). This variation is slightly stronger for countries in the far western Pacific south of the equator where the continental land masses have an effect (East Timor and Papua New Guinea). Near the equator some locations (Solomon Islands, Palau, Nauru, Kiribati and Tuvalu) experience two peaks in their annual air temperature cycle (around May and November).

Average monthly sea-surface temperature values are between average monthly mean and average monthly maximum air temperature values at most locations throughout the year. This reflects the small size of many islands and their small impact on local temperatures (Papua New Guinea is the main exception), and indicates the influence ocean temperatures have on the climate experienced on islands.

Compared to air and sea temperature there is greater variation in rainfall. The wettest months in countries in the north Pacific region, Palau, the Federated States of Micronesia and the Marshall Islands, occur when the ITCZ is strongest and displaced furthest north between May and August. Nauru, Kiribati and Tuvalu, all near or just south of the equator, experience their wettest months between December and March, when the ITCZ and the monsoon trough are furthest south. These countries are also influenced by the SPCZ, especially Tuvalu as it is further south. Rainfall is therefore higher in Tuvalu, which is also a consequence of the influence of the WPM.

Partner Countries south of 15°S experience a greater annual air and sea-surface temperature range compared to those further north. For example, at Nuku'alofa, Tonga, the summer to winter maximum and minimum air temperature ranges are more than 6°C. At these locations the air and sea temperature maximum is experienced at most sites between December and March. These are the wettest months and the period when the SPCZ is most active and furthest south. Peak tropical cyclone and Madden-Julian Oscillation activity also occurs during this period. In countries farthest from the equator, such as Niue and Tonga, the difference between wet season and dry season rainfall is reduced as more rainfall in the winter is received from passing cold fronts.

On small low-lying islands, the climatology of the key location may in fact represent that of the rest of the island and nearby islands. However, on larger elevated islands topography can have a significant effect, so the climate of the key location may not be applicable several kilometres away. For example, in Fiji rainfall is higher in Suva, which is exposed to the south-east trade winds, than in Nadi (not shown in Figure 2.10) which lies on what is predominantly the lee side of the same island. There can also be notable differences in climate within countries that are spread over a large area, e.g. the northern and southern Cook Islands.

Table 2.4: List of the Partner Countries and the main features that influence their climate. Also included is whether the country is regularly impacted by tropical cyclones and if it has significant topography leading to climatic effects.

Country	Main climate features and influences
Cook Islands	SPCZ, sub-tropical highs, trade winds, tropical cyclones, topography
East Timor	WPM, topography
Federated States of Micronesia	ITCZ, WPM, trade winds
Fiji	SPCZ, trade winds, sub-tropical highs, tropical cyclones, topography
Kiribati	ITCZ, SPCZ, trade winds
Marshall Islands	ITCZ, WPM (in some years), tropical cyclones
Nauru	ITCZ, SPCZ, trade winds
Niue	SPCZ, trade winds, sub-tropical highs, tropical cyclones
Palau	WPM, ITCZ, trade winds
Papua New Guinea	WPM, ITCZ, topography
Samoa	SPCZ, trade winds, sub-tropical highs, tropical cyclones, topography
Solomon Islands	SPCZ, WPM, tropical cyclones
Tonga	SPCZ, trade winds, sub-tropical highs, tropical cyclones, topography
Tuvalu	WPM, SPCZ, trade winds, sub-tropical highs, tropical cyclones
Vanuatu	SPCZ, trade winds, sub-tropical highs, tropical cyclones, topography

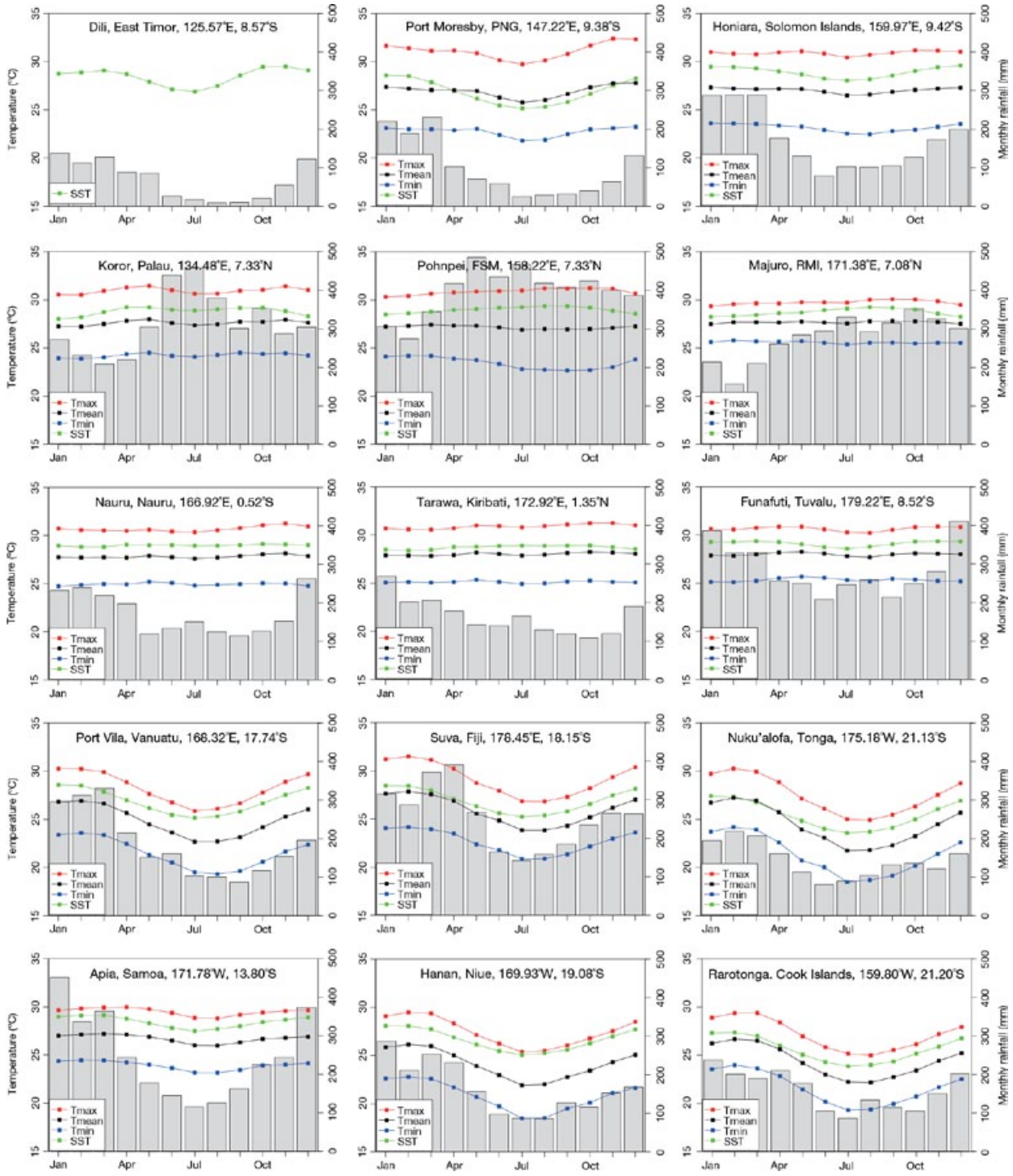

Figure 2.10: Monthly average maximum air temperature (red), mean air temperature (black), minimum air temperature (blue), sea-surface temperature (green) and average monthly rainfall (grey bars) at key locations in each of the Partner Countries. Station data over 1961–1990 were used.

2.6 Current Climate in the Region: Oceans

The ocean and atmosphere interact strongly in the tropical Pacific through the exchange of heat, water and momentum via surface winds. Surface winds affect the upper ocean in the first few tens of metres, driving surface currents and causing water to pile up in certain regions and to drop in others. This in turn generates pressure differences that can create currents extending from the surface to hundreds, or even thousands, of metres below. Surface winds also generate waves at the surface of the ocean which increase in size with the strength, duration and distance over which the wind blows.

While the atmosphere can drive changes in ocean circulation, temperature and salinity, the ocean's surface temperature also shapes the properties and circulation of the atmosphere, as described in previous sections. Movement of heat within the ocean also controls changes in atmospheric circulation and rainfall on interannual time scales. The most dramatic example of this is the wind and rainfall changes driven by shifts in the position of the warmest tropical Pacific waters as part of ENSO (Chapter 3).

The ocean in the PCCSP region has a number of important and unique temperature, salinity and circulation features that influence the overlying atmosphere and play a role in marine productivity.

2.6.1 Sea-Surface Temperature

In general, sea-surface temperature decreases consistently from the equator towards the poles. This is a consequence of the greater amount of solar energy entering the ocean at lower latitudes compared to higher latitudes. There are important regional deviations. Along the equator, easterly trade winds push the warm surface tropical waters towards the west. This forms an extensive pool of the world's warmest waters, the West Pacific Warm Pool, with temperatures exceeding 28–29ºC and covering an area of 15 million km^2 (Wyrtki, 1989; Figure 2.11). The Warm Pool stretches from the central Pacific to the far eastern Indian Ocean. The Indian Ocean portion of the Warm Pool is fed via a warm current (called the Indonesian Throughflow) from the Pacific Ocean (Hautala et al., 2001) via the Indonesian archipelago. The warm water abutting the western margin of the Pacific basin is forced downwards and as a result the very warm waters extends to a depth of up to 100 m (Figure 2.12).

While water is pushed westward in the direction of the winds directly at the equator, the easterly trade winds drive surface currents (in the top 10–50 m) that flow away from the equator in both hemispheres (Figure 2.11, top panel, blue arrows). This deviation of surface current direction from the prevailing wind direction is caused by the Coriolis effect, which is a consequence of the rotation of the Earth. These surface flows are termed Ekman currents. This causes a divergence of surface water away from the equator, draws sub-surface water to the surface in a process known as equatorial upwelling. A similar mechanism occurs adjacent to the South American continent. Here the south-easterly alongshore winds (in combination with the Coriolis effect) drive an offshore Ekman current that again causes coastal upwelling of deep water to the surface.

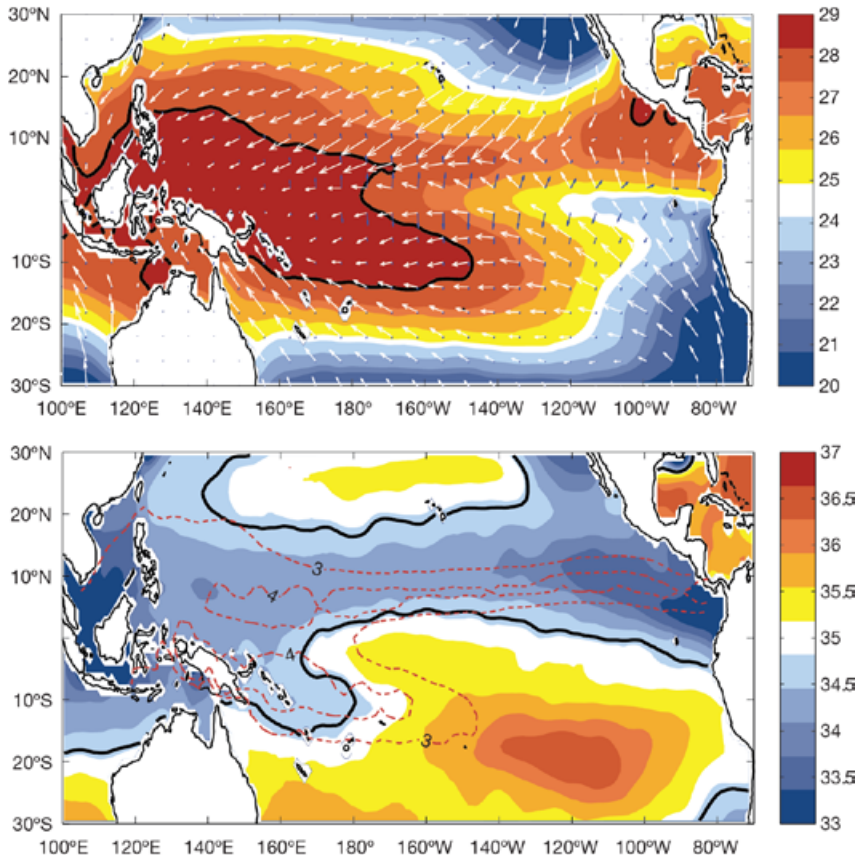

Figure 2.11: Long-term annual-average sea-surface temperature (˚C) (top) and sea-surface salinity (parts per thousand, ppt) (bottom) from the World Ocean Atlas 2005 Database. Thick black lines show the 28.5°C and 34.8 ppt contours, commonly used for the boundary of the Warm Pool. Also shown on the upper panel are the Quikcat wind stress vectors (white arrows) and surface Ekman currents (blue arrows, computed from windstress). Precipitation minus evaporation from ERA-40 reanalysis is shown on the lower panel (mm per day, red dashed contours). See text for explanations of these terms and Tables 2.2 and 2.3 for data sources.

The effect of the coastal and equatorial upwelling is that deeper, cooler and more nutrient-rich waters are pulled to the surface. This leaves a clear signature in the sea-surface temperatures with relatively cool water along the west coast of South America and along the equator in the eastern Pacific, known as the Equatorial Cold Tongue (Figure 2.11). While there is also equatorial upwelling in the western Pacific, because the Warm Pool extends to considerable depth, the upwelled water is still quite warm and does not produce surface cooling as it does in the eastern part of the Pacific basin.

2.6.2 Salinity and Nutrients

The pattern of sea-surface salinity (Figure 2.11) is strongly influenced by rainfall and evaporation patterns. In regions where rainfall exceeds evaporation (as it does in the tropical western Pacific), the salt concentration at the ocean surface is diluted, reducing salinity. The warm waters of the West Pacific Warm Pool and two bands of relatively warm water that straddle the equator centred near latitudes 10ºS and 7ºN (Figure 2.11) are the regions of high convective activity, surface wind convergence, and rainfall associated with the South Pacific and Intertropical Convergence Zones. As a result, they are also regions of relatively low surface salinity. The high rainfall over the Warm Pool relative to surrounding regions leads to the Warm Pool being bounded by a sharp salinity contrast (Maes et al., 2004).

In the tropical Pacific a large amount of heat and fresh water from rainfall enters the surface ocean and thus surface waters tend to be much warmer and fresher than sub-surface water. In the top few tens of metres of the ocean, strong vertical mixing occurs through the action of winds, waves and convective activity. This gives rise to a region where temperature and salinity, and therefore density, are well mixed and are almost constant with depth. This layer of the ocean is called the surface mixed layer.

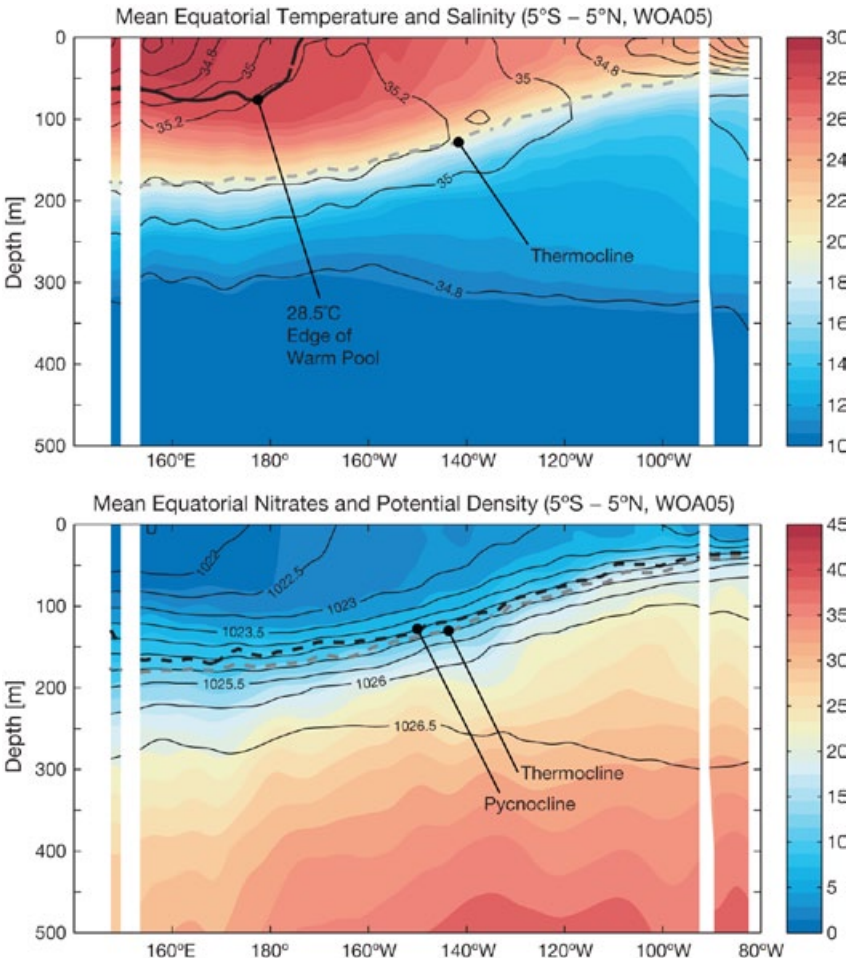

Figure 2.12: Ocean properties in the upper 500 m of the ocean near the equator. (Top) Average temperature (colours; °C) and salinity (line contours; parts per trillion) near the equator (5°S – 5°N). Superimposed are the Warm Pool location, commonly defined as temperatures greater than 28.5°C (black solid line), and the average thermocline depth (the depth of strongest vertical temperature change, grey dashed line). (Bottom) Average nitrate concentration (colours, micromoles per litre) and potential density (line contours, kg per cubic metre). Superimposed are average thermocline (grey dashed line) and pycnocline (the depth of strongest vertical density change, black dashed line) depths. Calculated from World Ocean Atlas 2005.

As noted, both temperature and salinity affect water density: warmer water is less dense than colder water, and fresher water is less dense than saltier water. As temperature decreases and salinity increases rapidly below the mixed layer, there is a sharp density increase below the mixed layer. The region of strongest vertical density change is called the pycnocline. The pycnocline separates an upper layer of relatively light (low density) water from the deep heavy (high density) water. The pycnocline acts as a barrier against mixing between the layers just as 'light' oil sitting on top of 'heavier' water is hard to mix together. The pycnocline gets shallower from west to east (Figure 2.12).

The depth at which the vertical temperature gradient is strongest is called the thermocline. Because density is determined to a large extent by temperature in tropical surface waters, the pycnocline and thermocline are at very similar depths over much of the ocean, and are commonly used to mean the same thing. An important exception occurs in regions of high rainfall (e.g. in the vicinity of the Warm

Pool and the convergence zones) where surface density is strongly reduced by the lower salinity, so the pycnocline sits at a shallower depth than the thermocline. This can have important consequences for interactions between the ocean and atmosphere.

This layering of ocean properties is known as stratification. Stratification strongly affects marine biological activity. Primary productivity (growth of marine plants/phytoplankton) only occurs in the surface ocean where sufficient light is available for photosynthesis. However photosynthesis and other metabolic activity require certain nutrients. The free nutrients are quickly consumed and depleted in the sun-lit (photic) surface ocean as a result of biological activity, but become much more abundant below these depths. This is because biological material falling downwards from the surface into the deep ocean is reprocessed by bacteria, releasing the locked up nutrients such as nitrate (Figure 2.12). Surface nutrients increase from west to east because of coastal and equatorial upwelling that supply the surface ocean with nutrient-rich colder water.

Ocean processes, such as the vertical currents associated with coastal and equatorial upwelling, work against the inherent ocean stratification and facilitate the transfer of deep nutrients up into the photic zone where they are used for biological production. Other processes that affect stratification include ocean mixing via strong winds or storms and convective activity, both of which can act to increase the depth of the mixed layer and entrain nutrient-rich deeper water. In the interior ocean, internal waves, often generated by tidal currents, move through the water and interact with the bottom of the ocean in shallow regions, causing vertical mixing. Ocean eddies (whirlpools of water that are many kilometres in diameter) are also important for mixing and are associated with strong vertical movement of water in their cores.

2.6.3 Ocean Currents

In addition to the Ekman currents that are confined to the first few tens of metres of the surface ocean, and the associated upwelling currents at the equator and along the South American coastline, there are a number of other important ocean currents in the Pacific Ocean (Figure 2.13). At higher latitudes the sub-tropical gyres (vast rotating masses of water extending downwards over a thousand metres) span the north and south extra-tropical regions. Their broad eastern equatorward flowing limbs extend across the central and eastern parts of the basin. In contrast, their western, poleward flowing limbs form narrow (100–200 km wide), fast flowing (sometimes exceeding 1 metre per second) jets (or western boundary currents) that hug the continental margins. The South Pacific western boundary current is the East Australian Current (EAC) (Figure 2.13). Its Northern Hemisphere counterpart is the Kurushio Current. The westward flow of the low-latitude limbs of the sub-tropical gyres extends across much of the tropical ocean in the form of the South and North Equatorial Currents in the Southern and Northern Hemispheres, respectively. The sub-tropical and tropical circulation is indirectly driven by the surface winds, in particular the south-east and north-east trade winds. Wind conditions are dramatically altered within the convergence zones, and as a result the prevailing westward currents of the South and North Equatorial Currents are interrupted in these areas. In fact, beneath the Intertropical Convergence Zone (Section 2.4.2) the prevailing current (the North Equatorial Counter Current) is reversed across most of the basin (Johnson et al., 2002). The corresponding current reversal beneath the less extensive South Pacific Convergence Zone (Section 2.4.1), the South Equatorial Counter Current, is confined to the western basin in the Southern Hemisphere (Gouriou and Toole, 1993).

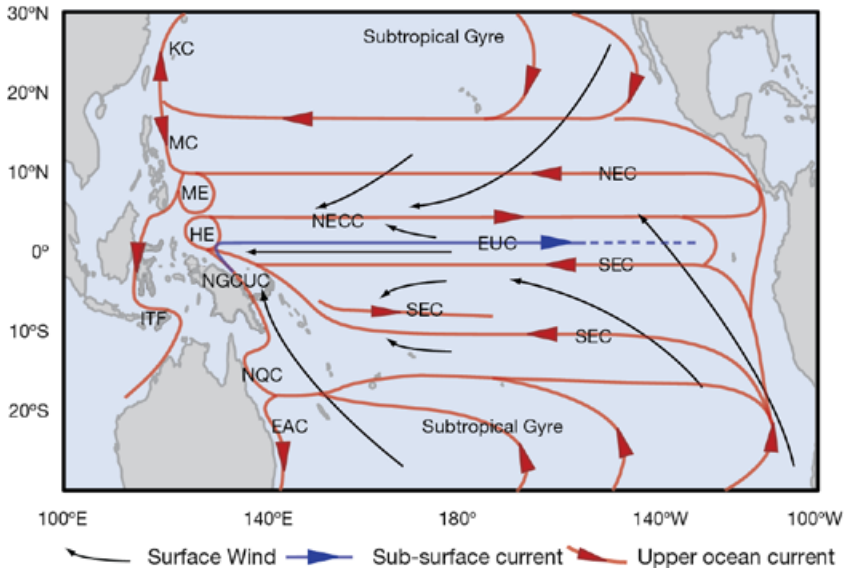

Figure 2.13: Schematic of upper ocean circulation and surface winds. Upper ocean currents range in depth from a less than 100 m to 2000–3000 m in the case of the sub-tropical gyres. Legend: East Australian Current (EAC); Equatorial Undercurrent (EUC); Halmahera Eddy (HE); Indonesian Throughflow (ITF); Kurushio Current (KC); Mindanao Eddy (ME); North Equatorial Current (NEC); North Equatorial Counter Current (NECC); New Guinea Coastal Current (NGCC); New Guinea Coastal Undercurrent (NGUC); North Queensland Current (NQC); South Equatorial Current (SEC); South Equatorial Counter Current (SECC); Modified from Tomczak and Godfrey (2003, Figure 8.6).

Water transported westward in the northern limb of the southern sub-tropical gyre divides at the Australian continental margin. Some of the water flows southwards as part of the East Australian Current, while the remainder flows northward as part of the North Queensland Current, and later the New Guinea Coastal Undercurrent. Water runoff from Papua New Guinea is thought to supply the New Guinea Coastal Undercurrent with high concentrations of dissolved iron (Mackey et al., 2002). At the equator this current feeds the Equatorial Undercurrent, a sub-surface current, which sits directly under the equator at a depth of more than 200 m in the west and about 50 m in the east. This narrow jet of water supplies the iron essential for biological productivity to the eastern Pacific.

In addition to the broad-scale circulations described, the ocean is densely populated with fine-scale currents that are associated with ocean eddies and fronts. Furthermore, as broad currents interact with the ocean floor or islands, they are deflected or channelled, forming local features including jets, island boundary currents and island eddies that have important biological implications. As the South Equatorial Current interacts with Vanuatu and New Caledonia, for example, the North and South Caledonia Jets and the North Vanuatu Jet are formed (Webb, 2000; Gourdeau et al., 2008; Ganachaud et al., 2008). In addition, high islands can also alter the strength and direction of the prevailing wind on the lee side, which can also drive local currents and upwelling.

2.6.4 Sea Level

The observed mean sea level for the period 1993–2002 derived from satellite altimeter, in situ measurements and a geoid model (Maximenko et al., 2009, data available from http://apdrc.soest.hawaii.edu/projects/DOT; Rio and Hernandez 2004, data available from http://www.aviso.oceanobs.com) reveals information about ocean currents as the upper ocean circulation approximately follows contours of constant sea-level height in the ocean interior (Figure 2.14). Along the equator, there is a strong zonal (east-to-west) sea-level slope, with sea level west of the International Date Line (180° longitude) about a half metre higher than that in the cold tongue region of the eastern equatorial Pacific and South American coastal regions. This zonal tilting of sea level on the equator is required to balance the trade winds pushing surface water westward. Higher sea level can also be found in the centres of sub-tropical gyres (about 20° to 40° N and S), with relatively strong (weak) zonal slope in the west (east), which is consistent with strong and narrow poleward western boundary currents and slow and wide equatorward return flow in the interior of the basin. There is a sea-level ridge around 5°N and a sea-level trough around 10°N, which is associated with the eastward-flowing North Equatorial Counter Current between these latitudes.

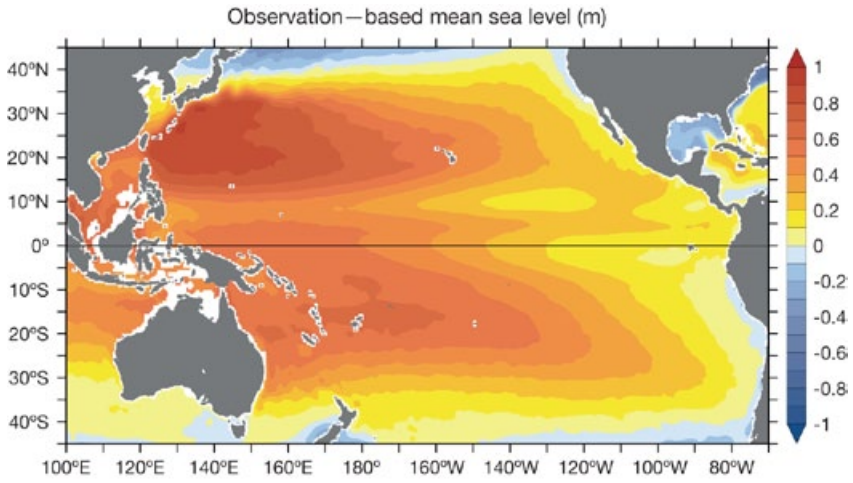

Figure 2.14: Mean sea level (in metres) from observations. The global mean has been removed. (From Maximenko et al., 2009).

2.7 Atmospheric and Oceanic Extremes

The seasons bring regular changes to climate in most Partner Countries. However, occasionally events occur that result in extreme rainfall, winds and temperatures, as well as flooding from storm surges and waves. The following sections describe the main short-term extremes that occur in the region. Year-to-year variability in extreme events, as well as the factors that cause this variability, are described in Chapter 3.

2.7.1 Tropical Cyclones

Each year, approximately 80 tropical cyclones form around the globe (Gray, 1979), with about one-third of them occurring in the Southern Hemisphere (Kuleshov, 2003). In the western North Pacific, about 30 tropical cyclones occur on average per year (Chan, 2005) which is more than for any other ocean basin in the world. Tropical cyclones dramatically affect maritime navigation and communities in many of the PCCSP Partner Countries and other island nations in the Pacific.

The Southern Hemisphere experiences most of its tropical cyclones during November-April, with a maximum in tropical cyclone frequencies during the January-March period when there is an average presence of one to two cyclones per day (Figure 2.15). On average about 2.2 cyclones are present on any given day in the Southern Hemisphere, with about 1 per day in the South Pacific around the end of February to the beginning of March. Very occasionally a cyclone may occur in the Southern Hemisphere on either side of the main cyclone season, in May and October.

The spatial distribution of the average number of tropical cyclones per year in the Southern Hemisphere (Figure 2.16) shows that the most tropical cyclones occur in the South Pacific in the area between the Australian coast and the International Date Line, from about 12°S to 22°S.

In the western North Pacific, the high number of tropical cyclones is due to the high frequency of favourable conditions for their development (Gray, 1979). For example, of all of the world's ocean basins, the western North Pacific has the highest

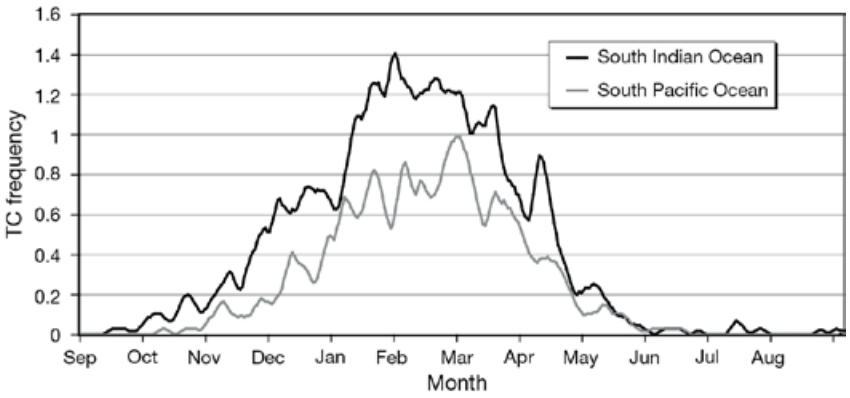

Figure 2.15: Seasonal profiles (1969/70–1998/99) of the average daily number of active tropical cyclones (TC) for the South Indian and the South Pacific Oceans (Source: Kuleshov, 2003).

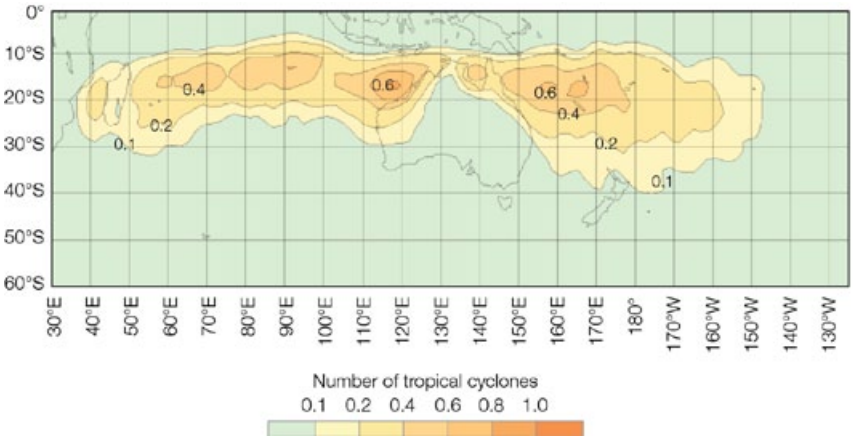

Figure 2.16: Average annual number of tropical cyclones per year in the Southern Hemisphere in an area 2° x 2° over the period, 1969/70 to 2005/06. Source: http://www.bom.gov.au/jsp/ncc/climate_averages/tropical-cyclones.

values of an index representing the potential for cyclone genesis (based on relative humidity, vertical wind shear, vorticity, sea-surface temperature and convective available potential energy; Camargo et al., 2007a). Cyclones in this region can form at any time throughout the year, with August having the highest frequency and January-March having the lowest frequency (Chan, 2005). There is also considerable interannual and inter-decadal variation in the number of tropical cyclones that occur in this region (Chan, 1985; Chan and Shi, 1996) and in the South Pacific (Callaghan and Power, 2010; Section 3.5.4). In the western North Pacific cyclones are referred to as typhoons.

2.7.2 Extreme Sea Levels

Extreme sea levels can cause significant coastal impacts, including inundation of low-lying coastal terrain, erosion of beaches, ecosystem loss, damage or destruction of coastal infrastructure, damage to crops and water supplies, and injury or loss of life. They are caused by a combination of three components: tides; seasonal or longer-term fluctuations due to changing wind, pressure and ocean temperature patterns such as ENSO; and short-term events due to weather, such as storm surge, ocean waves and tsunamis. Although tsunamis can cause the most devastating extreme sea-level events, they are not affected by climate and so will not be discussed further here. The contributions of tides, storm surge and ocean waves to sea-level extremes are illustrated in Figure 2.17. The forces that influence these different components of extreme sea level vary and will be discussed in turn in this section.

Astronomical tides are predictable events that are caused by the gravitational forces that arise from the movement of the Moon, Sun and other planetary bodies relative to the Earth. These motions cause the daily rise and fall of waters and the monthly variation in tidal heights (spring and neap tides; Figure 2.18a). In addition to variations on monthly time scales, there is also yearly variation in tidal heights, such that the highest spring tides tend to occur around the same time each year. Although the motions of the sun and moon cause different tides in different locations and no two years, even at the same location, are exactly the same, in most case the highest tides each year tend to occur either when the sun and the moon are closest to the equator (at the equinoxes, in March and October; Figure 2.18b) or when the declination of the sun is at its greatest (at the solstices, in December and June).

As discussed in detail in Chapter 3 (Section 3.6.3.2), ENSO has a major influence on sea levels across the Pacific and this can influence the occurrence of extreme sea levels. During La Niña events, strengthened trade winds cause higher than normal sea levels in the western tropical Pacific, and lower than normal levels in the east. Conversely, during El Niño events, weakened trade winds are unable to maintain the normal gradient of sea level across the tropical Pacific, leading to a drop in sea level in the west and a rise in the east. Pacific islands within about 10° of the equator are most strongly affected by ENSO-related sea-level variations.

Tropical cyclones can cause severe short-term sea-level extremes in the Pacific due to storm surges and/or ocean waves. Falling atmospheric pressures associated with cyclones draw the ocean surface upwards at a rate of 1 cm for each hPa drop in pressure, and onshore winds can build up water levels against the coast (wind setup). While cyclone intensity (measured by the minimum central pressure or maximum wind speed) strongly influences the severity of waves and storm surge, other tropical cyclone attributes such as size, direction and speed of movement also play an important role, as does the geomorphology of the coast itself.

Tropical cyclone-induced storm surges tend to be localised, and concentrated in the region of maximum onshore winds close to the cyclone centre. Whilst their impacts are potentially devastating, they are rare at any given location. On the other hand, ocean waves produced by such systems can propagate long distances in the deep ocean as swell, with little loss of energy, and can therefore impact a larger number of more distant coastlines. As the waves encounter shallow coastal waters, they steepen and break, progressively losing energy and producing an increase in coastal sea levels known as wave setup. Atolls with steep shelf margins may be particularly affected by remotely generated swell causing wave setup in lagoons, thereby contributing to sea-level extremes (Callaghan et al., 2006). As a wave breaks at the coast the maximum vertical extent of the wave uprush on a beach or structure above the still water level is known as wave runup (Figure 2.17).

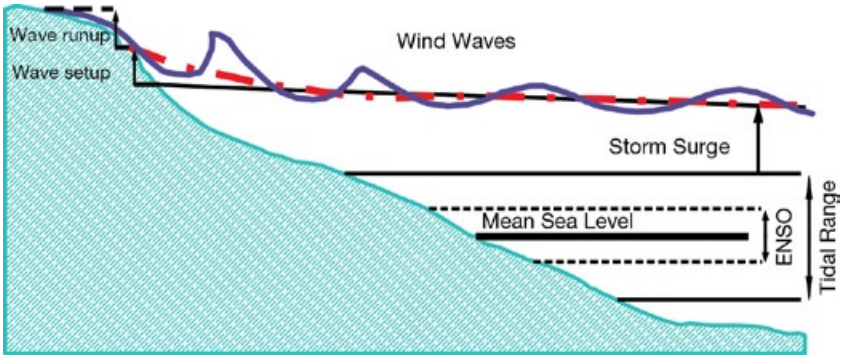

Figure 2.17: Diagram illustrating the contributions to sea-level extremes due to tides, ENSO, storm surge and wind-generated waves. The maximum sea level from the first three of these contributions is given by the thin black line at the top. Also shown are wave height (blue line) and wave set-up (red line).

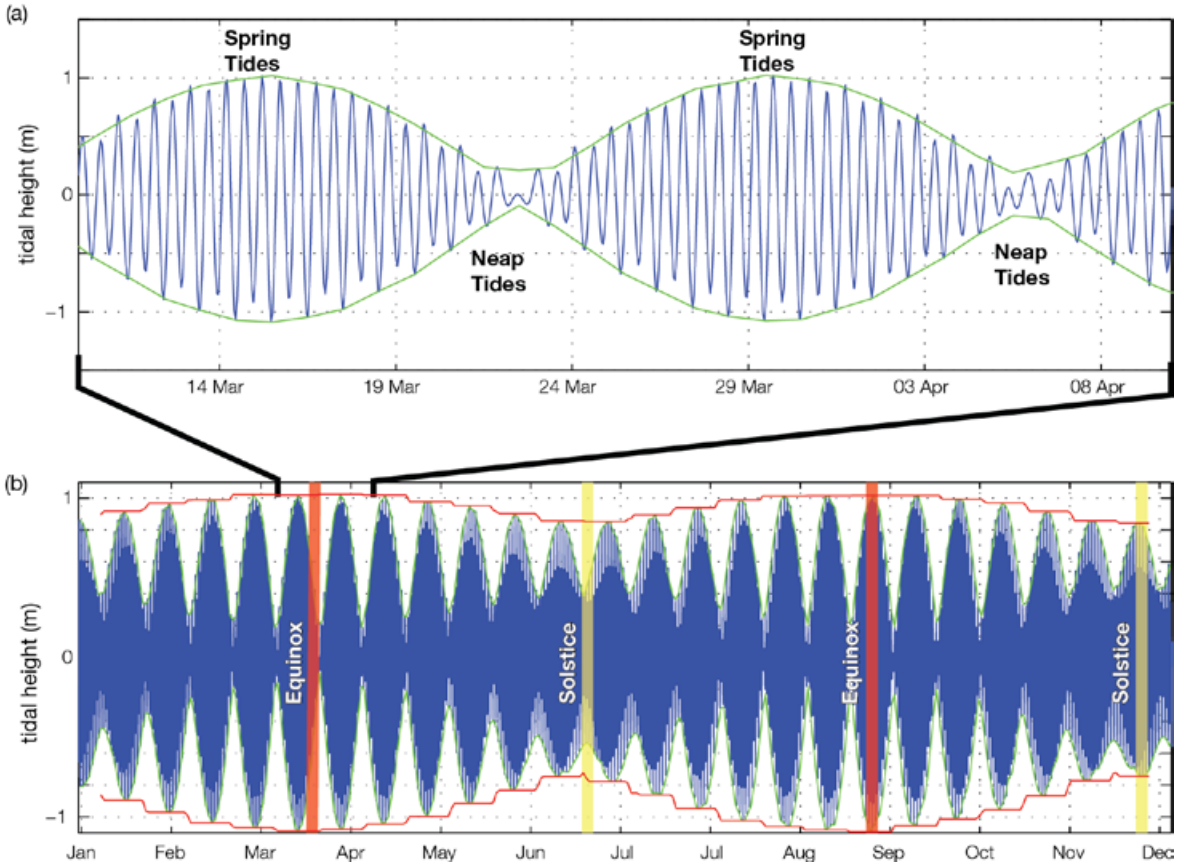

Figure 2.18: A tidal prediction for Tarawa, Kiribati using the five largest astronomic constituents to illustrate (a) spring and neap tides and (b) the semi-annual range in tides; (a) is over a one-month period centered on the March 2006 equinox, indicating times of spring and neap tides and (b) shows the entire year of 2006, indicating the times of the equinoxes and the solstices. In (a) and (b) the green lines indicate the maximum daily tidal range envelope and in (b) the red lines indicate the maximum fortnightly (two-week) tidal range.

The coastal impacts resulting from the cyclone-induced storm surges and waves are also a function of various coastal attributes, such as the shape of the sea bed (bathymetry), the shape of the coastline in relation to the cyclone path, and the landform (geomorphology). Wide and shallow continental shelves amplify the storm surge while bays and channels can funnel and increase the storm surge height. The presence of reefs will cause waves to break and lose energy before they reach coastal areas.

In summary, while weather events such as tropical cyclones may cause short-term sea-level extremes due to storm surges and/or high waves, it should be noted that the impacts of these events can be strongly moderated by other factors such as tides, seasonal variations in sea level and ENSO (Figure 2.17). The tidal range can experience large variations throughout the year so that the potential for a short-term extreme event coinciding with higher than normal background sea level is greater in some months in the year compared to others. Seasonal variations in sea level arise in some locations from variations in atmospheric circulation patterns and/or ocean currents. On interannual time scales, ENSO variability can affect both the weather events that cause short-term sea-level extremes and the background mean sea level (Chapter 3). The relative roles of these factors are investigated for PCCSP countries in Volume 2.

Coral reef, Funafuti, Tuvalu

Chapter 3
Observed Climate Variability and Trends

Summary

The IPCC Fourth Assessment Report (Hergerl et al., 2007) concluded that "anthropogenic warming of the climate system can be detected in temperature observations taken at the surface, in the troposphere and in the oceans", and that "greenhouse gas forcing has very likely caused most of the observed global warming over the last 50 years".

Studies also show that zonal average warming in the tropics and sub-tropics over the period 1901–2005 (Hergerl et al., 2007) is not reproduced in climate models with natural variability alone, but can be reproduced in climate models that include anthropogenic forcing incorporating increases in greenhouse gases.

- Collectively, the observed climate record of the PCCSP region indicates a climate in transition, driven by both natural and human influences.
- Palaeoclimate records indicate the Pacific is characterised by climate variability on a wide variety of time scales. Changes in the frequency and intensity of El Niño-Southern Oscillation (ENSO) activity over the past 12 000 years have been linked to widespread changes in climate impacts.
- Natural climate oscillations, e.g. ENSO, the Pacific Decadal Oscillation (PDO), the Interdecadal Pacific Oscillation (IPO), Southern Annular Mode (SAM), the Indian Ocean Dipole (IOD), and fluctuations in the key climatological features of the region (Intertropical Convergence Zone (ITCZ), South Pacific Convergence Zone (SPCZ), and West Pacific Monsoon (WPM)) are responsible for much of the variability in the atmosphere and ocean on seasonal to multi-decadal timescales.
- Temperature records from Pacific Island observation stations show a clear signal of warming over the past 50 years, with most stations warming at a rate between +0.08 and +0.20°C per decade over this time, consistent with global trends.
- Rainfall across the region has increased and decreased in response to natural climate variability. Over the past 50 years, rainfall totals increased to the north-east of the SPCZ, and declined to the south.
- There are no significant trends in the overall number of tropical cyclones, or in the number of intense tropical cyclones, in the South Pacific Ocean over the period 1981–2007. The number of severe tropical cyclones making landfall over eastern Australia has declined since the late 19th century, though this result is significant at the 90% level only.
- Sea-surface temperatures in the region have generally warmed since 1950. This warming has been partially attributed to increases in the concentration of greenhouse gases. However, temperature variations associated with the IPO/PDO also substantially influence the background trend.
- The western tropical Pacific Ocean has become significantly less salty over recent decades. Conversely, regions to the east have generally become saltier. Together, these changes suggest an intensification of the hydrological cycle.
- A distinctive pattern of intensified surface warming and sub-surface cooling, centred near a depth of 200 m is evident over the past 50 years in the Pacific Ocean. Climate models suggest this pattern is consistent with human-induced change.
- The Hadley Circulation has expanded poleward and the Walker Circulation has weakened. The weakening of the Walker Circulation over the past century is due to a combination of both natural changes and human-induced change.
- Sea level has risen globally and in the PCCSP region over recent decades. Extreme sea levels are also increasing, primarily as a result of increases in mean sea level.
- There is significant interannual variability of sea level in the region related to the ENSO cycle. Consequently, the pattern of trends in the altimeter record (since the start of satellite measurements in 1993) is not representative of longer-term trends.
- The acidity level of surface ocean waters is increasing (i.e. pH is reducing) due to the increased uptake of carbon dioxide due to the higher atmospheric concentrations that have resulted from human activities.

Anecdotally, people in the region are reporting climate change impacts, including more salt-water intrusions, changes in seasonal climate cycles, and more frequent occurrence of drought, fires, mudslides and coral bleaching (Box 3.1). However, little research has been conducted to quantify the relative importance of human-induced change and natural variability as causes of the observed trends in the PCCSP region.

3.1 Introduction

Climate variability in the PCCSP region occurs on interannual, decadal, centennial and longer time scales. Palaeoclimate records indicate that during the millennia before the Industrial Revolution (around 1750), the climate of the Pacific underwent large variations, primarily associated with changes in the intensity and frequency of the El Niño-Southern Oscillation (ENSO) (Cobb et al., 2003; Gergis and Fowler, 2009). However, in the past climate shifts were driven by natural mechanisms; it is now likely that they are also being driven by human influences (Trenberth et al., 2007).

The current way of life in the PCCSP region is based on the patterns of climate experienced over the past few centuries. The flora and fauna of the region have evolved within the climatic bounds exhibited over much longer time scales. If the mean climate shifts beyond these bounds, or changes more rapidly than seen before, many aspects of life may change. Many Pacific Islanders believe they have already seen the impacts of climate change (Box 3.1). Consequently, it is important to understand the range of climate variability experienced in the past in order to provide a context in which to interpret projections of future climate change. Understanding past variability also contributes to assessing the likely causes of climate change (discussed in Chapter 4).

This chapter summarises previous studies of observed climate variability and change in the region and describes the contributions made to this understanding by the PCCSP. The assessment of observed climate variability and change presented here is based on updated and improved meteorological and oceanographic datasets. This 'data rehabilitation' has involved significant collaboration with Partner Countries and resulted in improved data access and security, and enhanced scientific and technical capacity in the region. It is hoped that the increased knowledge and tools developed by the PCCSP will lead to improvements in the way Partner Countries manage and analyse the observational data required to detect and document climate variability and change in their respective countries.

3.2 Global Context

The evidence for global climate change is broad and compelling (Trenberth et al., 2007). Global mean surface air temperature, as determined by the HadCRUT3v global gridded dataset (Brohan et al., 2006) is estimated to have increased by 0.74°C from 1910–2010, with a trend of around 0.14°C per decade over the past 50 years (Figure 3.1). Global warming is confirmed by natural indicators such as melting glaciers and sea-ice, sea-level rise, earlier flowering and ripening dates, longer growing seasons, coral bleaching and poleward migration of plants and animals (Rosenzweig et al., 2007).

Further evidence of changes in the global climate comes from palaeoclimatic records reconstructed from sources such as ice cores, tree rings and corals. When modern instrumental temperature records are placed in the context of reconstructed temperature records over the past 2000 years, it is apparent that the Northern Hemisphere (where sufficient palaeoclimate records exist) is currently experiencing a rapid and unusual warming (Mann et al., 2009).

A lack of data makes it difficult to reconstruct a similar long record for the Southern Hemisphere. However, global datasets based on instrumental records clearly indicate that the PCCSP region has also warmed significantly since the early 20th century (Figure 3.1). Most of the region's warmest years in the instrumental record have occurred over the past two decades. The rate of warming in the PCCSP region appears to be slightly less than the global mean, with an increase of 0.60°C over the past century and a trend of 0.10°C per decade over the past 50 years (based on HadCRUT3v dataset; Brohan et al., 2006). The regional rate of increase is lower than the global rate because the region is dominated by ocean, and ocean temperatures are known to be increasing more slowly than land temperatures. Warming across the PCCSP region has not been uniform, with some datasets suggesting that data-sparse parts of the central equatorial Pacific have actually cooled over the past 50 years (Figure 3.2). It is unclear whether this cooling is real or an artefact of the analysis technique.

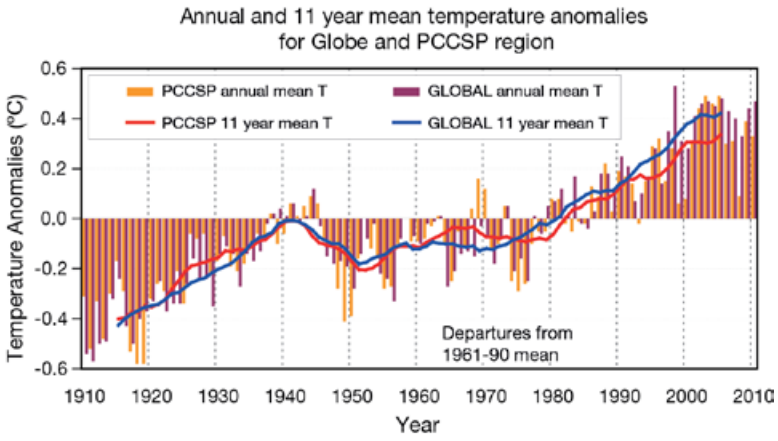

Figure 3.1: Annual mean surface air temperature anomalies from 1910–2010 for the globe and PCCSP region (120°E–210°E; 25°S–20°N), relative to the 1961–1990 mean. Solid lines indicate 11-year running means. (Based on HadCRUT3v dataset: Brohan et al., 2006).

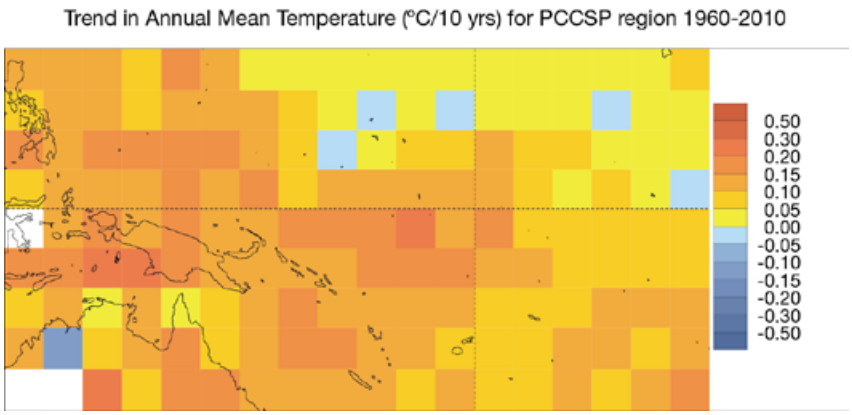

Figure 3.2: Trend in annual mean temperature (°C per decade) over 1960–2010, as determined by the HadCRUT3v global gridded temperature dataset (Brohan et al., 2006).

Box 3.1: Local Perceptions of a Changing Climate

There is general agreement amongst the communities of the Pacific Islands and East Timor that changes in weather and climate are occurring in their region. More change is believed to have occurred over the past decade than at any other time in human memory. Partner Country representatives have described local perceptions of climate change in their countries. These include:

- Shifts in seasonal patterns of rainfall and tropical cyclones.
- More frequent and extreme rainfall causing flooding and mudslides.
- More drought and fires.
- More hot days.
- Lower crop productivity.
- Spread of weeds, pest and diseases.
- More coral bleaching.
- More storm surges, coastal erosion and salt water contamination of freshwater springs and taro swamps.

Partner Country representatives have also reported that many Pacific Islanders believe that the impacts of climate change are being exacerbated by increased population and development, poor waste management and land degradation. Also, perceptions of vulnerability to climate change appear to differ between age, gender, religion, and socio-economic groups, with some studies indicating that urban and wealthier people generally feel less vulnerable to the impacts of climate change (Wongbusarakum, 2009).

While some of the climate changes noted by Pacific Island people are consistent with anthropogenic global warming, human memory can be quite subjective regarding extreme weather and climate events. It is also difficult to scientifically confirm many of these changes due to a lack of sufficient data, highlighting the need for improved observation networks in the region. Detection and attribution of climate changes in the Pacific is further complicated by large changes in ENSO activity over the past century (Power and Smith, 2007). Consequently, it can be difficult to distinguish between natural interdecadal changes and those due to anthropogenic climate change, particularly at the local scale.

Some regional-scale changes in the Pacific have been partly attributed to human activities, e.g. weakening of the Walker Circulation (Power and Kociuba, 2011), and warming in the Pacific mean surface temperature (Stott et al., 2010). However, little research has been conducted to determine whether the changes perceived by people in the islands are real, and if so, to quantify the relative contributions from human and natural climate influences. The PCCSP represents a coordinated effort to begin to address these knowledge gaps.

Participants from PCCSP Partner Countries and other countries came together at a PCCSP workshop in June 2010 to discuss perceptions of climate change in their countries.

3.3 Climate of the Pacific over the Past 12 000 Years

3.3.1 Changes in Climate over the Holocene

The period from approximately 12 000 years ago to the present is known as the Holocene. It was preceded by a cold, glacial period that peaked around 21 000 years ago at the Last Glacial Maximum. Global average sea level at that time was around 120 m lower than that of today, due to the vast amounts of water that were locked up in expanded (Northern Hemisphere) ice sheets. The climate of the Holocene has been relatively warm and stable, allowing humans to develop agriculture and permanent settlements. People migrated across much of the Pacific Basin during this time (Nunn, 2007), with significant societal changes possibly linked to ENSO-driven environmental variability (Allen, 2006) and long-distance travel potentially assisted by reversals in the direction of the trade winds during El Niño events (Anderson et al., 2006).

There have been a number of large-scale changes in Pacific climate during the Holocene. Evidence from marine sediment records suggests that the Intertropical Convergence Zone (ITCZ) was located further north during the early Holocene (Haug et al., 2001), which may have led to drier and more saline conditions in the West Pacific Warm Pool (Stott et al., 2004). The ITCZ is thought to have moved in response to shifts in seasonal solar radiation caused by changes in the Earth's orbit, with the changing position of the ITCZ driving variations in both the location and extent of the Indo-Pacific Warm Pool (Abram et al., 2009). The Asian monsoon is thought to have been stronger around 10 000 years ago and gradually weakened in response to the change in seasonal solar radiation (Wang et al., 2005). Lake level records from northern Australia suggest the Australian monsoon was stronger in the early Holocene (Wyrwoll and Miller, 2001). Stalagmites from Indonesia also suggest an increase in monsoon rainfall around 11 000 to 7000 years ago in association with rising global sea levels at this time (Griffiths et al., 2009).

During the past 10 000 years, ENSO variability is believed to have increased to its modern strength from a relatively weak level in the early Holocene (Tudhope et al., 2001). Proxy ENSO measures, such as charcoal evidence from northern Australia (Gagan et al., 2004); coral records (McGregor and Gagan, 2004); lake sediment records from Ecuador (Rodbell et al., 1999); and pollen records from northern Australia (Shulmeister and Lees, 1995), suggest that ENSO became stronger around 5000 years ago, with some evidence of a peak in activity around 2000 years ago (Woodroffe et al., 2003).

These changes would have had widespread impacts across the Pacific region, with likely increases in the frequency of extreme events such as droughts, floods, fires and tropical cyclones. Climate models suggest that the changes in ENSO activity during the Holocene were driven by changes in the seasonal incoming solar radiation associated with the precessional cycle of Earth's orbit (Brown et al., 2008; Phipps and Brown, 2010).

In New Zealand, the extent of Southern Alps ice has largely decreased over the Holocene (Schaefer et al., 2009), despite evidence that ice margin fluctuations and glacier re-advance episodes were numerous in the mid-to-late Holocene. Regional circulation dictates Southern Alps glacial activity and helps to modulate Southern Alps ice volume through changing precipitation and temperature regimes. Thus, ENSO, the Southern Annular Mode (Kidston et al., 2009; Ummenhofer et al., 2009), as well as the Interdecadal Pacific Oscillation, have probably combined to cause the glaciers to advance and retreat (Lorrey et al., 2010; 2011). Some of the past ice advances during the late Holocene occurred during Northern Hemisphere warm periods, indicating that Northern and Southern Hemisphere temperature changes have not always been in phase.

3.3.2 Changes in Climate over the Past 1000 Years

Variations in the global climate over the 1000-year period preceding the Industrial Revolution were driven by natural internal processes (e.g. ENSO) and natural external forcing factors (e.g. variations in solar output and stratospheric aerosols associated with major volcanic eruptions). Northern Hemisphere temperature reconstructions have identified a period of relatively warm temperatures (the Medieval Warm Period or Medieval Climate Anomaly) and a cooler period (the Little Ice Age). It is not clear if the Pacific region experienced the same climate variability (cf. Jansen et al., 2007).

The Medieval Climate Anomaly occurred around 1000–1300 A.D., and was associated with relatively high solar irradiance and low tropical volcanism. The warming found in reconstructions of Northern Hemisphere climate may not necessarily have been global. For example, a reconstruction using over 1000 different proxy records shows regions of both warming and cooling, with evidence for cool tropical eastern Pacific sea-surface temperatures (Mann et al., 2009). An 1100 year tree ring record from New Zealand (Cook et al., 2002) implies the local climate was around 0.3 to 0.5°C warmer than the 20th century mean during the period 1000–1300 A.D., while a coral record from Palmyra, in the central Pacific, indicates local temperatures may have been cooler than present at the time of the Medieval Climate Anomaly (Cobb et al., 2003).

A synoptic palaeoclimate approach (Lorrey et al., 2007) was used to reconstruct atmospheric circulation patterns over New Zealand from a network of proxy records. While the late Holocene circulation has been variable (Lorrey et al., 2008), the frequency of blocking (stagnant) pressure patterns over the south-west Pacific increased during the Medieval Climate Anomaly (Lorrey et al., 2011), and has a different signature than the Northern Hemisphere.

The Northern Hemisphere Little Ice Age (ca. 1400–1850 A.D.) was associated with reduced solar irradiance and increased volcanic activity. Again, there is some evidence that the Little Ice Age was not experienced globally. For example, the Palmyra coral record (Cobb et al., 2003) suggests that the central tropical Pacific was relatively warm at that time.

The Palmyra coral record also provides information about changes in ENSO over the past 1100 years. The record suggests that during the mid-17th century ENSO events were stronger and more frequent than modern events, whereas during periods in the 12th and 14th centuries, ENSO activity was greatly reduced (Cobb et al., 2003). A tree ring reconstruction of ENSO over a six century period using North American tree ring records (D'Arrigo et al., 2005) found reduced ENSO amplitude in the late 17th to 18th centuries. Reconstructions based on multiple climate proxies have also shown that ENSO activity during the 20th century was unusual in that a high proportion of extreme and protracted El Niño and La Niña events occurred during this time (Gergis and Fowler 2009; McGregor et al., 2010). The Palmyra coral record implies that changes in ENSO over the last millennium may have arisen from natural internal variability (Cobb et al., 2003).

3.4 Major Features of Climate Variability

3.4.1 El Niño-Southern Oscillation and the Walker Circulation

ENSO is a major feature of interannual (year-to-year) climate variability in the Pacific. ENSO is a natural cycle of the climate system, characterised by distinct patterns of change in winds, surface pressure, surface and sub-surface ocean temperatures, precipitation, cloudiness and convection across the tropical Pacific. Consequently, ENSO has a powerful influence on the climate of the region. All PCCSP Partner Countries are affected by ENSO in some way, although the magnitude and timing of this influence varies between countries.

The ENSO cycle is irregular, and most of its variability has periods of two to seven years. The two extreme phases of the ENSO cycle are El Niño and La Niña. An El Niño is characterised by warming of waters in the central and eastern Pacific Ocean and cooling in a 'horse-shoe' pattern in the western Pacific Ocean, extending to the north-east and south-west (Figure 3.3a). This is known as the 'canonical' El Niño pattern and results in a reduction in the east to west sea-surface temperature gradient, which drives the Walker Circulation. Consequently, the surface trade winds forming the lower branch of the Walker Circulation weaken during El Niño. This reduces the east to west sea-surface temperature difference, so the winds weaken further still. This completes a positive or self-reinforcing feedback loop. The existence of this feedback loop helps to make the tropical climate system unstable and this instability is partially responsible for the existence of ENSO. These changes in the atmosphere and ocean during El Niño also result in a displacement of the main area of convection from the western Pacific to east of the International Date Line. Opposite changes tend to occur during La Niña events, i.e. the central and eastern Pacific cools, trade winds strengthen and the main area of convection intensifies and moves further west than normal.

There are no universally agreed criteria to define El Niño or La Niña years. However, approximately one quarter of all years are usually defined as El Niño years, approximately one quarter as La Niña years and approximately one half as neutral years in which the anomalies described above are not apparent (Power and Smith, 2007).

El Niño and La Niña events usually begin to develop around May or June and last until the following March-May. However, while such events tend to follow a typical pattern of development, the strength and timing of each event is different, as is the exact pattern of sea-surface temperature, wind and convection changes, and hence impacts.

A variation on the traditional canonical sea-surface temperature pattern of El Niño events involves the maximum warming occurring in the central tropical Pacific, rather than in the east (Figure 3.3b). This modified pattern is known as a 'central Pacific El Niño', or an 'El Niño Modoki' (Ashok and Yamagata, 2009). Whereas a canonical El Niño has anomalous ascending air over a large area covering the central to eastern Pacific overlying warmer sea-surface temperatures, during an El Niño Modoki the ascending branch occurs only in the central Pacific. El Niño Modoki is associated with distinct climate impacts compared to canonical El Niño events (Kumar et al., 2006; Wang and Hendon, 2007; Ashok et al., 2007; Weng et al., 2007; Taschetto and England, 2009). For example, in some seasons the impacts over regions such as New Zealand and the western coast of United States are opposite to those of a canonical El Niño.

ENSO is associated with large rainfall variations in many Partner Countries (Figure 3.4). Generally, countries east of about longitude 160ºE and close to the equator experience above-average rainfall during an El Niño, while other countries, those west of longitude 160ºE or more than about 10º from the equator, experience drier than

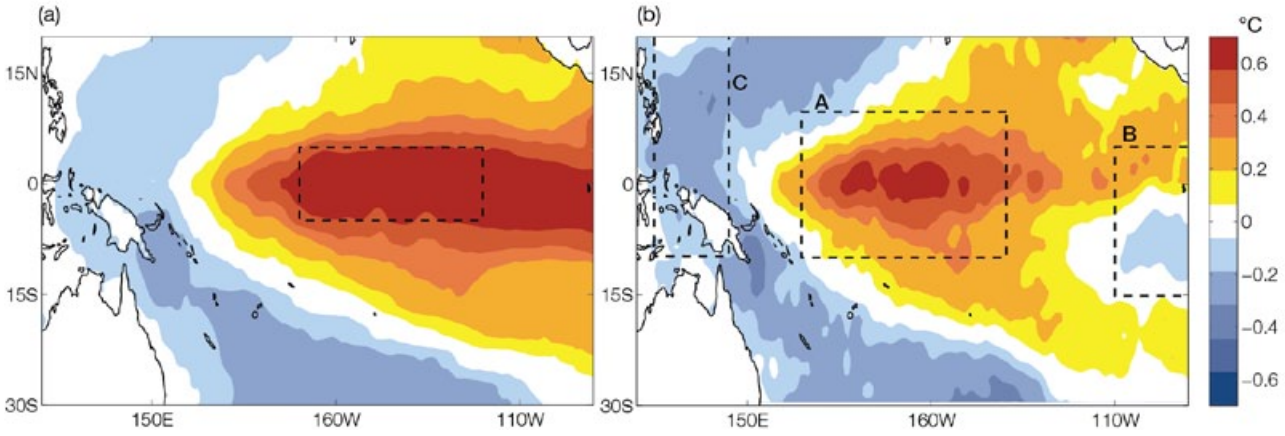

Figure 3.3: Sea-surface temperature anomalies (differences from average conditions) associated with (a) Canonical El Niño and (b) El Niño Modoki. (Source: Andrea Taschetto). Boxes show areas over which the (a) NINO 3.4 and (b) El Niño Modoki indices are calculated.

normal conditions. For most countries the average response in wet season rainfall is in the same direction for both canonical and El Niño Modoki events (Figure 3.4). However, in some places the response is weaker for El Niño Modoki, particularly for Partner Countries furthest to the south-east. Two exceptions are Nauru and Tarawa (Kirabati), due to these sites lying close to the centre of the largest sea-surface temperature anomalies that occur in Modoki events, and hence the greater response for El Niño Modoki.

ENSO is also associated with large year-to-year changes in the risks of drought, flood, tropical cyclones and coral bleaching throughout the region. Consequently, ENSO has significant impacts on agriculture, ecosystems, water resources, emergency management and disease (Philander, 1990, 2006; Power and Smith, 2007).

Numerous measures are used to monitor the status of ENSO. The Southern Oscillation Index (SOI) is an important example (Figure 3.5a). The SOI is calculated using the barometric pressure difference between Tahiti and Darwin, and is used as an indicator of the strength of the equatorial Walker Circulation and the Pacific trade winds (Power and Kociuba, 2010). A strong, persistently negative SOI is typical of El Niño conditions, while a strong and persistently positive SOI is indicative of La Niña.

Being a coupled ocean-atmosphere phenomenon, several measures of sea-surface temperature are used in conjunction with the SOI to monitor the oceanic component of ENSO. The Niño3.4 index (Figure 3.5b) measures the sea-surface temperature anomaly in the central and eastern Pacific between 170°W to 120°W and 5°S to 5°N (See Figure 3.3a). A strong, persistently positive Niño3.4 index (i.e. a warm central Pacific sea-surface temperature) corresponds to an El Niño event. Niño3.4 and the SOI are almost mirror images of each other, demonstrating the strong coupling between ocean and atmospheric changes.

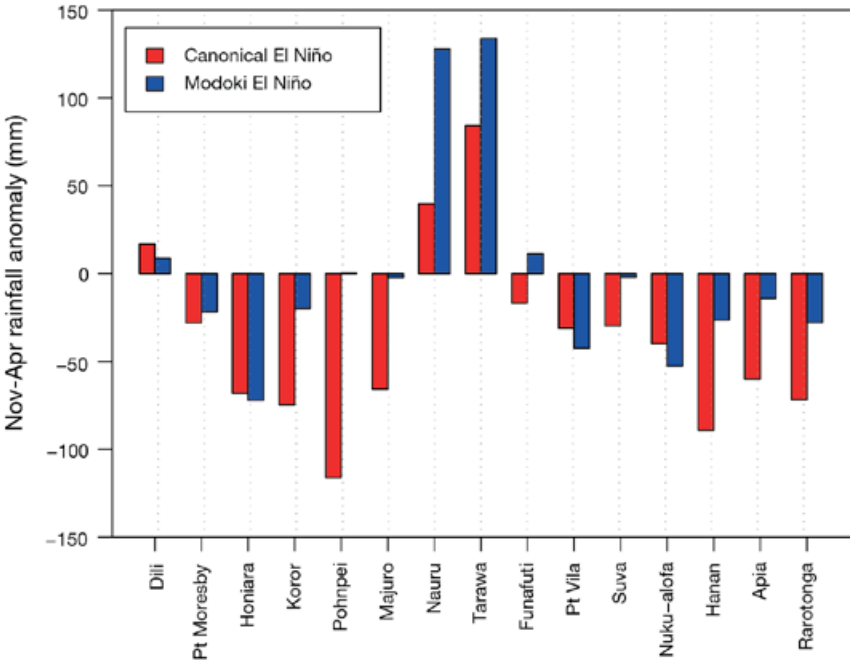

Figure 3.4: For sites in each Partner Country, differences between normal November to April rainfall and average rainfall during (red) Canonical El Niño events (years 1965, 1972, 1977, 1982, 1997, 2006, 2009) and (blue) Modoki El Niño events (years 1986, 1990, 1991, 1992, 1994, 2002, 2004).

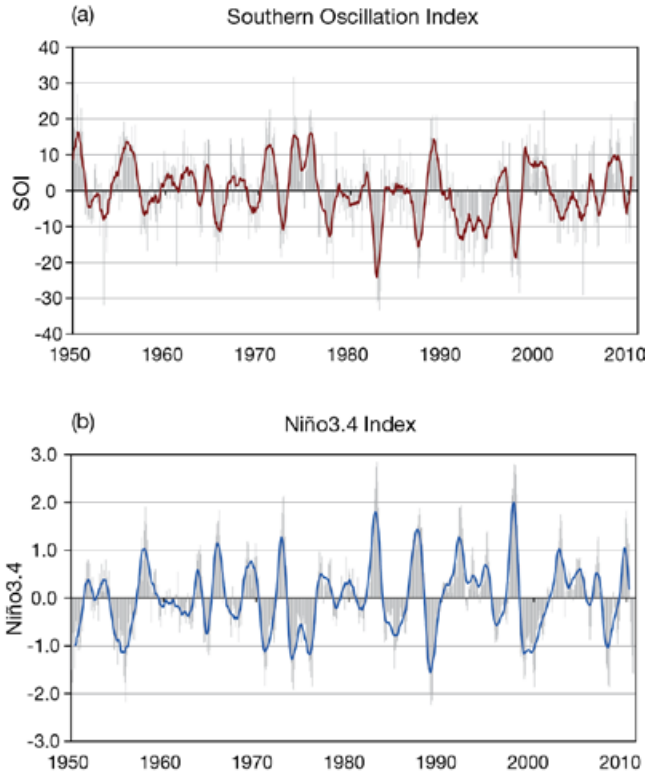

Figure 3.5: Monthly (a) SOI and (b) Niño3.4 values since 1950. Curves denote 12-month moving averages. (Source: SOI: http://www.bom.gov.au/climate/current/soihtm1.shtml; Niño3.4: ftp.cpc.ncep.noaa.gov/wd52dg/data/indices/sstoi.indices).

El Niño Modoki is measured by an El Niño Modoki Index (Ashok et al. 2007). Like the Niño3.4 index, it is calculated from average sea-surface temperature anomalies, but over three boxes: A: 165ºE–140ºW, 10ºS–10ºN; B: 110ºW–70ºW, 15ºS–5ºN; and C: 125º-145ºE, 10ºS–20ºN, so that this index is equal to A – 0.5*B – 0.5*C (See Figure 3.3b). Consequently, the index measures sea-surface temperature variations in the central equatorial Pacific Ocean against out-of-phase variations in the far eastern and far western Pacific Ocean.

Since the late 1970s the Modoki form of El Niño has become more frequent than the traditional El Niño (Ashok et al., 2007; Lee and McPhaden, 2010), with some scientists hypothesising that this might be related to anthropogenic global warming (Yeh et al., 2009). If so, this would suggest that this form of El Niño may become the dominant type in future.

In the past 100 years there have been interdecadal phases of strong and weak ENSO related to decadal variability from natural causes (Power et al. 2006; Collins et al. 2010). Along with the warming of the tropical Pacific in recent decades, there appears to have been a weakening of the Walker Circulation (Tanaka et al., 2004; Vecchi et al., 2006; Power and Smith, 2007; Collins et al., 2010; Power and Kociuba, 2010, in press). Theoretical arguments (Held and Soden, 2006) and model experiments (Vecchi et al., 2006) suggest that these changes are partly due to anthropogenic global warming. However, the changes can also be partially attributed to an increase in the frequency of El Niño events and a decrease in the frequency of La Niña events since 1975 (Fedorov and Philander, 2000; Power and Kociuba, 2010). Therefore the observed weakening of the Walker Circulation appears to have been driven both by global warming and random changes in the frequency of ENSO events.

Power and Kocuiba (in press) examined the weakening of the Walker Circulation in response to internally generated natural variability and external climate forcing by examining simulations from global climate models with different natural and anthropogenic forcing. Internally generated natural variability is variability arising from instabilities in the atmosphere-ocean system such as ENSO and the Interdecadal Pacific Oscillation. External forcing is the term climate scientists use to cover forcing due to anthropogenic changes in greenhouse gases and aerosols, and forcing arising from natural changes in insolation (solar radiation) and volcanic activity. Most of the response to external forcing over the 20th century typically comes from the anthropogenic forcing. Power and Kociuba (in press) concluded that both internally generated natural variability and external forcing is needed to explain the observed 20th century weakening of the Walker Circulation, and that the magnitude of weakening caused by external forcing is similar to that of natural climate variability. This highlights the fact that trends in the region will typically have both an anthropogenic and a natural contribution.

3.4.2 Pacific Decadal Oscillation and Interdecadal Pacific Oscillation

Climate in and around the Pacific Ocean varies substantially on decadal time scales (Power et al., 1999a,b; Mann et al., 2000; Hasegawa and Hanawa, 2003; Kiem et al., 2003; Verdon et al., 2004; Power and Smith, 2007; Callaghan and Power, 2010). Much of this variability has been linked to natural ENSO-like patterns of variability operating at decadal and interdecadal time scales called the Pacific Decadal Oscillation (PDO) (Figure 3.16; Mantua et al., 1997) and the Interdecadal Pacific Oscillation (IPO, Power et al., 1999a).

The interdecadal variability in IPO and PDO indices are very similar (Power et al., 1999b). In fact the PDO can be regarded as the North Pacific manifestation of the Pacific-wide IPO (Folland et al., 2002). Countries influenced by the IPO are the same as the countries influenced by ENSO.

ENSO-like patterns of decadal variability can, in theory, arise from random changes in ENSO activity from decade to decade (Power and Colman, 2006). For example, a decade dominated by El Niño (e.g. a decade with two El Niño events and no La Niña events) will tend to have an El Niño-like sea-surface temperature pattern, whereas a decade dominated by La Niña (e.g. a decade with three La Niña events and only one El Niño event) will tend to have a La Niña-like decadal sea-surface temperature pattern.

While random changes in ENSO activity from decade to decade help explain the observed IPO and the PDO, such random changes alone cannot fully explain the spatial patterns and spectral properties of the IPO or the PDO (Power and Colman, 2006; Newman et al., 2003). For example, the unsmoothed PDO index has a lower frequency character than indices used to track ENSO (Newman et al., 2003), and the spatial pattern of the IPO has a broader meridional (north-south) structure near the equator in the eastern Pacific than ENSO in both observations and models (cf. Figure 3.3a and Figure 3.16, top; Power and Colman, 2006). The differences arise because the PDO and the IPO indices are influenced by slow oceanic processes (e.g. the storage of heat in the upper ocean and its evolution) and low-frequency oceanic Rossby waves (very large disturbances in ocean circulation that propagate across ocean basins).

Changes in the phase of the IPO have been linked to significant changes in climate regimes across the Pacific. For example, the rapid transition from a negative to a positive IPO phase during the mid-1970s was associated with a shift to an El Niño dominated period (Figure 3.6). The IPO switched to a negative phase around the year 2000, and the past decade has been dominated by La Niña.

The involvement of slow, natural oceanic processes can make some of the multi-year and decadal variability linked to the IPO and PDO more predictable than for ENSO (Power and Colman, 2006; McGregor et al., 2007, 2008, 2010; Mochizuki et al., 2010). However, the extent to which this translates into predictability of surface variables such as rainfall is unclear, though likely small (Power et al., 2006). This is the subject of ongoing research (Collins et al., 2010).

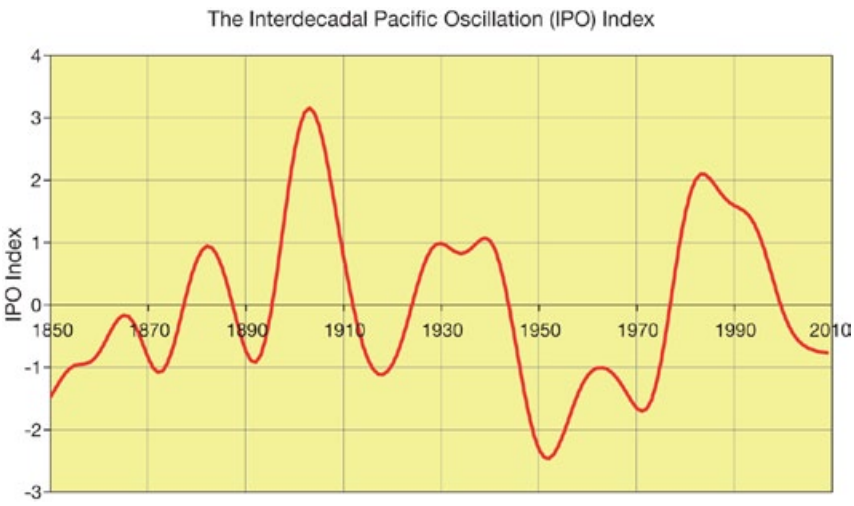

Figure 3.6: Time series of the Interdecadal Pacific Oscillation. (Data source: UKMO; Based on definition of Parker et al., 2007).

3.4.3 Intertropical Convergence Zone

The mean state of the ITCZ is described in Chapter 2. Seasonal and interannual variability in the position and intensity of the ITCZ can have significant impacts on low latitude Pacific nations due to its meridional narrowness and large rainfall gradients. As the mean seasonal shift of the ITCZ is relatively small, at only around 2° of latitude in the central Pacific, even small shifts in overall location can result in large impacts. As noted in Chapter 2, the PCCSP Partner Countries affected by the ITCZ are Palau, the Marshall Islands and the Federated States of Micronesia (see Table 2.4 and country reports in Volume 2 for further details).

Interannually, the ITCZ latitudinal location varies more in the December-February season than in June-August, with standard deviations of 1.5° and 0.6° of latitude respectively (Figure 3.7). Correlations with concurrent Niño3.4 temperatures are extremely high during both seasons (-0.94 and -0.85 respectively) indicating a strong link between ITCZ position and ENSO.

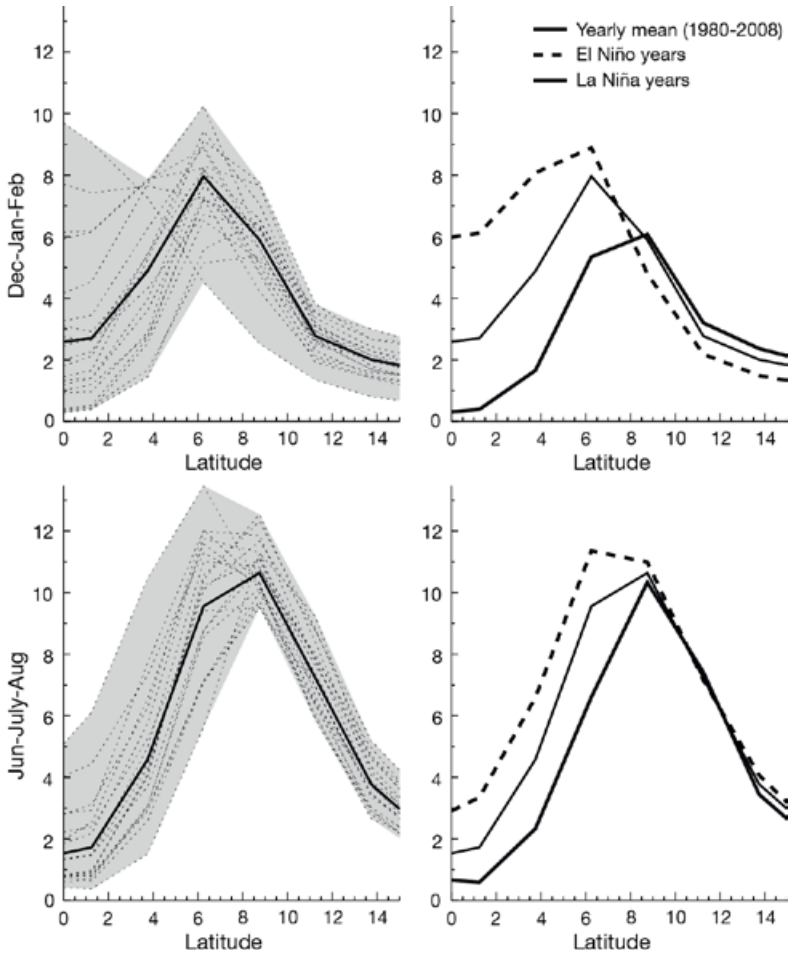

Figure 3.7: Observed meridional (north-south) variation of average precipitation for (top panels) December-February and (bottom panels) June-August for all years 1980–1999 (left panels) and for El Niño and La Niña years (right panels).

Over the 1979–1999 period the ITCZ, on average, was positioned around 3° closer to the equator during El Niño conditions than La Niña conditions; a difference larger than its mean seasonal variation. Rainfall amounts (again defined within the region 160°E–120°W, 0°–15°N) are also strongly correlated with Niño3.4 at around 0.74 in both the December-February and June-August seasons. A small downward trend in total rainfall is apparent over the 1979–1999 period for this region, and the trend is stronger in December-February than June-August.

3.4.4 Western Pacific Monsoon

The Western Pacific Monsoon is associated with a seasonal reversal of wind direction that brings heavy rainfall to the region north of Australia, extending from East Timor to the Solomon Islands. Variations in the timing, position, intensity, longevity and extent of the monsoon account for much of the rainfall variability in this region. As noted in Chapter 2, the PCCSP countries affected by the Western Pacific Monsoon are East Timor, Papua New Guinea and the Solomon Islands (see Table 2.4 and Volume 2 for further details).

The year-to-year variability in rainfall for December-February averaged over Southern Hemisphere box-1 (Figure 2.10) and June-August averaged over the Northern Hemisphere box (Figure 2.10) shows a downward trend during the 1980–1999 period (~90 mm per decade) for the Northern Hemisphere monsoon area, but only a weak downward trend for the Southern Hemisphere section (Figure 3.8). A strong correlation exists between rainfall in these regions and ENSO (shown in Figure 3.8 as seasonal mean Oceanic Niño3.4 Index, ONI), being -0.65 for the Northern Hemisphere box and -0.83 for Southern Hemisphere box-1.

The seasonal reversal of low-level winds is one measure of the regional extent of the monsoon (Wang, 2006). The extent of the westerly wind domain for each January during 1980–1999, as well the average extent for January during the same period, is shown in Figure 3.9. East Timor, Papua New Guinea and the Solomon Islands are within the monsoon region for all or most years. Vanuatu, Tuvalu and parts of Kiribati lie outside the average monsoon domain but nonetheless are affected by the monsoon during some years. In the Northern Hemisphere, Palau lies within the westerly domain during most years, while parts of the Federated States of Micronesia and Marshall Islands are only affected by the monsoon in some years.

Year-to-year variability in the extent of the monsoon-affected region is significant, especially on the eastern edge, where it varies by more than 5000 km between maximum and minimum extent. The north-south variability of the westerly wind domain is much less pronounced (Figure 3.9).

The time series of the position of the eastern edge of the westerly wind domain for December-February shows no long-term trend in the eastern extension of the monsoon domain during 1980–1999 for any of the three months (Figure 3.10). However, there is significant variability in the eastern edge within a single season, with the eastern edge moving on average by ~2500 km in every season. Between two different monsoon seasons, the variability in the position of the eastern edge of the monsoon domain is also large. The differences between the maximum and minimum extents are 2000 km for December, 1800 km for January and 2200 km for February. ENSO causes some of this variability. In fact, the two most extreme maximum eastern extents of the monsoon domain occurred during the strong El Niño years of 1983/84 and 1997/98 (Figure 3.10).

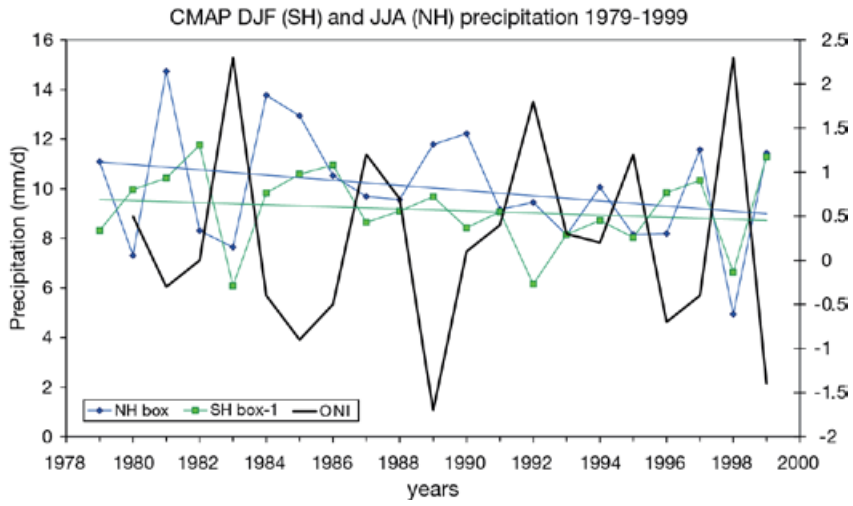

Figure 3.8: Seasonal mean rainfall (mm per day) averaged over Northern and Southern Hemisphere boxes (Northern Hemisphere box: 125–145°E; 5–10°N and Southern Hemisphere box-1: 120–150°E; 0–10°S, as shown in Figure 2.10). Seasonal averages are shown for June-August for the Northern Hemisphere box (blue) and for December-February for Southern Hemisphere box-1 (green) (Based on CMAP precipitation analysis). The Oceanic Niño3.4 Index (ONI) is shown in black.

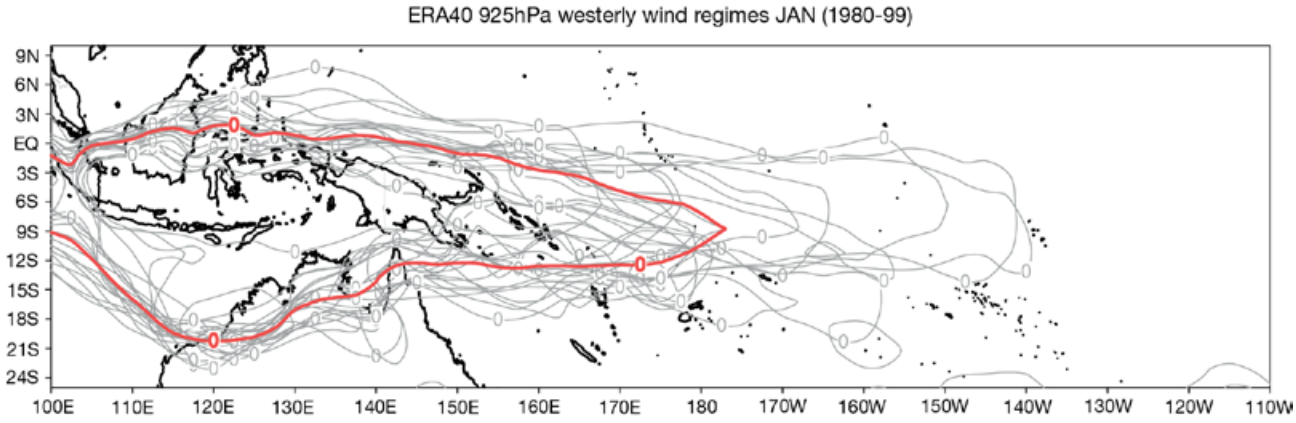

Figure 3.9: Interannual variability of the extent of the monsoon westerly wind domain during January. The extent for each individual January during 1980–1999 is shown in grey, with mean January extent during 1980–1999 shown in red. (Based on ERA-40 zonal winds at the 925 hPa level).

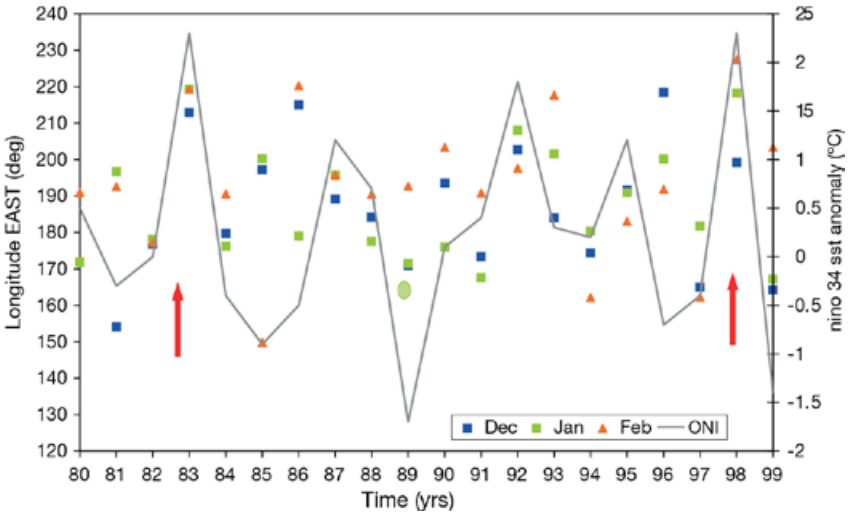

Figure 3.10: The most easterly position of the eastern edge of the monsoon westerly wind domain in December (blue), January (green) and February (orange) between 1980 and 1999. The December-February seasonal mean Oceanic Niño3.4 Index (ONI) is also shown (grey), with the major El Niños of 1983/84 and 1997/98 denoted by red arrows.

3.4.5 South Pacific Convergence Zone

The mean features of the SPCZ are described in Chapter 2. Fluctuations in the position of the SPCZ are a major cause of seasonal changes in rainfall, winds and tropical cyclone risk in many South Pacific Partner Countries. As noted in Chapter 2, the PCCSP countries affected by the SPCZ are the Cook Islands, Fiji, Kiribati, Nauru, Niue, Samoa, Solomon Islands, Tonga, Tuvalu and Vanuatu (Table 2.4 and Volume 2). The SPCZ Position Index is a measure of SPCZ location and is calculated as the normalised November-April difference at 9 am (local time) in mean sea-level pressure between Suva and Apia. It defines the latitude of the SPCZ between longitudes 180°W and 170°W (Folland et al., 2002).

The location of the SPCZ is closely linked with the phase of ENSO and the IPO/PDO (Folland et al., 2002). From the mid-1940s to the late 1970s, the SPCZ Position Index was more often negative than positive (Figure 3.11), indicating a tendency for the SPCZ to lie to the south-west of its mean position. Around 1980, the SPCZ Position Index underwent a rapid shift to more positive values, indicating a northward shift of the diagonal portion of the SPCZ, and a stronger sub-tropical high pressure belt (Griffiths et al., 2003). Since the late 1980s, the position of the SPCZ has oscillated around its long-term mean position.

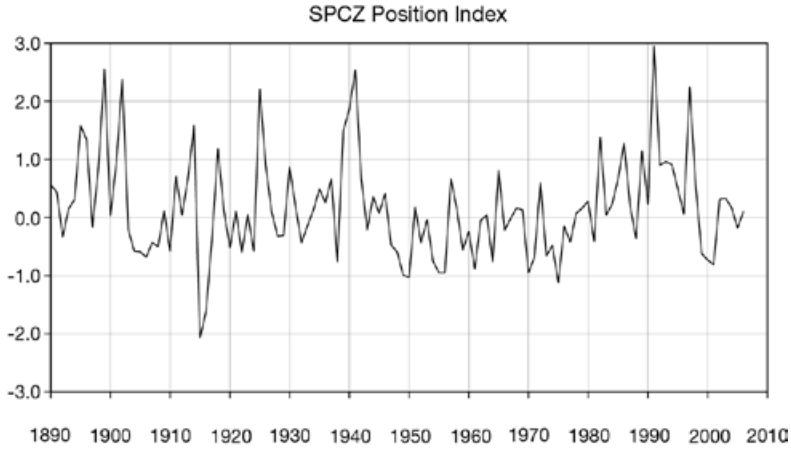

Figure 3.11: Index of the position of the South Pacific Convergence Zone during November-April (1891–2007). (Relative to the base period 1933–1992). Data courtesy of Jim Salinger.

3.4.6 Hadley Circulation

The Hadley Circulation is the dominant meridional circulation in the tropical atmosphere. Recent studies have suggested a poleward expansion of this circulation from the late 1970s using multiple datasets and methodologies (Birner, 2010; Hu and Fu, 2007; Siedel and Randel, 2007; Seidel et al., 2008). Many of these studies suggest that the observed expansion is larger in the Southern Hemisphere than the Northern Hemisphere. Lu et al. (2009) hypothesise that the expansion is a consequence of the radiative forcing associated with increased levels of greenhouse gases in the atmosphere and stratospheric ozone depletion. Changes to the intensity of the Hadley Circulation have been suggested (Mitas and Clement, 2005), although the magnitude of any such changes is unclear (Mitas and Clement, 2006).

As a whole, global climate models indicate a general meridional expansion and weakening of the Hadley Circulation in response to increased greenhouse gas forcing. This is hypothesised to be a result of increasing tropical static stability, which slows and weakens the overturning circulation. However, Johanson and Fu (2009) noted that the observed tropical expansion has proceeded more quickly than predicted by the models. They attribute this result to the role of stratospheric ozone depletion in driving the observed trends. The impacts of the expansion of the Hadley Circulation on Partner Countries remains poorly understood, but may turn out to be a significant consequence of global warming.

3.4.7 Southern Annular Mode

In the Southern Hemisphere extra-tropics the atmospheric circulation is dominated by strong mid-latitude westerly winds. There are important variations in the strength and the position of these winds: they tend to oscillate between being stronger and more poleward, or weaker and more equatorward. This characteristic pattern of variability in the westerlies is known as the Southern Annular Mode (SAM; Thompson and Wallace, 2000). While this feature primarily affects higher latitude land masses (Gillet et al., 2006; Hendon et al., 2007) and oceans (Sen Gupta and England, 2006), it may directly impact southern parts of the PCCSP region (south of about 20ºS) via changes in the atmospheric circulation. The SAM may also indirectly affect the wave climate of the region by modifying the large swell waves generated by storm activity in the Southern Ocean that can travel into the tropical Pacific and affect wave height (Hemer et al., 2008).

The SAM can be represented by an index based on the difference in pressure between 40ºS and 65ºS (Marshall, 2003). A positive SAM is associated with both a strengthening and poleward shift of the westerlies, and an intensification of storm activity. As a result, the sub-tropical high pressure systems that migrate from west to east at around latitude 30º (Section 2.3.1) move away from the equator as well, affecting local weather conditions. The reverse occurs during the negative phase of the SAM: the band of westerly winds are weaker and situated closer to the equator, with weaker storm activity and cold fronts located closer to the sub-tropics. The SAM may therefore affect the climate of all PCCSP countries in the South Pacific sub-tropics.

Since the mid-1960s the SAM has undergone a robust change towards its more positive phase (Thompson and Wallace, 2000; Marshall, 2003). Observational and modelling studies have demonstrated that these trends are consistent with a combination of recent stratospheric ozone depletion and enhanced greenhouse gas forcing (Fyfe et al., 1999; Thompson and Solomon, 2002; Gillett and Thompson, 2003; Cai and Cowan, 2007). The increase in storm intensity associated with the positive phase of the SAM could be expected to increase swell magnitudes in southern parts of the South Pacific (Hemer et al., 2008), but the southward shift in the location of the storm tracks may act to counteract the effect of this increased intensity.

Long-term changes in the SAM can also drive changes in the sub-tropical ocean circulation. Observational evidence suggests an increase in the strength of the South Pacific sub-tropical gyre since 1993, and an associated warming of the Tasman Sea (Roemmich et al., 2007).

3.4.8 Indian Ocean Dipole

The Indian Ocean Dipole (IOD) is a pattern of interannual variability in the tropical Indian Ocean basin that involves ocean-atmosphere interactions in the east-west direction (Saji et al., 1999; Webster et al., 1999; Yu and Rienecker 1999). A positive IOD event refers to a pattern of sea-surface temperature variability in which ocean-surface conditions are cool relative to the long-term average in the east equatorial Indian Ocean and warm in the west. A negative IOD event has the opposite pattern. Similar to ENSO, the IOD is associated with a positive feedback process involving winds that result in a shallower thermocline, influencing zonal sea-surface temperature gradients, which in turn reinforce the winds. An IOD event usually starts to develop in June and peaks in September-November.

The IOD influences climate both locally and in remote regions. For example, a positive IOD event is associated with droughts in East Asia (Guan and Yamagata, 2003), south-east Australia (Cai et al., 2005; Meyers et al., 2007; Cai et al., 2009a), Indonesia and East Timor (D'Arrigo and Smerdon, 2008), and flooding in parts of India and East Africa (short rains; Black et al., 2003). It also affects the Indian and Australian monsoons (Ashok et al., 2001). However, the IOD is a much weaker source of climate variability for the Pacific region than ENSO and its independence from ENSO remains a subject of scientific debate (Dommenget, 2010). Its influence on PCCSP Partner Countries other than East Timor is uncertain. Some evidence suggests a trend towards an increasing frequency of positive IOD events and decreasing frequency of negative IOD events (Cai et al., 2009b).

3.5 Variability and Change in the Atmosphere

3.5.1 Temperature

Previous studies of temperature trends in the Pacific used data recorded by the respective national meteorological services to show that temperatures generally increased throughout the Pacific Islands during the 20th century (Salinger, 1995; Folland et al., 2003). However, these trends have not been spatially uniform. Changes in temperature extremes have tended to follow those of mean temperatures, with most stations showing an increase in the occurrence of hot days and warm nights, and a decline in the number of milder days and cooler nights over the last four decades of the 20th century (Manton et al., 2001; Griffths et al., 2005).

Long-term temperature trends in the Pacific have been updated here by the PCCSP through collaboration with the national meteorological services in Partner Countries. These temperature records have undergone homogeneity assessment and adjustment (Wang, 2009) where appropriate to produce reliable analyses of temperature trends. Unfortunately only limited data could be sourced for East Timor and Nauru, preventing the calculation of trends for these Partner Countries.

The updated PCCSP region temperature records show clear and consistent warming over the past 50 years (Figure 3.12), with most stations recording trends around +0.08–0.20°C per decade over this time. The strongest warming is found in Papua New Guinea and French Polynesia. Trends in maximum and minimum temperatures are generally similar to those of mean temperature at most stations, apart from in Fiji, Tonga and Niue where there is a tendency for greater warming in the daytime. The amount of warming in the wet and dry seasons is also similar at most stations. The magnitude of background warming in PCCSP region temperature records over the past half-century is consistent with that expected from human-induced global warming.

3.5.2 Rainfall

Much of the variability in Pacific Island rainfall records is closely linked to ENSO and the IPO (Salinger et al., 2001), and directly attributable to shifts in the SPCZ or ITCZ (McCarthy et al., 2001; Folland et al., 2002). The effects of SPCZ movement on mean rainfall regimes in much of the South Pacific have been large in the past century. Increases of mean annual rainfall of 30% or more occurred north-east of the SPCZ between the most recent positive phase of the IPO (1978–1998), and the previous negative phase (1946–1977; Salinger et al., 2001). Decreases in mean annual rainfall to the south-west of the SPCZ were smaller, but both changes were consistent with a movement in the mean location of the SPCZ to the north-east.

Previous studies of rainfall trends show that over the 1961–2000 period, locations to the north-east of the SPCZ became wetter, with the largest trends occurring in the eastern Pacific Ocean (east of 160°W), while locations to the south-west of the SPCZ became drier (Griffiths et al., 2003). Trends in the frequency of rain days were generally similar to those of total annual rainfall, with more (less) rain days typically associated with more (less) total rainfall (Manton et al., 2001; Griffiths et al., 2003). Overall, rainfall changes determined by previous studies are consistent with the SPCZ having moved north-east over the 1960–2000 period (Figure 3.11).

Changes in extreme rainfall in the Pacific have been analysed by defining indices to measure extreme frequency, intensity, proportion of total rain and dry spell length (Manton et al., 2001; Griffiths et al., 2003). Trends in these indices have tended to mirror those of total rainfall. Changes in extreme rainfall during the last four decades of the 20th century are thus also consistent with the SPCZ having moved north-east.

Due to the paucity of rainfall station data in the Pacific, many of the global gridded precipitation datasets show large voids in the region. Consequently, rainfall trends are best analysed using station data. Rainfall series from land based stations have been updated and adjusted for homogeneity where appropriate, in collaboration with national meteorological services and other agencies in Pacific Island countries and East Timor.

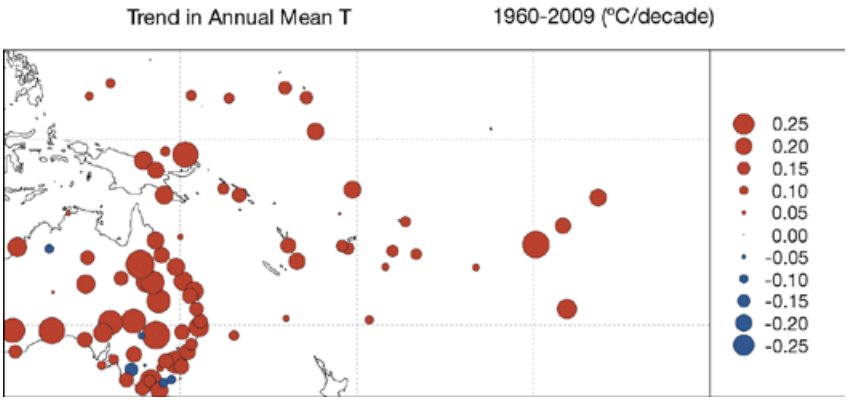

Figure 3.12: Sign and magnitude of trends in annual mean temperatures at Pacific Island meteorological stations for 1960–2009. Australian stations included for comparison.

The updated rainfall series clearly show the large interannual variability experienced in the tropical Pacific. This variability is large compared with the magnitude of long-term rainfall trends, making them less spatially coherent than those for temperature. Trends in total annual rainfall for the longest available rainfall records, indicate a general increase in rainfall totals north-east of the SPCZ over the past 50 years (Figure 3.13a), with mainly declines to the south-west of the SPCZ, and north of the ITCZ just west of the International Date Line. This pattern of change is generally reflected in both wet and dry seasons. However, the pattern of trends has changed markedly in the south-west Pacific over the past two decades (Figure 3.13b), consistent with a shift of the SPCZ back to its climatological position since 1990 (Figure 3.11).

Unlike changes in temperature, which are dominated by background global warming, the lack of a sustained trend in rainfall suggests that Pacific rainfall patterns continue to be strongly influenced by natural climate variability.

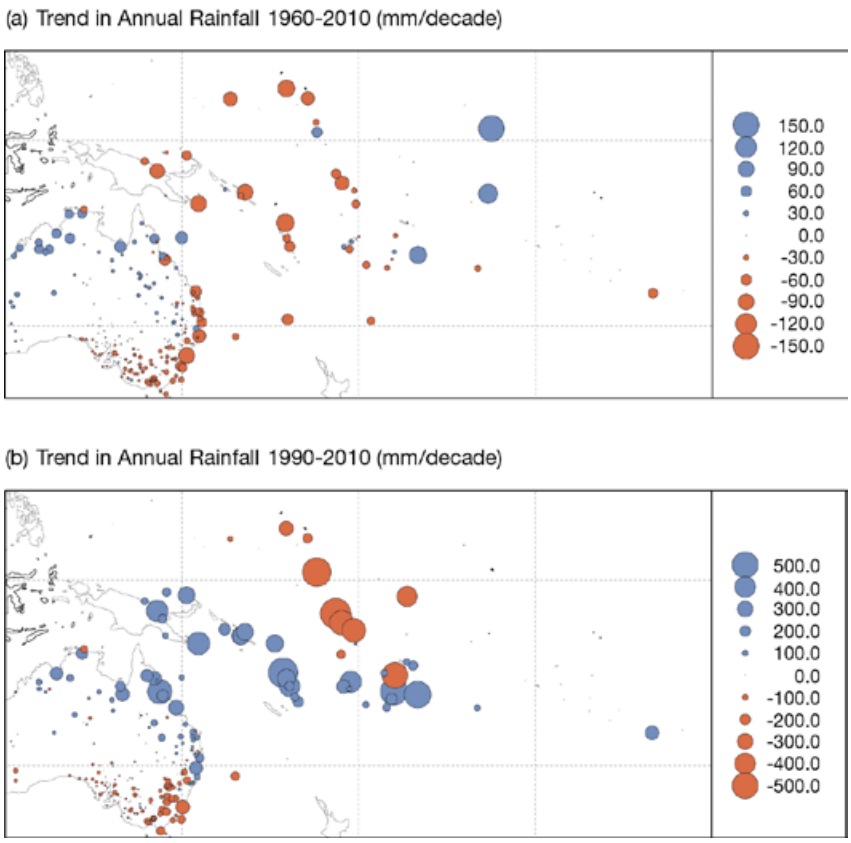

Figure 3.13: Trends in annual total rainfall at Pacific meteorological stations for (a) 1960–2010 and (b) 1990–2010. Note different scales on plots. Refer to Volume 2 of this report for individual station time series.

3.5.3 Tropical Cyclones

ENSO plays a role in modifying tropical cyclone risk throughout the tropical Pacific. When the western equatorial Pacific warms relative to the eastern equatorial Pacific during the La Niña phase, cyclones occur with greater frequency in the western Pacific, close to Australia (Figure 3.14). Conversely, during the El Niño phase, when the western equatorial Pacific is anomalously cool, the region of greatest cyclone occurrence is found further east.

The analysis of trends in the historical tropical cyclone record has been difficult. Some studies (Webster et al., 2005) describe trends towards more intense tropical cyclones in parts of the world, e.g. the North

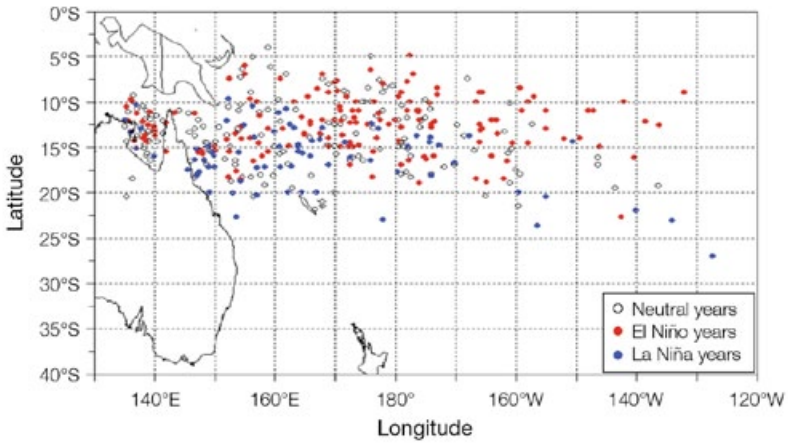

Figure 3.14: Locations where tropical cyclones formed over the South Pacific Ocean in neutral (grey), El Niño (red) and La Niña (blue) years during 1969–2006. Genesis location is defined as the point where tropical cyclone central pressure is estimated to have dropped to 1000 hPa or lower (Source: Kuleshov et al., 2009).

Atlantic Ocean and the north-west Pacific region, while other studies (Chan, 2006; Landsea et al., 2006; Curry et al., 2006) dispute these findings on the basis that changes in observation technology and analysis techniques over time have created spurious trends in the observational record. Using three different tropical cyclone archives, Song et al. (2010) found contrary trends in the proportion of intense tropical cyclones in the western North Pacific over the past few decades. They concluded that different algorithms used in determining tropical cyclone intensity in each of the archives may account for these discrepancies.

A rigorous analysis of the South Pacific tropical cyclone archive indicates no significant trends in the total number of tropical cyclones over 1981–2007, nor in the overall number of intense tropical cyclones in the South Pacific Ocean (Figure 3.15; Kuleshov et al., 2010). However, this is a very short period over which to examine trends in extreme events. As complete records of estimated tropical cyclone intensity are only available from 1981, studies of tropical cyclone numbers are limited to this time. It is important to note that the absence of overall trends for the South Pacific does not discount the possibility of local trends. However, as shown in the country summaries in Volume 2 of this publication, tropical cyclone numbers show large interannual variability at the local level, making it virtually impossible to identify long-term trends at local and national scales.

An analysis of published case studies, seasonal summaries, newspaper archives and historical society records dating back to the late 19th century (Callaghan and Power, 2010) indicates that the frequency of severe tropical cyclones making landfall over north-eastern Australia varies substantially on interannual, decadal and longer time scales. The sign and magnitude of trends calculated over 30-year periods varies greatly for these Australian landfalling tropical cyclones, highlighting the need for caution in making inferences about trends based on short time spans, such as the satellite era (from the 1970s). While the number of landfalls fell over the period 1872–2010, the declining trend is only significant at the 90% level. Callaghan and Power (2010) also concluded that prudent planning should reflect the possibility of a rapid return to the much higher landfall rates seen earlier in the record.

3.5.4 Other Variables

Studies of changes in atmospheric variables other than temperature, rainfall and tropical cyclones are rare for the Pacific region, reflecting a lack of available data. One study showed that trends in sunshine hours and 9 am cloud amount in the Pacific region over the 1951–1990 period were weak and mixed throughout the region (Salinger et al., 2001).

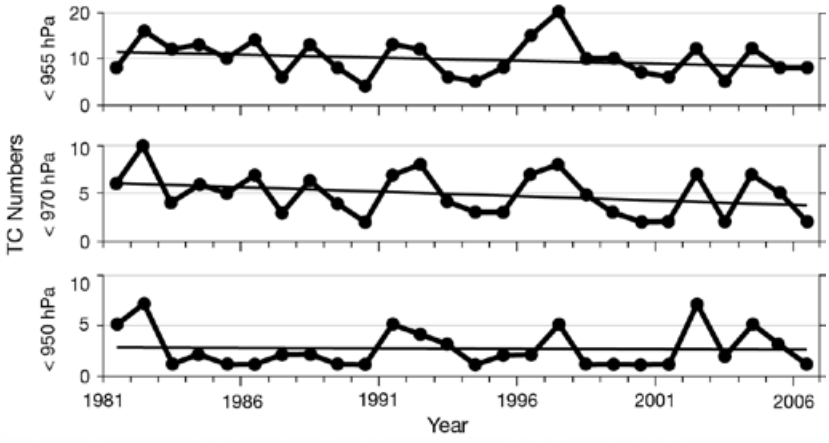

Figure 3.15: Number of tropical cyclones per year over the South Pacific Ocean for the 1981–2007 period. Series represent numbers of tropical cyclones with minimum central pressure of 995 hPa or lower (top), 970 hPa or lower (middle) and 950 hPa or lower (bottom). (Source: Kuleshov et al., 2010).

3.6 Variability and Change in the Ocean

The ocean dominates the PCCSP region. Changes to ocean characteristics affect marine biological systems and, in turn, the vital regional fisheries. In addition, interactions between the ocean and atmosphere mean that changes in the atmosphere, and on the islands, are strongly influenced by the state of the ocean. For example, ENSO owes its existence to oscillations in the location of warm water in the western Pacific Ocean and the resulting feedback this causes in the atmosphere. On longer time scales, the predominance of ocean in the region means that the regional mean temperature has risen more slowly than the global mean over recent decades.

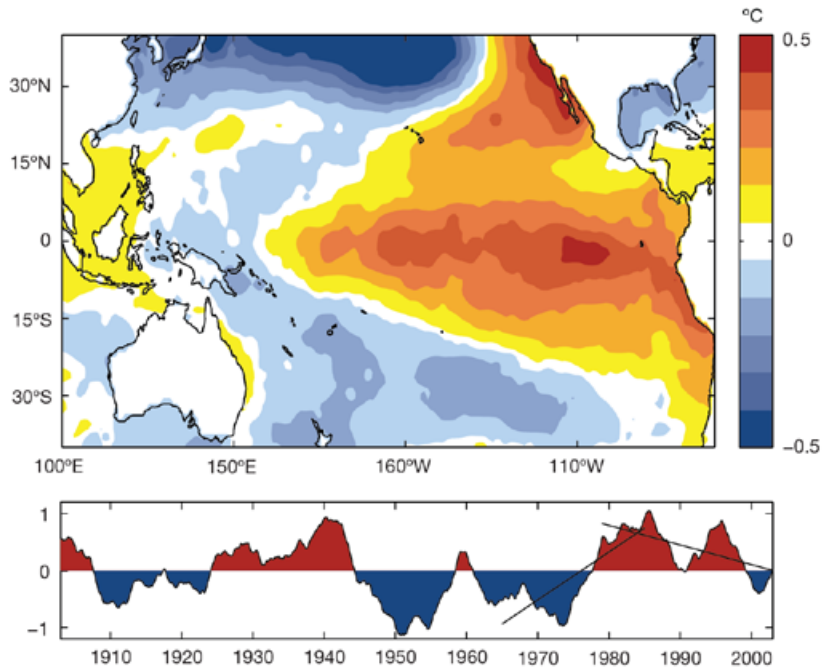

Figure 3.16: (Top) Pattern of sea-surface temperature associated with a positive, warm phase (+1 standard deviation) Pacific Decadal Oscillation (PDO) event. (Bottom) Time series of the PDO (red: warm phase, blue: cold phase) with linear trends for the periods 1979–2008 and 1965–1985 superimposed (Data source: HadISST).

3.6.1 Sea-Surface Temperature and Salinity

At tropical latitudes, year-to-year variability is often larger than seasonal changes. The predominant pattern of interannual change in the ocean is associated with ENSO (Section 3.4.1). On longer time scales, the PDO/IPO (Section 3.4.2) are associated with important modulations in large-scale ocean temperature and circulation. As already discussed, the pattern of sea-surface temperature changes associated with the PDO (Figure 3.16, top) are similar to those during ENSO, although the pattern extends further away from the equator, and the oscillation between positive and negative phases can take decades, rather than a few seasons (Figure 3.16, bottom). The existence of natural variability with such long time scales complicates the attribution of trends in ocean temperatures by making it difficult to determine what is related to global warming and what is simply part of natural variability.

There are a number of different sea-surface temperature datasets that, while based on essentially the same set of observations, use different interpolation methods to account for missing data. Based on two of these datasets the 50-year trends reveal broad-scale warming in most areas (Figure 3.17). However, as a consequence of data scarcity across parts of the tropical Pacific region, there is disagreement in the sign of the trends in some locations. This is further discussed in Deser et al. (2010). Cravatte et al. (2009) found that most datasets show a consistent long-term warming in the western Pacific, up to 0.75°C over 1959–2008, while there is less consistency in the central and eastern equatorial Pacific.

A further difficulty with trend calculation is related to the 'noise' associated with natural variability on interdecadal and longer time scales. The pattern of change varies considerably, depending on the time period over which the trend is computed. For example, over the 1979–2008 period, sea-surface temperatures show broad cooling in the eastern equatorial Pacific and warming in the west, while over 1965–1985 this pattern is essentially reversed (irrespective of the dataset used). While warming in the mean Pacific surface temperature has been partially attributed to human-induced global warming (Stott et al., 2010), part of the slowly varying changes evident can also be attributed to natural variability, e.g. IPO/PDO (see trend lines on Figure 3.16, bottom). Large swings in the IPO/PDO indices are often termed regime shifts in the climate dynamics (Mantua and Hare, 2002) and are associated with major biological and climate shifts. The extent to which these shifts are actually predictable on decadal time scales is the subject of ongoing research (Newman, 2003; Power et al., 2006; Power and Colman, 2006; Collins et al., 2010) and will be a major focus for the next IPCC Assessment Report (Taylor et al., 2009).

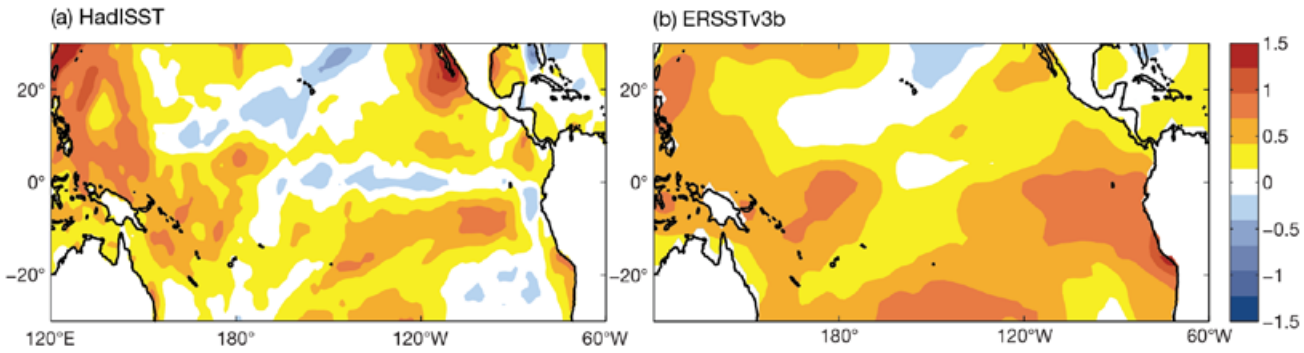

Figure 3.17: Comparison of linear trend in sea-surface temperature (°C per 50 years) over 1959–2008 for two observational datasets. (a) HadISST, http://badc.nerc.ac.uk/data/hadisst/; (b) ERSSTv3b, ftp.eclipse.ncdc.noaa.gov.

Salinity measurements in the equatorial Pacific Ocean are much sparser than temperature measurements, making the identification of trends even more difficult. Nevertheless, a significant freshening seems to have occurred over the western tropical Pacific, extending eastward under the low salinity ITCZ and SPCZ regions (Figure 3.18; Durack and Wijffels, 2010). Conversely, regions to the east have generally become saltier. These observations suggest that there has been an increase in rainfall relative to evaporation in the western tropical Pacific and an increase in evaporation relative to rainfall in the east, i.e. an intensification of the hydrological cycle across the equatorial Pacific over recent decades.

As the west equatorial Pacific Warm Pool has warmed and freshened during recent decades, the extent of the Warm Pool has grown considerably. For example, the area of water with temperatures exceeding 29.5°C has increased by 400–600% (Cravatte et al., 2009).

3.6.2 Sub-Surface Temperature and Salinity

To examine changes in temperatures below the ocean surface, a new observational dataset based on over 2.6 million historical temperature profiles has been developed. The analysis explicitly accounts for the effects of global and regional natural climate fluctuations (including ENSO, PDO, SAM and the North Atlantic Oscillation) and climate drivers (including increased greenhouse gases, stratospheric volcanic aerosols and total solar irradiance). A new salinity dataset has also been developed using over 1.6 million profiles of salinity, potential temperature and neutral density from historical archives and the international Argo project (Durack and Wijffels, 2010). The dataset extends from 1950–2008, which minimises bias in the trend calculation associated with ENSO.

A distinctive pattern of intensified surface warming and sub-surface cooling centred near a depth of 200 m is evident for the 1950–2008 period (Figure 3.19). The sub-surface

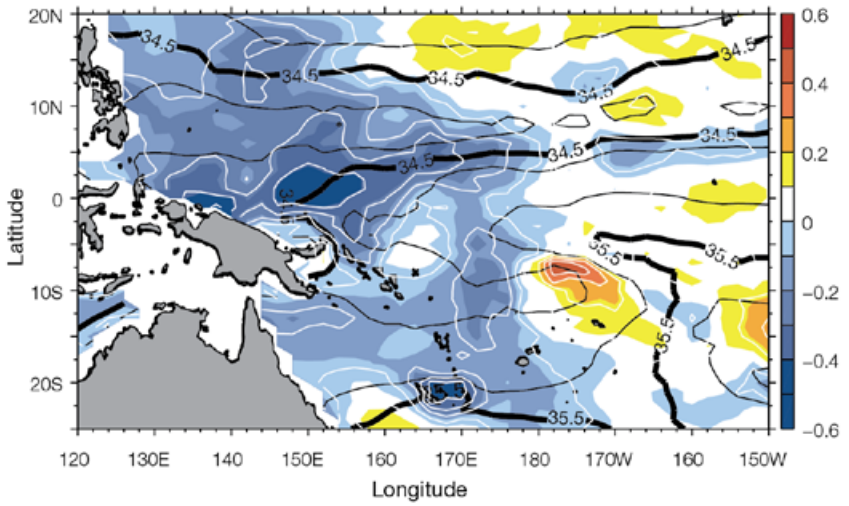

Figure 3.18: Surface salinity trend (psu per 50 years) in the tropical Pacific Ocean based on data from 1950–2008 (with 0.125 psu per 50 years contour interval shown in white). Mean salinity is overlaid in black (contour interval 0.25, and thick contours every 0.5). (Source: Durack and Wijffels, 2010).

cooling is probably a result of changes in the overlying wind field that causes the thermocline to be shallower (Han et al., 2006). A similar pattern of change, albeit with weaker magnitude, is evident in many of the climate model simulations of historical change (Chapter 4). As this change in the climate model simulations is due to increased concentrations of atmospheric greenhouse gases (and not natural climate variability) it suggests that the observed pattern is a result of human-induced changes, rather than natural variability.

The linear trend in sub-surface ocean temperature is larger than anything that can be explained by solar and volcanic activity, or by the natural fluctuations associated with the North Atlantic Oscillation, SAM and PDO. Only ENSO could potentially result in signals of this magnitude, but this is only true within the tropics. The temperature trend is statistically significant over most of the Pacific Ocean, however, and so cannot be fully explained without human-induced warming.

Large, significant and spatially coherent multi-decadal trends in salinity, down to a depth of 2000 m, are also evident in the Pacific. Much of the sub-surface change is consistent with an upward movement of the thermocline. Intensified surface warming and freshening both act to reduce upper ocean density, thus intensifying ocean stratification and suppressing vertical mixing, making it harder to bring sub-surface nutrients into the upper ocean (where they are used in primary production).

3.6.3 Sea Level, Waves and Surges

3.6.3.1 Past Sea-Level Change

Information on how sea level has changed through Earth's history provides valuable insight as to what sea levels might be possible in the future and what rates of change are feasible. The last time the Earth was essentially free of major ice sheets was about 35 million years ago. At that time the atmospheric carbon dioxide concentration was 1250 ± 250 ppm, the Earth was warmer as a result of larger atmospheric greenhouse gas concentration and sea level was about 70 m above present-day values (Alley et al., 2005). As greenhouse gas concentrations fell after this period, the Earth cooled and the major ice sheets formed, first in the Antarctic and then later in the Northern Hemisphere. Over the glacial cycles of the past 500 000 years, sea level has vacillated by more than 100 m as the great ice sheets, particularly those of northern Europe and North America, waxed and waned (Rohling et al., 2009).

During the last interglacial period (about 125 000 years ago) temperatures were about 3°C warmer than today due to a natural variation in the Earth's orbital parameters. These temperatures are similar to what could be expected late in the 21st century if greenhouse gas emissions continue to rise at the rate of the past decade. Analysis of geological records indicates a 95% probability that global sea level peaked at least 6.6 m higher than today but was unlikely (33% probability) to have exceeded 9.4 m (Kopp et al., 2009). About the time when global sea level was close to its current level or higher, the millennial average rate of global sea-level rise is very likely to have exceeded 5.6 m per millennium but is unlikely to have exceeded 9.2 m per millennium (Kopp et al., 2009). A record in the Red Sea indicates higher rates of 1.6 ± 0.8 m per century (Rohling et al., 2008). Higher rates of rise may have occurred over shorter periods but it is not yet possible to definitively quantify these from the available data. It may take some time for the ice sheet contributions to sea-level rise to accelerate to these rates but the palaeo-data highlight the long-term vulnerability of ice sheets to sustained global warming.

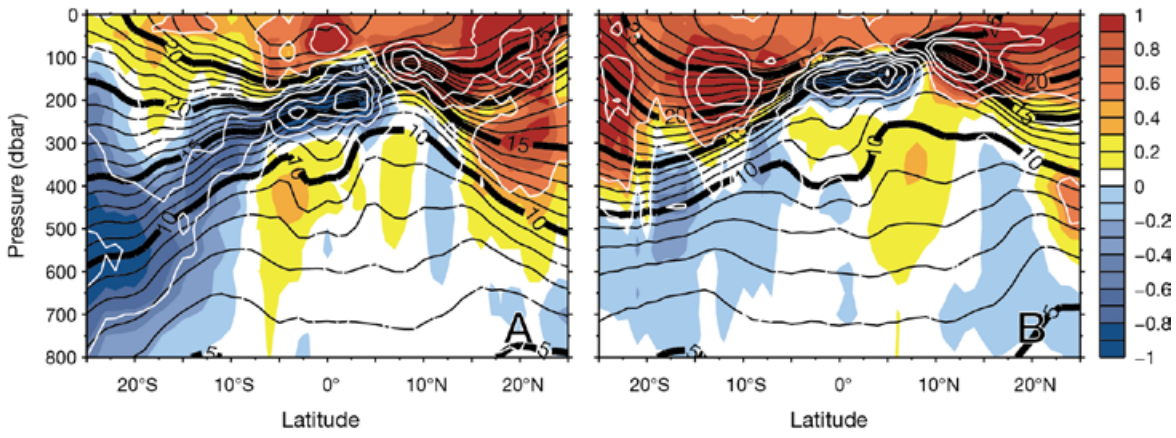

Figure 3.19: Temperature trend (ºC per 50 years) in the tropical Pacific Ocean based on the years 1950–2008. Mean temperature is overlaid in black (contour interval 1°C, and thick contours every 5°C), and temperature changes are contoured in white (contour interval 0.5°C from -2°C to +2°C). Vertical meridional sections at (A) 160°E and (B) 160°W are shown (Source: Durack and Wijffels, 2010).

From the last interglacial period to the last glacial maximum about 20 000 years ago, sea level fell by over 120 m as major ice sheets formed over northern America, Europe and Asia, and the Antarctic ice sheet grew (Lambeck and Chappell, 2001). From about 20 000 years ago until about 7 000 years ago, sea level rose rapidly at average rates of about 1 m per century for many millennia. Recent estimates (Stanford et al., 2011) suggest the highest rates during this period were probably less than 2.6 m per century (99% confidence limits), although Clark et al. (2002) have estimated rates of as large as 4 m per century. However, these conditions are probably not analogous to the 21st century sea-level change because of the much larger and lower latitude ice sheets present at that time. From about 7000 years ago, sea level rose much more slowly. Over the last two millennia up until the 19th century, the little available evidence indicates the rate of global sea-level rise was less than a few tenths of a millimetre per year (Lambeck et al., 2004; Kemp et al., 2009).

From the 19th century to the present, the few available long-term tide gauge records (Woodworth, 1990), evidence from salt marshes (Kemp et al., 2009; Donelly et al., 2004; Gerhels et al., 2005, 2006, 2008), and the available global sea-level estimates (Church and White, 2006, in press; Jevrejeva et al., 2006, 2008; Woodworth et al., 2009, 2011) all indicate an increase in the rate of rise.

3.6.3.2 Current Sea Level Variability and Change

ENSO has a major influence on sea levels across the Pacific, as illustrated in Figure 3.20. During La Niña events, strengthened trade winds push more water toward the west resulting in a higher than normal sea surface in the western tropical Pacific, and lower than normal levels in the east. Conversely, during El Niño events, weakened trade winds are unable to maintain the normal gradient of sea level across the tropical Pacific, leading to a drop in sea level in the west and a rise in the east.

The influence of ENSO can be seen at individual island locations in the PCCSP region. The in situ and satellite observations of sea level indicate interannual variations of over 200 mm. These observed sea levels have been plotted along with reconstructed sea levels over the period from 1950 to 2009 in Figure 3.21. (Reconstructed sea level uses advanced statistical techniques to combine contemporary tide gauge and satellite sea-level measurements to estimate pre-satellite sea level from tide gauge measurements alone. Section 2.2; Church et al. 2004, 2006). In this equatorial region, the in situ and satellite observations of sea level agree well with each other and the reconstructed sea levels.

As well as the influence of ENSO and other natural variability, sea level is also rising globally (Figure 3.22) and in the PCCSP region. The satellite altimeter record from 1993 to the present indicates that global averaged sea level has been rising at 3.2 ± 0.4 mm per year (Cazenave and Llovel, 2010; Church and White, in press). While in situ sea-level measurements do not have the same spatial coverage as the altimeter data, they can be used to make estimates of global averaged and regional sea-level variability and rise (Church and White, 2006, in press; Jevrejeva et al., 2006, 2008; Church et al. 2004, 2006). These estimates confirm the satellite altimeter record and indicate that global averaged sea level has been rising at about 1.7 ± 0.2 mm per year since 1900 (Church and White, in press). Together with other data, they also indicate the rate of rise has increased from the 19th to the 20th century (Bindoff et al., 2007) and during the 20th century (Church and White, 2006, in press; Jevrejeva et al., 2006).

Woodworth et al. (2009) considered the estimates of global averaged sea level and also the distribution of individual records around the globe. The two most prominent features were an increase in the rate of rise around the 1930s, and a decrease

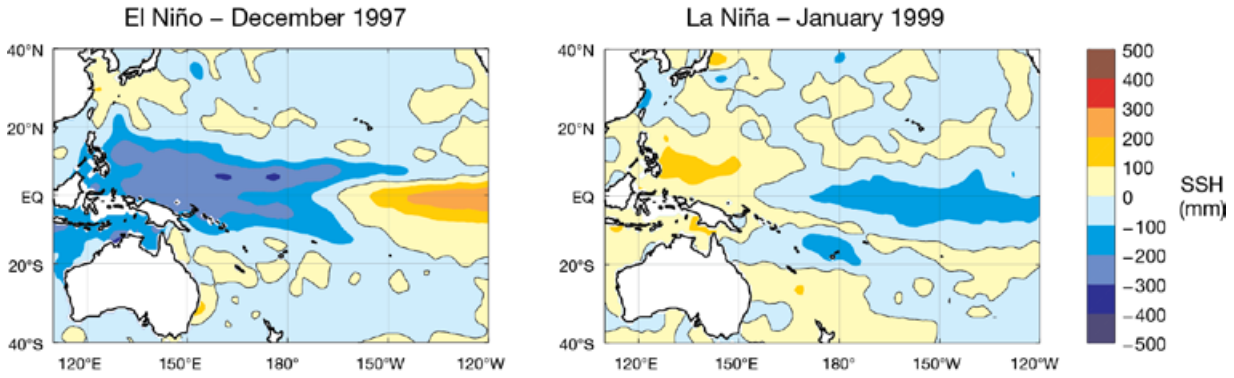

Figure 3.20: Sea-surface height variations relative to the long-term average (mm) across the Pacific during the December 1997 El Niño and January 1999 La Niña events. These are monthly averages from the satellite altimeter observations from 1993 to the present.

in the 1960s, which Houston and Dean (2011) considered in a subset of the global data. Major volcanic eruptions result in additional aerosol loading in the stratosphere and as a result some of the incoming solar radiation is reflected back to space leading to a short-term (a few years for the atmosphere) cooling of the Earth. The oceans also cool but have a substantially longer recovery time. The net effect is that the rate of rise since the 1960s would most likely have been larger if it were not for the impact of major volcanic eruptions in 1963, 1982 and 1991 (Church et al., 2005; Gregory et al., 2006). Also, the additional storage of water in dams (Chao et al., 2008) has slowed the rate of sea-level rise, although this has been partly offset by the depletion of ground water. It is not yet known whether the faster rate of increase since 1993 is due to decadal variability or a further acceleration in the long-term trend. Models indicate the recovery of the ocean from the eruption of Mount Pinatubo in 1991 would increase the rate of sea-level rise by about 0.6 mm per year. There is increasing evidence that the contribution to sea level due to mass loss from Greenland and Antarctica has increased over the past two decades (Velicogna, 2009; Rignot et al., 2011).

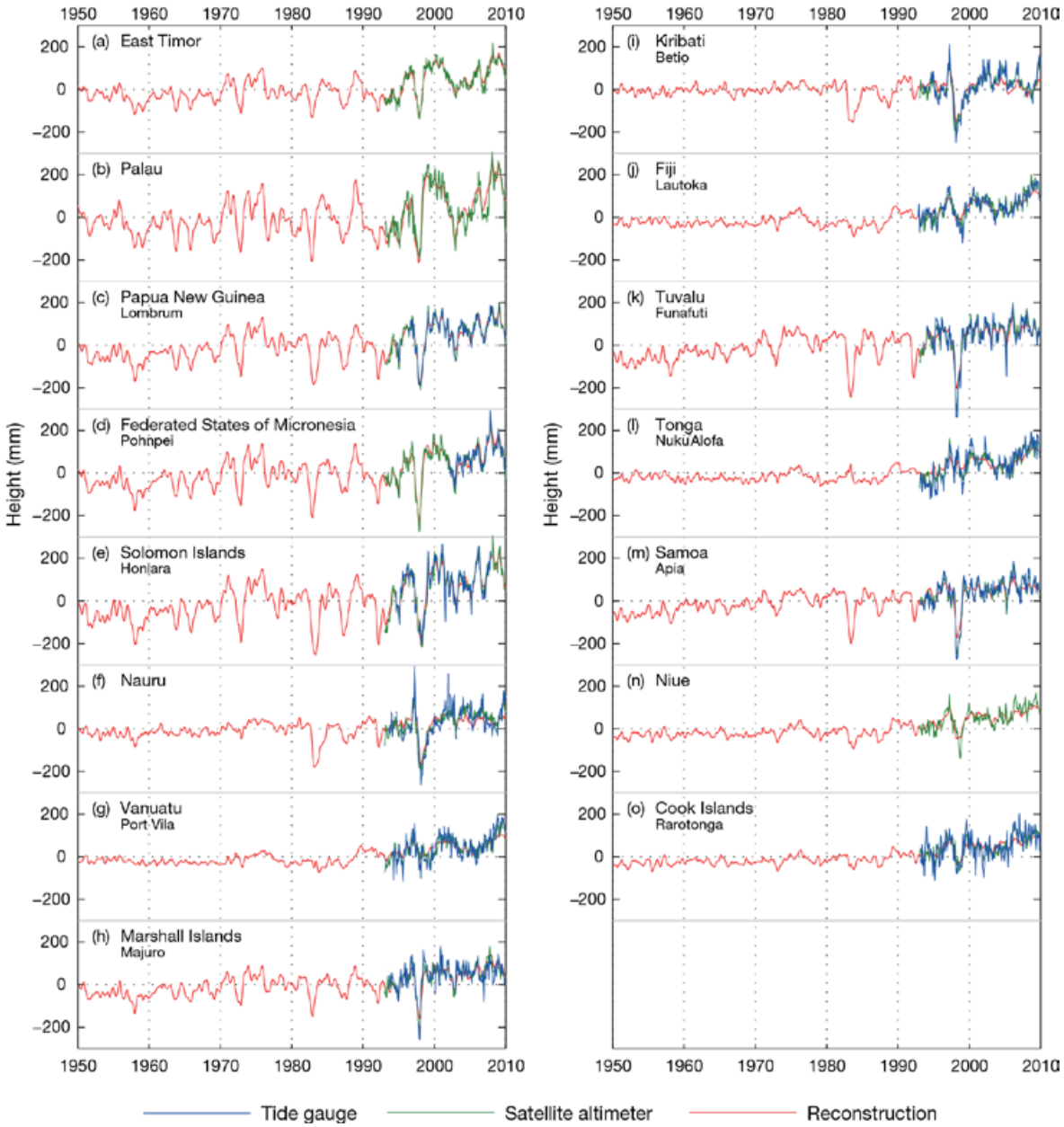

Figure 3.21: Time series of monthly tide gauge data (blue) from the South Pacific Sea Level and Climate Monitoring Project (where available), satellite-altimeter data (green, from 1993) and reconstructed (red) sea levels using both sources of data, for PCCSP Partner Countries (based on methods in Church et al., 2006).

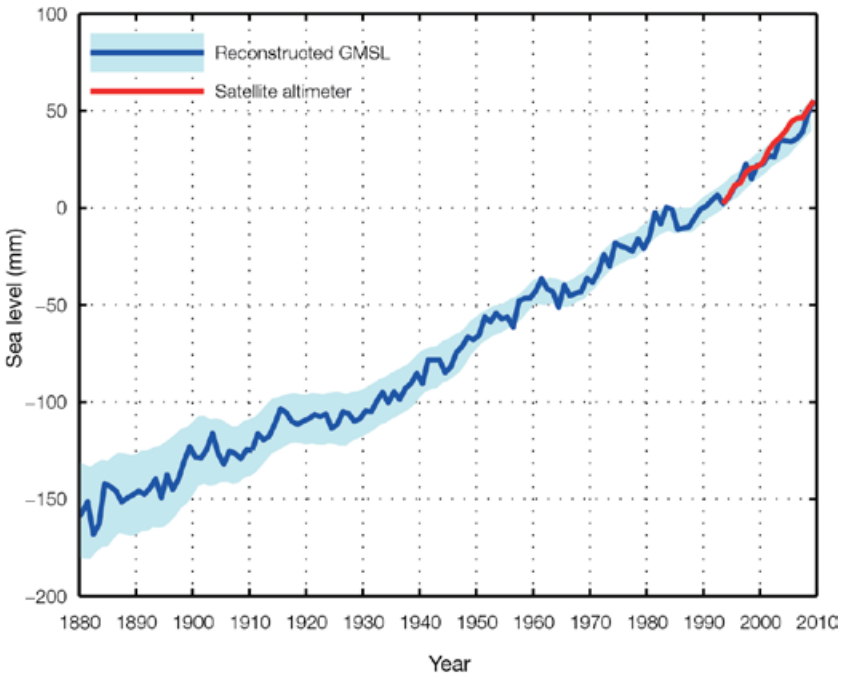

Figure 3.22: Annual global averaged sea level from 1880 to 2009 estimated from coastal and island sea-level data (blue) and from the satellite-altimeter data since 1993 (red). The one standard deviation uncertainty estimates plotted about the low passed (smoothed) sea level are indicated by the shading. The sea level estimated from the coastal and island data has an arbitrary datum and for convenience is set to zero in 1990. The altimeter data is set to the same value as the in situ data at the start of the satellite record in 1993 (following Church and White, in press).

Over the short period from 1993 to 2009, both the altimeter and in situ data indicate a higher than global average rate of rise in the western Pacific and eastern Indian Oceans, up to about three times the global average (Figure 3.23). However, because of the strong influence of ENSO and decadal variability on sea level in the region, this higher rate of rise is not necessarily representative of a longer time span. Merrifield (2011) argues that the high rates of sea-level rise in the western Pacific are a result of an intensification of the easterly trade winds across the tropical Pacific Ocean. For a longer time span, Church et al. (2006) examined the tide gauge records in the region and found the rate of relative sea-level rise (ocean relative to the land) was in the range -0.6 ± 0.5 mm per year to 6.7 ± 0.8 mm per year over varying time spans. Some of these records are likely to be affected by poorly known vertical land motions and poorly determined decadal variability.

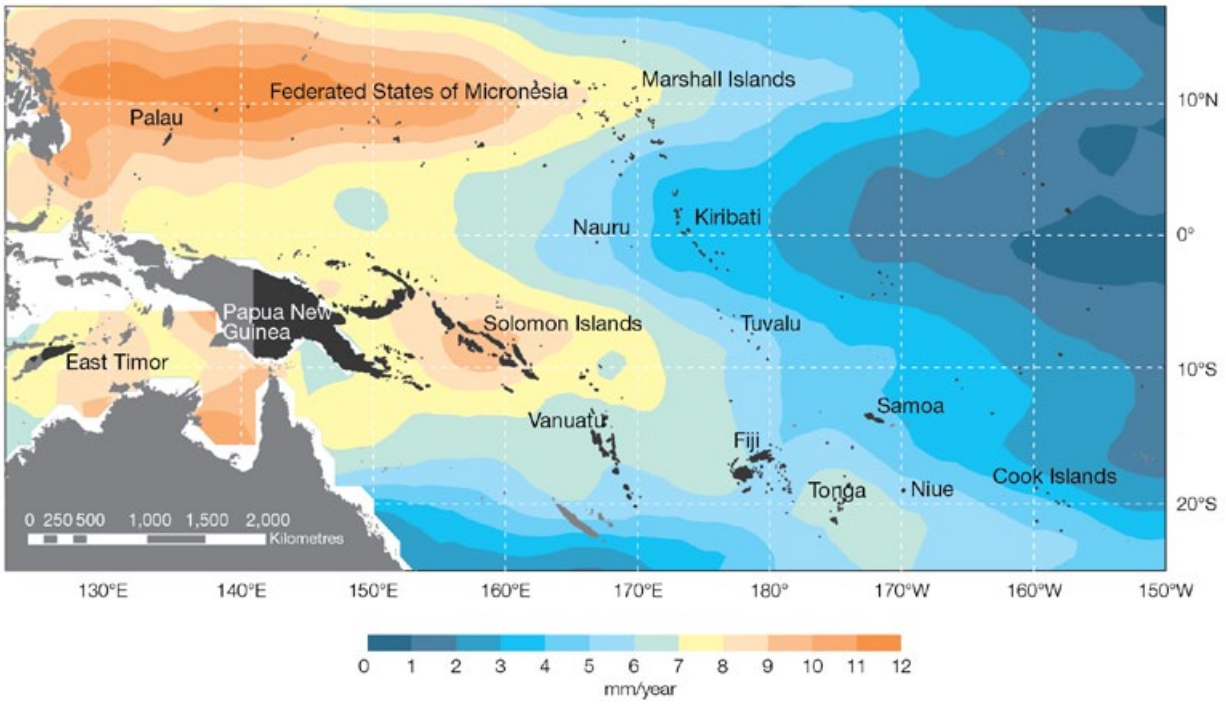

Figure 3.23: The regional distribution of sea-level rise measured by satellite altimeters from January 1993 through December 2009.

Trends in extreme sea level were analysed by Woodworth and Blackman (2004) at 141 tide gauges across the globe since 1975, including around 20 gauges in the tropical Pacific. By modifying the background state, rising sea levels and ENSO have a strong influence on the occurrence of extreme sea levels. Woodworth and Blackman (2004) showed that extreme sea levels are positively correlated with the SOI at tide gauges in the western tropical Pacific west of 180°, while gauges on the equator to the east of this are negatively correlated with the SOI. Menendez and Woodworth (2010) used sea-level records from 258 tide gauges across the globe, including over two dozen in the tropical Pacific, and found similar results. Hence, extreme high sea levels are more probable in the western Pacific (approximately to the west of 180°) during La Niña events, while to the east of 180° they are more probable during El Niño events. These relationships have been investigated in detail for the US-affiliated states (Guam, Palau, the Northern Mariana Islands, the Marshall Islands, the Federated States of Micronesia, and American Samoa) by Chowdhury et al. (2007, 2010) who noted that prediction of ENSO events can be used in early warning systems for sea-level extremes in the region.

For the highest 1% of sea levels, there are positive trends over decadal periods in most tide gauge records analysed (Woodworth and Blackman, 2004). These trends are similar to trends in mean sea level, leading to the conclusion that changes in mean sea level, and not changes in storminess, are driving current trends in extreme sea levels. Using two metrics for extreme sea levels, the 99th percentile sea level and the 50-year return period, Menendez and Woodworth (2010) also found that there has been an increasing trend in extreme sea levels globally, including in the PCCSP region, which has been more pronounced since the 1970s, and this trend is consistent with trends in mean sea level.

3.6.4 Ocean Circulation

A number of multi-decadal changes in ocean circulation have been observed in the Pacific region. As discussed in Section 3.4.6, there has been a poleward movement and acceleration of the sub-tropical westerlies over recent decades, associated with a more positive Southern Annular Mode. Dynamical arguments suggest that these wind changes should result in an increase in the strength of the South Pacific oceanic sub-tropical gyre. Such changes have indeed been identified in recent decades, via both in situ observations of ocean currents and satellite altimetry, which can be used to infer large-scale circulation patterns (Roemmich et al., 2007). However, the observational record is short, making trends sensitive to natural variability. These changes have also been found in 20th century simulations from most climate models that include interactive atmosphere and ocean components (Cai et al., 2005; Saenko et al., 2005).

As noted earlier, there appears to have been a weakening of the Walker Circulation and associated equatorial trade winds since 1975 (Vecchi et al., 2006; Zhang and Song, 2006; Power and Smith, 2007; Power and Kocuiba, 2010, in press), which might be expected to have had some influence on equatorial currents. Time series of currents are available from the array of instruments moored in discrete locations along the equatorial Pacific Tropical Atmosphere Ocean moorings (Hayes et al., 1991). These data confirm that large year-to-year variations in the strength of the sub-surface Equatorial Undercurrent (Figure. 2.13) is closely linked with changes in the overlying trade winds (Izumo, 2005). However, a discernable long-term trend is yet to be detected. At 110°W there is a small but statistically significant decrease in the strength of the surface South Equatorial Current but no significant trend is seen further west at 140°W.

3.6.5 Ocean Acidification

The ocean is a major sink for anthropogenic carbon dioxide (CO_2) and takes up about one quarter of the annual CO_2 emissions that result from human activities (Sabine et al., 2004; Le Quere et al., 2009). The CO_2 taken up by the ocean reacts in water and causes a decrease in the pH of the seawater that is referred to as ocean acidification. The pH change is accompanied by an increase in the concentration of total dissolved inorganic carbon, and a decrease in the dissolved carbonate ion concentration of the seawater (Feely et al., 2004). The decrease in dissolved carbonate ion concentrations causes a lowering of the seawater saturation states of the biogenic forms of calcium carbonate (aragonite, calcite and high magnesium calcite) that are secreted as shells or skeletal material by many key species in marine ecosystems (Feely et al., 2004).

The changes in the carbonate saturation states and in the pH of seawater predicted to occur this century have the potential to severely disrupt the health and sustainability of reef ecosystems (Guinotte and Fabry, 2008). While only a small number of species have been grown experimentally under high CO_2 conditions to mimic the acidification effects expected this century, evidence indicates that changes in carbonate saturation states may eventually lead to a condition where processes that act to degrade reefs (bioerosion, dissolution, storm damage) overcome the capacity of corals and other calcifiers to grow and maintain a healthy reef ecosystem (Manzello et al., 2008; Silverman et al., 2009). The reduction in seawater pH may also influence the lifecycle of marine organisms by altering long-term metabolic function, reproduction and growth, although the sensitivity to these changes is not well known (Fabry et al., 2008; Guinotte and Fabry, 2008; Munday et al., 2009; Munday et al 2010). Other stressors, like ocean warming, are likely to add to the ecosystem response (Anthony et al., 2008; Hoegh-Guldberg et al., 2007).

Since pre-industrial times, the pH of global surface waters is estimated to have declined by about 0.1 units, representing about a 30% increase in the hydrogen ion concentration (Feely et al., 2009). Observations made since the early 1990s in the sub-tropical North Pacific Ocean (Figure 3.24) show surface water pH decreases as the partial pressure of CO_2 (pCO_2) in the surface water increases as a result of CO_2 uptake driven by increasing concentrations of atmospheric CO_2. The same data also show a long-term decline in the seawater saturation states of the biogenic carbonates, aragonite and calcite. The saturation states are the product of the concentrations of dissolved calcium and carbonate ion concentrations in seawater, divided by the solubility products for calcite and aragonite, respectively.

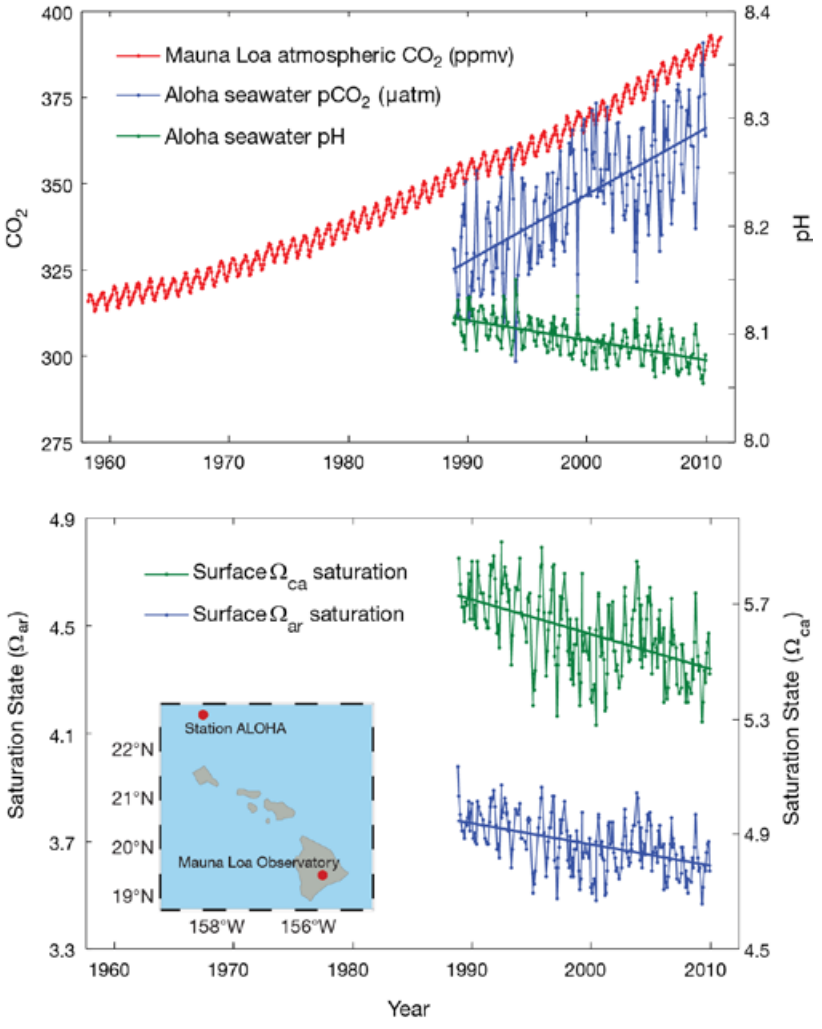

Figure 3.24: (Top) Atmospheric CO_2 measured at Mauna Loa Observatory (ppmv), and surface ocean pH and pCO_2 (µatm) at the Hawaii Ocean Time Series site, Station Aloha, in the sub-tropical North Pacific Ocean. (Bottom) Seawater calcite and aragonite saturation state data for surface waters at Station Aloha (Adapted from: Dore et al., 2009 and Feely et al., 2009).

Tropical reef-building corals secrete calcium carbonate as aragonite and tend to show a reduction in calcification at lower seawater aragonite saturation states (Langdon and Atkinson, 2005). Aragonite saturation states above about 4 are considered optimal conditions for healthy coral reef ecosystems, with values below 3.5 becoming increasingly marginal for supporting healthy coral reef growth (Guinotte et al., 2003).

Data collected in the Pacific region as a part of the Joint Global Ocean Flux Study/World Ocean Circulation Experiment CO_2 survey allow estimates to be made of the aragonite saturation states of seawater in the pre-industrial era and in the 1990s. In pre-industrial times, the saturation state values were above 4 throughout most of the sub-tropical and tropical Pacific Island region, apart from a small equatorial band east of 150°W (Figure 3.25, top). By the mid 1990s, the uptake of anthropogenic CO_2 had resulted in a widespread decline in the aragonite saturation state, with values slightly above 4 only found in the region of the South Equatorial Current and in the western Pacific (Figure 3.25, bottom). Values of aragonite and other carbonate saturation states have continued to decline since the 1990s and only the surface waters of the South Equatorial Current now have aragonite saturation states that remain at or slightly above values of 4.

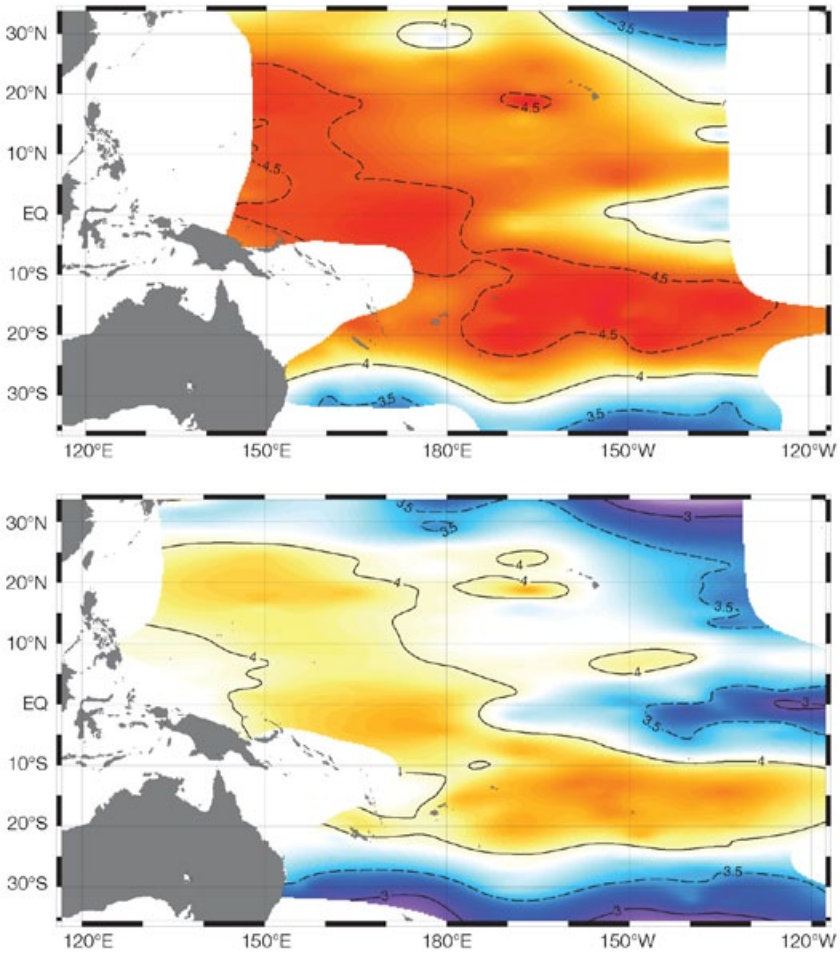

Figure 3.25: (Top) Seawater aragonite saturation state values calculated for the pre-industrial period (about 1765) using GLODAP data on dissolved inorganic carbon parameters (Lamb et al., 2002), including estimates of anthropogenic CO_2 (Sabine et al., 2004). (Bottom) The seawater aragonite saturation state calculated for JGOFS/WOCE CO_2 survey data collected in the 1990s (Data source: GLODAP data base, Carbon Dioxide Information Analysis Center, Oak Ridge, Tennessee, http://cdiac.ornl.gov/oceans/glodap/).

Climate science workshop, Samoa

Chapter 4
Climate Projection Methodology

Summary

In general, the Pacific Climate Change Science Program (PCCSP) climate projections were derived using output from global climate model simulations of the future climate, performed as part of the international Coupled Model Intercomparison Project (CMIP3). The projections focused on simulations corresponding to three Intergovernmental Panel on Climate Change (IPCC) future scenarios representing B1 (low), A1B (medium) and A2 (high) greenhouse gas emissions respectively, for three 20-year time periods (centred on 2030, 2055 and 2090). Since the skill of global climate models decreases at smaller spatial scales (e.g. at the scale of an individual country or island), a number of methods were used to enhance the resolution of the CMIP3 output locally (known as downscaling):

- Dynamical downscaling was conducted at 60 km horizontal resolution for the entire PCCSP region, using a high resolution atmospheric model driven by the changes in sea-surface temperature simulated by six CMIP3 models under the A2 (high) emissions scenario, with a focus on two 20-year future time periods (centred on 2055 and 2090).
- Dynamical downscaling was conducted at 8 km horizontal resolution for seven PCCSP Partner Country regions (each measuring approximately 1000 km x 1000 km), using a high resolution atmospheric model driven by the changes in sea-surface temperature simulated by three CMIP3 models under the A2 (high) emissions scenario, for two 20-year future time periods (centred on 2055 and 2090).
- Statistical downscaling was conducted for selected sites, using a statistical model that combines information regarding observed trends over recent decades with projected changes from the 60 km dynamical downscaling. Projections were calculated out to either 2040 or 2065 under the A2 (high) emissions scenario, depending on the quality and length of time that observational data is available.

Substantial and additional analysis of CMIP3 and/or dynamical downscaled output was required in order to provide sea-level, tropical cyclone and ocean acidification projections.

4.1 Introduction

The complexity of the climate system means that we cannot simply extrapolate past trends to forecast future conditions. Instead, mathematical representations of the Earth's climate system, called global climate models (Section 4.3), are used to simulate the fundamental processes driving weather and climate. These models are very complex and require substantial supercomputer resources. Over recent decades, global climate models have been developed and utilised extensively not only to project future climate change, but also to help better understand the present and past climate.

One of the key conclusions of the Intergovernmental Panel on Climate Change (IPCC) Fourth Assessment Report was that most of the global warming since the mid-20th century is very likely due to increases in greenhouse gas emissions from human activities (IPCC, 2007). Given the important role that these emissions have played in the climate of the past century, estimates of the evolution of these emissions over the coming decades are needed to simulate future climate change using climate models. Such estimates were provided by the IPCC Special Report on Emissions Scenarios (SRES), for use in climate research (Section 4.2). A number of research groups participated in a recent international climate model intercomparison project, for which they were required to apply a selection of the IPCC emissions scenarios to global climate model simulations of the future climate (Section 4.3.1). In this publication, climate projections for the broad PCCSP region were calculated from the output of this project (Section 4.4.1), while projection information at the country and/or individual island scale was obtained by further processing the output, using techniques known as dynamical downscaling and statistical downscaling (Sections 4.4.2, 4.5 and 4.6). For projections of sea level, tropical cyclones and ocean acidification, substantial additional analysis of the intercomparison project output and/or dynamically downscaled results was undertaken (Sections 4.7, 4.8 and 4.9).

4.2 Emissions Scenarios

Greenhouse gases such as water vapour, carbon dioxide (CO_2), methane and nitrous oxide are a vital feature of the Earth's climate, because they are able to trap long-wave radiation emitted from the Earth and therefore act to warm the lower atmosphere. In fact, in the absence of atmospheric greenhouse gases, the average temperature on Earth would be below freezing. However, the atmospheric concentration of these gases has been increasing since 1750, due to a rise in emissions from human activities. Most of the global warming since the mid-20th century is very likely due to this increase in human-related greenhouse gas emissions (IPCC, 2007).

To assist in modelling the future climate, the IPCC prepared 40 greenhouse gas and sulphate aerosol emissions scenarios for the 21st century that combine a variety of plausible assumptions about demographic, economic and technological factors likely to influence future emissions (IPCC, 2000). These include assumptions regarding population growth, energy generation and transport using fossil fuels, agriculture, land-clearing, industrial processes and waste. Each future scenario represents a variation within one of four storylines: A1, A2, B1 and B2 (Box 4.1), leading to a range of projected CO_2, methane, nitrous oxide, and sulphate aerosol emissions.

Box 4.1: Intergovernmental Panel on Climate Change Emissions Scenarios

The IPCC Special Report on Emissions Scenarios (SRES) developed 40 plausible futures based on various assumptions about demographic change, economic development and technological change (IPCC, 2000). These were grouped into four 'storylines' (A1, A2, B1 and B2).

A1. The A1 storyline describes a future world of very rapid economic growth, a global population that peaks in mid-century and declines thereafter, and the rapid introduction of new and more efficient technologies. Major underlying themes are convergence among regions, capacity building and increased cultural and social interactions, with a substantial reduction in regional differences with respect to per capita income. The A1 storyline develops into three scenario groups that describe alternative directions of technological change in the energy system. They are distinguished by their technological emphasis: fossil intensive (A1FI); non-fossil intensive energy sources and technologies (A1T); or a balance across all sources (A1B) (where balance is defined as not relying too heavily on one particular energy source, on the assumption that similar improvement rates apply to all energy supply and end use technologies).

A2. The A2 storyline describes a very heterogeneous world. The underlying theme is self-reliance and preservation of local identities. Fertility patterns across regions converge very slowly, resulting in a continuously increasing global population. Economic development is primarily regionally oriented and per capita economic growth and technological change is more fragmented and slower than for the other storylines.

B1. The B1 storyline describes a convergent world with the same global population as in the A1 storyline (one that peaks in mid-century and declines thereafter) but with rapid change in economic structures toward a service and information economy, with reductions in material intensity and the introduction of clean and resource efficient technologies. The emphasis is on global solutions to economic, social and environmental sustainability, including improved equity, but without additional climate initiatives.

B2. The B2 storyline describes a world in which the emphasis is on local solutions to economic, social and environmental sustainability. It is a world with a continuously increasing global population at a rate lower than A2, intermediate levels of economic development, and less rapid, and more diverse technological change than in the B1 and A1 storylines. Whilst the scenario is also oriented towards environmental protection and social equity, it is focused on local and regional levels.

Rather than consider all 40 future emissions scenarios, climate projection studies typically focus on a maximum of six scenarios: four so-called marker scenarios (A1B, A2, B1 and B2) and two additional illustrative scenarios (A1FI and A1T). For the purposes of the PCCSP, it was considered sufficient to consider only the B1, A1B and A2 scenarios, as these represent a low, medium and high emissions future respectively (Figure 4.1).

The final greenhouse gas concentration in the atmosphere depends not only on the rate of anthropogenic emissions, but also on the lifetime of the gases in the atmosphere and the ability of the biosphere and oceans to withdraw them from the atmosphere. For instance, CO_2 is continuously cycled between the atmosphere, ocean and land, which involves a range of processes with different time scales. Around half of the emitted CO_2 is removed from the atmosphere on a time scale of 30 years, a further 30% is removed within a few centuries, and the remaining 20% may stay in the atmosphere for thousands of years (Denman et al., 2007).

Due to its relatively high atmospheric concentration and potency as an absorber of long-wave radiation, CO_2 is often discussed alone, without reference to greenhouse gases that have a lesser cumulative influence on the temperature of the lower atmosphere (such as methane and nitrous oxide).

Carbon cycle models are used to calculate the atmospheric greenhouse gas concentrations that will arise from a given emissions scenario. These models include the uptake of emissions by the land and ocean, relevant climate feedbacks, and the gas transport and chemical reactions occurring in the atmosphere. For the 40 SRES emissions scenarios, carbon cycle models give estimates of atmospheric CO_2 concentrations for the year 2100 ranging from 500 to 1200 parts per million (ppmv) (Figure 4.1; Meehl et al., 2007b), compared to the 2010 concentration of 390 ppmv and the pre-industrial value of 280 ppmv (http://www.csiro.au/greenhouse-gases/; Meure et al., 2006; Etheridge et al., 1996). Since the release of the SRES report in 2000, observed greenhouse gas emissions have been tracking near the high end of the emissions scenarios (between A1B and A1FI), although there was a drop in 2008 due to the global financial crisis (Manning et al., 2010; Friedlingstein et al., 2010; Raupach and Canadell, 2010).

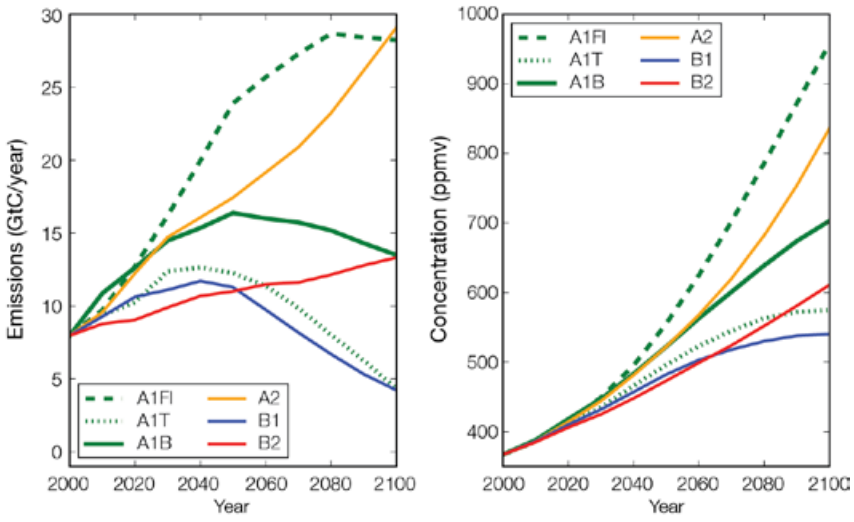

Figure 4.1: Global average carbon dioxide emissions in gigatonnes (thousand million tonnes) of carbon per year (GtC/yr) for the four marker (A1B, A2, B1 and B2) and two illustrative (A1FI and A1T) SRES future emissions scenarios (left), and the estimated resulting atmospheric carbon dioxide concentration in parts per million (ppmv; right). Projected changes in other greenhouse gases and aerosols can be found in Figure 10.26 of the IPCC Fourth Assessment Report (IPCC, 2007).

4.3 Global Climate Models

Global climate models are used to simulate the behaviour of the atmosphere, oceans, land surface and cryosphere (ice covered areas) over the entire planet. Variables such as temperature, rainfall and wind are calculated over a three-dimensional array of grid cells covering the globe and spaced typically 100–400 km apart, with around 40 layers through the depth of the ocean and around 40 layers through the height of the atmosphere, depending on the model (Figure 4.2). Typically, the time step is about half an hour, so climate models can simulate hourly to daily weather (the average weather over 30 years or more is called climate; Section 1.1). Weather conditions in the model change according to a set of mathematical rules based on the laws of physics, such as conservation of mass, energy and momentum. Processes that occur at spatial scales smaller than the model grid spacing, such as water droplet formation in clouds and turbulence in near-surface winds, are represented by parameterising the influence of these processes on the larger scale. Parameterisation is basically a complex method of estimation, which typically combines well-established laws of physics with observational data.

Many research institutions around the world develop and maintain their own global climate models. While these models are similar in many ways, subtle variations exist with respect to factors such as grid characteristics (e.g. spatial resolution), parameterisation schemes and model sub-components (e.g. some models include a representation of atmospheric chemistry, while others do not), which means that climate simulations arising from these models differ. In an attempt to coordinate the analysis of these differences, a number of international model intercomparison projects have been conducted in recent decades (Meehl et al., 2000). The most recent is known as the Coupled Model Intercomparison Project Phase 3 (CMIP3; Meehl et al., 2007a), and the output from this project formed the basis for many of the climate projections presented in both this publication (Section 4.4) and the IPCC Fourth Assessment Report (IPCC, 2007).

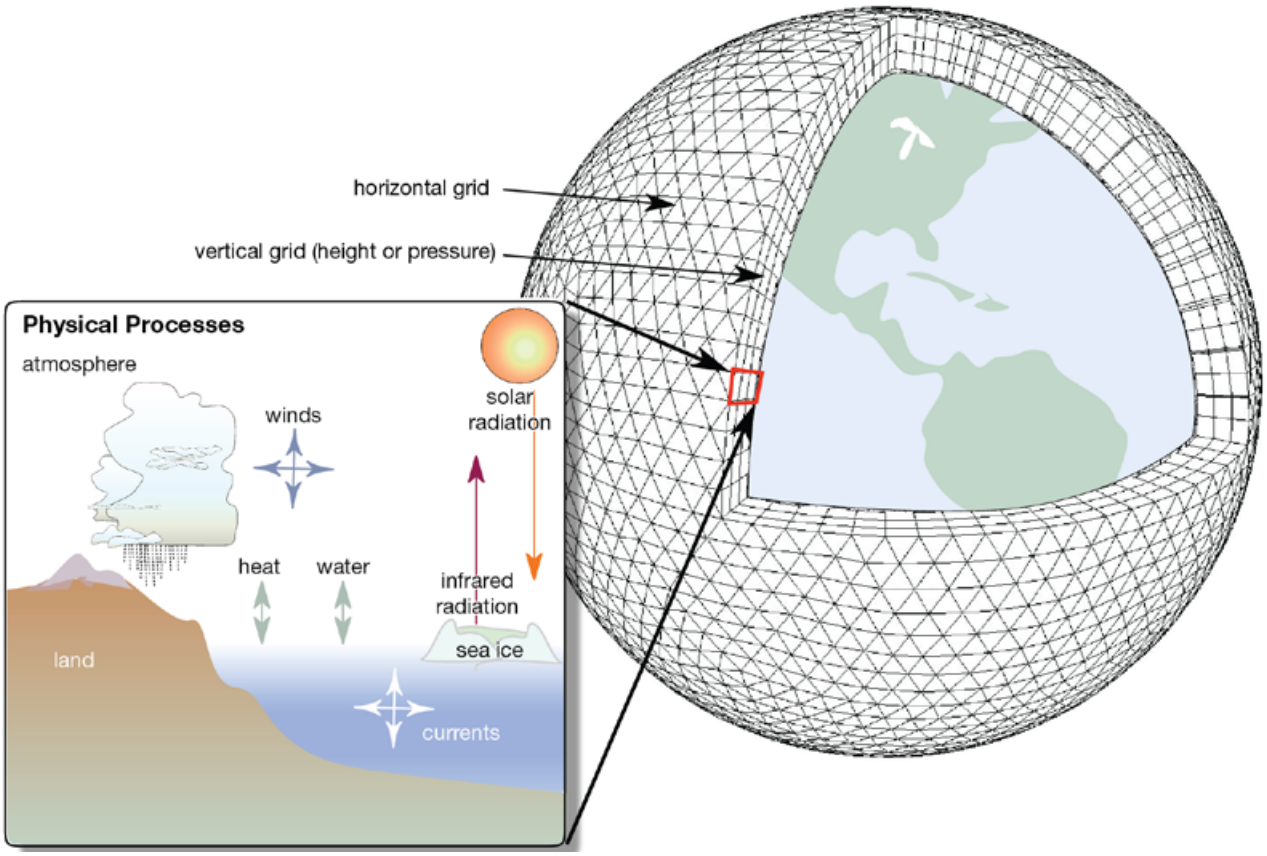

Figure 4.2: Schematic illustrating how the Earth is represented by a series of grid cells in global climate models. Some of the physical processes simulated in a typical global climate model are shown inset. (Source: Centre for Multiscale Modelling of Atmospheric Processes[1]).

[1] http://www.cmmap.org/learn/modeling/whatIs2.html

4.3.1 Coupled Model Intercomparison Project Phase 3

A total of 24 global climate models contributed model output to the CMIP3 project (Table 4.1), which is freely available from the Program for Climate Model Diagnosis and Intercomparison at Lawrence Livermore National Laboratory (www-pcmdi.llnl.gov). Participating institutions were required to perform a number of model simulations, each differing in terms of the external forcing applied to the climate system. External climate forcings are factors that can alter the energy balance of the Earth system (and thus the climate), and can be either natural (e.g. volcanic activity) or human-related (e.g. greenhouse gas and aerosol emissions).

The CMIP3 simulations relevant to the PCCSP include:

- **Pre-industrial control simulation (PIcntrl).** Incorporates a seasonally varying but annually unchanging external forcing indicative of the late 19th century (usually corresponding to 1870 conditions).
- **Climate of the 20th century simulation (20c3m).** Modelling groups initiated their global climate model from the PIcntrl (circa 1870) simulation and then imposed the natural and human-related forcing thought to be important for simulating the climate of the 20th and late 19th centuries.
- **Climate of the 21st century simulations.** Modelling groups initiated their global climate model from the 20c3m (circa 2000) simulation and then imposed the human-related forcing associated with one or more of the B1, A1B or A2 SRES emissions scenarios (Section 4.2). None of the modelling groups used the A1FI emissions scenario. These simulations were run until the end of the 21st century (and sometimes beyond).

Output from the PIcntrl and 20c3m simulations was used extensively in evaluating the CMIP3 models over the PCCSP region (Chapter 5), while a number of SRES emissions scenario simulations were used in determining PCCSP climate projections (Section 4.4). It should be noted that many institutions did not provide output for all the variables and SRES emissions scenarios requested by the CMIP3 organisers. In addition, the availability of monthly output is greater than for daily output, due to the extra data storage requirements associated with the latter. The availability of CMIP3 output relevant to this publication is outlined in Appendix 1.

Table 4.1: Participating CMIP3 climate models. For additional details see www-pcmdi.llnl.gov, Randall et al. (2007) and Santer et al. (2009).

	Model name	Institute (country)	Forcings[a]
1	BCCR-BCM2.0	Bjerknes Centre for Climate Research (Norway)	G,SD
2	CCSM3	National Center for Atmospheric Research (USA)	G,O,SD,BC,OC,SO,U
3	CGCM3.1(T47)[b]	Canadian Centre for Climate Modelling & Analysis (Canada)	G,SD
4	CGCM3.1(T63)[b]	Canadian Centre for Climate Modelling & Analysis (Canada)	G,SD
5	CNRM-CM3	Centre National de Recherches Météorologiques (France)	G,O,SD,BC
6	CSIRO-Mk3.0	CSIRO Marine and Atmospheric Research (Australia)	G,O,SD
7	CSIRO-Mk3.5	CSIRO Marine and Atmospheric Research (Australia)	G,O,SD
8	ECHAM5/MPI-OM	Max Planck Institute for Meteorology (Germany)	G,O,SD,SI
9	ECHO-G[b]	Meteorological Institute of the University of Bonn and Korea Meteorological Administration (Germany/Korea)	G,SD,SI
10	FGOALS-g1.0	Institute of Atmospheric Physics (China)	G,SD
11	GFDL-CM2.0	Geophysical Fluid Dynamics Laboratory (USA)	G,O,SD,BC,OC, LU,SO,V
12	GFDL-CM2.1	Geophysical Fluid Dynamics Laboratory (USA)	G,O,SD,BC,OC, LU,SO,V
13	GISS-AOM	Goddard Institute for Space Studies (USA)	G,SD,SS
14	GISS-EH	Goddard Institute for Space Studies (USA)	G,O,SD,SI,BC,OC,MD,SS,LU,SO,V
15	GISS-ER	Goddard Institute for Space Studies (USA)	G,O,SD,SI,BC,OC,MD,SS,LU,SO,V
16	INGV-SXG	Instituto Nazionale di Geofisica e Vulcanologia (Italy)	G,O,SD
17	INM-CM3.0[b]	Institute for Numerical Mathematics (Russia)	G,SD,SO
18	IPSL-CM4	Institut Pierre Simon Laplace (France)	G,SD,SI
19	MIROC3.2 (hires)	Center for Climate System Research (Japan)	G,O,SD,BC,OC,MD,SS,LU,SO,V
20	MIROC3.2 (medres)	Center for Climate System (Japan)	G,O,SD,BC,OC,MD,SS,LU,SO,V
21	MRI-CGCM2.3.2[b]	Meteorological Research Institute (Japan)	G,SD,SO
22	PCM	National Center for Atmospheric Research (USA)	G,O,SD,SO,V
23	UKMO-HadCM3	Hadley Centre for Climate Prediction and Research (UK)	G,O,SD,SI
24	UKMO-HadGEM1	Hadley Centre for Climate Prediction and Research (UK)	G,O,SD,SI,BC,OC,LU,SO,V

[a] **The climate forcing factors are G: Well-mixed greenhouse gases; O: Ozone; SD: Sulphate direct effect; SI: Sulphate indirect effect; BC: Black carbon; OC: Organic carbon: MD: Mineral dust; SS: Sea salt; LU: Land use; SO: Solar irradiance; and V: Volcanic aerosol.**

[b] Model adds artificial fluxes of heat (and in some cases fresh water and momentum) at the air-sea interface in order to prevent the model drifting towards an unrealistic state over long climate simulations. This process is known as flux adjustment and attracts concern because of its inherently non-physical nature, and because flux adjustments based on the present climate may not be valid in future climate simulations.

4.4 Climate Projection Methods

Climate models generate output for a wide range of variables, including temperature, rainfall, wind, humidity, evaporation, ocean salinity and solar radiation. The determination of climate projections for these variables therefore involves the direct analysis of climate model output. In particular, the CMIP3 archive of climate model output was used to determine the PCCSP large-scale climate variable projections (i.e. at the scale of the entire PCCSP region; Section 4.4.1).

While global climate models are useful for making large-scale climate projections, their skill decreases at finer temporal and spatial scales (Chapter 5). For instance, these models typically have insufficient horizontal grid resolution to explicitly represent small islands (i.e. the model just sees an area of ocean). This means that while they can simulate the large-scale climate conditions, they cannot account for some important local climate effects resulting from island shape and topography. A number of methods have been developed to try and overcome this limitation by enhancing the resolution of model output locally (Section 4.4.2). Of these methods, dynamical and statistical downscaling techniques were used to provide small-scale (i.e. country- and/or individual island-scale) PCCSP climate projections (Sections 4.5 and 4.6).

Unlike for typical climate variable projections, the PCCSP sea level, tropical cyclone and ocean acidity projections required substantial and additional analysis of CMIP3 and/or downscaled output, which sometimes incorporated other sources of information (see Sections 4.7, 4.8 and 4.9 respectively).

4.4.1 Large-Scale Projections

Large-scale ocean and atmosphere projections for the PCCSP region were calculated from CMIP3 climate model output for a B1 (low), A1B (medium) and A2 (high) SRES emissions scenarios (Box 4.1). Projections were given for three 20-year time periods centred on 2030 (2020–2039), 2055 (2046–2065) and 2090 (2080–2099), relative to 1990 (1980–1999) (Figure 4.3).

When formulating climate projections based on results from a number of different global climate models, a pragmatic and well-accepted approach is to combine the output and calculate a multi-model average (Knutti et al., 2010). However, while the practice of reporting multi-model average projections is well established, there are many variations on the precise methods used to formulate this average (Tebaldi and Knutti, 2007). These variations are typically associated with issues surrounding model skill in simulating the current climate, or the differing availability of data across emissions scenarios.

With respect to model skill, a number of CMIP3 models were found to simulate various key aspects of the Indo-Pacific climate less skilfully than other models (Section 5.5.1). For associated climate projections in this publication, these models were eliminated when calculating the multi-model average. Besides this skill-based elimination, all available CMIP3 models were typically included in calculating multi-model average projections, regardless of how many emissions scenarios they provided data for (see Appendix 1 for CMIP3 data availability). This approach is advantageous in terms of maintaining the largest possible sample size, however inconsistencies may arise in comparing projections between different variables and emissions scenarios. All included models were assigned equal weight in determining average projections, as opposed to an individual weight reflecting their respective skill, in accordance with recently published recommendations (Weigel et al., 2010). Unless otherwise stated, only the first model run was used for those models where multiple simulations are archived, for consistency with models that have only one simulation in the CMIP3 archive.

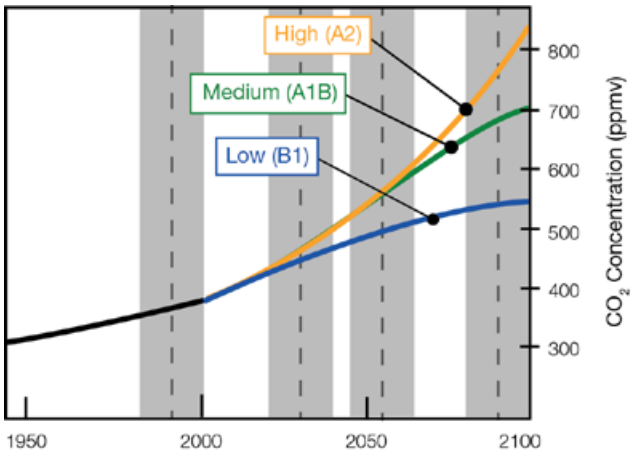

Figure 4.3: Large-scale projections for the PCCSP region were calculated from CMIP3 global climate model output for three 20-year periods centred on 2030, 2055 and 2090, relative to 1990 (shaded bars). These projections were determined for a low (B1), medium (A1B) and high (A2) future greenhouse gas emissions scenario (corresponding carbon dioxide concentrations are shown as blue, green and orange lines, respectively).

4.4.2 Small-Scale Projections

Given the relatively coarse spatial resolution of global climate model output, a variety of different methods have been developed to produce regional-scale projections for use in risk assessments (e.g. at the scale of an individual country or island). The choice of method must be matched to the intended application, taking into account local constraints of time, resources, human capacity and supporting infrastructure (Wilby et al., 2009). Options include:

- Sensitivity analysis. This entails running a climate impact model with observed climate data to establish a baseline level of risk, then re-running the model with the same input data, modified by selected changes in climate (e.g. a warming of 1, 2 or 3°C).
- Change factors. The changes in mean climate between a present and future period, as simulated by a climate model, are applied to observed climate data (e.g. the warming pattern from a CMIP3 model could be applied to observed data from the meteorological station in Rarotonga, Cook Islands).
- Climate analogues. Past climate data are used as an analogue for the future (e.g. the warming and sea level that occurred during the last interglacial period, 125,000 years ago).
- Trend extrapolation. Extension of recent climate trends into the future.
- Weather generation. Involves the use of a model that simulates time series of weather data, with statistical properties similar to observed weather data. These statistical properties can be modified for future climates using information from climate models.
- Dynamical downscaling. Involves the use of a finer resolution atmospheric climate model, driven by output from a global climate model. This provides better representation of topography and associated effects on local climate, such as rainfall in mountainous regions, as well as the potential to better simulate extreme weather features, such as tropical cyclones. This method is computationally intensive and the results are strongly dependent on the choice of both global climate model and fine resolution atmospheric model. In some cases, the projected changes can be applied directly to observed data, or statistically downscaled using observed data, for use in risk assessment.
- Statistical downscaling. This can be as simple as interpolating climate model output to a particular location, or as complex as constructing a statistical model that relates large-scale atmospheric variables and local-scale surface variables. Models of intermediate complexity are also popular. High-quality observed data are required for a number of decades to calibrate the statistical model, and results are strongly dependent on the choice of climate model.

The first five methods (sensitivity analysis, change factors, climate analogues, trend extrapolation and weather generation) are relatively easy to use, with low resource demands, but have significant disadvantages (Table 4.2). The remaining two methods (dynamical downscaling and statistical downscaling) are considered to have the most merit, despite increased complexity and higher demands on resources, and have been used to provide information regarding small-scale (i.e. country- and/or individual island-scale) climate change projections in the PCCSP (Sections 4.5 and 4.6).

Table 4.2: Options for creating regional climate projections, in order of increasing complexity and resource demands (modified from Table VI in Wilby et al. (2009)).

Method	Advantages	Disadvantages
Sensitivity analysis	1. Easy to apply 2. Requires no future climate change information 3. Shows most important variables/system thresholds 4. Allows comparisons between studies	1. Provides no insight into the plausibility/likelihood of associated impacts unless benchmarked to other scenarios 2. Impact model uncertainty seldom reported or unknown
Change factors	1. Easy to apply to observed data, assuming data from global climate models (GCMs) are available	1. Only changes baseline mean of the observed data, so changes in variability and sequencing of events remain unchanged 2. Limited applicability where changes in extreme events are important
Cliamte Analogues	1. Easy to apply 2. Requires no future climate change information 3. Reveals multi-sector impacts/vulnerability to past climate conditions or extreme events, such as a flood or drought episode	1. Assumes that the same socio-economic or environmental responses recur under similar climate conditions 2. Requires data on confounding factors such as population growth, technological advance, conflict
Trend extrapolation	1. Easy to apply 2. Reflects local conditions 3. Uses recent patterns of climate variability and change 4. Tools freely available	1. Typically assumes linear change 2. Trends (sign and magnitude) are sensitive to the choice/length of record 3. Assumes recent trend will persist, despite evidence for abrupt changes in the past 4. Needs high quality observational data for calibration
Weather generators	1. Modest computational demand 2. Provides daily or sub-daily weather variables 3. Preserves relationships between weather variables 4. Already in widespread use for simulating present climate 5. Tools freely available	1. Needs high quality observational data for calibration and verification 2. Assumes a constant relationship between large-scale circulation patterns and local weather 3. Scenarios are sensitive to choice of predictors and quality of GCM output 4. Scenarios are typically timeslice rather than transient 5. Difficulty reproducing interannual variability (e.g. due to ENSO) and tropical weather phenomena such as monsoons and tropical cyclones
Dynamical downscaling	1. Maps regional climate scenarios at 10–60 km resolution 2. Reflects underlying land-surface controls and feedbacks 3. Preserves relationships between weather variables 4. Often gives a better representation of coastal and mountain effects, and extreme weather events 5. Simulations with bias-corrected sea-surface temperatures should make the present climate simulation more realistic than the host GCM 6. Potentially can apply projected changes to observed data for risk assessments	1. Has a high computational and technical demand, which limits the number of GCMs, emissions scenarios and time periods that can be downscaled, so the range of uncertainty in projections tends to be sub-sampled 2. Projections are sensitive to choice of host GCM and high-resolution atmospheric model 3. Requires high quality observational data for model verification 4. Some biases potentially remain in the present climate simulation (e.g. too wet/dry), so caution is needed in using data directly in risk assessments 5. Need to assess model reliability before using in risk assessment 6. It should not be assumed that the dynamically downscaled projections are necessarily more reliable than projections based on the host model
Statistical downscaling	1. Modest computational demand 2. Site specific time series and other statistics, e.g. extreme event frequencies 3. Reduces biases in climate model data 4. Tools freely available	1. Requires high quality observational data over a number of decades for calibration and verification 2. Assumes a constant relationship between large-scale circulation patterns and local weather 3. Scenarios are sensitive to choice of forcing factors and host GCM or dynamical downscaling model 4. Choice of host GCM or dynamical downscaling model constrained by archived outputs 5. Hard to choose from the large variety of methods, each with pros and cons

4.5 Dynamical Downscaling

In dynamical downscaling, large-scale climate information from a global climate model is used as input to a finer resolution atmospheric model with more detailed topography, land use and coastal boundaries (the global climate model information is said to drive the finer resolution model). This allows atmospheric processes to be simulated with greater detail, possibly resulting in an improved representation of weather events (particularly extremes). However, finer resolution comes at the cost of increased computer time and data storage. This constrains the number of global climate models and emissions scenarios that can be downscaled, as well as the duration and geographic area of downscaled simulations. Therefore, dynamical downscaling tends to sub-sample the broader range of possible future climates simulated by global climate models.

4.5.1 Downscaling Methods

As for global climate models, there are many scientific institutions around the world that are involved in dynamical downscaling. There are a number of different approaches taken by these institutions, which can be summarised into three types:

- Limited time slice experiments with fine-resolution global atmospheric models.
- Fine-resolution atmospheric models embedded within global climate model output over a limited area (known as limited-area models).
- Stretched-grid atmospheric models with finer resolution over a region of interest and coarser resolution over the rest of the globe.

Given the computationally expensive nature of fine resolution atmospheric simulations over the entire globe, time slice simulations of only 20 or 30 years duration are run, as opposed to an entire climate run of 100 years or more. These simulations provide the most comprehensive depiction of the climate, at the expense of full temporal coverage.

Fine resolution, limited-area models are less computationally demanding, as they only simulate a restricted region of the globe. They are therefore able to provide much greater temporal coverage, but require significant amounts of input data from a host global climate model at their lateral boundaries (the limited-area model is said to be nested in the host model). Problems can arise at these boundaries due to differences in resolution, model physics and evolution of weather events between the global climate model and limited-area model.

Stretched-grid models provide a compromise between the global high resolution and limited-area approaches by providing finer resolution over the area of interest, while maintaining a coarser resolution for the remainder of the globe. Although a stretched-grid model simulates the atmosphere of the entire globe, the resolution can vary from approximately 60 km in the region of interest up to 400 km in other areas. This approach allows for better representation of local climate factors (e.g. topography), however it may compromise the simulation of distant factors that influence the regional climate of interest (e.g. the El Niño-Southern Oscillation influences regions located thousands of kilometres from the tropical Pacific Ocean).

4.5.2 Downscaling in the Pacific Climate Change Science Program

The dynamical downscaling conducted in the PCCSP consisted of a primary set of simulations from which climate projections were derived, as well as a series of additional simulations designed to assess the uncertainty associated with those projections. All primary simulations were completed using CSIRO's global stretched-grid, Conformal Cubic Atmospheric Model (CCAM; McGregor and Dix, 2008) run at 60 km horizontal resolution over the entire globe, while further downscaling to 8 km was conducted for selected Partner Countries. The additional simulations involved repeating the primary CCAM simulations with an alternative configuration for atmosphere/ocean interaction, as well as a series of simulations using five different limited-area models, in order to assess the influence of the selection of downscaling method on regional climate projections.

The CCAM model was chosen for the downscaling because it is a global atmospheric model, so it was possible to bias-adjust the sea-surface temperature in order to improve upon large-scale circulation patterns (Section 4.5.2.1). In addition, the use of a stretched grid eliminates the problems caused by lateral boundary conditions in limited-area models. The model has been well tested in various model intercomparisons and in downscaling projects over the Australasian region (Corney et al., 2010).

4.5.2.1 CCAM 60 km Global Simulations

These simulations were performed for six host global climate models (CSIRO-Mk3.5, ECHAM5/MPI-OM, GFDL-CM2.0, GFDL-CM2.1, MIROC3.2 (medres) and UKMO-HadCM3) that were deemed to have acceptable skill in simulating the climate of the PCCSP region (Section 5.5.1). For these simulations:

- The period 1961–2099 was simulated using the equivalent CO_2, direct aerosol effect and ozone distribution for the A2 (high) emissions scenario (except in simulating the current climate, which used 20c3m equivalents).
- Monthly, bias adjusted sea-surface temperature and sea-ice fraction output from the host global climate models was used. Bias adjustment refers to the removal of model errors in the present day, mean state climate. In this case, the sea-surface temperature bias adjustment was calculated by computing the monthly average biases of the global models for the 1971–2000 period, relative to the observed climatology, based upon the method of Reynolds (1988). These monthly biases were then subtracted from the global climate model monthly sea-surface temperature output throughout the simulation. This approach preserves the inter- and intra-annual variability and the climate change signal of the host global climate models (Nguyen et al., in press).
- No atmospheric input from the global climate models was used, as the bias adjusted sea-surface temperature is considered sufficient information to drive CCAM. In addition, the bias adjustment makes the global climate model atmospheric fields incompatible with the sea-surface temperature distributions. This procedure may be viewed as somewhat akin to the flux adjustment used in some global models (Table 4.1), however because no attempts are made to predict the ocean temperatures, only to downscale the atmosphere, the technique is acceptable in this context. It is assumed that the fixed, monthly adjustment is appropriate over the entire course of the simulation, which may be a disadvantage/limitation of the approach.
- The period 1961–2099 was simulated for the A2 (high) emissions scenario only.

4.5.2.2 CCAM 8 km Regional Simulations

The GFDL-CM2.1, UKMO-HadCM3 and ECHAM5 60 km CCAM global simulations were selected for further downscaling to 8 km. Of the six host models, these show a low, middle and high amount of global warming into the future, respectively. Due to the very high demand for computer resources when downscaling at 8 km resolution, the temporal and spatial extent of the simulations was limited. Only the 1980–1999, 2046–2065 and 2080–2099 time periods were simulated for seven 1000 km x 1000 km regions, including Papua New Guinea, East Timor, Fiji, Solomon Islands, Vanuatu, Samoa and the Federated States of Micronesia. These country regions were selected on the basis of five criteria:

1. Likely impact of model resolution on weather characteristics.
2. The desire to capture a range of climate regimes across the selected regions.
3. Mountainous terrain.
4. Population.
5. Discussion with Partner Countries.

4.5.2.3 Additional CCAM Simulations Using Alternative Settings

The primary 60 km CCAM and regional 8 km CCAM simulations were repeated with the inclusion of a 20-level mixed-layer ocean model and a thermodynamic sea-ice model, to allow for a more realistic interaction of the atmosphere, ocean and ice. A digital filter (Thatcher and McGregor, 2009) was used for the top 200 m of the mixed-layer ocean in order to keep the ocean simulation similar to the host global climate model.

4.5.2.4 Additional Limited-Area Model Simulations

Simulations at 50 km resolution were completed with five different limited-area models: PRECIS model (Jones et al., 2004), WRF model (Skamarock et al., 2008), Zetac model (Pauluis & Garner, 2006), MM5 model (Grell et al., 1994; Chen and Dudhia, 2001) and the RegCM3 model (Pal et al., 2007). The domain chosen was 145°E–170°W, 25°S–10°N and three sets of simulations were completed:

1. A simulation nested within the NCEP/DOE R-2 reanalyses dataset (Section 2.2) for the period 1981–2000, in order to evaluate the ability of the limited-area models to simulate the present day climate.
2. Simulations for the periods 1981–2000 and 2045–2065 nested in the output from the CCAM 60 km simulation driven by the GFDL-CM2.1 model, in order to evaluate projections arising from the limited-area models.
3. Additional simulations for some of the limited-area models using finer resolution and different model settings.

A summary of the downscaled simulations conducted for the PCCSP is given in Figure 4.4.

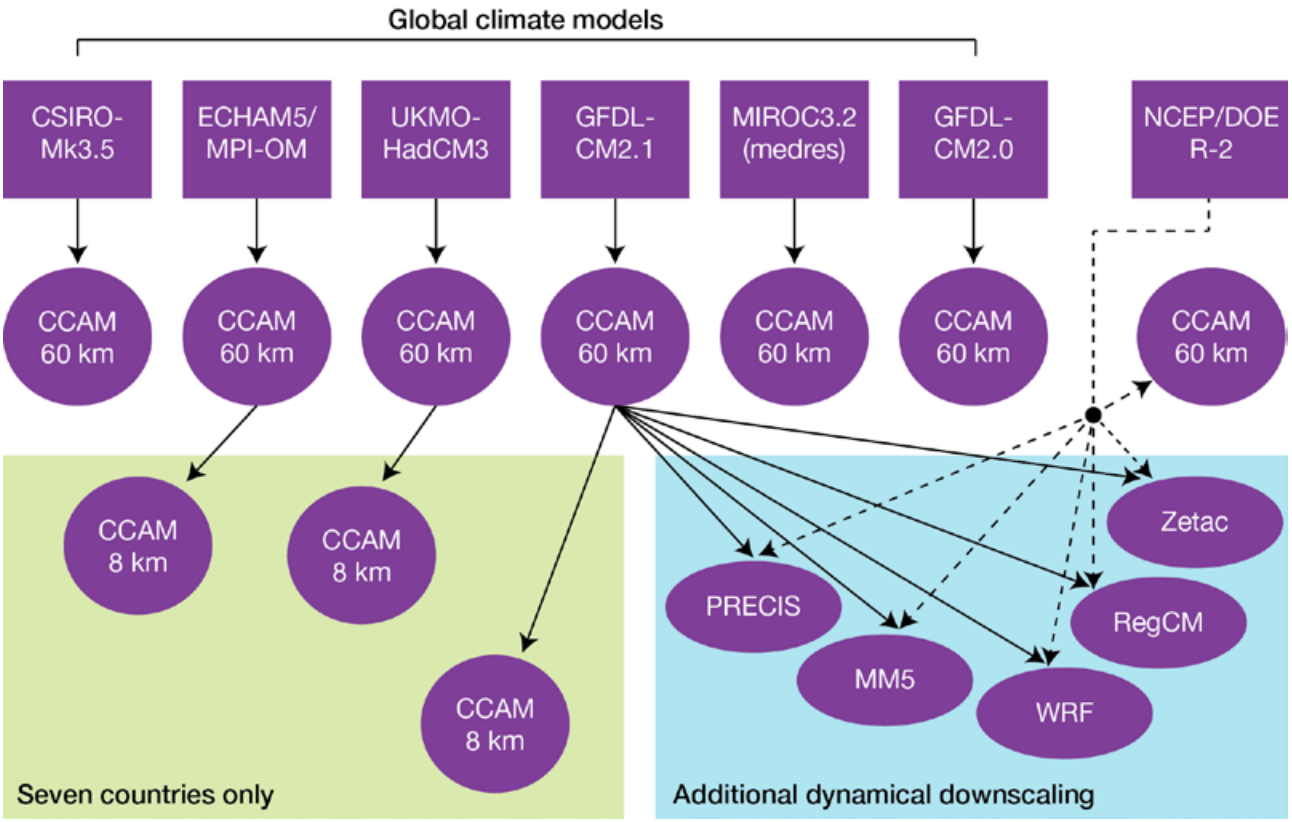

Figure 4.4: Summary of dynamical downscaling conducted in the PCCSP. All future time periods were simulated using the high (A2) emissions scenario.

4.6 Statistical Downscaling

Engagement with Partner Countries and other stakeholders has repeatedly emphasised that for strategic decision making there is often a preference for location-specific climate information over the large-scale information generally provided by global climate models (cf. Fowler et al., 2007; Murphy et al., 2009; Crimp et al., 2009; Kokic et al., 2007; Cao et al., 2003). This can be provided by statistical downscaling.

A recent IPCC guidance paper (Knutti et al., 2010) stated that four factors should be considered in assessing the likely future climate change in a region: historical change, process change (e.g. changes in the driving circulation), global climate change projected by global climate models and downscaled projected change. In the PCCSP, a statistical downscaling approach was developed and used that is consistent with these objectives. By establishing empirical relationships between coarse resolution climate variables and the local climate, the technique maintains important information regarding locally observed historic trends and variability, but also introduces important drivers of change from global climate models. Known as Linear Mixed Effect State-Space Modelling (Kokic et al., 2011), this technique was used in conjunction with a bootstrap (i.e. repeat sampling) simulation procedure based on quantile matching (Li et al., 2010) to simulate future daily climate. Compared to alternative approaches (Fowler et al., 2007), this technique has several advantages:

- The modelling and simulation accounts for seasonality and temporal and cross-variable dependencies in the locally observed data. The simulated daily data therefore exhibit quite realistic behaviour, which is important for subsequent application in research and risk assessments.
- The method forecasts the joint distribution of the climate variables, so the local climate variability as well as the change in the mean is projected.
- Time series can be generated continuously from past to future, which are suitable for direct use in risk assessments.

The Linear Mixed Effect State-Space method was used to downscale daily maximum temperature, minimum temperature and rainfall projections for 17 locations in seven Partner Countries (Table 4.3). Daily climate data archived by the US National Oceanic and Atmospheric Agency were used to build the statistical models, with the exception of Vanuatu, where high quality daily climate records from four climate stations were provided by the Vanuatu Meteorology and Geo-hazard Department. The selection of locations in each Partner Country was based on the length and quality of data available. In cases where data quality was severely compromised, these parts of the time series were removed.

Some specific aspects of the methodology are:

- Projections for a range of monthly summary statistics were made out to 2040 at all 17 locations, while for 12 locations the observational data were of sufficient length and quality to allow projections to be extended out to 2065 (Table 4.3).
- Daily time series were generated at all 17 locations for the period 1981–2000 and 2021–2040, and at 12 locations for 2046–2065.
- The projections were based on large-scale changes simulated by the CCAM 60 km simulations driven by the GFDL-CM2.1, UKMO-HadCM3 and ECHAM5 models, under the high (A2) emissions scenario.

Table 4.3: Climate station sites used for statistical downscaling. Locations where projections were made out to 2065 (as opposed to 2040) are indicated with an asterisk.

Country	Station names
Cook Islands	Rarotonga*
Federated States of Micronesia	Pohnpei*
Fiji	Matuku Nabouwalu Nadi airport* Nasouri* Vunisea*
Marshall Islands	Kwajalein Missle Majuro*
Samoa	Apia* Faleolo airport
Solomon Islands	Auki Honiara*
Vanuatu	Aneityum* Lamap* Pekoa* Sola*

4.7 Sea Level

Many factors need to be considered when making projections of future global sea level. These include:

- **Expansion / contraction of sea water (i.e. steric effects).** The ocean will expand if heated, and contract if cooled (known as the 'thermosteric' component of sea level).
- **Antarctic and Greenland ice sheets.** The melting and sliding into the ocean of these large ice sheets acts to raise sea level, while water is taken from the ocean and deposited on ice sheets (via evaporation and rainfall) when they grow.
- **Glaciers and ice caps.** These comprise all land ice except for the ice sheets of Greenland and Antarctica. While relatively small in comparison to the ice sheets, they have contributed more to sea-level rise during the 20th century than the ice sheets and are likely to provide a significant contribution to 21st century sea-level rise.
- **Terrestrial storage of water.** The storage of water on land by the building of dams and the depletion of ground water can act to lower and raise global sea level, respectively.

When considering regional sea level projections, there are two additional factors to consider:

- **Ocean dynamics.** Changes in ocean currents (often associated with changes in the surface winds) can alter the sea level of a given region. This is reflected in changes in ocean temperatures and salinity and changes in bottom pressure.
- **Mass distribution.** The redistribution of mass in response to changes in ice sheets, terrestrial reservoirs and glaciers and ice caps alters the loading of the Earth (resulting in vertical crustal motion) and the gravitational field, leading to a regional distribution in the amount of sea-level rise.

The CMIP3 models are only able to provide projections regarding the steric and ocean dynamics components of sea level (termed the modelled components of the projection). To obtain information regarding the Antarctic and Greenland ice sheets, glaciers and ice caps, terrestrial water storage or mass distribution, additional modelling techniques are required (i.e. the CMIP3 models do not include a representation of processes such as ice-sheet dynamics or terrestrial water storage).

Projections for the PCCSP region were calculated using essentially the same techniques as in the IPCC Fourth Assessment Report (Meehl et al., 2007b). The only difference was that unlike in that report, which provided no total sea-level rise projections on a regional scale, the regional distribution (including the mass distribution component) was calculated so that all the sea-level components could be summed regionally (Table 4.4; see Church et al. (2011) for more details). See Appendix 1 for a listing of the CMIP3 models used to formulate these projections.

Table 4.4: Summary of sea level projection methods used in the PCCSP. See Meehl et al. (2007b) and Church et al. (2011) for details.

Component	Method
Steric & ocean dynamic effects	Calculated using output from the CMIP3 models.
Ice sheets	Calculated using an empirical calibration scheme for surface mass balance as a function of temperature change, using the ice sheet mass balance temperature sensitivities reported by Gregory and Huybrechts (2006) and the temperature changes simulated by the CMIP3 models. As these sensitivities do not account for the possibility of further mass loss from a rapid dynamic response of the ice sheets (e.g. the discharge of ice into the ocean as icebergs), an additional component related to surface temperature change and the current estimated dynamic response of the ice sheets was also included. This additional component is known as the rapid ice contribution.
Glaciers & ice caps	Calculated using the CMIP3 projected temperature changes with respect to a climate in which glaciers were estimated to be in a steady state (somewhat cooler than the late 19th century), an estimate of the present volume of the world's glacier and ice caps, and an estimate of the sensitivity to temperature of the global glacier surface mass balance (Kaser et al., 2006).
Terrestrial storage	Recent research suggests that the global rate of dam building has slowed and reservoir storage is likely to be approximately stable to 2025, as sedimentation offsets any building of new dams (Lettenmaier and Milly, 2009). The depletion of ground water has increased over the last two decades and was likely greater than increases in reservoir storage by up to a few tenths of a millimetre per year (Konikow and Kendy, 2005; Wada et al., 2010). Continuation of recent trends would therefore suggest an additional sea-level rise of a few centimetres at most, however there are no formal projections of how this depletion will evolve through to 2100. Due to this lack of formal projections and the fact that recent trends suggest that sea level change associated with terrestrial storage is likely to be relatively small, this component was not included in the PCCSP projections.
Mass distribution	The changes in vertical land motion and the gravitational field resulting from changes in the mass balances of glaciers, ice caps and ice sheets were estimated, using the calculated projected changes in the ice sheets and by assuming that the spatial pattern of glacial and ice cap mass loss to the ocean in the 21st century would have a similar pattern to that observed from 1993 to 2007 (Cogley, 2009).
Other vertical land motion	Other than the response to changing glacier and ice sheet mass, no estimates of vertical land motion from the ongoing response of the Earth to changes in ice sheets since the last glacial maximum (or other local issues) were included in the projections.

4.8 Tropical Cyclones

The current generation of global climate models have difficulty in adequately simulating the features of the current climate known to strongly influence tropical cyclone numbers and intensity, (e.g. regional patterns of sea-surface temperature, ENSO, the West Pacific Monsoon and the SPCZ), and they have insufficient temporal and spatial resolution to capture the high wind speeds and other small-scale features associated with these systems. Despite these limitations, a number of methods exist for making projections of the frequency and location of tropical cyclone activity from global climate model output (Knutson et al., 2010). In general terms, these methods seek to either identify and utilise relationships between tropical cyclones and the large-scale environmental conditions that are known to affect their development, or to identify weather features that have the characteristics of a tropical cyclone (i.e. a closed low pressure system accompanied by strong winds and a warm core through the depth of the atmosphere) directly from climate model output (known as direct detection schemes).

The PCCSP projections of tropical cyclone frequency and location were derived using methods falling under both of these general categories:

- A method for inferring tropical cyclone activity from the large-scale environmental conditions, known as the Genesis Potential Index, was used to determine projections from CMIP3 model output (Section 4.8.1).
- The CSIRO Direct Detection scheme was applied to both CMIP3 and CCAM 60 km model output (Section 4.8.2).
- A new tropical cyclone detection method known as the Curvature Vorticity Parameter scheme was developed, which was applied to CMIP3 model output (Section 4.8.3).

In addition, the cyclonic wind hazard for both the current climate and for the future climate was assessed using Geoscience Australia's Tropical Cyclone Risk Model (Section 4.8.4).

4.8.1 Genesis Potential Index

Approaches that use the mean characteristics of the large-scale environment to build empirical indices that replicate the key features of tropical cyclone formation are all essentially updates of the Yearly Genesis Parameter (Gray, 1979). For instance, Royer et al. (1998) showed that the Yearly Genesis Parameter could not be used to address climate change and therefore refined this index by modifying the thermal component. More recently, Emanuel and Nolan (2004) have proposed the Genesis Potential Index (GPI), which uses the concept of Potential Intensity (Bister and Emanuel, 1998) to account for thermal conditions. The GPI was developed and tuned using the large-scale environmental conditions of the NCEP/DOE R-2 reanalyses and has since been used in a number of studies to infer tropical cyclone formation from global climate model output (Camargo et al., 2007b). In this study, the GPI was calculated for CMIP3 models deemed to have acceptable skill in simulating the Indo-Pacific climate (Section 5.5.1) and for which relevant daily model output was available (Appendix 1).

4.8.2 CSIRO Direct Detection Scheme

A number of approaches exist for the direct detection and tracking of tropical cyclone-like vortices in global climate model and downscaled model simulations (Bengtsson et al., 1982; Broccoli and Manabe, 1990; Walsh and Watterson, 1997; Camargo and Zebiak, 2002). However, due to the low resolution of global climate models and possible model biases and other deficiencies, tropical cyclone detection procedures invariably need to be adjusted to reproduce observed climatologies. Subjective adjustment can lead to model-specific and even basin-specific detection criteria (Camargo and Zebiak, 2002) which is less than ideal because model deficiencies are compensated for by the detection procedure, and the same model deficiencies are assumed to be present in the projected future climate. An effort to objectively determine detection criteria was proposed by Walsh et al. (2007), which incorporated a resolution-dependent wind speed threshold. While arguably an improvement because of its increased objectivity, it effectively retains model-dependent thresholds for all models of differing grid resolution.

The PCCSP approach to the direct detection of tropical cyclone-like vortices used a modified version of the Nguyen and Walsh (2001) detection scheme, coupled with the tracking scheme of Hart (2003), and is hereafter referred to as the CSIRO Direct Detection (CDD) method. The CDD method uses a wind speed threshold set at 70% of the value recommended by Walsh et al. (2007) and was tested on 20-years of ERA-Interim reanalysis data and tuned

to best reproduce the International Best Track Archive for Climate Stewardship (IBTrACS) observed database (see Section 2.2 for details of reanalysis and observational data). It was applied to outputs from the six CCAM 60 km simulations and CMIP3 models deemed to have acceptable skill in simulating the Indo-Pacific climate (Section 5.5.1) and for which suitable model output was available (Appendix 1).

4.8.3 Curvature Vorticity Parameter Scheme

An independent and objectively determined detection method (based on a Curvature Vorticity Parameter, CVP) was developed for use in the PCCSP. It draws on the large-scale processes known to be essential to tropical cyclone formation, which should be resolvable even in the output generated by relatively coarse resolution global climate models. In particular, recent studies (Dunkerton et al., 2009; Nolan, 2007) have identified the importance of high curvature vorticity and low- to mid-tropospheric relative humidity immediately prior to tropical cyclone formation. Thus, elevated curvature vorticity and relative humidity, as well as minimal vertical wind shear, have been incorporated into the detection algorithm.

As for the CDD method, the CVP scheme was tested on 20 years of ERA-Interim reanalysis data and tuned to best reproduce the IBTrACS observed database. No additional tuning or adjustments were made prior to applying the method to global climate model output, which provides greater confidence that future changes in tropical cyclone frequency actually represent changes in the frequency of tropical cyclone-like circulations that develop in the global models. The CVP scheme was applied to a subset of four CMIP3 models deemed to have acceptable skill in simulating the Indo-Pacific climate (Section 5.5.1) and for which suitable model output was available (Appendix 1).

4.8.4 Tropical Cyclone Wind Hazard

Geoscience Australia's Tropical Cyclone Risk Model (TCRM) is a statistical parametric model of tropical cyclone behaviour, enabling users to generate synthetic records of tropical cyclones representing many thousands of years of activity. It uses an auto-regressive model, similar to the model developed by Hall and Jewson (2007), to create synthetic tracks of tropical cyclone events based on the characteristics (speed, intensity, bearing, size and genesis location) of a record of tropical cyclone events. Once a set of synthetic tropical cyclone events has been created, a parametric wind field (Powell et al., 2005) and boundary layer model (Kepert, 2001) is applied to each track, and the maximum wind speed over the life of each event is captured. A generalised extreme value distribution is then fitted to the maximum wind speed values for each location (Hosking, 1990).

The wind hazard associated with current climate tropical cyclone activity was estimated by applying TCRM to the historical cyclone track record (from IBTrACS) over the PCCSP region. For future projections of wind hazard, TCRM was applied to tracks of tropical cyclone-like vortices detected in the CCAM 60 km simulations (using the CDD method).

4.9 Ocean Acidification

Ocean acidification describes the decrease in both seawater pH and carbonate ion concentration that occurs as CO_2 is absorbed from the atmosphere and reacts in seawater. One of the key carbon parameters to describe the change in carbonate ion concentration is the aragonite saturation state (Mucci, 1983). Projected changes in aragonite saturation and carbonate chemistry for the PCCSP region were calculated using an offline carbonate chemistry model. Three inputs were used to drive this model:

1. Projections of future ocean carbon uptake.
2. Empirical relationships between ocean carbonate chemistry and salinity.
3. Projections of temperature and salinity from the CMIP3 models.

The fields of temperature and salinity were derived by combining anomalies from model projections with observations (Antonov et al., 2006; Locarnini et al., 2006), while future oceanic carbon uptake was estimated using projected atmospheric CO_2 concentrations under different SRES emissions scenarios, observed seasonality (Takahashi et al., 2009) and future trends in uptake from the IPSL CM4-LOOP coupled climate carbon model (Marti et al., 2010). Projections were calculated for CMIP3 models for which sea-surface temperature and salinity output was available (Appendix 1).

Nuku'alofa, Tonga

Chapter 5
Climate Model Reliability

Summary

- Global climate models can simulate many aspects of climate, and generally give a reasonable representation of seasonal and interannual climate in the PCCSP region. Most models, however, show biases, such as a tendency for sea-surface temperatures along the equator to be too cold. Such biases must be taken into consideration when using the models for climate projections.
- The representation of the El Niño-Southern Oscillation (ENSO) in climate models has improved over the years but remains a challenge at the regional scale. For example, sea-surface temperature variability associated with ENSO tends to be too narrowly focused on the equator, too far to the west and variability away from the equator in the sub-tropical Pacific tends to be too small.
- Global climate models reproduce the observed pattern of the regional distribution of sea level reasonably well. Global climate models that include all factors that influence the climate generate similar temporal variability in global-averaged ocean thermal expansion to the observations, but a slightly smaller rate of rise over recent decades. Observations indicate sea level is currently rising at near the upper end of the projected range.
- The CSIRO Direct Detection, Genesis Potential Index and Curvature Vorticity Parameter projection methods generally performed well in reproducing the observed tropical cyclone climatology when applied to global climate models.
- An evaluation of the performance of 24 global climate models has identified a set of 18 models which provide a reasonable representation of climate over the PCCSP region. These models are used for constructing projections of future climate for the PCCSP region and for individual Partner Countries in Chapters 6 and 7.
- Dynamical downscaling models have finer resolution and can be used to obtain information at regional scales, including over topography or where coastal effects are important. Since this is very computer-intensive, the output from only six global models has been downscaled and used to provide additional projections information in Chapter 7.
- Bias-adjustment of the sea-surface temperatures and increased atmospheric model resolution improves the representation of some aspects of the current climate in the downscaled simulations. Moreover, downscaled projections can provide useful complementary information to projections from coarser global climate models. However, there is no guarantee that the downscaled projections are actually more reliable than the projections from the coarser global models.

5.1 Introduction

To make scientifically robust and confident projections of the future climate, it first has to be demonstrated that global or downscaled climate models are sufficiently realistic in simulating the present climate. Whether a model is skilful in simulating the present climate will depend on its ability to represent the long-term average and seasonal cycle of various atmosphere and ocean fields (e.g. temperature, rainfall, wind, salinity and sea level); important regional large-scale climate features (e.g. Intertropical Convergence Zone (ITCZ), South Pacific Convergence Zone (SPCZ) and West Pacific Monsoon); the major components of climate variability on various timescales (e.g. the El Niño-Southern Oscillation (ENSO), Pacific decadal variability); extreme weather events (e.g. heat waves, heavy rain, tropical cyclones); and long-term trends. In addition, climate models should be stable and not exhibit substantial model drift (model drift refers to spurious trends in climate simulations that occur in the absence of any change in factors that might be expected to induce change).

The level of agreement between model simulations and observations of the present climate is used as a method of assessing model reliability. It is assumed that a model which adequately simulates the present climate will provide more reliable projections of the future. As shown in this chapter, no one model is the best in representing all aspects of climate, and a range of models should be considered when making projections of future climate.

Because of the complexity of climate systems, and the wide range of climate change factors of interest to stakeholders, it is important that model evaluation considers a broad range of features, fields and processes – with a corresponding requirement for high quality observations. For some features (e.g. global gridded rainfall) more than one dataset is available, which can provide a useful measure of observational uncertainty. The various observational datasets used in this chapter (and publication) are described in Chapter 2 and listed (along with their abbreviations) in Table 2.2 for the atmosphere variables and Table 2.3 for the ocean variables.

The global climate models (CMIP3 models) assessed in this chapter are listed in Table 4.1, along with model numbers and names used throughout this publication. Features of global climate models, such as resolution and representation of physical processes, are discussed in general in Section 4.3, along with details of the CMIP3 suite of experiments. Most analysis in this chapter is carried out with respect to the climate of the 20th century experiments described in Section 4.3.1. Also described in Chapter 4 are the techniques used for dynamical and statistical downscaling and for the calculation of tropical cyclones and sea-level changes based on climate model output.

The performance of global climate models is evaluated for atmosphere variables, ocean variables, major climate features and patterns of variability and extremes in Section 5.2. The performance of dynamical and statistical downscaling is evaluated in Section 5.3. The simulation of tropical cyclones in climate models is evaluated in Section 5.4. A summary of the suitability of models for use in climate projections in the PCCSP region is provided in Section 5.5.

Box 5.1: Summary of Intergovernmental Panel on Climate Change Comments on Model Strengths and Weaknesses

Climate models are based on the laws of physics and can reproduce many observed features of the current climate and past climate changes. Confidence in model simulations is higher for some climate variables (e.g. temperature) than for others (e.g. rainfall). Confidence is also generally higher for changes on continental or larger scales than for sub-continental and island scales.

Confidence in the reliability of global climate models for climate projections has improved, based on tests of their ability to represent:

- Present day average climate and year-to-year variability.
- Observed climate trends in the recent past.
- Extreme events, such as storms and heatwaves.
- Climates from thousands of years ago.

Models show significant and increasing skill in representing many important mean climate features, such as the large-scale distributions of atmospheric temperature, rainfall, radiation and wind, and of oceanic temperatures, currents and sea-ice cover. Patterns of climate variability that are generally well-simulated include the advance and retreat of the major monsoon systems, the seasonal shifts of temperatures, storm tracks and rain belts. Simulations that include estimates of natural and human influences can reproduce the observed large-scale changes in surface temperature over the 20th century, including the global warming that has occurred during the past 50 years.

However, there remain significant deficiencies in models, stemming largely from the need to represent in approximate form (parameterise) some small-scale but key physical processes, such as cloud physics, radiation and rainfall processes. Importantly, errors or biases remain in a number of aspects of the simulation of tropical rainfall, ENSO and the Madden-Julian Oscillation, and tropical ocean temperatures. Relatively small-scale events such as tropical cyclones and thunderstorms are less skilfully reproduced. Finer resolution models tend to produce more realistic simulations, although increased resolution alone does not reduce some important biases.

In summary, climate models provide credible quantitative estimates of future climate change, particularly at larger scales. Some deficiencies remain at smaller scales. There will always be a range of uncertainty in climate projections. People doing impact assessments based on climate model projections need to understand and incorporate this uncertainty.

(Summary based on information in Chapter 8 of the Working Group 1 contribution to the IPCC Fourth Assessment Report (2007)).

5.2 Evaluation of CMIP3 Climate Models

In this section, the seasonal and annual mean climatology of the 24 CMIP3 models is compared with observations. First, key atmospheric variables are examined, then model ocean climatology is compared with observed ocean variables. The key features of mean climate and climate variability in the models are compared with observations, and finally the simulation of climate extremes is compared with the observed distribution of extremes.

5.2.1 Atmosphere Variables

In simulating the current climate, the CMIP3 models should ideally capture the observed mean state of the climate, the timing and strength of the seasonal cycle, and the location and magnitude of any spatial features. A number of statistics relevant to these aspects of a model simulation have been calculated (Table 5.1). Unless otherwise stated, the results presented for these statistics refer to the multi-model mean (plus/minus the inter-model standard deviation) of the all-observation test scores (i.e. the value obtained by averaging across the scores from all relevant observational datasets). These observational datasets include CMAP and GPCP for the rainfall analysis, and the ERA-40, NCEP/DOE R-2 and JRA25 datasets for surface temperature and wind (Table 2.2). A complete listing of the CMIP3 models that were assessed for each variable (i.e. the models that have monthly time scale data available for the climate of the 20th century simulation) is given in Appendix 1.

5.2.1.1 Surface Air Temperature

The vast majority of the CMIP3 models show a cold bias throughout much the PCCSP region (Figure 5.1; E_{bias}= -0.8 ± 0.8°C), which is largely responsible for the multi-model mean grid-point error magnitude of E_{abs} = 1.0 ± 0.5°C. The models are able to capture the general surface air temperature spatial pattern, however they tend to exaggerate the intensity and westward extent of the cool equatorial surface air associated with the oceanic cold tongue (r_p = 0.9 ± 0.1; $\sigma_{ratio,x}$ = 1.1 ± 0.1). The models also tend to slightly overestimate the amplitude of the seasonal cycle ($\sigma_{ratio,t}$ = 1.2 ± 0.3), however the phase of this cycle is relatively well represented (r_t = 0.8 ± 0.1).

5.2.1.2 Rainfall

The main large-scale features of the climatological rainfall in the PCCSP region, including the high rainfall areas associated with the tropical convergence zones and West Pacific Monsoon, are clearly present in most CMIP3 model simulations (Figure 5.2 and Section 5.2.3). However, discrepancies in the precise location of these simulated features generally lead to relatively large grid-point errors in the 1980–1999 annual mean rainfall field (E_{abs} = 1.8 ± 0.5 mm per day) and are reflected in the spatial correlation values obtained for each month (r_p = 0.7 ± 0.2). Given the pronounced differences between the CMAP and GPCP datasets with respect to the intensity of tropical rainfall (Yin et al., 2004; also see Figure 5.2 and discussion in Section 2.2.1), it is interesting to note that the amplitude of both the modelled seasonal cycle and spatial distribution of rainfall in the PCCSP region tends to compare more favourably with CMAP ($\sigma_{ratio,t}$ = 1.1 ± 0.3 and $\sigma_{ratio,x}$ = 1.1 ± 0.2) than GPCP ($\sigma_{ratio,t}$ = 1.5 ± 0.4 and $\sigma_{ratio,x}$ = 1.5 ± 0.3). The models compare similarly to CMAP and GPCP with respect to their ability to capture the phase of the seasonal cycle (r_t = 0.6 ± 0.1).

Table 5.1: Definition of the statistics used to assess the ability of the CMIP3 models to simulate surface air temperature, rainfall and the surface wind. Each statistic was calculated over the PCCSP region (as defined in Section 1.3) after interpolation to a common 2.5° latitude/longitude grid.

Aspect assessed	Statistical test	Data required
Mean state (bias)	Bias (or difference - model minus observed) in the spatial average value (E_{bias})	1980–1999 annual mean field
Mean state (error)	Grid point average of the magnitude of the difference between the model and observed field (E_{abs})	
Seasonal cycle (phase)	Grid point average temporal correlation (r_t)	Spatial field containing 12-step time series of the1980–1999 mean value for each month
Seasonal cycle (amplitude)	Grid point average temporal standard deviation ratio (model/observed; $\sigma_{ratio,t}$)	
Spatial features (location)	Monthly time step average spatial (or pattern) correlation (r_p)	1980–1999 mean field for each month
Spatial features (amplitude)	Monthly time step average spatial standard deviation ratio (model/observed; $\sigma_{ratio,x}$)	

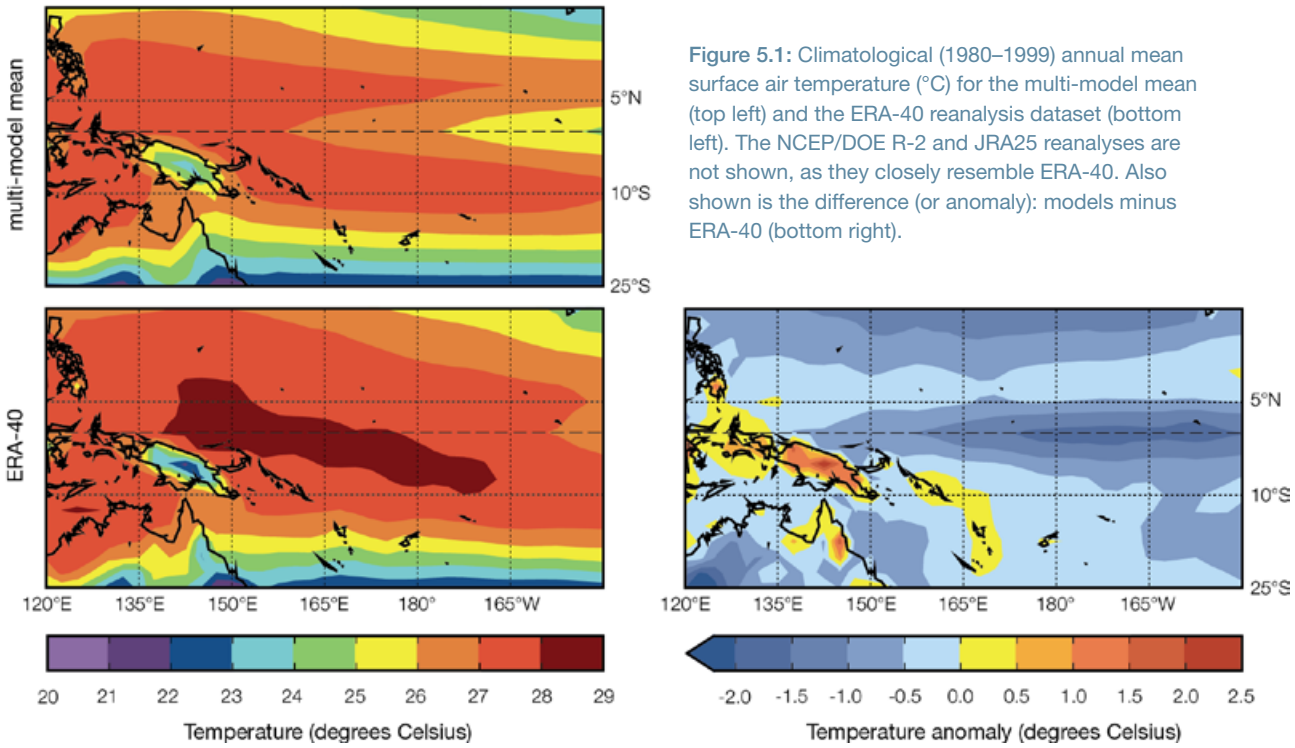

Figure 5.1: Climatological (1980–1999) annual mean surface air temperature (°C) for the multi-model mean (top left) and the ERA-40 reanalysis dataset (bottom left). The NCEP/DOE R-2 and JRA25 reanalyses are not shown, as they closely resemble ERA-40. Also shown is the difference (or anomaly): models minus ERA-40 (bottom right).

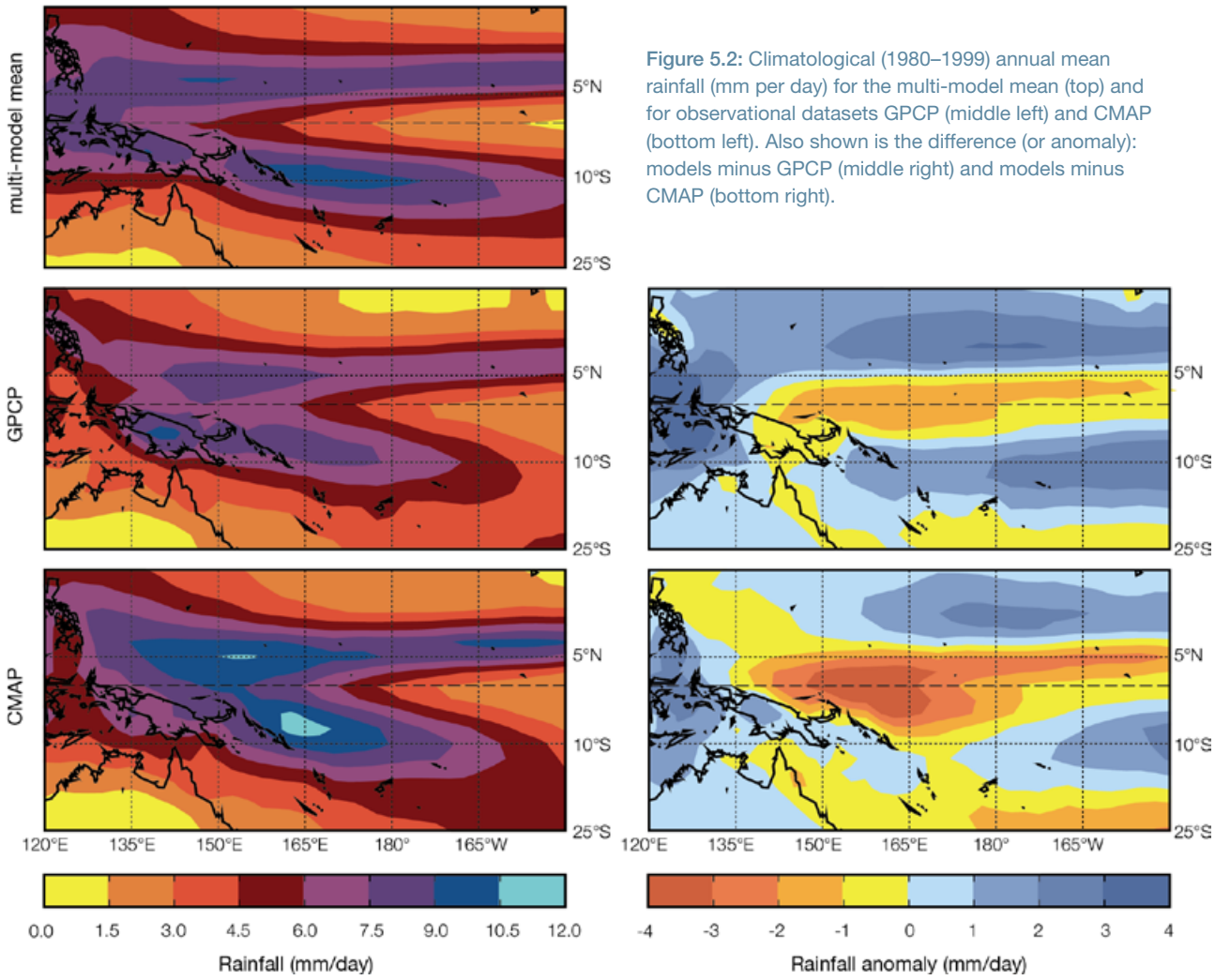

Figure 5.2: Climatological (1980–1999) annual mean rainfall (mm per day) for the multi-model mean (top) and for observational datasets GPCP (middle left) and CMAP (bottom left). Also shown is the difference (or anomaly): models minus GPCP (middle right) and models minus CMAP (bottom right).

5.2.1.3 Near-Surface Wind

The CMIP3 models tend to closely agree with observed climatological wind surface speed data (at 10 m above the ground) throughout most of the PCCSP region, except for the area immediately to the north and east of Papua New Guinea and the Solomon Islands (Figure 5.3). Over this area, the model tendency to overestimate the annual mean wind speed relates to model deficiencies in capturing the seasonal wind reversal associated with the West Pacific Monsoon (Section 5.2.3). Further, these sub-regional errors contribute greatly to the overall PCCSP region multi-model mean grid point error magnitude of E_{abs} = 0.9 ± 0.3 metres per second. The models have some difficulty in capturing the phase (r_t = 0.7 ± 0.1) and spatial pattern (r_p = 0.8 ± 0.1) of the seasonal cycle in wind speed.

The multi-model grid point error magnitude for wind direction is E_{abs} = 14.7 ± 4.3°, however on a sub-regional scale errors larger than 10° are typically confined to the region in and around Indonesia and Papua New Guinea. These directional errors may also arise from deficiencies in the simulation of the West Pacific Monsoon, however any mismatch between the model and reanalysis topography in the region would also be a factor. The models tend to underestimate the magnitude of the seasonal cycle in wind direction across the entire PCCSP region ($\sigma_{ratio,t}$ = 0.9 ± 0.2) and also show some difficulty in capturing the phase (r_t = 0.7 ± 0.1) and spatial pattern (r_p = 0.5 ± 0.1) of the seasonal cycle in wind direction.

5.2.1.4 Summary: Atmosphere Variables

In summary, the CMIP3 models are able to capture the broad-scale characteristics of the 1980–1999 average surface air temperature, rainfall and surface wind climatology. However they display some important deficiencies in simulating the finer details. In particular, the cold tongue bias influences the model simulated climate of Kiribati and Nauru, while many other Partner Countries are influenced by biases in the location of the tropical convergence zones (SPCZ and ITCZ) and the representation of seasonal wind reversals associated with the West Pacific Monsoon. The INM-CM3.0 and PCM models provide consistently poor simulations of the average climate across all atmospheric variables examined (Irving et al., in press). It is recommended that these models are not used for projections of future climate in Chapters 6 and 7 (Section 5.5).

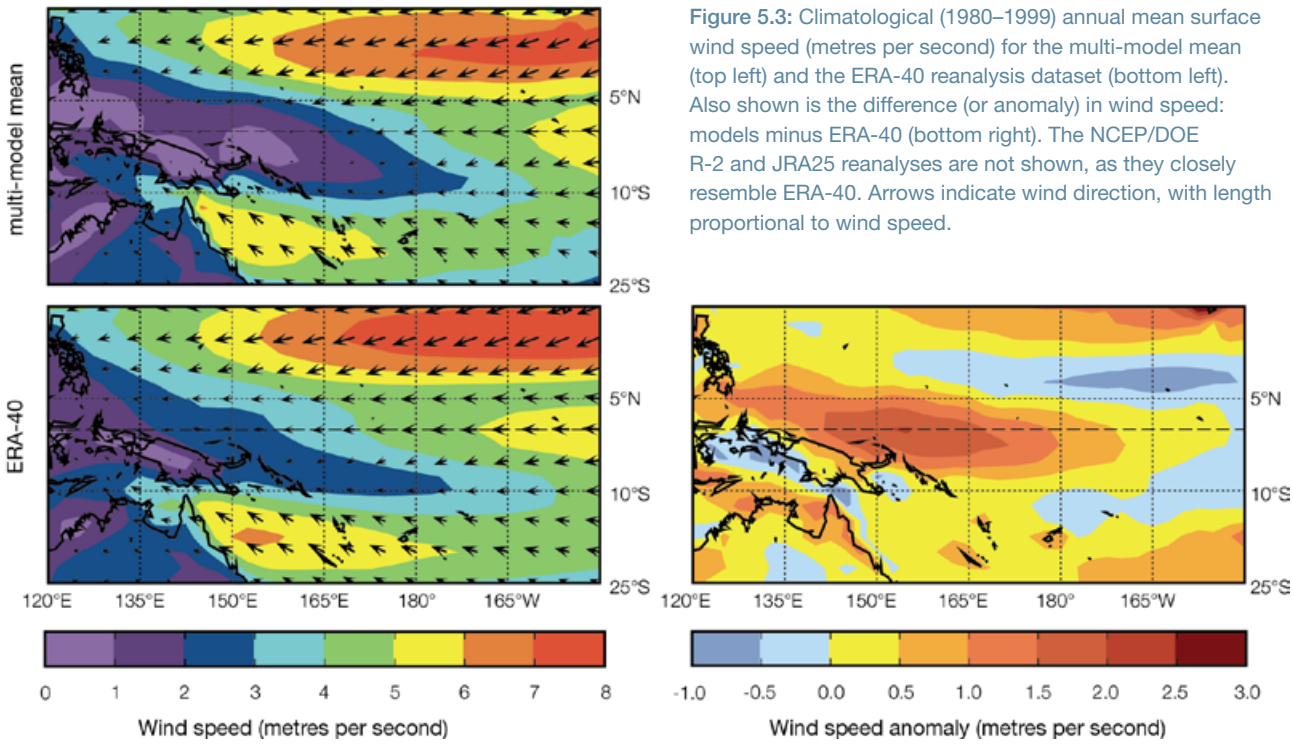

Figure 5.3: Climatological (1980–1999) annual mean surface wind speed (metres per second) for the multi-model mean (top left) and the ERA-40 reanalysis dataset (bottom left). Also shown is the difference (or anomaly) in wind speed: models minus ERA-40 (bottom right). The NCEP/DOE R-2 and JRA25 reanalyses are not shown, as they closely resemble ERA-40. Arrows indicate wind direction, with length proportional to wind speed.

5.2.2 Ocean Variables

5.2.2.1 Sea-Surface Temperature

Comparison of observed and multi-model mean sea-surface temperature (Figure 5.4) shows that important large-scale features are generally captured with some degree of fidelity in the simulations. These include: (1) the West Pacific Warm Pool, (2) the warm bands straddling the equator and (3) the cold tongue in the eastern Pacific. However, systematic errors are also evident. The difference between the multi-model mean and observations of sea-surface temperature is ~0.7°C on average at any given location (root mean square error is 0.73°C). Across the equatorial region, this error is considerably larger, as the sea-surface temperature is too cool in the majority of models. Despite a zonal (east-west) sea-surface temperature difference that is close to observations in many of the models, the cold tongue extends too far into the western Pacific, thereby reducing the extent of the Warm Pool and making it generally too cold. This bias is also manifest in air temperatures and has implications for the wind distribution, the location of the atmospheric convergence, and hence rainfall.

Considerable differences in sea-surface temperature distribution are evident across the models (Figure 5.5). Two models (GISS-ER and GISS-AOM) show little evidence of an equatorial cold tongue and consequently a lack of distinct convergence zones. This indicates a significant failing in their ability to properly capture tropical processes. In a few models (in particular INM-CM3.0 and BCCR-BCM2.0) the cold tongue reaches well into the western basin – a bias that adversely affects mean rainfall in the western Pacific region. Average sea-surface temperatures over the Pacific region are systematically too low, which also affects surface air temperatures (Figure 5.1). While two models are about 0.5°C too warm, the majority (including three of the flux-adjusted models) are more than 0.5°C too cold. Both the BCCR-BCM2.0 and CNRM-CM3.0 models are more than 1.8°C too cold.

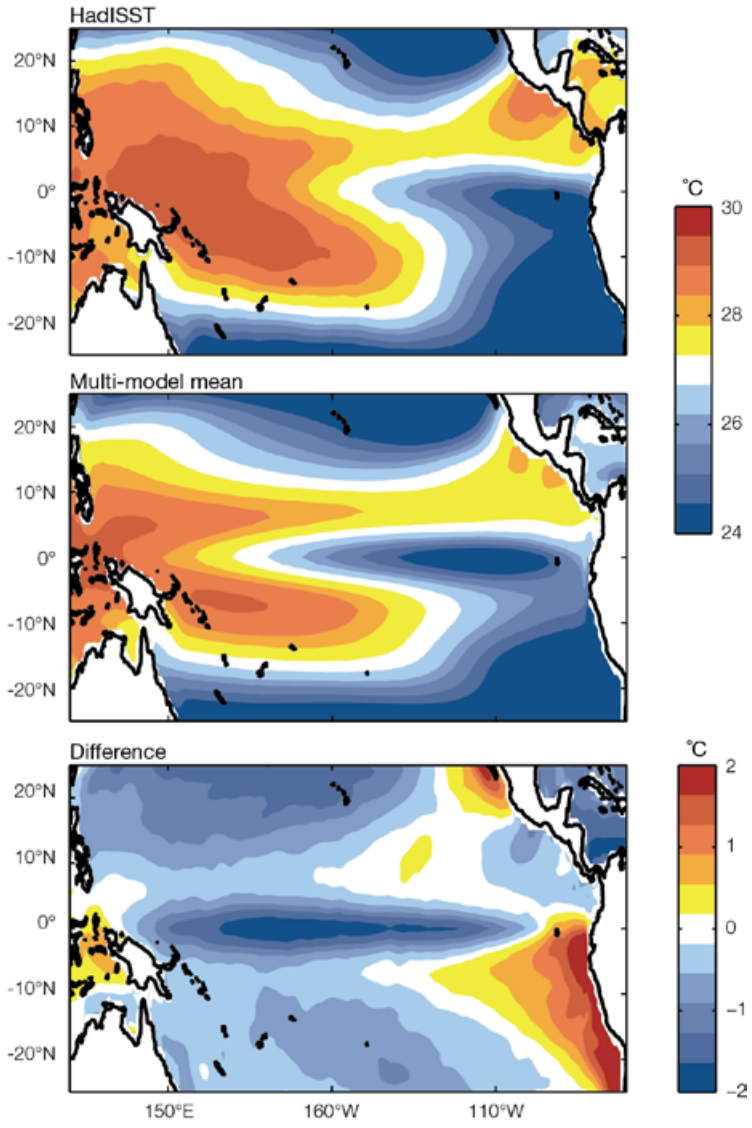

Figure 5.4: Climatological (1980–1999) annual mean sea-surface temperature (°C) for the observed HadISST dataset (top) and the multi-model mean (middle). Also shown is the difference, i.e. models minus observations (bottom).

5.2.2.2 Sea-Surface Salinity

The large-scale observed features in sea-surface salinity are captured in the multi-model mean of the PCCSP region (Figure 5.6), in particular, the low salinity under the convergence zones, where high rainfall levels dilute the salinity concentration, and the high salinity in the south-eastern Pacific where there is low rainfall and high rates of evaporation. Examination of individual models shows very different sea-surface salinity patterns and a large spread in regional averages (Figure 5.5). While the majority of models have average salinities between 34.3 and 35.2 practical salinity units (psu) in the PCCSP region, three models (CSIRO-Mk3.5, UKMO-HadCM3 and PCM) have average salinities below 33.9 psu (Figure 5.5). The multi-model root mean square error for sea-surface salinity in the region is ~0.48 psu.

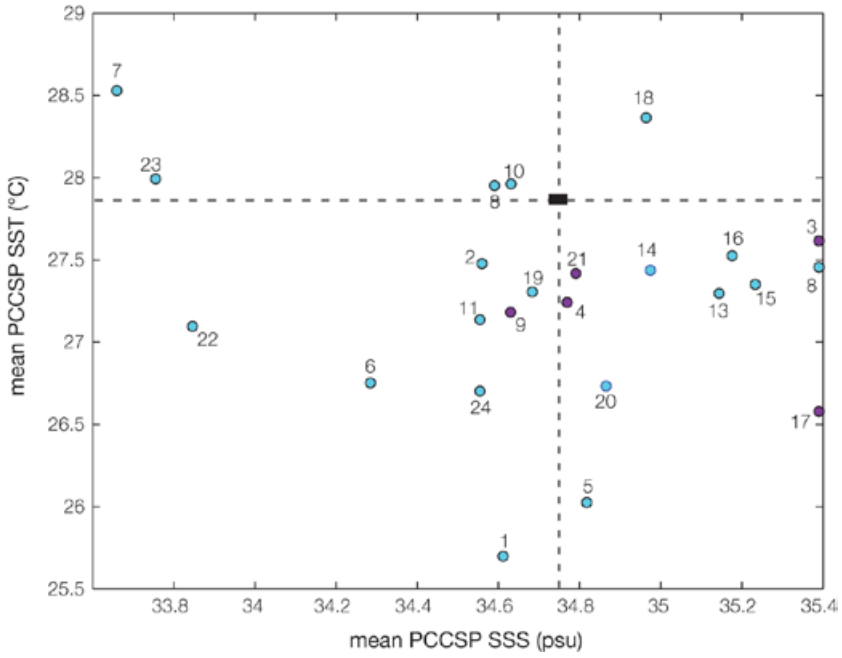

Figure 5.5: Average (1980–1999) PCCSP region sea-surface temperature and sea-surface salinity for individual CMIP3 models (numbered circles, see Table 4.1 for model numbers). The observed range (black box) spans two sea-surface temperature (SST) (HadISST and ERSSTv3) and two sea-surface salinity (SSS) (CARS06 and WOA05) observational datasets. Purple circles indicate flux-adjusted models (see the Glossary).

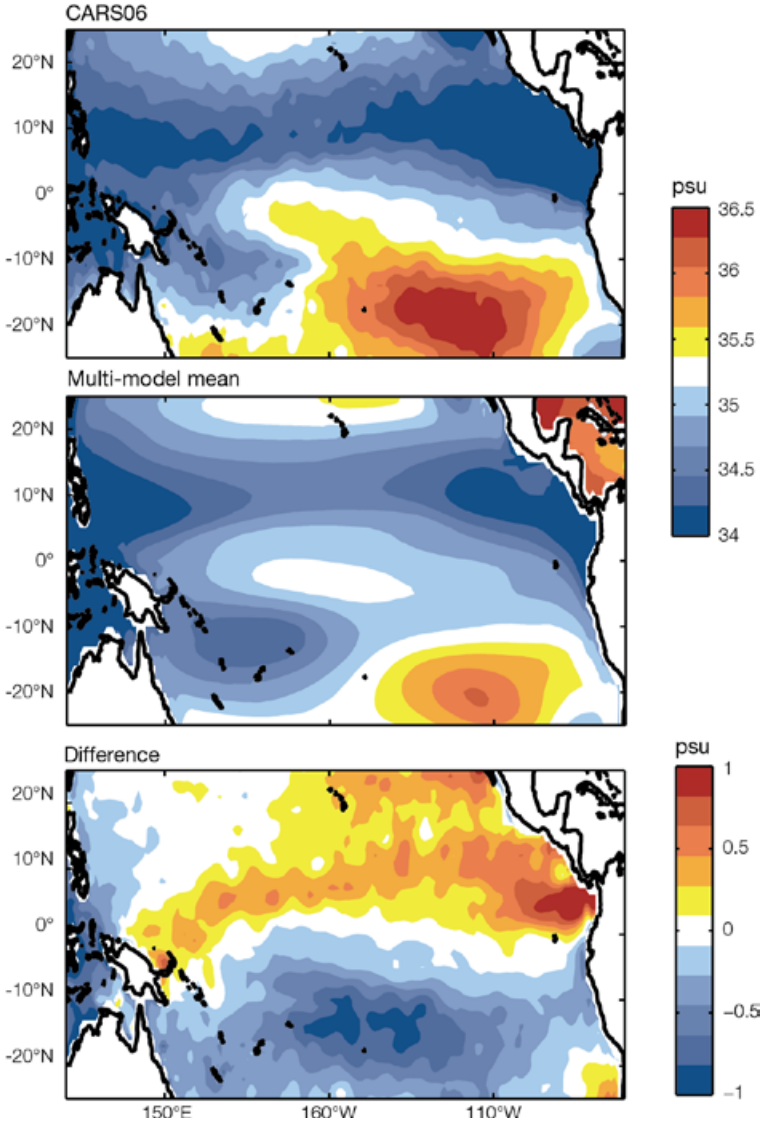

Figure 5.6: Climatological (1980–1999) annual mean sea-surface salinity (psu) for observed CARS06 dataset (top) and multi-model mean (middle). Also shown is the difference, i.e. models minus observations (bottom).

5.2.2.3 Trends and Variability

An important test for climate models is how well they are able to simulate known climate variability on interannual time scales, and how well they can reproduce historical trends. Such an assessment is complicated by the fact that observations are often sparse (particularly prior to the mid-20th century) and often come from multiple sources, making it difficult to combine observations into a consistent record.

A comparison of observed PCCSP region sea-surface temperature trends with individual climate models shows that all the models simulate a warming over the latter half of the 20th century (Figure 5.7). However, there is considerable spread, with some models producing more than double the observed warming, and others showing a very weak warming. Despite this, the multi-model mean compares well with observations. This does not imply that the multi-model mean is necessarily the best predictor of future climate.

The Pacific Decadal Oscillation is important (Chapter 3) as it can enhance or suppress ENSO impacts on decadal time scales. While most models simulate a Pacific Decadal Oscillation reasonably well, a number of models underestimate its strength, and three models (BCCR-BCM2.0, GISS-AOM and GISS-ER) give a sea-surface temperature response to the Pacific Decadal Oscillation that is of the wrong sign (Figure 5.7).

In addition to appropriately simulating natural variability such as ENSO and the Pacific Decadal Oscillation, models should be able to respond realistically to changes in insolation and to major volcanic eruptions. All models (except MIROC3.2 (medres)) that include the effect of volcanoes correctly simulate a cooling in the PCCSP region associated with increased volcanic activity, although the response is generally considerably larger than observed (Figure 5.7). In addition, all models, (except for GFDL-CM2.1) that include changes in insolation, simulate a warming in the PCCSP region associated with increased insolation.

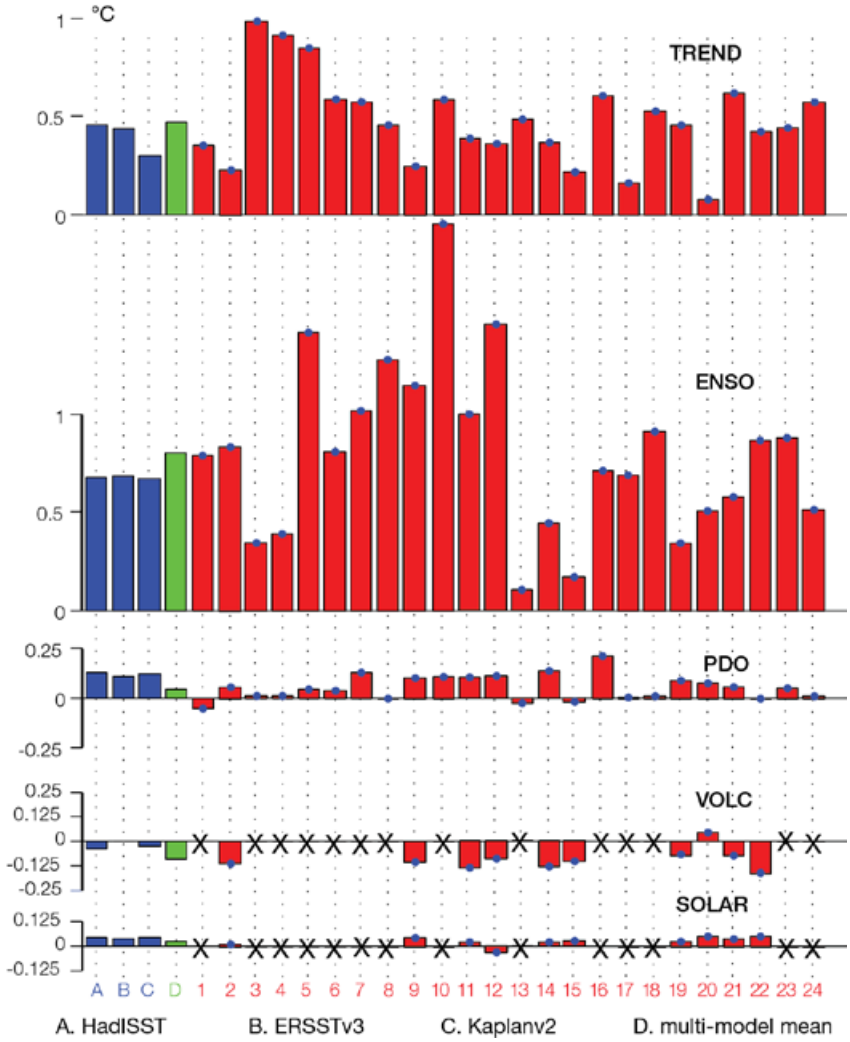

Figure 5.7: Sea-surface temperature trend (1950–2000) and the strength of sea-surface temperature variability associated with ENSO, Pacific Decadal Oscillation, volcanic and solar forcing for three observational datasets (HadISST, ERSSTv3b and Kaplanv2), the multi-model mean, and the CMIP3 models. ENSO and Pacific Decadal Oscillation strength relate to the sea-surface temperature response in the Niño3.4 region, 5°N–5°S, 120°W–170°W (as both of these phenomena have very different regional responses) while other forcing and the sea-surface temperature trend relates to the full PCCSP region (as changes are regionally homogeneous). X indicates models that do not incorporate solar and/or volcanic forcing in the 20th century simulation. See Table 4.1 for model numbers.

5.2.2.4 Sub-Surface Trends

Understanding what goes on beneath the ocean surface is fundamental to fully understanding climate variability and change. The ocean has absorbed about 90% of the total additional heat from global warming and about half of the CO_2 emitted since industrialisation (Sabine et al., 2004). Its huge inertia means that changes are less subject to the short-term fluctuations that are ubiquitous for atmospheric properties. Hence ocean heat content and sea-level change is often a more reliable indicator of climate change. The ocean plays a central role in ENSO and longer-term variability and takes part in important feedback processes that modulate the rate of long-term atmospheric warming. Physical ocean processes such as mixing are also vital for bringing essential nutrients into the surface ocean. These nutrients maintain biological productivity and ultimately the fisheries that are so important for the region.

The sub-surface temperature trend (1950–2000) shows a surface-intensified warming in both the models and observations consistent with increased greenhouse gas concentrations (Figure 5.8). Counter-intuitively, there is also a region of cooling centred near the equator at about 200 m depth. This cooling is consistent with a weakening in the equatorial trade winds that (through ocean processes) cause the thermocline to become shallower (Han et al., 2006) lifting the deeper cold water upwards. While the observed warming-cooling pattern could be caused by natural variability (McPhaden and Zhang, 2004), the fact that it is reproduced in the climate models (albeit with reduced intensity) suggests that the pattern is, in part, related to increased greenhouse gas concentrations. This is consistent with atmospheric studies that attribute the weakening of the Walker Circulation and the associated Pacific trade winds to both natural variability and the influence of greenhouse gases (Power and Kociuba, in press).

5.2.2.5 Climate Model Drift

Climate models that include historical or projected increases in atmospheric greenhouse gas concentrations would be expected to exhibit a global warming trend, with associated changes in other climate characteristics (e.g. rainfall, circulation). Conversely, climate simulations with greenhouse gas concentrations held fixed (i.e. control simulations) would be expected not to exhibit long-term trends. Many models do, however, have trends in their control simulations as a result of imperfections in the representation of physical processes in the models. Such spurious trends are referred to as climate model drift (Power, 1995). This is problematic, as a model that exhibits drift within the control simulation will also exhibit similar drift in the historical and projection simulations. The model drift therefore erroneously affects any global warming signal in the model output. Drift must therefore be accounted for when it is large.

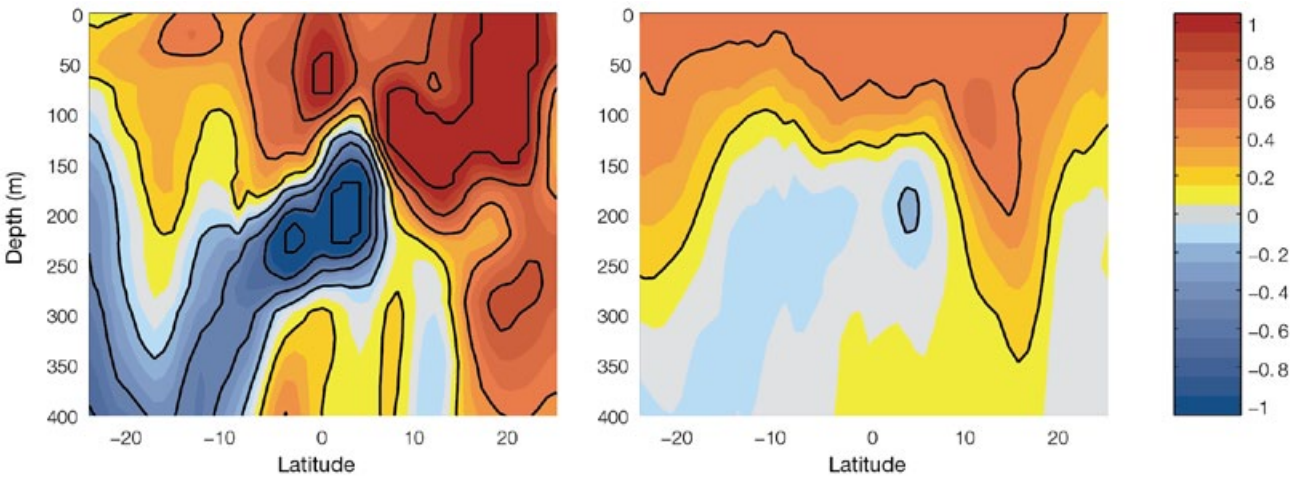

Figure 5.8: Linear trend across the equator at 165°E in sub-surface ocean temperatures based on the multi-model mean (right) and an observational reconstruction (left; Durack and Wijffels, 2010). Units are °C per 50 years; black contours every 0.2°C per 50 years.

The typical error introduced by model drift (if not accounted for) in the simulated trend for the PCCSP region is shown in Figure 5.9. For most models, the trend associated with model drift is less than 20% of the simulated 1950–2000 sea-surface temperature trend. In one model (INGV-SXG) the drift error is particularly pronounced, exceeding 40%. Model drift introduces a greater error in rainfall, with most models showing an error of 10 to 40%. Two models, MRI-CGCM2.3.2 and INGV-SXG, have rainfall drift errors that exceed 60%. In general, INGV-SXG shows high levels of drift in all climate variables. In addition, it is not possible to correct for model drift for this model as a concurrent control simulation is unavailable.

Model drift becomes relatively less important for projections as the anthropogenic climate signal become larger. In addition, model drift tends to be randomly distributed across models (i.e. it will make a trend larger in some models and smaller in others). As a result, model drift tends to be negligible when considering multi-model means. Model drift is often most important in the ocean, particularly at greater depth. As a result, ocean model fields used in projections of ocean variables (other than sea level) have been corrected for model drift by subtracting the drift in the control experiment from corresponding projection simulations.

5.2.2.6 Sea Level

Mean Sea-Level Pattern

The observed sea-level pattern was presented in Section 2.6.4 (see Chapter 4 and Gregory et al. (2001) for a description of techniques to calculate sea level from the models).

Globally, the modelled sea level reproduces the large-scale features of the observed pattern but some models have a higher correlation with the observations and a smaller root mean square error than others (not shown). For the tropical and sub-tropical Pacific basin, there is a similar level of agreement but some models have closer agreement with the observations (Figure 5.10). There is a smaller root mean square error and larger spatial correlation for the multi-model mean sea-level distribution (for the 17 models available) than the individual models (Table 5.2, Figure 5.10 and Figure 5.11), where larger inter-model differences of regional sea-level patterns can be seen (Figure 5.10). The root mean square error between the mult-model mean and the observations is 0.09 m (Table 5.2 and Figure 5.11) over the region (120°E–70°W, 45°S–45°N) and the spatial correlation is very high at 0.97 (Table 5.2).

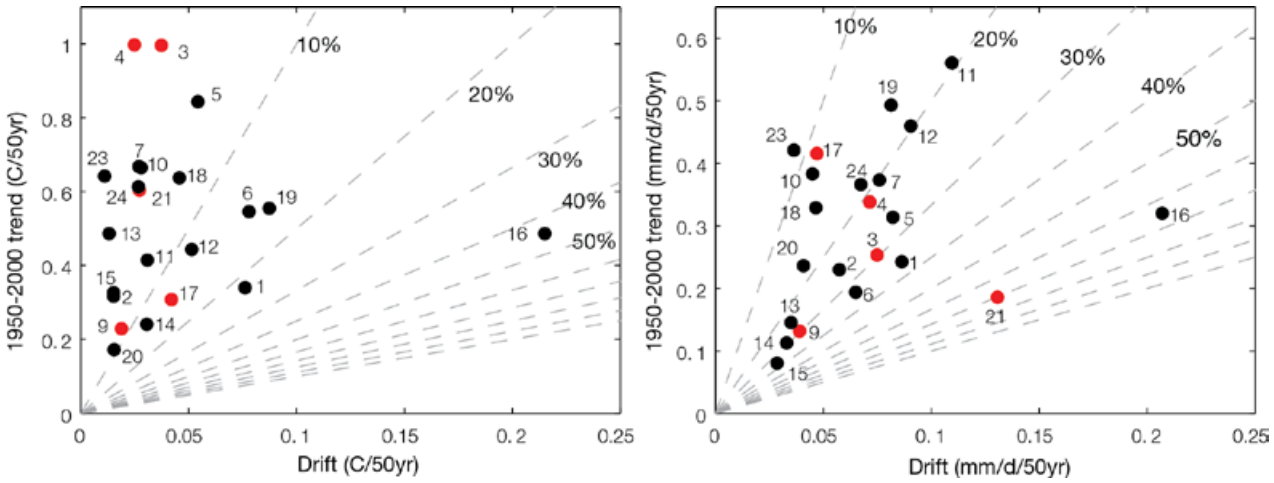

Figure 5.9: Relative size of climate drift in the CMIP3 models (based on their respective simulation with fixed greenhouse gases concentrations: the control run) versus the simulated 1950–2000 trend (where greenhouse gases concentrations follow historical levels) for surface air temperature (left) and rainfall (right). Model numbers are defined in Table 4.1 (Model 16 is INGV-SXG). Red dots indicate models that use flux adjustment (a correction made to some models to reduce the effect of model drift, see Glossary).

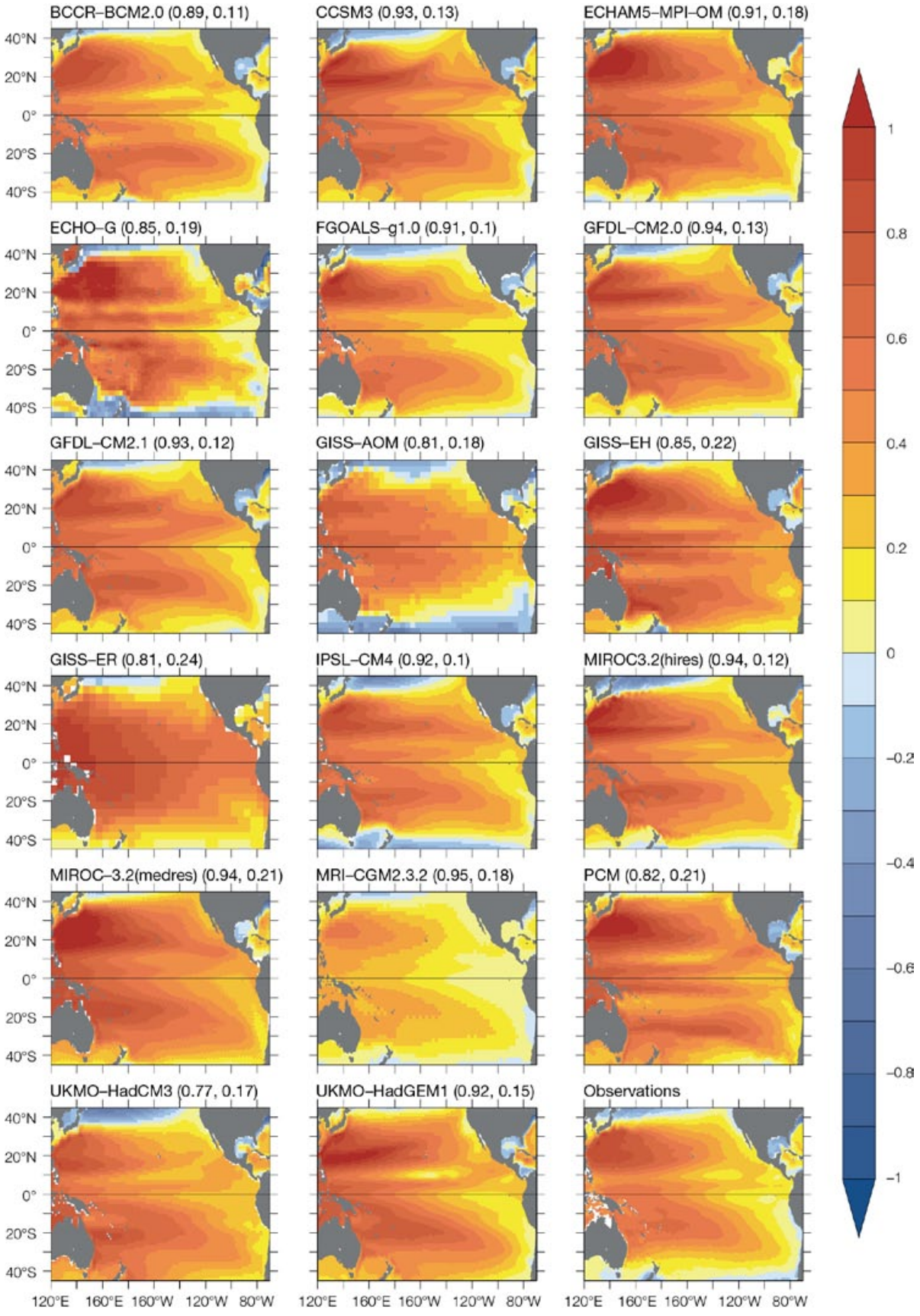

Figure 5.10: Tropical and sub-tropical Pacific basin mean sea level (in metres) from each climate model and observations for the period 1993–2000. The first number in brackets above each panel is the spatial correlation of mean sea level between each climate model and the observations for the tropical and sub-tropical Pacific basin (120°E–70°W, 45°S–45°N), while the second number is root mean square error. The global mean, averaged over the same period, is removed from each panel.

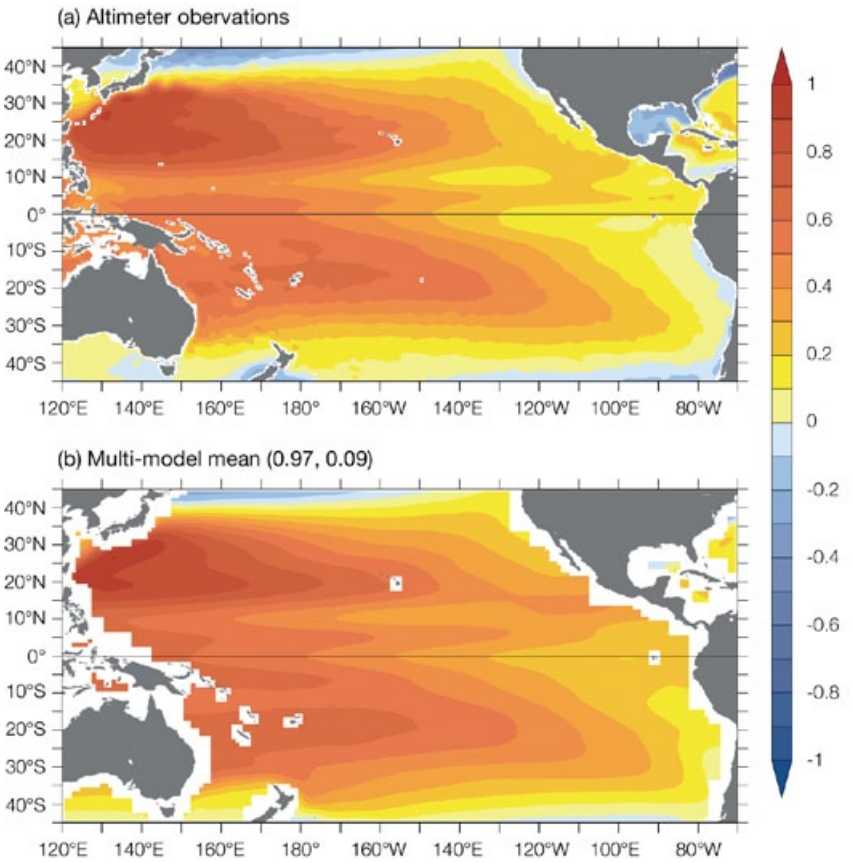

Figure 5.11: Tropical and sub-tropical Pacific basin mean sea level (in metres) based on (a) observations and (b) the multi-model mean for the period 1993–2000. The spatial correlation between (a) and (b) is 0.97, while the root mean square error is 0.09 m. The global mean is removed from each panel.

Table 5.2: Spatial correlation and root mean square (RMS) error of mean sea level (in metres) between each climate model and observation for the period 1993–2000 over the tropical and sub-tropical Pacific basin (120°E–70°W, 45°S–45°N).

Climate model	Spatial correlation	RMS error (m)
BCCR-BCM2.0	0.89	0.11
CCSM3	0.93	0.13
ECHAM5/MPI-OM	0.91	0.18
ECHO-G	0.85	0.19
FGOALS-g1.0	0.91	0.10
GFDL-CM2.0	0.94	0.13
GFDL-CM2.1	0.93	0.12
GISS-AOM	0.81	0.18
GISS-EH	0.85	0.22
GISS-ER	0.81	0.24
IPSL-CM4	0.92	0.10
MIROC3.2(hires)	0.94	0.12
MIROC3.2(medres)	0.94	0.21
MRI-CGCM2.3.2	0.95	0.18
PCM	0.82	0.21
UKMO-HadCM3	0.77	0.17
UKMO-HadGEM1	0.92	0.15
Multi-model mean	0.97	0.09

Sea-Level Trends

Robust projections of sea-level rise depend critically on understanding the ability to adequately represent past sea-level changes in model simulations. In the IPCC Fourth Assessment Report (Bindoff et al., 2007) it was pointed out that the inability to satisfactorily explain the observed sea-level rise over decades has been a significant limitation in all of the IPCC assessments to date and a barrier to narrowing projections of sea-level rise.

Consistent with these results, Rahmstorf et al. (2007) showed that the observed sea level from tide gauges (1990–2001) and from satellite altimeter data (1993–2006) was rising at the upper limit of the projections from the IPCC (2001). Church et al. (2011) have also compared the observed sea-level rise derived from an improved sea-level reconstruction (Church and White, in press) and a longer altimeter time series, with the projected sea-level rise based on the IPCC projections (2007). By the end of the observational time series, both the reconstructed and altimeter sea-level datasets are close to the top of the projections.

Climate model simulations that only included the impact of greenhouse gases (and not the natural climate-influencing factors such as solar variability and stratospheric aerosols from large volcanic eruptions) have significantly larger trends and significantly less variability (Domingues et al., 2008) than simulations with improved upper-ocean heat content and steric sea-level trends (Domingues et al., 2008; Ishii and Kimoto, 2009; Levitus et al., 2009). In contrast, the variability in models that do include these natural climate-influencing factors is similar to the observed ocean variability but the trend in both ocean heat content and thermosteric sea-level rise is slightly smaller than the observations (Domingues et al., 2008). Model simulations which include natural factors also suggest that steric sea level would have fallen by several

millimetres following the eruption of Mount Pinatubo in 1991 and that the ocean recovery from this cooling could add about 0.5 mm per year to the rate of steric sea-level rise over the decade from 1993, coincident with the first decade of high quality satellite altimeter observations (Church et al., 2005; Gregory et al., 2006).

There have been updated glacier and ice cap mass inventories (Radic and Hock, 2010) resulting in a larger ice volume estimate, and permitting the mass changes of Greenland and Antarctica to be explicitly included in projections. The dataset of glacier mass balance has been expanded by using the 'geodetic' observations of glacier volume change in addition to the surface mass-balance observations (Cogley, 2009). Radic and Hock (2011) have allowed for glacier and ice cap hypsometry (changing area with altitude) in recent projections. Most recently, LeClercq et al. (2011) have used glacier length observations together with the surface mass balance observations compiled by Cogley (2009) to estimate glacier and ice cap contributions to sea level since 1800. Current methods reproduce these observations but significant uncertainty in parameters used for projections remain and the methods used in the IPCC (2007) report do not allow glacier and ice cap contributions to come to a new equilibrium in a warmer climate.

In the IPCC (2007) report, the ice sheet projections were completed using empirically calibrated schemes for melting as a function of temperature change. More recent work employs climate models at high resolution in the ice sheet regions and incorporates detailed physical models of the surface energy balance, melting and runoff, and snow accumulation, both for Greenland (Fettweis, 2007) and Antarctica (Krinner, 2007). In the IPCC (2007) report, it was recognised that the current suite of ice sheet models was not capable of adequately simulating a potential rapid response of the ice sheets to global warming.

Much attention has been directed in recent years to developing improved models of ice sheet dynamics, and some first results are now available (Joughin et al., 2010). More are expected as an outcome of two large ongoing activities, the SeaRISE project supported by NASA, and the EU-funded ice2sea project.

5.2.2.7 Summary: Ocean Variables

In summary, while climate models are able to reproduce most of the important oceanic features, natural variability in the ocean, and the direction of historical changes, there are still significant biases that must be considered when applying these models to projections. The INGV-SXG model displays a large climate drift in all variables, and does not provide a corresponding control simulation to correct for climate drift. It is recommended that this model is not used for projections of future climate in Chapters 6 and 7 (Section 5.5).

Global climate models reproduce the observed pattern of the regional distribution of sea level with a fair degree of realism. Models that include natural and human emissions as climatic factors have similar temporal variability in global-averaged ocean thermal expansion as the observations, but a slightly smaller rate of rise over recent decades.

5.2.3 Climate Features and Patterns of Variability

In this section, the ability of models to simulate the major features and patterns of variability of climate in the PCCSP region is evaluated. A detailed description of the observed climate features (the SPCZ, ITCZ and West Pacific Monsoon) and components of climate variability (ENSO and the Indian Ocean Dipole) is given in Chapters 2 and 3.

5.2.3.1 El Niño-Southern Oscillation

As ENSO is a major component of climate variability in the PCCSP region, it is essential that it is well simulated in climate models. To simulate ENSO, a climate model needs to accurately simulate atmosphere-ocean interactions on all relevant time and space scales. In particular, a model requires a realistic mean climate, including the Walker Circulation and zonal and vertical ocean temperature gradients; realistic daily to weekly wind variability that helps trigger ENSO events; variations in the thermocline depth and slope; and appropriate ocean-atmosphere interactions. A key factor in successfully simulating all these features is sufficient spatial and temporal resolution to represent small-scale processes, such as ocean eddies. Other important model characteristics include realistic convection processes, representation of clouds and the feedbacks between clouds and radiation.

The adequate simulation of all these features contributes to a more realistic representation of the spatial pattern and strength of ENSO events, the frequency of events, the characteristics of different types of events, and the link between ENSO and climate variables such as rainfall. Reproducing ENSO-like behaviour in climate models is a very complex task and it is a significant achievement that, unlike two decades ago, most climate models simulate an ENSO-like phenomenon. The climate models involved in the CMIP3 comparisons (Section 4.3.1) perform much more realistically than previous generations of models because resolution, model formulation and representation of sub-grid scale processes (parameterisations) have been improved. Thus, many models are extremely useful tools for studying ENSO and its impacts (Guilyardi et al., 2009; Collins et al., 2010).

Challenges in simulating ENSO behaviour still remain. Of the CMIP3 models, a small minority fail to adequately reproduce ENSO variability, probably due to coarse

ocean resolution (van Oldenborgh et al., 2005). Two models in particular (GISS-AOM and GISS-ER) show virtually no ENSO-like variability. The remaining models have a pattern of El Niño warming that extends too far into the western Pacific (Figure 5.12). This means that in some models, some Pacific Islands experience sea-surface temperature anomalies of the wrong sign and therefore the opposite impact of the El Niño event to what is observed. This bias also explains most of the error in the sea-surface temperature pattern correlations for canonical ENSO.

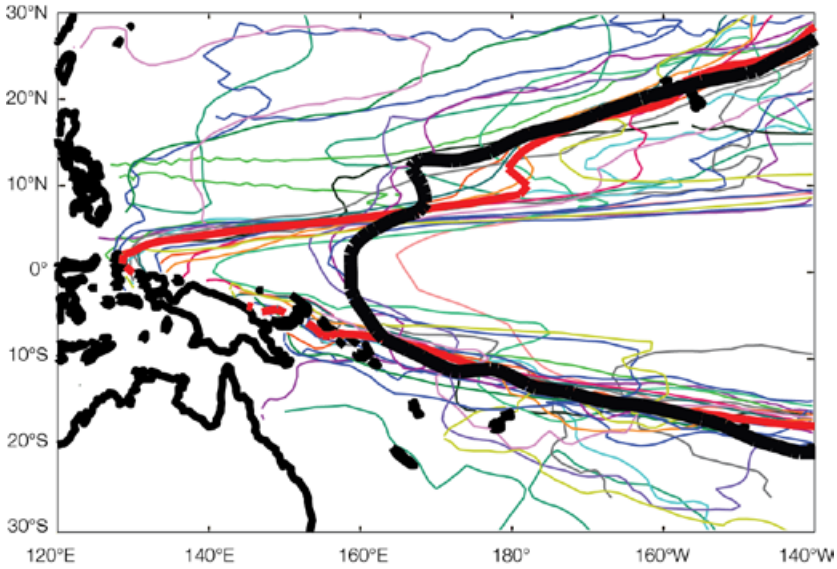

Figure 5.12: Zero-line for sea-surface temperature response to ENSO for individual model (thin lines), multi-model mean (thick red) and observed (HadISST, thick black). During an El Niño event, warming (cooling) occurs to the east (west) of this line. Clearly evident is the large systematic bias in the model sea-surface temperature response over the equatorial western Pacific. This has important implications for the rainfall response to ENSO, which tends to increase (decrease) over warmer (cooler) waters.

Every El Niño and La Niña event is different, but they have been observed to fall into two types based on the spatial patterns of sea-surface temperature anomalies that occur: the canonical ENSO and the El Niño Modoki (Section 3.4.1). The El Niño Modoki is thought to have become more prevalent in recent decades. It remains an ongoing topic of research whether this is due to natural variability or anthropogenic factors (Yeh et al., 2009).

CMIP3 models show varying degrees of skill in reproducing the strength and frequency of ENSO events. Observed ENSO events undergo a highly irregular two to seven year oscillation, but in some models ENSO events occur too often and too regularly, e.g. an El Niño or La Niña every two years (Randall et al., 2007), or too seldom (Joseph and Nigam, 2006). The variability of the strength of canonical and Modoki events (measured by standard deviation of Niño3.4 and El Niño Modoki Index respectively, Figure 5.13 left), vary substantially from very weak to overly strong. In general, models with excessively strong canonical ENSO variability also have excessively strong Modoki variability, or too weak for both, reflecting general sea-surface temperature variability in the tropics.

The Modoki pattern was identified in observations as the second most important pattern in explaining monthly variability of sea-surface temperature in the tropical Pacific region (Ashok et al., 2007). The first pattern is the canonical El Niño pattern of sea-surface temperature variability, which accounts for 45% of tropical sea-surface temperature variability, compared to 12% for El Niño Modoki. The observed spatial patterns of the two modes are very similar to the patterns in Figure 3.4. In order to determine whether the spatial patterns of these forms of variability in the CMIP3 models correspond to those observed, they have been calculated for all models and for observations (HadISST) from their linearly de-trended monthly sea-surface temperatures from 1975–1999, using Empirical Orthogonal Function analysis (von Storch and Zwiers, 2000). Pattern correlations between the observed and model patterns (Figure 5.13 right) show that most of the CMIP3 models do not successfully distinguish the canonical and Modoki types of ENSO variability. The canonical ENSO pattern is reasonably well reproduced by most models (pattern correlation, r_p is above 0.6 for most models), but in general they do not reproduce the Modoki pattern well (r_p is below 0.6 for most models). Only a small number of models produce a second mode of variability that is recognisably similar to the observed Modoki pattern. From the results shown here it also is clear that several models do not reproduce realistic variability for either canonical or Modoki ENSO.

The overly westward extension of sea-surface warming during El Niño events in most models has important implications for the rainfall response to ENSO, which tends to increase over warmer waters and decrease over cooler waters. This is evident from model rainfall maps (Figure 5.14, models 2 and 3), particularly in the region east of Papua New Guinea. Almost all models have an ENSO-related rainfall response in the wrong direction in parts of the western Pacific. Also, those models with weak sea-surface temperature variability tend to have a weak rainfall response (Figure 5.14, model 1), and those with excessively strong sea-surface temperature variability have a strong rainfall response (model 2). Models with realistic ENSO sea-surface temperature variability show a more realistic rainfall response (model 3).

Many models simulate errors in the ENSO related changes in temperature or rainfall that influence particular Partner Countries. As the line between regions of warmer and cooler water during ENSO events is shifted too far west in many models (Figure 5.12), countries may have the wrong sea-surface temperature anomaly during El Niño and La Niña events. The pattern of rainfall response to ENSO events is also shifted too far west in many models, and is too strong or too weak in some models (Figure 5.14). Therefore, models may not simulate the correct changes in rainfall during El Niño and La Niña events for some Partner Countries.

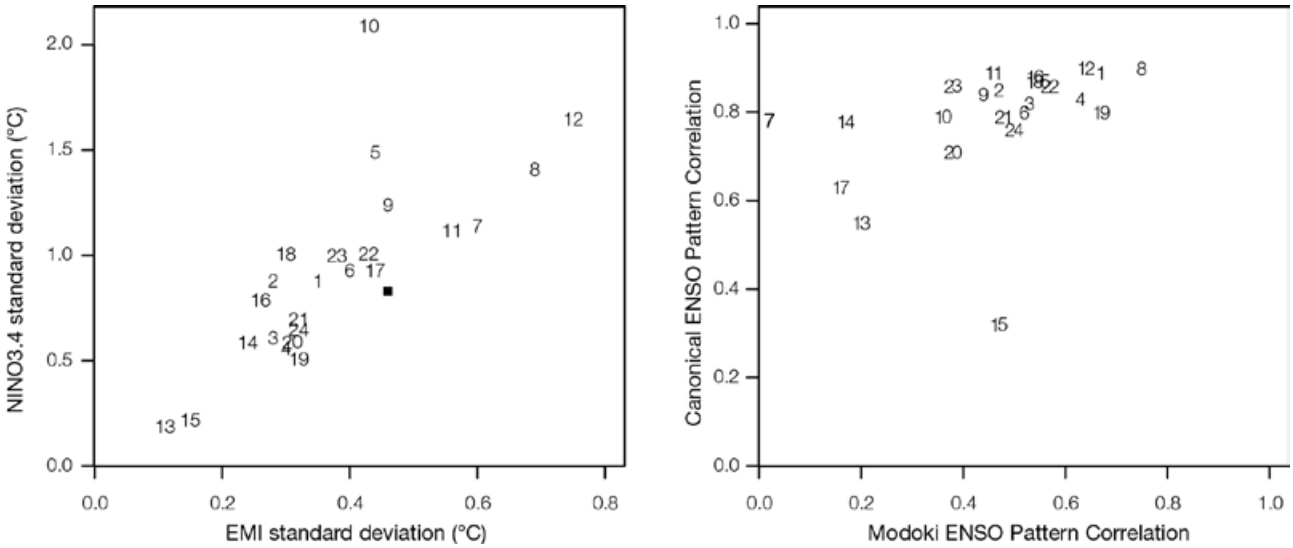

Figure 5.13: (Left) Variability (standard deviations) of the Niño3.4 Index and El Niño Modoki Index in the 24 CMIP3 climate model simulations (model numbers given in Table 4.1). The black square shows the observed standard deviations. (Right) Pattern correlations of canonical (Mode 1) and Modoki ENSO (Mode 2) spatial patterns of sea-surface temperature variability for each model with the observed patterns.

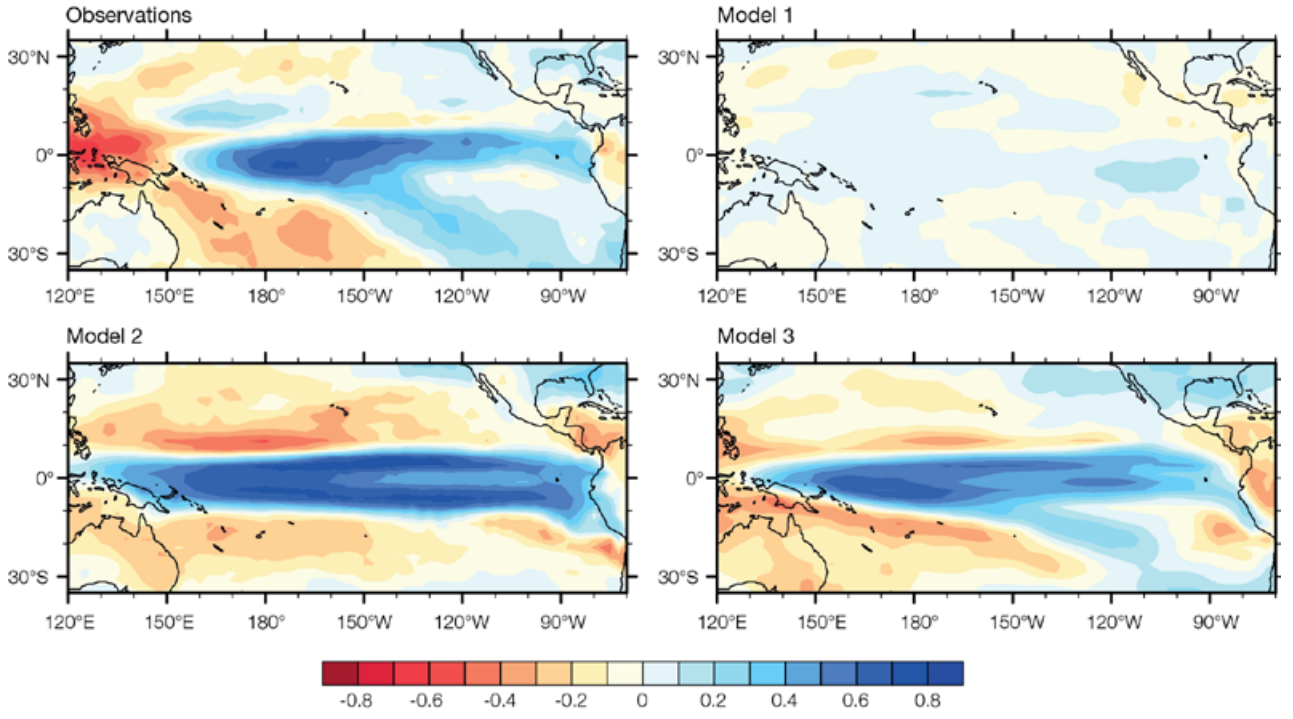

Figure 5.14: Observed (top left) and model (top right and bottom panels) rainfall response to a canonical El Niño event for three models. Contours represent the correlation coefficient between monthly Niño3.4 and rainfall. Positive correlations (blue) show where rainfall typically increases during El Niño events, and negative correlations (red) show where rainfall typically decreases during El Niño events.

5.2.3.2 Indian Ocean Dipole

The simulation of the Indian Ocean Dipole (IOD, Section 3.4.7) in CMIP3 models may be relevant to climate projection for regions affected by the IOD, including East Timor. Most CMIP3 models show some skill in reproducing the spatial pattern of surface temperatures that corresponds to the observed IOD. However the multi-model mean IOD pattern has a stronger east-west gradient than observed (Cai et al., 2009c). In five CMIP3 models (ECHO-G, IPSL-CM4, GISS-AOM, GISS-ER and INM-CM3.0), the IOD sea-surface temperature pattern is unrealistic, with a weak or negative correlation between the observed pattern and the model patterns (Cai et al., 2009c).

5.2.3.3 South Pacific Convergence Zone

The observed SPCZ is described in detail in Chapter 2. The simulation of the SPCZ in the CMIP3 global climate models is examined using December-February and June-August mean rainfall from the last two decades of the 20th century climate simulations compared with CMAP observed rainfall (Table 2.2). The SPCZ position is identified from the line of maximum rainfall in the South Pacific, extending from around 150°E towards the south-east.

The observed CMAP and multi-model mean rainfall for the December-February and June-August seasons (Figure 5.15) show that the observed SPCZ is more intense during December-February, and extends further into the south-east Pacific. During June-August, the ITCZ is more intense than the SPCZ, and the SPCZ breaks into distinct tropical and sub-tropical components. The multi-model mean rainfall also shows a distinct SPCZ band, which is most intense during December-February. The multi-model mean SPCZ has an orientation that is too zonal (east-west), rather than sloping to the south-east, and does not extend far enough into the sub-tropics in the eastern Pacific. In June-August, the multi-model mean rainfall does not show the sub-tropical section of the SPCZ located at around 30°S.

While most models are able to simulate a separate ITCZ and SPCZ, a small number of models do not show a distinct SPCZ (for individual model performance, see Brown et al., in press). GISS-AOM and GISS-ER simulate a single rainfall band over the equator, while MIROC3.2 (medres) and MIROC3.2 (hires) simulate an SPCZ that does not extend east of the International Date Line.

Observations show that the SPCZ tends to move north-east during El Niño years and south-west during La Niña years (Folland et al., 2002; Vincent et al., 2011). The majority of models reproduce this movement of the SPCZ in response to ENSO. This underpins the ability of the models to simulate the influence of ENSO on rainfall and atmospheric circulation in the South Pacific (Brown et al., in press) because ENSO impacts on rainfall and circulation are largely linked to shifts in the SPCZ in this region.

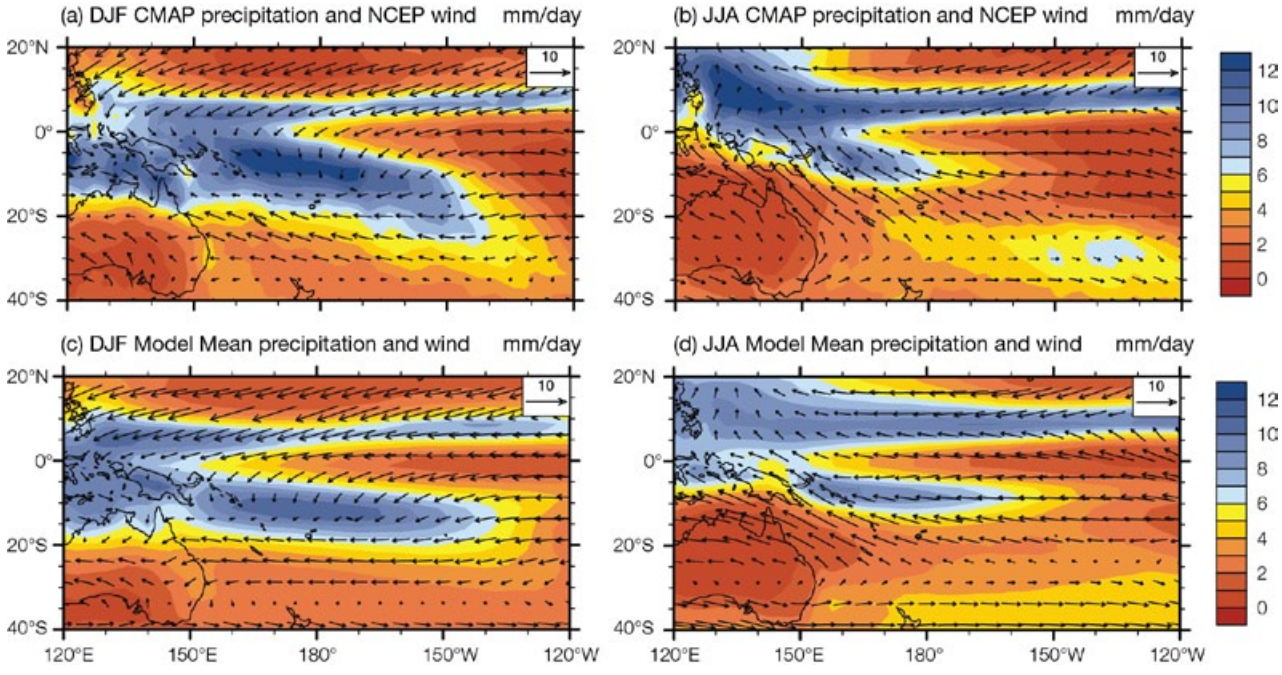

Figure 5.15: (Top left): Observed December-February seasonal mean rainfall (from CMAP; see Table 2.2) and near-surface wind (from NCEP). (Top right): As for top left panel but for June-August. (Bottom left): Multi-model mean December-February seasonal mean rainfall and near-surface wind. (Bottom right): As for bottom left panel but for June-August.

5.2.3.4 Intertropical Convergence Zone

Climate models typically simulate a narrow, zonal rainfall maximum corresponding to the ITCZ, with the exception of three models (GISS-AOM, GISS-ER and MIROC3.2(hires)) which show no Northern Hemisphere ITCZ branch in the western Pacific. These three models should therefore not be used for regional projections in that area. In the central and eastern Pacific, many models display a double ITCZ, with a Southern Hemisphere branch that is not found in the observations. In the multi-model mean there is too much rain in the south-eastern Pacific, with associated December-February northerly wind anomalies over the equator (in the observations this is a region of persistent southerlies).

The observed seasonal variation of the position of the ITCZ has an amplitude of approximately 2° of latitude, with maximum southward extent (although still in the Northern Hemisphere) in February, and a broad maximum of the northern extent between July and September (Waliser and Gautier, 1993). Models represent the December-February location well on average, but show an excessive northward displacement in July-September (Figure 5.16); a bias that occurs in almost all models. Models on average reproduce the seasonal cycle of ITCZ rainfall amounts reasonably well, although uncertainties in the observations are large in this region, precluding stronger conclusions. On interannual time scales, most models are able to reproduce the equatorward shift under El Niño conditions and the poleward shift under La Niña conditions found in the observations (Chapter 3), except for those models not showing significant ENSO variability.

5.2.3.5 West Pacific Monsoon

In the Southern Hemisphere the West Pacific Monsoon consists of the seasonal reversal of wind direction over the region to the north of Australia, extending from East Timor to the Solomon Islands. The observed December-February monsoon winds are north-westerly, and bring convection and heavy rainfall predominantly to East Timor, Indonesia, Papua New Guinea and the Solomon Islands (Figure 5.15 (a) and (b)). In the Northern Hemisphere, corresponding seasonal reversals affect Palau and the Federated States of Micronesia. The spatial pattern of rainfall and winds associated with the monsoon is reasonably well simulated by the multi-model mean (Figure 5.15 (c) and (d)).

Over the Southern Hemisphere box-1 region (Figure 2.10), all models simulate easterly winds that prevail during June-August and most models also simulate either a weakening or a reversal of the zonal wind component during December-February (Figure 5.17). Four models (GISS-AOM, GISS-EH, IPSL-CM4 and MIROC3.2(medres)) fail to simulate a reversal in wind direction.

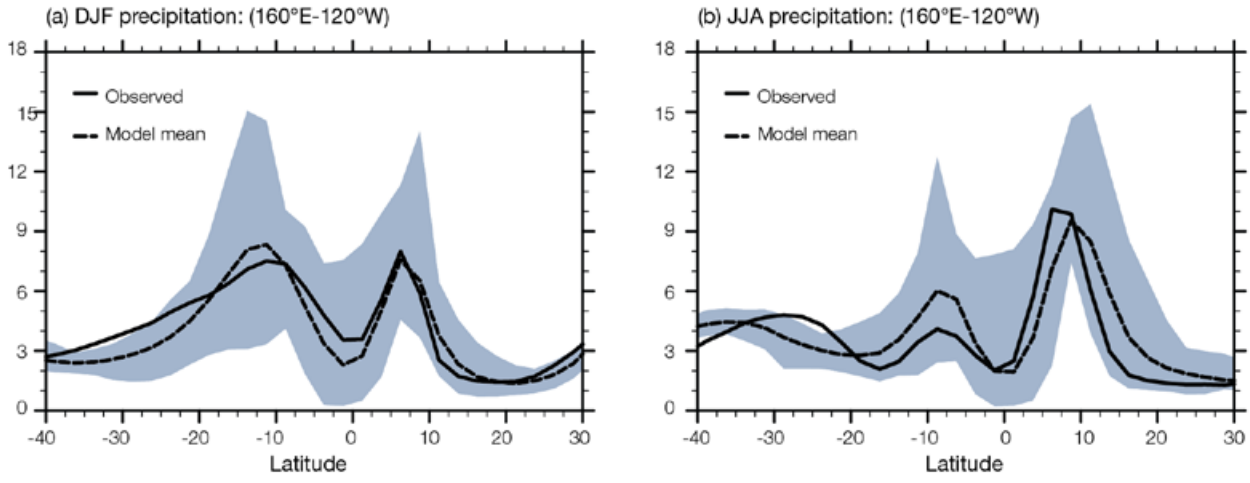

Figure 5.16: Zonal average rainfall for (a) December-February, and (b) June-August, across the Pacific (160°E–120°W). CMAP (Table 2.2) observations and multi-model means are shown as solid and dashed lines, with the inter-model range as blue shading.

When the seasonal rainfall contrast is expressed as the ratio of the December-February rainfall total divided by the June-August rainfall total over the Southern Hemisphere box-1 region (Figure 2.10), the observed ratio is close to two according to the CMAP data (Figure 5.18). Almost all the models simulate a ratio greater than one, with the exception of GISS-EH, which fails to simulate an enhancement of rainfall during the monsoon season.

Overall, with only a few exceptions, the CMIP3 climate models capture the major climatic features of the monsoon, including the seasonal reversal of the surface winds and the dominance of summer rainfall over winter rainfall. Of the four models without wind reversal, one, IPSL-CM4, has a reasonable rainfall seasonality, and the wind reversal failure is marginal. Consequently, three models (GISS-AOM, GISS-ER and MIROC3.2(medres)) do not adequately simulate the West Pacific Monsoon wind reversal and rainfall seasonality.

5.2.3.6 Summary: Climate Features and Patterns of Variability

Most of the 24 CMIP3 global climate models are able to reproduce the major climate features (SPCZ, ITCZ and West Pacific Monsoon) and modes of variability (ENSO, Interdecadal Pacific Oscillation and Pacific Decadal Oscillation). Two models (GISS-AOM and GISS-ER) show virtually no ENSO-like variability. These two models also fail to simulate a distinct SPCZ and ITCZ. In addition, MIROC3.2(medres) and MIROC3.2(hires) simulate an SPCZ that does not extend to the east of the International Date Line. Three models fail to simulate the West Pacific Monsoon wind reversal and rainfall seasonality (GISS-AOM, GISS-ER and MIROC3.2(medres)).

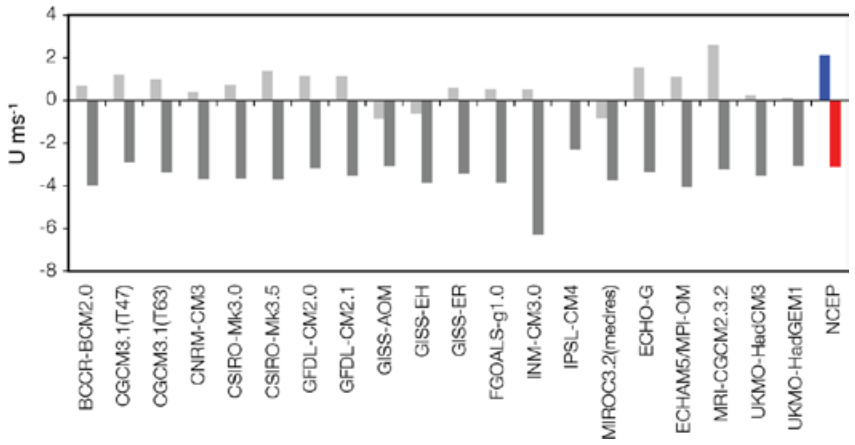

Figure 5.17: Seasonal surface zonal (easterly) winds as simulated by CMIP3 models for the Southern Hemisphere box-1 region (Figure 2.10) in December-February (light grey) and June-August (dark grey). Observed (NCEP, Table 2.2) zonal winds for December-February (blue) and June-August (red). Note that surface winds are only available for 20 CMIP3 models.

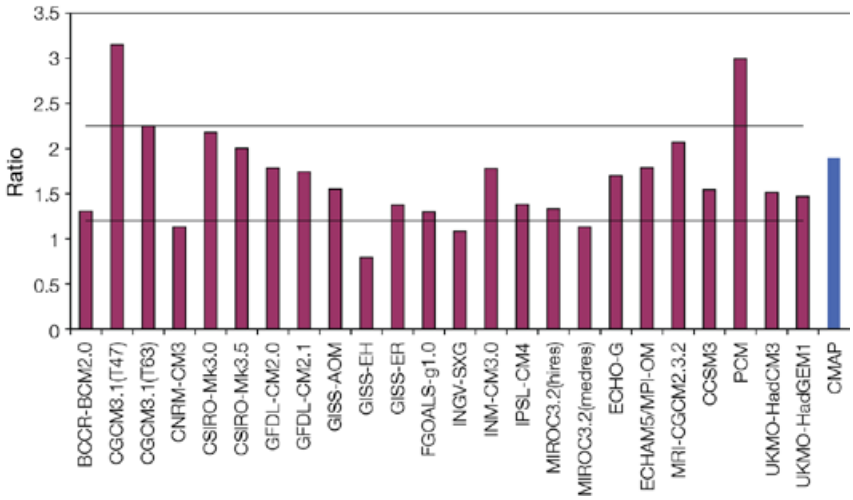

Figure 5.18: The ratio of December-February to June-August rainfall as simulated by CMIP3 models for the Southern Hemisphere box-1 region (Figure 2.10) (purple). The observed rainfall ratio (CMAP, Table 2.2) is indicated in blue. The black lines encompass the multi-model mean plus and minus one standard deviation.

5.2.4 Extremes

As a first step in assessing extreme events, an overview of the ability of the models to simulate the full spectrum of daily maximum temperature, minimum temperature and rainfall over the period 1980–1999 was obtained by calculating the Probability Density Function (PDF) overlap skill score (Perkins et al., 2007; Figure 5.19). In the context of daily maximum surface air temperature, for example, the PDF overlap skill score determines the degree to which a model simulates the correct number of cold, mild and hot days. Scores can range from 0.0 (no skill) to 1.0 (highest possible skill). The test is performed on the empirical distributions of the observed and model data, rather than a parametric distribution fitted to each dataset.

While the PDF overlap skill score is useful in gaining an overview of the ability of climate models to simulate the full spectrum of daily climate, it is not very useful for capturing rare and extreme events (e.g. the hottest day of the year has a relative frequency of 0.003, and is therefore barely visible on a PDF of daily maximum temperature). For this reason, the model bias was calculated for a number of commonly used statistics that capture the magnitude and frequency of extreme daily maximum temperature, minimum temperature and rainfall events (Table 5.3).

Unless otherwise stated, the results presented for all bias statistics refer to the multi-model mean (plus/minus the inter-model standard deviation) of the all observation test scores (the value obtained by averaging across the scores from the ERA-40, NCEP/DOE R-2 and JRA25 datasets). Only limited amounts of daily data are available for CMAP and GPCP, so these datasets could not be used for the rainfall analysis. A list of the CMIP3 models for which daily data are available is given in Appendix 1. The only exception to this listing is for the rainfall statistics, where GISS-ER and GISS-EH were excluded due to their outlying poor performance.

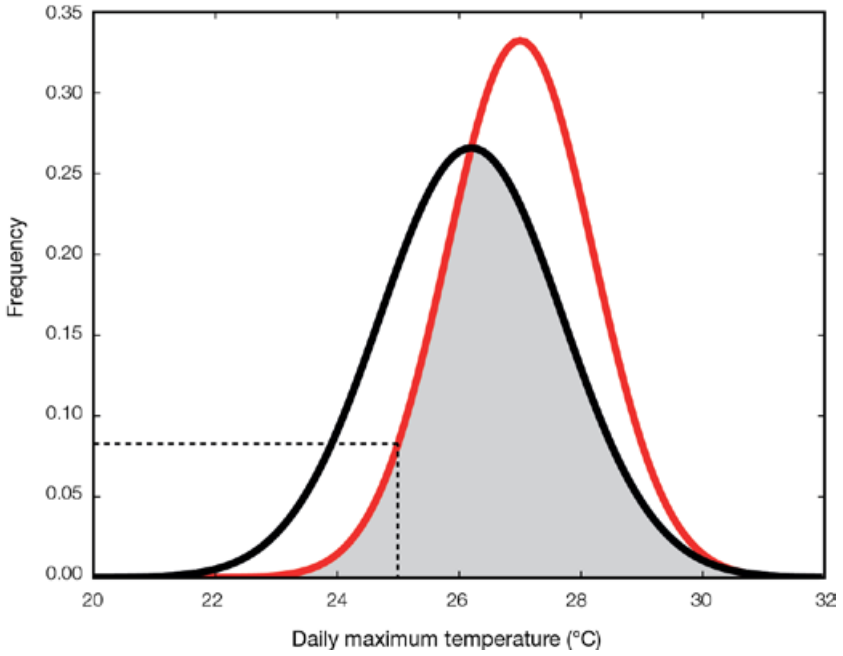

Figure 5.19: Schematic diagram illustrating the information contained in a Probability Density Function (PDF) and the PDF overlap skill score. A PDF provides information on the frequency of an event in a given sample. For example, for the red PDF a daily maximum temperature of 25°C occurs on 8% of days (a relative frequency of 0.08). As indicated by the grey shading, the PDF overlap skill score measures the degree of commonality (or overlap) between modelled (e.g. red PDF) and observed (e.g. black PDF) daily data.

Table 5.3: Definition of the statistics used to assess the ability of the models to capture the magnitude and frequency of extreme events.

Test	Description	Variables
1-in-20-year return value bias (B_{RV20})[a]	Difference (model minus observed) in the magnitude of the event that occurs on average only once every 20 years	Maximum temperature Minimum temperature Rainfall
90th percentile bias (B_{90pctl})	Difference in the value that is exceeded on only 10% of days	Maximum temperature Minimum temperature Rainfall
10th percentile bias (B_{10pctl})	Difference in the value that is exceeded on all but 10% of days	Maximum temperature Minimum temperature Rainfall
Heat wave duration index bias (B_{HWDI})[b,c]	Difference in the average length of a heat wave (defined as five or more consecutive days with a maximum temperature above ($\mu + 2\sigma$)°C of the observational data)	Maximum temperature
Warm nights (WN)[b]	Percentage of days where the minimum temperature is ≥ 90th percentile of the observational data (i.e. a perfect score is 10%)	Minimum temperature
Highest 5-day rainfall total bias (B_{RX5})[b]	Difference in the magnitude of the highest 5-day rainfall total	Rainfall
Extreme rainfall contribution index bias (B_{R95pT})[b]	Difference in the percentage of total annual rainfall that comes from intense rainfall events (defined as more intense than the 95th percentile)	Rainfall

μ = mean; σ = standard deviation

[a]Calculated using the Generalised Extreme Value distribution (Coles, 2001; Kharin et al., 2005)

[b]See http://cccma.seos.uvic.ca/ETCCDMI/ for details

[c]Threshold was modified from the original ETCCDMI definition, to better reflect the Indo-Pacific climate.

5.2.4.1 Surface Air Temperature

The ability of the CMIP3 models to reproduce the full spectrum of daily maximum and daily minimum surface air temperature is very similar. Both variables are particularly well simulated in the South Pacific, with ensemble average PDF overlap skill scores of up to 0.8 achieved in the vicinity of Vanuatu, Fiji and Tonga (Figure 5.20, inset). However, the equatorial Pacific is less well simulated, with scores as low as 0.3 near Kiribati and Nauru. These low equatorial scores can be explained by a general underestimation of the mean and overestimation of the variance in daily temperature (Figure 5.20) which may be related to the aforementioned cold bias and tendency of the models to overestimate the amplitude of the seasonal temperature cycle (Section 5.2.1.1).

With respect to the magnitude of rare and extreme temperature events, the 1-in-20-year maximum daily temperature tends to be slightly underestimated by the models throughout most of the PCCSP region (B_{RV20} = -1.0 ± 0.8°C), while the 1-in-20-year minimum daily temperature is either slightly over- or underestimated, depending on the location and particular model. The models tend to overestimate the maximum heat wave duration throughout the PCCSP region (B_{HWDI} = 6.4 ± 4.7 days) and the number of warm nights (*WN* = 17 ± 12%).

5.2.4.2 Rainfall

The CMIP3 models have a similar ability in simulating the full spectrum of daily rainfall throughout the PCCSP region, with multi-model average spatial PDF overlap skill scores all within the narrow range of 0.6 to 0.8 (Figure 5.21, inset). The nature of the differences between the model and observed PDF, however, differs depending on location (Figure 5.21). Throughout most of the PCCSP region, the models generally underestimate the number of days at both ends of the observed daily rainfall distribution (i.e. the number of days of both heavy rain and little to no rain). In contrast, the models tend to overestimate the number of days of little or no rain in the vicinity of Kiribati and Nauru. This contrasting performance may be related to the influence of the cold tongue bias (Section 5.2.2.1 and Box 5.2).

Consistent with this underestimation of the frequency of extreme rainfall events, the CMIP3 models also generally underestimate the intensity. This is evident from a tendency to underestimate the intensity of the 1-in-20-year event (B_{20RV} = -54 ± 28 mm per day), the contribution of heavy rainfall events to the annual rainfall total (B_{R95pT} = -3.1 ± 2.2%) and the highest 5-day rainfall total (B_{RX5} = -109 ± 67 mm). These model deficiencies in representing the frequency and intensity of extreme rainfall events may be partly explained by the failure of coarse resolution climate models to fully represent intense, localised rainfall features.

5.2.4.3 Summary: Extremes

In summary, although the CMIP3 models show some skill in representing the broad PDF of temperature and rainfall (as evidenced by the overlap statistic) they tend to underestimate the frequency and intensity of present day extreme (high) temperature and rainfall events. This finding may be related in part to the relatively coarse resolution of these models. Biases tend to be most pronounced in the vicinity of Kiribati and Nauru, which is likely due to the influence of the cold tongue bias. The PCM model provides a relatively poor simulation of present day temperature extremes, while the GISS-ER and GISS-EH models provide a poor simulation of present day rainfall extremes (see Perkins, in press for details). It is recommended that these models are not used for projections of future climate in Chapters 6 and 7 (Section 5.5).

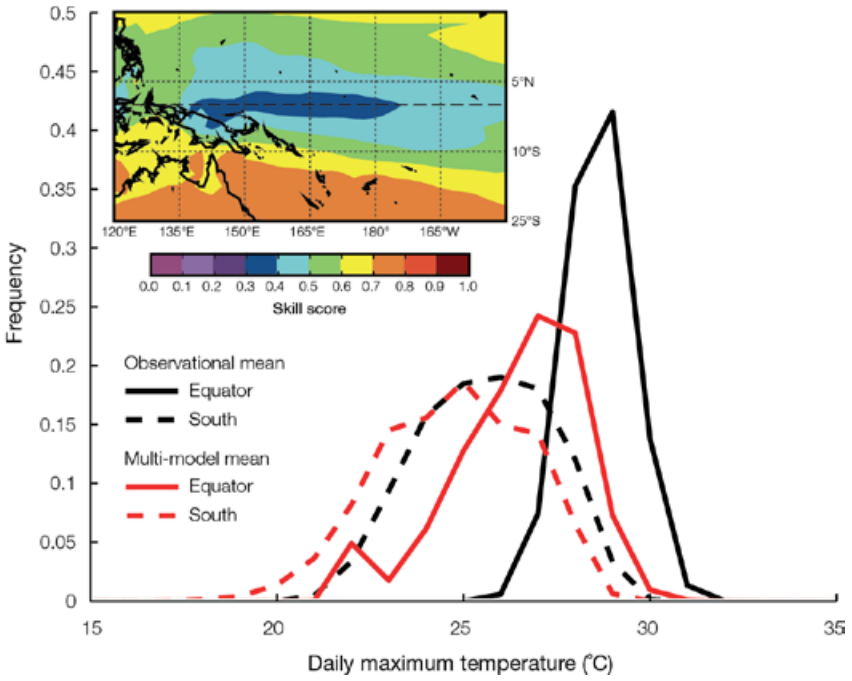

Figure 5.20: Multi-model mean and observed mean (ERA-40, NCEP/DOE R-2 and JRA25 average) 1980–1999 maximum daily surface air temperature PDFs for two locations: south (170°W, 20°S) and equator (175°E, 0°). Inset: Multi-model mean PDF overlap skill score for the 1980–1999 daily maximum surface air temperature, averaged over the observational datasets.

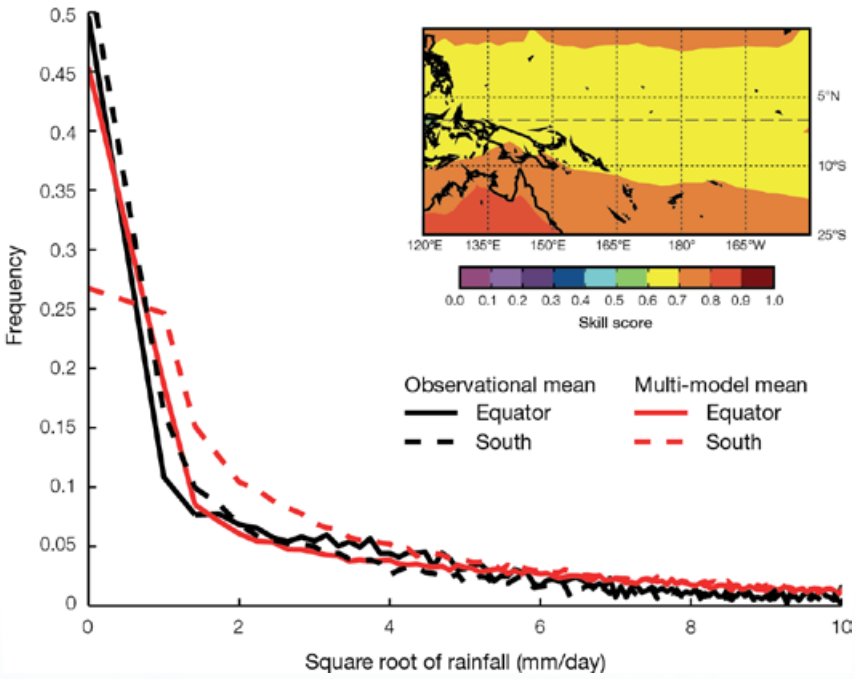

Figure 5.21: Multi-model mean (GISS-EH and GISS-ER excluded) and observed mean (ERA-40, NCEP/DOE R-2 and JRA25) 1980–1999 daily rainfall PDFs for two locations: south (170°W, 20°S) and equator (175°E, 0°). Inset: Multi-model mean PDF overlap skill score for the 1980–1999 daily rainfall, averaged over the observational datasets.

Box 5.2: CMIP3 Model Biases in the PCCSP Region

In general, the CMIP3 global climate models are able to represent essential aspects of the most important large-scale climate features of the Pacific region. These include representing the geographic and temporal patterns of sea-surface temperature and wind speed and direction, and the approximate shape, location and seasonality of the major convergence regions, e.g. SPCZ, ITCZ, and their associated rainfall. This provides confidence in the use of models for regional climate projections.

However, a number of common model biases and errors are apparent which lead to important limits in this confidence. Perhaps the most significant of these arise from a tendency for models to extend the Pacific equatorial cold tongue too far to the west, resulting in western and central equatorial Pacific sea-surface temperatures which are too cold (Figure 5.4). Maximum temperature biases occur in the vicinity of Nauru and Kiribati, however other countries are also affected, as this bias affects large-scale patterns of wind and rainfall, and thereby many aspects of broader Pacific climate and climate variability.

Both model sea-surface temperatures and surface air temperatures are lower than observed in this region, with resultant rainfall totals significantly too low, particularly near the equator. This manifests as an artificial split between the ITCZ and SPCZ, the latter of which is too east-west orientated (Figure 5.15). The ITCZ is also located too far off the equator in December-February. In addition, winds are consistently too strong here, with direction errors (at over 10°) being largest in the Pacific basin (Figure 5.3). The cold tongue bias also affects ENSO variability, in particular pushing the pattern of response too far to the west, with consequences for the interannual variation of surface temperatures and rainfall at low latitudes in the western Pacific (Figure 5.12).

It is critical that such biases and shortcomings are borne in mind when interpreting model output for practical applications within the region. They also provide some of the most significant challenges for ongoing research (Chapter 8).

Flux adjustment in global climate models may reduce some of these biases, but leads to uncertainty over their ability to simulate climate variability and the response to climate forcing.

5.3 Evaluation of Dynamical and Statistical Downscaling

In evaluating the dynamical downscaling performed with the CCAM model (Section 4.5.2), a number of comparisons have been made:

- A comparison of the large-scale PCCSP region present day climate simulated by CCAM (i.e. the 60 km resolution simulations) with observations and the six host global climate models (Section 5.3.1.1). Note that the six models chosen for downscaling here were not the top six performing members in the previous global climate model evaluation. They were selected based upon the research of Smith and Chandler (2010) because they generally scored high in this study and tended to have good interannual variability, such as ENSO. However, as the sea-surface temperature biases were corrected before being used by CCAM, and no atmospheric data from the global model was used, the performance of the global climate model does not directly relate to the accuracy of the downscaled simulations.
- A comparison of the small-scale present day climate simulated by CCAM (i.e. the 8 km resolution simulations) with relevant high resolution observations (Section 5.3.1.2). This analysis was conducted for two regions: Papua New Guinea and Fiji.
- A comparison of the performance of CCAM with additional dynamical downscaling simulations (Section 5.3.3).

5.3.1 CCAM Large-Scale (60 km) Climate

Using the same statistics and observational datasets as in Section 5.2.1, the CCAM 60 km simulations were upscaled to a common 2.5° latitude/longitude grid. This allowed for large-scale temperature, rainfall and extreme weather comparisons to be made against observations and the six host global climate models.

5.3.1.1 Surface Air Temperature

The evaluation of present day surface air temperature (Table 5.4) shows general improvement in the downscaled simulations versus the host global models. In particular, the downscaled simulations provide an:

- Improved mean state (E_{abs} = 0.55 vs. 1.03°C).
- Improved phase (r_t = 0.93 vs. 0.77) and amplitude ($\sigma_{ratio,t}$ = 1.07 vs. 1.21) of the seasonal cycle.
- Improved location (r_p = 0.97 vs. 0.90) and amplitude ($\sigma_{ratio,x}$ = 1.05 vs. 1.17) of spatial features.

The absence of any pronounced cold tongue bias appears to be the main factor behind improvements in the mean state and spatial pattern (Figure 5.22). This is due to the sea-surface temperature bias adjustment in the CCAM method. Also note the improved representation of the temperature over the land masses due to better resolved topography in the CCAM 60 km simulations, as for

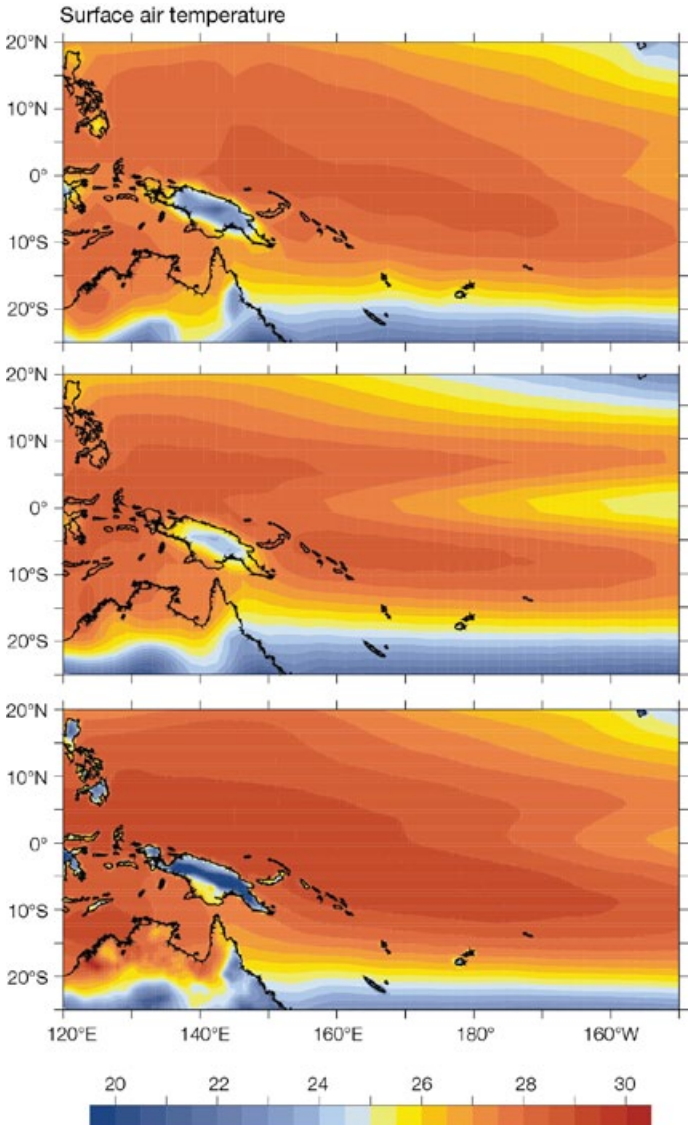

Figure 5.22: Annual mean surface air temperature for 1980–1999 ERA-40 reanalysis dataset (top), for the global climate model multi-model mean (middle) and CCAM 60 km six-model mean (bottom).

Papua New Guinea and Fiji, for example. The warm bias in the CCAM simulations is the result of a parameterisation of the sea-surface temperature enhancement when there are light winds and sunny skies. It appears as though this effect may be too large in these simulations. This can be seen in the evaluation statistics of the individual downscaled simulations (Table 5.4).

5.3.1.2 Rainfall

The evaluation of recent historical rainfall (Table 5.5) shows general improvement in the downscaled simulations versus the host global climate model. In particular, the downscaled simulations provide:

- Improved mean state (E_{abs} = 1.33 vs. 1.88 mm per day).
- Improved spatial pattern (r_p = 0.76 vs. 0.68).
- Slightly poorer seasonal cycle (r_t = 0.51 vs. 0.59).

It is difficult to comment on the amplitude of the seasonal cycle or the spatial features of the region, due the large differences between the amplitude of CMAP and GPCP (Yin et al., 2004; also see Figure 5.2 and discussion in Section 2.2.1.4). However, it is interesting to note that the outputs of global climate models compared more favourably with CMAP, while the downscaled runs compared more favourably with GPCP. An improved orientation of the SPCZ and the absence of excessive rainfall in the far west of the PCCSP region (i.e. the region influenced by the West Pacific Monsoon) appear to be the main factors behind improvements in the mean state and spatial pattern in CCAM (Figure 5.23). Note that for the CCAM simulations, the statistics for the various simulations are fairly similar, while the statistics for the global climate models vary significantly. Although the biases in the CCAM simulations (around 1 mm per day) are worse than the outputs of global climate models, the mean absolute errors are less. Evidently, the global climate models have both positive and negative errors in various regions which cancel out to give a smaller bias, but larger mean absolute errors.

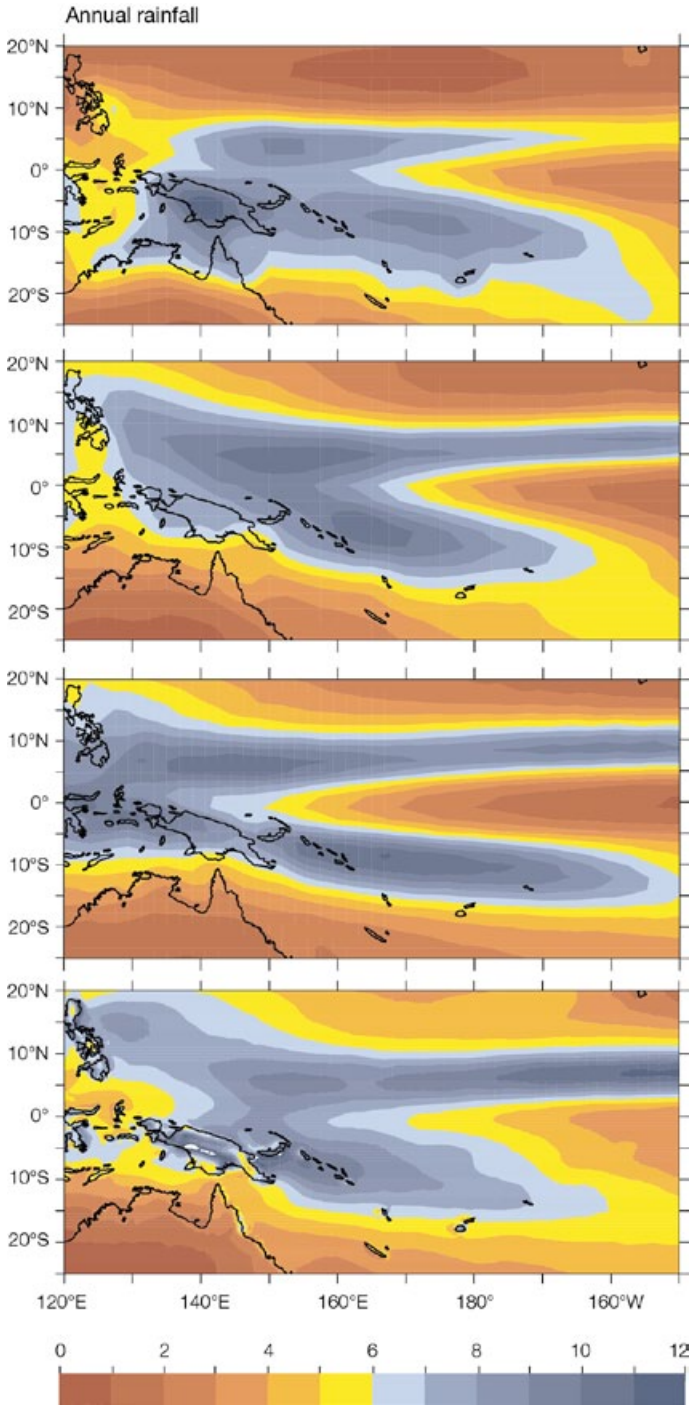

Figure 5.23: 1980–1999 annual mean rainfall (mm per day) for GPCP data (top), CMAP data (middle top), multi-model mean of the six global climate models that were downscaled (middle bottom) and multi-model mean of six CCAM 60 km models (bottom).

Table 5.4: Combined statistics for global climate multi-model mean and CCAM 60 km multi-model mean simulations for surface air temperature against ERA-40, NCEP2 and JRA25 reanalysis. Bold values show better results for multi-model means (top) and also for pairs of global climate model-CCAM simulations (middle and bottom sections). For comparison, statistics for the multi-model means of the 23 global climate models and for the six individual host global climate models and CCAM 60 km simulations are also given (top). Statistics are defined in Table 5.1.

Surface air temperature (entire PCCSP region)	Bias (°C)	E_{abs} (°C)	r_t	r_p	$\sigma_{ratio,t}$	$\sigma_{ratio\,x}$
Multi-model means						
Average (all 23 global climate models)	-0.76	1.02	0.74	0.89	1.18	1.08
Average of 6 global climate models	**-0.40**	1.03	0.77	0.90	1.21	1.17
Average of 6 downscaled models	0.50	**0.55**	**0.93**	**0.97**	**1.07**	**1.05**
Individual global model simulations						
CSIRO-Mk3.5	1.01	1.04	0.80	0.89	1.13	1.18
GFDL-CM2.0	-1.33	1.35	0.77	0.93	1.44	1.28
GFDL-CM2.1	-0.94	0.98	0.73	0.93	1.44	1.22
ECHAM5/MPI-OM	**0.16**	**0.46**	0.81	0.93	**1.05**	**1.04**
MIROC3.2 (medres)	-1.46	1.51	0.71	0.89	1.19	1.04
UKMO-HadCM3	**0.14**	0.86	0.83	0.85	**1.00**	1.25
Individual CCAM simulations						
CCAM (CSIRO-Mk3.5)	**0.54**	**0.58**	**0.94**	**0.97**	**1.06**	**1.06**
CCAM (GFDL-CM2.0)	**0.49**	**0.54**	**0.93**	**0.98**	**1.07**	**1.05**
CCAM (GFDL-CM2.1)	**0.52**	**0.57**	**0.93**	**0.97**	**1.08**	**1.05**
CCAM (ECHAM5/MPI-OM)	0.52	0.56	**0.94**	**0.98**	1.08	1.06
CCAM (MIROC3.2 (medres))	**0.43**	**0.49**	**0.93**	**0.97**	**1.09**	1.04
CCAM (UKMO-HadCM3)	0.53	**0.57**	**0.94**	**0.97**	1.06	**1.05**

Table 5.5: As for Table 5.4, but for rainfall. Observational data is from CMAP and GPCP.

Rainfall (entire PCCSP region)	Bias (mm/day)	E_{abs} (mm/day)	r_t	r_p	$\sigma_{ratio,t}$	$\sigma_{ratio\,x}$
Multi-model means						
Average (all 23 global climate models)	0.39	1.77	0.55	0.63	1.25	1.27
Average of 6 global climate models	**0.62**	1.88	**0.59**	0.68	1.31	1.40
Average of 6 downscaled models	1.00	**1.33**	0.51	**0.76**	**0.92**	**0.90**
Individual global model simulations						
CSIRO-Mk3.5	**0.75**	1.86	**0.66**	0.73	1.37	1.41
GFDL-CM2.0	**0.55**	1.60	**0.67**	0.76	1.49	1.50
GFDL-CM2.1	**1.04**	1.75	**0.62**	0.67	1.40	1.27
ECHAM5/MPI-OM	**0.95**	2.46	0.50	0.57	1.35	1.45
MIROC3.2 (medres)	**-0.13**	1.23	**0.53**	0.70	**1.02**	1.10
UKMO-HadCM3	**0.56**	2.39	0.55	0.67	1.23	1.68
Individual CCAM simulations						
CCAM (CSIRO-Mk3.5)	1.10	**1.37**	0.52	**0.78**	**0.97**	**0.97**
CCAM (GFDL-CM2.0)	0.94	**1.31**	0.54	0.76	**0.91**	**0.85**
CCAM (GFDL-CM2.1)	1.11	**1.44**	0.50	**0.75**	**0.91**	**0.89**
CCAM (ECHAM5/MPI-OM)	1.04	**1.31**	**0.55**	**0.78**	0.93	**0.93**
CCAM (MIROC3.2 (medres)	0.82	**1.20**	0.43	**0.73**	**0.89**	0.88
CCAM (UKMO-HadCM3)	0.97	**1.35**	0.55	**0.76**	**0.92**	**0.87**

5.3.1.3 Extremes

Evaluation of the 1-in-20-year maximum daily air temperature (Figure 5.24) shows large values of over 44°C in the reanalyses over Australia and fairly uniform values of around 30°C over the Pacific Ocean, with slightly lower values in the north-eastern and southern regions. The global climate models capture this pattern, but have higher values than the reanalyses. The upscaled CCAM 60 km simulations have even larger values over the ocean, but are closer to the reanalyses over Australia. The raw CCAM 60 km simulations have slightly higher values than the upscaled results, indicating that upscaling tends to slightly dampen the extremes.

The CCAM 8 km results for Fiji are fairly uniform, with lower temperatures to the south, similar to the CCAM 60 km results. In addition, some variation is seen across the islands, with lower values in the mountains and higher values in the lowlands for the southern island and generally lower values for the northern island. For Papua New Guinea, the 8 km variations are much more pronounced, with lower extremes clearly evident over the high mountains and higher values over the lowlands. This pattern was also partially captured in the CCAM 60 km simulations (not upscaled).

Evaluation of the percentage of days with heavy rainfall (20–50 mm) shows agreement between the mean of the five global climate models for which daily data were available and that were used to downscale, and the mean of the CCAM 60 km simulations (Figure 5.25), while the combined global climate model values appear to be too large, i.e. many of the global models appear to be simulating too many heavy rain days.

The CCAM 8 km percentage of heavy rain days for Fiji and Papua New Guinea (bottom row of Figure 5.25) shows a complex pattern, with higher values (greater than 20% of days with heavy rainfall) along the eastern edges of the Fiji Islands and lower values (around 2% of days with heavy rainfall) over western portions of the islands. Over Papua New Guinea, the largest percentage of heavy rain days is along mountain slopes and over the Solomon Sea, with fewer days over the Coral Sea and most inland areas. The lack of available quality-controlled, high-resolution gridded daily rainfall observational data prevents validation of these values.

The PDF overlap statistic used in the global climate models evaluation (Section 5.2.4) is also applied here to evaluate the extremes in the CCAM 60 km simulations. Evaluation scores in Figure 5.26 are for multi-model means for all CMIP3 models with available daily data (top), the five global climate models with daily data used to drive the CCAM (middle), and the six CCAM 60 km downscaled simulations (bottom). The PDF statistic for daily rainfall shows general agreement for all three, with some improvement in using CCAM compared to the global climate models. For daily maximum temperature, improvement is not evident. This is potentially related to the CCAM simulations having a greater temperature spread (wider PDF) than the reanalyses, giving a smaller PDF statistic score.

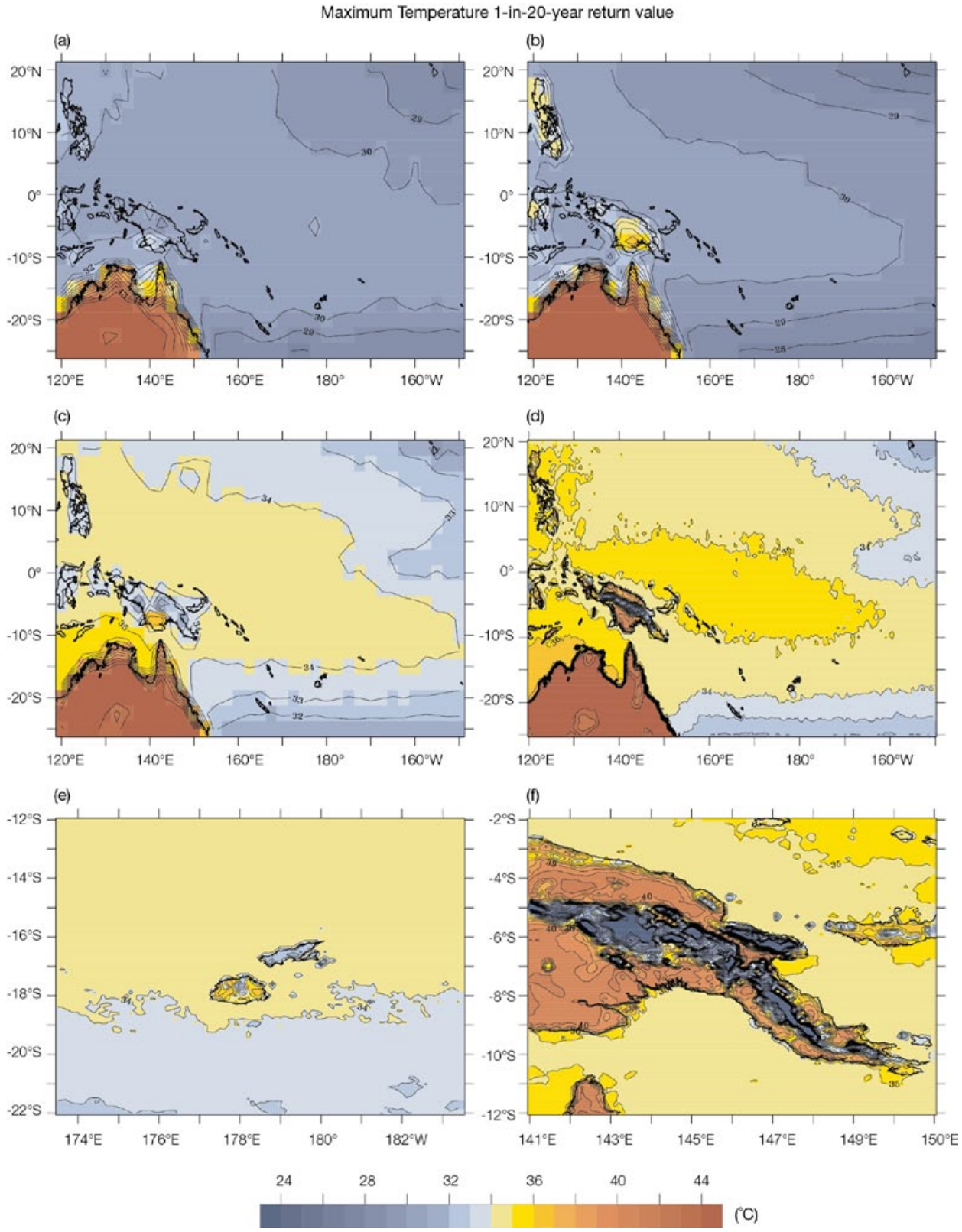

Figure 5.24: 1980–1999 1-in-20-year return maximum daily air temperature. Multi-model mean of (a) three reanalyses (NCEP2, ERA-40 and JMA25), (b) five global climate models, (c) six CCAM 60 km simulations upscaled to a 2.5 degree resolution grid, (d) six CCAM 60 km simulations on a 0.5 degree grid, (e) three CCAM 8 km simulations for Fiji, (f) three CCAM 8 km simulations for Papua New Guinea.

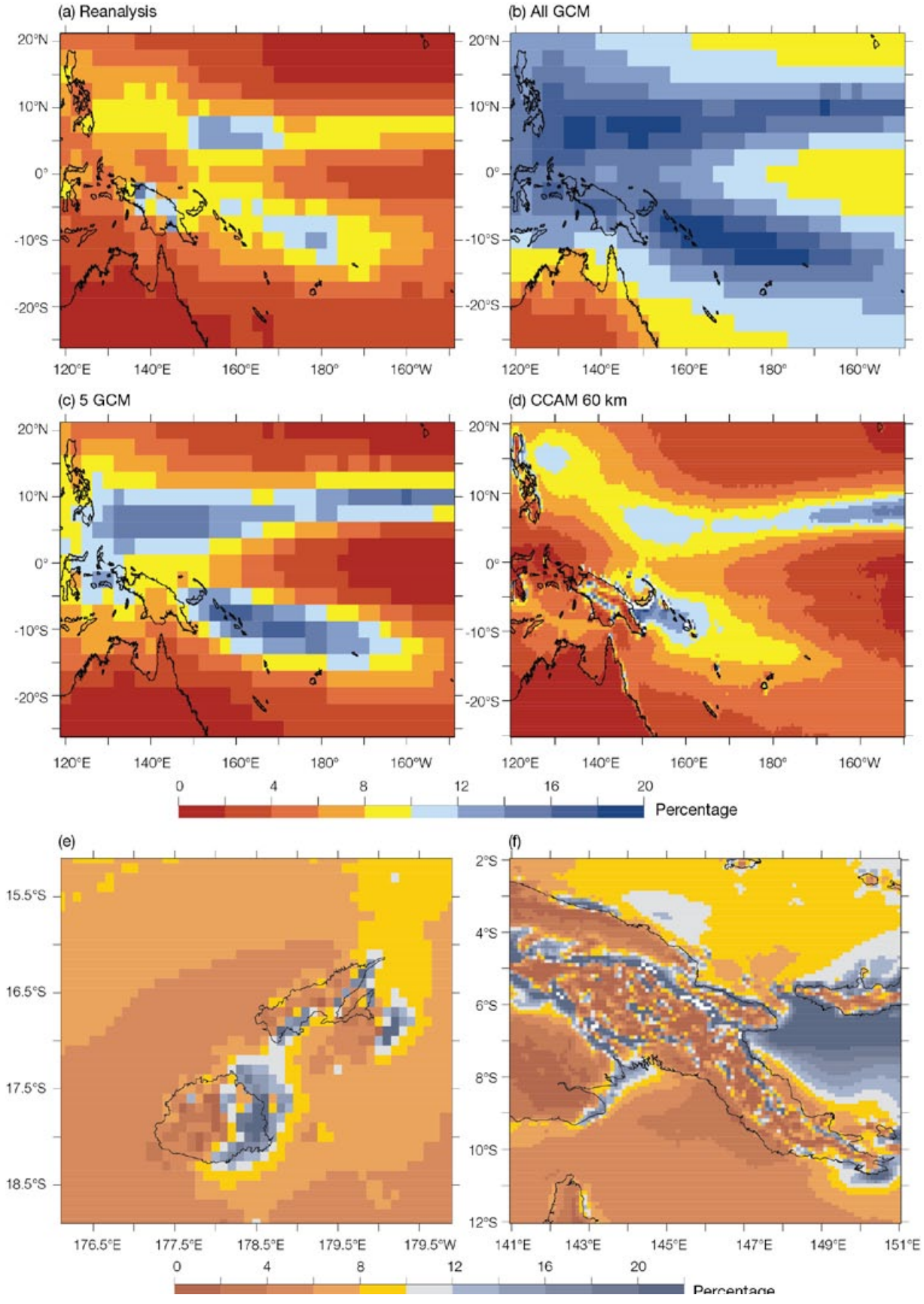

Figure 5.25: 1980–1999 percentage days with heavy rainfall (20–50 mm). Multi-model mean of three reanalyses (NCEP2, ERA40 and JMA25) (top left), average of all global climate models (top right), average of five global climate models (middle left), average of six CCAM 60 km simulations (middle right), average of three CCAM 8 km simulations for Fiji (bottom left) and average of three CCAM 8 km simulations for Papua New Guinea (bottom right).

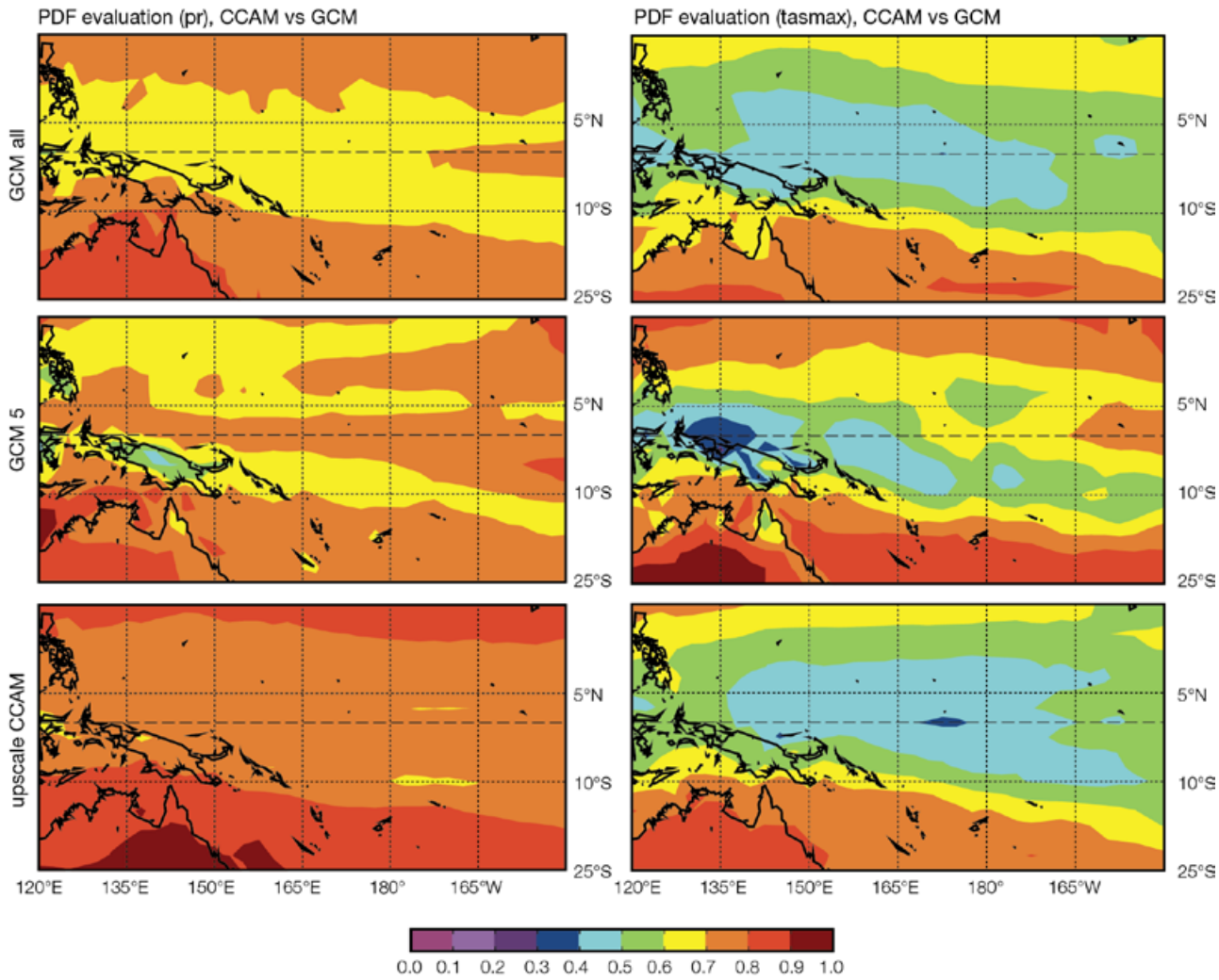

Figure 5.26: PDF statistic for annual rainfall (left) and maximum temperature (right). Multi-model mean for all global climate models (top), for five global climate models (middle), and six CCAM 60 km simulations averaged to 2.5 degree grid for validation (bottom).

5.3.2 CCAM Small-Scale (8 km) Climate

As demonstrated in the previous section, the CCAM 60 km multi-model mean rainfall simulations show a general statistical improvement over the mean values for all global climate models. By further downscaling to 8 km, the rainfall pattern can be better resolved and the effects of topographical and other local features can be incorporated. See, for example, the study by Lal et al. (2008) which showed the benefits of high resolution by using CCAM with 8 km resolution to downscale NCEP reanalyses over Fiji for 10 years. As explained previously, due to computational and time constraints, only three of the six CCAM 60 km simulations were further downscaled to 8 km. In this section, validation for Papua New Guinea and Fiji is presented. A more complete validation for these and other 8 km downscaled regions will be presented in a future technical report.

One of the issues in evaluating rainfall for the 8 km CCAM simulations is the lack of high-resolution gridded datasets to compare against. The TRMM satellite-based dataset chosen is available at 25 km resolution for the period 1998–2010 only, while the CRU dataset is at 50 km and is based upon station data (hence land only (Section 2.2.1)).

Evaluation of the downscaled annual rainfall for Papua New Guinea is presented in Figure 5.27. The top row in Figure 5.27 shows the rainfall pattern at 200 km resolution, approximately the resolution of the global climate models. Although the overall pattern in the various models is similar to the TRMM data, the magnitude is slightly better captured by the 8 km simulation. However, the key reason for the higher resolution simulations is to give more detail than is available from the coarse resolution global climate models. In particular, the pattern of higher rainfall along the slopes of the mountains is better captured by the 60 km simulations, and in even more detail in the 8 km simulations, though the observational dataset is not fine enough to evaluate if all the added detail is realistic.

Comparison of the upper row with the lower row demonstrates the added information at the higher resolutions. The validity of the technique has been shown in a previous study by Lal et al. (2008) using the same model for regional climate simulations over Fiji.

A similar comparison of rainfall for Fiji is shown in Figure 5.28. Fiji is made up of smaller islands than Papua New Guinea, with less complex topography. Again, the top row shows that all models capture the large-scale pattern reasonably well, with more rainfall to the north and less to the south. At the full resolution of the various datasets (bottom row), the topographic effect on the rainfall begins to show, with more rainfall on the eastern side of the main islands and less on the western sides (Lal et al., 2008). This is mainly a result of the easterly trade winds flowing over mountains on the island, rising on the eastern side, resulting in more rainfall, and descending on the downwind side, causing less rainfall.

5.3.2.1 Rainfall and Temperature Validation for Nadi, Fiji

As indicated in the previous section, as finer resolution downscaled simulations are run, more detail in the simulations is provided than is available in gridded observational datasets. An alternative method of validation is to compare model grid point data with station observations. In this section, the simulations from global climate models and CCAM simulations are evaluated for Nadi, Fiji. The observed rainfall climatology from various datasets for 1980–1999 is shown in Figure 5.29 (left). There is greater rainfall in November-April, with less rainfall in the other months. All datasets have generally similar seasonal cycles, though some differences are evident, especially in February, March and December.

Comparisons of rainfall for the global climate models, CCAM 60 km simulations and CCAM 8 km simulations are shown in Figure 5.29 (right). The larger spread of the global climate models (shown by the green dashed lines) is evident, with a tendency to underestimate the seasonal cycle of rainfall. The CCAM 60 km simulations of the seasonal rainfall cycle are closer to the station observations than those of the global climate model. The 8 km simulations tend to best capture the rainfall cycle, though they tend to overestimate rainfall amounts.

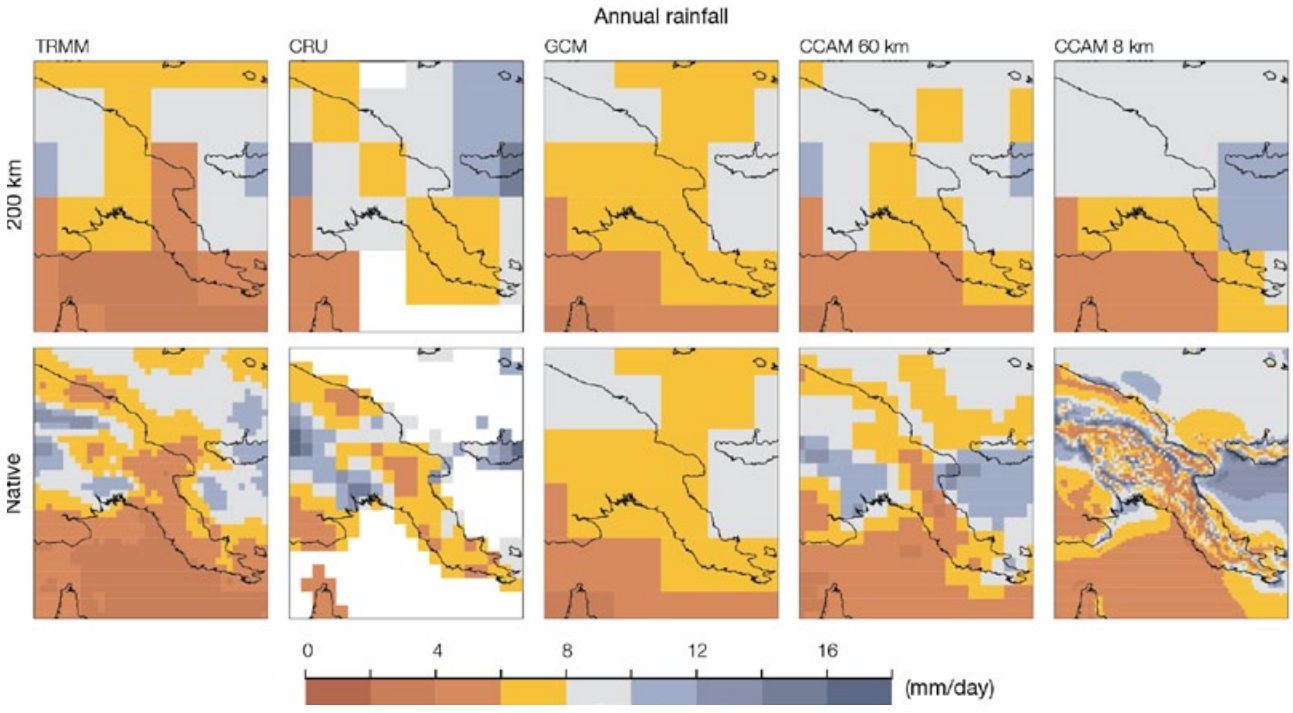

Figure 5.27: Papua New Guinea 1980–1999 annual rainfall climatology (mm per day) for TRMM satellite data (left); CRU data set (middle left); six global climate models multi-model mean (middle); six CCAM 60 km multi-model mean (middle right); and three CCAM 8 km multi-model mean (right). Top row all re-gridded to 200 km grid, bottom row all on the original grid for each dataset.

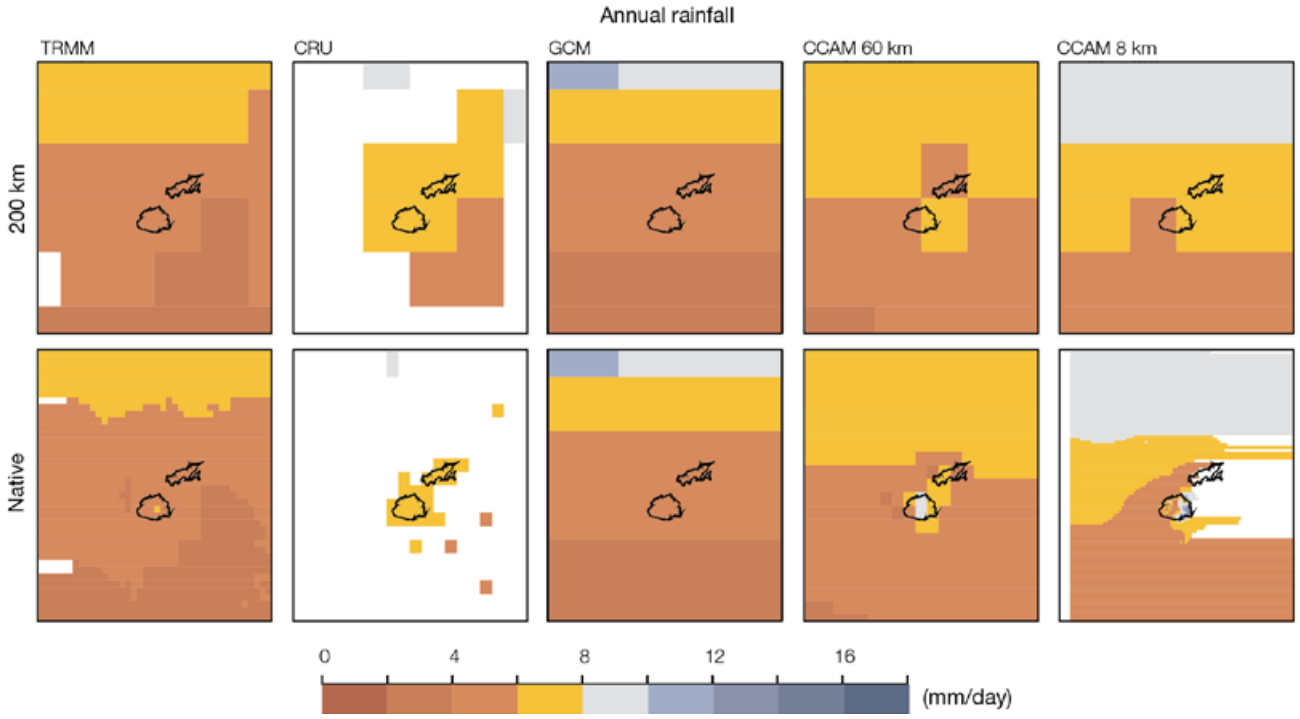

Figure 5.28: Fiji 1980–1999 annual rainfall climatology (mm per day) for TRMM satellite data (left); CRU (middle left); six global climate models model mean (middle); six CCAM 60 km multi-model mean (middle right); and three CCAM 8 km multi-model mean (right). Top row all re-gridded to 200 km grid, bottom row all on the original grid for each dataset.

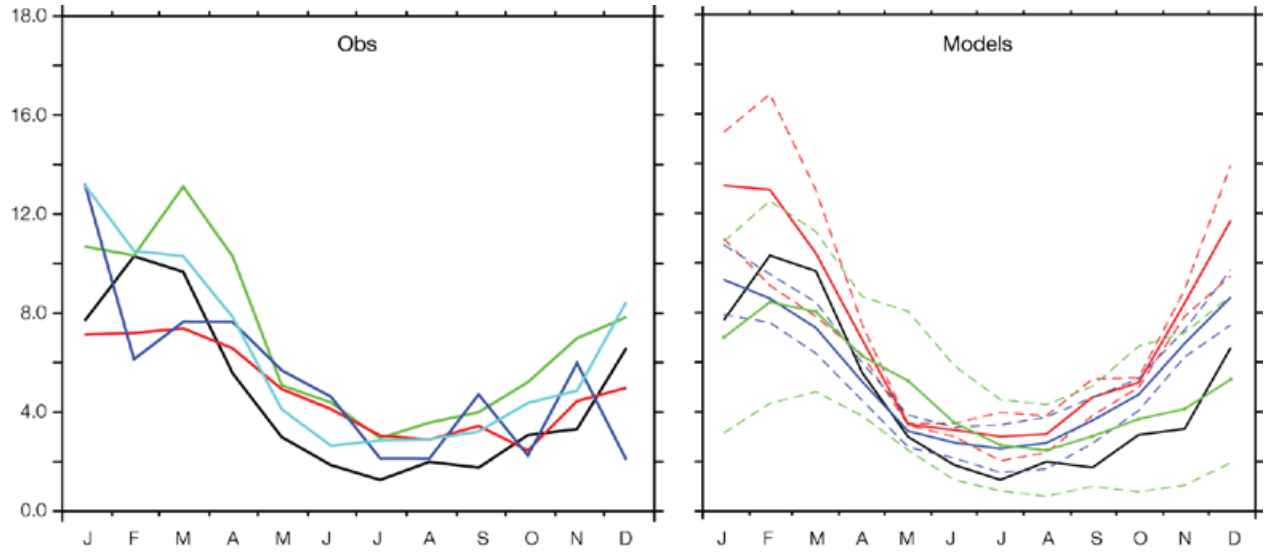

Figure 5.29: Evaluation of 1980–1999 rainfall (mm per day) for Nadi, Fiji. (Left) Monthly plot from various observational data sources: Nadi observations (black line), CMAP (red line), CRU (blue line), GPCP (green line) and TRMM (cyan line). (Right) Monthly plots for Nadi observations (black line), average of the global climate models (solid green line with +/- two standard deviations dashed green lines), CCAM 60 km (solid blue line with +/- two standard deviations dashed blue lines) and CCAM 8 km (solid red line with +/- two standard deviations dashed red lines).

The validation of daily temperature for Nadi, Fiji is presented in Figure 5.30. The multi-model means for the global climate models and the CCAM 60 km simulations show quite good agreement with the station observations, although the global climate models tend to be warmer by around 1°C from February to July. The CCAM 60 km simulations also have a cold bias of about 1°C for most of the year. The CCAM 8 km simulations are closest to the observed seasonal cycle of temperature. The seasonal cycle of maximum and minimum surface air temperature (Figure 5.31) indicates a cold bias in maximum temperatures and warm bias for minimum temperatures in the CCAM 60 km simulations. The CCAM 8 km simulations are very close to the observed maximum temperatures, with a 1°C cold bias in minimum temperatures.

Probability plots of the daily temperature for the various runs are also shown in Figure 5.30 (right). In general, all simulations capture the observed distribution reasonably well, though the global climate models tend to have a flatter peak to the distribution (green line), while the CCAM 60 km (blue line) and 8 km (blue line) simulations capture the peak more accurately, though with a probability slightly too high. In general, the global climate models have too broad a distribution, while the CCAM simulations have too narrow a distribution.

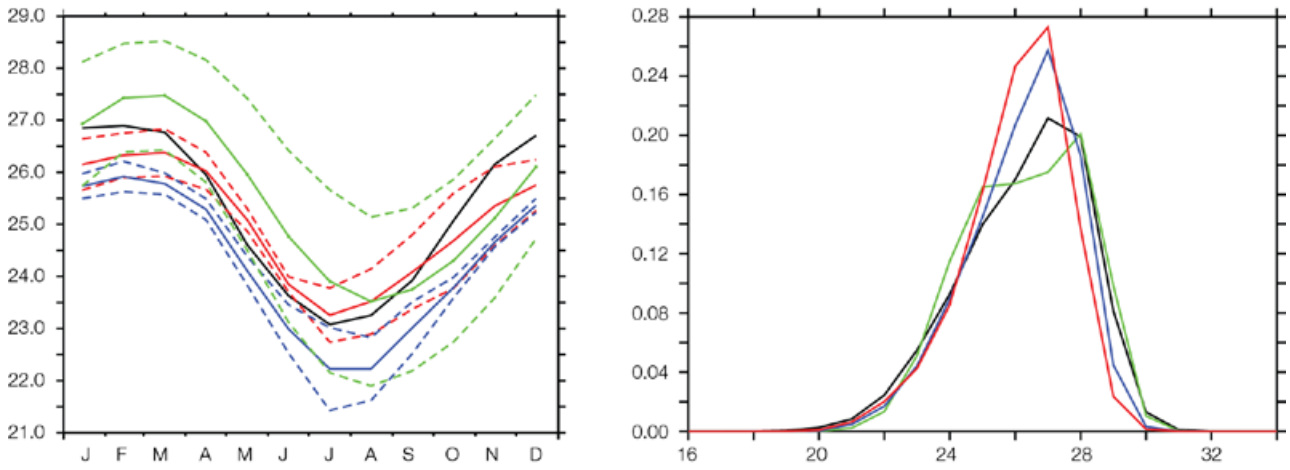

Figure 5.30: Evaluation of 1980–1999 monthly average temperature (mm per day) for Nadi, Fiji. (Left) Monthly plots for Nadi observations (black line), global climate models (solid green line with +/- two standard deviations dashed), CCAM 60 km (solid blue line with +/- two standard deviations dashed) and CCAM 8 km (solid red line with +/- two standard deviations). (Right) Frequency distribution plots for surface air temperature using same colour scheme as in the left hand figure.

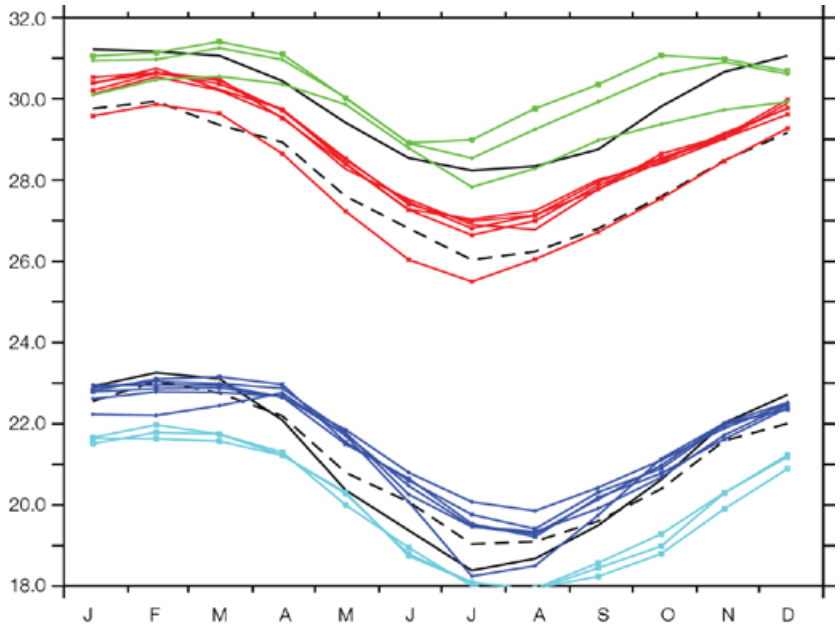

Figure 5.31: Monthly plots of surface air maximum (Tmax) and minimum (Tmin) temperatures (°C) for the grid point representing Nadi, Fiji for the period 1980–1999. Nadi observed Tmax and Tmin are thick black line; CRU observed values at nearest grid point are dashed black line, individual CCAM 60 km simulated Tmax are red and Tmin are blue; while individual CCAM 8 km simulated Tmax are green and Tmin are cyan.

5.3.3 Additional Regional Climate Model Simulations

In this section, validation of the various additional regional climate model simulations which were completed for the PCCSP is summarised briefly. As was noted in Chapter 4, there were three sets of runs completed: one set nested directly within NCEP2 for 1980–2000, and two sets nested within the CCAM 60 km simulations driven by GFDL-CM2.1 GCM sea-surface temperatures, one for the period 1980–2000 and the other for the period 2045–2065 (Figure 4.4). Results for the first two sets of regional climate simulations are presented in this section, while those of the third are presented in Chapter 7.

Comparison of the annual rainfall for the various regional climate models nested in the NCEP2 reanalyses (Figure 5.32) shows a large range of results. A key element of regional climate modelling is the level of impact provided by the lateral boundary conditions. Some of the models used some large-scale forcing (CCAM - top right centre, WRF - middle left, and Zetac - middle right) which provides an additional constraint on the simulation in the interior of the domain. However, this does not seem to have made significant impact on the quality of the simulations. CCAM has too strong an ITCZ, while most other models are too weak, apart from PRECIS, which is the best at capturing the ITCZ. For the southern portion of the domain, all models have difficulty correctly capturing the position and intensity of the SPCZ, with WRF probably the best. The impact on the simulation of using different convection parameterisation schemes can be seen by comparing the four examples for RegCM in the bottom row of Figure 5.32. Significant variation can be seen between the various runs. The way the models treat convection can have a very large impact on the quality of the simulation results, especially in this region.

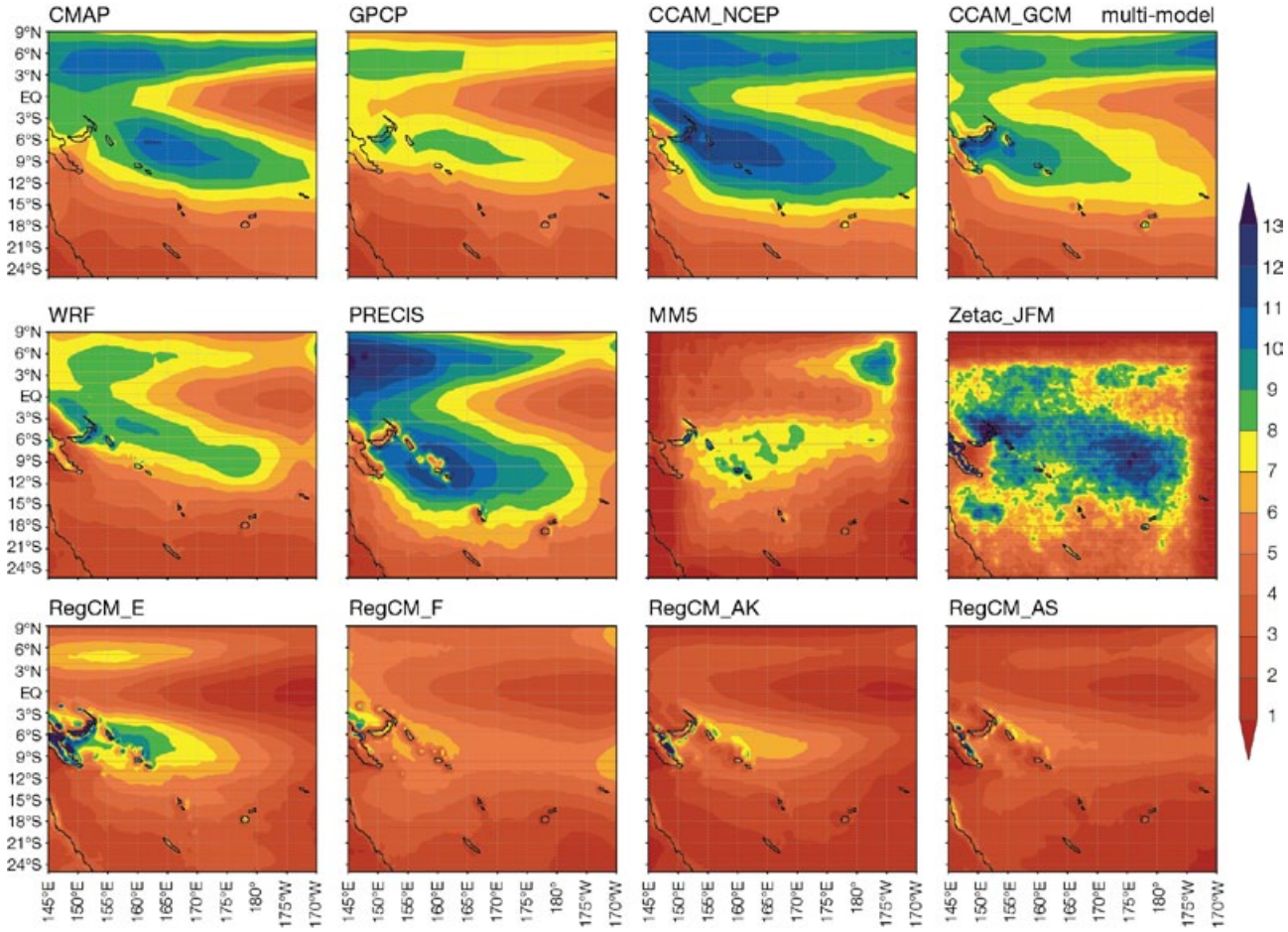

Figure 5.32: Annual rainfall (mm per day) for observed datasets and additional regional climate model simulations nested within the NCEP2 reanalyses. (Top): Observed datasets CMAP (left) and GPCP (centre left). CCAM at 60 km run with spectral nudging of large-scale fields of temperature, winds and surface pressure (centre right) and CCAM 60 km multi-model mean of runs using GCM sea-surface temperatures (right). (Middle): Various regional climate models nested directly within 6-hourly NCEP2 reanalyses. Note that the Zetac model is only for January-March, not annual. (Bottom): RegCM model run with four different convection schemes: Emanuel (left), Grell with Fritsch-Chappell (centre left), Anthes-Kuo (centre right) and Grell with Arakawa-Schubert (right).

Validation statistics, similar to those presented for global climate models and CCAM 60 km simulations (Table 5.5) are presented in Table 5.6 for runs nested within NCEP2 for the period 1980–1999. The statistics are computed over the simulation domain, excluding some boundary rows where the limited-area models have problems (Section 4.5.1). The PRECIS model has the lowest bias and mean absolute error, while CCAM has the lowest root mean square error and correlation, i.e. it captures the pattern best. The results support the discussion of Figure 5.32.

For the second set of climate change simulations, the regional models were nested within a global climate model. Here, the data from the CCAM 60 km simulations with bias-corrected sea-surface temperatures from the GFDLCM2.1 global climate model were used to drive the lateral boundary conditions of the limited-area models. In order to assess the impact of this technique, the validation statistics were recomputed for 1980–2000 from these simulations (Table 5.7). Again, the PRECIS model bias is the lowest, though the CCAM 60 km simulation has the lowest mean absolute error and root mean square error. Interestingly, although there is some decrease in quality of the simulations, the statistics do not show large changes when compared with the runs nested within NCEP. This suggests that the lateral boundary data were not causing significant negative impact on the limited area models' climatology.

In summary, the MM5 regional model did not perform satisfactorily, with large error statistics and poor pattern correlation, and will not be used in the downscaled projections in Chapter 7.

Table 5.6: Validation of annual rainfall for various regional climate models nested within the NCEP2 reanalyses for the period 1980–1999. The verifying dataset is the CMAP dataset. Equivalent comparison of GPCP rainfall analysis with CMAP is shown in last row. Bold numbers show best performance of the models.

Annual rainfall (mm per day) (Nested within NCEP2)	Bias	E_{abs}	RMS error	r_p
CCAM60	1.05	1.13	**1.38**	**0.93**
WRF	-1.14	1.26	1.49	0.92
PRECIS	**0.46**	**1.05**	1.41	0.86
MM5	-2.67	2.95	3.64	0.46
REGCM_E	-2.27	2.58	3.14	0.57
REGCM_FC	-2.58	2.65	3.06	0.75
REGCM_AS	-3.78	3.84	4.30	0.51
REGCM_AK	-3.88	3.93	4.35	0.57
GPCP	-1.10	1.21	1.38	0.96

Table 5.7: Validation of annual rainfall for various regional climate models nested within the CCAM 60 km simulations using GFDL-CM2.1 sea-surface temperatures for the period 1980–1999. Verifying dataset is the CMAP dataset. Bold numbers show best performance of the models.

Annual rainfall (mm per day) (Nested within CCAM 60 km GFDLCM2.1)	Bias	E_{abs}	RMS error	r_p
CCAM60	0.29	**0.91**	**1.30**	**0.85**
WRF	-1.42	1.68	1.90	**0.85**
PRECIS	**0.23**	1.41	1.72	0.84
MM5	1.27	5.52	7.20	0.58
REGCM_E	-0.68	1.60	2.34	0.67

5.3.4 Evaluation of Statistical Downscaling

To evaluate the statistical downscaling methodology used in this project (Section 4.7), an example comparison between the simulated temperature and rainfall data and the observed data at Nadi, Fiji is presented (Figure 5.33).

This figure shows that the statistical downscaling and bootstrap simulation procedure is capable of representing the year on year variation of standard deviations of temperature (top panel), and also is able to accurately represent the short-term autocorrelation structure of the temperature and rainfall data (four subplots on the lower panels). Further validation at this specific location is shown in Figure 5.34. The Linear Mixed Effect State-Space Model (Section 4.6) predicts minimum and maximum temperature and proportion of rain days well, but median rainfall on rain days is less well predicted. This is not unexpected and is similar to experience from dynamic models. Similar plots were obtained for all other locations for which statistical downscaling was performed. These also indicated that temperature was predicted quite accurately by the model and that rainfall was less well predicted. Further out of sample validation results of the Linear Mixed Effect State-Space Model can be found in Kokic et al. (2011).

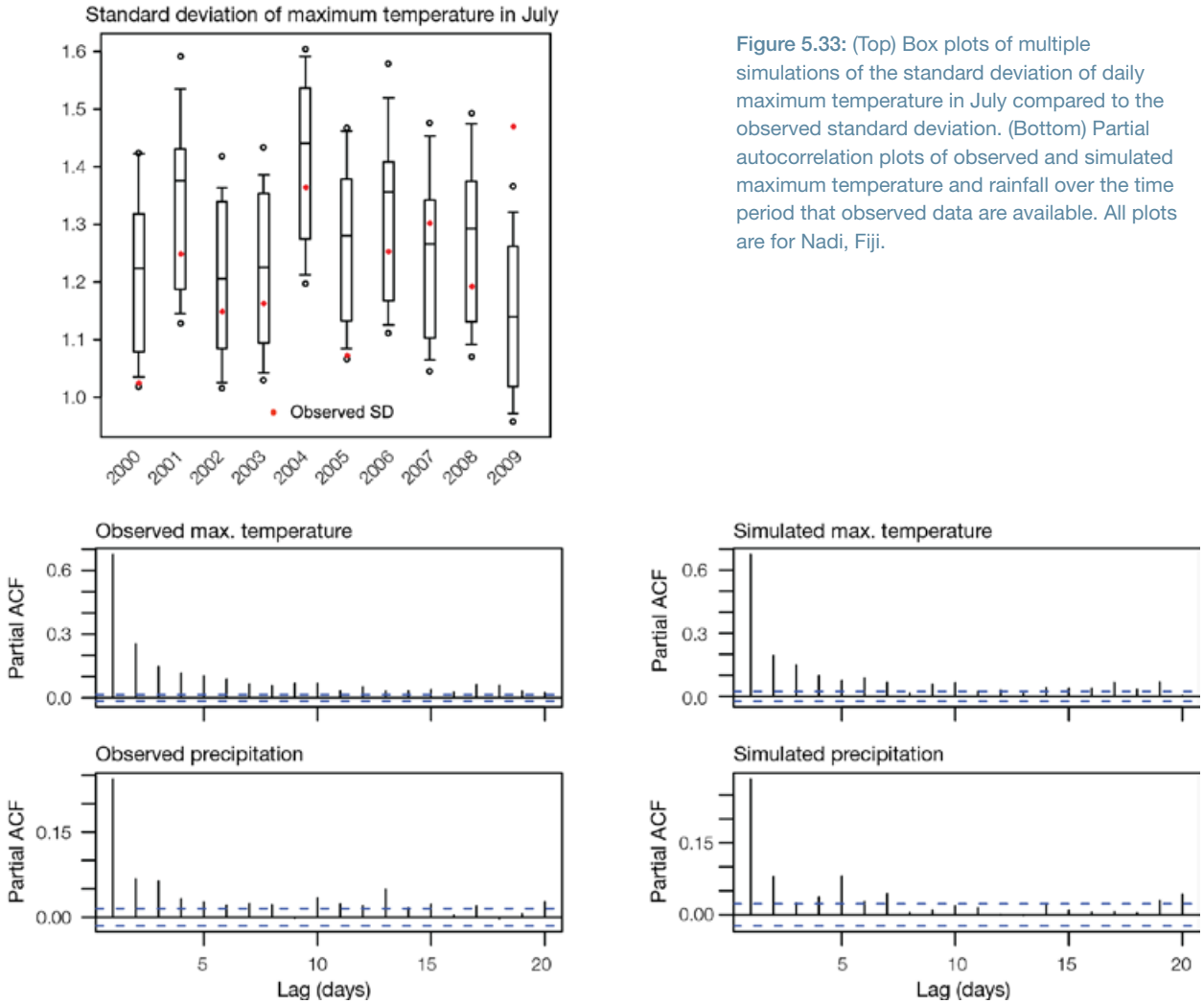

Figure 5.33: (Top) Box plots of multiple simulations of the standard deviation of daily maximum temperature in July compared to the observed standard deviation. (Bottom) Partial autocorrelation plots of observed and simulated maximum temperature and rainfall over the time period that observed data are available. All plots are for Nadi, Fiji.

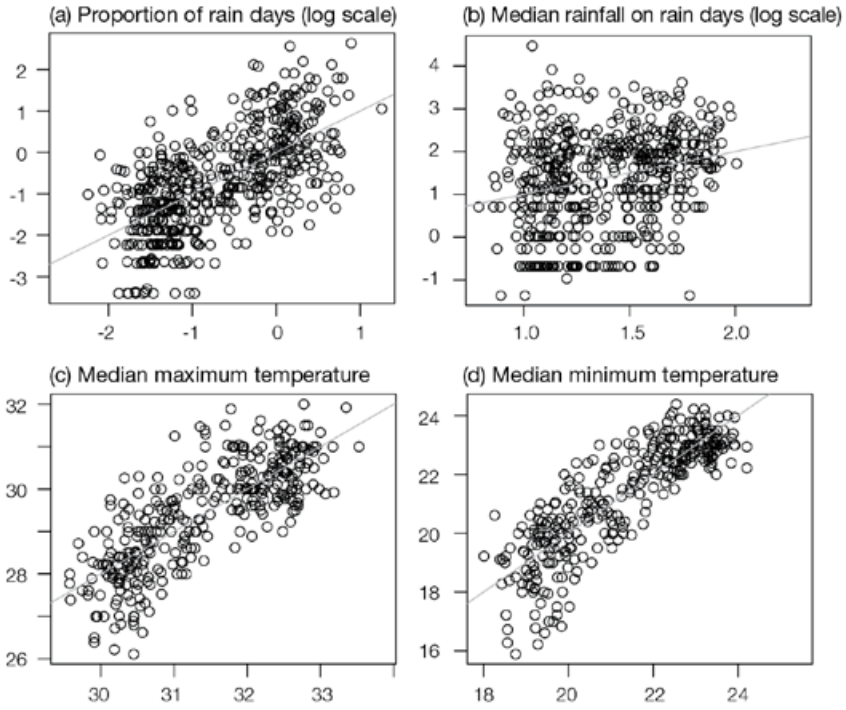

Figure 5.34: Observed monthly data versus predicted values from the Linear Mixed Effect State-Space Model. All plots are for Nadi, Fiji.

5.3.5 Summary: Dynamical and Statistical Downscaling

The dynamically downscaled simulations provide an improved, more detailed representation of most aspects of the current climate. At higher resolutions, the simulations are able to capture more detailed topographic and coastal effects of the islands on the atmospheric flow. One issue is the lack of suitable observational datasets to validate the downscaled simulations. Gridded datasets are of generally coarser resolution than the simulations. Comparing downscaled results against stations is also not totally appropriate, since the model simulations give a grid box average rather than the point value of a station.

The utility of validating the statistical downscaled results is less clear since the model is trained on the observational data. Care must be used not to interpret the accuracy of the statistical downscaled results for the current climate as an indication of the reliability of the technique for future climates.

In summary, although better performance of the downscaled results for most aspects of the current climate does build confidence in their use in projecting future climates, there is still some uncertainty that the downscaled models will perform accurately in a future climate, and the results must be used with a degree of caution, as with global climate model simulations.

5.4 Tropical Cyclones in Global and Downscaled Models

5.4.1 Introduction

It is difficult to make climate change projections of tropical cyclone activity. There are two fundamental reasons for this. The first is that the features of a tropical cyclone that cause damage occur at a spatial scale smaller than can be resolved by the climate models, particularly global climate models. These include the eye wall, the zone of high winds, heavy rainfall, wave action and storm surge. A consequence of this is that the models do not adequately simulate tropical cyclone behaviour when applied to current climate. Conventional wisdom suggests that without developing appropriate scale reduction or downscaling techniques, the models cannot be used to project future behaviour of tropical cyclones with any confidence (Knutson et al., 2010). However, the direct application to climate models of the Curvature Vorticity Parameter (CVP) method (Section 5.4.3.1) and a modified CSIRO Tropical Cyclone detector and tracker (modified using insight developed in this project) has yielded promising results.

The second reason for the difficulty in making projections of tropical cyclone behaviour is that the features of current climate that strongly influence tropical cyclone numbers and intensity have some systematic biases in climate models. These include the regional patterns of sea-surface temperature as well as the major climate features and patterns of variability in the PCCSP region, including ENSO, the ITCZ, West Pacific Monsoon and the SPCZ. The tropical cyclone research carried out for the PCCSP mainly addressed the first of these issues: the horizontal resolution or downscaling problem. The methods used are those described in Section 4.8 of this publication.

5.4.2 Tropical Cyclones in Downscaled Models

The CCAM modelling system used in this study includes bias-corrected sea-surface temperature as a boundary condition inherited from the host global climate model, and thus is expected to have significantly different regional circulation features to the host. Theoretically, the 60 km horizontal resolution enables more realistic cyclone circulations to develop than in the host global climate model. These circulations are detected using the CSIRO Direct Detection (CDD) method described in Section 4.8.

The spatial distribution of tropical cyclone genesis locations, detected from CCAM using the six different host global climate models for the late 20th century (1981–2000) compare well with each other and with the observed climatology derived from the IBTrACS data (Figure 5.35). Overall, the late 20th century cyclone climatology is well reproduced in the Southern Hemisphere. However, it underestimates cyclone frequency in the Northern Hemisphere in the eastern North Pacific and the North Atlantic. The performance is more apparent in Figure 5.36 which shows the observed and downscaled annual cyclone numbers for four of the six models, globally, by hemisphere and in three PCCSP sub-basins.

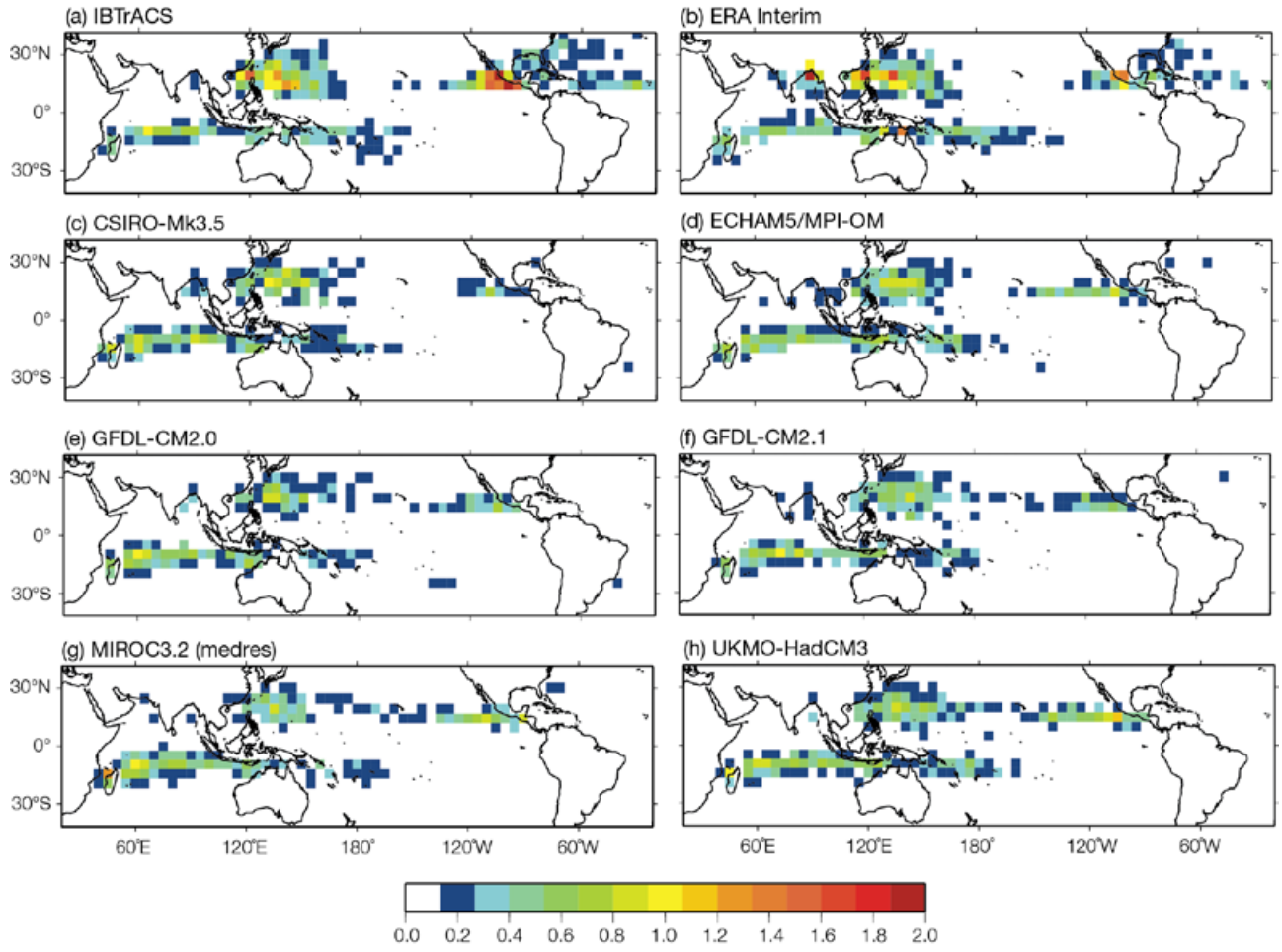

Figure 5.35: Spatial distribution of annual tropical cyclone genesis (a) in IBTrACS data, (b) detected in ERA-Interim using the CSIRO Direct Detection method and (c-h) detected in CCAM simulations for different host global climate models. Occurrence is expressed as the number of cyclone formations per year within a 5 x 5 degree grid cell.

Over the PCCSP region, results show that CCAM is able to reproduce the climatology of tropical cyclone numbers well in the south-west Pacific sub-basin (0–35ºS; 130–170ºE; Figure 5.36d) and the north Pacific sub-basin (0–15ºN; 130º–180ºE; Figure 5.36f). However, the spatial distribution of tropical cyclones detected in the South Pacific shows fewer tropical cyclones east of 180º longitude, which explains the lower number of cyclones detected in the south-east Pacific sub-basin (0–35ºS; 170ºE–130ºW) compared to the observed climatology (Figure 5.36e). One needs to be aware of the greater uncertainty in cyclone frequency projections in this sub-basin due to the weaker performance of the downscaled models, which has implications for country specific projections for the PCCSP Partner Countries that reside in that sub-basin (which include Fiji, Tuvalu, Samoa, Tonga, Niue and Cook Islands, as well as eastern parts of Vanuatu and the Solomon Islands).

5.4.3 Tropical Cyclones in Global Climate Models

Three analysis methods have been applied to the outputs from global climate models. These methods are (1) the Curvature Vorticity Parameter method, (2) the CSIRO Direct Detection method and (3) the Genesis Potential Index. These are described in detail in Section 4.8. Assessment of the late 20th century tropical cyclones in global models based on these methods is discussed in this section, and the results are compared with the observed tropical cyclone climatology.

5.4.3.1 Curvature Vorticity Parameter Method

The performance of the objective Curvature Vorticity Parameter (CVP) detection technique (Section 4.8.3) developed in this study has been assessed and applied directly to global climate models. This approach complements the CCAM-based downscaling method and provides an independent assessment of the ability of global models to generate tropical cyclone-like structures. A comparison of Figure 5.37(a) and (b) shows the detection method reproduces the observed spatial distribution of tropical cyclones and tropical cyclone numbers well. Figure 5.38 also shows that the observed annual tropical cyclone numbers (red bars) and those detected using the CVP approach (green bars) also compare well globally, in the two hemispheres, and in the three PCCSP sub-basins.

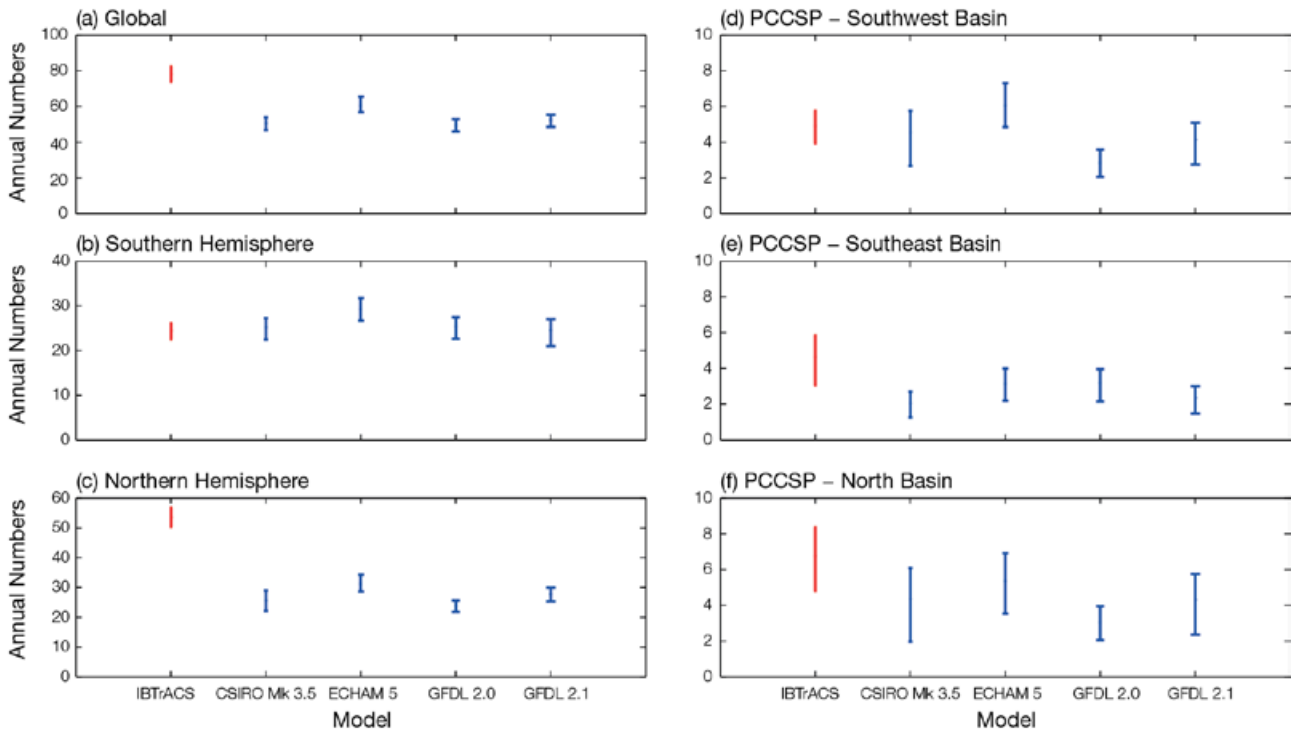

Figure 5.36: Annual number of tropical cyclones simulated using the CCAM downscaling methodology for different host models, and that observed in the IBTrACS data, in different hemispheres (left) and in the PCCSP region (right). Bars indicate distribution in annual mean number of tropical cyclones (at the 95% significance level) obtained via a statistical technique known as bootstrap sampling (i.e. repeat sampling).

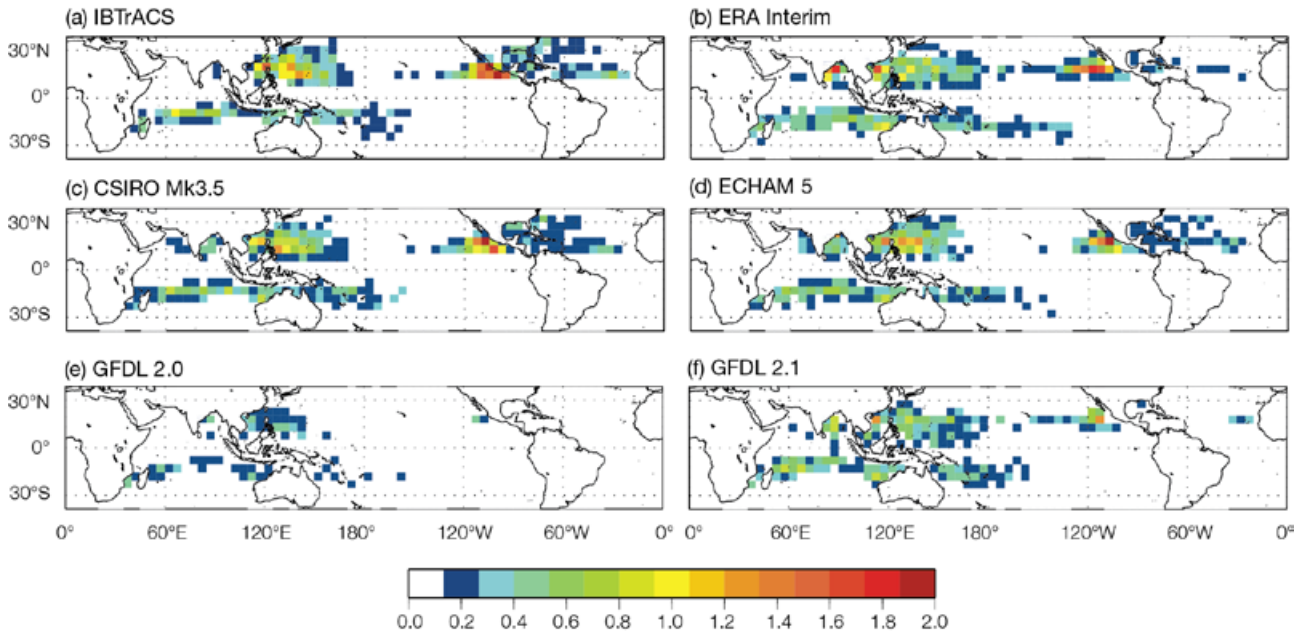

Figure 5.37: Spatial distribution of annual tropical cyclone genesis (a) in IBTrACS data, (b) detected in ERA-Interim and (c-f) detected in different global climate models using the Curvature Vorticity Parameter method. Occurrence is expressed as the number of cyclone formations per year within a 5 x 5 degree grid cell.

The global climate models (excluding GFDL-CM2.0[1]) reproduce the observed spatial distribution of tropical cyclones well (Figure 5.37), although the mean annual tropical cyclone numbers show some variation between the models (blue bars in Figure 5.38). Like the downscaled results, too few cyclones are detected in the North Atlantic. The healthier cyclone numbers in the north-east Pacific compared to the downscaled results (excluding GFDL-CM2.0), contribute to the overall better reproduction of the Northern Hemisphere cyclone climatology (compare Figure 5.36c and Figure 5.38c).

In the PCCSP region using the CVP technique, two global climate models (ECHAM5/MPI-OM and GFDL-CM2.1) reproduce the total number of tropical cyclones very well (i.e. errors of only 5% and 7% respectively, not shown). However, when divided into different basins, differences between the observed and detected tropical cyclone numbers become more apparent (Figure 5.38d-e). For example, ECHAM5/MPI-OM and CSIRO-Mk3.5, in the south-east (Figure 5.38e) and northern sub-basin (Figure 5.38f), respectively, deviate substantially from climatology. The overestimation in ECHAM5/MPI-OM is due to more tropical cyclones detected east of 180° (Figure 5.37d) than those observed.

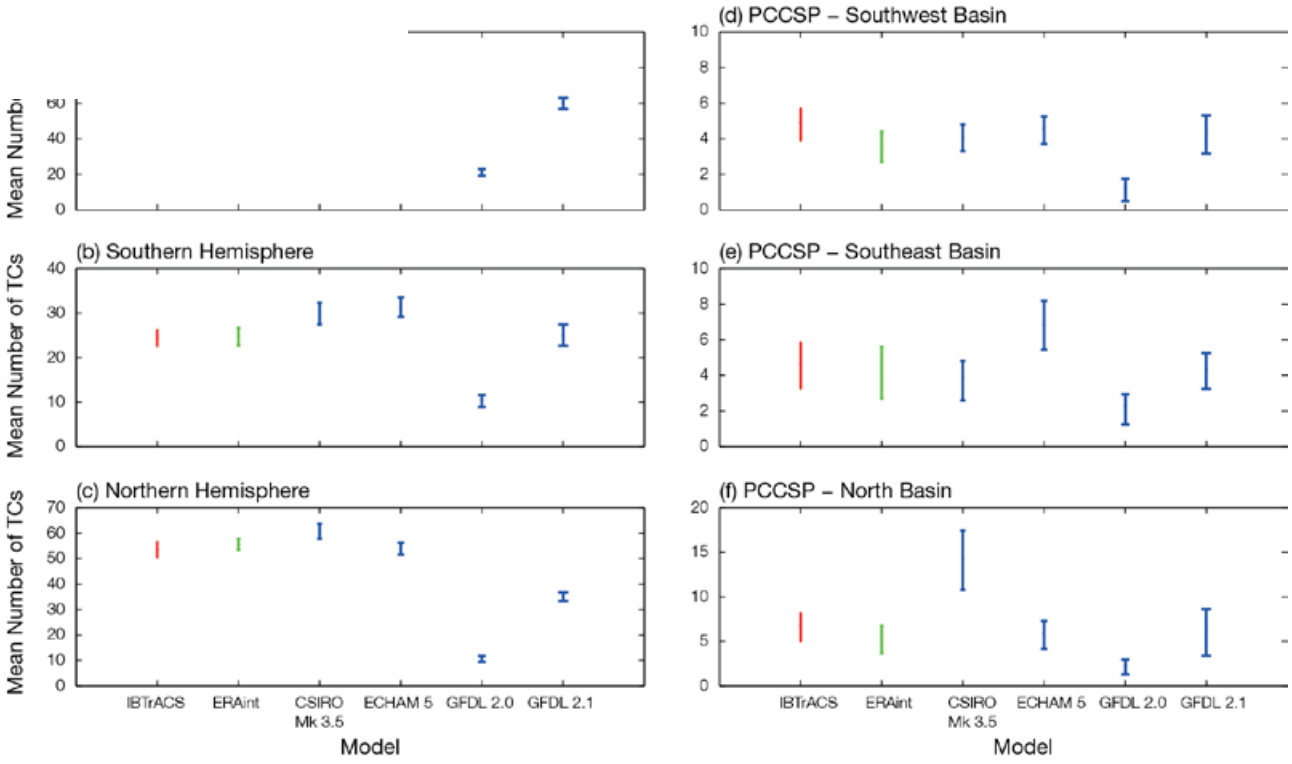

Figure 5.38: Annual number of tropical cyclones detected in different global climate models using the Curvature Vorticity Parameter scheme, and that observed in the IBTrACS data, in different hemispheres (left) and in the PCCSP region (right). Bars indicate distribution in annual mean number of tropical cyclones (at the 95% significance level) obtained via a statistical technique known as bootstrap sampling (i.e. repeat sampling).

[1] The Curvature Vorticity Parameter technique uses humidity as a detection criterion. Due to a dry bias in the GFDL-CM2.0 model many circulations were not detected. The CSIRO Direct Detection technique does not use humidity and is thus not negatively affected by the dry bias.

5.4.3.2 CSIRO Direct Detection Method

The CSIRO Direct Detection (CDD) method (Section 4.8.2) has been applied to nine global climate models for which appropriate data are available (Figure 5.39). The average spatial distribution of tropical cyclones compares favourably with the observed climatology although there is significant variation between the models in the details of this distribution. For example, there are no tropical cyclone-like vortices detected in the PCCSP region in the MIROC3.2 (medres) model. Thus the MIROC3.2 (medres) model was not used in further analysis using the CDD and results are based upon the eight models that produce realistic cyclone climatologies over the study region. In common with the methods described above, the CDD method applied to global models detects few cyclones in the North Atlantic.

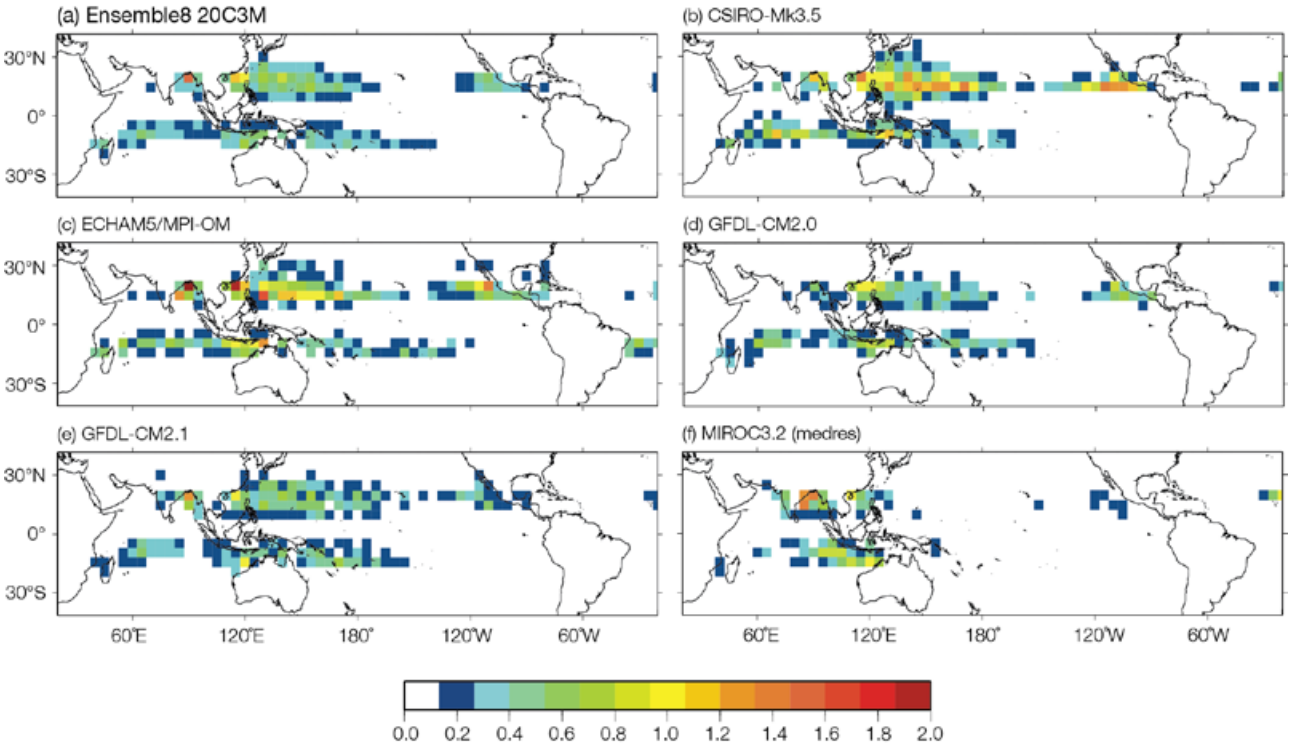

Figure 5.39: Spatial distribution of annual tropical cyclone genesis numbers using the CDD method applied to the CMIP3 global models. (a) is the average climatology based on the results from 8 global models with realistic cyclone climatology and (b-f) are individual results for a subset of the global models considered. Occurrence is expressed as the number of cyclone formations per year within a 5 x 5 degree grid cell.

5.4.3.3 Genesis Potential Index Method

The Genesis Potential Index (GPI, Section 4.8.1) of Emanuel and Nolan (2004) was calculated for the 17 CMIP3 global models for which daily data are available. A subset of 14 models[2] that were found to satisfactorily represent the large-scale climate features of the region is used in the analysis shown in Figure 5.40. The GPI method, a measure of the large-scale environmental conditions conducive to cyclone formation, was developed and calibrated using the NCEP reanalyses. When applied to the outputs of global models or other reanalyses, there can be large differences in results, as illustrated in Figure 5.40(b) and (c). When averaged over the 14 models, the more intense values of the index represent the observed genesis regions reasonably well (Figure 5.40(a)), although the spatial extent of the main genesis regions is too large.

5.4.4 Tropical Cyclone Wind Risk Hazard

Tropical cyclones present a significant hazard to countries situated in the warm tropical waters of the western Pacific. The hazards posed by these severe storms include extreme winds, storm surge inundation, salt water intrusion into ground water supplies, and flooding and landslides caused by the intense rainfall. Despite high exposure to tropical cyclones, there have been few studies attempting to quantify the hazard posed by these severe storms to this region. An exception is a limited number of detailed case studies that have been performed in support of developing a regional disaster insurance scheme similar to that implemented in the Caribbean (Shorten et al., 2003; Shorten et al., 2005). This study aims to address the limited understanding of the extreme wind hazard in this region by evaluating the wind hazard from tropical cyclones using a combination of historical tracks and downscaled climate models with Geoscience Australia's Tropical Cyclone Risk Model (TCRM, Section 4.8.4).

Historical track data from the IBTrACS tropical cyclone database for the period 1981–2008 were fed into TCRM to generate estimates of the maximum 3-second gust wind speed from tropical cyclones for a given return period. The 500-year return period wind speed is used as the primary measure of wind hazard for the following analysis since it is suitable for considering the design loads on residential buildings (AS/NZS 1170.0:2002). It should be noted that these estimates are of regional wind speed and do not account for local factors such as terrain roughness, wind shielding effects and topographic acceleration.

The results are presented in Table 5.8 for each of the 15 PCCSP Partner Countries. Where available, the 500-year return period wind

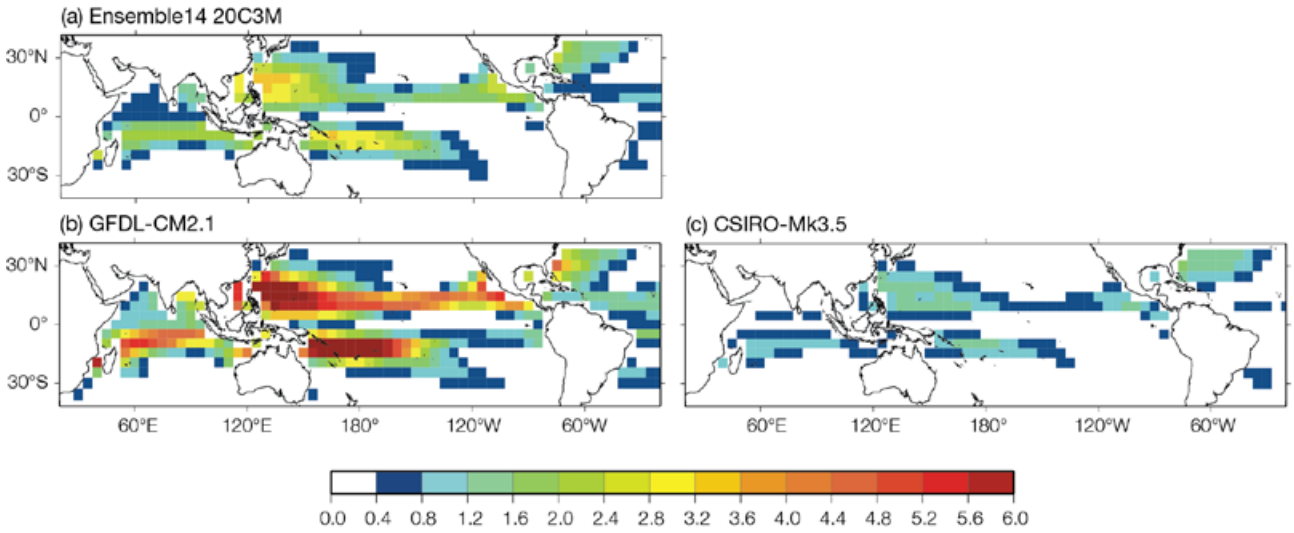

Figure 5.40: Spatial distribution of annual tropical cyclone genesis numbers using the GPI method applied to the CMIP3 global climate models, (a) is the average climatology based on the results from 14 global models and (b) and (c) are results for the GFDL-CM2.1 and CSIRO-Mk3.5 models respectively. Occurrence is expressed as the number of cyclone formations per year within a 5 x 5 degree grid cell. Note that the scale in this figure differs from Figure 5.35.

[2] The unsatisfactory global climate models that were removed from this analysis are those identified in Section 5.5.1

loading standard for each of the countries (HB 212-2002) is provided as a reference. The 500-year return period wind speed estimated from TCRM is found to exceed the design wind speeds by between 15% and 30%. These results may not be unreasonable, however, given that there is evidence that the current wind loading standards may underestimate the cyclonic wind hazard (Rattan and Sharma, 2005). Spatial maps of the 500-year return period cyclonic winds are shown in Figure 5.41.

5.4.5 Summary: Simulation of Tropical Cyclones

The CDD and CVP projection methods have provided realistic late 20th century tropical-cyclone climatologies and are suitable for cyclone detection of the late 21st century climate simulations introduced in Chapter 7. These are subsequently used to produce projected changes in tropical cyclone frequency and wind hazard by the late 21st century for the PCCSP region.

Table 5.8: Cyclonic wind hazard (metres per second) for the PCCSP Partner Countries. Values are taken as the median wind hazard found in a 2 degree x 2 degree region centred on each country's capital city.

Country	Return period wind hazard				Standard
	25yr	50yr	100yr	500yr	500yr
Cook Islands	68	77	84	95	-
East Timor	44	55	62	75	-
Federated States of Micronesia	50	58	64	74	-
Fiji	58	64	69	76	66
Kiribati	-	-	-	-	-
Marshall Islands	54	64	71	82	-
Nauru	-	-	-	-	-
Niue	63	71	77	86	-
Palau	57	65	71	80	-
Papua New Guinea	33	42	48	58	45
Samoa	62	69	75	84	66
Solomon Islands	34	41	46	53	45
Tonga	64	70	75	82	66
Tuvalu	35	41	46	53	-
Vanuatu	69	75	79	86	66

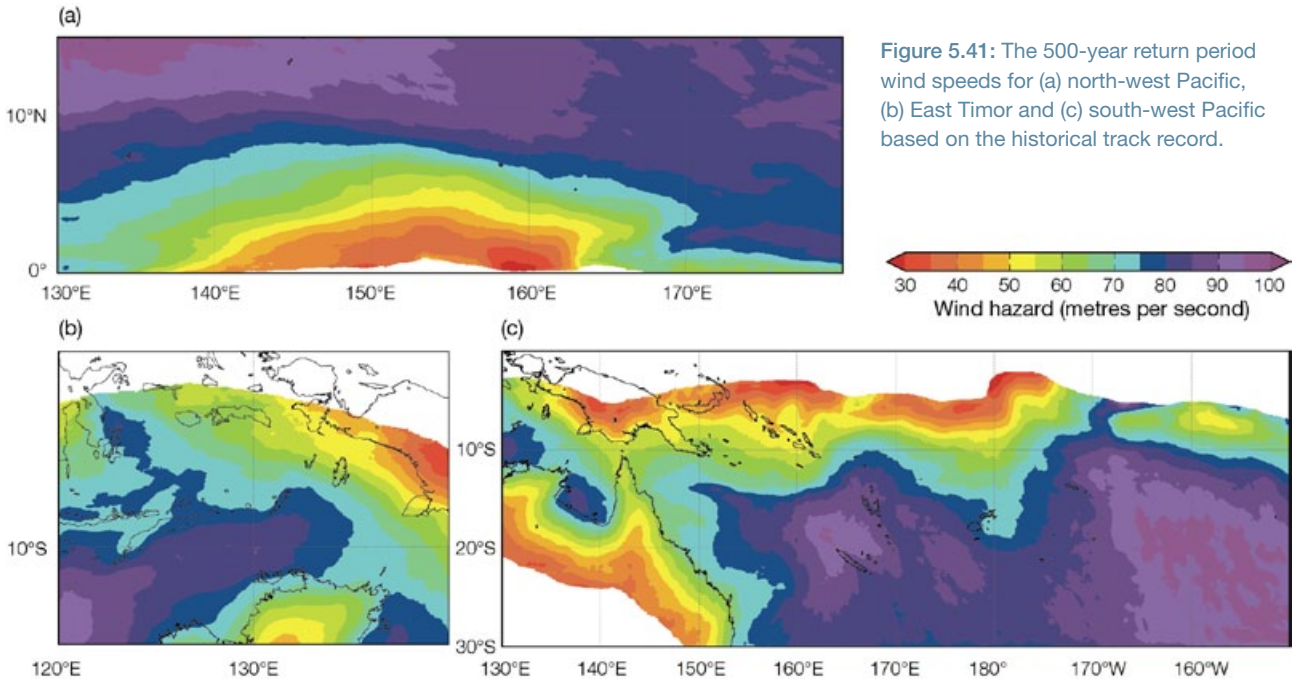

Figure 5.41: The 500-year return period wind speeds for (a) north-west Pacific, (b) East Timor and (c) south-west Pacific based on the historical track record.

5.5 Model Reliability and Implications for Projections

5.5.1 Use of Global Models for Climate Projections

As demonstrated throughout this chapter, the ability of individual CMIP3 models to simulate the western Pacific climate can vary depending on which aspect of a model simulation is considered. While this makes it difficult to identify a group of best performing models, it is possible to identify a small subset of models that perform consistently poorly across many aspects of a climate model simulation, or that perform poorly on critical aspects of a simulation. The approach adopted for determining climate change projections for the PCCSP region has been to equally weight all participating CMIP3 models, with the option of eliminating any models that display unsatisfactory performance in simulating key aspects of the Pacific climate (see Section 4.4.1 for justification of this approach).

To assist in the identification of poor performing models, much of the model evaluation summarised in Sections 5.2.1, 5.2.2 and 5.2.3 (or slight variations thereof) was combined in order to calculate a normalised skill score for each model, with respect to the simulation of surface air temperature, rainfall, surface wind, SPCZ, ITCZ, West Pacific Monsoon, ENSO, model drift and long-term sea-surface temperature trends over the PCCSP region (Irving et al., in press; Figure 5.42).

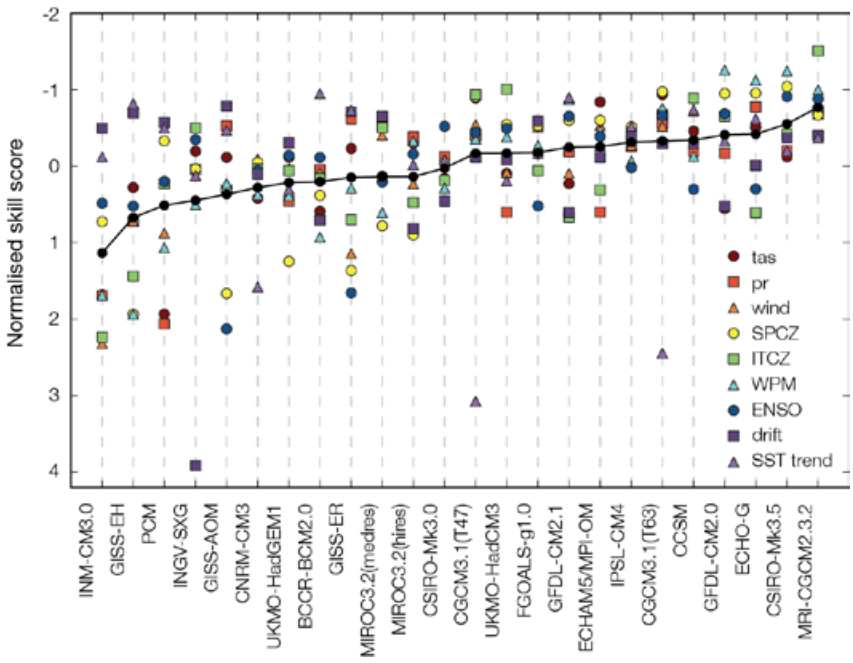

Figure 5.42: Summary of the normalised CMIP3 model skill scores for surface air temperature (tas), rainfall (pr), surface wind (speed and direction combined), SPCZ, ITCZ, West Pacific Monsoon, ENSO, drift and long-term sea-surface temperature trends (see Irving et al., in press for details). The connected solid black dots represent the average skill score across all categories. Increasingly negative scores indicate better model performance.

From the results of Irving et al. (in press) and additional analysis presented in the individual sections of this chapter, the following models were eliminated in calculating all PCCSP climate projections, for the reasons outlined (see also Table 5.9):

- GISS-EH, INM-CM3.0 and PCM: These models perform particularly poorly with respect to the simulation of many aspects of the present day climate over the PCCSP region (Sections 5.2.1 and 5.2.4).
- INGV-SXG: This model has a large climate drift (Section 5.2.2.5) and does not provide the required control simulation data to remove this drift from projected changes.
- GISS-AOM and GISS-ER: These models perform particularly poorly with respect to their simulation of the present day ENSO (Section 5.2.3.1), which was considered to be a critical aspect of the PCCSP region climate.

In addition, the following models were eliminated for specific projections, due to critical deficiencies relating to isolated climate features:

- MIROC3.2(hires) and MIROC3.2(medres): These models were eliminated in determining projections of future SPCZ activity, as they perform particularly poorly in simulating the present day characteristics of the SPCZ (Section 5.2.3.3; Brown et al., in press).
- MIROC3.2(hires): This model was eliminated in determining projections of future ITCZ activity, as it performs particularly poorly in simulating the present day characteristics of the ITCZ (Section 5.2.3.4).
- MIROC3.2(medres): This model was eliminated in determining projections of future West Pacific Monsoon activity, as it performs particularly poorly in simulating the present day characteristics of the monsoon (Section 5.2.3.5).

Table 5.9: CMIP3 models eliminated for the purposes of determining climate projections, based on an evaluation of their present day climate simulation.

Type of projection	Eliminated models	Reason for elimination
All projections	GISS-AOM GISS-ER	Very weak or no ENSO (both models) and a poor simulation of extreme events (GISS-ER)
	INGV-SXG	Model drift too large
	GISS-EH INM-CM3.0 PCM	Overall poor performance (all three models) and a poor simulation of extreme events (GISS-EH, PCM)
SPCZ projections	MIROC3.2(hires) MIROC3.2(medres)	SPCZ poorly simulated
ITCZ projections	MIROC3.2(hires)	ITCZ poorly simulated
West Pacific Monsoon projections	MIROC3.2(medres)	West Pacific Monsoon poorly simulated

5.5.2 Use of Downscaled Models for Climate Projections

The large-scale climate of the CCAM global simulations was found to be closer to observations than the corresponding CMIP3 climate models in some aspects but less in other respects. These simulations do not fully incorporate atmosphere-ocean feedbacks which have been shown to be important for capturing some features, such as monsoon processes (cf. Wang et al., 2005). For these reasons, downscaled projections of changes in these climate features need to be treated with caution.

Further, due to the computational cost, only a limited number of the global climate models and emissions scenarios have been downscaled, so the full range of possible projections has not been sampled. While not all aspects of the large-scale CCAM climate represent an improvement over the CMIP3 global climate models, the 8 km resolution simulations substantially improve the simulation of local climate influences associated with factors such as topography and coastline. As with all projections, it is necessary to assess and understand the physical mechanisms associated with the various changes. In light of these findings, the level of confidence associated with downscaled climate projections is not uniform across the PCCSP region.

Pacific Climate Futures training, Federated States of Micronesia

Chapter 6
Projections Based on Global Climate Models

Summary

- The climate change projections in this chapter are based on simulations from up to 18 global climate models for three emissions scenarios: B1 (low), A1B (medium) and A2 (high). Results are given for three future 20-year periods centred on 2030, 2055 and 2090, relative to a 20-year period centred on 1990.
- The projected warming over the PCCSP region is about 70% as large as the global average warming for all emissions scenarios. Regional warming is expected to be greatest near the equator. Large increases in the incidence of extremely hot days and warm nights are also projected.
- Increases in annual mean rainfall are projected to be most prominent near the South Pacific Convergence Zone (SPCZ) and Intertropical Convergence Zone (ITCZ), while the remainder of the region is generally expected to experience little change. Little change is projected in the annual number of rainy days, except for increases near the equator. A widespread increase in the number of heavy and extreme rain days is projected.
- Increases in potential evapotranspiration are expected. The ratio of annual average rainfall to potential evapotranspiration decreases in most regions (increased aridity), except near the equator where the relatively large projected rainfall increases exceed the smaller changes in potential evapotranspiration.
- Surface wind speed generally decreases in the equatorial and northern parts of the region, while increases are indicated in the south, but these changes are projected to be relatively small in most locations. Changes in wind direction are very small.
- Projected changes in humidity and solar radiation are also relatively small (less than 5% by 2090).
- Sea-surface salinity is expected to decrease in the West Pacific Warm Pool. The regional pattern of change closely matches projected changes in net rainfall (i.e. rainfall minus evaporation). The intensified warming and freshening at the surface is projected to make the surface ocean less dense compared to the deep ocean, so the ocean becomes more stratified.
- Sea level is projected to rise. However, improved understanding of the processes responsible for ice-sheet changes are urgently required to improve estimates of the rate and timing of 21st century and longer-term sea-level rise. For the PCCSP region, total sea-level rise is projected to be similar to the global average.
- The projected growth in atmospheric carbon dioxide concentration is expected to cause further ocean acidification leading to increasingly marginal conditions for sustaining healthy coral growth and reef ecosystems.
- The El Niño-Southern Oscillation (ENSO) will continue to be a major source of climate variability. However the impacts of global warming on ENSO amplitude and frequency are unclear.
- While broad-scale patterns of change are physically plausible and relatively consistent between models (at least in the vicinity of the ITCZ and SPCZ), the small-scale details of these projections should be interpreted with caution, given the deficiencies in model simulations of the current climate described in Chapter 5.

6.1 Introduction

The Intergovernmental Panel on Climate Change (IPCC) gives broad-scale projections for the Pacific (Mimura et al., 2007). Annual mean temperature and rainfall projections are averaged over two large Pacific regions (the North Pacific and the South Pacific), for three 30-year periods (2010–2039, 2040–2069 and 2070–2099), based on results from seven global climate models and four emissions scenarios. The projected warming is slightly greater in the north than the south, and rainfall tends to increase in the north with no clear direction of change in the south. An increase in the frequency of extremely high temperatures is likely, with more heavy rainfall and more intense cyclones, but the global total number of cyclones may decrease. Global average sea-level may rise 0.18 to 0.59 m by 2080–2099, relative to 1980–1999, but larger increases cannot be ruled out.

The level of regional detail in the IPCC projections is limited over the PCCSP region. In this chapter, more detail is provided. The climate change projections developed are based on simulations from up to 18 global climate models for three emissions scenarios (B1, A1B and A2, which are low, medium and high respectively).

Results are given for three future 20-year periods: 2020–2039 (denoted 2030), 2045–2064 (denoted 2055) and 2080–2099 (denoted 2090). Changes are relative to 1980–1999 (denoted 1990) (Figure 4.3). The selection of years and emissions scenarios is limited by data availability. The selection of models is based on those considered most reliable in Chapter 5 (Table 5.9).

The presentation of climate projections for the PCCSP region in this chapter focuses on multi-model mean changes (or multi-model median for variables with large outliers). While these may be considered to represent central estimates, this chapter also refers to the spread of individual model projections, relevant model biases and deficiencies (Chapter 5), the consistency of the projections with observed changes over recent decades (Chapter 3) and the physical plausibility of each projection. For a more detailed discussion on the full range of possible futures simulated for each country, see Volume 2.

6.2 Atmospheric Projections

Projected surface changes in air temperature, rainfall, wind, solar radiation, relative humidity and potential evapotranspiration are presented for the entire PCCSP region. More detailed atmospheric projections for the PCCSP region are available in Perkins et al. (in press), and for individual countries in Volume 2.

6.2.1 Surface Air Temperature

For all time periods, seasons, emissions scenarios and locations within the PCCSP region, mean air temperature (1.5 m above the ground) is projected to increase throughout the 21st century. The multi-model mean projections indicate a 0.5–1.0°C rise in annual mean temperature under all emissions scenarios by 2030, relative to the 1990 reference period (Figure 6.1). By 2055, the warming is generally 1.0–1.5°C with regional differences depending on the emissions scenario. By 2090, the warming is generally 1.5–2.0°C for B1 (low) emissions, around 2.0–2.5°C for A1B (medium) emissions, and around 2.5–3.0°C for A2 (high) emissions. This divergence of warming with time is consistent with the respective carbon dioxide (CO_2) concentration paths for each emissions scenario (Figure 4.1). Although not shown, seasonal projections (May-October; November-April) of surface air temperature are very similar to annual projections.

Despite the high level of model agreement in the direction and magnitude of temperature change (Perkins et al., in press), it should be noted that the models share common biases in the PCCSP region that directly influence the surface temperature projections. In particular, the largest warming occurs in the vicinity of Kiribati and Nauru, where the models are known to display a cold tongue bias with respect to their simulation of the current climate (Section 5.2.1.1 and Box 5.2). Temperature projections in this region may therefore be associated with a lower level of confidence than other locations (Volume 2).

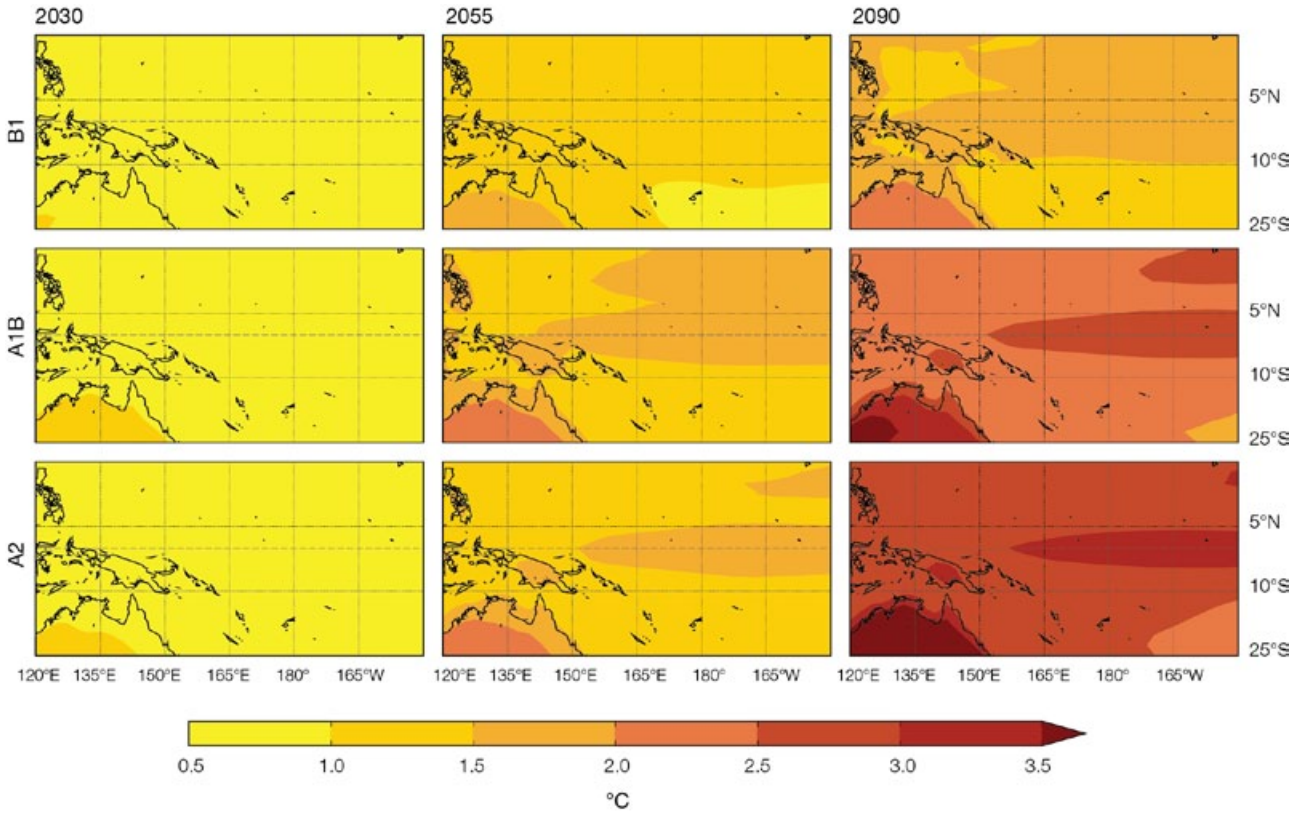

Figure 6.1: Projected multi-model mean changes in annual mean surface air temperature for 2030, 2055 and 2090, relative to 1990, under the B1 (low), A1B (medium) and A2 (high) emissions scenarios. All models agree on the direction of change in all locations.

The projected warming over the PCCSP region is less than the global average for all emissions scenarios, with the ratio between the PCCSP region and global change approximately constant at 0.7 throughout the 21st century (Figure 6.2). This phenomenon is linked to the fact that the global oceans have been warming (and are projected to warm into the future) at a lower rate than global land areas (c.f. Sections 3.2 and 6.3). As the PCCSP region has a higher percentage of ocean surface than the global average, it follows that temperature increases in the region would be less than those seen globally. The physical mechanism behind this land-sea contrast is not just a transient effect due to the larger heat capacity of the oceans, but an inherent feature of the climate system related to the different moisture availability over the land and ocean (Joshi et al., 2007; Dommenget, 2009).

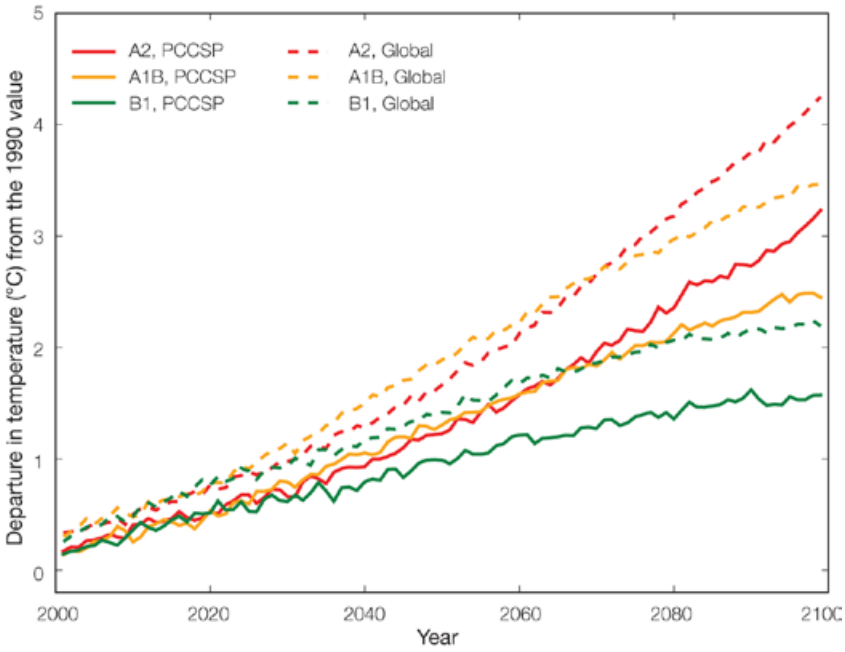

Figure 6.2: Projected multi-model mean changes in the spatial average global and PCCSP region annual mean surface air temperature for the 21st century, relative to 1990, under the B1 (low), A1B (medium) and A2 (high) emissions scenarios.

6.2.2 Rainfall

Wetter conditions are projected over most of the PCCSP region in the future (Figure 6.3). Strong increases in annual mean rainfall are projected in the vicinity of the Intertropical Convergence Zone (ITCZ) and South Pacific Convergence Zone (SPCZ), associated with increased moisture convergence in a warmer climate (Sections 6.4.3 and 6.4.5). In these regions, at least 80% of the models agree on an increase in rainfall. The largest increases are found immediately to the north of Papua New Guinea and the Solomon Islands.

The multi-model mean projections indicate increases in annual rainfall of 0–0.3 mm per day by 2030 throughout most of the PCCSP region, rising to 0.3–0.6 mm per day between latitudes 5°N and 10°S, for all emissions scenarios. By 2055, the increases are generally similar to 2030, but reach 0.9–1.2 mm per day between latitudes 5°N and 10°S, with decreases of 0–0.3 mm per day between Vanuatu and Tonga in the B1 (low) and A1B (medium) emissions scenarios. By 2090, the increases are generally similar to 2055, but reach 1.2–1.5 mm per day for B1 (low) emissions and 1.5–1.8 mm per day for A1B (medium) and A2 (high) emissions between latitudes 5°N and 10°S (Figure 6.3).

On a seasonal basis, rainfall increases are widespread during November-April and associated with an intensification of the SPCZ and West Pacific Monsoon (Figure 6.4; Sections 6.4.4 and 6.4.5). Rainfall increases are also projected during May-October in the deep tropics (Section 6.4.3), while decreases in rainfall are projected to the south of the SPCZ mean position, between Vanuatu and the Cook Islands.

While this broad-scale pattern of rainfall change is both physically plausible and relatively consistent between models (at least in the deep tropics and in the vicinity of the SPCZ), the small-scale details of these projections should be interpreted with caution, given known biases in model simulations of the current climate. In particular, the orientation of the SPCZ tends to be overly zonal (east-west) in most simulations (Section 5.2.3.3), while the seasonal migration of the ITCZ tends to be overestimated during the Northern Hemisphere summer (Section 5.2.3.4). The models also substantially underestimate current rainfall in the vicinity of Kiribati and Nauru, in association with the cold tongue bias (Section 5.2.1.2).

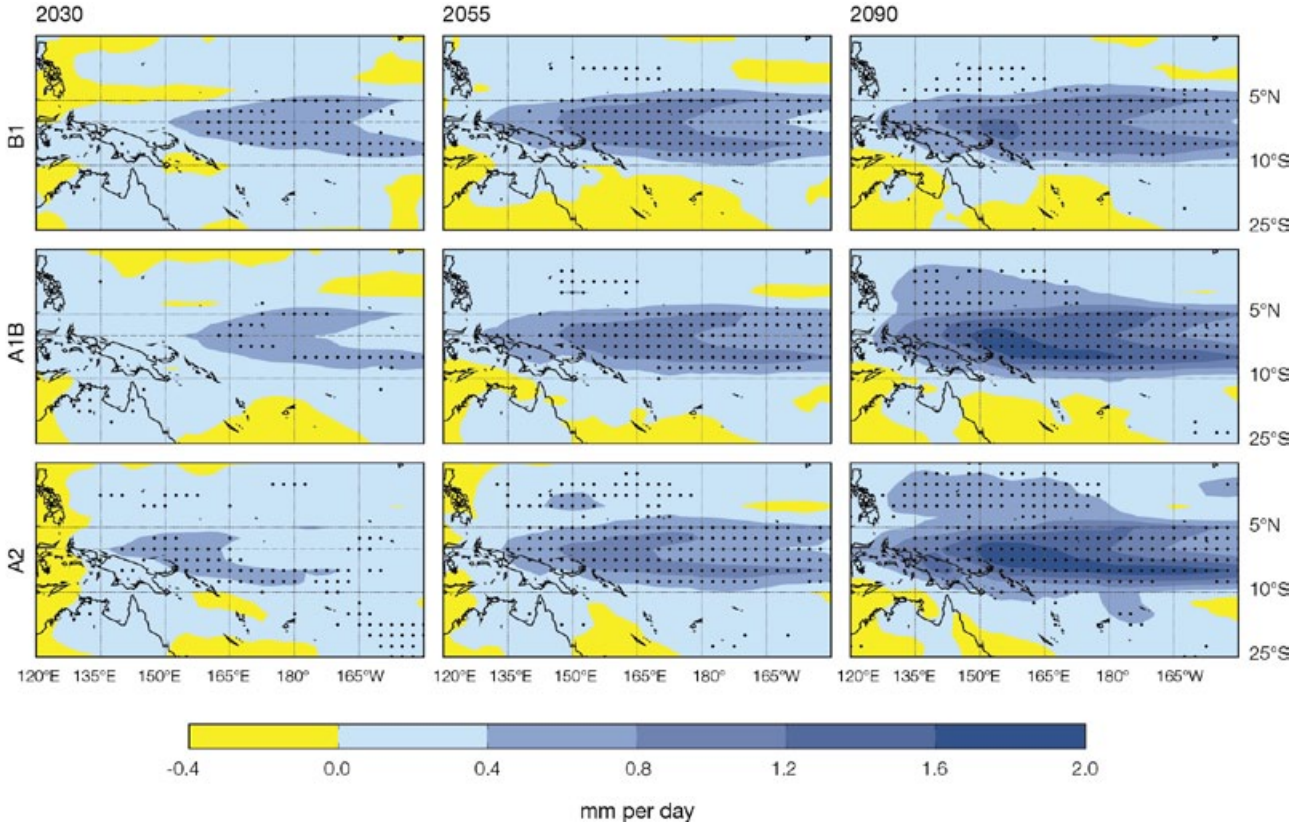

Figure 6.3: Projected multi-model mean changes in annual rainfall (mm per day) for 2030, 2055 and 2090, relative to 1990, under the B1 (low), A1B (medium) and A2 (high) emissions scenarios. Regions where at least 80% of models agree on the direction of change are stippled.

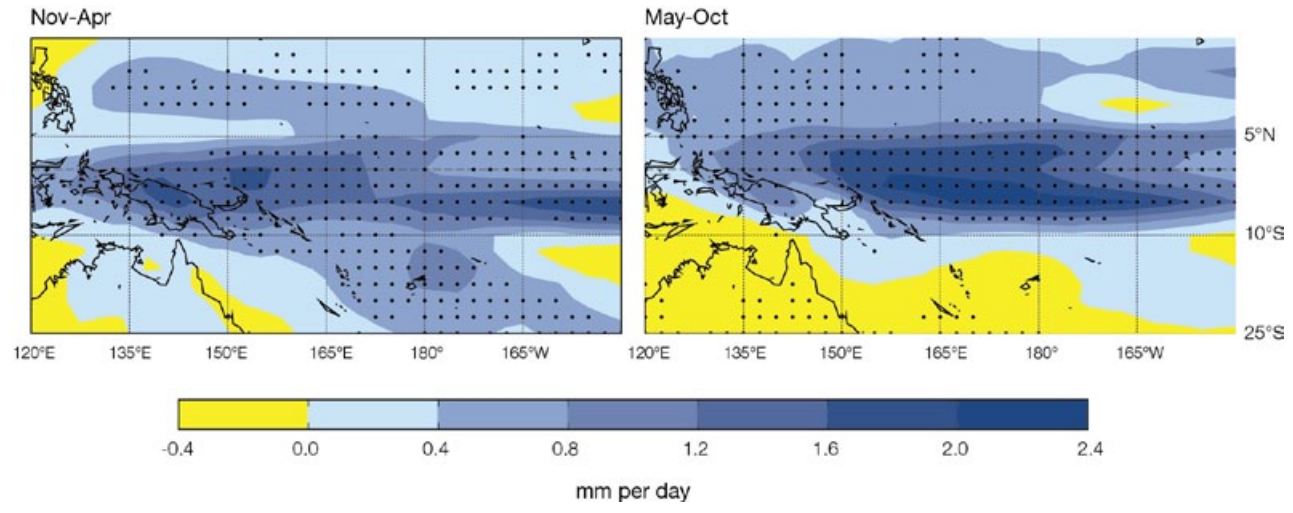

Figure 6.4: Projected multi-model mean changes in November-April (left) and May-October (right) mean rainfall for 2090, relative to 1990, under the A2 (high) emissions scenario. Regions where at least 80% of models agree on the direction of change are stippled.

6.2.3 Near-Surface Wind

Near-surface wind speed (10 m above the ground) is generally projected to decrease in the equatorial and northern parts of the PCCSP region, while increases are projected in the south (Figure 6.5). However, the multi-model annual and seasonal median changes are relatively small in most locations, with values of typically less than ±0.5 metres per second (± ~10%) projected for all emissions scenarios and time periods. Wind speed in the vicinity of the Cook Islands is an exception, where the May-October mean wind speed is projected to increase by up to 1.5 metres per second (~40%) in 2090 under the A2 (high) scenario.

From a physical standpoint, these wind speed increases in the south-east of the PCCSP region have been linked to the relatively low rate of sea-surface temperature increase in that region (Xie et al., 2010), while the wind speed decline projected for the equatorial PCCSP region is consistent with a weakening of the Walker Circulation (Vecchi and Soden, 2007b; Power and Kociuba, in press). The models tend to closely agree with observed annual mean wind speed data throughout most of the PCCSP region, so the projections are considered robust. However, the models tend to overestimate the annual mean wind speed immediately to the north and east of Papua New Guinea and the Solomon Islands, so projections are considered less reliable there (Section 5.2.1.3).

Projected multi-model median changes in annual and seasonal wind direction are typically less than 3° throughout much of the PCCSP region, for all emissions scenarios and time periods. As such, no large-scale, fundamental shift in the near-surface circulation is indicated.

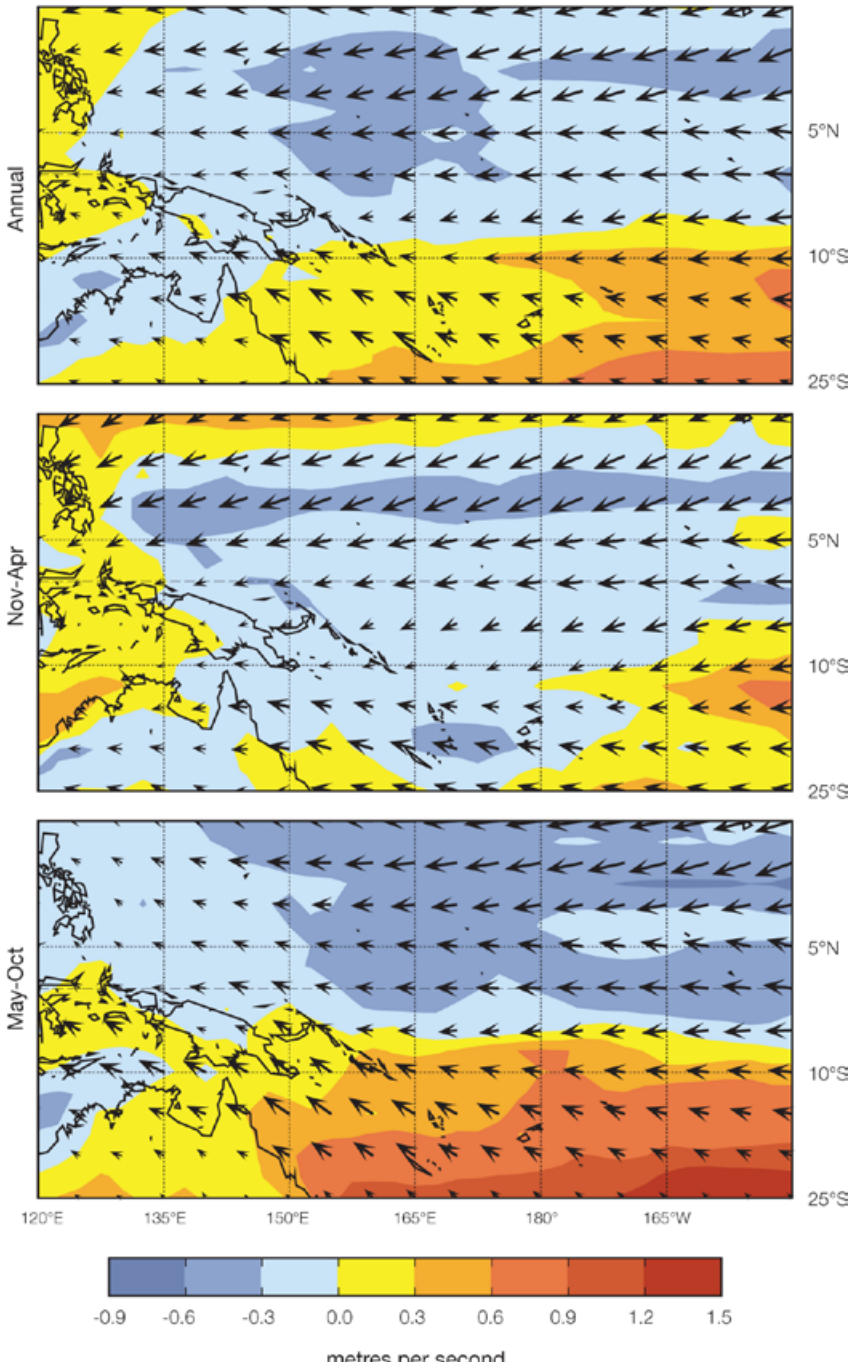

Figure 6.5: Projected multi-model median change in annual and seasonal mean wind speed (metres per second) for 2090, relative to 1990, under the A2 (high) emissions scenario. For reference, the multi-model median 1990 annual mean wind field is indicated by arrows. Projected changes for 2030 and 2055 and lower emission scenarios tend to be of smaller magnitude but similar spatial structure.

6.2.4 Surface Solar Radiation

Given the strong link between changes in cloud cover and surface solar radiation, projected multi-model mean changes in annual surface solar radiation closely resemble those for rainfall. For instance, the projected decline in surface solar radiation in the deep tropics (latitudes 10°S to 5°N) and in the vicinity of the SPCZ (Figure 6.6) is consistent with the projected increase in rainfall in these areas (through an associated increase in cloudiness; Figures 6.3 and 6.4). In fact, multi-model mean decreases in annual surface solar radiation of up to -14 Watts per square metre (~5%) are projected for 2090 under the A2 (high) scenario, in the region immediately to the north of Papua New Guinea and the Solomon Islands. For locations not influenced by the SPCZ or ITCZ, projected decreases in surface solar radiation are relatively small, with individual model projections tending to cluster relatively close to and either side of no change. As for rainfall, small-scale details in projected surface solar radiation need to be interpreted with caution, due to known biases in model simulations of the ITCZ and SPCZ (Sections 5.2.3.3 and 5.2.3.4), in addition to the cold tongue bias (Section 5.2.1.1).

6.2.5 Near-Surface Humidity

Relative humidity is defined as the amount of water vapour in the air, relative to the maximum amount of water vapour that the air is able to hold, without it condensing (expressed as a percentage). Projected changes in near-surface relative humidity (1.5 m above the ground) tend to be small, with spatial multi-model mean values ranging from changes of between -0.5 to +0.5% in 2030 for the B1 (low) scenario, to -0.5 to +1.5% in 2090 for the A2 (high) scenario (Figure 6.7).

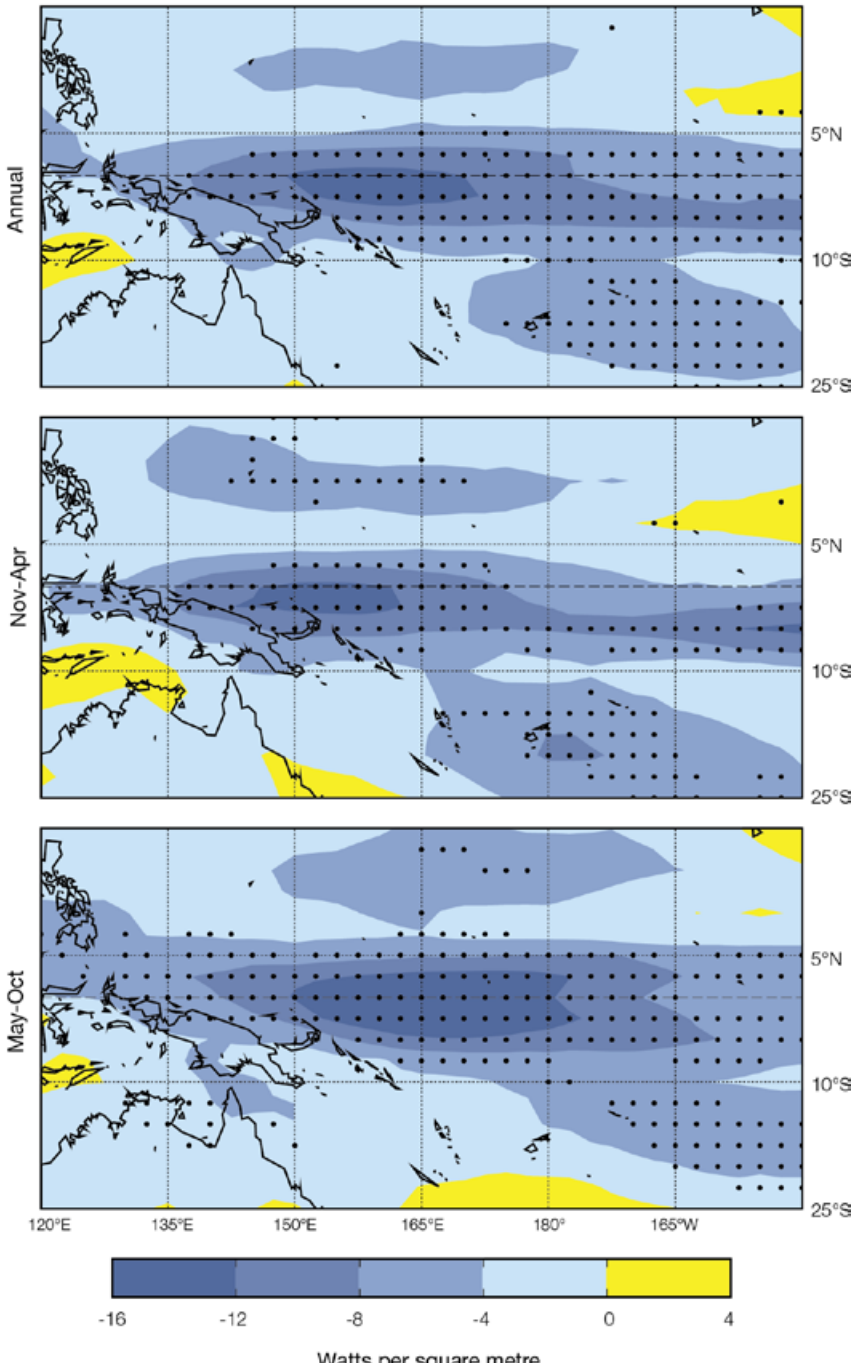

Figure 6.6: Projected multi-model mean changes in annual and seasonal mean surface solar radiation (Watts per square metre) for 2090, relative to 1990, under the A2 (high) emissions scenario. Projected changes for earlier years and less intense emissions scenarios tend to be of smaller magnitude but similar spatial structure. Regions where at least 80% of models agree on the direction of change are stippled.

Although small in magnitude, these projections consistently indicate declining relative humidity in locations associated with large land masses, such as Papua New Guinea and East Timor. This is likely due to the fact that there is a limited supply of water over vast expanses of land, meaning the actual amount of water vapour in the air cannot increase at the same rate as the water vapour holding capacity of the atmosphere (which increases as temperature increases). Due to the essentially unlimited supply of water for evaporation from the vast expanses of ocean, decreases in relative humidity of similar magnitude are not seen elsewhere throughout the PCCSP region. A physical reason for regional contrasts that are not related to water availability, such as the presence of relatively high projected changes in the south of the PCCSP region, is an area of ongoing research (Sherwood et al., 2010).

6.2.6 Potential Evapotranspiration

Evapotranspiration is the sum of evaporation from the land surface (e.g. from the soil and bodies of water such as lakes and rivers) and transpiration from vegetation. Potential evapotranspiration is therefore defined as the evapotranspiration that would take place if there was an unlimited water supply (Morton, 1983). It is a representation of the environmental demand for evapotranspiration, which depends upon both the amount of energy available to evaporate water, and the strength of the wind available to transport water vapour from the surface up into the lower atmosphere. Potential evapotranspiration is therefore highest in hot, sunny (high surface solar radiation), dry (low relative humidity), and windy conditions.

Throughout much of the PCCSP region, annual mean potential evapotranspiration is projected to increase into the future (Figure 6.8). The spatial consistency of this finding suggests that the projected increase in annual mean temperature (which promotes an increase in potential evapotranspiration) dominates the future evolution of potential evapotranspiration, overwhelming the influence of changes in other related variables, such as solar radiation. An exception to this general rule is evident for a small region extending from immediately north of Papua New Guinea and the Solomon Islands eastwards beyond Nauru and Tuvalu, where approximately half of the CMIP3 models project a decrease in potential evapotranspiration.

It is useful to consider these projected changes to the environmental demand for evapotranspiration in the context of future rainfall changes. In particular, projected changes in the ratio of annual average rainfall and potential evapotranspiration (known as the aridity index; Middleton and Thomas, 1992) can be used to infer long-term changes in the balance between these two important hydrological parameters. Throughout much of the PCCSP region, a slight decrease in the aridity index is projected into the future, indicating that the projected increase in environmental demand for moisture is not being matched by sufficient increases in rainfall (i.e. the environment becomes slightly more arid; Figure 6.8). In the vicinity of Kiribati, Nauru and Tuvalu however, the relatively large projected rainfall increases overwhelm the smaller changes in potential evapotranspiration, meaning that the aridity index is projected to increase (these regions are projected to become less arid).

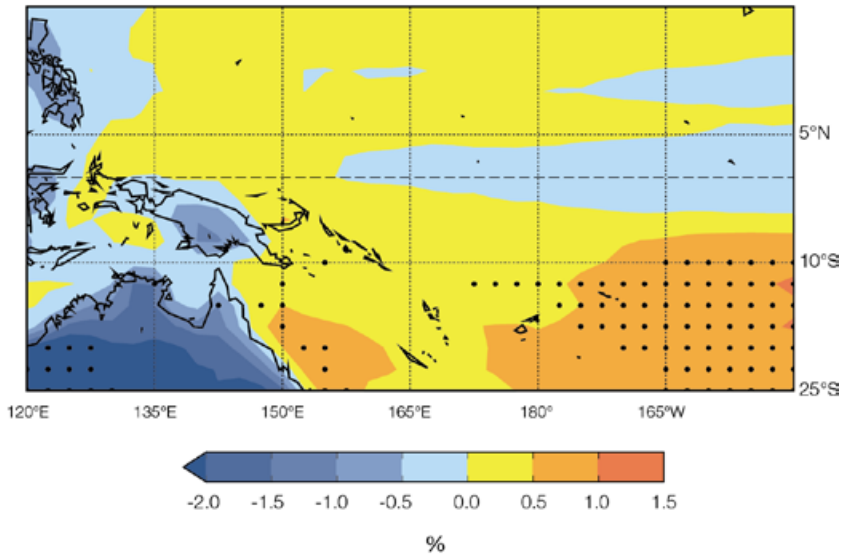

Figure 6.7: Projected multi-model mean change (%) in annual relative humidity for 2090, relative to 1990, for the A2 (high) emissions scenario. Projected changes for earlier years and less intense emissions scenarios tend to be of smaller magnitude but similar spatial structure. Regions where at least 80% of models agree on the direction of change are stippled.

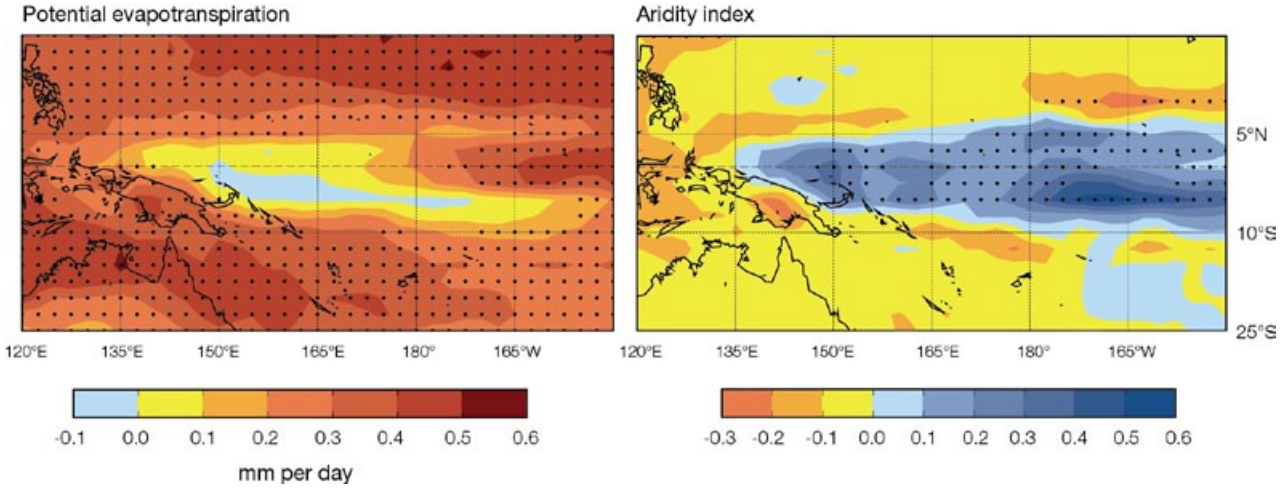

Figure 6.8: Projected multi-model median change in annual mean potential evapotranspiration (mm per day) and aridity index, (rainfall/potential evaporation), for 2090, relative to 1990, for the A2 (high) emissions scenario. Note that a negative change in the aridity index indicates a shift towards a more arid environment. Projected changes for earlier years and less intense emissions scenarios tend to be of smaller magnitude but similar spatial structure. Regions where at least 80% of models agree on the direction of change are stippled.

6.2.7 Extreme Temperature and Rainfall

Changes in the mean climate are almost inevitably associated with changes in the frequency and intensity of extreme events. For instance, a rise in mean temperature may be associated with an increase (decrease) in the number of extremely hot (cold) days, while a rise in mean rainfall may be associated with an increase in the number of heavy rain days, at the expense of light rain days (Figure 6.9). However, due to the inherent complexity of the climate system, changes in extremes are not always consistent with changes in the mean, so it is generally not appropriate to simply extrapolate mean climate projections when considering extreme events. Instead, a number of descriptive indices (Frich et al., 2002; Alexander et al., 2006; Klein Tank et al., 2009) and statistical modelling techniques (Coles et al., 2001; Kharin et al., 2005; Kharin et al., 2007) are used to capture changes in the magnitude and frequency of extreme weather events from daily data.

In this section, daily CMIP3 data have been analysed to provide projected changes in a number of commonly used extreme maximum temperature, minimum temperature and rainfall indices (Table 6.1), as well as a drought index. Since the availability of daily CMIP3 data is less than that for monthly data, both in terms of the number of contributing models (Appendix 1, Table A2) and the future time periods offered, projections are presented for two 20-year periods centred on 2055 and 2090. For those projections where the changes are relatively uniform and of the same direction across the PCCSP region, the regional average multi-model mean change (plus or minus twice the inter-model standard deviation) is provided only for 2090 under the A2 (high) scenario.

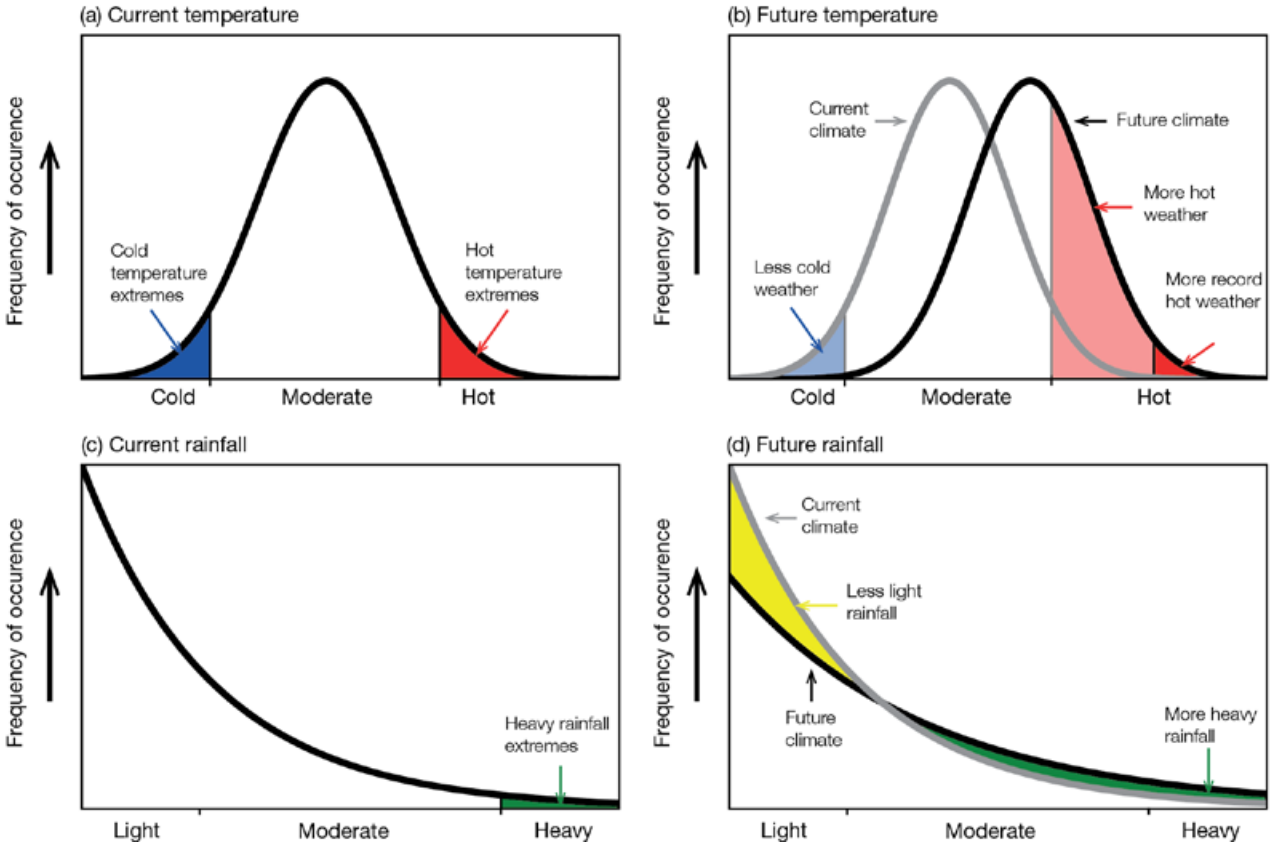

Figure 6.9: Typical changes to the occurrence of extreme events in response to a hypothetical increase in mean temperature and rainfall. Panels (a) and (c) represent the current climate and demonstrate averages and extremes for temperature and rainfall, respectively. Panels (b) and (d) show the changes in extreme events arising from an increase in mean temperature and rainfall, respectively. Adapted from figure ES.1 of the US Climate Change Science Program, Karl et al., (2009).

Table 6.1: Statistics used to project changes in the magnitude and frequency of extreme events.

Statistic	Description	Variables
1-in-20-year return value [a]	Extreme daily value that occurs on average only once every 20 years The change in this statistic relative to the base period (1980–1999) is denoted ΔP_{20RV}	Maximum temperature Minimum temperature Rainfall
90th percentile	The value that is only exceeded on 10% of days	Maximum temperature Minimum temperature Rainfall
10th percentile	The value that is surpassed on all but 10% of days	Maximum temperature Minimum temperature Rainfall
Highest 5-day total rainfall [b]	Magnitude of the highest 5-day rainfall total The change in this statistic relative to the base period (1980–1999) is denoted ΔP_{RX5}	Rainfall
Extreme rainfall contribution index [b]	Percentage of total annual rainfall that comes from intense rainfall events (defined as more intense than the 99th percentile) The change in this statistic relative to the base period (1980–1999) is denoted $\Delta P_{R99pTOT}$	Rainfall
Rainy day	Any day where more than 1 mm of rain falls	Rainfall
Light, moderate and heavy rain day[c]	Any day where 1–10 mm (light), 10–20 mm (moderate) or 20–50 mm (heavy) of rain falls	Rainfall

[a] Calculated using the Generalised Extreme Value distribution (Coles et al., 2001; Kharin et al., 2005)
[b] See http://cccma.seos.uvic.ca/ETCCDMI/ for details
[c] Categories defined by Dai (2006) and Sun et al. (2006).

6.2.7.1 Surface Air Temperature Extremes

Projected changes in surface air temperature extremes, both in terms of their magnitude and spatial structure, are highly consistent with mean temperature projections presented in Section 6.2.1. The projected multi-model mean increase in the annual 10th percentile, 90th percentile and 1-in-20-year minimum and maximum daily temperature all range from 0.5 to 1.5°C for 2055 under the B1 (low) scenario, to 2.0 to 3.5°C for 2090 under the A2 (high) scenario. As such, it appears that the daily temperature distribution is projected to shift to warmer values, with little change to the range (or spread) of values. This differs from projections for many other regions of the globe, where minimum temperatures are projected to increase at a faster rate than maximum temperatures, indicating a change in the spread of the distribution as well as the location (Meehl et al., 2007b; Kharin et al., 2007).

The spatial distribution of changes in extreme surface air temperature is comparable to that of mean surface air temperature. For example, under the A2 (high) emissions scenario by 2055, the 1-in-20-year maximum daily temperature event increases by up to 2°C over Papua New Guinea, and in the central and north-east of the PCCSP region; and by 2090 the area with the smallest increase of 2.5°C is situated in the south-west of the region, with increases of up to 3°C projected for the majority of the region (Figure 6.10). Such patterns and magnitudes are also projected for near-surface air temperature (Figure 6.1), however there are some regional differences, most notably that the warming in the central equatorial part of the region is 0.5°C less in the maximum 1-in-20-year event than for mean surface air temperature (Figures 6.10 and 6.1, respectively).

Over all locations, the current 1-in-20-year maximum daily temperature event is projected to increase in frequency. Given the relatively narrow range of daily temperatures that many (particularly near-equatorial) PCCSP Partner Countries experience, the projected increases in frequency are significantly larger than what is expected over land based regions (Kharin et al., 2007). Due to the shift of the overall temperature distribution towards warmer conditions, there are no projected occurrences of the current 1-in-20-year daily minimum temperature in 2030 and beyond.

The uncertainty associated with extreme temperature projections is higher than for mean temperature projections. This is due to a larger spread in the model projections around the multi-model mean value (Perkins, in press), in addition to the fact that the CMIP3 models tend to underestimate the magnitude of temperature extremes in the current climate (Section 5.2.4.1).

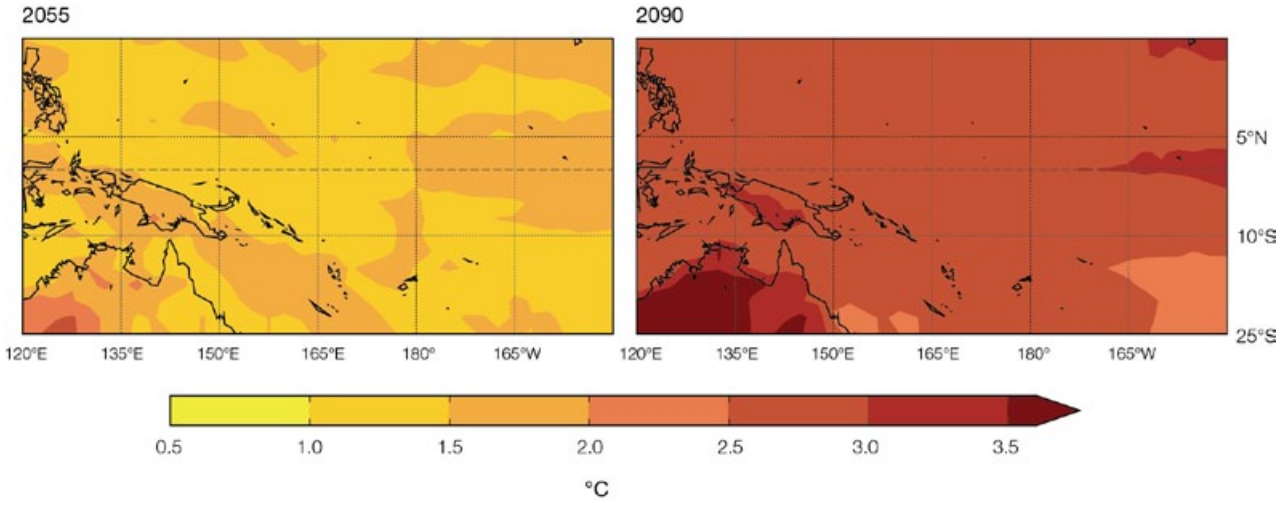

Figure 6.10: Projected multi-model mean changes in the 1-in-20-year maximum daily surface air temperature (°C) for 2055 and 2090, relative to 1990, under the A2 (high) emissions scenario. All models agree on the direction of change in all locations.

6.2.7.2 Extreme Daily Rainfall

A widespread increase in the number of heavy rain days (20–50 mm) is projected by the climate models for the A2 (high) emissions scenario. The annual numbers of rain days (over 1 mm), light rain days (1–10 mm) and moderate rain days (10–20 mm) are projected to increase near the equator, with little change elsewhere in the region (Figure 6.11).

For the A2 (high) scenario, this shift towards a rainfall distribution that includes more heavy rain days is projected to be accompanied by an increase in the intensity of extreme events (ΔP_{20RV} = 25 ± 70 mm or 35 ± 90%). Consequently, the maximum five-day rainfall total is also projected to increase in all locations (ΔP_{RX5} = 55 ± 200 mm or 30 ± 95%), and for most locations a greater percentage of annual rainfall is projected to come from intense rainfall events ($\Delta P_{R99pTOT}$ = 5 ± 10%). Extreme rainfall events that currently occur once every 20 years on average are generally simulated to occur four times per 20-year period, on average, by 2055 and seven times per 20-year period, on average, by 2090 under the A2 (high) scenario. It is clear that these projected increases in extreme rainfall are more pronounced than for the mean rainfall projections (Section 6.2.2).

Due to the large spread in projections between the CMIP3 climate models, and to the fact that all models tend to underestimate the current intensity and frequency of extreme rainfall events (Section 5.2.4.2), these projections must be interpreted with caution.

6.2.7.3 Drought

The standardised precipitation index (SPI; Lloyd-Hughes and Saunders, 2002) is a measure of drought based solely on rainfall (excluding the effect of evapotranspiration). It is computed by fitting a probability density function to the frequency distribution of rainfall which is summed over the timescale of interest (Lloyd-Hughes and Saunders, 2002). In this case, monthly precipitation is used and the timescale of interest is 12 months, chosen to reflect the time required for water deficit conditions to significantly affect various agricultural and hydrological systems. Each monthly value is the total precipitation for the previous 12 months. The probability distribution is then transformed to a standardised normal distribution. Negative SPI values are indicative of drought conditions while positive values are

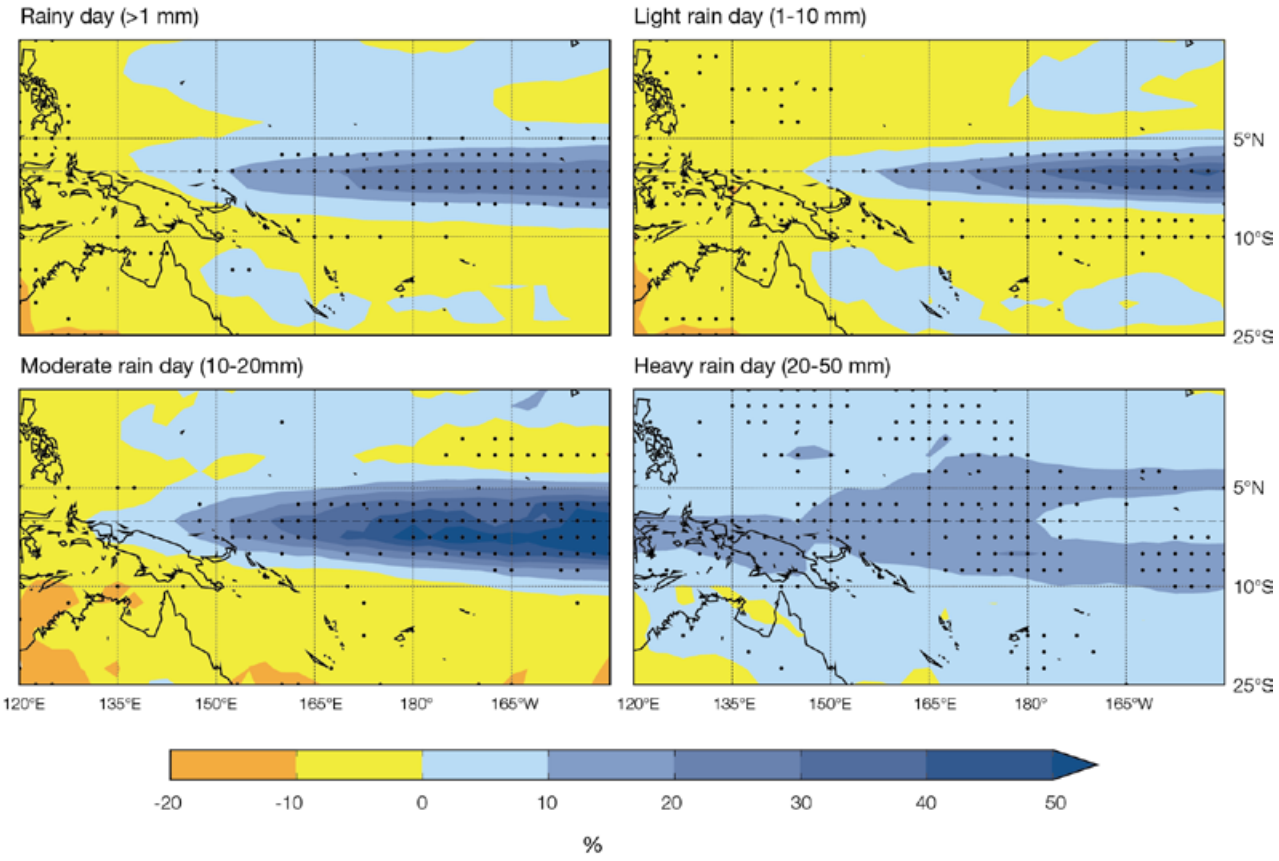

Figure 6.11: Projected multi-model mean change in the number of rainy (>1 mm), light rain (1–10 mm), moderate rain (10–20 mm) and heavy rain (20–50 mm) days between 1990 and 2090, for the A2 (high) emissions scenario. Regions where at least 80% of models agree on the direction of change are stippled.

indicative of water surplus conditions. Over the 21st century, the SPI for a given region has a mean of zero, due to normalisation. In general, there is a trend from negative to positive SPI values (i.e. fewer droughts toward the end of the century).

For all emissions scenarios, the frequency of moderate droughts (SPI values between -1.00 and -1.49) are projected to decline in the central Pacific (Figure 6.12). Over the eastern equatorial cold tongue region (Section 5.2.1.1), moderate droughts occur 3-4 times every 20 years by 2030, decreasing to 2-3 times by 2090. Over the central western Pacific (including Papua New Guinea, the Solomon Islands and southern Palau), moderate droughts occur 1-2 times every 20 years by 2030, decreasing to 0-1 times by 2090, particularly under the A2 (high) scenario. For the rest of the PCCSP region, the occurrence of moderate droughts remains as 1-2 times every 20 years, with the exception of a decrease in the north (over the Marshall Islands and Federated States of Micronesia) under the A2 (high) scenario.

Similar patterns are also evident for mild droughts (SPI values between 0 and -0.99) and severe droughts (SPI values between -1.50 and -1.99). Mild droughts decrease in the central Pacific from 9 times every 20 years by 2030 to 4-6 times every 20 years by 2090. Severe droughts decrease from 1-2 times every 20 years by 2030 to 0-1 times every 20 years by 2090. The largest decrease is simulated under the A2 (high) scenario, where the increase in rainfall is the highest (Figure 6.3). Regional projections of drought frequency are discussed for each country in Volume 2.

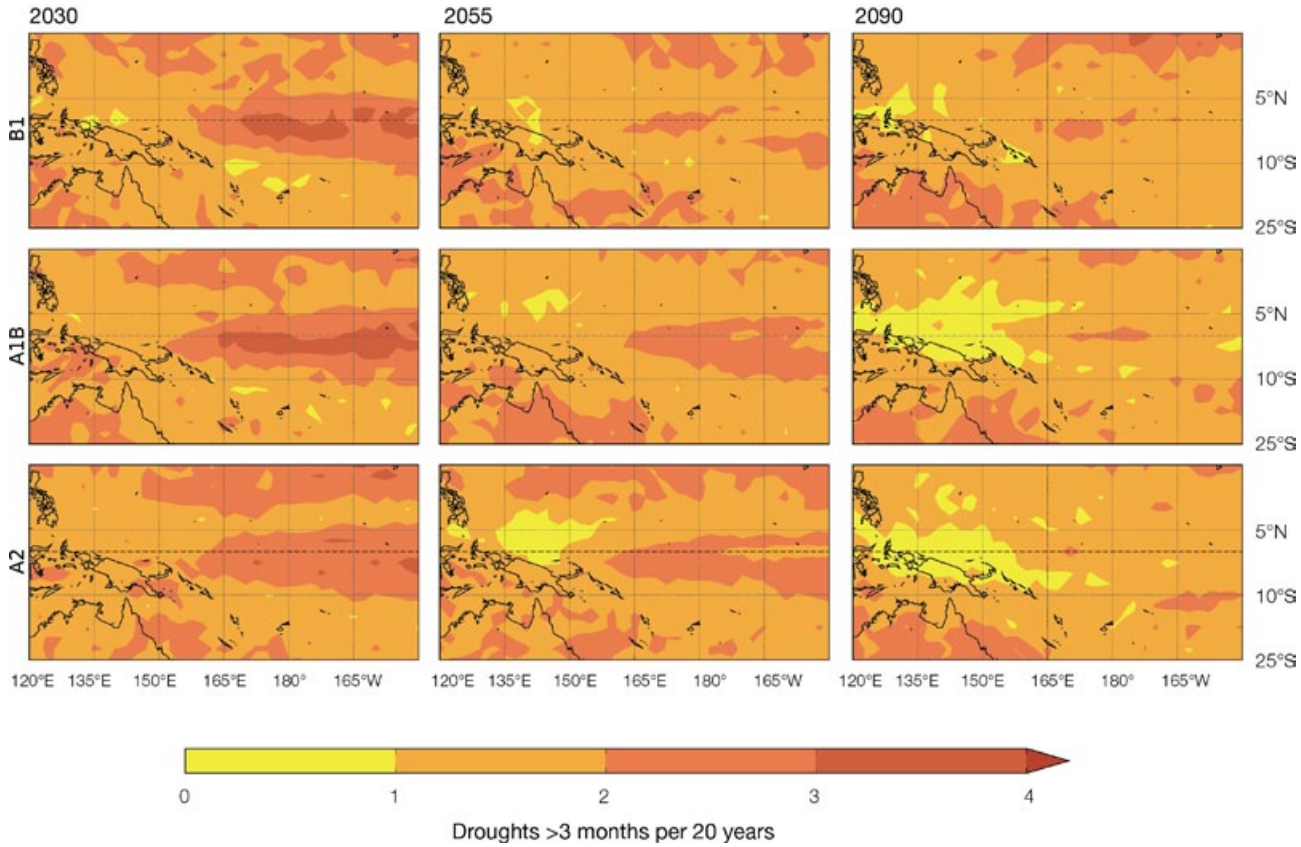

Figure 6.12: Frequency of moderate drought defined by the standardised precipitation index (SPI) under the B1 (low), A1B (medium) and A2 (high) scenarios for 20-year periods centred on 2030, 2055 and 2090. Frequency is defined as the number of times during the 20-year period where the SPI is between -2.00 to -2.99 for at least three consecutive months (Lloyd-Hughes and Saunders, 2002).

6.3 Ocean Projections

This section considers sea-surface temperature, sea-surface salinity, stratification and ocean circulation. Sea-level rise is addressed in Section 6.5 and ocean acidification is covered in Section 6.6.

Projections have been derived for three 20-year periods centred on 2030, 2055 and 2090, relative to a 20-year period centred on 1990. This is based on all available CMIP3 climate models, except those deemed unsatisfactory in their ability to simulate the aspects of the current climate (Chapter 5). The number of available models differs between each variable and emissions scenario (Appendix 1, Table A3).

6.3.1 Ocean Temperature and Salinity

Warming and freshening in the western tropical Pacific Ocean have already been observed over recent decades (Section 3.6; Cravatte, 2009).

In addition, climate models have consistently shown such changes for the 20th century and project acceleration into the future under the influence of human-induced global warming. For the PCCSP region, sea-surface temperatures are projected to increase by 1.4 ± 0.7°C, 2.2 ± 0.8°C and 2.6 ± 0.6°C and sea-surface salinities are projected to decrease by 0.22 ± 0.3 psu, 0.32 ± 0.4 psu and 0.34 ± 0.4 psu between 1990 and 2090 for the B1 (low), A1B (medium) and A2 (high) scenarios respectively (Figure 6.13), where the range is estimated as a two standard deviation spread over climate model projections. Differences in the rate of sea-surface temperatures rise between the A1B and A2 scenarios only emerge at the very end of the century because it is then that CO_2 concentrations for the A2 scenario start to overtake A1B (Figure 4.1). For the first few decades of the 21st century, CO_2 concentrations for A1B slightly exceed those of A2.

The spread in future sea-surface salinity changes across the models is considerably larger than for sea-surface temperature, reflecting in part large inter-model differences in the representation of mean rainfall.

Many of the climate models indicate a maximum warming in the central equatorial Pacific, with the least warming occurring in the south-eastern Pacific (Figure 6.14). The pattern of equatorial warming has been shown to be related to a complicated set of factors, including greater cloud cover in combination with weaker westward surface flow in the eastern Pacific, and weaker upwelling of sub-surface water combined with a stronger vertical temperature gradient in the western Pacific (DiNezio et al., 2009). The weak warming in the south-eastern Pacific may be linked to the stronger projected winds in that region that will tend to cool the ocean (Xie et al., 2009).

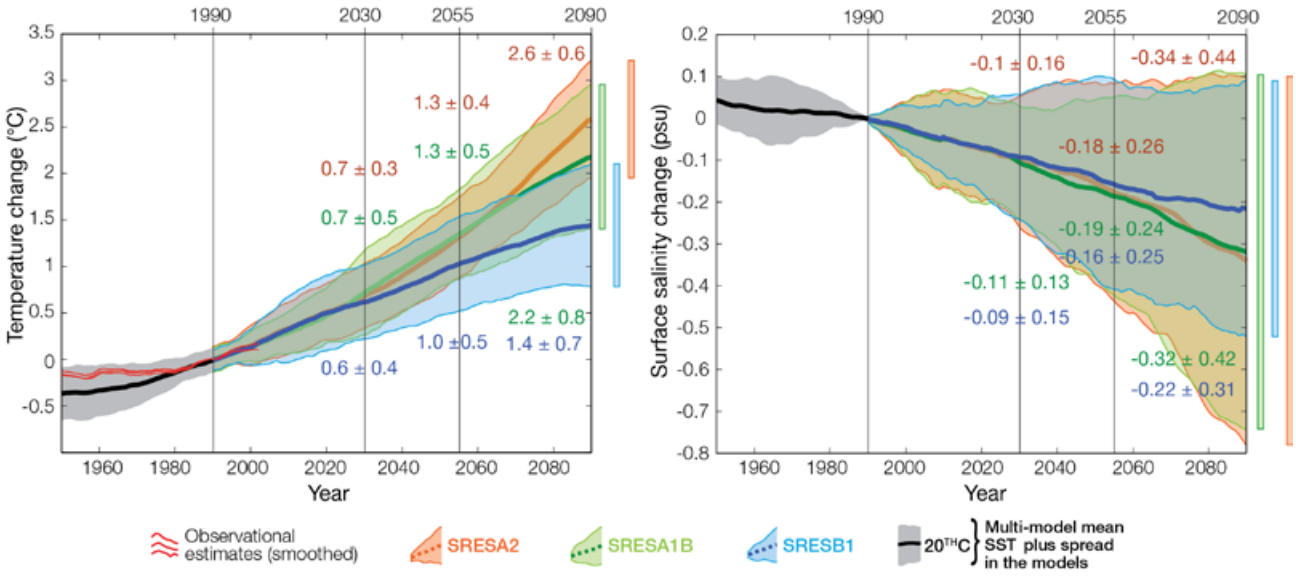

Figure 6.13: Evolution of multi-model average sea-surface temperatures (°C) (left) and sea surface salinity (psu) (right) for the PCCSP region for 1950–1990 (black) and three post-1990 scenarios (B1-green, A1B-blue and A2-red). The shaded envelope indicates ± two standard deviations. Numbers indicate mean change in sea-surface temperature or salinity (plus or minus the corresponding multi-model standard deviation) for three time slices (2030, 2055 and 2090) relative to 1990. The red line (left) is observational estimate from HadISST. Where possible de-drifting has involved the removal of any linear trend in the control simulation for 1900–2150. While the ECHAM5/MPI-OM model has no sea-surface temperature control run available for de-drifting, the equivalent control run for surface air temperature shows relatively minor drift, and the model has been included in this analysis.

Regional differences in projected salinity changes (Figure 6.14) closely match projected changes in net rainfall (i.e. rainfall minus evaporation). The largest increases in rainfall occur in the western equatorial Pacific, and on the inner flanks of the convergence zones, with reduced rainfall in the south-east. This results in a strong freshening in most of the PCCSP region (with high agreement between models), except in the far eastern and particularly south-eastern parts of the domain, where there is a suggestion of increased salinity.

The West Pacific Warm Pool provides the energy to sustain western Pacific convection and the tropical atmospheric circulation. It is an important factor in El Niño-Southern Oscillation (ENSO) variability; it can modulate the intensification of tropical cyclones, and its eastern edge is an important indicator of the location of vital tuna stocks on inter annual time scales (Lehodey et al., 1997). The projected changes for the West Pacific Warm Pool show a massive increase in extent (defined here as temperatures above 29˚C), with the edge of the pool moving many thousands of kilometres to the east along the equator over coming decades (Figure 6.14). While the fresh water pool also shows a substantial increase in area, the changes are considerably less than the Warm Pool. This indicates that the threshold sea-surface temperature for convective activity must also be increasing over time so that the area of strongest convection does not expand with the 29˚C isotherm (see also Johnson and Xie, 2010 and references therein).

The projected changes in temperature and salinity with depth, averaged over the PCCSP region (Figure 6.15), show that the surface intensified warming and freshening will cause the surface ocean to become considerably less dense compared to the deep ocean, i.e. the ocean becomes more stratified (with 100% model agreement). There is also a clear projected increase in ocean stratification (as measured by the buoyancy frequency squared, which depends on the vertical density gradient) between about 50 m and 100 m depth. These depths are associated with the upper pycnocline, which marks the boundary between high nutrients (below) and depleted nutrients (above) (Chapter 2). This increase in stratification acts to inhibit mixing, thereby reducing the supply of nutrients from the deep to the surface ocean, with consequences for biological productivity (Ganachaud et al., 2011). Implications of the projected changes for ocean biology, particularly fisheries, are discussed in detail in Bell et al. (2011).

6.3.2 Ocean Circulation

Theoretical arguments for a surface warming and an intensification of the hydrological cycle also suggest that the tropical atmospheric circulation, including the equatorial trade winds, should weaken (Held and Soden, 2006) as the troposphere warms. Observational evidence indicates that such a slowdown may have already occurred (Vecchi et al., 2006; Power and Smith, 2007; Power and Kociuba, 2010, in press). Climate models do indeed project a consistent slowdown of the equatorial trade winds with a weakening of surface winds over much of the Northern Hemisphere extra-tropics and a corresponding strengthening in the Southern Hemisphere. Surface Ekman currents (wind driven flow that is deflected by the Earth's rotation) in the upper few tens of metres of the ocean, are directly driven by surface winds. The direction of flow is complicated by the rotation of the planet, causing surface currents to be deflected to the right (left) of the direction of the wind in the Northern (Southern) Hemisphere. No deflection occurs at the equator (where the Coriolis effect vanishes). Thus in

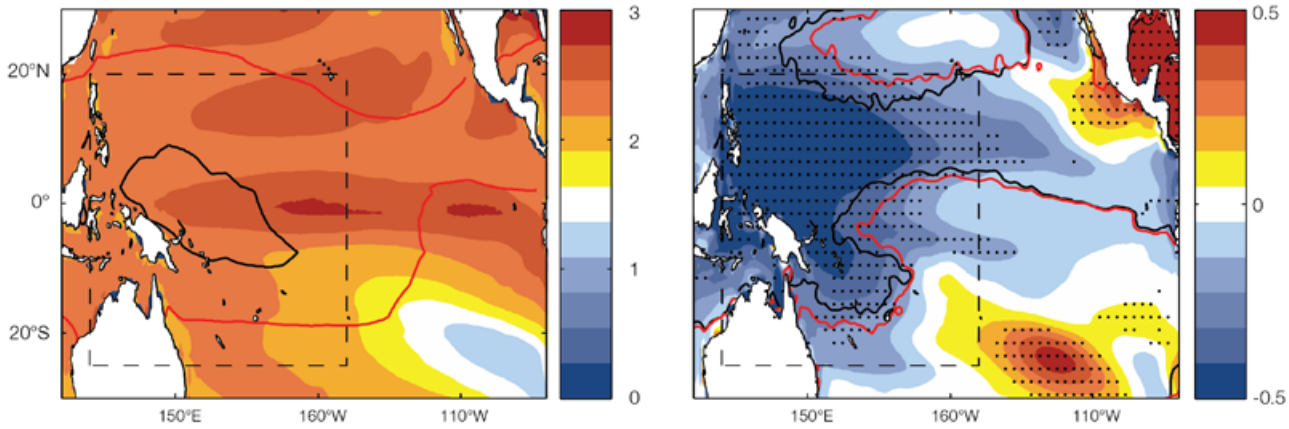

Figure 6.14: Multi-model mean change in sea-surface temperature (°C) (left) and sea-surface salinity (psu) (right) over the tropical Pacific region for the A2 (high) scenario, for a 20-year period centred on 2090 relative to 1990. Superimposed on the sea-surface temperature change is the observed (HadISST) Warm Pool extent (black contour, for waters with mean annual temperature exceeding 29°C) and projected Warm Pool extent (red contour, computed as 1990 observed sea-surface temperature + projected warming). Superimposed on sea-surface salinity change is the observed (black, from CARS06) and projected (red) location of the edge of the 'fresh pool' defined by the 34.8 psu contour. Stippling for sea-surface salinity represents areas where there is at least 80% agreement in the sign of the change across the models. Drift correction has been applied to all models.

regions of projected decreases in surface wind strength, surface currents will also tend to weaken. Just to the north and south of the equator, the mean equatorial trade winds drive a mean surface Ekman current with a component directed away from the equator. This divergent surface flow normally generates upwelling along the equator, with an associated convergent surface flow and downwelling off the equator, driving a shallow vertical circulation (the tropical overturning cell). The projected slow-down of the equatorial trade winds drives a weakening of the surface Ekman flow and consequently a slowdown of the tropical overturning cell.

Model projections show the changes in the volume transport (measured in millions of cubic metres per second; Sv) for some of the major regional currents (Figure 6.16). There is a robust acceleration of the northern branch of the sub-tropical gyre, which forms the extra-tropical part of the South Equatorial Current. This change is part of a large-scale intensification of the sub-tropical gyre including the East Australian Current (Cai and Cowan, 2007; Sen Gupta et al., 2009). Conversely, the part of the South Equatorial Current close to the equator weakens as a direct response to the weakening trade winds. While there is a projected weakening in the multi-model mean, there exists poor agreement across the models. Similarly, circulation changes in the Northern Hemisphere are not very consistent across the models. In a number of models there are projected increases in the sub-surface Equatorial Undercurrent, in part related to greater flow in the New Guinea Coastal Undercurrent which feeds the Equatorial Undercurrent. Finally, the Indonesian Throughflow, which represents the only conduit for tropical water to pass from the Pacific to the Indian Ocean, shows a robust decrease in water transport, from about 9 Sv to 7 Sv in the multi-model mean.

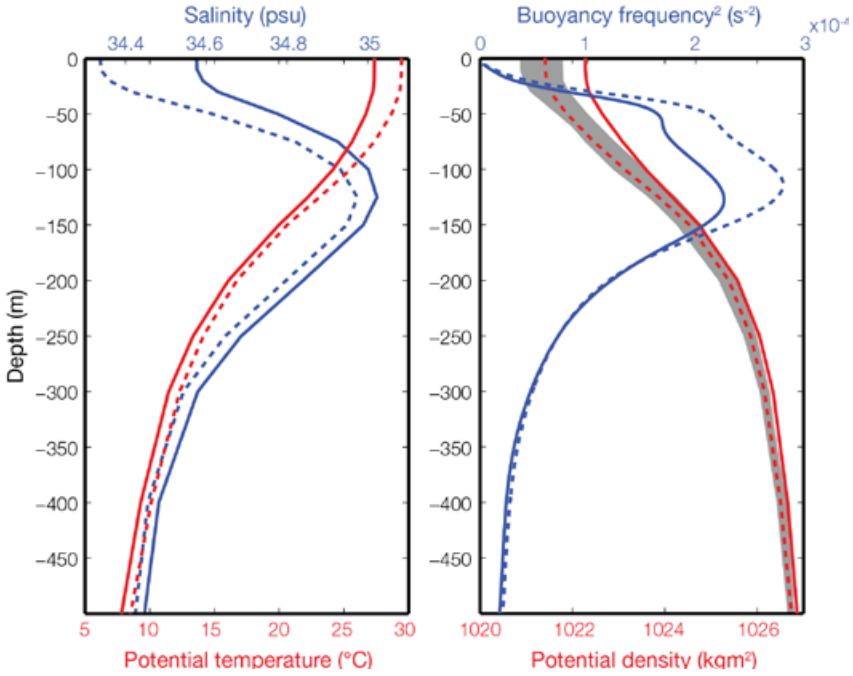

Figure 6.15: Ocean changes with depth. (Left) PCCSP regional average multi-model mean potential temperature (red) and salinity (blue), for the period 1980–1999 (solid) and 2080–2099 (dashed) for A1B scenario. (Right) PCCSP regional average multi-model mean potential density (red) and buoyancy frequency squared (blue), for 1980–1999 (solid) and 2080–2099 (dashed) for A1B (medium) scenario. Grey shading indicates the full range of projected density changes based on all models used (Chapter 4, Table A3). The buoyancy frequency N is defined as $(N^2 = \frac{1}{\rho}\frac{\partial \rho}{\partial z}$, where ρ is density and z is depth).

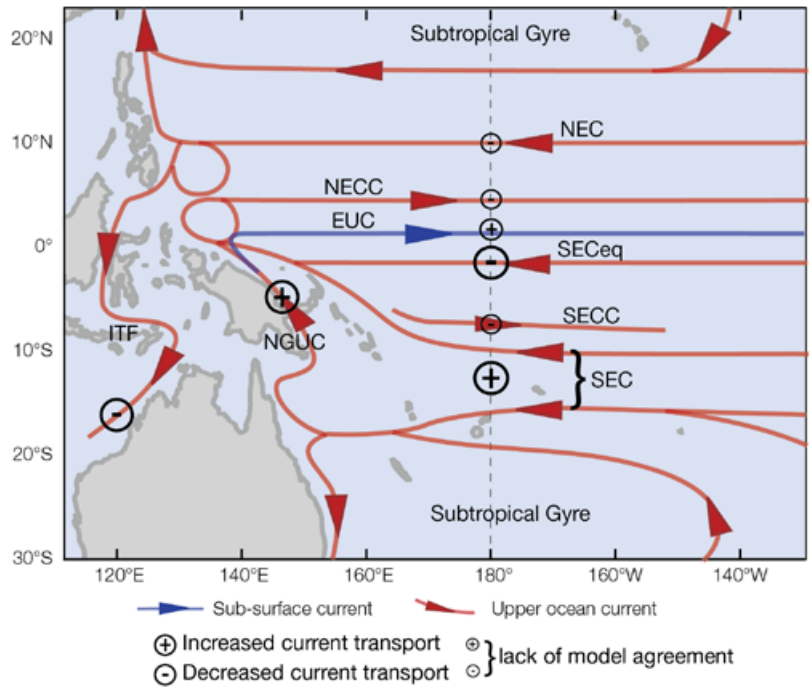

Figure 6.16: Schematic showing some of the major upper ocean currents and whether they are projected to increase or decrease in the future. Key: Equatorial Undercurrent (EUC); Indonesian Throughflow (ITF); North Equatorial Current (NEC); North Equatorial Counter Current (NECC); New Guinea Coastal Undercurrent (NGUC); South Equatorial Current (SEC); South Equatorial Counter Current (SECC).

6.4 Key Climate Features and Variability

6.4.1 El Niño-Southern Oscillation

ENSO events are responsible for significant climate variability in most Partner Countries. Even small changes to various aspects of ENSO could profoundly alter Pacific climate: the frequency and/or intensity of El Niño and La Niña events, and the details of their characteristics, such as where the strongest El Niño-related increase in sea-surface temperature occurs.

Projected changes in the average climate of the Pacific relevant to ENSO (Sections 6.2 and 6.3) are: increasing sea-surface and near-surface air temperatures, with the strongest warming on the equator; a flattening and shallowing of the thermocline (Yeh et al., 2009); an increase in ocean stratification; and a weakening of the Walker Circulation, with a decrease in the pressure gradient across the tropical Pacific (Vecchi et al., 2006; Power and Smith, 2007; Power and Kociuba, 2010, in press). As they are related to positive or negative feedbacks, some of these changes favour an intensification of ENSO variability and some favour a weakening. As a result, the exact nature of ENSO under conditions of global warming has many uncertainties (Collins et al., 2010).

The strength of the Niño3.4 and ENSO Modoki Indices for the CMIP3 climate model simulations for the 2078–2098 period using the A2 (high) scenario, relative to 1979–1999 in the 20th century simulations (Figure 6.17) shows that changes in the two indices are closely related across the different models. This suggests that sea-surface temperature variability changes in each model are fairly consistent across a broad equatorial Pacific region. All the models indicate that ENSO will remain an important factor in year-to-year variability in the future. However, studies of palaeoclimate suggest that ENSO has exhibited very different behaviours in past climates (Chapter 3).

Global warming has very likely driven changes in mean rainfall, temperature and other important climatic variables (Hegerl et al., 2007; Meehl et al., 2007b) in many countries (including PCCSP Partner Countries). As ENSO events are responsible for some of the variability about these means in most Partner Countries, climatic conditions experienced during ENSO events will very likely change if they have not already (Power and Smith, 2007). For example, if El Niño tends to warm a particular region then temperatures experienced during future El Niño events will tend to be higher than the temperatures experienced during past El Niño events.

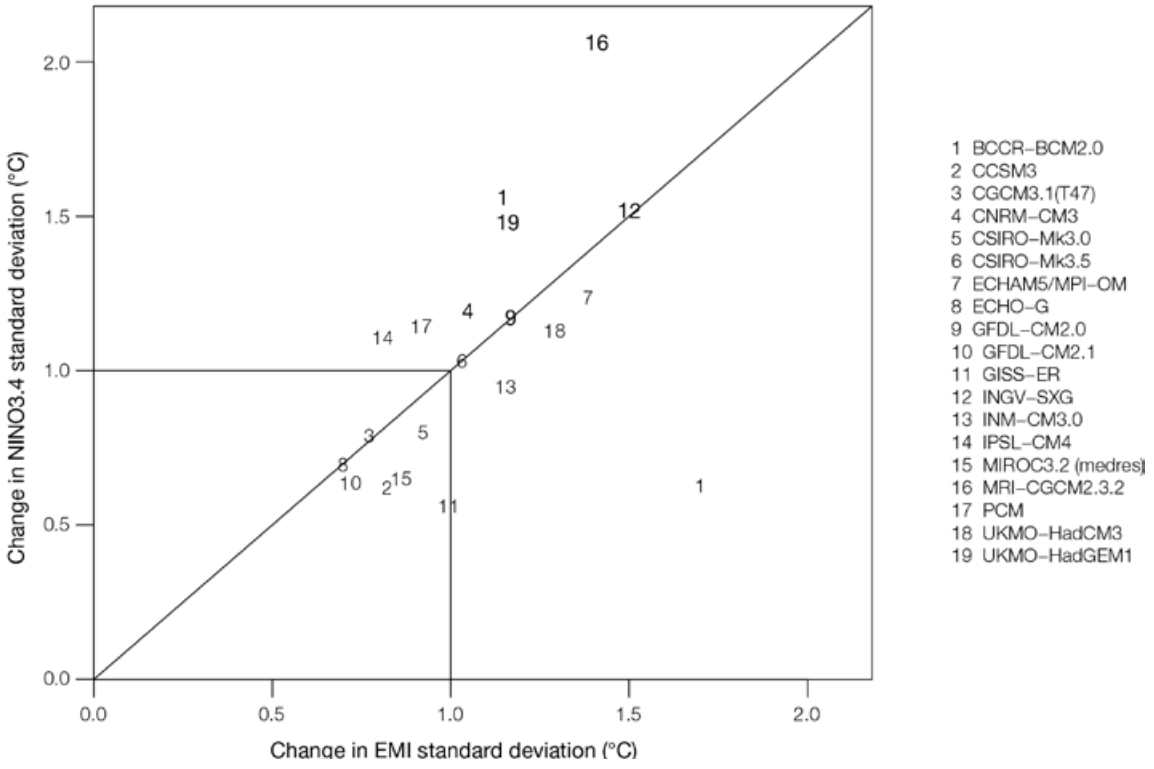

Figure 6.17: The ratio of A2 (high) scenario (2078–2098) to 20th century (1979–1999) model simulated variability (standard deviations) in the Niño3.4 and ENSO Modoki Indices (EMI) for 19 climate models. Numbers greater than one show increased variability in the future, while those less than one show decreased variability. The GISS-ER, INGV-SXG, INM-CM3.0 and PCM models are considered less reliable than the others (see Chapter 5).

It should be noted that any changes in ENSO variability, as seen in these projections, may be due to interdecadal variability in the strength of events, rather than any global warming signal. In the period 2057–2077, the relative changes in the two ENSO indices are slightly different for each model, but the range across all models is similar to that for 2078–2098. For some of the CMIP3 models, the changes in variability in the two periods are in opposite directions, but in the majority only the size of the changes are different, suggesting that some of the projected change is due to decadal variability, with the remainder due to global warming.

The models are generally poor in reproducing the pattern of sea-surface temperature variability associated with ENSO Modoki in the 20th century, and so little can be ascertained on the probable evolution of the Modoki under the A2 (high) scenario. However, this analysis (based on the Modoki index calculated across three boxes – see Section 3.4.1) shows no large, or consistent, change across the CMIP3 simulations.

The sea-surface temperature pattern across the Pacific region associated with the Interdecadal Pacific Oscillation (IPO) shares some features of the pattern of warming observed over the 20th century (Meehl et al., 2009). This means that in coming decades, depending on the phase of the IPO, natural interdecadal temperature variability may act to either enhance or reduce the warming driven by continued increases in greenhouse gas concentrations in locations where the IPO influences sea-surface temperatures. This same variability may also act over the next few decades to favour more El Niño or more La Niña type conditions. However, over longer time periods the global warming signal will dominate temperatures in the region.

Also, given the lack of evidence that ENSO variability will change significantly, over longer periods neither El Niño nor La Niña events would be expected to be significantly more prevalent than the other.

Therefore, while year-to-year variability in the PCCSP region will continue to be largely driven by ENSO, climate models do not provide consistent projections of changes in the frequency, intensity and patterns of future El Niño and La Niña events.

6.4.2 Indian Ocean Dipole

The frequency of positive Indian Ocean Dipole (IOD) events has been increasing in recent decades (Section 3.4.7). Climate models suggest that a more positive IOD-like mean-state will continue with easterly wind trends and a shallowing thermocline over the eastern Indian Ocean, associated with a weakening of the Walker Circulation (Vecchi and Soden, 2007b). A multi-model average shows a slower warming rate in the eastern Indian Ocean than in the western Indian Ocean (Cai et al., 2011), with a consistent rainfall response by way of lower rainfall over the eastern Indian Ocean regions, including East Timor (Figures 6.3 and 6.4).

However, there is no systematic multi-model analysis of how the IOD frequency and amplitude will change. It is anticipated that a more positive IOD-like mean state would be associated with an increase in the positive IOD amplitude and/or frequency. For example, a study using the GFDL model showed that there is little change in the positive IOD amplitude (Zheng et al., 2010), although the frequency of positive IOD events increases. Further research is required to assess the degree of consensus amongst models regarding projected changes in IOD frequency and amplitude.

6.4.3 Intertropical Convergence Zone

Under conditions of anthropogenically induced climate change, the multi-model mean projections using 16 CMIP3 models show a general increase in tropical rainfall, with increases occurring in a broad band (rather than confined to the ITCZ) extending fairly uniformly and zonally from around 10°S to 5°N across the Pacific (Figure 6.3). This pattern can be largely attributed to increased moisture convergence associated with warmer air temperatures (Christensen et al., 2007), although additional dynamics-related changes complicate the picture regionally in individual models (Chou et al., 2008). Changes in rainfall, averaged over the region north of the equator encompassing the ITCZ (160°E–120°W, 0–15°N), show a general increase in June-August (high levels of model consensus), with little change in December-February, thereby amplifying the current seasonal cycle (Figure 6.18a). Using the 6 mm per day contour to define the ITCZ, there is an increase in the area of the ITCZ in all models in June-August, and in all but three in December-February (Moise and Delage, in press). This corresponds to a modest expansion of around 5% per °C of Pacific warming, primarily through an increase in the width of the ITCZ. A 25–30% increase in annual mean rainfall is simulated by the end of the century within the ITCZ under the A2 (high) scenario.

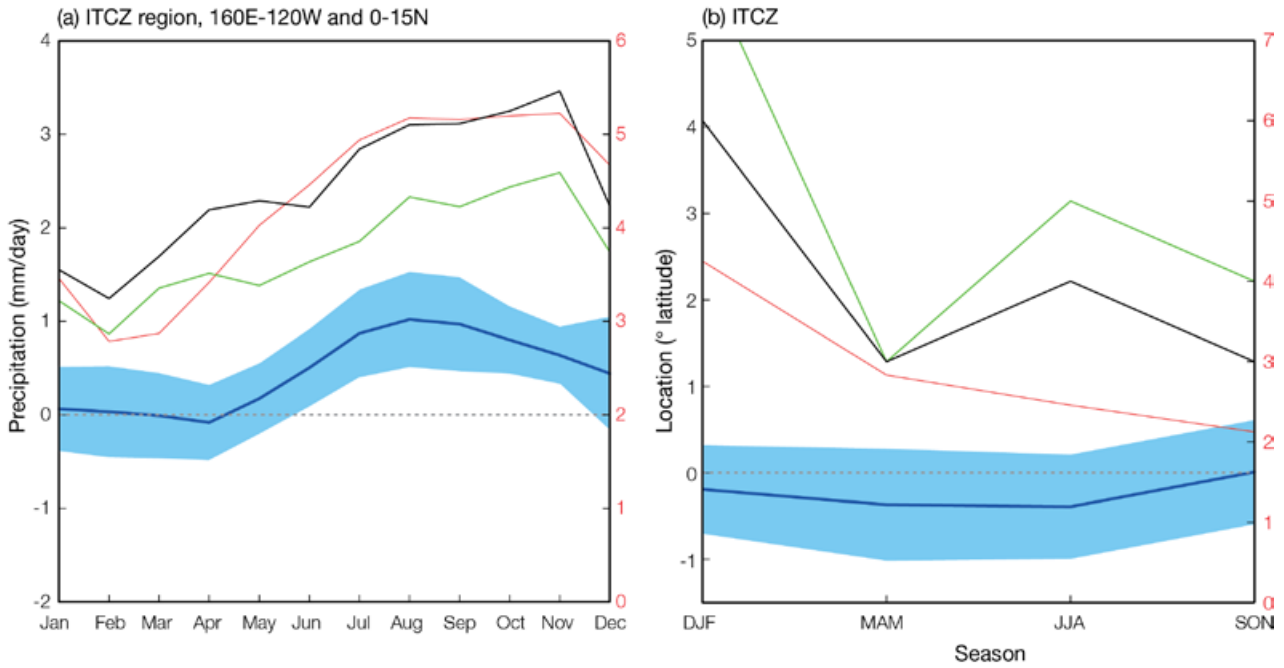

Figure 6.18: (a) Projected changes in average monthly rainfall (mm per day; relating to the left y-axis scale) over the ITCZ region (defined by 160°E–120°W, 0–15°N). The multi-model mean is shown as the thick blue line, with the shaded regions encompassing the spread (standard deviation) between individual model simulations. Also shown is the mean model 20th century annual cycle of monthly rainfall in red (mm per day; relating to the right y-axis scale) and observations from the GPCP (green) and CMAP (black) datasets respectively. (b) Projected changes in location (latitude; relating to the left y-axis scale) of the ITCZ. Also shown is the mean model and observed 20th century location of ITCZ (latitude; relating to the right y-axis scale). Line colours correspond to those in (a). Climate change results in both (a) and (b) show 2079–2098 A2 (high) emissions minus 1980–1999. Included are all models providing A2 (high) scenario results, except those listed in Table 5.9 as performing poorly.

Given the broad areal extent of the tropical rainfall increases exhibited by the CMIP3 models, only relatively small systematic geographical shifts are projected for the ITCZ location. Results using a line fitting method (Brown et al., 2011) between the longitudes 160°E and 120°W, show that the maximum shifts in particular models in individual seasons are modest, at less than 2° of latitude (Figure 6.18b), with the east-west orientation ('slope') of the ITCZ having little systematic change on average (not shown). In the multi-model mean, models show a small displacement (less than 0.5°) towards the equator in March-May and June-August (small compared with a mean location at 8°N), with a spread (standard deviation) much larger than the projected displacement, highlighting the significant degree of disagreement in these projections. For December-February and September-November, there is no change apparent in mean ITCZ location. This result is not sensitive to whether all CMIP3 models are used, or when those which show lower skill are excluded.

In summary, under the A2 (high) scenario, the ITCZ is projected to move equatorward in some seasons and broaden, but only by a very small amount (less than 2° of latitude), with substantial disagreement between individual models on the magnitude of the shift. A more robust projection is for significant rainfall increases, but these occur both in the ITCZ itself and in the surrounding (particularly equatorial) region.

6.4.4 West Pacific Monsoon

The West Pacific Monsoon region is rarely discussed exclusively in climate change scientific literature and the following discussion is based on results covering larger regions that either include or directly affect the West Pacific Monsoon. Under global warming, the Walker Circulation affects South Asian monsoon variability in such a way that the role of the Pacific Ocean dominates, and that of the Indian Ocean is secondary (Meehl and Arblaster, 2003). Climate projections show an increase in rainfall during the Asian monsoon, along with an increase in the interannual season-averaged variability. However, the uncertain role of aerosols in general, and carbon aerosols in particular, complicates

the monsoon rainfall projections (Meehl et al., 2007b). This region is also affected by the cold tongue bias present in all global climate models (Section 5.2.3.5).

There is no significant projected change in the westerly winds over the region, even though the results differ across individual models. There is a general tendency for an amplification of the seasonal cycle of rainfall in the West Pacific Monsoon region, as shown by the projected changes in average monthly rainfall over both the three monsoon regions (Southern Hemisphere box-1, Southern Hemisphere box-2 and Northern Hemisphere, as defined in Section 2.5.3), relative to the 20th century multi-model mean (Figure 6.19). There is fairly strong model agreement on the amplification as indicated by the shaded areas. Interestingly, models simulate this amplification only during the initial phase of the wet season in the Northern Hemisphere region while the Southern Hemisphere box-1 region has a consistent increase throughout the wet season, and the Southern Hemisphere box-2 region has a consistent increase for the entire year. The latter result is consistent with the fact that Southern Hemisphere box-2 lies at the eastern edge of the monsoon affected region and receives high rainfall throughout the year.

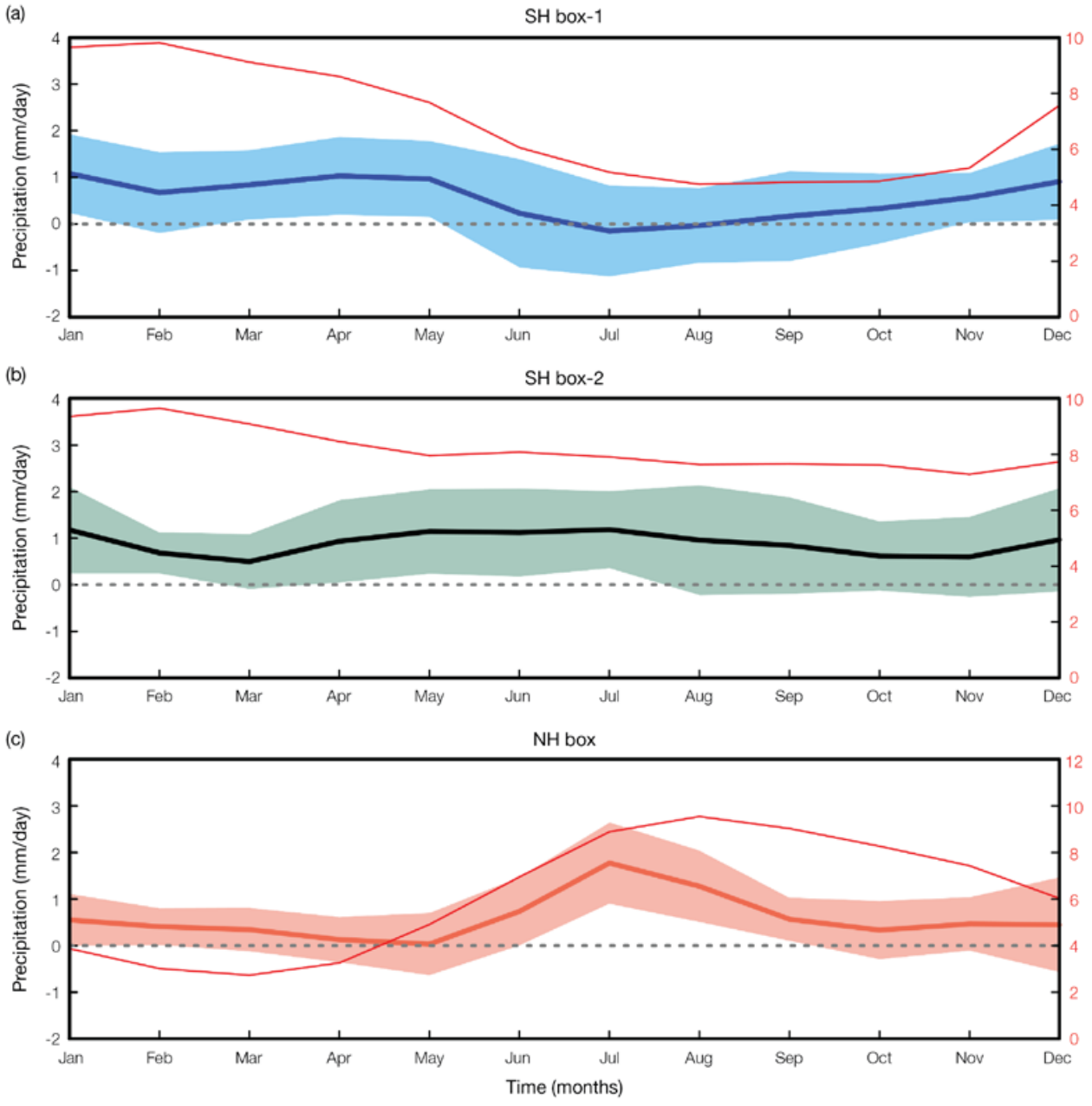

Figure 6.19: Projected changes in average monthly rainfall (mm per day) over the three monsoon regions (SH box-1, SH box-2 and NH, as defined in Section 2.5.3) for 2090, relative to 1990. The multi-model mean for the A2 (high) scenario is shown as the solid thick line; the shaded regions encompass the spread (standard deviation) of the individual model simulations. Also shown is the 20th century annual cycle in red (relating to the right y-axis).

Simulated changes in both low level zonal winds and rainfall in the Southern Hemisphere box-1 region under the A2 (high) emissions scenario from 14 CMIP3 climate models are shown in Figure 6.20. The changes refer to the difference between the two periods (2080–2099) and (1980–1999). This shows that the projected changes favour increases in rainfall while at the same time there is little evidence for a consistent weakening or strengthening of the accompanying low level winds.

As noted previously, monsoon variability is also strongly tied to ENSO, with drought risk increasing during El Niño events, but there is little agreement among climate models with respect to how future climate change may alter the frequency or intensity of El Niño events (Section 6.4.1).

6.4.5 South Pacific Convergence Zone

Future rainfall increases in Pacific region climate are projected to be greatest in the regions of the tropical convergence zones, due to increased atmospheric moisture transport, with the multi-model average change in rainfall showing an increase in the western and central South Pacific, and a decrease in the eastern South Pacific (Christensen et al., 2007). Changes in the position of the SPCZ have been observed in recent decades (Chapter 3), but there is evidence that these may be related to the Interdecadal Pacific Oscillation rather than anthropogenic climate warming (Griffiths et al., 2003).

For the PCCSP study, changes in the SPCZ position and intensity were examined for 16 global climate model simulations, driven by the A2 (high) emissions scenario (Brown et al., in press). The analysis focuses on December-February, when the SPCZ is most intense. The sample of models examined is the same as for other atmospheric projections, except that MIROC3.2(medres) is excluded as this model does not produce a well defined SPCZ (Brown et al., 2011).

Using a simple linear fit to the position of the SPCZ, based on the band of maximum rainfall, the December-February seasonal mean position of the SPCZ is calculated for the last two decades of the 20th century, and compared with the last two decades of the 21st century (Figure 6.21). There is no systematic northward or southward shift in the mean position of the SPCZ, and no systematic shift in the slope of the SPCZ line. One model shows a large increase in the SPCZ slope and a southward shift in latitude due to a change in the width and eastern extent of the SPCZ, and another model shows a northward shift of the SPCZ (see Brown et al., (in press) for details of individual models).

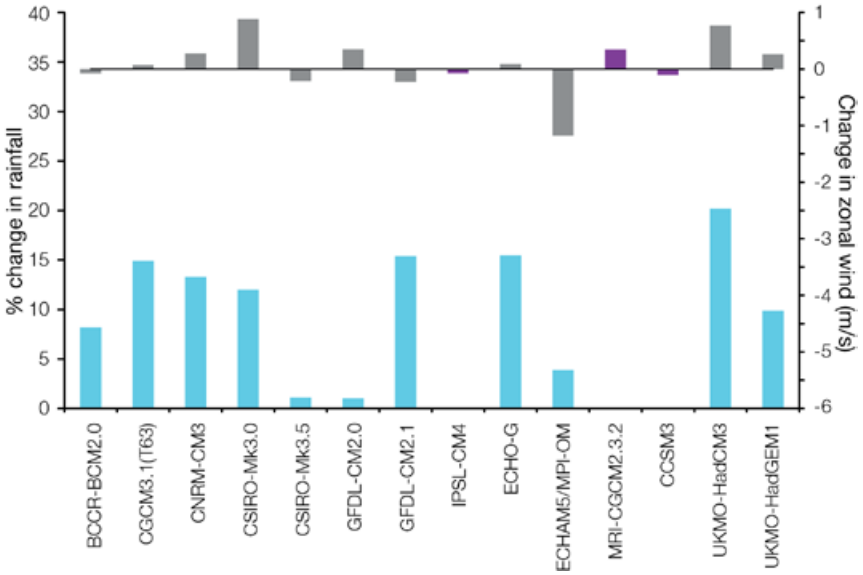

Figure 6.20: Projected changes in December-February zonal (east-west) wind speed (metres per second) and rainfall (%) for the Southern Hemisphere box-1 region (defined in Section 2.5.3) from 14 CMIP3 model results for the A2 (high) emissions scenario. The 1980–1999 mean low level zonal wind-speeds are indicated by the purple bars, while the wind-speed changes (2080–2099 minus 1980–1999) are indicated by the dark grey bars. The accompanying percentage differences in rainfall are indicated by the blue bars.

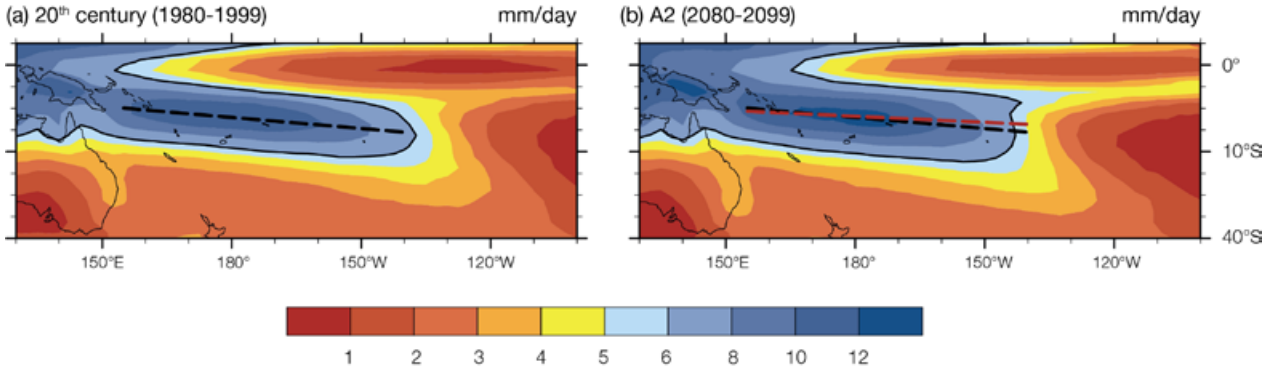

Figure 6.21: The 16 model mean position of the SPCZ in the late 20th and 21st centuries (A2 (high) emissions scenario), as defined by December-February rainfall (mm per day). The black contour shows the 6 mm per day rainfall threshold, giving the approximate edge of the SPCZ. The black dashed line indicates the position of maximum rainfall during 1989–1999, while the red dashed line indicates the position during 2080–2099 for the A2 (high) emissions scenario. See Brown et al., (2011) for details of linear fit method.

Using the 6 mm per day rainfall threshold to define the edge of the SPCZ, changes in the area and intensity of the SPCZ are also calculated. In December-February, the area of the SPCZ increases in the A2 (high) emissions simulations in all models. The majority of models also show an increase in the mean and maximum rainfall within the SPCZ. Overall, there is evidence for more intense SPCZ rainfall in December-February, which is consistent with a stronger hydrological cycle and increased moisture transport in a warmer climate.

At the eastern edge of the SPCZ, between around 150°W to 120°W, there is a decrease in December-February mean rainfall in most models (see Brown et al., in press) and in the multi-model mean (Figure 6.21). This reduction is associated with a relatively small sea-surface temperature increase in the region of the southern sub-tropical anticyclone, and strengthened surface trade winds in this region. The eastern edge of the SPCZ thus appears to contract westwards in the climate change simulations.

Therefore, during December-February, there is a consistent increase in mean and maximum SPCZ rainfall and in the area of the SPCZ in the wet season, with the SPCZ rainfall band becoming wider in most models. There is also a consistent westward contraction of the eastern edge of the SPCZ, associated with a stronger circulation and reduced surface wind convergence in the region to the east of around 150°W in this season. However, there is no consistent shift in the position or slope of the SPCZ in the wet season.

During May-October, the SPCZ in the current climate is generally weaker and closer to the equator than in December-February (Chapter 2 and Chapter 5). In the future, most models project an increase in rainfall within the SPCZ during May-October, with the largest increases on the equatorward side, leading to a shift in the SPCZ towards the equator.

Most CMIP3 models do not accurately simulate the observed diagonal orientation of the SPCZ or the extension of SPCZ rainfall into the extra-tropics in December-February or May-October (Chapter 5). Therefore, the regional-scale changes in rainfall and winds associated with the SPCZ may not be correctly located in the model projections.

6.5 Sea-Level Rise

Projections of sea-level rise require consideration of ocean thermal expansion, the melting of glaciers and ice caps, the surface mass balance and dynamic response of the ice sheets of Antarctica and Greenland, and any changes in storage of water in dams, (Section 4.7). Summaries of sea-level rise issues and recent results can be found in Church et al. (2001), Meehl et al. (2007b), Church et al. (2008, 2010), Milne et al. (2010), Slangen et al. (2010) and Church et al. (2011).

6.5.1 Intergovernmental Panel on Climate Change Projections of Global Averaged Sea-Level Rise for the 21st Century

The projections of the global average sea-level rise by the IPCC Fourth Assessment Report (IPCC 2007; Meehl et al., 2007b) are comprised of two sets of contributions and are for 2090–2099 compared with the average over 1980–1999. The first set includes contributions from ocean thermal expansion, the melting of glaciers and ice caps, the Greenland and Antarctic ice sheet surface mass balances, and the slow dynamic response included in current ice sheet models (Table 6.2). These contributions can be estimated with currently available coupled ocean-atmosphere models and models used to represent the response of land ice to changing atmospheric conditions. The projected ranges given, for the 5% to 95% confidence limits, are from 18 to 38 cm for the B1 (low) emissions scenario to 26 to 59 cm for the A1FI (very high) emission scenario (Meehl et al., 2007b) (Section 5.2.2.6).

In addition, the IPCC Fourth Assessment recognised that these models did not include uncertainties in climate-carbon cycle feedbacks and that there was insufficient understanding to accurately quantify the contribution that might come from any rapid change in ice discharge from the Greenland and Antarctic ice sheets (termed rapid ice here). Using simple scaling arguments, they suggested that the above estimates could increase by up to about 20 cm (17 cm in Table 6.2). However, they recognised that larger values cannot be excluded but that understanding of the relevant processes was "too limited to assess their likelihood or provide a best estimate or an upper bound for sea-level rise" (IPCC, 2007). The sum of all of these contributions to estimate the total sea-level rise is given in Figure 6.22 (see Church et al., 2011 for more details) with the total range across scenarios of about 18 to 80 cm.

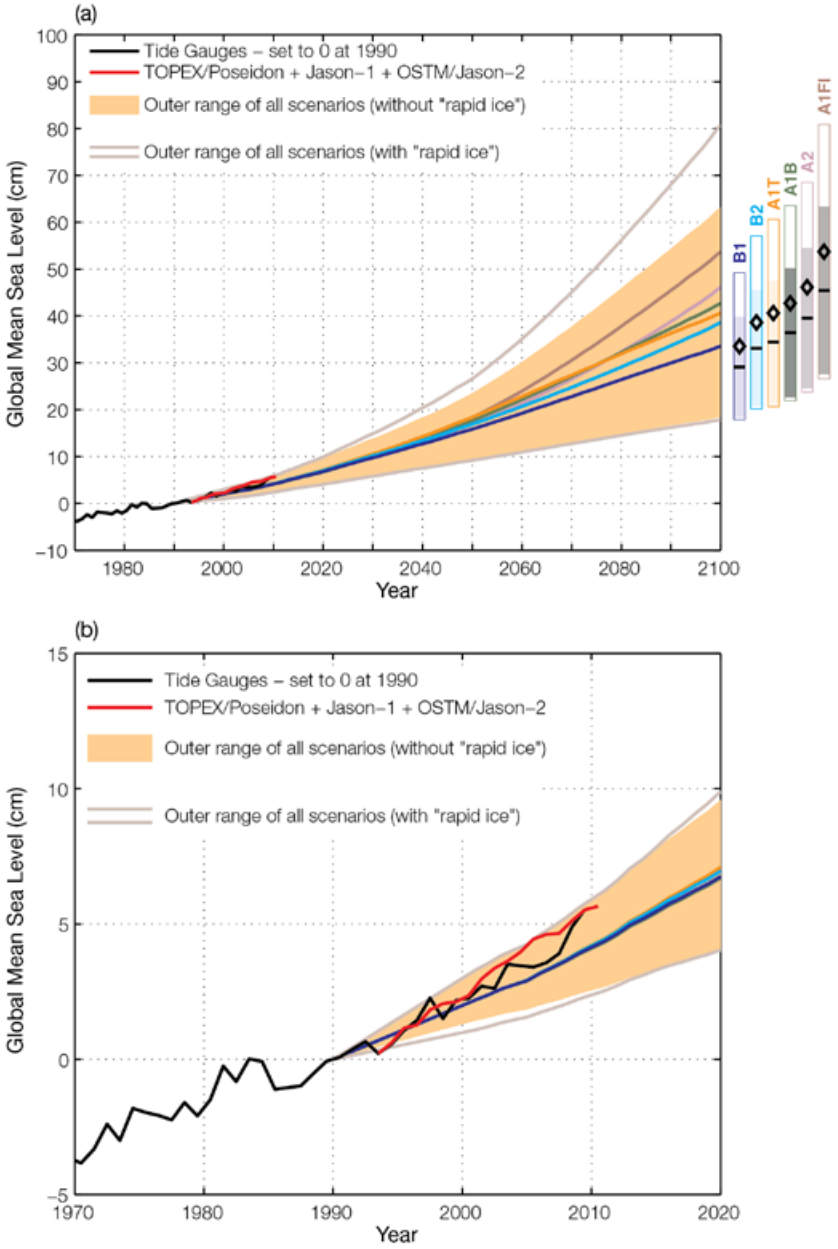

Figure 6.22: Global averaged projections of sea-level rise for six IPCC greenhouse gas emissions scenarios to (a) 2100 and (b) 2020 with respect to 1990. The full range of projections without (with) any rapid ice component is shown by shaded region (outer light lines). The continuous coloured lines from 1990 to 2100 are the central value of the projections including the rapid ice contribution. The bars at the right in (a) are the range of projections in 2100 for the various named scenarios. The horizontal lines (diamonds) in the bars are the central values without (with) the rapid ice sheet contribution. The observational estimates of global averaged sea level estimated from tide gauges and the satellite altimeter data are shown in black and red respectively. The tide gauge data is set to zero at the start of the projections in 1990 and the altimeter data is set equal to the tide gauge data at the start of the record in 1993. The projections are based on the IPCC Fourth Assessment results. From Church et al. (2011).

Table 6.2: The IPCC Fourth Assessment projections of global average sea-level rise during the 21st century and its components under six IPCC emissions scenarios. The upper row in each pair gives the 5 to 95% range (m) of the rise in sea level between 1980–1999 and 2090–2099. The lower row in each pair gives the range of the rate of sea-level rise (mm per year) during 2090–2099. The land ice sum comprises glaciers and ice caps and ice sheets, including dynamics, but excludes the scaled-up ice sheet discharge (see text) which is given separately in line G. The sea-level rise comprises thermal expansion and the land ice sum. Note that for each scenario the lower (upper) bound for sea-level rise is larger (smaller) than the sum of the lower (upper) bounds of the contributions, since the uncertainties of the contributions are largely independent. Reproduced from Meehl et al. (2007b).

		B1		B2		A1B		A1T		A2		A1FI	
A.Thermal expansion	m	0.10	0.24	0.12	0.28	0.13	0.32	0.12	0.30	0.14	0.35	0.17	0.41
	mm/yr	1.1	2.6	1.6	4.0	1.7	4.2	1.3	3.2	2.6	6.3	2.8	6.8
B. Glacial and ice cap	m	0.07	0.14	0.07	0.15	0.08	0.15	0.08	0.15	0.08	0.16	0.08	0.17
	mm/yr	0.5	1.3	0.5	1.5	0.6	1.6	0.5	1.4	0.6	1.9	0.7	2.0
C. Greenland ice sheet surface mass balance	m	0.01	0.05	0.01	0.06	0.01	0.08	0.01	0.07	0.01	0.08	0.02	0.12
	mm/yr	0.2	1.0	0.2	1.5	0.3	1.9	0.2	1.5	0.3	2.8	0.4	3.9
D. Antarctic ice sheet surface mass balance	m	-0.10	-0.02	-0.11	-0.02	-0.12	-0.02	-0.12	-0.02	-0.12	-0.03	-0.14	-0.03
	mm/yr	-1.4	-0.3	-1.7	-0.3	-1.9	-0.4	-1.7	-0.3	-2.3	-0.4	-2.7	-0.5
E = B + C + D.	m	0.04	0.18	0.04	0.19	0.04	0.20	0.04	0.20	0.04	0.20	0.04	0.23
Land ice sum	mm/yr	0.0	1.8	-0.1	2.2	-0.2	2.5	-0.1	2.1	-0.4	3.2	-0.8	4.0
F = A + E.	m	0.18	0.38	0.20	0.43	0.21	0.48	0.20	0.45	0.23	0.51	0.26	0.59
Sea level rise	mm/yr	1.5	3.9	2.1	5.6	2.1	6.0	1.7	4.7	3.0	8.5	3.0	9.7
G. Scaled-up ice sheet discharge	m	0.00	0.09	0.00	0.11	-0.01	0.13	-0.01	0.13	-0.01	0.13	-0.01	0.17
	mm/yr	0.0	1.7	0.0	2.3	0.0	2.6	0.0	2.3	-0.1	3.2	-0.1	3.9

6.5.2 Post-Intergovernmental Panel on Climate Change Fourth Assessment Results

Recent results (since 2007) indicate an increased contribution over the past decade from glaciers and ice caps (Cogley, 2009) and the ice sheets (Velicogna, 2009; Rignot et al., 2011). In particular, discharge from glaciers and ice streams of the Greenland and Antarctic ice sheets are showing signs of a dynamic response, potentially leading to a more rapid rate of rise than can occur from surface melting alone. Using kinematic constraints, Pfeffer et al. (2008) estimated that sea-level rise greater than 2 m by 2100 was physically untenable and that a more plausible estimate was about 80 cm, consistent with the upper end of the IPCC estimates and the present rate of rise. This value still requires a significant acceleration of the ice sheet contributions.

The last two IPCC assessments and recent publications (Rahmstorf et al., 2007; Church et al., 2011; Figure 6.22b) indicate the rate of sea-level rise is currently near the upper limit of the projections (including the scaled-up ice discharge). This does not imply that sea level will continue to follow this upper limit. This observation has raised concern that the IPCC projections may be underestimates, especially given the current inability to adequately model the ice sheets' response to global warming, and has led to the development of several semi-empirical models of sea-level rise (Rahmstorf, 2007; Horton et al., 2008; Grinsted et al., 2009; Vermeer and Rahmstorf, 2009). These semi-empirical models all give larger rates of rise during the 21st century (upper values as high as 1.8 m) than the Fourth Assessment projections. However, significant concerns have been raised about the robustness of these projections on several grounds (Holgate et al., 2007; Schmith et al., 2007; Lowe and Gregory, 2010; Church et al., 2011) and they should be used with caution until these limitations are more fully understood.

A recent comprehensive study exploring high-end climate change scenarios for flood protection in the Netherlands (Vellinga et al., 2009; Katsman et al., in press) did not adopt these semi-empirical models and instead suggested a global-averaged upper-end sea-level rise scenario of 0.55 to 1.1 m by 2100.

Improved understanding of the processes responsible for ice sheet changes are urgently required to improve estimates of the rate and timing of 21st century and longer-term sea-level rise. This understanding is developing rapidly, and early results (Joughin et al., 2010) are consistent with the IPCC Fourth Assessment projections. However, there are not yet robust projections of the dynamic response of the Greenland and Antarctic ice sheets for the 21st century or beyond. The next IPCC report is likely to contain substantially improved assessment of potential ice sheet contributions.

6.5.3 Regional Distribution of Sea-Level Rise During the 21st Century

The regional distribution of sea-level rise is important because it is the regional or local sea-level change and local land motion that most directly impacts society and the environment. Satellite-altimeter data show significant regional variations in the rate of sea-level rise (Figure 3.20), with some regions having experienced substantially larger rates than the global-averaged rate of rise since 1993. However, this regional variation in the relatively short altimeter record is at least partly a result of climate variability, particularly in the equatorial Pacific Ocean.

During the 21st century, there will be two significant reasons for the departure of regional sea-level change from the global averaged rise (Figure 6.23). These are associated with climate and ocean variability and the associated ocean dynamics, and the changing distribution of water on the Earth (Section 4.7). The latter changes the surface loading of the Earth and thus the vertical motion of the surface of the Earth, and also changes the gravitational field thus changing the regional height of the ocean surface.

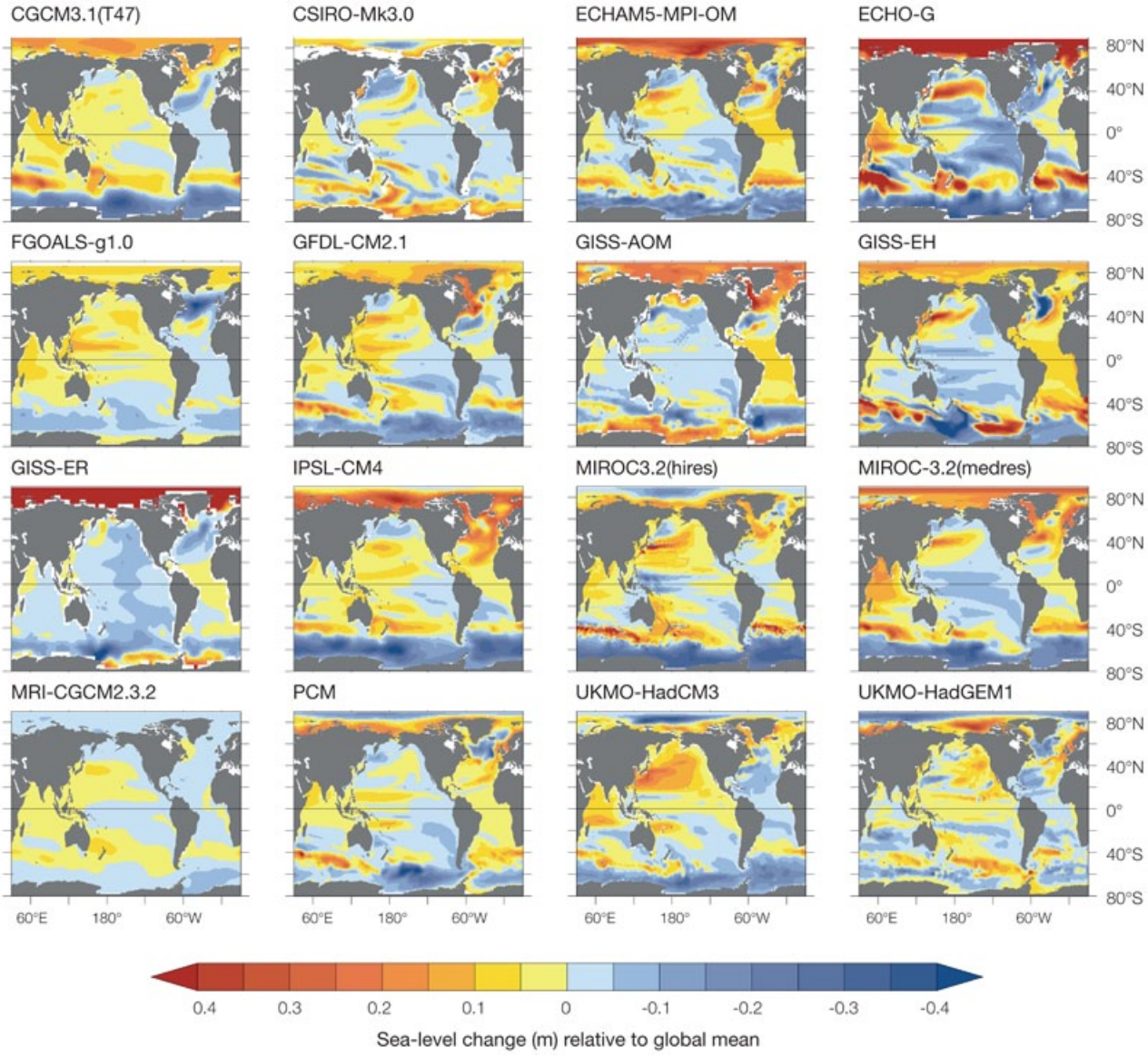

Figure 6.23: The global distribution of sea-level rise (m) in 16 models available from the CMIP3 experiment for the A1B (medium) scenario. The global mean sea-level rise has been subtracted from each panel and the rise is for the 2081–2100 period compared with the 1981–2000 period.

6.5.3.1 Ocean Dynamical Changes

On a global scale, the response of sea-levels to global warming is not spatially uniform (Figures 6.23 and 6.24), with some regions experiencing higher or lower sea-level change than the global average.

The regions where global climate models tend to agree with each other on future sea-level change for the period 2081–2100 compared with 1981–2000 occupy only a small percentage of the globe. However, there are some common features in the model responses. Within the tropical Pacific, two-thirds of the models indicate that sea-level rise is lower than the global-averaged rise in a band running from Papua New Guinea to southern South America, i.e. most of south-easterly trade winds prevailing regions (Figure 6.24). Slightly higher sea-level change can be found in the region east of Australia and in the eastern Indian Ocean. Such regional patterns of sea-level change can be mainly attributed to regional wind-stress changes and the resultant vertical movement of the thermocline, especially the intensification of south-easterly trade winds. Wind stress changes cause a vertical movement of the water column (and hence changes in density) through Ekman dynamics and Rossby wave dynamics (Qiu and Chen, 2006; Timmermann et al., 2010). Wind-stress change can also induce gyre-circulation change, such as the barotropic circulation from Sverdrup theory (Sverdrup, 1947), though such barotropic gyre-circulation change usually has secondary effects on sea-level change, especially in low-latitudes (Lowe and Gregory, 2006). The intensification of south-easterly winds is related to the regional patterns of sea-surface temperature change in the tropical South Pacific with maximum warming on the equator and minimum warming in the south-eastern tropical Pacific. Thus the regional sea-level change in the tropical Pacific is part of complex ocean-atmosphere interaction on climate change time scales, as discussed by Timmermann et al. (2010).

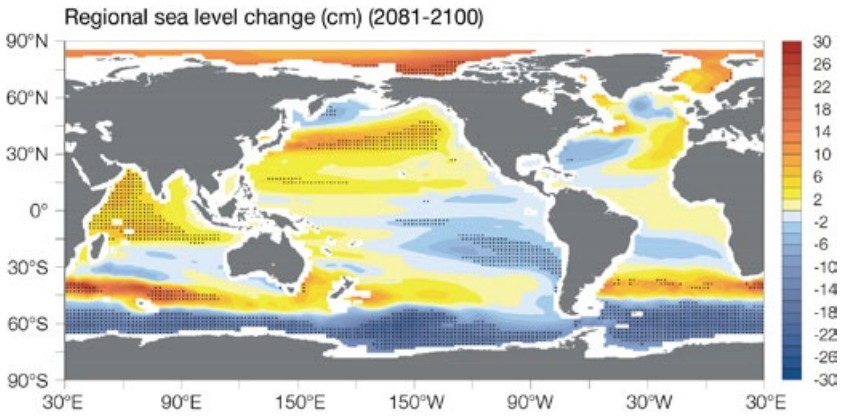

Figure 6.24: The global distribution of regional sea-level change (in cm) due to ocean density and circulation change during 2081–2100 relative to 1981–2000, derived from 13 available CMIP3 models subjected to the A1B (medium) scenario. The global mean is removed, thus positive (negative) values indicate higher (lower) local sea-level change than global average. Stippling denotes that regions where climate models tend to agree, defined as the regions where the magnitude of multi-model mean exceeds the inter-model standard deviation.

The spatial standard deviation (relative to the global average) of multi-model mean of sea-level change relative to period 1981–2000 under the A1B (medium) scenario is 0.032, 0.056 and 0.083 metres globally for the periods 2021–2040, 2046–2065 and 2081–2100, respectively (refer to Figure 6.25 for tropical Pacific), which implies the spatial variability in the pattern of regional sea-level change increases over the next 100 years (Pardeans et al., 2010; Yin et al., 2010).

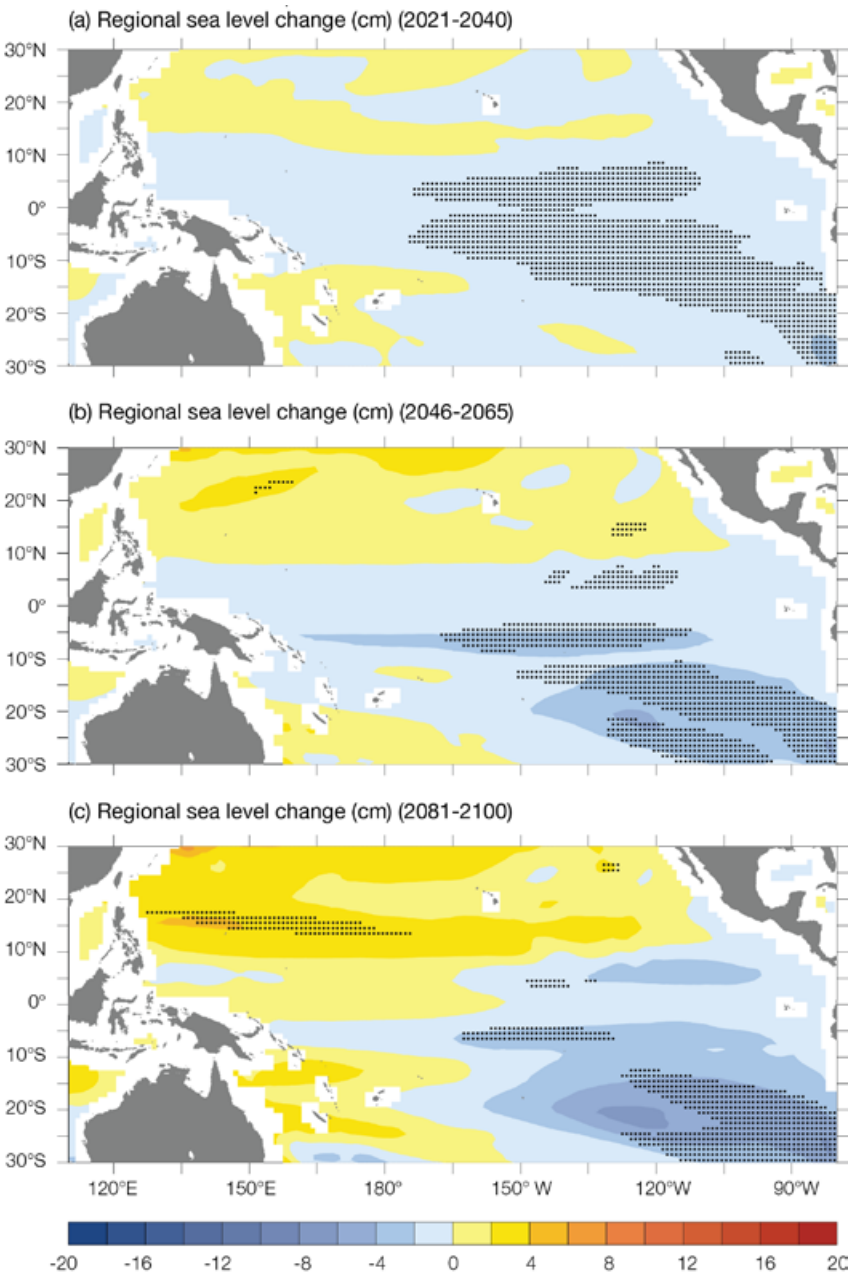

Figure 6.25: Regional sea-level change (in cm) for the PCCSP region due to ocean density and circulation change during (a) 2021–2040, (b) 2046–2065 and (c) 2081–2100 relative to 1981–2000, derived from 13 available CMIP3 models subjected to the A1B (medium) scenario. The global mean is removed, thus positive (negative) values indicate higher (lower) local sea-level change than global average. Stippling denotes regions where climate models tend to agree, defined as the regions where the magnitude of multi-model mean exceeds the inter-model standard deviation.

Regional dynamic sea-level change patterns simulated by CMIP3 climate models can be mostly explained by regional steric sea-level change calculated over the full ocean depth (Figure 6.26). Steric sea-level change is derived from the vertical integral of sea water density change, which can be further divided into a thermosteric component (i.e. associated with temperature change) and halosteric component (i.e. associated with salinity change). For global mean steric sea-level change, the thermosteric component plays a dominant role, while the halosteric component has a minor role (Church et al., 2010). Nonetheless, both components have comparable effects in regional sea-level change distributions, and tend to compensate each other in many regions (Figure 6.26; Yin et al., 2010). Though thermosteric sea-level change is positive almost everywhere (Landerer et al., 2007), thermal expansion in the tropical Pacific is generally less than the global average, by about -4 to -6 cm (Figure 6.26). Both the global hydrological cycle change and ocean circulation change (especially the Atlantic Meridional Overturning Circulation) redistribute salt among different basins and thus lead to halosteric sea-level change (Yin et al., 2010). The tropical and North Pacific are projected to be fresher and have a halosteric sea-level change of about +4 to +6 cm (Figure 6.26). However, while progress is being made, there is still insufficient understanding of what controls the regional pattern of steric sea-level rise.

Superimposed on the long-term trends in sea level are interannual and decadal variations (as discussed in Chapter 3) which will continue into the future. Coastal communities will be impacted by the combination of the long-term sea-level rise, the natural variability in sea level and of course extreme sea-level events caused by storms and waves.

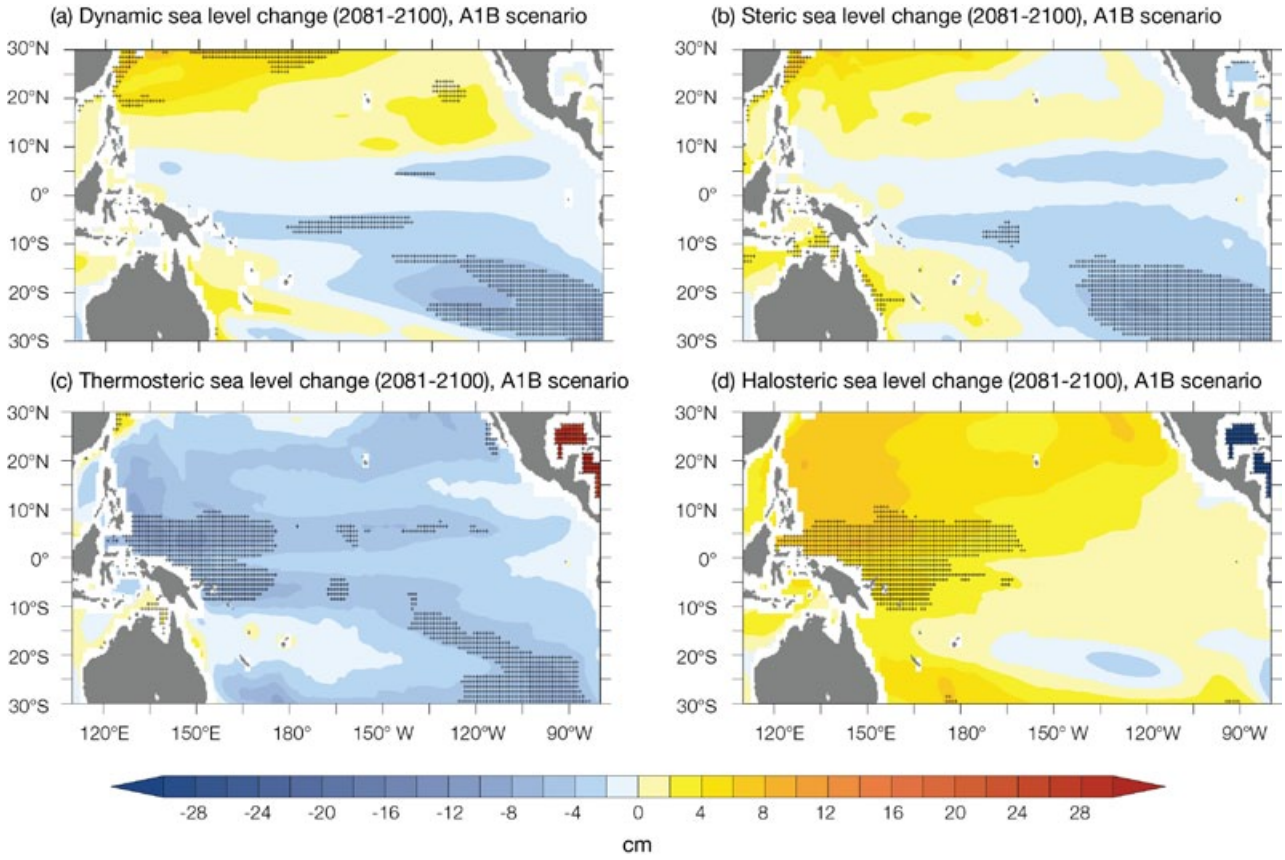

Figure 6.26: (a) Regional dynamic sea-level change (in cm) for the PCCSP region due to ocean density and circulation change during 2081–2100 relative to 1981–2000, derived from 13 available CMIP3 models subjected to the A1B (medium) scenario. (b) Steric (c) thermosteric and (d) halosteric sea-level change (in cm) over full ocean depth during 2081–2100 relative to 1981–2000, derived from 11 available CMIP3 models subjected to the A1B (medium) scenario. The global mean is removed from each panel, thus positive (negative) values indicate higher (lower) local sea-level change than global average. Stippling denotes that regions where climate models tend to agree, defined as the regions where the magnitude of multi-model mean exceeds the inter-model standard deviation.

6.5.3.2 Ocean Mass Changes

In addition to changes in ocean conditions, changes in the mass of the ice sheets (and glaciers and ice caps) also influence the regional distribution of sea-level rise through corresponding changes in the Earth's gravitational field and the elastic movement of the Earth's crust, called sea-level fingerprints (Mitrovica et al., 2001, 2009). As a result, the contribution from the ice sheets implies a lower relative sea level near decaying ice sheets (Greenland and the West Antarctic ice sheets) and a larger than the globally averaged rise (up to about 20–30%) far from the decaying ice sheets. Gomez et al. (2010) demonstrates that these regional distributions may be an important stabilisation factor for the ice sheets because of a local sea-level fall. Ice sheet contributions to future sea-level rise may have a disproportionate impact in some far-field regions. Indeed, in the PCCSP region, contributions from the glaciers and ice caps, and the Greenland and Antarctic ice sheets are all about 20% above the global average rise from each of these contributions (Mitrovica et al., 2001, 2009).

6.5.3.3 Total Regional Sea Level Change

In various studies, the global averaged sea-level rise has been combined with the ocean dynamical response and these regional fingerprints make regional projections of sea-level rise for particular regions (Katsman et al., in press) and worldwide (Kopp et al., 2010; Slangen et al., 2010).

PCCSP scientists have combined global averaged sea-level rise from coupled atmosphere-ocean models with the regional changes resulting from ocean dynamics and mass redistribution and regional fingerprints to estimate the total regional sea-level change for the tropical and sub-tropical Pacific region for the A1B (medium) emissions scenario. The small local ongoing response of the solid Earth to changes since the last glacial maximum has not been included (Church et al., 2011; Figure 6.27). The glacier and ice sheet fingerprint was calculated assuming that the spatial pattern of mass loss to the ocean in the 21st century had a similar pattern to that from 1993 to 2007 (Cogley, 2009). The surface mass balance changes over Greenland and Antarctica were assumed uniform.

One-third of the rapid ice contribution was assumed to come from Greenland and two-thirds from the West Antarctic ice sheet. The total projections of sea-level change (Figure 6.27) are non-uniform with a slightly above global average rise in the western Pacific and Indian Oceans and in a band extending around the oceans at about latitude 40°S. For the PCCSP region (Figure 6.28), the less than global average ocean dynamical sea-level rise and the larger than average sea-level rise as a result of the gravitational/elastic responses counteract such that the total sea-level rise is similar to the global average. Similar patterns are calculated for other greenhouse gas scenarios and time frames.

In addition to the regional changes associated with present day changes in mass there are ongoing changes in relative sea level associated with changes in surface loading over the last glacial cycle (glacial isostatic adjustment) and local tectonic motions. The glacial isostatic motions are relatively small for the PCCSP region.

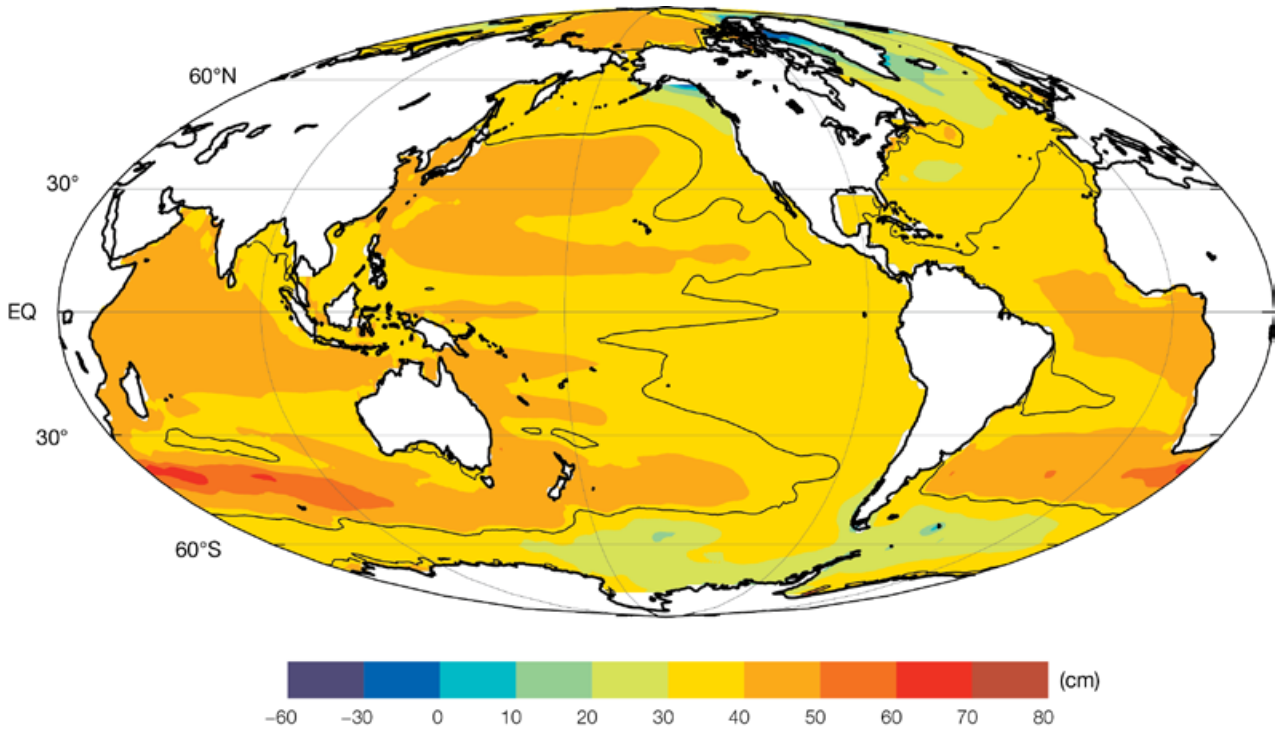

Figure 6.27: The regional distribution of the projections of sea-level change for 2090 compared to 1990, combining the global average sea-level projections, the dynamic ocean departure from the global average and the regional changes associated with the changing mass distribution in the cryosphere for the A1B (medium) scenario. The black contour is the average value at 2090 of 38 cm dividing those regions with above and below average sea-level rise. From Church et al. (2011).

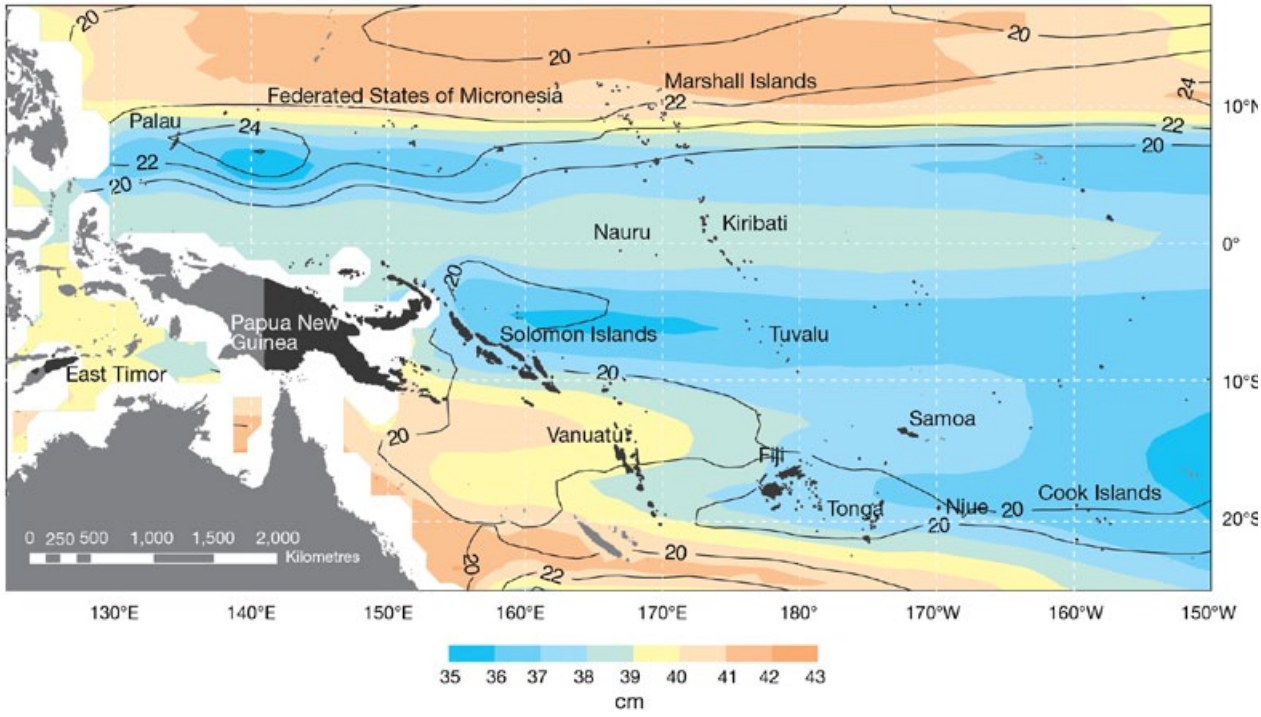

Figure 6.28: The sea-level projections (in cm) for the A1B (medium) emissions scenario in the PCCSP region for 2081–2100 relative to 1981–2000 are indicated by the shading, with the uncertainty indicated by the contours. The distribution of the projections of sea-level change are estimated by combining the global average sea-level projections, the dynamic ocean departure from the global average and the regional changes associated with the changing mass distribution in the cryosphere.

6.5.4 Sea-Level Rise Beyond 2100

It is critically important to recognise that the oceans and the ice sheets take a long time to respond to changes in climate. As a result, sea-level rise will continue for centuries after 2100.

Glaciers and ice caps (outside the polar regions) contain a limited mass of ice (less than about 50 cm of equivalent sea-level rise if they were all to melt (Radic and Hock, 2010)), so their contribution to sea-level rise is limited. However, ocean thermal expansion will continue for centuries, even after greenhouse gas concentrations in the atmosphere have been stabilised, due to the slow transfer of heat from the surface to the deep ocean. The eventual sea-level rise would be dependent on the concentration of greenhouse gases and atmospheric temperatures; climate model simulations suggest of the order of 0.5 m per degree Celsius of global warming (Meehl et al., 2007b).

The Antarctic and Greenland ice sheets are the biggest concerns for longer-term sea-level rise. The area and mass of melt from the Greenland ice sheet (which contains enough water to raise sea level by about 7 m) is increasing. Model simulations indicate that surface melting of the Greenland ice sheet will increase more rapidly than snowfall, leading to a threshold in temperature above which there is an ongoing decay of the Greenland ice sheet over millennia. This threshold is estimated as a global-averaged temperature rise of just 3.1 ± 0.8°C (one standard deviation) above pre-industrial temperatures (Gregory and Huybrechts, 2006). With unmitigated emissions of greenhouse gases, the world is likely to pass this threshold during the 21st century, committing the world to metres of sea-level rise, although from surface melting alone this would take millennia. The Antarctic ice sheet presently experiences little surface melting and its contribution to sea level is dependent on changes in the surface mass balance and the currently uncertain dynamic response.

6.6 Ocean Acidification

Ocean acidification results from the net uptake of CO_2 released to the atmosphere through human activities. The net uptake causes a decline in seawater pH and a decrease in dissolved carbonate ion concentrations (Feely et al., 2004). The decrease in carbonate ion concentrations leads to a lowering of the seawater saturation state of carbonate minerals (Feely et al., 2009), including aragonite, which is the form of calcium carbonate precipitated by reef building corals and many other key reef organisms (Guinotte and Fabry, 2008). Studies indicate that coral growth rates typically decline as the aragonite saturation state of waters decrease with potential to impact the growth of coral reef ecosystems (Langdon and Atkinson, 2005). Other calcifying organisms may also be impacted leading to weaker reef structures (Manzello et al., 2008), greater susceptibility to external stresses like warming (Anthony et al., 2008), and shifts in ecosystems (Hoegh-Guldberg et al., 2008).

Changes in the seawater aragonite saturation state (Figure 6.29) over the 21st century were estimated in the PCCSP region using data from six climate models (CGCM3.1(T47), CNRM-CM3, CSIRO-Mk3.5, GFDL-CM2.0, MIROC3.2 (medres) and UKMO-HadCM3), which are in turn used to drive an offline carbonate chemistry model. The six models are those that had the required projections of salinity and temperature change under low, medium and high emissions scenarios (B1, A1B and A2, respectively). To drive these models three inputs were used: (1) projections of future ocean carbon uptake, (2) empirical relationships between ocean carbonate chemistry and salinity, and (3) projections of temperature and salinity. The future oceanic carbon uptake was derived from projected atmospheric CO_2 concentrations under the different emissions scenarios, observed seasonality in surface partial pressure of CO_2 (Takahashi et al., 2009), and future trends in uptake from the IPSL CM4-LOOP coupled climate carbon model (Marti et al., 2010).

The results show: (1) the key driver for ocean acidification is the atmospheric CO_2 concentration, and the magnitude and rate of ocean acidification is proportional to this concentration; (2) for the first half of this century, the low, medium and high emissions scenarios (B1, A1B and A2, respectively) result in similar atmospheric CO_2 concentrations, and the change in aragonite saturation state for this period is largely independent of the emissions scenario; (3) over the second half of this century, the aragonite saturation state in the entire PCCSP region will continue to decline with the greatest changes occurring under the highest (A2) emission scenario; (4) the lowest values in this century will occur in the eastern equatorial Pacific, to the east of 160°W (the easternmost islands of Kiribati), with the highest values in the region of the South Equatorial Current, between approximately latitudes 5°S and 20°S (Cook Islands, Samoa, Tuvalu).

Marine environments with seawater values of aragonite saturation states greater than 4 are generally considered optimal for coral growth, with values below 3.5 becoming increasingly marginal for sustaining healthy coral growth and reefs (Kleypas et al., 1999; Guinotte et al., 2003). Other calcifying organisms may also be impacted, leading to weaker reef structures (Manzello et al., 2008), greater susceptibility to external stresses like warming (Anthony et al., 2008), and shifts in ecosystems to species more resilient to acidification (Hoegh-Guldberg et al., 2008). As saturation states continue to decline, reef ecosystems could change from conditions of net growth to net dissolution (loss) of carbonate (Silverman et al., 2009).

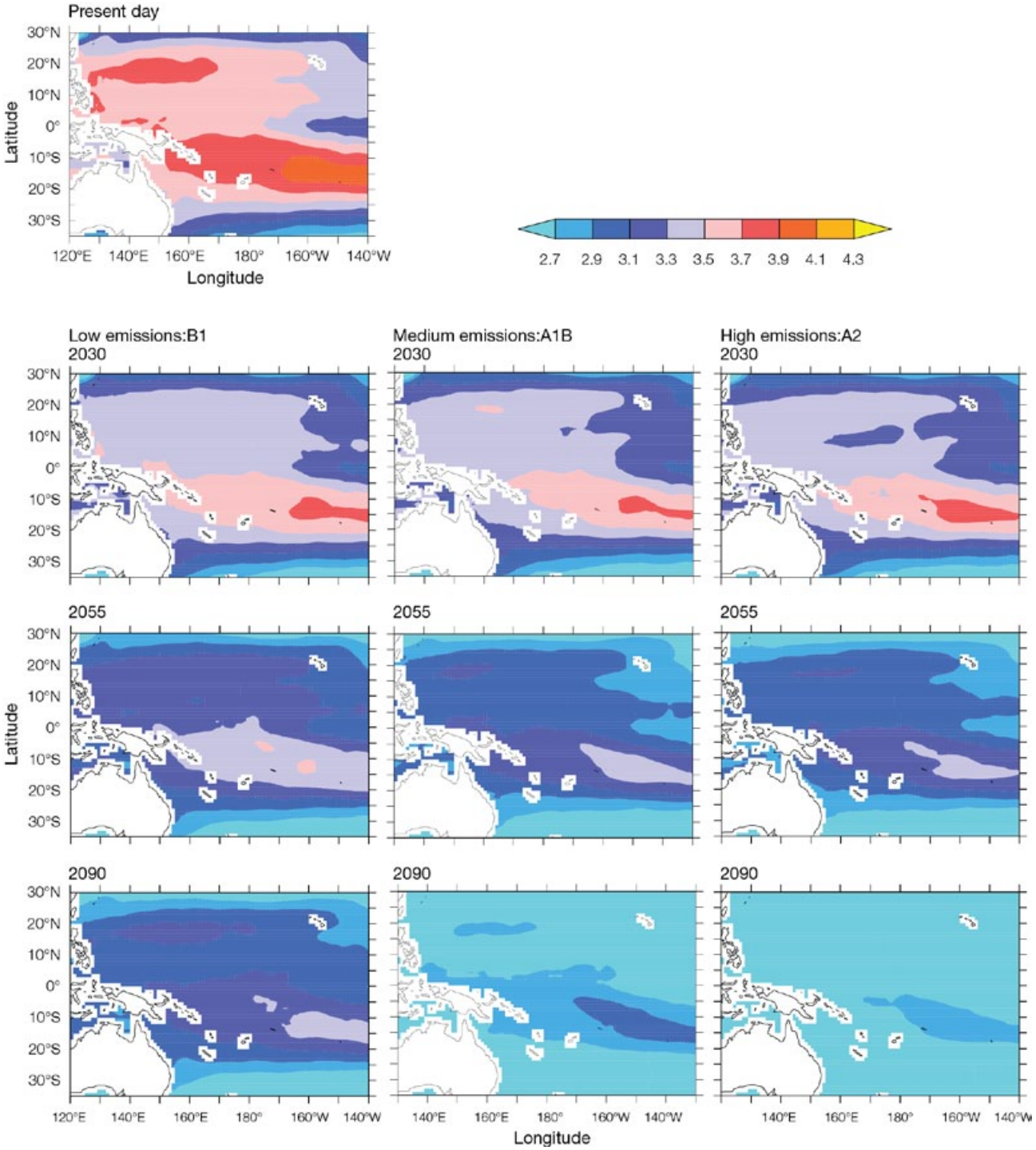

Figure 6.29: The multi-model mean of annual maximum values of aragonite saturation state in surface waters for the present day and in 2030, 2055 and 2090 from six climate models. The B1 (low), A1B (medium) and A2 (high) emissions scenarios are shown.

6.7 Synthesis of Projections

This synthesis of regional projections focuses on multi-model mean changes and may therefore be considered to represent central estimates. For more information at the country-scale regarding the spread of individual model projections, the impact of relevant model deficiencies, physical plausibility, and the consistency of the projections with observed changes over recent decades, see Volume 2. Uncertainties in climate projections are summarised in Box 6.1.

6.7.1 Summary of Atmospheric Projections

Temperature: The projected warming over the PCCSP region is about 70% as large as the global average warming for all emissions scenarios. The projected regional warming is around 0.5–1.0°C by 2030, regardless of the emissions scenario. By 2055, the warming is generally 1.0–1.5°C with regional differences depending on the emissions scenario. By 2090, the warming is generally 1.5–2.0°C for B1 (low) emissions, around 2.0–2.5°C for A1B (medium) emissions, and around 2.5–3.0°C for A2 (high) emissions. Large increases in the incidence of heat waves, extremely hot days and warm nights are also projected.

Rainfall: In the PCCSP region, increases in annual mean rainfall are projected to be most prominent near the SPCZ (affecting the Cook Islands, Fiji, Nauru, Niue, Samoa, the Solomon Islands, Tonga, Tuvalu, Vanuatu and Kiribati) and ITCZ (affecting Federated States of Micronesia, Kiribati, Marshall Islands, Nauru, Palau and Papua New Guinea), with little change in the remainder of the region. The annual numbers of rain days (over 1 mm), light rain days (1–10 mm) and moderate rain days (10–20 mm) are projected to increase near the equator, with little change elsewhere in the region. There is a widespread increase in the number of heavy rain days (20–50 mm). Extreme rainfall events that currently occur once every 20 years on average are generally simulated to occur four times per 20-year period, on average, by 2055 and seven times per 20-year period, on average, by 2090 under the A2 (high) scenario. Droughts are expected to occur less often.

Solar radiation: Consistent with the projected rise in annual mean rainfall throughout much of the PCCSP region, solar radiation is projected to decline due to increased cloudiness. The largest decreases in solar radiation occur near the ITCZ and SPCZ.

Humidity: Little change in relative humidity is projected through most of the PCCSP region. This is because while a warmer atmosphere can hold more water vapour, the amount of water vapour in the air can also be expected to increase due to the essentially unlimited supply of moisture from the vast expanses of ocean in the region.

Wind: Surface wind speed generally decreases in the equatorial and northern parts of the PCCSP region, while increases are indicated in the south, but these changes are projected to be relatively small in most locations. Projected changes in wind direction are very small.

Potential evapotranspiration: Increases in potential evapotranspiration are expected. The ratio of annual average rainfall to potential evapotranspiration decreases in most regions (increased aridity), except near Kiribati, Nauru and Tuvalu where the relatively large projected rainfall increases overwhelm the smaller changes in potential evapotranspiration.

6.7.2 Summary of Ocean Projections

Sea-surface temperature: Increases are expected with maximum warming in the central equatorial Pacific and least warming in the south-eastern Pacific. The West Pacific Warm Pool (defined here as temperatures above 29°C) increases in extent, with the edge of the pool moving many thousands of kilometres east along the equator over coming decades.

Sea-surface salinity: Decreases are expected with regional differences closely matching projected changes in rainfall and evaporation. The intensified warming and freshening at the surface is projected to make the surface ocean become less dense compared to the deep ocean, so the ocean becomes more stratified. This increase in stratification acts to inhibit mixing, thereby reducing the supply of nutrients from the deep to the surface ocean, with consequences for biological productivity.

Sea level: Projections of sea-level rise require consideration of ocean thermal expansion, the melting of glaciers and ice caps, the surface mass balance and dynamic response of the ice sheets of Antarctica and Greenland, and changes in terrestrial water storage. Recent results indicate that global-mean sea-level rise greater than 2 m by 2100 is physically untenable and that a more plausible estimate is about 80 cm, consistent with the upper end of the IPCC estimates and the present rate of rise. Other results suggest a global-averaged upper-end sea-level rise scenario of 0.55 to 1.1 m by 2100. However, improved understanding of the processes responsible for ice sheet changes is urgently required to improve estimates of the rate and timing of 21st century and longer-term sea-level rise. For the PCCSP region, the less than global average ocean dynamical sea-level rise and the larger than average sea-level rise as a result of the gravitational/elastic responses, counteract such that the total sea-level rise is slightly larger than the global average.

Ocean acidification: The projected growth in atmospheric CO_2 concentration is expected to cause further ocean acidification. Aragonite saturation values below 3.5 are projected to become more widespread and increasingly marginal for sustaining healthy coral growth and reefs. The lowest values are projected to occur in the eastern equatorial Pacific to the east of 160°W (the easternmost islands of Kiribati), with the highest values in the region of the South Equatorial Current, between approximately latitudes 5°S and 20°S (Cook Islands, Samoa, Tuvalu).

6.7.3 Summary of Projected Changes in Key Climate Features and Variability

El Niño-Southern Oscillation (ENSO): Year-to-year variability in the region will continue to be largely driven by ENSO. Unfortunately, climate models do not provide consistent projections of changes in the frequency, intensity and patterns of future El Niño and La Niña events. As the climate changes, however, some aspects of the climate experienced in some regions during El Niño and La Niña events may differ from what was experienced in the past. For example, if El Niño tends to warm a particular region, then future El Niño events will tend to be warmer than El Niño events experienced in the past.

Indian Ocean Dipole (IOD): Climate models suggest that a more positive IOD-like mean-state will continue with easterly wind trends and a shallowing thermocline over the eastern Indian Ocean, associated with a weakening of the Walker Circulation. Further research is required to assess the degree of consensus amongst models regarding projected changes in IOD frequency and amplitude.

South Pacific Convergence Zone (SPCZ): In the wet season (November-April), the SPCZ is not expected to shift position, but there is some evidence of an equatorward shift in the dry season (May-October). Increased rainfall is projected within the SPCZ in the wet season in particular, due to increased atmospheric moisture content in a warmer climate. Many models also suggest that the eastern edge of the SPCZ will become drier in the wet season as the trade winds in the south-east Pacific become stronger.

Intertropical Convergence Zone (ITCZ): Changes in rainfall averaged over the ITCZ show a general increase in June-August, with little change in December-February, thereby amplifying the current seasonal cycle. There is an increase in the area of the ITCZ in all models in June-August, and in all but three in December-February. Models suggest the ITCZ may shift equatorward in March-May and June-August, although displacement is small.

West Pacific Monsoon: There is a general tendency for an amplification of the seasonal cycle of rainfall in the West Pacific Monsoon region. Westerly winds over the region show a relatively weak enhancement in December-February, while in June-August there are enhanced westerlies in the Northern Hemisphere contrasting with weaker westerlies in the Southern Hemisphere.

Box 6.1: Climate Projection Uncertainties

- Since it is uncertain how society will evolve over this century, it is difficult to know exactly how anthropogenic emissions of greenhouse gases and aerosols will change. Each of the 40 emission scenarios produced by the IPCC is considered plausible, with the range of uncertainty increasing over the 21st century.
- There are subtle differences between models associated with the representation of key physical processes. These important differences result in a range of climate projections for a given emission scenario.
- While climate models are all based on the same physical laws, they are not perfect representations of the real world. Climate models are not equally skilful in simulating the climate of the Pacific. A rigorous evaluation of the ability of the models to simulate the present climate revealed that while most models are able to capture the broad-scale climate features of the region, a number of deficiencies exist, particularly for tropical rainfall. When a country is located in a region with model deficiencies, less confidence can be placed on climate projections.
- Models differ in their estimates of the strength of different feedbacks in the climate system, particularly cloud feedbacks, oceanic heat uptake and carbon cycle feedbacks.
- Direct and indirect aerosol impacts on the magnitude of the temperature response, on clouds and on precipitation remain uncertain.
- Future changes in the Greenland and Antarctic ice sheet mass are a major source of uncertainty that affect sea-level rise projections.
- Confidence in projections is higher for some variables (e.g. temperature) than for others (e.g. precipitation), and it is higher for larger spatial scales and longer averaging periods.
- Some of the most difficult aspects of understanding and projecting changes in regional climate relate to possible changes in the circulation of the atmosphere and oceans, and their patterns of variability.
- Many important small-scale processes cannot be represented explicitly in models, and so must be included in approximate form as they interact with larger-scale features. This is partly due to limitations in computing power, but also results from limitations in scientific understanding or in the availability of detailed observations of some physical processes.
- Downscaling methods have been specifically developed for the study of regional- and local-scale climate change, but these have advantages and disadvantages.
- When interpreting projected changes in the mean climate, it is important to remember that natural climate variability (e.g. the state of the El Niño-Southern Oscillation) will be superimposed and can cause conditions to vary substantially from the long-term mean from one year to the next, and sometimes from one decade to the next.

Damage caused by Tropical Cyclone Pat, Cook Islands, February 2010.
Photo: National Environment Service, Government of the Cook Islands

Chapter 7
Projections Based on Downscaling

Summary

- Downscaled projections are provided that complement, but do not replace, the projections discussed in Chapter 6.
- The Conformal Cubic Atmospheric Model (CCAM) 60 km downscaled projections for the Pacific Climate Change Science Program region are broadly consistent with those of the global climate models presented in Chapter 6. However, some differences between these and the CCAM projections are noted, such as bands of rainfall decrease around latitudes 8°N and 8°S. These projections are also supported by the additional downscaling results using a variety of other regional climate models.
- The CCAM 8 km downscaled projections show regional-scale variations of the climate change signal, largely related to the topography of Partner Countries.
- Statistical downscaling shows slightly less warming, more consistent with the observed trends.
- Tropical cyclone frequency in the PCCSP region is likely to decrease by the late 21st century. There is a moderate level of confidence in these projections, with little consistency found in the magnitude of the projected changes between either the models or the three analysis methods.
- Most simulations project an increase in the proportion of the most severe storms in the south-west Pacific and a southward movement in the latitude at which maximum intensity occurs.
- Most simulations project an increase in the proportion of storms occurring in the weaker categories in the Northern basin.
- Theory and high-resolution modelling also suggest that climate change may lead to a global increase in tropical cyclone intensity of about 2–11%.
- For the South Pacific, most models indicate a reduction in cyclonic wind hazard north of 20°S and regions of increased hazard south of 20°S. This coincides with the projected increase in the number of tropical cyclones occurring south of 20°S and with a poleward shift in the latitude at which storms are most intense.
- For the North Pacific region (between the equator and 15°N), there is a general reduction in cyclonic wind hazard between the current and future climate simulations as a result of a decrease in storm frequency close to the equator.

7.1 Introduction

This chapter deals with climate projections, including projections for extreme events such as tropical cyclones, based on dynamical and statistical downscaling. The methodologies are described in Chapter 4. Dynamically downscaled projections are presented for the CCAM 60 km simulations. This is followed by projections for Fiji and Papua New Guinea based upon two of the seven CCAM 8 km simulations. In Section 7.3, projections are presented for seven of the 17 sites that were statistically downscaled. Projected changes in tropical cyclones are presented using various techniques in Section 7.4. The results are summarised in Section 7.5.

- Downscaled PCCSP projections are generated using both dynamical and statistical downscaling.
- Dynamically downscaled atmospheric projections are provided at 60 km resolution using changes in sea-surface temperatures from six global climate models (Sections 4.1.2 and 4.3), driven by the A2 (high) emission scenario. Projections for two time periods centred on 2055 and 2090 are provided.
- Additional dynamically downscaled atmospheric projections are provided at 8 km resolution over seven PCCSP country regions each measuring 1000 x 1000 km^2 using CCAM, including changes in sea-surface temperatures from three global climate models, driven by the A2 high emissions scenario (Section 4.3). Projections are provided for two time periods centred on 2055 and 2090.
- Statistically downscaled projections for a total of 17 sites in seven Partner Countries for 2030 are provided. Projections out to 2055 are provided in some instances where observational data are of sufficient quality and length (approximately 40 years).
- Projected changes in tropical cyclones for the PCCSP region are obtained using several methods.
- Details of the methods underpinning the projections presented in this chapter were provided in Chapter 4.

7.2 Dynamical Downscaling

Dynamical downscaling is a methodology for providing more detailed climate projection information for a specific region. The technique uses broad-scale climate data from global climate models as input data for a finer resolution atmospheric model (see detailed discussion in Chapter 4). The main advantage of dynamical downscaling methods is that they rely on physically based modelling techniques similar to those used by the global models, but applied to regional scales (10–100 km). Dynamical downscaling is a process-based approach to how the rainfall, winds and temperatures change as global air temperatures increase. Dynamical methods can also be useful for studying extreme events (e.g. tropical cyclones).

7.2.1 CCAM Downscaling at 60 km Resolution

The first step in dynamical downscaling in this study was to run CCAM with a global grid of 60 km resolution using bias-adjusted sea-surface temperatures from six global climate models for the period 1961–2099. Projections based upon these simulations are presented here and compared with those from the host global models.

7.2.1.1 Surface Air Temperature

The projected changes in near-surface maximum and minimum air temperature (Figure 7.1) are similar to those from the host global models since the changes in the sea-surface temperatures in the simulations using CCAM are the same as those for the global models. In general, the warming across the region is 2–3°C by the end of the 21st century for the A2 (high) emissions scenario, although some regions warm by more than 3°C. Although not shown, the simulation using sea-surface temperatures from the UKMO-HadCM3 model warms the least (around 2.5°C). The simulation using sea-surface temperatures from CSIRO-Mk3.5 warms the most (closer to 3.5°C). The mean maximum temperature change based on the average of all six models shows generally greater warming along the equator in the central and eastern Pacific, as well as over Australia and surrounding oceans, whilst the least warming occurs over the south-eastern

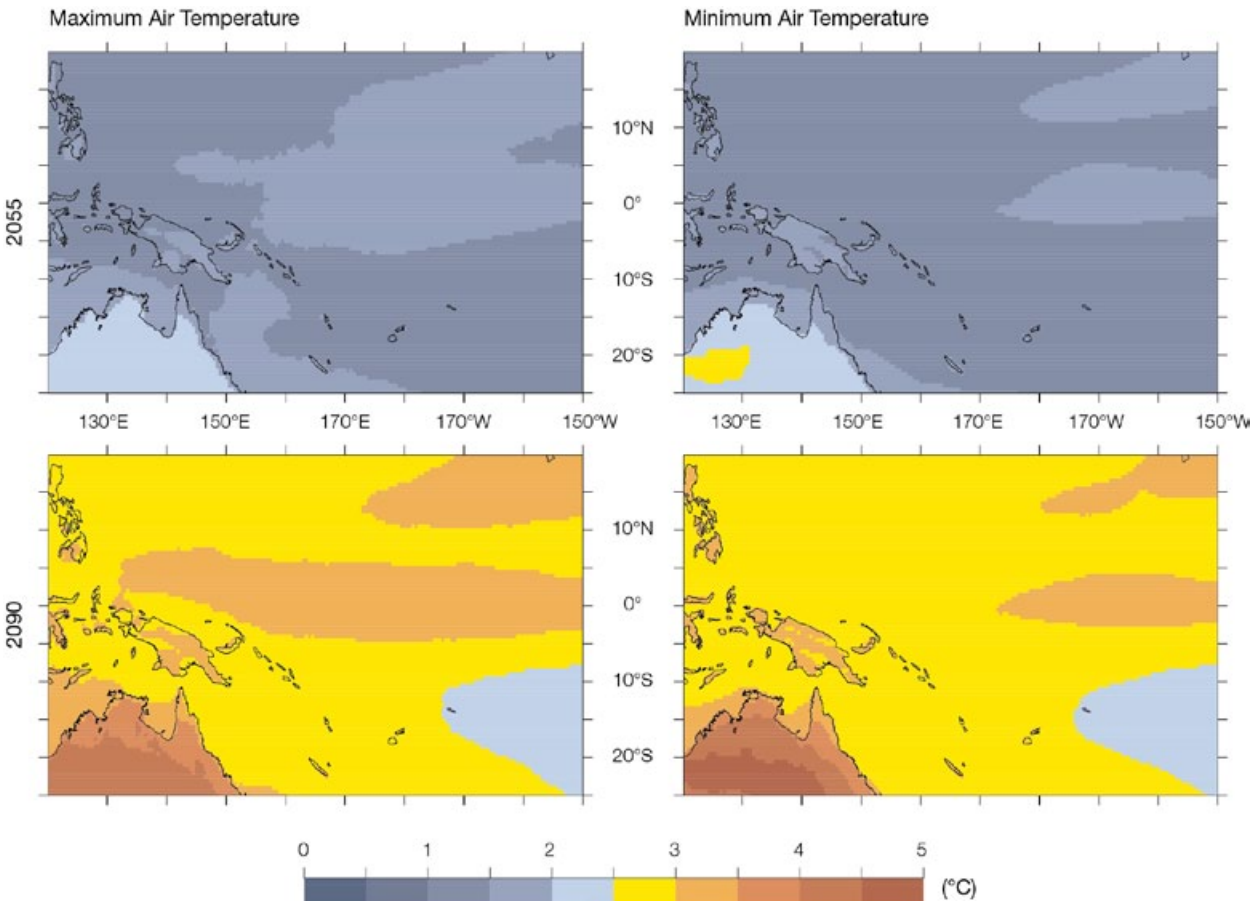

Figure 7.1: Increases in annual maximum near-surface air temperature (°C) (left) and minimum temperature (right) in 2055 (top) and 2090 (bottom) relative to 1990 for the CCAM 60 km multi-model simulations using the A2 (high) emissions scenario.

Pacific. Minimum temperature changes show a similar spatial pattern (see Figure 6.2 for comparison with mean surface-temperature changes in the global models). Also note the increased warming over the better resolved land areas in the downscaled results.

7.2.1.2 Rainfall

Simulations driven by the six host sea-surface temperatures downscaling to 60 km with CCAM (Figure 7.2 for November-April and Figure 7.3 for May-October) show that the broad-scale changes in rainfall are generally similar to those of the host models, with increases along the equator and smaller changes elsewhere. These results suggest a significant influence of the sea-surface temperature changes on the rainfall changes. There is an increase in rainfall of approximately 2–3 mm per day along the equator, with a decrease in rainfall of up to 2 mm per day for latitudes around 8° north and south of the equator. The location and intensity of these changes are different in the host models and the downscaling model. In general, the largest increases in rainfall in the CCAM simulations are closer to the equator, while the greatest increases in the global models tend to be located at about latitude 5°S, especially in the central and eastern portions of the domain. These differences could be related to the downscaling method chosen, which corrects some of the sea-surface temperatures biases in the global models (see discussions in Chapter 4 and Chapter 5).
The decreases in rainfall in the downscaled simulations north and south of the equatorial region also tend to be somewhat larger and cover a much broader area than in the global models, particularly in the period November-April. A possible explanation for the rainfall differences in CCAM and the global models relates to changes in the Hadley Circulation, since with enhanced convection along the equator, there is greater ascent of air. Compensating subsidence to the north and south will tend to suppress the rainfall. In the finer-resolution CCAM simulations, this compensating subsidence appears to be stronger than in the global models. As will be shown later, some of the additional downscaled simulations also show similar rainfall decreases on either side of the equatorial region, which suggest this is related to resolution. This is an area for further research.

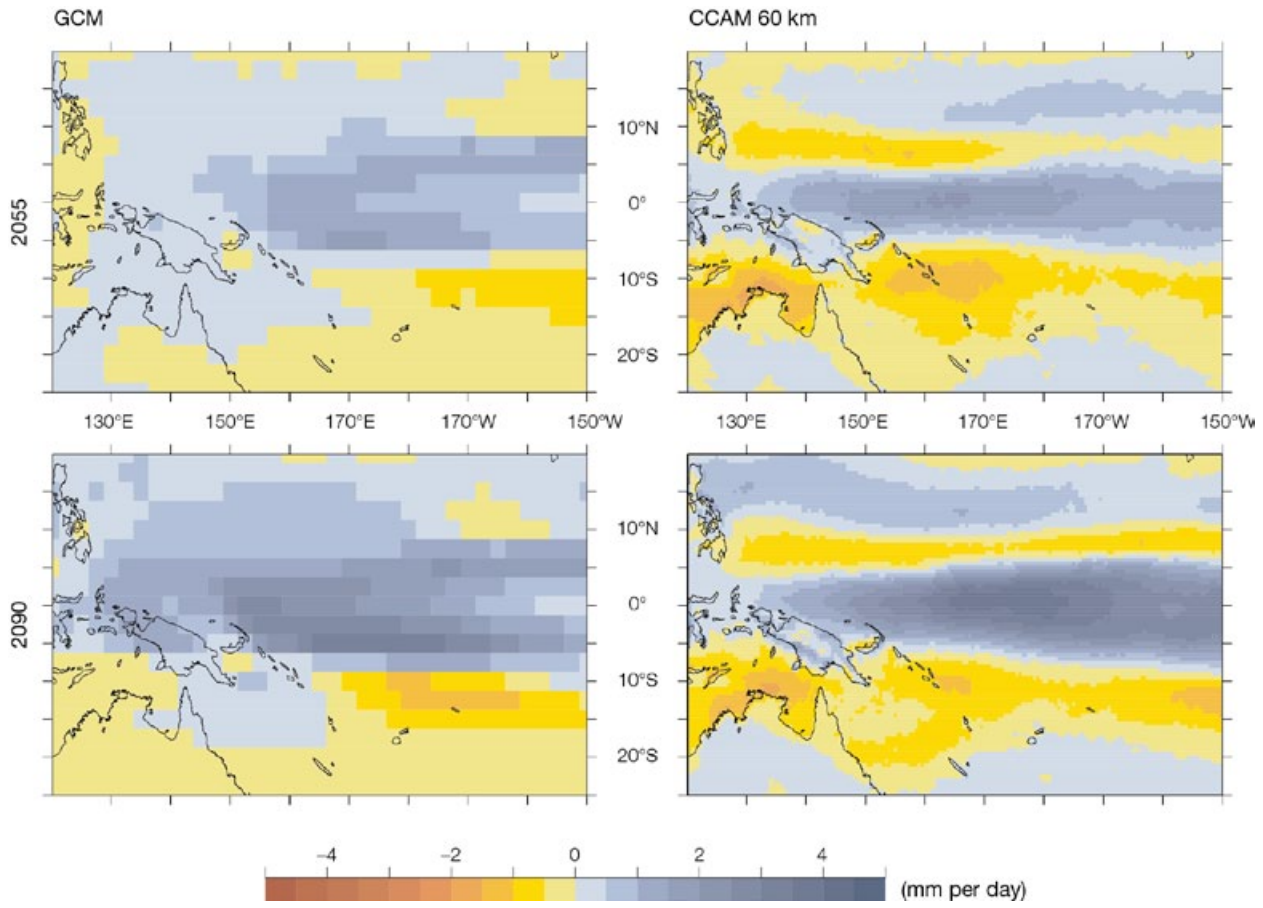

Figure 7.2: Multi-model mean change in November-April rainfall (mm per day) in global climate models (left) and CCAM 60 km simulations (right), each consisting of the same six models, for the period centred on 2055 (top) and 2090 (bottom), relative to 1990, using the A2 (high) emissions scenario.

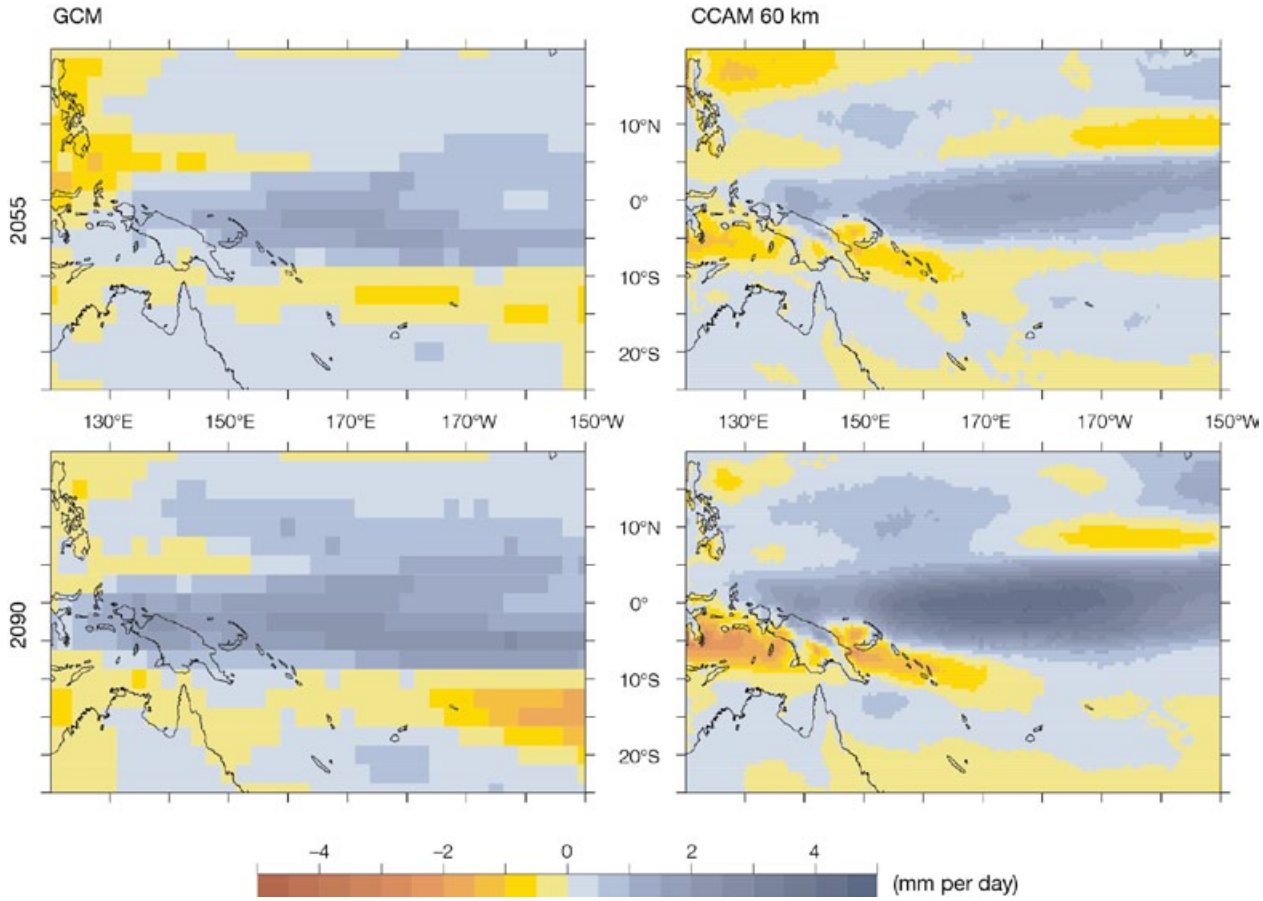

Figure 7.3: Multi-model mean change in May-October rainfall (mm per day) in global climate models (left) and CCAM 60 km simulations (right), each consisting of the six models, for the periods centred on 2055 (top) and 2090 (bottom), relative to 1990, using the A2 (high) emissions scenario.

In order to check the consistency of these rainfall changes among the six downscaled simulations, the annual rainfall changes from 2055 and 2090 were compared (Figure 7.4). As indicated earlier, results show that the largest increases are along the equator, with greater increases by 2090. Bands of rainfall decreases around latitudes 8°N and 8°S are also evident. The six CCAM simulations all agree on the equatorial increase in rainfall due to the greater warming of the sea-surface temperatures along the equator. Most simulations (five out of six) also show a decrease in rainfall in bands to the north and south of this increase. While the global models show a similar equatorial increase, they tend not to show the decreases to the north and south (Chapter 6).

The changes in rainfall along the South Pacific Convergence Zone (SPCZ) are small, though there is some agreement in decreases around Vanuatu and over the south central Pacific. Rainfall decreases are evident over the oceans north of Australia and East Timor, and are very consistent across all the downscaled results.

7.2.1.3 Surface Wind Speed

CCAM simulations of the projected change in wind speed (at 10 m above the surface) over the PCCSP region (Figure 7.5) do not indicate a major change in wind speed by the end of the 21st century, with a projected reduction in wind speed of less than 1 metre per second on average. The magnitude of wind speed decreases is 0.5 metre per second in south-western regions. The MIROC3.2 (medres)-based CCAM simulation shows the greatest increases, but this model is considered unreliable in the SPCZ and West Pacific Monsoon regions. The general pattern of wind speed change is similar to the global climate models (Figure 6.5), although increases south of the equator are slightly less than for the global models.

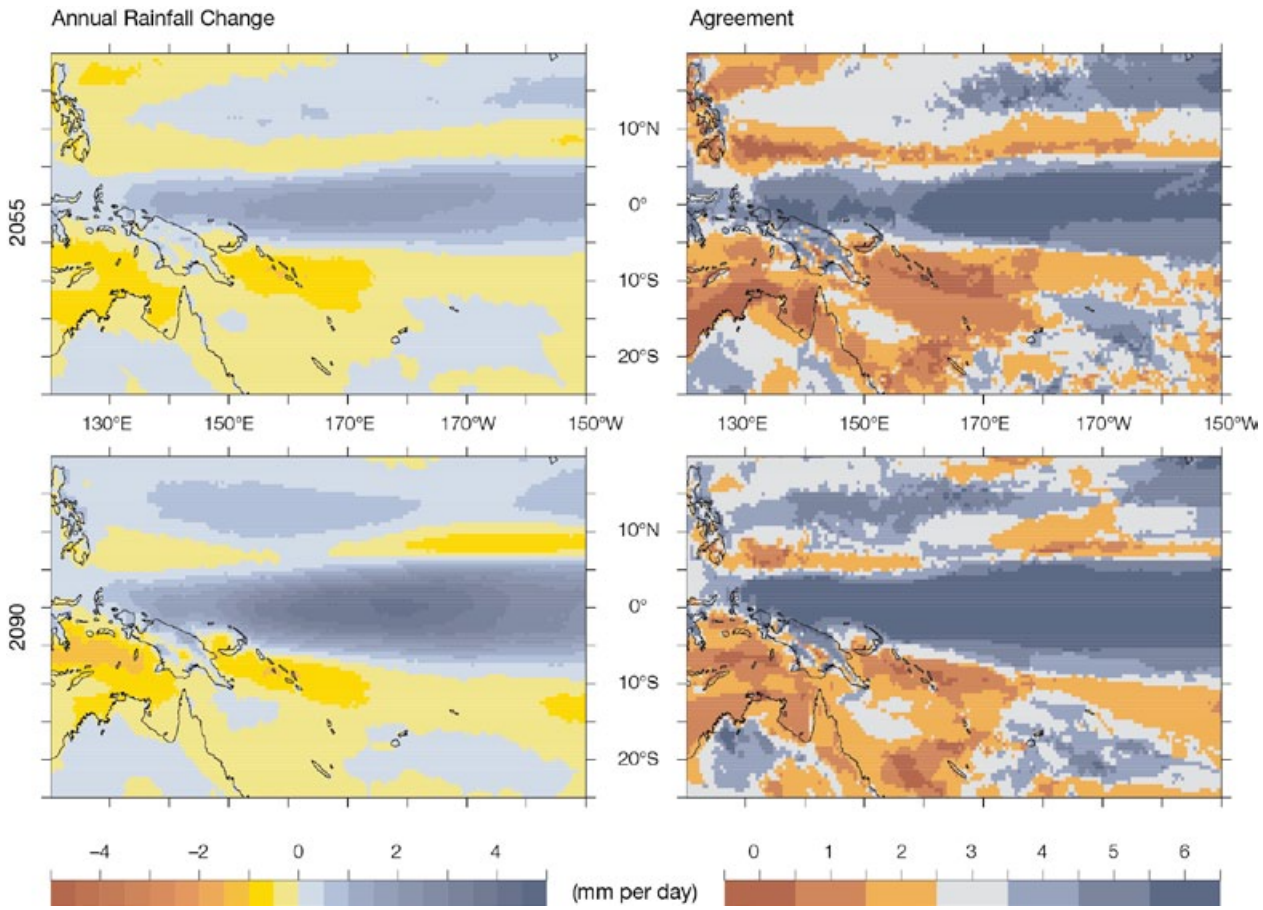

Figure 7.4: Annual change in rainfall (mm per day) between the periods centred on 2055 (top left) and 2090 (bottom left) relative to 1990, and the agreement on an increase in the six CCAM simulations for the same two periods (right top and bottom). 0 means all models show a decrease, 6 means all show an increase.

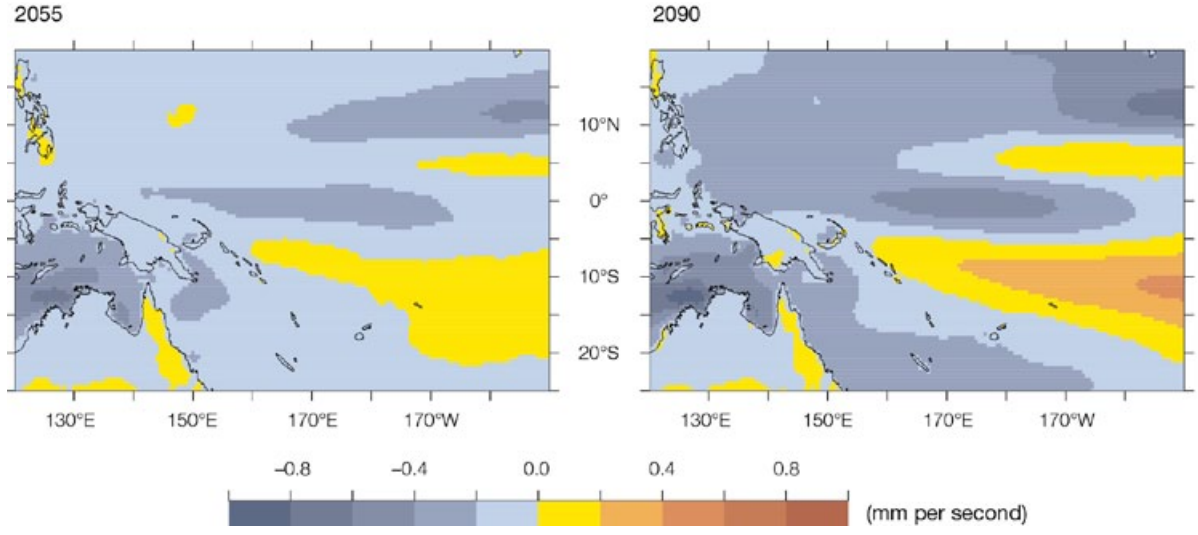

Figure 7.5: Mean change in annual 10 m wind speed (metres per second) between the periods centred on 2055 (left) and 2090 (right) relative to 1990 (from the multi-model mean of the six CCAM 60 km simulations, for the A2 (high) emissions scenario).

7.2.1.4 Heavy Rainfall

Projected changes in number of days per year with heavy rainfall (that is, days with daily rainfall between 20 and 50 mm) by 2090 are given in Figure 7.6. There are increases along the equator in the multi-model means of all of the global climate models, as well as for the five global models with daily data that were downscaled and the six CCAM 60 km simulations. The mean of all global climate models shows increases of 5-10 days per year, while the 5-global model mean has increases of up to 20 days per year near Vanuatu and Papua New Guinea. The pattern of change is similar for the two sets of global model simulations, with one band of increase south of the equator near 5°S and another band near 5°N. The CCAM 60 km simulations show much larger increases in number of heavy rainfall days (more than 35 days per year in some areas), and the locations are more centred on the equator. In addition, there are decreases (more than 10 days per year) near Vanuatu and north of Australia.

7.2.2 CCAM Projections Downscaled to 8 km Resolution

Three of the CCAM 60 km simulations (driven by sea-surface temperatures from host global climate models ECHAM5, HADCM3, and GFDL2.1) for the A2 (high) emissions scenario were further downscaled to 8 km resolution over seven regions, each measuring approximately 1000 x 1000 km^2. This was conducted to assess the impact of the finer resolution downscaled results on the projected changes. Two 20-year time periods were completed, centred respectively on 2055 and 2090, and compared to the 20-year period centred on 1990. The seven regions selected were Papua New Guinea, East Timor, Fiji, Solomon Islands, Vanuatu, Samoa and the Federated States of Micronesia. In the next section, summary results for two regions are examined; more detailed assessment and results for the other regions will be presented in a future technical report.

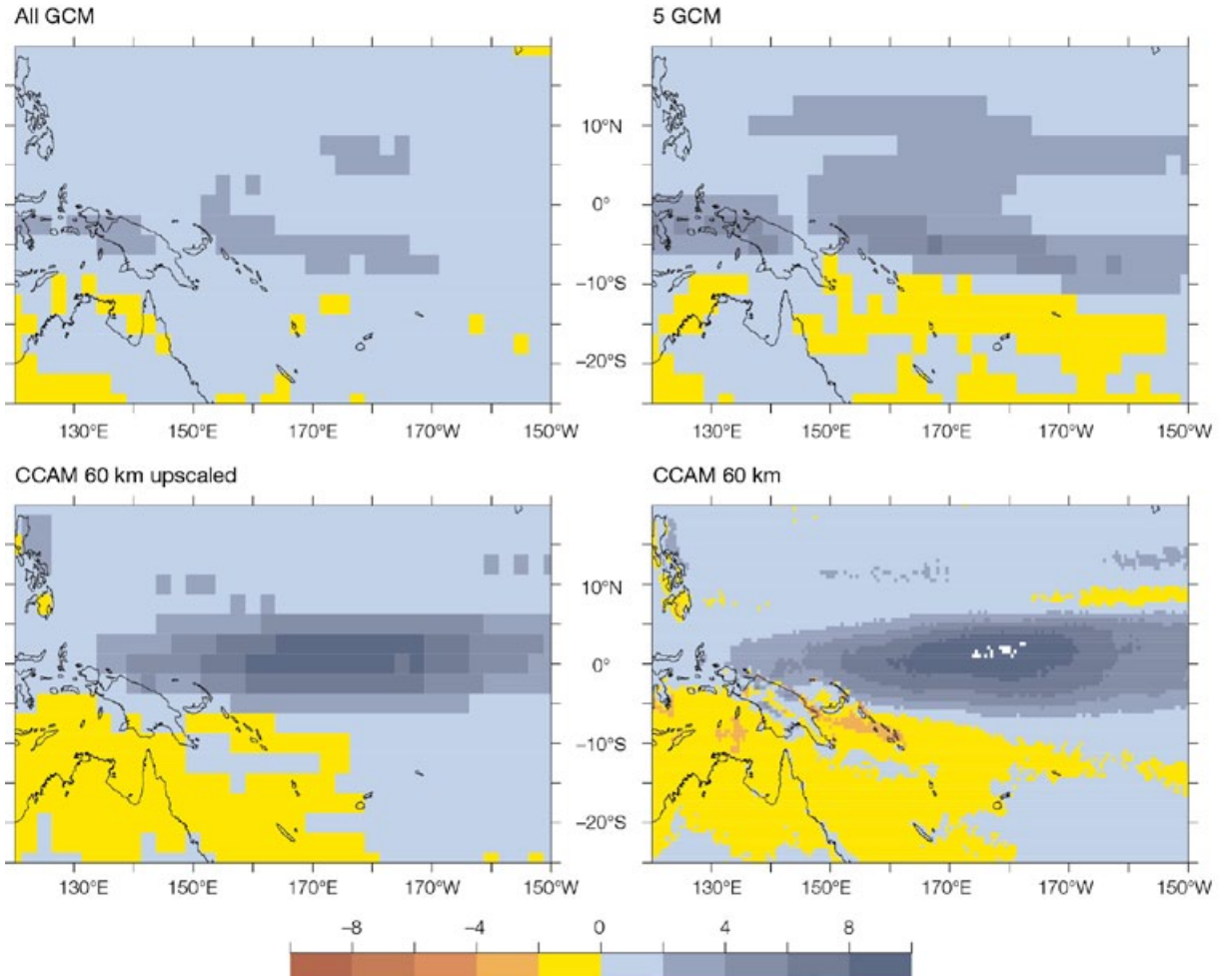

Figure 7.6: Change in number of heavy rain days between 2090 and 1990 using multi-model means of all global climate models (top left), five global models used for downscaling with daily data (top right) and CCAM 60 km simulations. Upscaled (bottom left) and on original grid (bottom right).

7.2.2.1 Detailed Analysis of Two Regions at 8 km Resolution

In this section, two regions are analysed in order to explore any improvement in the detail of local projections, particularly over mountainous areas (Section 4.5.2). Papua New Guinea was chosen since this region has the most varied and mountainous topography. Fiji was also selected since it has some mountainous topography and is of moderate size for a Pacific Island nation. In addition, two stations on Fiji with observational data available are further analysed. The following results need to be treated with caution because they are based on a very limited sample of global climate models and only one dynamical downscaling model.

Over Fiji, the downscaled 8 km simulations show maximum temperature increases of 2–2.5°C over the ocean (Figure 7.7), with greater warming over the land (up to 3–3.5°C over the western side of Viti Levu, the south-west island) in May-October. In November-April, the maximum temperature increase is 2.5–3°C. Minimum temperatures increase similarly (2–2.5°C in May-October and 2.5–3°C in November-April), with around 0.5°C greater warming evident over the land.

The projected rainfall changes show increases of 0.5–1 mm per day in May-October (Figure 7.7), with greater increases (up to 1.5 mm per day) along the eastern side of the islands. Rainfall decreases of 0.5–1 mm per day are evident in November-April, especially along the southern and eastern side of the islands. In addition, there is some increase in rainfall over the north-west side of Viti Levu.

Over Papua New Guinea during May-October, the maximum temperature increase is around 2.5°C over the ocean (Figure 7.8) and 3–4°C over the land. In November-April, the ocean warms 2.5°C while the land warms 3.5–4°C. Minimum temperatures increase around 2.5°C over the oceans and around 3°C over land in May-October and 2.5–3°C over the oceans and 3–3.5°C over land in November-April.

The projected rainfall changes for Papua New Guinea (Figure 7.8) show a complicated pattern related to the topography. There are rainfall increases over the ocean to the north and south of Papua New Guinea, and some decreases between Papua New Guinea and New Britain. Over land, the projected rainfall increases are along the northern slopes of the mountain ranges, with some decreases on the southern sides. There are general projected decreases of rainfall across the region in May-October, apart from some increases along the mountain ranges.

These results demonstrate the added information that dynamical downscaling provides. The high resolution (8 km) simulations can capture some of the effects of the topography and land-sea contrast on the climate projections. As seen in the temperature projections, the greater warming over land versus the oceans is captured. Spatial variations in the projected rainfall changes are also evident. (For further discussion of how downscaling can add value to coarser resolution models, see Corney et al., 2010; Frauke et. al., 2011; Kanamitsu and DeHann, 2011; Rockel et. al., 2008.)

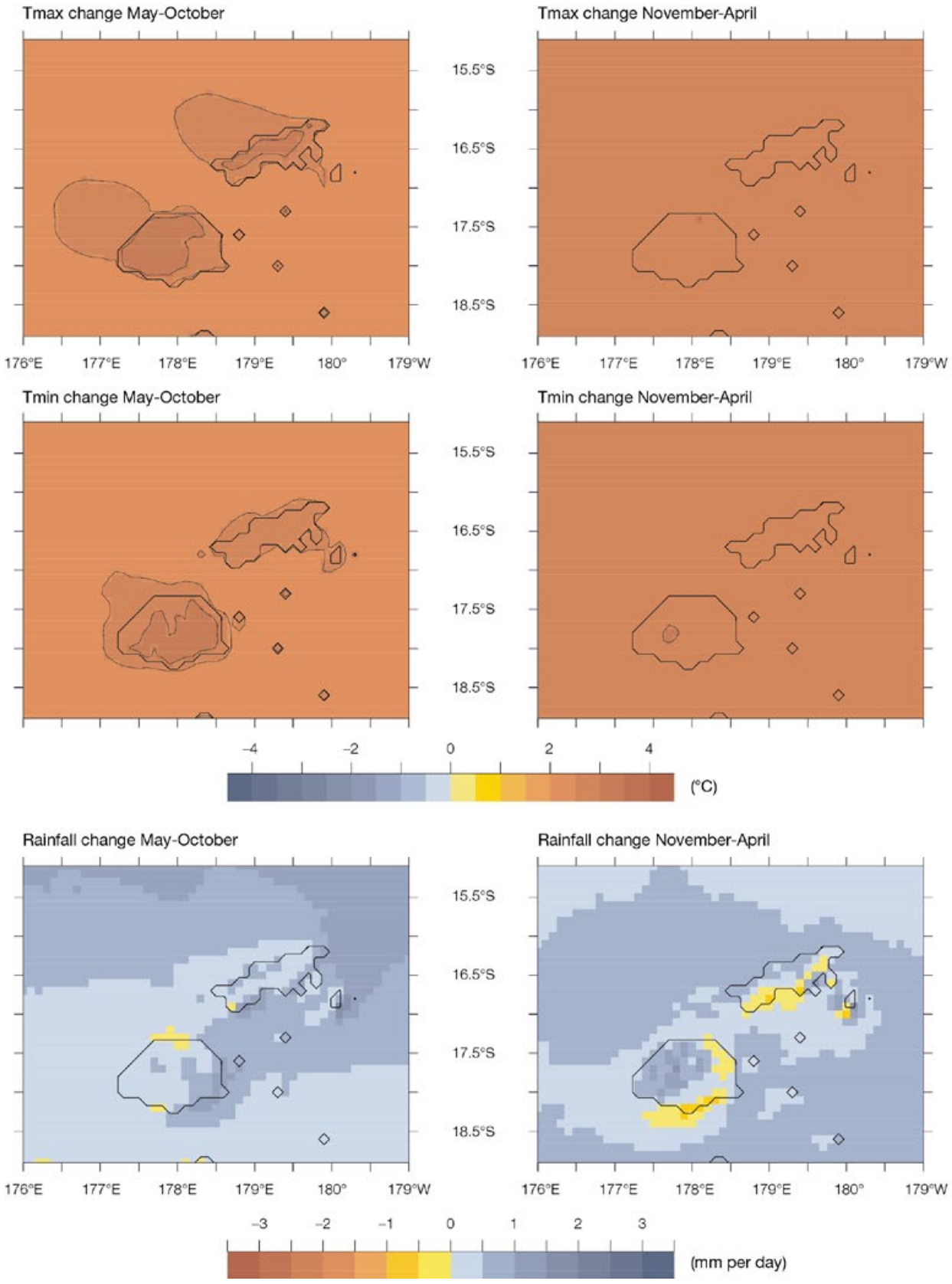

Figure 7.7: Projected temperature and rainfall changes for Fiji in 2090 relative to 1990 from CCAM 8 km multi-model mean simulations, for the A2 (high) emissions scenario. Left panels are May-October and right panels are November-April. Top row is changes in maximum surface air temperature (°C), middle row is changes in minimum surface air temperature (°C) and bottom row is changes in mean rainfall (mm per day).

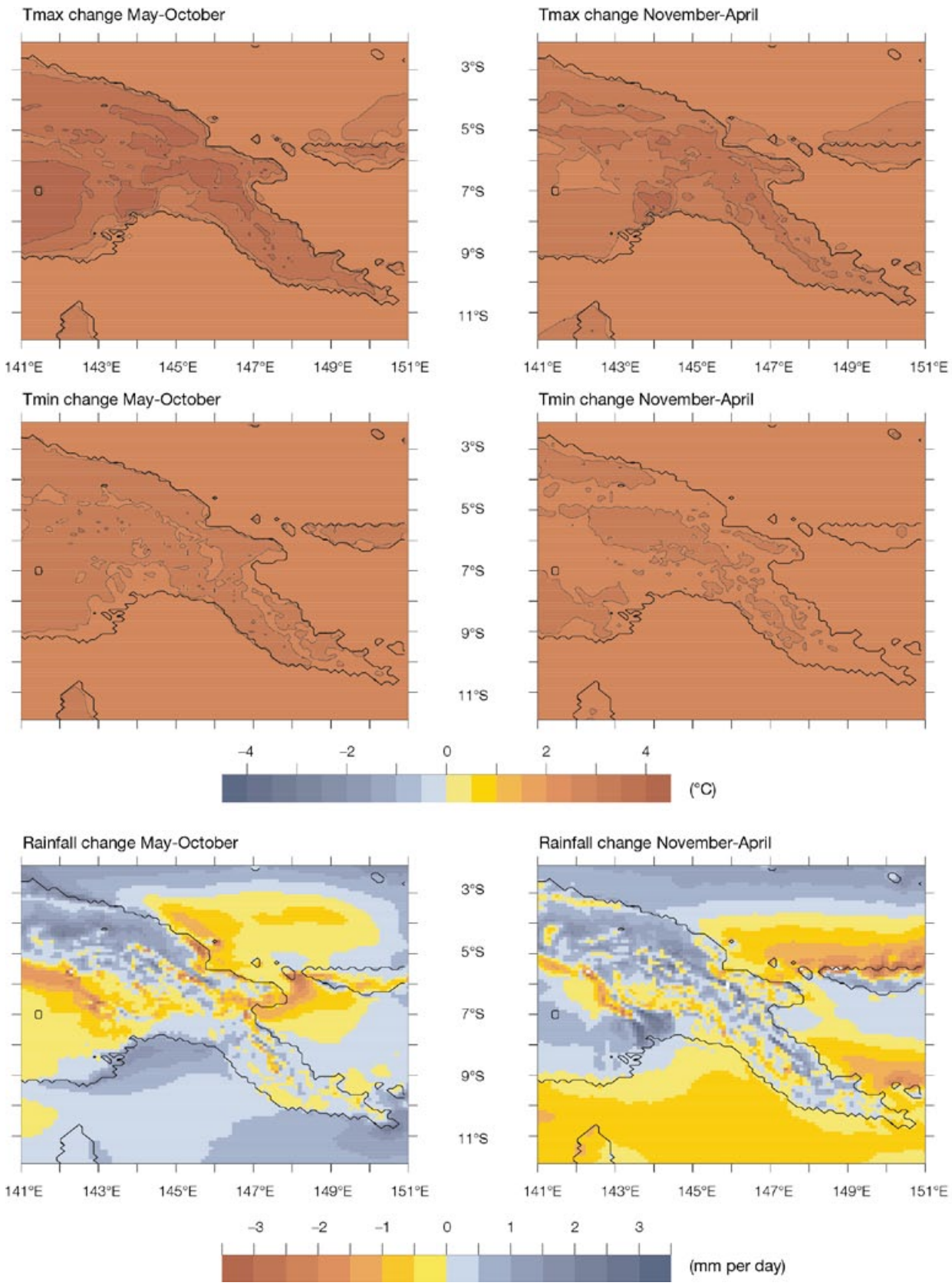

Figure 7.8: Projected changes in temperature and rainfall for Papua New Guinea in 2090 relative to 1990 from CCAM 8 km multi-model mean simulations, for the A2 (high) emissions scenario. Left panels are May-October and right panels are November-April. Top row is changes in maximum surface air temperature (°C), middle row is changes in minimum surface air temperature (°C) and bottom row is changes in rainfall (mm per day).

7.2.2.2 Seasonal Temperature and Rainfall Changes at Selected Locations

Changes in seasonal rainfall and temperature can also be significant. The comparison of changes in temperature and rainfall for Nadi, Fiji for the global climate models, CCAM 60 km simulations, and CCAM 8 km simulations are presented in Figure 7.9. As was indicated in Figure 7.7, which covers all of Fiji, the temperature increases about 1.5°C by 2055 and by 2.5–3°C by 2090. There are slightly greater temperature increases in the middle of the year, most noticeably in the 8 km simulations, where increases are around 3.5°C.

There are only slight rainfall changes by 2055 in the global climate models and the CCAM 60 km results. The 8 km simulations show small increases at Nadi throughout most of the year. By the end of the century, all simulations show rainfall increases in the first half of the year, with greater increases in the 8 km simulations than in the 60 km simulations. The second half of the year shows little change in rainfall (Figure 7.9, lower right).

The seasonal changes in temperature and rainfall for Nausori, Fiji are presented in Figure 7.10. As was indicated in Figure 7.7, the temperature warms about 1.5°C by 2055 and by 2.5–3°C by 2090. There is slightly greater warming in the first half of the year (nearing 3°C) while warming is only 2.5°C later in the year. Note that the changes for the global models are similar for Nadi and Nausori, since they are separated by just over 100 km, less than the grid spacing of the models.

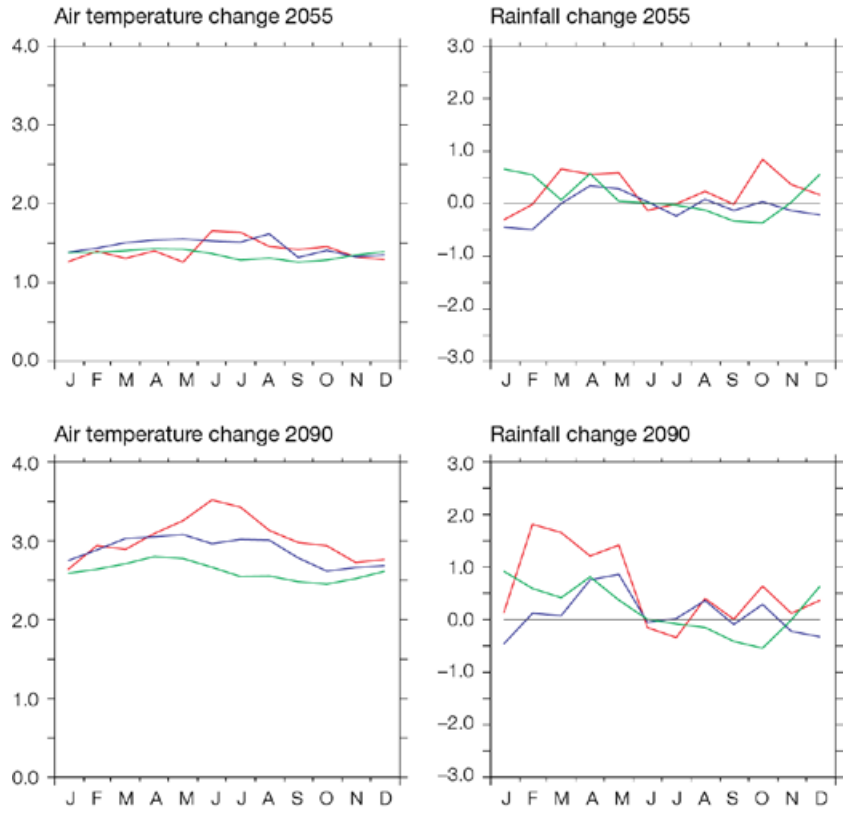

Figure 7.9: Monthly changes in surface air temperature (left, ˚C) and rainfall (right, mm per day) for Nadi, Fiji, showing changes in 2055 (top) and 2090 (bottom) relative to 1990, for the A2 (high) emissions scenario. Green lines are changes for global climate models, blue are changes for CCAM 60 km, red are changes for CCAM 8 km simulations.

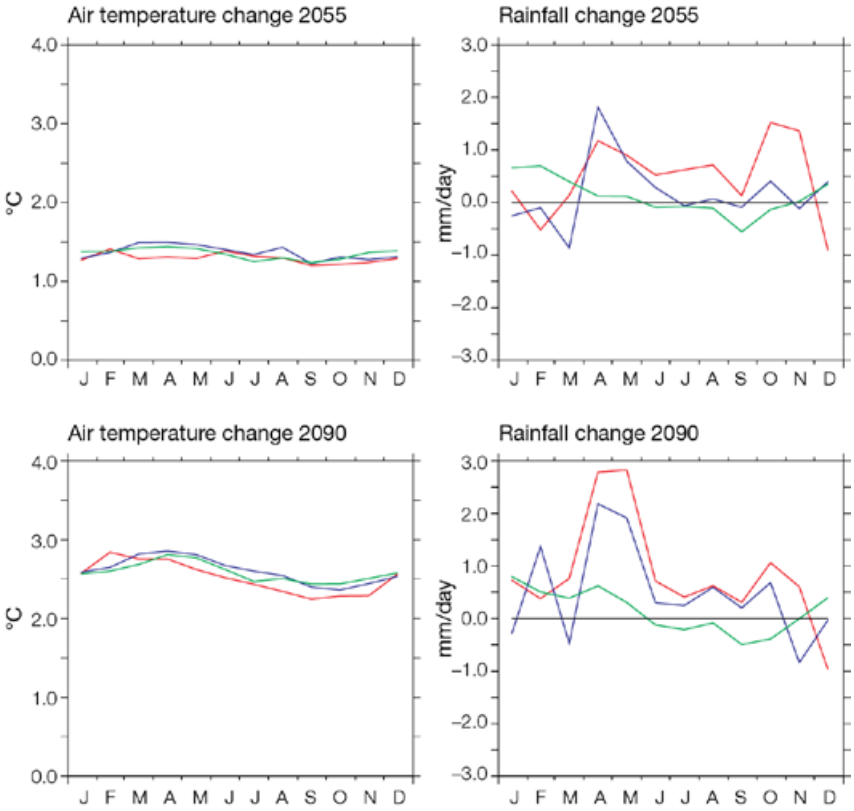

Figure 7.10: Monthly changes in temperature (left, ˚C) and rainfall (right, mm per day) for Nausori, Fiji, showing changes in 2055 (top) and 2090 (bottom) relative to 1990, for the A2 (high) emissions scenario. Green lines are changes for global climate models, blue are changes for CCAM 60 km, red are changes for CCAM 8 km.

Rainfall generally increases throughout the year for Nausori, though the changes in the global models are very small (and show some decreases in second half of the year). In the CCAM 60 km and 8 km downscaled projections, the rainfall increases are greatest in April and May.

7.2.2.3 Changes in Probability Density Functions of Temperature and Rainfall at Selected Locations

In order to assess the changes in the frequency of various daily rainfall amounts and to compare the various projected changes, the frequency distribution or probability density functions (PDF) of temperature and rainfall changes for two locations in Fiji are analysed. Fiji was selected since it is a relatively small, mountainous island, not resolved by the global climate models, has only one grid point at 60 km, and is reasonably well resolved at 8 km grid spacing. It is expected that the benefits of downscaling will be more evident at finer resolution. It should be noted that looking at only selected locations can be misleading as an indication of broader changes, since as was shown previously, there can be significant gradients of change over small distances related to local effects such as topography.

Changes in the PDFs of temperature and rainfall for Nadi are shown in Figure 7.11. As expected with global warming, there is a decrease in frequency of cooler temperatures and an increase in frequency of warmer temperatures. There is a slightly greater shift to warmer temperatures in the 8 km results because of the greater warming of the better-resolved land mass.

The projected changes in the rainfall PDF are generally small, with changes of only 1–2% in frequency. By 2055, the global climate models show little change in the frequency of rainfall, although there are slight decreases in light rainfall and slight increases in heavy rainfall. The CCAM 60 km and 8 km results show decreases in frequency of no rain days. The 60 km results show about 1% increase in frequency of the 4–10 mm per day rain days and decreases in frequencies for rain days greater than 10 mm per day. The 8 km results show increases in frequency of the 6–16 mm per day rain days. By 2090, the changes in frequency are generally similar to those for 2055.

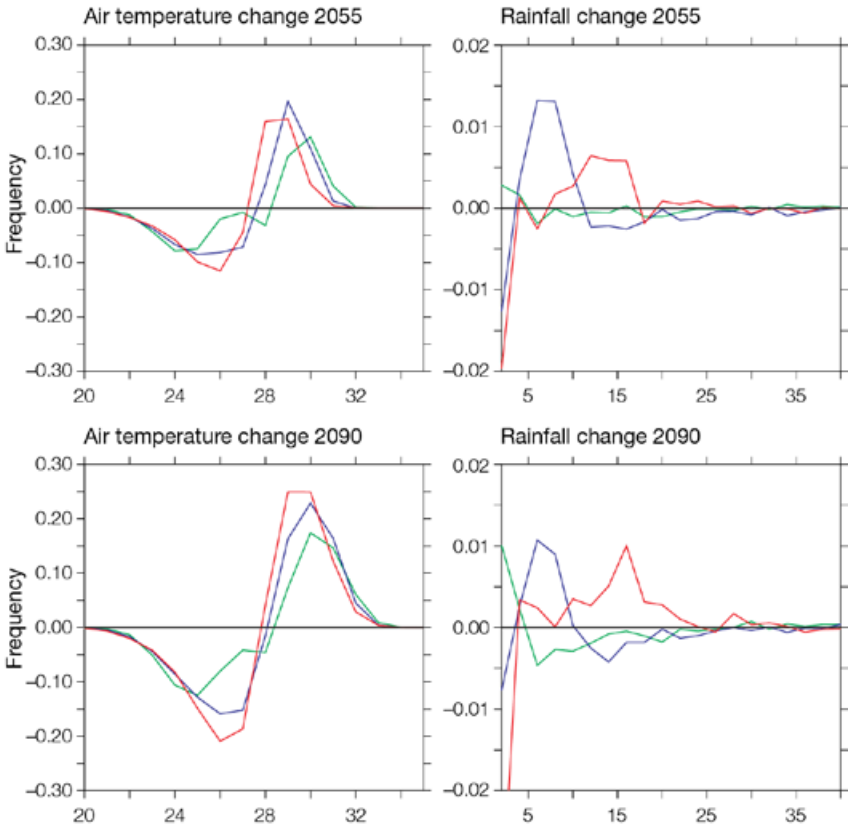

Figure 7.11: Changes in probability density functions for temperature (left, °C) and rainfall (right, mm per day) for Nadi, Fiji. Top row shows changes in 2055 relative to 1990, and bottom shows changes in 2090 relative to 1990, for the A2 (high) emissions scenario. Green lines are changes for global climate models, blue are changes for CCAM 60 km, red are changes for CCAM 8 km.

Changes in the PDFs of temperature and rainfall for Nausori are shown in Figure 7.12. There is a decrease in frequency of cooler temperatures and an increase in frequency of warmer temperatures, as for Nadi. The changes in the 8 km results show less of an increase than the 60 km simulations. The likely cause of this is related to the ocean influence on land. For the 60 km grid, a land point is 60 km away from the ocean, so coastal land points will have only minimal oceanic influence. For the 8 km grid, coastal land points are closer to ocean grid points, and hence the ocean will have a much greater influence, especially when there is onshore flow. For Nausori on the upwind side of Fiji, the effect of the weaker warming of the ocean relative to the land will be greater in the 8 km grid than in the 60 km grid. In the global models, Fiji is an ocean point. As a result, for Nausori, the 8 km projected temperature changes are closer to the global models than the 60 km results. Note this is not the case for Nadi, since Nadi is on the leeward side of the island and will be less influenced by the ocean.

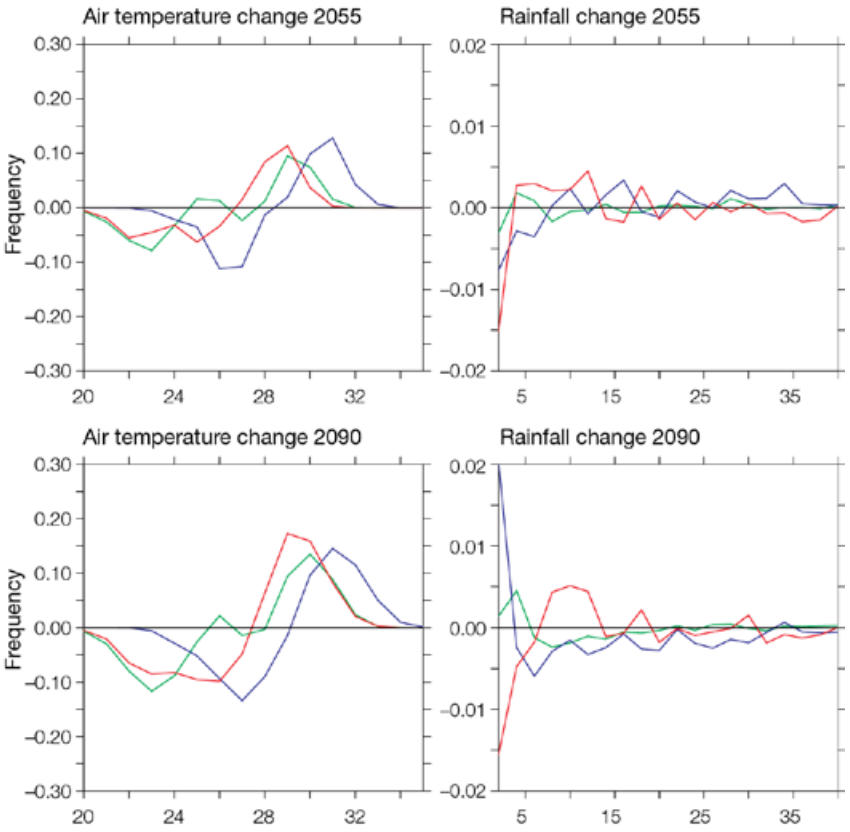

Figure 7.12: Changes in probability density functions for temperature (left, °C) and rainfall (right, mm per day) for Nausori, Fiji. Top row shows changes in 2055 relative to 1990; bottom shows changes in 2090 relative to 1990, for the A2 (high) emissions scenario. Green lines are changes for global climate models, blue are changes for CCAM 60 km, red are changes for CCAM 8 km.

The changes in rainfall PDF are very small by 2055, though all models tend to show a decrease in no or light rain days. By 2090, the global climate model changes are still small, but the 60 km projections show increases in no rain days, and decreases in other rainfall days. However, the 8 km results show a continued decrease in the frequency of no rain days, and an increase in frequency of moderate rain days with 8–12 mm per day.

7.2.2.4 Extremes

Changes in the frequency of the 1-in-20-year daily maximum air temperature for Fiji at 2055 and 2090 are shown in Figure 7.13. Increases in extreme maximum temperatures are mostly less than 2°C by 2055, but they increase to over 4°C by 2090 over land. Over the ocean, changes are around 3°C. For rainfall, the projected change in the number of heavy rainfall days (annual frequency of daily rainfall between 20 mm and 50 mm) are presented in Figure 7.14 for 20-year periods centred at 2055 and 2090. By 2055, the number of heavy rainfall days increases only slightly to the east and north of Fiji, and decreases slightly to the south-west. By 2090, the increases to the north of Fiji are greater than five days per year, while there are some decreases along the eastern side of Viti Levu. There are also some increases of over five days over central parts of the island. Note that Fiji lies in a region of small changes in the global climate models and CCAM 60 km simulations (Figure 7.6).

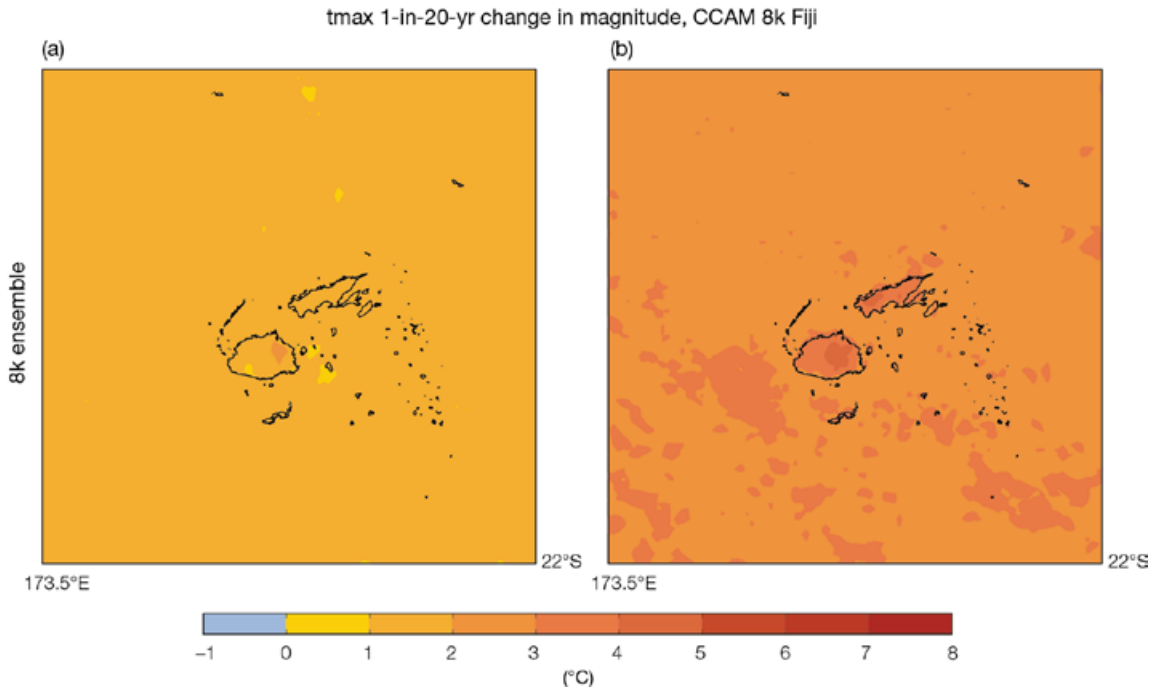

Figure 7.13: Change in magnitude of 1-in-20-year daily maximum air temperature events (°C) for Fiji, showing changes between the periods (a) 2055 and (b) 2090 relative to 1990, for the CCAM 8 km multi-model mean with the A2 (high) emissions scenario.

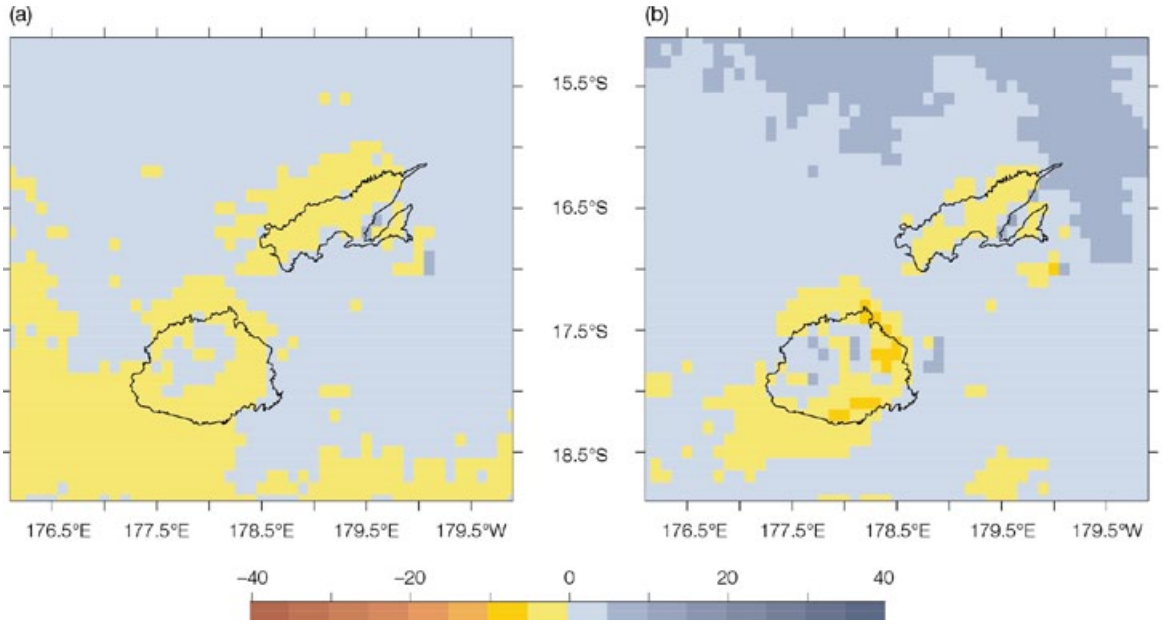

Figure 7.14: Change in the number of days with heavy daily rainfall for Fiji, showing changes between the periods 2055 (a) and 2090 (b) relative to 1990, for the CCAM 8 km multi-model mean with the A2 (high) emissions scenario.

Changes in the 1-in-20-year daily maximum air temperature for Papua New Guinea are shown in Figure 7.15. Increases in extreme maximum temperatures are projected to be mostly less than 2°C by 2055, except for the higher mountains where changes of over 2°C are evident. However, by 2090, the extreme daily temperatures increase over the mountains by more than 5°C. Over the ocean, increases are around 2.5°C. The number of heavy rain days per year (Figure 7.16) increases by more than five days to the north of Papua New Guinea, as well as over some mountainous regions and over the Gulf of Papua by 2055. There are also decreases of more than five days in heavy rain days along the north of New Britain, the Solomon and Coral Seas and in a band extending inland from the Gulf of Papua. By 2090, the general pattern is similar, but the changes are slightly larger.

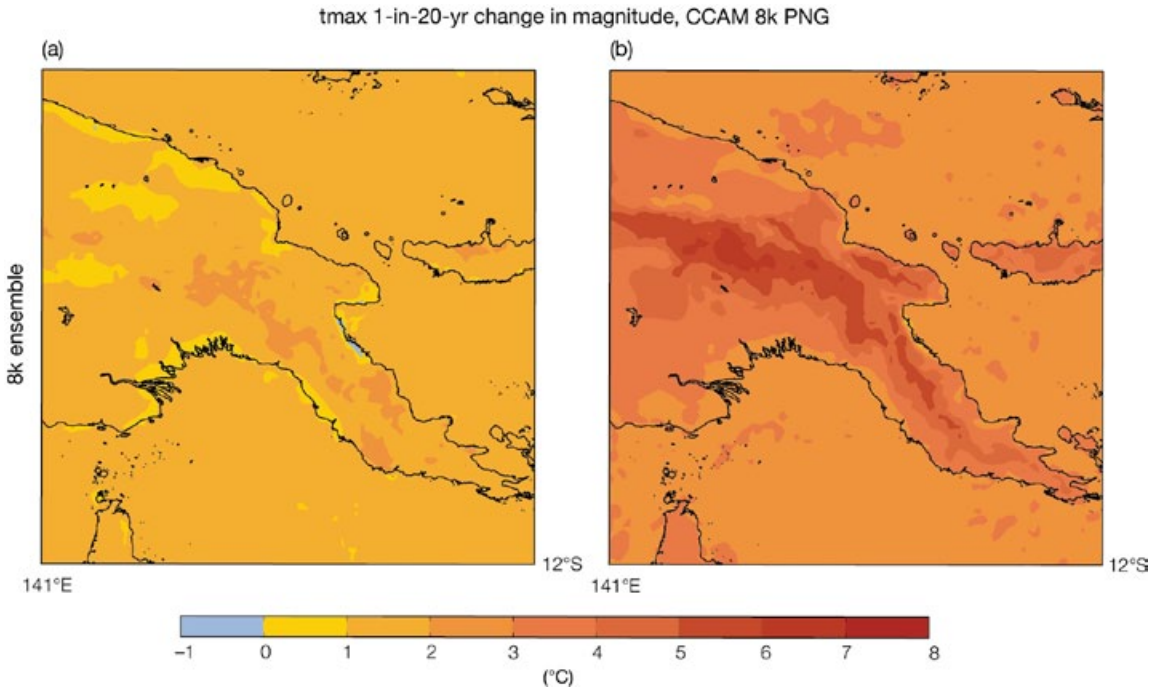

Figure 7.15: Change in magnitude of 1-in-20-year daily maximum air temperature (°C) events, showing projected changes for Papua New Guinea between the periods (a) 2055 and (b) 2090 relative to 1990, for the CCAM 8 km multi-model mean with the A2 (high) emissions scenario.

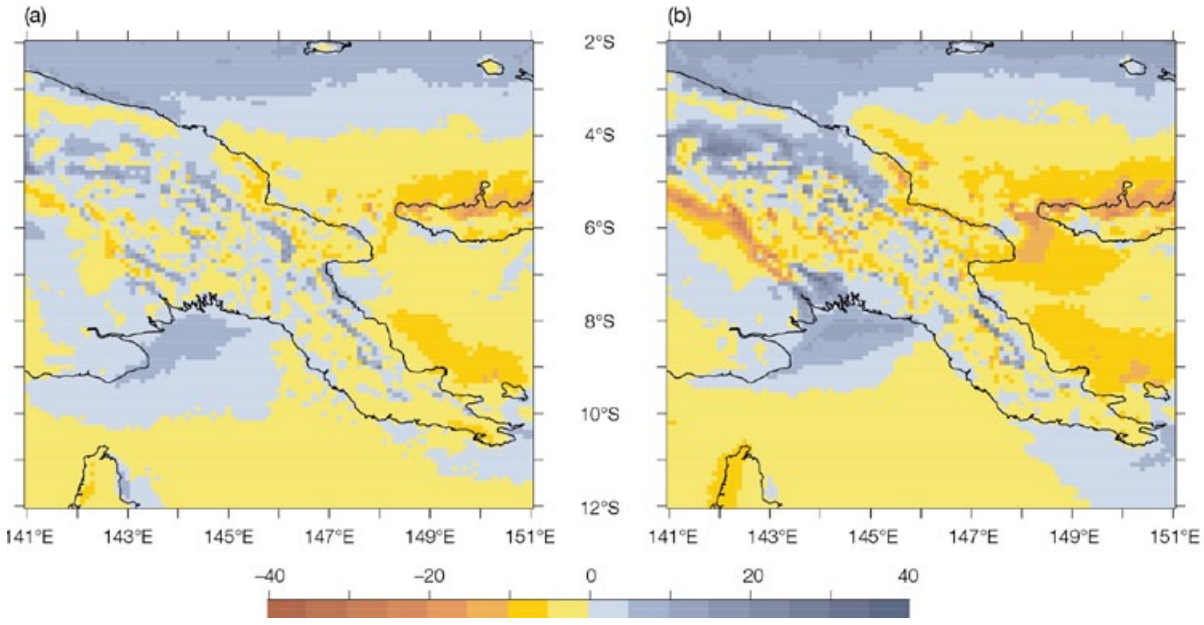

Figure 7.16: Change in the projected number of days with heavy daily rainfall for Papua New Guinea, showing changes between the periods (a) 2055 and (b) 2090 relative to 1990, for the CCAM 8 km multi-model mean with the A2 (high) emissions scenario.

7.2.3 Additional Regional Climate Model Results

Rainfall projections from the additional downscaling simulations are presented in Figure 7.17. The host global climate model is GFDL2.1, which was downscaled to 60 km with CCAM before providing data to the additional downscaled simulations. All simulations except the MM5 simulation, which was excluded due to its poor representation of the current climate (Section 5.3.3), show increases in rainfall along the equator of 1 to 3 mm per day. To the north and south of this increase, there tend to be bands of decrease, similar to the CCAM 60 km results. These bands of decreased rainfall are not as evident in the global models (Figure 6.4). There is less consistency in the results in the western portion of the domain. It is possible that the increased rainfall along the equator gives rise to greater upward motion, with compensating subsidence to the north and south causing an associated decrease in rainfall. These results may also be a result of the finer resolution, but the processes causing these changes need further investigation.

These results are some of the first multi-model dynamically downscaled simulations for the equatorial Pacific. Although there are some differences in the projected rainfall changes between the models, the differences are much less than among the various global models. This is possibly due to all models having the same bias-corrected sea-surface temperatures. In addition, all models used the same CCAM 60 km atmospheric conditions as lateral boundary conditions. However, the downscaled simulations all used different model dynamics, physics and model set-ups.

7.2.4 Dynamical Downscaling Summary

Dynamical downscaling at 50 to 60 km resolution indicates increased rainfall near the equator, between about 10°N and 10°S. Projected drying outside this band is likely as a result of the more intense rainfall along the equator. The models used in this study have very different dynamics, physics and set-up. The fact that they produce similar results adds confidence to the projections. In addition, the 8 km dynamical downscaling results are able to capture the significant effects of the mountainous topography on projected changes in temperature and rainfall across islands, as well as the seasonal variations of rainfall rate and location, and the greater warming of the islands than the surrounding oceans. Although it must be remembered that high-resolution dynamically downscaled models do not provide conclusive evidence of future climate, they are able to suggest trends that cannot be captured by models with coarser grids, where the islands are not resolved.

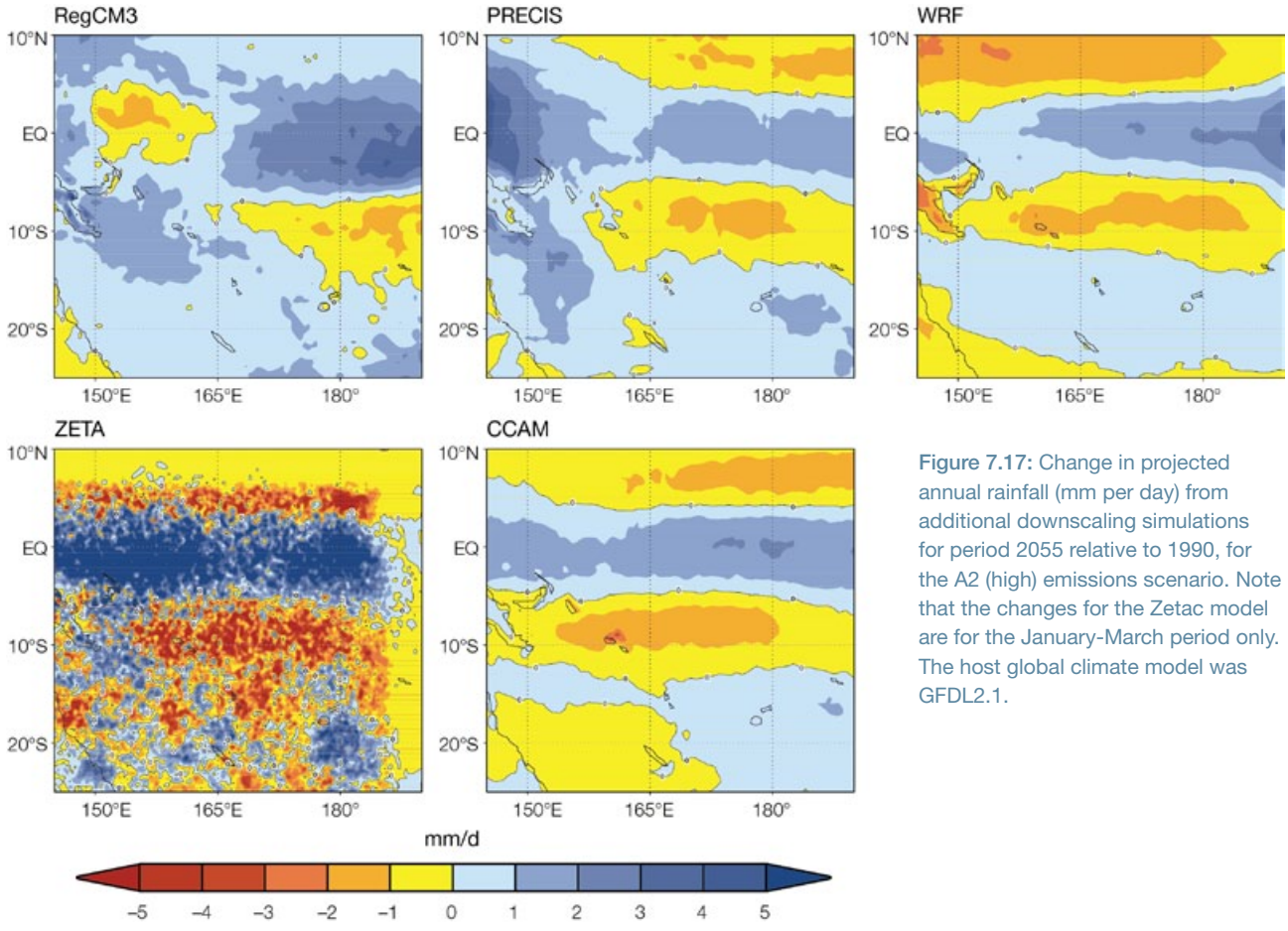

Figure 7.17: Change in projected annual rainfall (mm per day) from additional downscaling simulations for period 2055 relative to 1990, for the A2 (high) emissions scenario. Note that the changes for the Zetac model are for the January-March period only. The host global climate model was GFDL2.1.

7.3 Statistical Downscaling

Despite the significant improvement in spatial detail achieved via dynamic downscaling, this approach still has some limitations regarding accurately resolving all physical and synoptic-scale features, as well as predicting trends in climate at specific locations (Section 7.2). This is where statistical downscaling may play an important bridging role by empirical modelling of the relationship between carefully selected covariates from CCAM 60 km simulations and observed climate at specific locations over the observation period. The statistical approach selects the best set of covariates for each location which include the variable being downscaled, e.g. rainfall or temperature, as well as others such as sea-level pressure, total cloud and water mixing ratio.

The relationships between these covariates and the station observations are then used by the statistical model to make projections. Future changes in the CCAM covariates are used to produce station-scale future projections. This implies that the observed trends of climate at a specific location will influence the future projected value at that location. For this reason only locations with high quality data and long observational histories were chosen for downscaling.

7.3.1 Statistical Downscaling Results

The results of statistical downscaling (Table 7.1) based on output from three of the CCAM 60 km simulations (Section 4.6) show a projected increase in average daily rainfall in most locations for most host models, except for the Marshall Islands, where average daily rainfall is projected to decline in two out of the three cases. In some locations, the range of rainfall projections is quite wide, e.g. in the Federated States of Micronesia and the Marshall Islands, which indicates that rainfall is projected with less certainty in these locations. Average maximum and minimum temperature are consistently projected to increase in all locations regardless of which CCAM simulation is used to drive the statistical downscaling.

A comparison of median historical changes in temperature and rainfall between station observations and CCAM downscaled simulation data (not shown) revealed that results from the ECHAM5/MPI-OM model were most closely aligned with station changes across the Pacific. For this reason, the discussion and tables that follow focus on results from the ECHAM5/MPI-OM model. In most locations and seasons, rainfall is projected to increase (Table 7.2). A decline in daily rainfall across all seasons is projected in the Marshall Islands and a somewhat smaller decline across all seasons is projected for Samoa. In the case of the Marshall Islands, this is due to reductions in the intensity of rain, coupled with the increase in rain days, whereas for Samoa no decline in rain days is projected. The findings for these two locations are supported by the observed trends in the climate data at these locations. For example, for Majuro, Marshall Islands, the trend in median rainfall on rain days is -0.12 ± 0.02 mm per year, and the trend in rain days is +0.4 ± 0.06 % per year over the time period that data have been observed. Given the length of this observation time period (1973–2009) we can be quite confident that these trend estimates are not overly influenced by short-term effects.

For Nadi, Fiji, the number of rain days is projected to have little change by 2021–2040 (Table 7.2). However the median and 90th percentiles of rainfall are projected to increase, suggesting that events may decline in frequency but increase in severity. Again, this result is supported by trends in the observed data: the median rainfall on rain days increases at the rate of 0.08 ± 0.02 mm per year and the number of rain days decreases by 0.3 ± 0.1% per year over the observation period (1961–2009).

A comparison of the average change in rainfall projected by the dynamically downscaled ECHAM5/MPI-OM model compared to the statistical downscaled projections shows some differences (Table 7.2). These differences may be due to statistically significant differences in the trend of observed climate data and dynamically downscaled ECHAM5/MPI-OM data at the specific locations (highlighted by * in Table 7.2). For example, at Lamap in Vanuatu the trend in observed rainfall is 0.06 mm per year whereas for the dynamically downscaled ECHAM5/MPI-OM data over the same time period it is a very small decline. The statistical model not only uses dynamically downscaled ECHAM5/MPI-OM rainfall to project the future changes, but other variables such as sea-level pressure, temperature, and total cloud as well.

Table 7.1: Change in statistically downscaled climatic statistics projected for seven locations in the Pacific between 1981–2000 and 2021–2040. The statistical downscaling projections are based on output from three CCAM simulations (Section 4.6) under the A2 (high) emissions scenario. Values are sorted in ascending order.

Location	Change in average rainfall (mm per day)			Change in median maximum temperature (°C)			Change in median minimum temperature (°C)		
Rarotonga, Cook Islands	0.0	0.3	0.3	0.3	0.8	0.9	0.3	0.6	0.8
Pohnpei, Federated States of Micronesia	-0.1	0.1	1.1	0.3	0.3	0.6	0.1	0.2	0.2
Nadi, Fiji	0.1	0.2	0.2	0.3	0.7	0.7	0.5	0.7	0.8
Majuro, Marshall Islands	-0.7	-0.2	0.2	0.3	0.4	0.4	0.2	0.3	0.3
Apia, Samoa	-0.1	0.1	0.1	0.3	0.4	0.4	0.2	0.4	0.5
Honiara, Solomon Islands	0.0	0.5	0.6	0.1	0.2	0.4	0.2	0.3	0.5
Lamap, Vanuatu	0.2	0.3	0.9	0.4	0.7	0.9	0.2	0.5	0.5

Table 7.2: Change in statistically downscaled rainfall statistics projected for seven locations in the Pacific between 1981–2000 and 2021–2040. The statistical downscaling projections are driven by output from the dynamically downscaled ECHAM5/MPI-OM model under an A2 (high) emissions scenario.

Location	Season	Mean rainfall (mm per day) 1981–2000[a]	Percent of rain days 1981–2000	Change in percentage of rain days	Change in rainfall (mm per day)			
					On rain days only		Overall average change	CCAM (ECHAM5/ MPI-OM)
					Median	90th pctl		
Rarotonga, Cook Islands*	Oct-Mar	4.4	45	6	0.3	6.2	0.3	0.0
	Apr-Sep	3.6	39	5	0.1	-3.1	0.2	-0.1
	All	4.0	42	5	0.2	1.6	0.3	0.0
Pohnpei, Federated States of Micronesia*	Oct-Mar	11.8	81	4	-0.1	0.3	0.2	-0.5
	Apr-Sep	13.9	85	4	-0.3	0.4	0.1	-0.6
	All	12.8	83	4	-0.2	0.3	0.1	-0.5
Nadi, Fiji*	Oct-Mar	6.7	46	-1	0.6	1.2	0.3	0.0
	Apr-Sep	2.6	24	-1	0.3	0.6	0.1	-0.1
	All	4.6	35	-1	0.5	0.9	0.2	0.0
Majuro, Marshall Islands	Oct-Mar	8.8	73	3	-0.3	-0.7	-0.1	-0.5
	Apr-Sep	9.5	79	2	-0.5	-1.4	-0.3	-0.2
	All	9.1	76	2	-0.4	-1.0	-0.2	-0.3
Apia, Samoa	Oct-Mar	7.5	53	0	-0.3	-0.7	-0.1	0.0
	Apr-Sep	4.3	39	0	-0.2	-1.1	-0.1	-0.1
	All	6.0	46	0	-0.2	-0.9	-0.1	0.0
Honiara, Solomon Islands*	Oct-Mar	5.1	42	-1	0.0	-1.8	-0.1	-0.5
	Apr-Sep	3.0	37	-1	0.0	-1.1	0.0	-0.6
	All	4.0	39	-1	0.0	-1.5	0.0	-0.5
Lamap, Vanuatu*	Oct-Mar	8.0	63	2	0.4	2.0	0.4	-0.1
	Apr-Sep	4.9	51	2	0.4	1.8	0.3	-0.3
	All	6.5	57	2	0.4	1.9	0.3	-0.2

[a] where observed data are available during reference period

* Statistically significant different trends observed between the climate station and dynamically downscaled data

In terms of temperature, a consistent pattern of warming is projected at all locations, ranging between 0.1 and 0.5°C by 2021–2040 (Tables 7.3 a,b). Generally, the increases projected by statistical downscaling are slightly less than those predicted from the dynamically downscaled ECHAM5/MPI-OM model. As noted in the tables there are some significant differences between the observed climate at a particular station location and the dynamically downscaled climate over a comparable period. These differences in climatic means as well as trends result in the differences in the projections between the statistical and dynamic approaches.

The statistically downscaled results are partly influenced by the observed trend (within the data used to train the statistical model), which includes both global warming trends and changes in natural variability, as well as other effects not necessarily captured by the downscaled simulations. The dynamically downscaled results, while including long-term effects of global warming, may not accurately capture all the local synoptic changes occurring and this may result in the divergence between trends over the historical period.

Hence, some of the differences between the dynamically and statistically downscaled results may be the result of the relative importance of localised changes and how consistent they are with broader regional and global anthropogenic change (Timm and Diaz, 2009). This is an area of further research.

The projected increase in minimum temperatures appears greater than maximum temperatures in most locations (Tables 7.3 a,b). The pattern of warming for both maximum and minimum temperatures is greatest for both the 10th percentile and median temperatures and less so for the 90th percentile temperatures. This is consistent with predictions derived directly from both global climate models and dynamical downscaling.

Table 7.3a: Change in statistically downscaled maximum temperature statistics projected for seven locations in the Pacific between 1981–2000 and 2021–2040. The statistical downscaling projections are driven by output from the dynamically downscaled ECHAM5 model under an A2 (high) emissions scenario.

Location	Season	Mean maximum temperature (°C) 1981–2000	Change in maximum temperature (°C)			CCAM (ECHAM5): change in mean temperature (°C)
			10th percentile	Median	90th percentile	
Rarotonga, Cook Islands*	Oct-Mar	28.8	0.4	0.3	0.4	0.5
	Apr-Sep	26.8	0.3	0.3	0.4	0.5
	All	27.8	0.3	0.3	0.4	0.5
Pohnpei, Federated States of Micronesia*	Oct-Mar	31.2	0.5	0.2	0.3	0.4
	Apr-Sep	31.8	0.4	0.4	0.3	0.5
	All	31.5	0.4	0.3	0.3	0.4
Nadi, Fiji	Oct-Mar	31.1	0.4	0.3	0.2	0.5
	Apr-Sep	29.5	0.4	0.3	0.2	0.5
	All	30.3	0.4	0.3	0.2	0.5
Majuro, Marshall Islands	Oct-Mar	30.3	0.2	0.3	0.3	0.4
	Apr-Sep	30.6	0.3	0.3	0.3	0.4
	All	30.4	0.3	0.3	0.3	0.4
Apia, Samoa*	Oct-Mar	30.6	0.3	0.3	0.2	0.5
	Apr-Sep	30.1	0.3	0.2	0.2	0.5
	All	30.3	0.3	0.3	0.2	0.5
Honiara, Solomon Islands*	Oct-Mar	31.1	0.3	0.1	0.1	0.4
	Apr-Sep	30.8	0.2	0.1	0.1	0.5
	All	31.0	0.3	0.1	0.1	0.4
Lamap, Vanuatu*	Oct-Mar	30.1	0.4	0.4	0.4	0.6
	Apr-Sep	28.6	0.5	0.5	0.5	0.7
	All	29.4	0.5	0.4	0.5	0.6

* Statistically significant different trends observed between the climate station and dynamically downscaled data

Table 7.3b: Change in statistically downscaled minimum temperature statistics projected for seven locations in the Pacific between 1981–2000 and 2021–2040. The statistical downscaling projections are driven by output from the dynamically downscaled ECHAM5 model under the A2 (high) emissions scenario.

Location	Season	Mean minimum temperature (°C) 1981–2000	Change in minimum temperature (°C)			CCAM (ECHAM5): change in mean temperature (°C)
			10th percentile	Median	90th percentile	
Rarotonga, Cook Islands*	Oct-Mar	22.9	0.5	0.3	0.2	0.5
	Apr-Sep	20.8	0.4	0.3	0.2	0.5
	All	21.9	0.4	0.3	0.2	0.5
Pohnpei, Micronesia*	Oct-Mar	23.7	0.2	0.1	0.2	0.4
	Apr-Sep	23.3	0.0	0.1	0.0	0.5
	All	23.5	0.1	0.1	0.0	0.4
Nadi, Fiji*	Oct-Mar	22.8	0.6	0.5	0.1	0.5
	Apr-Sep	20.7	0.6	0.5	0.3	0.5
	All	21.7	0.6	0.5	0.2	0.5
Majuro, Marshall Islands*	Oct-Mar	26.0	0.1	0.4	0.2	0.4
	Apr-Sep	25.7	0.2	0.1	0.2	0.4
	All	25.8	0.2	0.3	0.2	0.4
Apia, Samoa	Oct-Mar	24.3	0.2	0.2	0.0	0.5
	Apr-Sep	23.7	0.1	0.1	0.0	0.5
	All	24.0	0.2	0.2	0.0	0.5
Honiara, Solomon Islands	Oct-Mar	23.1	0.1	0.2	0.4	0.4
	Apr-Sep	22.6	0.2	0.2	0.0	0.5
	All	22.9	0.2	0.2	0.1	0.4
Lamap, Vanuatu*	Oct-Mar	22.9	0.4	0.2	0.1	0.6
	Apr-Sep	22.2	0.5	0.3	0.2	0.7
	All	22.5	0.4	0.2	0.2	0.6

* Statistically significant different trends observed between the climate station and dynamically downscaled data

Time series information has also been generated as part of the statistical downscaling activities for the 17 locations (Table 4.3). An example has been provided of some monthly statistics for Lamap in Vanuatu (Figure 7.18). The figure shows that there is, as expected, strong within-season variation and interannual variation of the data as well as a slightly increasing rate over time of the upward trend of some variables. There is also a slight increase projected over time of the variation of median monthly rainfall on rain days.

7.3.2 Statistical Downscaling Summary

Statistical downscaling projections are somewhat different to those based upon global and dynamically downscaled models. In part, this is a result of the statistical model being based upon both observed local trends and large-scale dynamically downscaled outputs. In addition, statistical downscaling is designed to deliver information at a given station, and thus takes into consideration local influences on climate and weather.

Dynamical models produce information across a grid of varying resolution and thus may not account for all these local effects. The differences between dynamical and statistically derived projections are being examined and are the basis of future research.

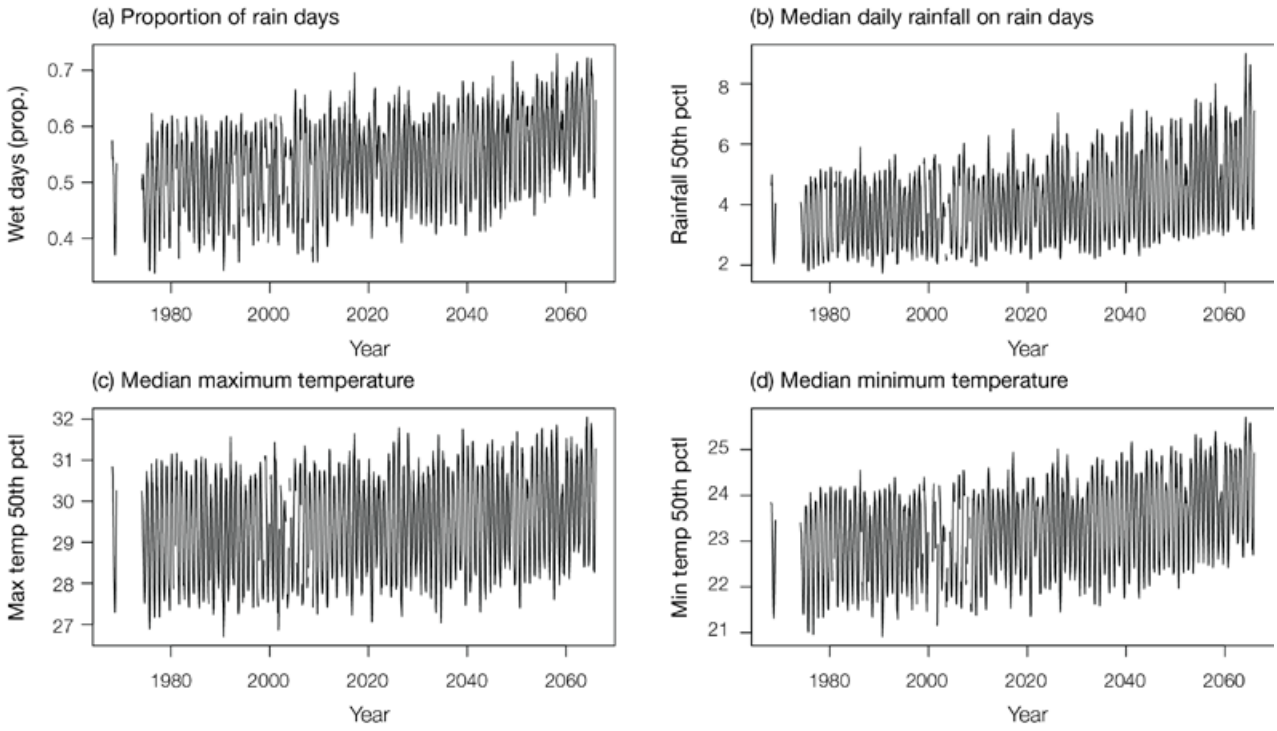

Figure 7.18: Statistically downscaled time series projections to 2065 for Lamap, Vanuatu. The statistical downscaling projections are driven by output from the dynamically downscaled ECHAM5/MPI-OM model under an A2 (high) emissions scenario.

7.4 Tropical cyclone projections

7.4.1 Introduction

Tropical cyclones are among the most destructive weather phenomena on Earth. The associated strong winds coupled with heavy rainfall and possible storm surges often have devastating consequences for life and property in various tropical regions of the world. In the tropical Pacific, small island developing States such as those in the PCCSP region are very vulnerable to catastrophic impacts of tropical cyclones. Determining realistic future changes in tropical cyclone activity (such as frequency and intensity) is therefore important for these areas. However, projection of realistic future changes in tropical cyclone activity at a regional spatial scale is still an unresolved issue; partly due to large variations in modelling results (Knutson et al., 2010) and partly due to model deficiencies in representing the large-scale environmental conditions that are known to influence tropical cyclones, including patterns of variability such as the El Niño-Southern Oscillation and large-scale climate features such as the South Pacific Convergence Zone (Brown et al., 2011).

Despite the global climate models' inadequacies in representing regional scales, the reproduction of current climate of tropical cyclones on larger scales was shown in Chapter 5 to be quite promising, due to the use of the multiple projection methods. These results provide some confidence in the projections of future changes in tropical cyclone frequency for the PCCSP region. Here the projected change in tropical cyclone frequency is defined in terms of the percentage change between the current climate (1980–1999) and the future climate for the A2 (high) scenario (2080–2099).

At the global scale, modelling studies consistently project a decrease in mean tropical cyclone frequency ranging from 6 to 34% by the late 21st century (Knutson et al., 2010). This decrease is more robust in the Southern Hemisphere than in the Northern Hemisphere, and may be due to a combination of increased vertical wind shear in the Southern Hemisphere, and smaller increases in sea-surface temperature compared with the Northern Hemisphere.

In individual basins, projected 21st century changes are highly variable, with both increases and decreases in frequency of more than 50%. Theory and high-resolution modelling also suggest that climate change may lead to an increase in cyclone intensity by about 2–11%.

In an attempt to provide more specific projections of tropical cyclone frequency for individual countries, the PCCSP region is divided into three sub-basins. These are the south-west basin (0–40ºS; 130–170ºE), the south-east basin (0–40ºS; 170ºE-130ºW) and the north basin (0–15ºN; 130–180ºE). The results of the cyclone frequency projections for the three basins from the different methods described in Section 4.8 are presented in Table 7.4 and Figure 7.19 (for a subset of the models and methods). Projected changes in cyclone intensity are also described. Changes in wind risk hazard are evaluated for the study region by applying the Tropical Cyclone Risk Model to tracks of tropical cyclone-like vortices detected in downscaled global climate models.

Table 7.4: Projected percentage change in tropical cyclone frequency between the current climate (1980–1999) and the late 21st century (2080–2099). Blue (red) shading indicates a statistically significant decrease (increase) in projected tropical cyclone frequency at the 95% confidence interval. Blue (red) numbers indicate projected decreases (increases) in tropical cyclone frequency that are not statistically significant. CCAM refers to the 60 km dynamically downscaled simulations. The CVP, CDD and GPI methods are described in Section 4.8. Significance level testing is not available for the GPI method.

Model	South-east basin				South-west basin				North basin			
	Projection method											
	CCAM	CVP	CDD	GPI	CCAM	CVP	CDD	GPI	CCAM	CVP	CDD	GPI
CSIRO-Mk3.5	-65	+10	+10	-60	-45	+50	+20	-70	0	+10	0	-80
ECHAM5/MPI-OM	-50	-20	+25	-35	-80	-30	+15	-25	-80	-25	+5	-30
GFDL-CM2.0	-70		-30	-20	-60		-35	-5	-45		0	+5
GFDL-CM2.1	-50	-10	-30	-25	-70	-20	-25	-5	-50	-10	-30	-5
MIROC3.2 (medres)	-90			-75	-80			-85	-50			-85
UKMO-HadCM3	-55			-30	-55			+10	-30			+15
BCCR-BCM2.0			-90	-5			-90	+10			-100	+15
CGCM3.1			+30	-20			+30	-10			-5	-10
CNRM-CM3			-20	-35			+10	-20			-5	-30
MRI-CGCM2.3.2			0	-25			-15	-5			0	0
CSIRO-Mk3.0				-50				-55				-65
UKMO-HadGEM1				-5				+5				+15
IPSL-CM4				-20				-15				-20
ECHO-G				-35				-25				-25
ENSEMBLE	-60	-6	-13	-30	-65	0	-11	-20	-45	-5	-17	-20

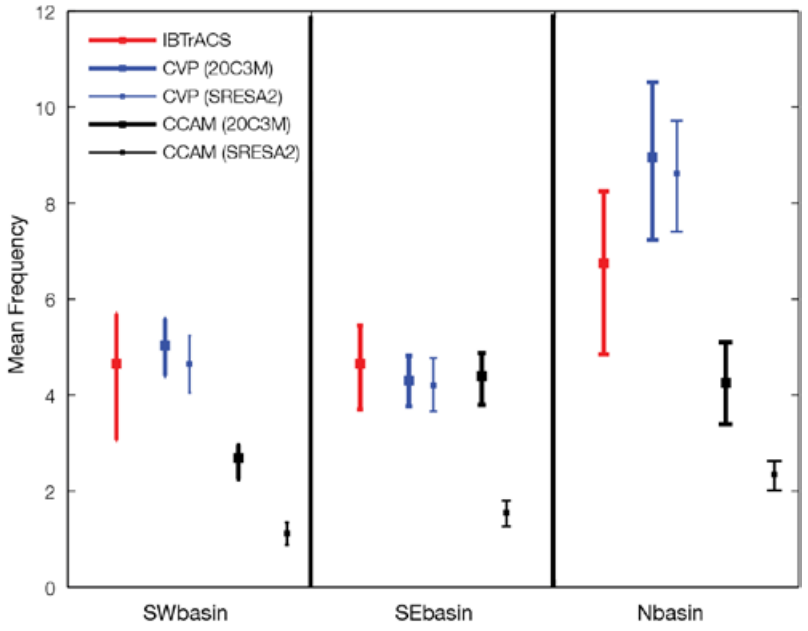

Figure 7.19: Average of all models of the late 21st century projected annual tropical cyclone frequency for the three sub-basins of the PCCSP region using the CCAM downscaling technique (thin black) and the Curvature Vorticity Parameter (CVP) method (thin blue). Also shown are the annual cyclone frequencies for the current climate for the CCAM downscaling technique (thick black) and the CVP method (thick blue). Red lines indicate observed mean tropical cyclone frequency. Bars denote 95% confidence interval. A change is considered likely if there is no overlap between current and future climate bars. Results are based on outputs from the CSIRO-Mk3.5, ECHAM5/MPI-OM, GFDL-CM2.0 and GFDL-CM2.1 global climate models (CVP) and CCAM simulations based on these global models.

7.4.2 Tropical Cyclone Frequency Projections in Downscaled Models

Overall, the CCAM results project a likely decrease in tropical cyclone frequency for all three sub-basins by the late 21st century (Figure 7.19). These decreases in frequency range from 50–70% for the south-east basin, 45–80% for the south-west basin and 0–80% for the north basin (Table 7.4).

In the south-east basin, the decrease in the CCAM multi-model average cyclone frequency as determined by the CSIRO Direct Detection technique, is clearly evident when comparing Figures 7.20a and 7.20b, with greatest decrease in the longitude band of 170–180ºE (Figures 7.20c, 7.20d), and near the latitude of 15ºS. Similarly, the greatest projected decrease in frequency for the south-west basin occurs mainly in the Coral Sea region (15ºS; 150–170ºE), where tropical cyclones are frequently spawned. For the north basin, the projected decrease occurs mainly in the region 10ºN; 130–150ºE (Figure 7.20e).

The location of cyclone genesis is just one component in the cyclone risk for a region. The risk for a region is also determined by the track, duration and intensity of storms traversing the region. The changes in cyclone numbers and days from the six CCAM simulations have been calculated (not shown). Most models show a small increase in the number of tropical cyclones occurring south of 20°S although there is little consistency between the models in the spatial pattern of the projected change. The change in intensity is discussed in detail later in this chapter.

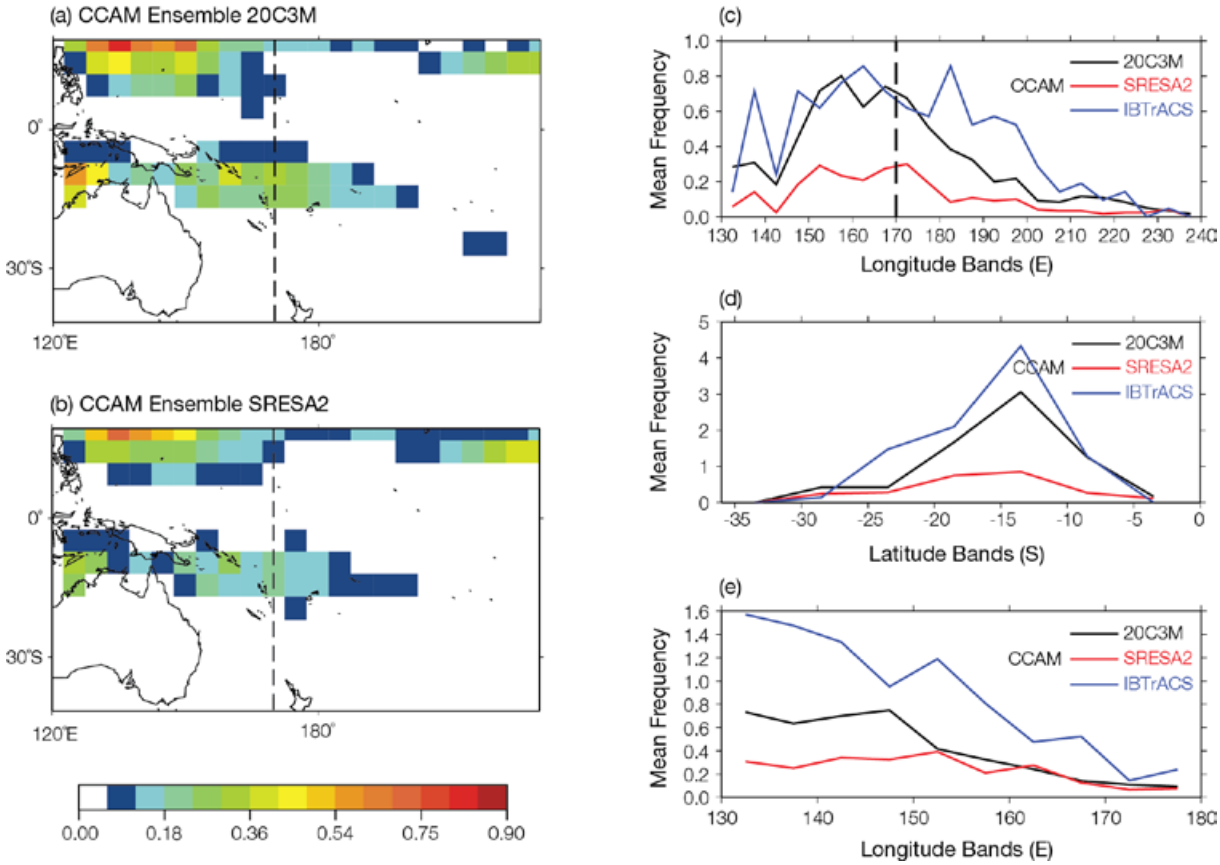

Figure 7.20: Multi-model mean distribution of tropical cyclone frequency (in 5º × 5º boxes) obtained using the CSIRO Direct Detection technique applied to the 65 km CCAM model for (a) current climate, (1980–1999, labelled 20C3m) and (b) late 21st century using the A2 high emissions scenario (2080–2099, labelled SRESA2). Cyclone frequency distributions are also shown in 5º (c) longitudinal and (d) latitudinal bands for the South Pacific and (e) longitudinal band for the north-west Pacific south of 20ºN. The dashed line at 170ºE in (c) separates the eastern and western basins of the South Pacific.

7.4.3 Cyclone Frequency Projections in Global Climate Models

In general, the Curvature Vorticity Parameter (CVP) approach discussed in Section 4.8 is based on output from three global climate models. It projects a small decrease in tropical cyclone frequency for the PCCSP region by the late 21st century (Figure 7.19). In the south-east basin, the projected change ranges from a 20% decrease for the ECHAM5/MPI-OM model to a 10% increase for the CSIRO-Mk3.5 model (Table 7.4). However, these changes are not statistically significant at the 95% level. The spatial distribution of tropical cyclone formation locations determined by taking the multi-model mean of the three global models shows no substantial change between the current (Figure 7.21a) and future (Figure 7.21b) distributions.

For the south-west basin, two global climate models (GFDL-CM2.1 and ECHAM5/MPI-OM) project a decrease in tropical cyclone numbers by about 20–30%. The CSIRO-Mk3.5 model, on the other hand, projects a likely increase of about 50%. A small decrease in tropical cyclone numbers is also projected for the north basin. However, this decrease is not statistically significant at the 95% level.

On average, the CSIRO Direct Detection (CDD) method discussed in Section 4.8 projects a multi-model average decrease in tropical cyclone genesis frequency for the PCCSP region by the late 21st century (Table 7.4 and Figure 7.22). However, there is little confidence in this projected change for the southern Pacific as in both the south-east basin and in the south-west basin, four out of eight models project a likely increase in tropical cyclone frequency and four out of eight models project a likely decrease in tropical cyclone frequency. In the northern basin there is greater confidence in the change as only one model projects a likely increase in tropical cyclone frequency.

7.4.4 Cyclone Frequency Projections from the Genesis Potential Index

The Genesis Potential Index (GPI) methodology has the advantage that more models (14) can be considered in the development of projections for changes in cyclone frequency.

The GPI method projects decreases of between 20% and 30% for the three basins (Figure 7.23). In the south-east basin, all models project a decrease in frequency with projected changes ranging from 5% to 70%. In the south-west basin, 11 out of 14 models project a decrease in the frequency with projected changes ranging from an increase of 10% to a decrease of 85%. In the north basin, the changes range from an increase of 15% to a decrease of 80%. Ten out of 14 models project a decrease in frequency for this basin.

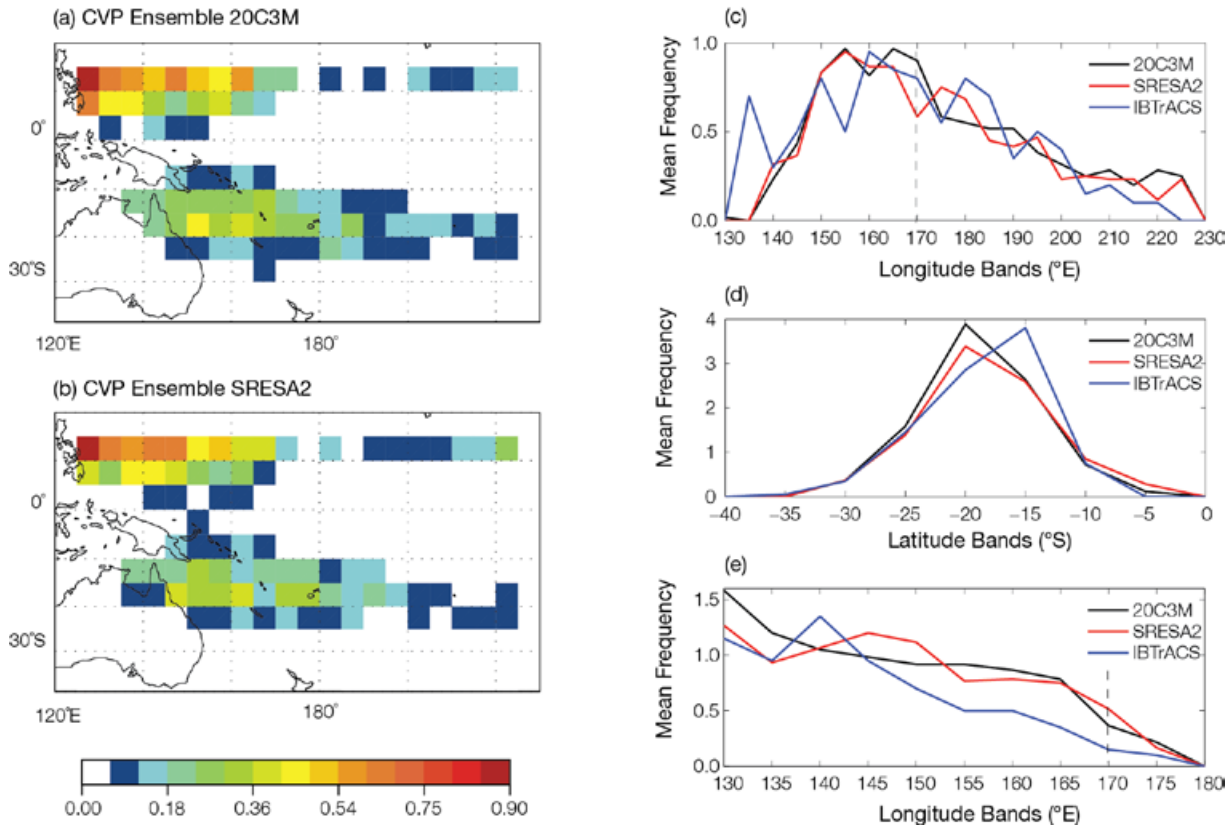

Figure 7.21: Multi-model mean distribution of tropical cyclone frequency (in 5° × 5° boxes) obtained using the CVP approach for (a) current climate (labelled 20C3m) and (b) late 21st century using the A2 (high) emissions scenario (labelled SRESA2). Cyclone frequency distributions are also shown in 5° (c) longitudinal and (d) latitudinal bands for the South Pacific and (e) longitudinal band for the north-west Pacific south of 20°N. The dashed line at 170°E in (c) separates the eastern and western basins of the South Pacific.

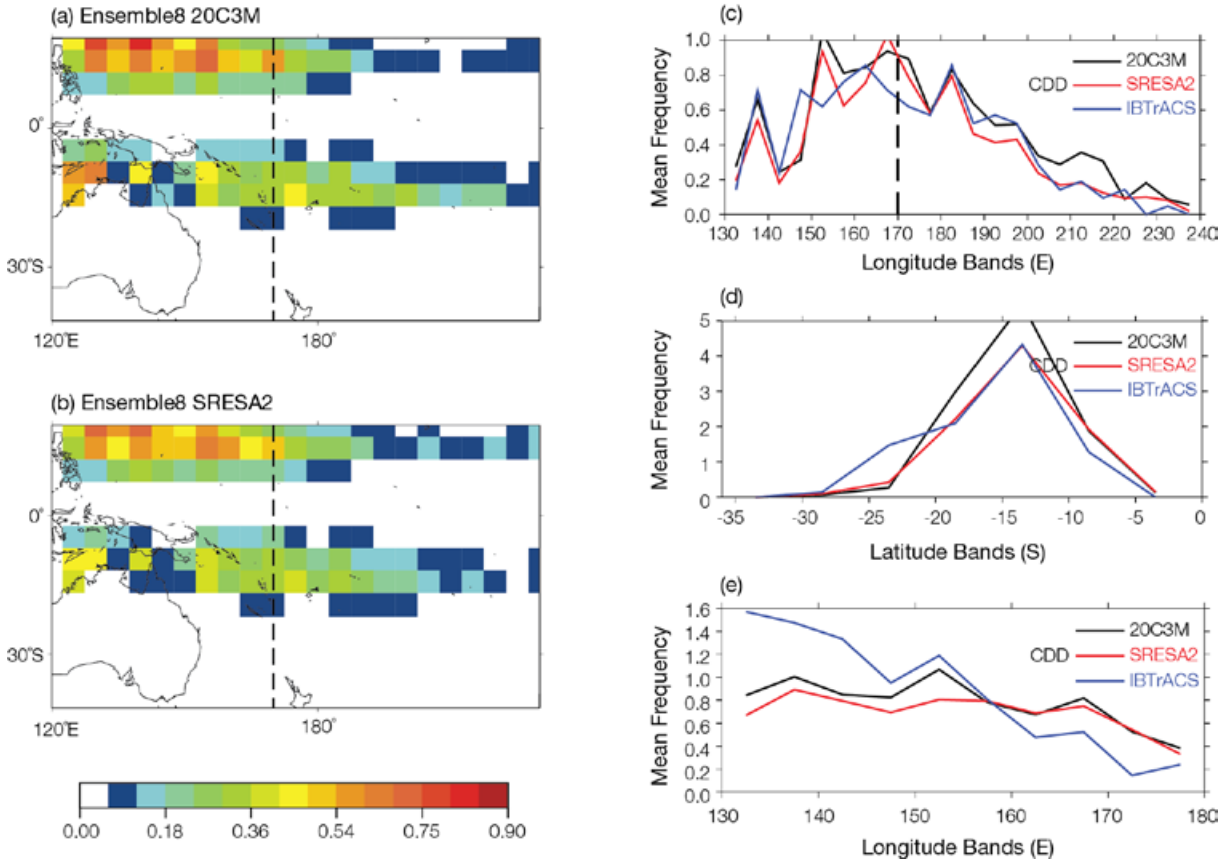

Figure 7.22: Multi-model mean distribution of tropical cyclone frequency (in 5° × 5° boxes) obtained using the CDD method on global climate model data for (a) current climate (labelled 20C3m) and (b) late 21st century using the A2 (high) emissions scenario (labelled SRESA2). Cyclone frequency distributions are also shown in 5° (c) longitudinal and (d) latitudinal bands for the South Pacific and (e) longitudinal band for the north-west Pacific south of 20°N. The dashed line at 170°E in (c) separates the eastern and western basins of the South Pacific.

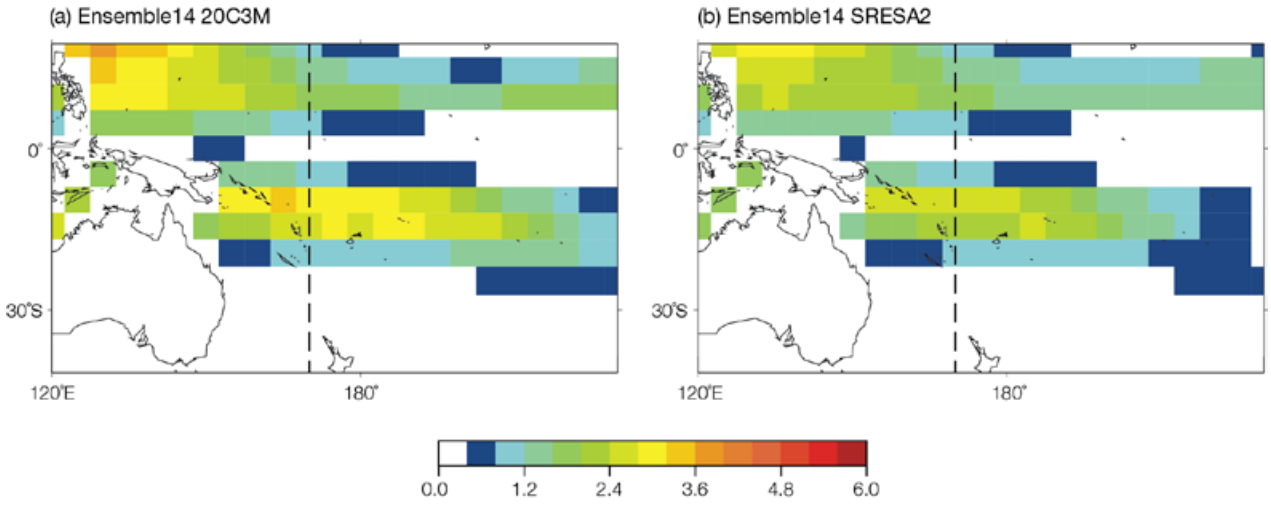

Figure 7.23: Multi-model mean distribution of tropical cyclone frequency (in 5° × 5° boxes) obtained using the GPI method for (a) current climate (labelled 20C3m) and (b) late 21st century using the A2 (high) emissions scenario (labelled SRESA2).

7.4.5 Cyclone Intensity Projections

The development of projections for changes in cyclone intensity requires that features such as the bands of heavy precipitation that accompany a cyclone and the eye wall (the zone of high winds that causes damage) are resolved by a model. However, these features occur at a spatial scale smaller than can be resolved by either global or regional climate models and thus the development of projections of changes in tropical cyclone intensity is difficult. However, a number of research groups have attempted to provide such projections and the results of those studies that are applicable to the South Pacific are summarised in Table 7.5. Note that the A1B, not the A2 emissions scenario, has been used here.

The PCCSP has used three methods to estimate projected changes in intensity. The first of these uses the Maximum Potential Intensity (MPI) component of the GPI, the second method uses the storm maximum wind speed simulated in the cyclone-like vortices detected in the CCAM simulations, and the third method scales the CCAM projections for use in the Tropical Cyclone Risk Model. The results using the MPI method are summarised in Table 7.6. In this analysis no attempt has been made to provide basin-specific projections – the projected changes apply to the full PCCSP study region.

Most models project a decrease in the MPI across the PCCSP region. The projected decrease is largest in the models that project the greatest decrease in the frequency. Models that project either a moderate decrease or slight increase in frequency also project small increases in the MPI.

Table 7.5: A summary of the projections of tropical cyclone intensity in the South Pacific, extracted from global modelling studies for a warmer climate under the A1B (medium) emissions scenarios or a three times carbon dioxide concentration. Bold text in the Technique column indicates type of analysis used. The projections of changes are in either the average intensity or the maximum intensity of cyclones in the South Pacific. In the far right column, projected decreases in frequency are in bold. (Adapted from Knutson et al., 2010).

Tropical cyclone intensity changes (%)	**Model**	**Technique**	**Emissions scenario**	**Measure of cyclone intensity**	**Projection time period**	**Change in maximum wind speed in the South Pacific** (percentage change or frequency change, as noted)
Vecchi and Soden, (2007a)	CMIP3 18-model	Potential Intensity calculations from the output of global models **Statistical downscaling**	A1B	Max wind speed	100yr trend	+ 1%
Emanuel et al. (2008)	CMIP3 7-model	**Statistical downscaling**	A1B	Max wind speed	2181–2200 minus 1981–2000	-1%
Oouchi et al. (2006)	MRI/JMA time slice experiment with global model TL959 L60 (~20km)	**Dynamical downscaling**	A1B	Average intensity (wind speed)	1982–1993 minus 2080–2099	-2%
Oouchi et al. (2006)	MRI/JMA time slice experiment with global model TL959 L60 (~20km)	**Dynamical downscaling**	A1B	Average annual maximum intensity (wind speed)	1982–1993 minus 2080–2099	-22%
Walsh et al. (2004)	Australia CSIRO DARLAM regional model	**Dynamical downscaling**	$3xCO_2$	Central pressure	2061–2090 minus 1961–1990	**+26%** **P<970 mb**
Leslie et al. (2007)	USA OU-CGCM with high-res. window.	**Dynamical downscaling**	IPCC estimated CO_2 from 1970–1999, and IS92a increasing concentration from 2000–2050	Wind speed	2000 to 2050 control and IS92a (6 members)	**+100% #>30m/s by 2050**

The results based on the storm maximum wind speed from the cyclone-like vortices detected in the CCAM simulations are presented in Figure 7.24. This analysis includes calculations of the proportion of storms in the late 21st century climate (2080–2099) that are stronger than the current climate 50th percentile, 75th percentile and 90th percentile wind speeds and the proportion of storms that are weaker than the 25th and 10th percentile wind speeds. If the proportion of storms in the late 21st century lies above the current climate curve, then there is an increase in the proportion of storms that are stronger (or weaker) than in the current climate. The analysis has been conducted for the north basin and the southern Pacific (south-east basin and south-west basin combined) and shows different behaviour in intensity changes for the two basins. In the north basin, only one CCAM simulation (based on CSIRO-Mk3.5) projects an increase in the proportion of storms that will occur in the stronger categories. Most simulations project an increase in the proportion of storms occurring in the weaker categories.

In the southern Pacific, five of the six simulations show an increase in the proportion of the most severe storms (those stronger than the current climate 90th percentile storm maximum wind speed). The latitude of maximum intensity in the southern Pacific is projected to move south by 5° of latitude from approximately 18°S in the current climate to approximately 23°S in the late 21st century.

The results of Figure 7.24 are consistent with finer resolution modelling studies such as those of Bender et al. (2011). They show that models that are able to realistically simulate the intensity of cyclones show an increase in the proportion of storms occurring in the strongest categories. These results should, however, be used with caution. The resolution of the models considered in this analysis is not fine enough to quantify changes in the intensity of tropical cyclones. Projections of changes in tropical cyclone intensity require the use of specialised models that are run with horizontal grid spacing of 5 km or less.

Table 7.6: Projected changes in GPI for each of the sub-basins and projected changes in Maximum Potential Intensity (MPI) for the PCCSP region for the late 21st century using the A2 (high) emissions scenario.

	GPI change			MPI change (%)
Model	SW	SE	N	
CSIRO-Mk3.5	-60	-70	-80	-59
ECHAM5/MPI-OM	-35	-25	-30	-13
GFDL-CM2.0	-20	-5	+5	1
GFDL-CM2.1	-25	-5	-5	1
MIROC3.2 (medres)	-75	-85	-85	-50
UKMO-HadCM3	-30	+10	+15	5
BCCR-BCM2.0	-5	+10	+15	6
CGCM3.1	-20	-10	-10	-9
CNRM-CM3	-35	-20	-30	-5
MRI-CGCM2.3.2	-25	-5	0	-2
CSIRO-Mk3.0	-50	-55	-65	-37
UKMO-HadGEM1	-5	+5	+15	13
IPSL-CM4	-20	-15	-20	-10
ECHO-G	-35	-25	-25	-7

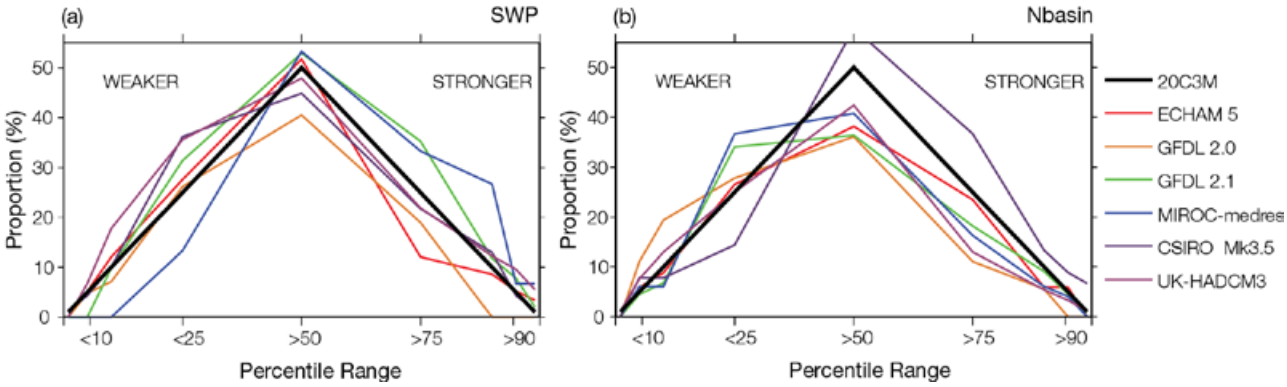

Figure 7.24: The proportion of projected storms in the late 21st century climate (2080–2099) that are stronger than the current climate (1980–1999) 50th percentile, 75th percentile and 90th percentile wind speeds and the proportion of storms that are weaker than the 25th and 10th percentile wind speeds in the CCAM simulations for (a) the southern Pacific and (b) the north basin.

7.4.6 Cyclonic Wind Hazard Projections

The Tropical Cyclone Risk Model used tracks of tropical cyclone-like vortices detected in the CCAM model as proxies for tropical cyclones. These were then used in the Tropical Cyclone Risk Model to produce estimates of the cyclonic wind hazard for both the current climate and late 21st century for the South Pacific (130°E–150°W, 30°S–0°) and the north-west Pacific (130°E–180°, 0°-15°N).

As described earlier and in Chapter 5, the CCAM simulations produce storms that are both less frequent and less intense than the real world. To overcome this, the frequency and intensity of the current climate simulations were re-scaled to match the historical record. This scaling was then held fixed for each future climate simulation. The resulting change in wind hazard between the current and future climate reflects the combined effect of changes to the frequency, intensity and track locations of the tropical cyclone-like vortices.

Maps of the relative change in the 500-year return period wind hazard between the current climate and the 20-year period centred on 2090 were created for each simulation. There is not a high degree of consistency between the spatial patterns of the projected change in wind hazard between the six simulations. This is illustrated by Figure 7.25, which shows the projected hazard change for the GFDL-CM2.1 and CSIRO-Mk3.5-based simulations. There were, however, some common trends shown in each of the model simulations. For the South Pacific, most models indicate a reduction in cyclonic wind hazard north of latitude 20ºS and some regions of increased hazard south of latitude 20ºS. Note, however, that the spatial patterns of these regions of increased wind hazard differs between models (c.f. Figures 7.25a and 7.25c). This increase in wind hazard coincides with the projected increase in the number of tropical cyclones occurring south of 20°S that was noted earlier. Similar increases have previously been found in the modelling study of Leslie et al. (2007). The poleward shift in cyclone frequency was found to also coincide with a poleward shift in the more intense storms. For the North Pacific region (between the equator and 15°N), there is a general reduction in cyclonic wind hazard between the current and future climate simulations as a result of a decrease in storm frequency close to the equator.

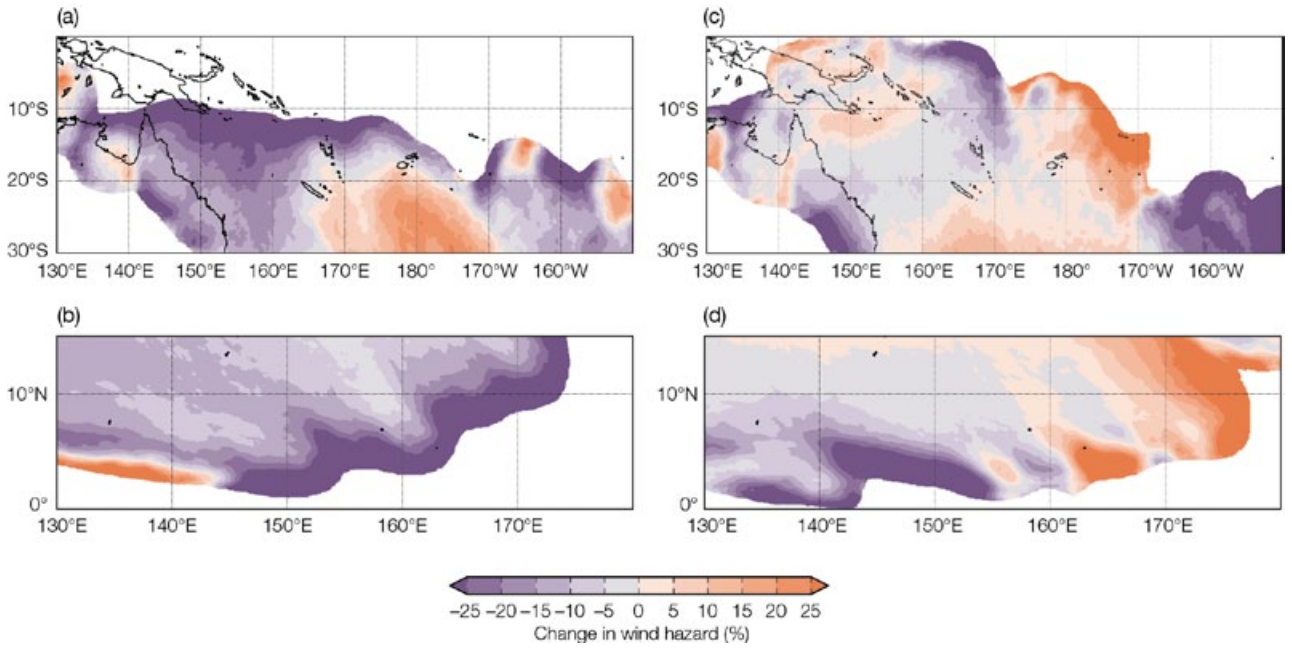

Figure 7.25: Percentage change in 500-year return period cyclonic wind speeds projected for the South Pacific (a and c) and the north-west Pacific (b and d) based on GFDL-CM2.1 (a and b) and CSIRO-Mk3.5 (c and d) for the late 21st century using the A2 (high) emissions scenario.

7.5 Downscaling Summary

The CCAM 60 km downscaled projections for the PCCSP region are broadly consistent with those of the global climate models presented in Chapter 6. However, some differences between global models and CCAM projections are noted, such as bands of rainfall decrease around latitudes 8°N and 8°S. These projections are also supported by the additional downscaling results using a variety of other regional climate models. The CCAM 8 km downscaled projections show regional-scale variations of the climate change signal, largely related to the topography of the Pacific Islands. Statistical downscaling shows slightly less warming, more consistent with the observed trends.

Projections of changes in tropical cyclone frequency based upon CMIP3 global climate models and CCAM show a number of important differences. The analysis of the global models using the CVP and CDD techniques shows that they are able to reproduce the climatology of tropical cyclones for the current climate. However, when these techniques are applied to the outputs from these models to provide projections of changes in frequency for the late 21st century, there is considerable variability in the projected changes between both the global models and the two techniques. Similarly, application of the GPI technique to the global model outputs also shows considerable variability between the models in projected changes in the occurrence of tropical cyclones affecting the study region.

In contrast, when the CDD technique is applied to CCAM outputs the projected changes show little variability between the six simulations considered. This may be due to the use of a single modelling system for the downscaled runs analysed. Importantly, the CCAM simulations underestimate the occurrence of tropical cyclones occurring east of 180°E. This deficiency should be considered when using tropical cyclone projections based upon these simulations.

Projections based upon these different modelling systems and analysis techniques show that tropical cyclone frequency in the PCCSP region is likely to decrease by the late 21st century. There is a moderate level of confidence in this projection, with little consistency found in the magnitude of the projected changes between either the models or the analysis methods.

Most simulations project an increase in the proportion of the most severe storms in the south-west Pacific and a southward movement in the latitude at which maximum intensity occurs. In the northern basin, most simulations project an increase in the proportion of storms occurring in the weaker categories. For the South Pacific, most models indicate a reduction in cyclonic wind hazard north of 20°S and regions of increased wind hazard south of 20°S. This coincides with the projected increase in the number of tropical cyclones occurring south of 20°S and with a poleward shift in the latitude at which storms are most intense. For the North Pacific region, there is a general reduction in cyclonic wind hazard between the current and future climate simulations as a result of a decrease in storm frequency close to the equator.

Koror, Palau

Chapter 8
Conclusions and Further Research to Advance Pacific Climate Science

8.1 Introduction

While there has been progress on many fronts to monitor, document, understand and project climate change relevant to the Pacific Climate Change Science Program's (PCCSP) Partner Countries, there are still many challenges. Further work to strengthen the scientific understanding of Pacific climate change is required to inform adaptation and mitigation strategies. Ongoing research in the following areas can contribute to the advancement of climate science in the PCCSP region.

8.1.1 Expand Ocean and Atmosphere Measurements in the Pacific Climate Change Science Program Region

There has been a marked decline in the total number of land based climate observation (measurement) stations in Partner Countries over the past few decades. These climate measurement stations need to be re-opened and upgraded, and the network needs to be expanded. The increased exchange of data between nations of the region will strengthen the ability of Partner Countries to monitor climate.

There is also a need to increase and recover meteorological and oceanographic data in the PCCSP region. The quality of historical climate observations in some countries is not high enough to reliably document variability or trends, and, despite improvements in ocean and satellite observations of the Pacific over the past few decades, the longer climate record of the Pacific region is generally sparse compared to other parts of the globe.

To this end, the rescue and rehabilitation of observational climate data, including the identification of new data sources and digitisation of hard copy data, is expanding the availability of climate data in Partner Countries, but requires continuing effort. The collation of other forms of historical data such as photographs, newspaper records and anecdotal evidence of change, is required to complement the instrumental monitoring of climate change. Given the relatively short duration of the instrumental records, palaeoclimate data also have an important role in extending the climate and sea-level records of this region.

Apart from the regional sea-level network, data documenting ocean changes are sparse, particularly regarding the sub-surface properties of the ocean, ocean chemistry and biological productivity changes. Greater use of ships of opportunity (volunteer merchant ships which routinely transit strategic shipping routes and carry instruments to measure ocean variables), or ocean gliders (remotely operated underwater vehicles, also carrying sensors to measure ocean characteristics) in the region will be beneficial. Expanded monitoring of ocean chemistry including acidification is urgent. Further analysis of historical sea-level observations is also required to provide a more continuous record of sea-level change.

A greater understanding of the role of tides, storm surges and waves in sea-level extremes would be facilitated by the addition of in situ wave observations throughout the region. This would include strategically located wave buoys and tide gauges. In quantifying the impacts of climate change on the coast in terms of both inundation and erosion, more comprehensive monitoring of shoreline changes and high resolution elevation surveys are needed throughout the region.

8.1.2 Advance the Understanding of Current Climate, Climate Variability and Climate Trends

A better understanding of climate features and patterns of variability in the PCCSP region is needed. For example, despite the key role of the South Pacific Convergence Zone in the climate of many Partner Countries, the processes governing it are still not fully understood. Issues such as this can be addressed through the continued use of observations and climate models. The imminent arrival of many new climate models through the international Coupled Model Intercomparison Project Phase 5 (CMIP5), and use of the Australian Climate Community Earth-System Simulator (ACCESS) for experimentation specifically targeted to issues of importance to the PCCSP region, provide exciting new opportunities on this front.

Trends in climate are evident over the Pacific as a whole, including the PCCSP region, however the extent to which these trends are attributable to natural variability and to human activities is not yet well understood. Greater clarity on this issue, and more reliable estimates of past variability in the atmosphere and the ocean – including extreme events – will help strengthen the credibility and communication of future climate projections in the region.

8.1.3 Improve Climate Models and Climate Change Projections

Models from the Coupled Model Intercomparison Project Phase 3 (CMIP3) have several limitations that restrict a full understanding of the past and projection of the future climate. The new set of global model projections from CMIP5 and the Intergovernmental Panel on Climate Change (IPCC) Fifth Assessment Report (due 2014) will provide new information about past and future climate, with a wider range of emissions scenarios and improved models.

CMIP5 will provide a standard set of model simulations to: (1) evaluate how realistic the models are in simulating the recent past, (2) provide projections of future climate change on two time scales, near-term (out to about 2035) and long-term (out to 2100 and beyond), and (3) explore the role of different factors and feedbacks such as clouds and the carbon cycle.

The ability of these next generation climate models to simulate climate in the PCCSP region needs to be assessed, and ongoing work to improve climate models needs to continue. Future model evaluation should also take advantage of the new enhanced regional climate dataset obtained from station records through the PCCSP.

Updating future climate projections for the PCCSP region using these new CMIP5 climate models is a priority. These projections need to be integrated more closely in specific case studies examining the impacts of climate change and developing adaptation strategies.

Greater attention needs to be given to assessing how statistical and dynamical downscaling can complement the global climate models. Downscaling of ocean projections is also required to understand changes to biological systems and impacts on fisheries and aquaculture.

One of the greatest sources of uncertainty in climate projections is the lack of consistency in projected El Niño-Southern Oscillation changes. Uncertainty can be better quantified and possibly reduced through closer study of systematic biases in the climate models associated with the El Niño-Southern Oscillation, the cold tongue and the South Pacific Convergence Zone. These model issues are likely to be interrelated and will require improvements to cloud physics, increased ocean resolution, and better representation of sub-annual atmospheric variability.

Uncertainty in sea-level projections is dominated by the future dynamic response of the Greenland and Antarctic ice sheets. Reducing uncertainty will require ongoing in situ and satellite observations, process studies and improved ice sheet (cryosphere) models, and the evaluation of climate models and their ability to simulate steric sea-level rise, as well as glacial and ice cap changes.

More detailed and rigorous testing of sea level and ocean heat content simulated by climate models is required, including the inter comparison of models and understanding the reasons for the differences between them. The models need to be critically compared with the available historical observations so as to improve understanding of interannual and decadal variability.

Regional projections of ocean acidification are based on coarse resolution climate models, so they do not represent localised changes in carbonate chemistry that result from net calcification and production within reefs, which can feedback to the acidification response. In order to reduce uncertainties of how reef systems will respond to acidification, a hierarchy of models and observations at reef and regional scales will be required. These models will also need to include ecological responses to other stressors including coral bleaching and pollution.

Climate models provide credible quantitative estimates of future climate change, particularly at larger scale, however some deficiencies remain at smaller scales. There will always be a range of uncertainty in climate projections. It is important that this uncertainty is understood and incorporated into any future impact assessments based on climate model projections.

8.1.4 Improve Understanding of Tropical Cyclones and Extreme Events

Continued use of climate models to make projections of tropical cyclone behaviour including frequency, location, intensity, rainfall and movement remains a high priority for the PCCSP region. Projections of changes in tropical cyclone intensity and extreme rainfall require the use of fine-resolution (less than 5 km) non-hydrostatic models which are able to represent small-scale features of the cyclone eye wall. The current methods used to predict the number of cyclones often provide conflicting results, reflecting a poor understanding of the relationship between cyclone activity and the surrounding large-scale circulation. A better understanding of the reasons why tropical cyclone activity varies from year to year will improve understanding and possibly lead to more robust projections. Projections of tropical cyclone activity in the future would also be more robust if the theoretical understanding of cyclone formation, intensity and frequency is enhanced.

To date there has been no systematic documentation of the effects of tropical cyclones in the PCCSP region. Daily time series of rainfall, sea level and wind need to be examined in order to document the contribution of tropical cyclones to extreme events in the current climate.

8.2 Conclusions

The IPCC Fourth Assessment Report (2007) concluded that a renewed international agenda to assess the vulnerability of small islands is needed, based on the most recent projections and newly available tools, to provide small islands with a firmer basis for future planning. The work of the PCCSP has addressed some of the key areas identified in the IPCC report as they relate to the Pacific islands and East Timor and has sought to enhance the capacity of the Partner Countries to collaborate in this research.

While some shortcomings, primarily in data availability and resolution of regional models, still remain, the PCCSP represents a coordinated, regionally focused research effort to directly address these issues.

There are many important steps to be taken on the way to implementing sound adaptation measures. An understanding of past and future climate change is fundamental, but it is only one step. This information has to be applied in impact models, vulnerability assessments, and ultimately long-term planning and decision support services.

Scientific research and capacity building have to proceed hand in hand. A long-term, inter-agency coordinated effort is required to further understand climate change science in the PCCSP region and to deliver the information in a manner that can inform and help shape adaptation strategies. This will assist the region in implementing the Pacific Islands Framework for Action on Climate Change and subsequent policies, and contribute to the sustainable development of the Partner Countries.

Blowholes, Tongatapu

Appendix 1
CMIP3 Models Used in Climate Projections

For many of the climate projections presented in Chapters 6 and 7, CMIP3 data were either analysed directly (e.g. temperature, rainfall) or used to calculate a climate variable (e.g. surface relative humidity, potential evapotranspiration) or diagnostic (e.g. Genesis Potential Index, aragonite saturation state) of interest (Table A1). However, many research institutions participating in CMIP3 did not provide data for all the model variables and SRES emission scenarios requested by the project organisers. As such, data availability is inconsistent for different variables, emission scenarios (i.e. A2, A1B and B1) and output frequencies (i.e. daily or monthly).

Information on the CMIP3 model data used in providing information on each PCCSP climate variable / diagnostic is therefore provided here (Table A2, Table A3, Table A4). It should be noted that:

- For any given variable and timescale, where data are available for one or more of the A2, A1B or B1 scenarios, data are also available for the corresponding 'Climate of the Twentieth Century' (20c3m) simulation.
- Due to high data archiving costs, daily GCM data are typically only available for the periods 1980–1999, 2046–2065 and 2080–2099. No such limitations apply for monthly data.
- For certain variables and emission scenarios, modelling groups provided data for multiple simulations of the same model, using slightly different initial conditions. The information outlined here indicates the models for which at least one simulation is available.
- The CMIP3 data are freely available, along with detailed documentation, from the Program for Climate Model Diagnosis and Intercomparison at Lawrence Livermore National Laboratory (www-pcmdi.llnl.gov).

Table A1. CMIP3 model variables required to provide information on each PCCSP variable / climate diagnostic.

PCCSP variable / climate diagnostic	Required model output (CMIP3 naming convention)
Surface air temperature	Surface air temperature (tas)
Daily maximum surface air temperature	Daily maximum surface air temperature (tasmax)
Daily minimum surface air temperature	Daily minimum surface air temperature (tasmin)
Rainfall	Precipitation (pr)
Surface wind	Calculated from zonal surface wind speed (uas) and meridional surface wind speed (vas)
Solar radiation	Surface downwelling shortwave radiation (rsds)
Surface relative humidity	Calculated from surface specific humidity (huss), sea level pressure (psl), surface altitude (orog) and surface air temperature (tas) data
Potential evapotranspiration	Calculated from surface downwelling shortwave radiation (rsds), surface air temperature (tas), surface altitude (orog), (calculated) surface relative humidity and precipitation (pr) data (Morton, 1983)
Sea surface temperature	Sea surface temperature (tos)
Sea surface salinity	Salinity (so)
Ocean temperature	Sea water potential temperature (thetao)
Ocean salinity	Salinity (so)
Ocean density	Calculated from potential temperature (thetao) and salinity (so) data
Ocean circulation	Calculated from eastward seawater velocity (uo) and northward seawater velocity (vo)
Buoyancy frequency squared	Calculated from potential temperature (thetao) and salinity (so) data
Steric sea level	Calculated from potential temperature (thetao) and salinity (so) data
Dynamic component of sea level	Sea surface elevation (zos)
Genesis potential index	Calculated from sea surface temperature (tos), sea level pressure (psl), air temperature (ta), specific humidity (hus), zonal wind speed (ua) and meridional wind speed (va) data
Curvature vorticity parameter	Calculated from air temperature (ta), specific humidity (hus), zonal wind speed (ua) and meridional wind speed (va) data
CSIRO direct detection method	Requires sea level pressure (psl), air temperature (ta), zonal wind speed (ua), meridional wind speed (va) data
Aragonite saturation state (Ωar)	Requires sea surface temperature (tos) and sea surface salinity (so) data

Table A2. CMIP3 models used in calculating atmospheric projections requiring daily timescale data.

		Temperature[a]			Rainfall			Tropical cyclones[b]		
		A2	A1B	B1	A2	A1B	B1	CVP	CDD	GPI
1	BCCR-BCM2.0									
2	CCSM3									
3	CGCM3.1 (T47)									
4	CGCM3.1 (T63)									
5	CNRM-CM3									
6	CSIRO-Mk3.0									
7	CSIRO-Mk3.5									
8	ECHAM5/MPI-OM									
9	ECHO-G									
10	FGOALS-g1.0									
11	GFDL-CM2.0									
12	GFDL-CM2.1									
13	*GISS-AOM*									
14	*GISS-EH*									
15	*GISS-ER*									
16	*INGV-SXG*									
17	*INM-CM3.0*									
18	IPSL-CM4									
19	MIROC3.2 (hires)									
20	MIROC3.2 (medres)									
21	MRI-CGCM2.3.2									
22	*PCM*									
23	UKMO-HadCM3									
24	UKMO-HadGEM1									
	Total models used	**11**	**15**	**15**	**14**	**16**	**16**	**4**	**10**	**14**

Pale blue cells denote those models and scenarios used in calculating projections. Italicised model names indicate those models excluded due to unacceptable performance in simulating the current climate (Section 5.5.1)

[a]Refers to both the daily maximum and minimum surface air temperature

[b]The Curvature Vorticity Parameter (CVP), CSIRO Direct Detection (CCD) scheme and Genesis Potential Index (GPI) were only calculated for the A2 emission scenario.

Table A3. CMIP3 models used in calculating atmospheric projections requiring monthly timescale data.

	Model name	Surface air temperature, rainfall			Surface wind			Solar radiation			Surface relative humidity, potential evapotranspiration		
		A2	A1B	B1	A2	A1B	B1	A2	A1B	B1	A2	A1B	B1
1	BCCR-BCM2.0												
2	CCSM3												
3	CGCM3.1 (T47)												
4	CGCM3.1 (T63)												
5	CNRM-CM3												
6	CSIRO-Mk3.0												
7	CSIRO-Mk3.5												
8	ECHAM5/MPI-OM												
9	ECHO-G												
10	FGOALS-g1.0												
11	GFDL-CM2.0												
12	GFDL-CM2.1												
13	*GISS-AOM*												
14	*GISS-EH*												
15	*GISS-ER*												
16	*INGV-SXG*												
17	*INM-CM3.0*												
18	IPSL-CM4												
19	MIROC3.2 (hires)												
20	MIROC3.2 (medres)												
21	MRI-CGCM2.3.2												
22	*PCM*												
23	UKMO-HadCM3												
24	UKMO-HadGEM1												
	Total models used	**15**	**18**	**17**	**13**	**16**	**15**	**15**	**18**	**16**	**9**	**11**	**10**

Pale blue cells denote those models and scenarios used in calculating projections. Italicised model names indicate those models excluded due to unacceptable performance in simulating the current climate (Section 5.5.1).

Table A4. CMIP3 models used in calculating oceanic projections requiring monthly timescale data.

	Model name	Sea surface temperature			Sea surface salinity[a]			T, S, density, buoyancy, steric sea level[b]			Dynamic sea level			Circulation			Ωar
		A2	A1B	B1	A2	A1B	B1		A1B			A1B			A1B		All[c]
1	BCCR-BCM2.0																
2	CCSM3																
3	CGCM3.1 (T47)																
4	CGCM3.1 (T63)																
5	CNRM-CM3																
6	CSIRO-Mk3.0																
7	CSIRO-Mk3.5																
8	ECHAM5/MPI-OM																
9	ECHO-G																
10	FGOALS-g1.0																
11	GFDL-CM2.0																
12	GFDL-CM2.1																
13	*GISS-AOM*																
14	*GISS-EH*																
15	*GISS-ER*																
16	*INGV-SXG*																
17	*INM-CM3.0*																
18	IPSL-CM4																
19	MIROC3.2 (hires)																
20	MIROC3.2 (medres)																
21	MRI-CGCM2.3.2																
22	*PCM*																
23	UKMO-HadCM3																
24	UKMO-HadGEM1																
	Total models used	**14**	**16**	**16**	**11**	**15**	**13**		**11**			**13**			**15**		**6**

Pale blue cells denote those models and scenarios used in calculating projections. Italicised model names indicate those models excluded due to unacceptable performance in simulating the current climate (Section 5.5.1)

[a]Model numbers are greater for sea surface salinity than for salinity through the depth of the ocean, as PCCSP researchers approached CMIP3 modelling groups requesting additional surface salinity data.

[b]Refers to the potential temperature (T), salinity (S), potential density and buoyancy frequency squared through the depth of the ocean.

[c]The same models were used for the A2, A1B and B1 scenarios.

Ωar = Aragonite saturation state.

Coastline, Nauru

References

Abram, N.J., McGregor, H.V., Gagan, M.K., Hantoro, W.S., and Suwargadi, B.W., (2009), Oscillations in the southern extent of the Indo-Pacific Warm Pool during the mid-Holocene: *Quaternary Science Reviews*, v. 28, p. 2794-2803.

Adler, R.F., Huffman, G.J., Chang, A., Ferraro, R., Xie, P.P., Janowiak, J., Rudolf, B., Schneider, U., Curtis, S., Bolvin, D., Gruber, A., Susskind, J., Arkin, P., and Nelkin, E., (2003), The version-2 global precipitation climatology project (GPCP) monthly precipitation analysis (1979–present): *Journal of Hydrometeorology*, v. 4, p. 1147-1167.

Alexander, L.V., Zhang, X., Peterson, T.C., Caesar, J., Gleason, B., Tank, A.M.G.K., Haylock, M., Collins, D., Trewin, B., Rahimzadeh, F., Tagipour, A., Kumar, K.R., Revadekar, J., Griffiths, G., Vincent, L., Stephenson, D.B., Burn, J., Aguilar, E., Brunet, M., Taylor, M., New, M., Zhai, P., Rusticucci, M., and Vazquez-Aguirre, J.L., (2006), Global observed changes in daily climate extremes of temperature and precipitation: *Journal of Geophysical Research-Atmospheres*, v. 111.

Allen, M.S., (2006), New ideas about late Holocene climate variability in the central Pacific: *Current Anthropology*, 47, 521-35.

Alley, R.B., Clark, P.U., Huybrechts, P. And Joughin, I., (2005), Ice-sheet and sea-level changes: *Science*, v. 310, p. 456-460

Anderson, A., Chappell, J., Gagan, M.K., and Grove, R., (2006), Prehistoric maritime migration in the Pacific islands: an hypothesis of ENSO forcing: *Holocene*, v. 16, p. 1-6.

Anthony, K.R.N., Kline, D.I., Diaz-Pulido, G., Dove, S., and Hoegh-Guldberg, O., (2008), Ocean acidification causes bleaching and productivity loss in coral reef builders: Proceedings of the National Academy of Sciences of the United States of America, v. 105, p. 17442-17446.

Antonov, J. I., R. A. Locarnini, T. P. Boyer, A. V. Mishonov, and H. E. Garcia, (2006), World Ocean Atlas 2005, Volume 2: Salinity. S. Levitus, (ed.) NOAA Atlas NESDIS 62, U.S. Government Printing Office, Washington, D.C., 182 pp.

Ashok, K., Behera, S.K., Rao, S.A., Weng, H.Y., and Yamagata, T., (2007), El Nino Modoki and its possible teleconnection: *Journal of Geophysical Research-Oceans*, v. 112.

Ashok, K., Guan, Z.Y., and Yamagata, T., (2001), Impact of the Indian Ocean Dipole on the relationship between the Indian monsoon rainfall and ENSO: *Geophysical Research Letters*, v. 28, p. 4499-4502.

Ashok, K., and Yamagata, T., (2009), The El Nino with a difference: *Nature*, v. 461, p. 481-484.

AS/NZS 1170.2:2002, (2002): *Structural design actions, Part 2: Wind actions*. Australian Standards/ New Zealand Standards.

Barry, R.G., and Chorley, R.J., (1992), Atmosphere, weather, and climate: London ; New York, Routledge, xxi, 392 p. p.

Bell, J.D., J.E. Johnson, and A.J Hobday, (eds.), (2011): *Vulnerability of Tropical Pacific Fisheries and Aquaculture to Climate Change*. Secretariat of the Pacific Community (SPC), Noumea, New Caledonia.

Bender, M.A., Knutson, T.R., Tuleya, R.E., Sirutis, J.J., Vecchi, G.A., Garner, S.T., and Held, I.M., (2010), Modeled Impact of Anthropogenic Warming on the Frequency of Intense Atlantic Hurricanes: *Science*, v. 327, p. 454-458.

Bengtsson, L., Bottger, H., and Kanamitsu, M., (1982), Simulation of Hurricane-Type Vortices in a General-Circulation Model: *Tellus*, v. 34, p. 440-457.

Beranger, K., Barnier, B., Gulev, S., and Crepon, M., (2006), Comparing 20 years of precipitation estimates from different sources over the world ocean: *Ocean Dynamics*, v. 56, p. 104-138.

Bindoff, N.L., J. Willebrand, V. Artale, A, Cazenave, J. Gregory, S. Gulev, K. Hanawa, C. Le Quéré, S. Levitus, Y. Nojiri, C.K. Shum, L.D. Talley and A. Unnikrishnan, (2007): Observations: Oceanic Climate Change and Sea Level. In: *Climate Change 2007: The Physical Science Basis*. *Contribution of Working Group I to the Fourth Assessment Report of the Intergovernmental Panel on Climate Change* [Solomon, S., D. Qin, M. Manning, Z. Chen, M. Marquis, K.B. Averyt, M. Tignor and H.L. Miller (eds.)]. Cambridge University Press, Cambridge, United Kingdom and New York, NY, US

Birner, T., (2010), Recent widening of the tropical belt from global tropopause statistics: Sensitivities*:* *Journal of Geophysical Research-Atmospheres*, v. 115.

Bister, M., and Emanuel, K.A., (1998), Dissipative heating and hurricane intensity: *Meteorology and Atmospheric Physics*, v. 65, p. 233-240.

Black, E., Slingo, J., and Sperber, K.R., (2003), An observational study of the relationship between excessively strong short rains in coastal East Africa and Indian Ocean SST: *Monthly Weather Review*, v. 131, p. 74-94.

Bosilovich, M.G., Chen, J.Y., Robertson, F.R., and Adler, R.F., (2008), Evaluation of global precipitation in reanalyses: *Journal of Applied Meteorology and Climatology*, v. 47, p. 2279-2299.

Broccoli, A.J., and Manabe, S., (1990), Can Existing Climate Models Be Used to Study Anthropogenic Changes in Tropical Cyclone Climate: *Geophysical Research Letters*, v. 17, p. 1917-1920.

Brohan, P., Kennedy, J.J., Harris, I., Tett, S.F.B., and Jones, P.D., (2006), Uncertainty estimates in regional and global observed temperature changes: A new data set from 1850: *Journal of Geophysical Research-Atmospheres*, v. 111.

Brown, J. R., Moise, A. F. and Delage, F. P., (in press), Changes in the South Pacific Convergence Zone in IPCC AR4 future climate projections: *Climate Dynamics*, doi:10.1007/s00382-011-1192-0.

Brown, J., Collins, M., Tudhope, A.W., and Toniazzo, T., (2008), Modelling mid-Holocene tropical climate and ENSO variability: towards constraining predictions of future change with palaeo-data: *Climate Dynamics*, v. 30, p. 19-36.

Brown, J.R., Power, S.B., Delage, F.P., Colman, R.A., Moise, A.F., and Murphy, B.F., (2011), Evaluation of the South Pacific Convergence Zone in IPCC AR4 Climate Model Simulations of the Twentieth Century: *Journal of Climate*, v. 24, p. 1565-1582.

Cai, W.J., and Cowan, T., (2007), Trends in Southern Hemisphere circulation in IPCC AR4 models over 1950-99: Ozone depletion versus greenhouse forcing: *Journal of Climate*, v. 20, p. 681-693.

Cai, W., Cowan, T., and Sullivan, A., (2009a), Recent unprecedented skewness towards positive Indian Ocean Dipole occurrences and its impact on Australian rainfall: *Geophysical Research Letters*, v. 36.

Cai, W., Shi, G., Cowan, T., Bi, D., and Ribbe, J., (2005), The response of the Southern Annular Mode, the East Australian Current, and the southern mid-latitude ocean circulation to global warming: *Geophysical Research Letters*, v. 32.

Cai, W., Sullivan, A., and Cowan, T., (2009b), Climate change contributes to more frequent consecutive positive Indian Ocean Dipole events: *Geophysical Research Letters*, v. 36.

Cai, W., Sullivan, A., and Cowan, T., (2009c), How rare are the 2006–2008 positive Indian Ocean Dipole events? An IPCC AR4 climate model perspective: *Geophysical Research Letters*, v. 36.

Cai, W., Sullivan, A., Cowan, T., Ribbe, J., and Shi, G., (2011), Simulation of the Indian Ocean Dipole: A relevant criterion for selecting models for climate projections: *Geophysical Research Letters*, v. 38.

Callaghan, D.P., Nielsen, P., Cartwright, N., Gourlay, M.R., and Baldock, T.E., (2006), Atoll lagoon flushing forced by waves: *Coastal Engineering*, v. 53, p. 691-704.

Callaghan, J. and Power, S.B., (2010), Variability and decline in the number of severe tropical cyclones making land-fall over eastern Australia since the late nineteenth century: *Climate Dynamics*, v. 37, issue 3-4, p. 647-662

Camargo, S.J., Emanuel, K.A., and Sobel, A.H., (2007a), Use of a genesis potential index to diagnose ENSO effects on tropical cyclone genesis: *Journal of Climate*, v. 20, p. 4819-4834.

Camargo, S.J., Sobel, A.H., Barnston, A.G., and Emanuel, K.A., (2007b), Tropical cyclone genesis potential index in climate models*: Tellus Series a-Dynamic Meteorology and Oceanography*, v. 59, p. 428-443.

Camargo, S.J., and Zebiak, S.E., (2002), Improving the detection and tracking of tropical cyclones in atmospheric general circulation models: *Weather and Forecasting*, v. 17, p. 1152-1162.

Cao, L., Klijn, N. and Gleeson, T. (2003), Modelling the effects of a temporary loss of export markets in case of a foot and mouth disease outbreak in Australia: preliminary results on costs to Australian beef producers and consumers: *Agribusiness Review*, v. 11, p.1-18.

Cazenave, A., and Llovel, W., (2010), Contemporary Sea Level Rise: *Annual Review of Marine Science*, v. 2, p. 145-173.

Chan, J.C.L., (1985), Tropical Cyclone Activity in the Northwest Pacific in Relation to the El-Nino Southern Oscillation Phenomenon: *Monthly Weather Review*, v. 113, p. 599-606.

Chan, J.C.L., (2005), Interannual and interdecadal variations of tropical cyclone activity over the western North Pacific: *Meteorology and Atmospheric Physics*, v. 89, p. 143-152.

Chan, J.C.L., (2006), Comment on “Changes in tropical cyclone number, duration, and intensity in a warming environment”: *Science*, v. 311.

Chan, J.C.L., and Shi, J.E., (1996), Long-term trends and interannual variability in tropical cyclone activity over the western North Pacific: *Geophysical Research Letters*, v. 23, p. 2765-2767.

Chao, B.F., Wu, Y.H. and Li, Y.S. (2008), Impact of Artificial Reservoir Water Impoundment on Global Sea Level. *Science*, 320, 212-214.

Chen, F., and Dudhia, J., (2001), Coupling an advanced land surface-hydrology model with the Penn State-NCAR MM5 modeling system. Part II: Preliminary model validation: *Monthly Weather Review*, v. 129, p. 587-604.

Chou, C., Neelin, J.D., Chen, C.A., and Tu, J.Y., (2009), Evaluating the “Rich-Get-Richer” Mechanism in Tropical Precipitation Change under Global Warming: *Journal of Climate*, v. 22, p. 1982-2005.

Chowdhury, M.R., Chu, P.S., and Schroeder, T., (2007), ENSO and seasonal sea-level variability - A diagnostic discussion for the US-Affiliated Pacific Islands: *Theoretical and Applied Climatology*, v. 88, p. 213-224.

Chowdhury, M. R., Chu, P.-S., Zhao, X. Schroeder, T.A. and Marra, J.J. (2010), Sea level extremes in the U.S.-Affiliated Pacific Islands – a coastal hazard scenario to aid in decision analyses. *J. Coast Conservation*, v. 14, p. 53-62.

Christensen, J.H., Hewitson, B., Busuioc, A., Chen, A., Gao, X., Held, I., Jones, R., Kolli, R.K., Kwon, W-T., Laprise, R., Magaña Rueda, V., Mearns, L., Menéndez, C.G., Räisänen, J., Rinke, A., Sarr, A. and Whetton, P., (2007), Regional Climate Projections. In: *Climate Change 2007: The Physical Science Basis*. *Contribution of Working Group I to the Fourth Assessment Report of the Intergovernmental Panel on Climate Change* [Solomon, S., D. Qin, M. Manning, Z. Chen, M. Marquis, K.B. Averyt, M. Tignor and H.L. Miller (eds.)]. Cambridge University Press, Cambridge, United Kingdom and New York, NY, USA.

Church J.A., Gregory J.M, Huybrechts P., Kuhn M., Lambeck K., Nhuan M.T., Qin D. & Woodworth P.L. (2001), Changes in Sea Level. In: *Climate Change 2001: The Scientific Basis. Contribution of Working Group 1 to the Third Assessment Report of the Intergovernmental Panel on Climate Change*, [Houghton, J.T., Y. Ding, D.J. Griggs, M. Noguer, P. van der Linden, X. Dai, K. Maskell and C.I. Johnson, (eds.)], pp.639-694, Cambridge University Press, Cambridge.

Church, J.A., Gregory, J.M., White, N.J., Platten, S.M., and Mitrovica, J.X., (2011), Understanding and Projecting Sea Level Change: *Oceanography*, v. 24, p. 130-143.

Church, J.A., and White, N.J., (2006), A 20th century acceleration in global sea-level rise: *Geophysical Research Letters*, v. 33.

Church, J. A. and N.J. White (in press), Sea-level rise from the late 19th to the early 21st Century. *Surveys in Geophysics*, doi:10.1007/s10712-011-9119-1.

Church, J.A., White, N.J., Aarup, T., Wilson, W.S., Woodworth, P.L., Domingues, C.M., Hunter, J.R., and Lambeck, K., (2008), Understanding global sea levels: past, present and future: *Sustainability Science*, v. 3, p. 9-22.

Church, J.A., White N.J. and Arblaster, J.M. (2005). Significant decadal-scale impact of volcanic eruptions on sea level and ocean heat content. *Nature*, v. 438, p. 74-77.

Church, J.A., White, N.J., Coleman, R., Lambeck, K., and Mitrovica, J.X., (2004), Estimates of the regional distribution of sea level rise over the 1950–2000 period: *Journal of Climate*, v. 17, p. 2609-2625.

Church, J.A., White, N.J., and Hunter, J.R., (2006), Sea-level rise at tropical Pacific and Indian Ocean islands: *Global and Planetary Change*, v. 53, p. 155-168.

Church, J.A., P.L. Woodworth, T. Aarup and W. S. Wilson, (eds.), (2010): *Understanding Sea-level Rise and Variability*. Wiley-Blackwell Publishing, Chichester, UK. 427 pp.

Clark, P.U., Mitrovica, J.X., Milne, G.A., and Tamisiea, M.E., (2002), Sea-level fingerprinting as a direct test for the source of global meltwater pulse IA: *Science*, v. 295, p. 2438-2441.

Cobb, K.M., Charles, C.D., Cheng, H., and Edwards, R.L., (2003), El Nino/Southern Oscillation and tropical Pacific climate during the last millennium: *Nature*, v. 424, p. 271-276.

Cogley, J.G., (2009), Geodetic and direct mass-balance measurements: comparison and joint analysis: *Annals of Glaciology*, v. 50, p. 96-100.

Coles, S., Bawa, J., Trenner, L., and Dorazio, P., (2001), An introduction to statistical modeling of extreme values: London, Springer, ix, 208 p.

Collins, M., An, S.I., Cai, W.J., Ganachaud, A., Guilyardi, E., Jin, F.F., Jochum, M., Lengaigne, M., Power, S., Timmermann, A., Vecchi, G., and Wittenberg, A., (2010), The impact of global warming on the tropical Pacific ocean and El Nino: *Nature Geoscience*, v. 3, p. 391-397.

Cook, E.R., Palmer, J.G., and D'Arrigo, R.D., (2002), Evidence for a 'Medieval Warm Period' in a 1,100 year tree-ring reconstruction of past austral summer temperatures in New Zealand: *Geophysical Research Letters*, v. 29.

Corney S.P., Katzfey, J.J., McGregor, J.L., Grose, M.R., Bennett, J.C., White, C.J., Holz, G.K., Gaynor, S.M., and Bindoff N.L., (2010), Climate Futures for Tasmania: climate modelling technical report, Antarctic Climate and Ecosystems Cooperative Research Centre, Hobart.

Cravatte, S., Delcroix, T., Zhang, D.X., McPhaden, M., and Leloup, J., (2009), Observed freshening and warming of the western Pacific Warm Pool: *Climate Dynamics*, v. 33, p. 565-589.

Crimp, S., Howden, M., Laing, A., Gaydon, D. Gartmann, A., Brown, P. and Nelson, R. (2009), Managing future agricultural production in a variable and changing climate. In the proceedings of the *International Scientific Congress on Climate Change – Global Risks, Challenges and Decisions*, Copenhagen 2009, 10–12 March, p. 328-332.

Curry, J.A., Webster, P.J., and Holland, G.J., (2006), Mixing politics and science in testing the hypothesis that greenhouse warming is causing a global increase in hurricane intensity: *Bulletin of the American Meteorological Society*, v. 87, p. 1025-1037.

Dai, A., (2006), Precipitation characteristics in eighteen coupled climate models: *Journal of Climate*, v. 19, p. 4605-4630.

D'Arrigo, R., Cook, E.R., Wilson, R.J., Allan, R., and Mann, M.E., (2005), On the variability of ENSO over the past six centuries: *Geophysical Research Letters*, v. 32.

D'Arrigo, R., and Smerdon, J.E., (2008), Tropical climate influences on drought variability over Java, Indonesia*: Geophysical Research Letters*, v. 35.

Davidson, N.E., Mcbride, J.L., and Mcavaney, B.J., (1983), The Onset of the Australian Monsoon during Winter Monex - Synoptic Aspects*: Monthly Weather Review*, v. 111, p. 496-516.

De Szoeke, S.P., and Xie, S.P., (2008), The tropical eastern Pacific seasonal cycle: Assessment of errors and mechanisms in IPCC AR4 coupled ocean - Atmosphere general circulation models: *Journal of Climate*, v. 21, p. 2573-2590.

Dee, D.P., Uppala, S.M., Simmons, A.J., Berrisford, P., Poli, P., Kobayashi, S., Andrae, U., Balmaseda, M.A., Balsamo, G., Bauer, P., Bechtold, P., Beljaars, A.C.M., van de Berg, L., Bidlot, J., Bormann, N., Delsol, C., Dragani, R., Fuentes, M., Geer, A.J., Haimberger, L., Healy, S.B., Hersbach, H., Holm, E.V., Isaksen, L., Kallberg, P., Kohler, M., Matricardi, M., McNally, A.P., Monge-Sanz, B.M., Morcrette, J.J., Park, B.K., Peubey, C., de Rosnay, P., Tavolato, C., Thepaut, J.N., and Vitart, F., (2011), The ERA-Interim reanalysis: configuration and performance of the data assimilation system: *Quarterly Journal of the Royal Meteorological Society*, v. 137, p. 553-597.

Delcroix, T., Henin, C., Porte, V. and Arkin, P., (1996), Precipitation and sea surface salinity in the tropical Pacific. *Deep Sea Research*, v. 43, p. 1123-1141.

Denman, K.L., G. Brasseur, A. Chidthaisong, P. Ciais, P. Cox, R.E. Dickinson, D. Hauglustaine, C. Heinze, E. Holland, D. Jacob, U. Lohmann, S. Ramachandran, P.L. da Silva Dias, S.C. Wofsy, and X. Zhang, (2007): Couplings Between Changes in the Climate System and Biogeochemistry. In: *Climate Change 2007: The Physical Science Basis*. *Contribution of Working Group I to the Fourth Assessment Report of the Intergovernmental Panel on Climate Change.* [Solomon, S., D. Qin, M. Manning, Z. Chen, M. Marquis, K.B. Averyt, M. Tignor, and H.L. Miller (eds.)]. Cambridge University Press, Cambridge, United Kingdom and New York, NY, USA.

Deser, C., Phillips, A.S. and Alexander, M.A. (2010). Twentieth century tropical sea surface temperature trends revisited. *Geophysical Research Letters*, v. 37.

DiNezio, P.N., Clement, A.C., Vecchi, G.A., Soden, B.J., and Kirtman, B.P., (2009), Climate Response of the Equatorial Pacific to Global Warming: *Journal of Climate*, v. 22, p. 4873-4892.

Domingues, C.M., Church, J.A., White, N.J., Gleckler, P.J., Wijffels, S.E., Barker, P.M., and Dunn, J.R., (2008), Improved estimates of upper-ocean warming and multi-decadal sea-level rise: *Nature*, v. 453, p. 1090-U6.

Dommenget, D., (2010), An objective analysis of the observed spatial structure of the tropical Indian Ocean SST variability. *Climate Dynamics*, v. 36, issue 11-21, p. 2129-2145

Donnelly, J.P., Cleary, P., Newby, P., and Ettinger, R., (2004), Coupling instrumental and geological records of sea-level change: Evidence from southern New England of an increase in the rate of sea-level rise in the late 19th century: *Geophysical Research Letters*, v. 31.

Dore, J.E., Lukas, R., Sadler, D.W., Church, M.J. and Karl, D.M. (2009), Physical and biogeochemical modulation of ocean acidification in the central North Pacific. *Proceedings of the National Academy of Sciences of the United States of America*, v. 106, p. 12235-12240.

Dunkerton, T.J., Montgomery, M.T., and Wang, Z., (2009), Tropical cyclogenesis in a tropical wave critical layer: easterly waves: *Atmospheric Chemistry and Physics*, v. 9, p. 5587-5646.

Dunn, J.R., and Ridgway, K.R., (2002), Mapping ocean properties in regions of complex topography: *Deep-Sea Research Part I-Oceanographic Research Papers*, v. 49, p. 591-604.

Durack, P.J., and Wijffels, S.E., (2010), Fifty-Year Trends in Global Ocean Salinities and Their Relationship to Broad-Scale Warming: *Journal of Climate*, v. 23, p. 4342-4362.

Emanuel, K.A., and Nolan, D.S., (2004), Tropical cyclone activity and global climate*: Bulletin of the American Meteorological Society*, v. 85, p. 666-667.

Etheridge, D.M., Steele, L.P., Langenfelds, R.L., Francey, R.J., Barnola, J.M., and Morgan, VI., (1996), Natural and anthropogenic changes in atmospheric CO_2 over the last 1000 years from air in Antarctic ice and firn: *Journal of Geophysical Research-Atmospheres*, v. 101, p. 4115-4128.

Fabry, V.J., Seibel, B.A., Feely, R.A., and Orr, J.C., (2008), Impacts of ocean acidification on marine fauna and ecosystem processes: *Ices Journal of Marine Science*, v. 65, p. 414-432.

Fedorov, A.V., and Philander, S.G., (2000), Is El Nino changing?: *Science*, v. 288, p. 1997-2002.

Feely, R.A., Doney, S.C., and Cooley, S.R., (2009), Ocean Acidification: Present Conditions and Future Changes in a High-CO_2 World: *Oceanography*, v. 22, p. 36-47.

Feely, R.A., Sabine, C.L., Lee, K., Berelson, W., Kleypas, J., Fabry, V.J., and Millero, F.J., (2004), Impact of anthropogenic CO_2 on the $CaCO_3$ system in the oceans: *Science*, v. 305, p. 362-366.

Fettweis, X., (2007), Reconstruction of the 1979–2006 Greenland ice sheet surface mass balance using the regional climate model MAR: *The Cryosphere Discussions,* v. 1, (1), p. 123-168.

Folland, C.K., Renwick, J.A., Salinger, M.J., and Mullan, A.B., (2002), Relative influences of the Interdecadal Pacific Oscillation and ENSO on the South Pacific Convergence Zone: *Geophysical Research Letters*, v. 29.

Folland, C.K., Salinger, M.J., Jiang, N., and Rayner, N.A., (2003), Trends and variations in South Pacific island and ocean surface temperatures: *Journal of Climate*, v. 16, p. 2859-2874.

Fowler, H.J., Blenkinsop, S., and Tebaldi, C., (2007), Linking climate change modelling to impacts studies: recent advances in downscaling techniques for hydrological modelling: *International Journal of Climatology*, v. 27, p. 1547-1578.

Frauke, F., Rockel, B., von Storch, H., Winterfeldt, J., and Zahn, M., (2011), Regional climate models add value to global model data: *Bulletin of the American Meteorological Society*, doi: 10.1175/2011BAMS3061.1.

Frich, P., Alexander, L.V., Della-Marta, P., Gleason, B., Haylock, M., Tank, A.M.G.K., and Peterson, T., (2002), Observed coherent changes in climatic extremes during the second half of the twentieth century: *Climate Research*, v. 19, p. 193-212.

Friedlingstein, P., Houghton, R.A., Marland, G., Hackler, J., Boden, T.A., Conway, T.J., Canadell, J.G., Raupach, M.R., Ciais, P., and Le Quere, C., (2010), Update on CO_2 emissions: *Nature Geoscience*, v. 3, p. 811-812.

Fyfe, J.C., Boer, G.J., and Flato, G.M., (1999), The Arctic and Antarctic oscillations and their projected changes under global warming: *Geophysical Research Letters*, v. 26, p. 1601-1604.

Gagan, M.K., Hendy, E.J., Haberle, S.G., and Hantoro, W.S., (2004), Post-glacial evolution of the Indo-Pacific Warm Pool and El Nino-Southern Oscillation: *Quaternary International*, v. 118-19, p. 127-143.

Ganachaud, A., Gourdeau, L., and Kessler, W., (2008), Bifurcation of the subtropical south equatorial current against New Caledonia in December 2004 from a hydrographic inverse box model*: Journal of Physical Oceanography*, v. 38, p. 2072-2084.

Ganachaud, A., Sen Gupta, A., Orr, J., Wijffels, S., Ridgway, K., Hemer, M., Maes, C., Steinberg, C., Tribollet, A., Qiu, B., and Kruger, J., (2011), Observed and expected changes to the tropical Pacific Ocean, in *Vulnerability of Fisheries and Aquaculture in the Tropical Pacific to Climate Change*. Secretariat of the Pacific Community (SPC), Noumea, New Caledonia., edited by J. D. Bell, J. E. Johnson, and A. J. Hobday.

Garcia, H. E., R. A. Locarnini, T. P. Boyer, and J. I. Antonov, (2006): *World Ocean Atlas 2005, Volume 4: Nutrients (phosphate, nitrate, silicate)*. S. Levitus, (ed.), NOAA Atlas NESDIS 64, U.S. Government Printing Office, Washington, D.C., 396 pp.

Gehrels, W.R., Hayward, B., Newnham, R.M., and Southall, K.E., (2008), A 20th century acceleration of sea-level rise in New Zealand: *Geophysical Research Letters*, v. 35.

Gehrels, W.R., Kirby, J.R., Prokoph, A., Newnham, R.M., Achterberg, E.P., Evans, H., Black, S., and Scott, D.B., (2005), Onset of recent rapid sea-level rise in the western Atlantic Ocean: *Quaternary Science Reviews*, v. 24, p. 2083-2100.

Gehrels, W.R., Marshall, W.A., Gehrels, M.J., Larsen, G., Kirby, J.R., Eiriksson, J., Heinemeier, J., and Shimmield, T., (2006), Rapid sea-level rise in the North Atlantic Ocean since the first half of the nineteenth century: *Holocene*, v. 16, p. 949-965.

Gergis, J.L., and Fowler, A.M., (2009), A history of ENSO events since AD 1525: implications for future climate change: *Climatic Change*, v. 92, p. 343-387.

Gill, A.E., (1982), Atmosphere-ocean dynamics: New York, Academic Press, xv, 662 p. p.

Gillett, N.P., Kell, T.D., and Jones, P.D., (2006), Regional climate impacts of the Southern Annular Mode: *Geophysical Research Letters*, v. 33.

Gillett, N.P., and Thompson, D.W.J., (2003), Simulation of recent Southern Hemisphere climate change: *Science*, v. 302, p. 273-275.

Gomez, N., Mitrovica, J.X., Huybers, P., and Clark, P.U., (2010), Sea level as a stabilizing factor for marine-ice-sheet grounding lines: *Nature Geoscience*, v. 3, p. 850-853.

Gourdeau, L., Kessler, W.S., Davis, R.E., Sherman, J., Maes, C., and Kestenare, E., (2008), Zonal jets entering the coral sea: *Journal of Physical Oceanography*, v. 38, p. 715-725.

Gouriou, Y., and Toole, J., (1993), Mean Circulation of the Upper Layers of the Western Equatorial Pacific-Ocean: *Journal of Geophysical Research-Oceans*, v. 98, p. 22495-22520.

Gray, W. M., (1979), Hurricanes: Their formation structure and likely role in tropical circulation. In: *Meteorology over the tropical oceans*, D.B. Shaw, (ed.), Royal Meteorological Society, p. 155-218

Gregory, J.M., and Huybrechts, P., (2006), Ice-sheet contributions to future sea-level change: *Philosophical Transactions of the Royal Society a-Mathematical Physical and Engineering Sciences*, v. 364, p. 1709-1731.

Gregory, J.M, Lowe, J.A. and Tett, S.F.B., (2006). Simulated global-mean sea level changes over the last half-millennium. *Journal of Climate*, v. 19, issue 18, p. 4576-4591.

Grell, G.A., J. Dudhia and D.R. Stauffer, (1994), A description of the fifth-generation Penn System/ NCAR Mesoscale Model (MM5). NCAR Technical Note NCAR/ TN–398+STR, 121 pp.

Griffiths, G.M., Chambers, L.E., Haylock, M.R., Manton, M.J., Nicholls, N., Baek, H.J., Choi, Y., Della-Marta, P.M., Gosai, A., Iga, N., Lata, R., Laurent, V., Maitrepierre, L., Nakamigawa, H., Ouprasitwong, N., Solofa, D., Tahani, L., Thuy, D.T., Tibig, L., Trewin, B., Vediapan, K., and Zhai, P., (2005), Change in mean temperature as a predictor of extreme temperature change in the Asia-Pacific region: *International Journal of Climatology*, v. 25, p. 1301-1330.

Griffiths, G.M., Salinger, M.J., and Leleu, I., (2003), Trends in extreme daily rainfall across the South Pacific and relationship to the South Pacific Convergence Zone: *International Journal of Climatology*, v. 23, p. 847-869.

Griffiths, M.L., Drysdale, R.N., Gagan, M.K., Zhao, J.X., Ayliffe, L.K., Hellstrom, J.C., Hantoro, W.S., Frisia, S., Feng, Y.X., Cartwright, I., Pierre, E.S., Fischer, M.J., and Suwargadi, B.W., (2009), Increasing Australian-Indonesian monsoon rainfall linked to early Holocene sea-level rise: *Nature Geoscience*, v. 2, p. 636-639.

Grinsted, A., Moore, J.C., and Jevrejeva, S., (2010), Reconstructing sea level from paleo and projected temperatures 200 to 2100 ad: *Climate Dynamics*, v. 34, p. 461-472.

Guan, Z.Y., and Yamagata, T., (2003), The unusual summer of 1994 in East Asia: IOD teleconnections: *Geophysical Research Letters*, v. 30.

Guilyardi, E., Wittenberg, A., Fedorov, A., Collins, M., Wang, C.Z., Capotondi, A., van Oldenborgh, G.J., and Stockdale, T., (2009), Understanding El Nino in Ocean-Atmosphere General Circulation Models Progress and Challenges: *Bulletin of the American Meteorological Society*, v. 90, p. 325-340.

Guinotte, J.M., Buddemeier, R.W., and Kleypas, J.A., (2003), Future coral reef habitat marginality: temporal and spatial effects of climate change in the Pacific basin: *Coral Reefs*, v. 22, p. 551-558.

Guinotte, J.M., and Fabry, V.J., (2008), Ocean acidification and its potential effects on marine ecosystems: *Year in Ecology and Conservation Biology 2008*, v. 1134, p. 320-342.

Guttman, N.B., (1989), Statistical Descriptors of Climate: *Bulletin of the American Meteorological Society*, v. 70, p. 602-607.

HB 212-2002, (2002): *Design Wind Speeds for the Asia-Pacific Region*. Standards Australia International.

Hall, T.M., and Jewson, S., (2007), Statistical modelling of North Atlantic tropical cyclone tracks: *Tellus Series a-Dynamic Meteorology and Oceanography*, v. 59, p. 486-498.

Han, W.Q., Meehl, G.A., and Hu, A.X., (2006), Interpretation of tropical thermocline cooling in the Indian and Pacific oceans during recent decades: *Geophysical Research Letters*, v. 33.

Hart, R.E., (2003), A cyclone phase space derived from thermal wind and thermal asymmetry: *Monthly Weather Review*, v. 131, p. 585-616.

Hasegawa, T., and Hanawa, K., (2003), Decadal-scale variability of upper ocean heat content in the tropical Pacific: *Geophysical Research Letters*, v. 30.

Haug, G.H., Hughen, K.A., Sigman, D.M., Peterson, L.C., and Rohl, U., (2001), Southward migration of the intertropical convergence zone through the Holocene: *Science*, v. 293, p. 1304-1308.

Hautala, S.L., Sprintall, J., Potemra, J.T., Chong, J.C., Pandoe, W., Bray, N., and Ilahude, A.G., (2001), Velocity structure and transport of the Indonesian Throughflow in the major straits restricting flow into the Indian Ocean: *Journal of Geophysical Research-Oceans*, v. 106, p. 19527-19546.

Hayes, S.P., Mangum, L.J., Picaut, J., Sumi, A., and Takeuchi, K., (1991), Toga-Tao - a Moored Array for Real-Time Measurements in the Tropical Pacific-Ocean: *Bulletin of the American Meteorological Society*, v. 72, p. 339-347.

Hegerl, G.C., F. W. Zwiers, P. Braconnot, N.P. Gillett, Y. Luo, J.A. Marengo Orsini, N. Nicholls, J.E. Penner and P.A. Stott, (2007), Understanding and Attributing Climate Change. In: *Climate Change 2007: The Physical Science Basis. Contribution of Working Group I to the Fourth Assessment Report of the Intergovernmental Panel on Climate Change* [Solomon, S., D. Qin, M. Manning, Z. Chen, M. Marquis, K.B. Averyt, M. Tignor and H.L. Miller (eds.)]. Cambridge University Press, Cambridge, United Kingdom and New York, NY, USA.

Held, I.M., and Soden, B.J., (2006), Robust responses of the hydrological cycle to global warming: *Journal of Climate*, v. 19, p. 5686-5699.

Hemer, M.A., Simmonds, I., and Keay, K., (2008), A classification of wave generation characteristics during large wave events on the Southern Australian margin: *Continental Shelf Research*, v. 28, p. 634-652.

Hendon, H.H., and Liebmann, B., (1990a), A Composite Study of Onset of the Australian Summer Monsoon: *Journal of the Atmospheric Sciences*, v. 47, p. 2227-2240.

Hendon, H.H., and Liebmann, B., (1990b), The Intraseasonal (30-50 Day) Oscillation of the Australian Summer Monsoon: *Journal of the Atmospheric Sciences*, v. 47, p. 2909-2923.

Hendon, H.H., Thompson, D.W.J., and Wheeler, M.C., (2007), Australian rainfall and surface temperature variations associated with the Southern Hemisphere annular mode: *Journal of Climate*, v. 20, p. 2452-2467.

Hoegh-Guldberg, O., Mumby, P.J., Hooten, A.J., Steneck, R.S., Greenfield, P., Gomez, E., Harvell, C.D., Sale, P.F., Edwards, A.J., Caldeira, K., Knowlton, N., Eakin, C.M., Iglesias-Prieto, R., Muthiga, N., Bradbury, R.H., Dubi, A., and Hatziolos, M.E., (2007), Coral reefs under rapid climate change and ocean acidification: *Science*, v. 318, p. 1737-1742.

Holgate, S., Jevrejeva, S., Woodworth, P., and Brewer, S., (2007), Comment on "A semi-empirical approach to projecting future sea-level rise": *Science*, v. 317.

Horton, R., Herweijer, C., Rosenzweig, C., Liu, J.P., Gornitz, V., and Ruane, A.C., (2008), Sea level rise projections for current generation CGCMs based on the semi-empirical method: *Geophysical Research Letters*, v. 35.

Hosking, J.R.M., (1990), L-Moment - Analysis and Estimation of Distributions Using Linear-Combinations of Order-Statistics: *Journal of the Royal Statistical Society Series B-Methodological*, v. 52, p. 105-124.

Houston, J. R. and Dean, R.G., (2011), Sea-Level Acceleration Based on U.S. Tide Gauges and Extensions of Previous Global-Gauge Analyses: *Journal of Coastal Research*, v. 27, p. 409-417.

Hu, Y., and Fu, Q., (2007), Observed poleward expansion of the Hadley circulation since 1979: *Atmospheric Chemistry and Physics*, v. 7, p. 5229-5236.

Huffman, G.J., Adler, R.F., Arkin, P., Chang, A., Ferraro, R., Gruber, A., Janowiak, J., McNab, A., Rudolf, B., and Schneider, U., (1997), The Global Precipitation Climatology Project (GPCP) Combined Precipitation Dataset: *Bulletin of the American Meteorological Society*, v. 78, p. 5-20.

IPCC, (2000): *Emissions Scenarios. Special Report of the Intergovernmental Panel on Climate Change*. Nakicenovic, N., and R. Swart, (eds). Cambridge University Press, UK. 570 pp.

IPCC, (2007): *Climate Change 2007: The Physical Science Basis. Contribution of Working Group 1 to the Fourth Assessment Report of the Intergovernmental Panel in Climate Change* [Solomon, S, D. Qin, M. Manning, Z. Chen, M. Marquis, K.B. Ayert, M. Tignor and H.L. Miller (eds.)]. Cambridge University Press, Cambridge, United Kingdom and New York, NY, USA, 996 pp.

Irving D.B., Perkins S.E., Brown J.R., Sen Gupta A., Moise A.F., Murphy B.F., Muir L.C., Colman R.A., Power S.B., Delage F.P., Brown J.N., (in press), Evaluating global climate models for climate change projections in the Pacific island region, *Climate Research*, doi: 10.3354/cr01028

Ishii, M., and Kimoto, M., (2009), Reevaluation of historical ocean heat content variations with time-varying XBT and MBT depth bias corrections: *Journal of Oceanography*, v. 65, p. 287-299.

Izumo, T., (2005), The equatorial undercurrent, meridional overturning circulation, and their roles in mass and heat exchanges during El Nino events in the tropical Pacific ocean: *Ocean Dynamics*, v. 55, p. 110-123.

Jansen, E., J. Overpeck, K.R. Briffa, J.-C. Duplessy, F. Joos, V. Masson-Delmotte, D. Olago, B. Otto-Bliesner, W.R. Peltier, S. Rahmstorf, R. Ramesh, D. Raynaud, D. Rind, O. Solomina, R. Villalba and D. Zhang, (2007): Palaeoclimate. In: *Climate Change 2007: The Physical Science Basis. Contribution of Working Group I to the Fourth Assessment Report of the Intergovernmental Panel on Climate Change* [Solomon, S., D. Qin, M. Manning, Z. Chen, M. Marquis, K.B. Averyt, M. Tignor and H.L. Miller (eds.)]. Cambridge University Press, Cambridge, United Kingdom and New York, NY, USA.

Jevrejeva, S., Grinsted, A., Moore, J.C., and Holgate, S., (2006), Nonlinear trends and multiyear cycles in sea level records: *Journal of Geophysical Research-Oceans*, v. 111.

Jevrejeva, S., Moore, J. C., Grinsted, A. and Woodworth, P.L. (2008) Recent global sea level acceleration started over 200 years ago?, *Geophysical Research Letters*, v. 35.

Jiang, H.Y., and Zipser, E.J., (2010), Contribution of Tropical Cyclones to the Global Precipitation from Eight Seasons of TRMM Data: Regional, Seasonal, and Interannual Variations: *Journal of Climate*, v. 23, p. 1526-1543.

Johanson, C.M., and Fu, Q., (2009), Hadley Cell Widening: Model Simulations versus Observations: *Journal of Climate*, v. 22, p. 2713-2725.

Johnson, G.C., Sloyan, B.M., Kessler, W.S., and McTaggart, K.E., (2002), Direct measurements of upper ocean currents and water properties across the tropical Pacific during the 1990s: *Progress in Oceanography*, v. 52, p. 31-61.

Johnson, N.C., and Xie, S.P., (2010), Changes in the sea surface temperature threshold for tropical convection: *Nature Geoscience*, v. 3, p. 842-845.

Jones, R.G., Noguer, M., Hassell, D.C. Hudson, D., Wilson, S.S., Jenkins, G.J., and Mitchell, J.F.B. (2004), Generating high resolution climate change scenarios using PRECIS. Met Office Hadley Centre, Exeter, UK, 40 pp.

Joseph, R., and Nigam, S., (2006), ENSO evolution and teleconnections in IPCC's twentieth-century climate simulations: Realistic representation?: *Journal of Climate*, v. 19, p. 4360-4377.

Joshi, M.M., Gregor,y J.M., Webb, M.J., Sexton, D.M.H. and Johns, T.C. (2007) Mechanisms for the land/sea warming contrast exhibited by simulations of climate change. *Climate Dynamics,* v. 30, p. 455-465.

Joughin, I., Smith, B.E., and Holland, D.M., (2010), Sensitivity of 21st century sea level to ocean-induced thinning of Pine Island Glacier, Antarctica: *Geophysical Research Letters*, v. 37.

Kalnay, E., Kanamitsu, M., Kistler, R., Collins, W., Deaven, D., Gandin, L., Iredell, M., Saha, S., White, G., Woollen, J., Zhu, Y., Chelliah, M., Ebisuzaki, W., Higgins, W., Janowiak, J., Mo, K.C., Ropelewski, C., Wang, J., Leetmaa, A., Reynolds, R., Jenne, R., and Joseph, D., (1996), The NCEP/NCAR 40-year reanalysis project: *Bulletin of the American Meteorological Society*, v. 77, p. 437-471.

Kanamitsu, M. and DeHaan L., (2011), The added value index: A new metric to quantify the added value of regional models: *Journal of Geophysical Research*, v. 116.

Kanamitsu, M., Ebisuzaki, W., Woollen, J., Yang, S.K., Hnilo, J.J., Fiorino, M., and Potter, G.L., (2002), Ncep-Doe Amip-Ii Reanalysis (R-2): *Bulletin of the American Meteorological Society*, v. 83, p. 1631-1643.

Kaplan, A., Cane, M.A., Kushnir, Y., Clement, A.C., Blumenthal, M.B., and Rajagopalan, B., (1998), Analyses of global sea surface temperature 1856-1991: *Journal of Geophysical Research-Oceans*, v. 103, p. 18567-18589.

Karl, T.R.; J.M. Melillo, T.C. Peterson, (eds.), (2009): *Global Climate Change Impacts in the United States*. Cambridge University Press. http://www.globalchange.gov/publications/reports/scientific-assessments/us-impacts.

Kaser, G., Cogley, J.G., Dyurgerov, M.B., Meier, M.F., and Ohmura, A., (2006), Mass balance of glaciers and ice caps: Consensus estimates for 1961–2004: *Geophysical Research Letters*, v. 33.

Katsman, C.A., Sterl, A., Beersma, J.J., van den Brink, H.W., Church, J.A., Hazeleger, W., Kopp, R.E., Kroon, D., Kwadijk, J., Lammersen, R., Lowe, J., Oppenheimer, M., Plag, H.-P., Ridley, J., von Storch, H., Vaughan, D.G., Vellinga, P., Vermeersen, L.L.A., van de Wal, R.S.W. and Weisse, R., (in press). Exploring high-end scenarios for local sea level rise to develop flood protection strategies for a low-lying delta - the Netherlands as an example. *Climatic Change*, doi:10.1007/s10584-011-0037-5.

Kemp, A.C., Horton, B.P., Culver, S.J., Corbett, D.R., van de Plassche, O., Gehrels, W.R., Douglas, B.C., and Parnell, A.C., (2009), Timing and magnitude of recent accelerated sea-level rise (North Carolina, United States): *Geology*, v. 37, p. 1035-1038.

Kepert, J., (2001), The dynamics of boundary layer jets within the tropical cyclone core. Part I: Linear theory: *Journal of the Atmospheric Sciences*, v. 58, p. 2469-2484.

Kharin, V.V., Zwiers, F.W., and Zhang, X.B., (2005), Intercomparison of near-surface temperature and precipitation extremes in AMIP-2 simulations, reanalyses, and observations: *Journal of Climate*, v. 18, p. 5201-5223.

Kharin, V.V., Zwiers, F.W., Zhang, X.B., and Hegerl, G.C., (2007), Changes in temperature and precipitation extremes in the IPCC ensemble of global coupled model simulations: *Journal of Climate*, v. 20, p. 1419-1444.

Kidston, J., Renwick, J. A. and McGregor, J., (2009), Hemispheric-scale seasonality of the Southern Annular Mode and impacts on the climate of New Zealand: *Journal of Climate*, v. 22, p. 4759-4770.

Kiem, A.S., Franks, S.W., and Kuczera, G., (2003), Multi-decadal variability of flood risk: *Geophysical Research Letters*, v. 30.

Kiladis, G.N., Vonstorch, H., and Vanloon, H., (1989), Origin of the South-Pacific Convergence Zone: *Journal of Climate*, v. 2, p. 1185-1195.

Kim, H.J., Wang, B., and Ding, Q.H., (2008), The Global Monsoon Variability Simulated by CMIP3 Coupled Climate Models: *Journal of Climate*, v. 21, p. 5271-5294.

Klein Tank, A.M.G., Zwiers, F.W., and Zhang, X., (2009): *Guidelines on analysis of extremes in a changing climate in support of informed decisions for adaptation*. WMO Climate Data and Monitoring, WCDMP-No.72, 56 pp.

Kleypas, J.A., McManus, J.W., and Menez, L.A.B., (1999), Environmental limits to coral reef development: Where do we draw the line?: *American Zoologist*, v. 39, p. 146-159.

Knutson, T.R., McBride, J.L., Chan, J., Emanuel, K., Holland, G., Landsea, C., Held, I., Kossin, J.P., Srivastava, A.K., and Sugi, M., (2010), Tropical cyclones and climate change: *Nature Geoscience*, v. 3, p. 157-163.

Knutti, R., Abramowitz, G., Collins, M., Eyring, V., Gleckler, P.J., Hewitson, B. and Mearns, L., (2010): Good Practice Guidance Paper on Assessing and Combining Multi Model Climate Projections. In*: Meeting Report of the Intergovernmental Panel on Climate Change Expert Meeting on Assessing and Combining Multi Model Climate Projections* [Stocker, T.F., D. Qin, G.-K. Plattner, M. Tignor, and P.M. Midgley (eds.)]. IPCC Working Group I Technical Support Unit, University of Bern, Bern, Switzerland.

Knutti, R., Furrer, R., Tebaldi, C., Cermak, J., and Meehl, G.A., (2010), Challenges in Combining Projections from Multiple Climate Models: *Journal of Climate*, v. 23, p. 2739-2758.

Kokic, P., Crimp, S., and Howden, M., (2011), Forecasting climate variables using a mixed-effect state-space model*: Environmetrics*, v. 22, p. 409-419.

Kokic, P., Nelson, R., Meinke, H., Potgieter, A., and Carter, J., (2007), From rainfall to farm incomes-transforming advice for Australian drought policy. I. Development and testing of a bioeconomic modelling system: *Australian Journal of Agricultural Research*, v. 58, p. 993-1003.

Konikow, L.F., and Kendy, E., (2005), Groundwater depletion: A global problem: *Hydrogeology Journal*, v. 13, p. 317-320.

Kopp, R.E., Simons, F.J., Mitrovica, J.X., Maloof, A.C., and Oppenheimer, M., (2009), Probabilistic assessment of sea level during the last interglacial stage: *Nature*, v. 462, p. 863-867.

Krinner, G., Magand, O., Simmonds, I., Genthon, C., and Dufresne, J.L., (2007), Simulated Antarctic precipitation and surface mass balance at the end of the twentieth and twenty-first centuries: *Climate Dynamics*, v. 28, p. 215-230.

Krishna, R., (2009), Brief history of the Fiji Meteorological Service, Information Sheet No.2. Climate Services Division, Fiji Meteorological Service.

Kuleshov, Y., (2003), Tropical cyclone climatology for the Southern Hemisphere. Part I. Spatial and temporal profiles of tropical cyclones in the Southern Hemisphere. *Commonwealth of Australia, Bureau of Meteorology*. 20 pp.

Kuleshov, Y., Fawcett, R., Qi, L., Trewin, B., Jones, D., McBride, J., and Ramsay, H., (2010), Trends in tropical cyclones in the South Indian Ocean and the South Pacific Ocean: *Journal of Geophysical Research-Atmospheres,* v. 115, p. -.

Kuleshov, Y., Ming, F.C., Qi, L., Chouaibou, I., Hoareau, C., and Roux, F., (2009), Tropical cyclone genesis in the Southern Hemisphere and its relationship with the ENSO: *Annales Geophysicae*, v. 27, p. 2523-2538.

Kumar, K.K., Rajagopalan, B., Hoerling, M., Bates, G., and Cane, M., (2006), Unraveling the mystery of Indian monsoon failure during El Nino: *Science*, v. 314, p. 115-119.

Kummerow, C., Barnes, W., Kozu, T., Shiue, J., and Simpson, J., (1998), The Tropical Rainfall Measuring Mission (TRMM) sensor package: *Journal of Atmospheric and Oceanic Technology*, v. 15, p. 809-817.

Kummerow, C., Simpson, J., Thiele, O., Barnes, W., Chang, A.T.C., Stocker, E., Adler, R.F., Hou, A., Kakar, R., Wentz, F., Ashcroft, P., Kozu, T., Hong, Y., Okamoto, K., Iguchi, T., Kuroiwa, H., Im, E., Haddad, Z., Huffman, G., Ferrier, B., Olson, W.S., Zipser, E., Smith, E.A., Wilheit, T.T., North, G., Krishnamurti, T., and Nakamura, K., (2000), The status of the Tropical Rainfall Measuring Mission (TRMM) after two years in orbit: *Journal of Applied Meteorology*, v. 39, p. 1965-1982.

Lal, M., McGregor, J.L., and Nguyen, K.C., (2008), Very high-resolution climate simulation over Fiji using a global variable-resolution model: *Climate Dynamics*, v. 30, p. 293-305.

Lamb, M.F., Sabine, C.L., Feely, R.A., Wanninkhof, R., Key, R.M., Johnson, G.C., Millero, F.J., Lee, K., Peng, T.H., Kozyr, A., Bullister, J.L., Greeley, D., Byrne, R.H., Chipman, D.W., Dickson, A.G., Goyet, C., Guenther, P.R., Ishii, M., Johnson, K.M., Keeling, C.D., Ono, T., Shitashima, K., Tilbrook, B., Takahashi, T., Wallace, D.W.R., Watanabe, Y.W., Winn, C., and Wong, C.S., (2002), Consistency and synthesis of Pacific Ocean CO_2 survey data: *Deep-Sea Research Part Ii-Topical Studies in Oceanography*, v. 49, p. 21-58.

Lambeck, K., Anzidei, M., Antonioli, F., Benini, A., and Esposito, A., (2004), Sea level in Roman time in the Central Mediterranean and implications for recent change: *Earth and Planetary Science Letters*, v. 224, p. 563-575.

Lambeck, K., and Chappell, J., (2001), Sea level change through the last glacial cycle: *Science*, v. 292, p. 679-686.

Landerer, F.W., Jungclaus, J.H., and Marotzke, J., (2007), Regional dynamic and steric sea level change in response to the IPCC-A1B scenario: *Journal of Physical Oceanography*, v. 37, p. 296-312.

Landsea, C.W., Harper, B.A., Hoarau, K., and Knaff, J.A., (2006), Can we detect trends in extreme tropical cyclones?: *Science*, v. 313, p. 452-454.

Langdon, C., and Atkinson, M.J., (2005), Effect of elevated pCO(2) on photosynthesis and calcification of corals and interactions with seasonal change in temperature/ irradiance and nutrient enrichment: *Journal of Geophysical Research-Oceans*, v. 110.

Le Quere, C., Raupach, M.R., Canadell, J.G., Marland, G., Bopp, L., Ciais, P., Conway, T.J., Doney, S.C., Feely, R.A., Foster, P., Friedlingstein, P., Gurney, K., Houghton, R.A., House, J.I., Huntingford, C., Levy, P.E., Lomas, M.R., Majkut, J., Metzl, N., Ometto, J.P., Peters, G.P., Prentice, I.C., Randerson, J.T., Running, S.W., Sarmiento, J.L., Schuster, U., Sitch, S., Takahashi, T., Viovy, N., van der Werf, G.R., and Woodward, F.I., (2009), Trends in the sources and sinks of carbon dioxide: *Nature Geoscience*, v. 2, p. 831-836.

Leclercq, P.W., Oerlemans, J. and Cogley, J.G., (2011), Estimating the Glacier Contribution to Sea-Level Rise for the Period 1800–2005, *Surveys in Geophysics*, doi: 10.1007/s10712-011-9121-7.

Lee, T., and McPhaden, M.J., (2010), Increasing intensity of El Nino in the central-equatorial Pacific: *Geophysical Research Letters*, v. 37.

Lehodey, P., Bertignac, M., Hampton, J., Lewis, A., and Picaut, J., (1997), El Nino Southern Oscillation and tuna in the western Pacific: *Nature*, v. 389, p. 715-718.

Leslie, L.M., Karoly, D.J., Leplastrier, M., and Buckley, B.W., (2007), Variability of tropical cyclones over the southwest Pacific Ocean using a high-resolution climate model: *Meteorology and Atmospheric Physics*, v. 97, p. 171-180.

Lettenmaier, D.P., and Milly, P.C.D., (2009), Land waters and sea level: *Nature Geoscience*, v. 2, p. 452-454.

Levitus, S., Antonov, J.I., Boyer, T.P., Locarnini, R.A., Garcia, H.E., and Mishonov, A.V., (2009), Global ocean heat content 1955–2008 in light of recently revealed instrumentation problems: *Geophysical Research Letters*, v. 36.

Li, H.B., Sheffield, J., and Wood, E.F., (2010), Bias correction of monthly precipitation and temperature fields from Intergovernmental Panel on Climate Change AR4 models using equidistant quantile matching: *Journal of Geophysical Research-Atmospheres*, v. 115.

Lloyd-Hughes, B., and Saunders, M.A., (2002), A drought climatology for Europe: International *Journal of Climatology*, v. 22, p. 1571-1592.

Locarnini, R.A., Antonov, J.I., Garcia, H.E., and Levitus, S., (2006), World ocean atlas 2005, NOAA atlas NESDIS 61-64: National Oceanic and Atmospheric Administration., United States. National Environmental Satellite Data and Information Service and National Oceanographic Data Center (U.S.). Ocean Climate Laboratory, Silver Spring, MD, U.S. Dept. of Commerce.

Lorrey, A., Fowler, A.M., and Salinger, J., (2007), Regional climate regime classification as a qualitative tool for interpreting multi-proxy palaeoclimate data spatial patterns: A New Zealand case study: *Palaeogeography Palaeoclimatology Palaeoecology*, v. 253, p. 407-433.

Lorrey, A., Goodwin, I., Renwick, J. And Browning, S., (2011), Blocking circulation anomalies in the Tasman Sea region during the Medieval Climate Anomaly, PAGES news, vol 19, 1, 22-24.

Lorrey, A.M., Vandergoes, M., Almond, P., Renwick, J.A., Stephens, T., Bostock, H., Mackintosh, A., Newnham, R., Williams, P.W., Ackerley, D. and Fowler, A.M., (in press), Palaeocirculation across New Zealand during the Last Glacial Maximum at ~21ka: *Quaternary Science Reviews*.

Lorrey, A.M, Vandergoes, M., Renwick, J., Newnham, R., Ackerley, D., Bostock, H., Williams, P.W., King, D.N.T., Neil, H., Harper, S., Mackintosh, A., Goff, J., McFadgen, B., Martin, T. and Chappell, P., (2010), A Regional Climate Regime Classification synthesis for New Zealand covering three critical periods of the late Quaternary: the last 2000 years, the mid-Holocene, and the end of the Last Glacial Coldest Period. NIWA Client Report AKL2010-025 prepared for the University of Auckland. 231 pp.

Lorrey, A., Williams, P., Salinger, J., Martin, T., Palmer, J., Fowler, A., Zhao, J.X., and Neil, H., (2008), Speleothem stable isotope records interpreted within a multi-proxy framework and implications for New Zealand palaeoclimate reconstruction: *Quaternary International*, v. 187, p. 52-75.

Lowe, J. A. and Gregory, J.M. (2010). A sea of uncertainty. *Nature Reports Climate Change*, Published online: 6 April 2010, doi:10.1038/climate.2010.30.

Lowe, J.A., and Gregory, J.M., (2006), Understanding projections of sea level rise in a Hadley Centre coupled climate model: *Journal of Geophysical Research-Oceans*, v. 111.

Lu, J., Deser, C., and Reichler, T., (2009), Cause of the widening of the tropical belt since 1958: *Geophysical Research Letters*, v. 36.

Mackey, D.J., O'Sullivan, J.E., and Watson, R.J., (2002), Iron in the western Pacific: a riverine or hydrothermal source for iron in the Equatorial Undercurrent?: *Deep-Sea Research Part I-Oceanographic Research Papers*, v. 49, p. 877-893.

Madden, R.A., and Julian, P.R., (1994), Observations of the 40-50-Day Tropical Oscillation - a Review: *Monthly Weather Review*, v. 122, p. 814-837.

Maes, C., Picaut, J., Kuroda, Y., and Ando, K., (2004), Characteristics of the convergence zone at the eastern edge of the Pacific warm pool: *Geophysical Research Letters*, v. 31.

Mann, M.E., Bradley, R.S. and Hughes, M.K., (2000). Long-term variability in the El Nino Southern Oscillation and associated teleconnections. In: *El Nino and the Southern Oscillation: Multiscale Variability and its Impacts on Natural Ecosystems and Society* [Diaz, H.F., and V. Markgraf (eds.)]. Cambridge University Press, Cambridge, UK, 357-412.

Mann, M.E., Zhang, Z.H., Rutherford, S., Bradley, R.S., Hughes, M.K., Shindell, D., Ammann, C., Faluvegi, G., and Ni, F.B., (2009), Global Signatures and Dynamical Origins of the Little Ice Age and Medieval Climate Anomaly: *Science*, v. 326, p. 1256-1260.

Manning, M.R., Edmonds, J., Emori, S., Grubler, A., Hibbard, K., Joos, F., Kainuma, M., Keeling, R.F., Kram, T., Manning, A.C., Meinshausen, M., Moss, R., Nakicenovic, N., Riahi, K., Rose, S.K., Smith, S., Swart, R., and van Vuuren, D.P., (2010), Misrepresentation of the IPCC CO_2 emission scenarios: *Nature Geoscience*, v. 3, p. 376-377.

Manton, M.J., Della-Marta, P.M., Haylock, M.R., Hennessy, K.J., Nicholls, N., Chambers, L.E., Collins, D.A., Daw, G., Finet, A., Gunawan, D., Inape, K., Isobe, H., Kestin, T.S., Lefale, P., Leyu, C.H., Lwin, T., Maitrepierre, L., Ouprasitwong, N., Page, C.M., Pahalad, J., Plummer, N., Salinger, M.J., Suppiah, R., Tran, V.L., Trewin, B., Tibig, I., and Yee, D., (2001), Trends in extreme daily rainfall and temperature in Southeast Asia and the South Pacific: 1961–1998: *International Journal of Climatology*, v. 21, p. 269-284.

Mantua, N.J., and Hare, S.R., (2002), The Pacific decadal oscillation: *Journal of Oceanography*, v. 58, p. 35-44.

Mantua, N.J., Hare, S.R., Zhang, Y., Wallace, J.M., and Francis, R.C., (1997), A Pacific interdecadal climate oscillation with impacts on salmon production: *Bulletin of the American Meteorological Society*, v. 78, p. 1069-1079.

Manzello, D.P., Kleypas, J.A., Budd, D.A., Eakin, C.M., Glynn, P.W., and Langdon, C., (2008), Poorly cemented coral reefs of the eastern tropical Pacific: Possible insights into reef development in a high-CO_2 world: *Proceedings of the National Academy of Sciences of the United States of America*, v. 105, p. 10450-10455.

Marshall, G.J., (2003), Trends in the southern annular mode from observations and reanalyses: *Journal of Climate*, v. 16, p. 4134-4143.

Marti, O., Braconnot, P., Dufresne, J.L., Bellier, J., Benshila, R., Bony, S., Brockmann, P., Cadule, P., Caubel, A., Codron, F., de Noblet, N., Denvil, S., Fairhead, L., Fichefet, T., Foujols, M.A., Friedlingstein, P., Goosse, H., Grandpeix, J.Y., Guilyardi, E., Hourdin, F., Idelkadi, A., Kageyama, M., Krinner, G., Levy, C., Madec, G., Mignot, J., Musat, I., Swingedouw, D., and Talandier, C., (2010), Key features of the IPSL ocean atmosphere model and its sensitivity to atmospheric resolution: *Climate Dynamics*, v. 34, p. 1-26.

Matthews, A.J., Hoskins, B.J., Slingo, J.M., and Blackburn, M., (1996), Development of convection along the SPCZ within a Madden-Julian oscillation: *Quarterly Journal of the Royal Meteorological Society*, v. 122, p. 669-688.

Maximenko, N., Niiler, P., Rio, M.H., Melnichenko, O., Centurioni, L., Chambers, D., Zlotnicki, V., and Galperin, B., (2009), Mean Dynamic Topography of the Ocean Derived from Satellite and Drifting Buoy Data Using Three Different Techniques: *Journal of Atmospheric and Oceanic Technology*, v. 26, p. 1910-1919.

McCarthy, J.J., O.F., Canziani, N.A. Leary, D.J. Dokken, and K.S. White, (eds). (2001): *Climate Change 2001: Impacts, Adaptation and Vulnerability. Contribution of Working Group II to the Third Assessment Report of the Intergovernmental Panel on Climate Change*. Cambridge University Press: Cambridge, UK.

McGregor, H.V., and Gagan, M.K., (2004), Western Pacific coral delta O-18 records of anomalous Holocene variability in the El Nino-Southern Oscillation: *Geophysical Research Letters*, v. 31.

McGregor, J.L., and Dix, M.R., (2008), An updated description of the Conformal-Cubic atmospheric model: *High Resolution Numerical Modelling of the Atmosphere and Ocean*, p. 51-75

McGregor, S., Holbrook, N.J. and Power, S.B. (2007), Interdecadal sea surface temperature variability in the equatorial Pacific Ocean. Part I: the role of off- equatorial wind stresses and oceanic Rossby waves: *Journal of Climate*, v. 20, p. 2643-2658.

McGregor, S., Timmermann, A., and Timm, O., (2010), A unified proxy for ENSO and PDO variability since 1650: *Climate of the Past*, v. 6, p. 1-17.

McPhaden, M.J., and Zhang, D.X., (2004), Pacific Ocean circulation rebounds: *Geophysical Research Letters*, v. 31.

Meehl, G.A., and Arblaster, J.M., (2003), Mechanisms for projected future changes in south Asian monsoon precipitation: *Climate Dynamics*, v. 21, p. 659-675.

Meehl, G. A., Boer, G.J., Covey, C., Latif, M. and Stouffer, R.J., (2000), The Coupled Model Intercomparison Project (CMIP): *Bulletin of the American Meteorological Society*, v. 81, p. 313-318.

Meehl, G.A., Covey, C., Delworth, T., Latif, M., McAvaney, B., Mitchell, J.F.B., Stouffer, R.J., and Taylor, K.E., (2007a), The WCRP CMIP3 multimodel dataset - A new era in climate change research: *Bulletin of the American Meteorological Society*, v. 88, p. 1383-1394.

Meehl, G.A., Hu, A.X., and Santer, B.D., (2009), The Mid-1970s Climate Shift in the Pacific and the Relative Roles of Forced versus Inherent Decadal Variability: *Journal of Climate*, v. 22, p. 780-792.

Meehl, G.A., T.F. Stocker, W.D. Collins, P. Friedlingstein, A.T. Gaye, J.M. Gregory, A. Kitoh, R. Knutti, J.M. Murphy, A. Noda, S.C.B. Raper, I.G. Watterson, A.J. Weaver and Z.-C. Zhao, (2007b): Global Climate Projections. In: *Climate Change 2007: The Physical Science Basis*. *Contribution of Working Group I to the Fourth Assessment Report of the Intergovernmental Panel on Climate Change* [Solomon, S., D. Qin, M. Manning, Z. Chen, M. Marquis, K.B. Averyt, M. Tignor and H.L. Miller (eds.)]. Cambridge University Press, Cambridge, United Kingdom and New York, NY, USA.

Menendez, M., and Woodworth, P.L., (2010), Changes in extreme high water levels based on a quasi-global tide-gauge data set: *Journal of Geophysical Research-Oceans*, v. 115.

Merrifield, M.A., (2011), A shift in western tropical Pacific sea-level trends during the 1990s, *Journal of Climate*. (in press).

Meure, C.M., Etheridge, D., Trudinger, C., Steele, P., Langenfelds, R., van Ommen, T., Smith, A., and Elkins, J., (2006), Law Dome CO_2, CH_4 and N_2O ice core records extended to 2000 years BP: *Geophysical Research Letters*, v. 33.

Meyers, G., McIntosh, P., Pigot, L., and Pook, M., (2007), The years of El Nino, La Nina, and interactions with the tropical Indian ocean: *Journal of Climate*, v. 20, p. 2872-2880.

Middleton, N., Thomas, D.S.G., and United Nations Environment Programme, (1997), World atlas of desertification: London, Arnold, x,182 p. p.

Milne, G.A., Gehrels, W.R., Hughes, C.W., and Tamisiea, M.E., (2009), Identifying the causes of sea-level change: *Nature Geoscience*, v. 2, p. 471-478.

Mimura, N., L. Nurse, R.F. McLean, J. Agard, L. Briguglio, P. Lefale, R. Payet and G. Sem, (2007): Small islands. In: *Climate Change 2007: Impacts, Adaptation and Vulnerability. Contribution of Working Group II to the Fourth Assessment Report of the Intergovernmental Panel on Climate Change*, M.L. Parry, O.F. Canziani, J.P. Palutikof, P.J. van der Linden and C.E. Hanson, (eds.), Cambridge University Press, Cambridge, UK, 687-716.

Mitas, C.M., and Clement, A., (2005), Has the Hadley cell been strengthening in recent decades?: *Geophysical Research Letters*, v. 32.

Mitas, C.M., and Clement, A., (2006), Recent behavior of the Hadley cell and tropical thermodynamics in climate models and reanalyses: *Geophysical Research Letters*, v. 33.

Mitrovica, J.X., Gomez, N., and Clark, P.U., (2009), The Sea-Level Fingerprint of West Antarctic Collapse: *Science*, v. 323, p. 753.

Mitrovica, J.X., Tamisiea, M.E., Davis, J.L., and Milne, G.A., (2001), Recent mass balance of polar ice sheets inferred from patterns of global sea-level change: *Nature*, v. 409, p. 1026-1029.

Mochizuki, T., Ishii, M., Kimoto, M., Chikamoto, Y., Watanabe, M., Nozawa, T., Sakamoto, T.T., Shiogama, H., Awaji, T., Sugiura, N., Toyoda, T., Yasunaka, S., Tatebe, H., and Mori, M., (2010), Pacific decadal oscillation hindcasts relevant to near-term climate prediction: *Proceedings of the National Academy of Sciences of the United States of America*, v. 107, p. 1833-1837.

Moise, A.F. and F.P. Delage, (in press). New climate model metrics based on object-orientated pattern matching of rainfall. *Journal of Geophysical Research*, v. 116, p. 2011 doi:10.1029/2010JD015318

Morton, F.I., (1983), Operational estimates of areal evaporation and their significance to the science and practice of hydrology. *Journal of Hydrology,* v. 66 p. 1-76.

Mucci, A., (1983), The Solubility of Calcite and Aragonite in Seawater at Various Salinities, Temperatures, and One Atmosphere Total Pressure: *American Journal of Science*, v. 283, p. 780-799.

Munday, P.L., Dixson, D.L., McCormick, M.I., Meekan, M., Ferrari, M.C.O., and Chivers, D.P., (2010), Replenishment of fish populations is threatened by ocean acidification: *Proceedings of the National Academy of Sciences of the United States of America*, v. 107, p. 12930-12934.

Munday, P.L., Donelson, J.M., Dixson, D.L. and Endo, G.G.K., (2009), Effects of ocean acidification on the early life history of a tropical marine fish: *Proceedings of the Royal Society B*, v. 276, p. 3275-3283.

NASA Quick Scatterometer, (2000), QuikSCAT Science Data Product, User's Manual, Overview & Geophysical Data Products, Version 2.0-Draft, Jet Propulsion Laboratory, California Institute of Technology, Doc. D-18053, May 2000

New, M., Hulme, M., and Jones, P., (1999), Representing twentieth-century space-time climate variability. Part I: Development of a 1961–90 mean monthly terrestrial climatology: *Journal of Climate*, v. 12, p. 829-856.

Newman, M., Compo, G.P., and Alexander, M.A., (2003), ENSO-forced variability of the Pacific decadal oscillation: *Journal of Climate*, v. 16, p. 3853-3857.

Nguyen, K. C., Katzfey, J. J., and McGregor J. L., (in press), Global 60 km simulations with CCAM: Evaluation over the tropics: *Climate Dynamics*, doi: 10.1007/s00382-011-1197-8.

Nguyen, K.C., and Walsh, K.J.E., (2001), Interannual, decadal, and transient greenhouse simulation of tropical cyclone-like vortices in a regional climate model of the South Pacific: *Journal of Climate*, v. 14, p. 3043-3054.

Nolan, D.S., (2007), What is the trigger for tropical cyclogenesis?: *Australian Meteorological Magazine*, v. 56, p. 241-266.

Nunn, P.D., (2007), Climate, environment and society in the Pacific during the last millennium: *Developments in Earth & Environmental Sciences*, 6: Science Direct, (online service) Amsterdam, Netherlands ; Boston [Mass.], Elsevier, p. xiv, 302 p.

Onogi, K., Tslttsui, J., Koide, H., Sakamoto, M., Kobayashi, S., Hatsushika, H., Matsumoto, T., Yamazaki, N., Kaalhori, H., Takahashi, K., Kadokura, S., Wada, K., Kato, K., Oyama, R., Ose, T., Mannoji, N., and Taira, R., (2007), The JRA-25 reanalysis: *Journal of the Meteorological Society of Japan*, v. 85, p. 369-432.

Oort, A.H., and Yienger, J.J., (1996), Observed interannual variability in the Hadley circulation and its connection to ENSO: *Journal of Climate*, v. 9, p. 2751-2767.

Pal, J.S., Giorgi, F., Bi, X.Q., Elguindi, N., Solmon, F., Gao, X.J., Rauscher, S.A., Francisco, R., Zakey, A., Winter, J., Ashfaq, M., Syed, F.S., Bell, J.L., Diffenbaugh, N.S., Karmacharya, J., Konare, A., Martinez, D., da Rocha, R.P., Sloan, L.C., and Steiner, A.L., (2007), Regional climate modeling for the developing world - The ICTP RegCM3 and RegCNET: *Bulletin of the American Meteorological Society*, v. 88, p. 1395.

Pardaens, A.K., Gregory, J.M., and Lowe, J.A., (2011), A model study of factors influencing projected changes in regional sea level over the twenty-first century: *Climate Dynamics*, v. 36, p. 2015-2033.

Parker, D., Folland, C., Scaife, A., Knight, J., Colman, A., Baines, P., and Dong, B.W., (2007), Decadal to multidecadal variability and the climate change background: *Journal of Geophysical Research-Atmospheres*, v. 112.

Pauluis, O., and Garner, S., (2006), Sensitivity of radiative-convective equilibrium simulations to horizontal resolution: *Journal of the Atmospheric Sciences*, v. 63, p. 1910-1923.

Perkins, S.E., (in press), Biases and model agreement in projections of climate extremes over the tropical Pacific: *Earth Interactions*, doi: 10.1175/2011EI395.1

Perkins, S.E., Irving D.B., Brown J.R., Power, S.B., Moise, A.F., Colman, R.A. and Smith, I., (in press), CMIP3 ensemble climate projections over the western tropical Pacific based on model skill, *Climate Research*.

Perkins, S.E., Pitman, A.J., Holbrook, N.J., and McAneney, J., (2007), Evaluation of the AR4 climate models' simulated daily maximum temperature, minimum temperature, and precipitation over Australia using probability density functions: *Journal of Climate*, v. 20, p. 4356-4376.

Pfeffer, W.T., Harper, J.T., and O'Neel, S., (2008), Kinematic constraints on glacier contributions to 21st-century sea-level rise: *Science*, v. 321, p. 1340-1343.

Philander, S.G., (1990), El Niño, La Niña, and the southern oscillation: San Diego, Academic Press, ix, 293 p. p.

Philander, S.G, (2006) Our Affair with El Niño: How We Transformed an Enchanting Peruvian Current into a Global Climate Hazard. Princeton University Press, pp. 288.

Phipps, S.J., and Brown, J.N., (2010), Understanding ENSO dynamics through the exploration of past climates: *IOP Conference Series: Earth and Environmental Science*, 9.

Powell, M., Soukup, G., Cocke, S., Gulati, S., Morisseau-Leroy, N., Hamid, S., Dorst, N., and Axe, L., (2005), State of Florida hurricane loss projection model: Atmospheric science component: *Journal of Wind Engineering and Industrial Aerodynamics*, v. 93, p. 651-674.

Power, S.B., (1995), Climate Drift in a Global Ocean General-Circulation Model: *Journal of Physical Oceanography*, v. 25, p. 1025-1036.

Power, S., Casey, T., Folland, C., Colman, A., and Mehta, V., (1999), Inter-decadal modulation of the impact of ENSO on Australia: *Climate Dynamics*, v. 15, p. 319-324.

Power, S., and Colman, R., (2006), Multi-year predictability in a coupled general circulation model: *Climate Dynamics*, v. 26, p. 247-272.

Power, S., Haylock, M., Colman, R., and Wang, X.D., (2006), The predictability of interdecadal changes in ENSO activity and ENSO teleconnections: *Journal of Climate*, v. 19, p. 4755-4771.

Power, S., and G. Kociuba, (in press), The impact of global warming on the Southern Oscillation Index. *Climate Dynamics*, doi:10.1007/s00382-010-0951-7.

Power, S.B. and Kociuba, G. (2011), What caused the observed 20th century weakening of the Walker circulation? *Journal of Climate* (in press) doi: 10.1175/2011JCLI4101.1

Power, S.B., and Smith, I.N., (2007), Weakening of the Walker Circulation and apparent dominance of El Nino both reach record levels, but has ENSO really changed?: *Geophysical Research Letters*, v. 34, issue 18.

Power, S., Tseitkin, F., Mehta, V., Lavery, B., Torok, S., and Holbrook, N., (1999), Decadal climate variability in Australia during the twentieth century: *International Journal of Climatology*, v. 19, p. 169-184.

Qiu, B., and Chen, S.M., (2006), Decadal variability in the large-scale sea surface height field of the South Pacific Ocean: Observations and causes: *Journal of Physical Oceanography*, v. 36, p. 1751-1762.

Radic, V., and Hock, R., (2010), Regional and global volumes of glaciers derived from statistical upscaling of glacier inventory data: *Journal of Geophysical Research-Earth Surface*, v. 115, p. -.

Radic, V., and Hock, R., (2011), Regionally differentiated contribution of mountain glaciers and ice caps to future sea-level rise: *Nature Geoscience*, v. 4, p. 91-94.

Rahmstorf, S., (2007), A semi-empirical approach to projecting future sea-level rise: *Science*, v. 315, p. 368-370.

Rahmstorf, S., Cazenave, A., Church, J.A., Hansen, J.E., Keeling, R.F., Parker, D.E., and Somerville, R.C.J., (2007), Recent climate observations compared to projections: *Science*, v. 316, p. 709.

Randall, D.A., R.A. Wood, S. Bony, R. Colman, T. Fichefet, J. Fyfe, V. Kattsov, A. Pitman, J. Shukla, J. Srinivasan, R.J. Stouffer, A. Sumi and K.E. Taylor, 2007: Cilmate Models and Their Evaluation. In: *Climate Change 2007: The Physical Science Basis. Contribution of Working Group I to the Fourth Assessment Report of the Intergovernmental Panel on Climate Change* [Solomon, S., D. Qin, M. Manning, Z. Chen, M. Marquis, K.B. Averyt, M.Tignor and H.L. Miller (eds.)]. Cambridge University Press, Cambridge, United Kingdom and New York, NY, USA.

Rattan, S. P. and R. N. Sharma, (2005), Extreme value analysis of Fiji's wind record: *The South Pacific Journal of Natural Science*, 23.

Raupach, M.R., and Canadell, J.G., (2010), Carbon and the Anthropocene: *Current Opinion in Environmental Sustainability*, v. 2, p. 210-218.

Rayner, N.A., Brohan, P., Parker, D.E., Folland, C.K., Kennedy, J.J., Vanicek, M., Ansell, T.J., and Tett, S.F.B., (2006), Improved analyses of changes and uncertainties in sea surface temperature measured in situ sice the mid-nineteenth century: The HadSST2 dataset: *Journal of Climate*, v. 19, p. 446-469.

Rayner, N.A., Parker, D.E., Horton, E.B., Folland, C.K., Alexander, L.V., Rowell, D.P., Kent, E.C., and Kaplan, A., (2003), Global analyses of sea surface temperature, sea ice, and night marine air temperature since the late nineteenth century: *Journal of Geophysical Research-Atmospheres*, v. 108.

Reynolds, R.W., (1988), A real-time global sea surface temperature analysis: *Journal of Climate*, v. 1, p. 75-86.

Ridgway, K.R., Dunn, J.R., and Wilkin, J.L., (2002), Ocean interpolation by four-dimensional weighted least squares - application to the waters around Australasia: *Journal of Atmospheric and Oceanic Technology*, v. 19, p. 1357-1375.

Rignot, E., Velicogna, I., van den Broeke, M.R., Monaghan, A., and Lenaerts, J., (2011), Acceleration of the contribution of the Greenland and Antarctic ice sheets to sea level rise: *Geophysical Research Letters*, v. 38.

Rio, M.H., and Hernandez, F., (2004), A mean dynamic topography computed over the world ocean from altimetry, in situ measurements, and a geoid model: *Journal of Geophysical Research-Oceans*, v. 109.

Rockel, B., Castro, C.L., Pielke, R.A., von Storch, H., and Leoncini, G., (2008), Dynamical downscaling: Assessment of model system dependent retained and added variability for two different regional climate models: *Journal of Geophysical Research-Atmospheres*, v. 113.

Rodbell, D.T., Seltzer, G.O., Anderson, D.M., Abbott, M.B., Enfield, D.B., and Newman, J.H., (1999), An similar to 15,000-year record of El Nino-driven alluviation in southwestern Ecuador: *Science*, v. 283, p. 516-520.

Roemmich, D., Gilson, J., Davis, R., Sutton, P., Wijffels, S., and Riser, S., (2007), Decadal spinup of the South Pacific subtropical gyre: *Journal of Physical Oceanography*, v. 37, p. 162-173.

Rohling, E.J., Grant, K., Bolshaw, M., Roberts, A.P., Siddall, M., Hemleben, C., and Kucera, M., (2009), Antarctic temperature and global sea level closely coupled over the past five glacial cycles: *Nature Geoscience*, v. 2, p. 500-504.

Rohling, E.J., Grant, K., Hemleben, C., Siddall, M., Hoogakker, B.A.A., Bolshaw, M., and Kucera, M., (2008), High rates of sea-level rise during the last interglacial period: *Nature Geoscience*, v. 1, p. 38-42.

Rosenzweig, C., G. Casassa, D.J. Karoly, A. Imeson, C. Liu, A. Menzel, S. Rawlins, T.L. Root, B. Seguin, P. Tryjanowski, (2007): Assessment of observed changes and responses in natural and managed systems. In: *Climate Change 2007: Impacts, Adaptation and Vulnerability. Contribution of Working Group II to the Fourth Assessment Report of the Intergovernmental Panel on Climate Change*, M.L. Parry, O.F. Canziani, J.P. Palutikof, P.J. van der Linden and C.E. Hanson, (eds.), Cambridge University Press, Cambridge, UK, 79-131.

Royer, J.F., Chauvin, F., Timbal, B., Araspin, P., and Grimal, D., (1998), A GCM study of the impact of greenhouse gas increase on the frequency of occurrence of tropical cyclones: *Climatic Change*, v. 38, p. 307-343.

Sabine, C.L., Feely, R.A., Gruber, N., Key, R.M., Lee, K., Bullister, J.L., Wanninkhof, R., Wong, C.S., Wallace, D.W.R., Tilbrook, B., Millero, F.J., Peng, T.H., Kozyr, A., Ono, T., and Rios, A.F., (2004), The oceanic sink for anthropogenic CO_2: *Science*, v. 305, p. 367-371.

Saenko, O.A., Fyfe, J.C., and England, M.H., (2005), On the response of the oceanic wind-driven circulation to atmospheric CO_2 increase: *Climate Dynamics*, v. 25, p. 415-426.

Saji, N.H., Goswami, B.N., Vinayachandran, P.N., and Yamagata, T., (1999), A dipole mode in the tropical Indian Ocean: *Nature*, v. 401, p. 360-363.

Salinger, M.J., (1995), Southwest Pacific Temperatures - Trends in Maximum and Minimum Temperatures: *Atmospheric Research*, v. 37, p. 87-99.

Salinger, M.J., Renwick, J.A., and Mullan, A.B., (2001), Interdecadal Pacific Oscillation and South Pacific climate: *International Journal of Climatology*, v. 21, p. 1705-1721.

Santer, B.D., Taylor, K.E., Gleckler, P.J., Bonfils, C., Barnett, T.P., Pierce, D.W., Wigley, T.M.L., Mears, C., Wentz, F.J., Bruggemann, W., Gillett, N.P., Klein, S.A., Solomon, S., Stott, P.A., and Wehner, M.F., (2009), Incorporating model quality information in climate change detection and attribution studies: *Proceedings of the National Academy of Sciences of the United States of America*, v. 106, p. 14778-14783.

Schaefer, J.M., Denton, G.H., Kaplan, M., Putnam, A., Finkel, R.C., Barrell, D.J.A., Andersen, B.G., Schwartz, R., Mackintosh, A., Chinn, T., and Schluchter, C., (2009), High-Frequency Holocene Glacier Fluctuations in New Zealand Differ from the Northern Signature: *Science*, v. 324, p. 622-625.

Schmith, T., Johansen, S., and Thejll, P., (2007), Comment on "A semi-empirical approach to projecting future sea-level rise": *Science*, v. 317.

Secretariat of the Pacific Regional Environment Programme (SPREP), (2005), Pacific Islands Framework for Action on Climate Change 2006–2015, http://www.sprep.org/att/publication/000438_PI_Framework_for_Action_on_Climate_Change_2006_2015_FINAL.pdf.

Seidel, D.J., Fu, Q., Randel, W.J., and Reichler, T.J., (2008), Widening of the tropical belt in a changing climate: *Nature Geoscience*, v. 1, p. 21-24.

Seidel, D.J., and Randel, W.J., (2007), Recent widening of the tropical belt: Evidence from tropopause observations: *Journal of Geophysical Research-Atmospheres*, v. 112.

Sen Gupta, A., and England, M.H., (2006), Coupled ocean-atmosphere-ice response to variations in the Southern Annular Mode: *Journal of Climate*, v. 19, p. 4457-4486.

Sen Gupta, A., Santoso, A., Taschetto, A.S., Ummenhofer, C.C., Trevena, J., and England, M.H., (2009), Projected Changes to the Southern Hemisphere Ocean and Sea Ice in the IPCC AR4 Climate Models: *Journal of Climate*, v. 22, p. 3047-3078.

Sherwood, S.C., Ingram, W., Tsushima, Y., Satoh, M., Roberts, M., Vidale, P.L., and O'Gorman, P.A., (2010), Relative humidity changes in a warmer climate: *Journal of Geophysical Research-Atmospheres*, v. 115.

Shorten, G. G., S. Goosby, K. Granger, K. Lindsay, P. Naidu, S. Oliver, K. Stewart, V. Titov and G. Walker, (2003): Developing Risk-Management Options for Disasters in the Pacific Region. SOPAC Joint Contribution Report 147.

Shorten, G. G., S. Schmall and S. Oliver, (2005): Building capacity to insure against disaster in Tuvalu. SOPAC Technical Report 380.

Shulmeister, J., and Lees, B.G., (1995), Pollen Evidence from Tropical Australia for the Onset of an Enso-Dominated Climate at C 4000 Bp: *Holocene*, v. 5, p. 10-18.

Silverman, J., Lazar, B., Cao, L., Caldeira, K., and Erez, J., (2009), Coral reefs may start dissolving when atmospheric CO_2 doubles: *Geophysical Research Letters*, v. 36.

Skamarock, W. C., J. B. Klemp, J. Dudhia, D. O. Gill, D. M. Barker, M. G. Duda, X.-Y.Huang, W. Wang, and J. G. Powers (2008), A Description of the Advanced Research WRF Version 3, NCAR Technical Note, NCAR, Boulder, CO, USA

Slangen, A., Katsman, C., van de Wal, R., Vermeersen, L., and Riva, R., (in press), Towards regional projections of twenty-first century sea-level change based on IPCC SRES scenarios. *Climate Dynamics*, doi:10.1007/s00382-011-1057-6

Smith, I., and Chandler, E., (2010), Refining rainfall projections for the Murray Darling Basin of south-east Australia-the effect of sampling model results based on performance: *Climatic Change*, v. 102, p. 377-393.

Smith, T.M., Reynolds, R.W., Peterson, T.C., and Lawrimore, J., (2008), Improvements to NOAA's historical merged land-ocean surface temperature analysis (1880–2006): *Journal of Climate*, v. 21, p. 2283-2296.

Smythe, S.M.B. 1864. Ten months in the Fiji Islands: With an introduction and appendix by Colonial W.J. Smythe, John Henry and James Parker, Oxford and London. Digital version available at Google books http://books.google.com/

Song, J.J., Wang, Y.A., and Wu, L.G., (2010), Trend discrepancies among three best track data sets of western North Pacific tropical cyclones: *Journal of Geophysical Research-Atmospheres*, v. 115.

Stanford, J. D., Heminway, R., Rohling, E. J., Challenor, P. G., Medina-Elizalde, M. and Lester, A. J., (2011). Sea-level probability for the last deglaciation: A statistical analysis of far-field records. *Global and Planetary Change*, (in press), doi:10.1016/j.gloplacha.2010.11.002

Steiner, J.T., (1980): The Climate of the South-West Pacific Region, a review for pilots. New Zealand Meteorological Service Publication No. 166, Wellington, New Zealand, 35 pp.

Storch, H.v., and Zwiers, F.W., (2001): Statistical analysis in climate research. Cambridge, UK ; New York, Cambridge University Press, x, 484 p.

Stott, L., Cannariato, K., Thunell, R., Haug, G.H., Koutavas, A., and Lund, S., (2004), Decline of surface temperature and salinity in the western tropical Pacific Ocean in the Holocene epoch: *Nature*, v. 431, p. 56-59.

Stott, P. A., Gillett, N. P., Hegerl, G. C., Karoly, D. J., Stone, D. A., Zhang, X. and Zwiers, F. (2010). Detection and attribution of climate change: a regional perspective. *Wiley Interdisciplinary Reviews: Climate Change*, v. 1, p. 192-211.

Streten, N. A., and Zillman, J.W., (1984): Climate of the South Pacific Ocean. *World Survey of Climatology, Climates of the Oceans*. Vol. 15. Elsevier, 716 pp.

Sun, Y., Solomon, S., Dai, A., and Portmann, R.W., (2006), How often does it rain?: *Journal of Climate*, v. 19, p. 916-934.

Sverdrup, H.U., (1947), Wind-Driven Currents in a Baroclinic Ocean - with Application to the Equatorial Currents of the Eastern Pacific: *Proceedings of the National Academy of Sciences of the United States of America*, v. 33, p. 318-326.

Takahashi, T., Sutherland, S.C. and Kozyr, A. (2010). Global Ocean Surface Water Partial Pressure of CO_2 Database: Measurements Performed During 1957–2009, (Version 2009). ORNL/CDIAC-152, NDP-088(V2009). Carbon Dioxide Information Analysis Center, Oak Ridge National Laboratory, U.S. Department of Energy, Oak Ridge, Tennessee, doi: 10.3334/CDIAC/otg.ndp088(V2009).

Tanaka, H.L., Ishizaki, N., and Kitoh, A., (2004), Trend and interannual variability of Walker, monsoon and Hadley circulations defined by velocity potential in the upper troposphere: *Tellus Series a-Dynamic Meteorology and Oceanography*, v. 56, p. 250-269.

Taschetto, A.S., and England, M.H., (2009), El Nino Modoki Impacts on Australian Rainfall: *Journal of Climate*, v. 22, p. 3167-3174.

Taylor, K.E., Stouffer, R.J. and Meehl, G.A. (2009): A Summary of the CMIP5 Experiment Design. http://www-pcmdi.llnl.gov/

Tebaldi, C., and Knutti, R., (2007), The use of the multi-model ensemble in probabilistic climate projections: *Philosophical Transactions of the Royal Society a-Mathematical Physical and Engineering Sciences*, v. 365, p. 2053-2075.

Thatcher, M., and McGregor, J.L., (2009), Using a Scale-Selective Filter for Dynamical Downscaling with the Conformal Cubic Atmospheric Model: *Monthly Weather Review*, v. 137, p. 1742-1752.

Thompson, C.S., (1986): The climate and weather of Tonga. New Zealand Weather Service Misc. Publ, 188(5), 60 pp.

Thompson, D.W.J., and Solomon, S., (2002), Interpretation of recent Southern Hemisphere climate change: *Science*, v. 296, p. 895-899.

Thompson, D.W.J., and Wallace, J.M., (2000), Annular modes in the extratropical circulation. Part I: Month-to-month variability: *Journal of Climate*, v. 13, p. 1000-1016.

Timm, O., and Diaz, H.F., (2009), Synoptic-Statistical Approach to Regional Downscaling of IPCC Twenty-First-Century Climate Projections: Seasonal Rainfall over the Hawaiian Islands: *Journal of Climate*, v. 22, p. 4261-4280.

Timmermann, A., McGregor, S., and Jin, F.F., (2010), Wind Effects on Past and Future Regional Sea Level Trends in the Southern Indo-Pacific: *Journal of Climate*, v. 23, p. 4429-4437.

Tolman, H. L., (2002): User manual and system documentation of WAVEWATCH-III version 2.22. http://polar.ncep.noaa.gov/mmab/papers/tn222/MMAB_222.pdf, NOAA / NWS / NCEP / OMB technical note 222, 133 pp.

Tomczak, M. and Godfrey, J.S., (2003): Regional Oceanography: an Introduction. 2nd improved edition. Daya Publishing House, Delhi. 390p.

Trenberth, K.E., (1976), Spatial and Temporal Variations of Southern Oscillation: *Quarterly Journal of the Royal Meteorological Society*, v. 102, p. 639-653.

Trenberth, K.E., P.D. Jones, P. Ambenje, R. Bojariu, D. Easterling, A. Klein Tank, D. Parker, F. Rahimzadeh, J.A. Renwick, M. Rusticucci, B. Soden and P. Zhai, (2007): Observations: Surface and Atmospheric Climate Change. In: *Climate Change 2007: The Physical Science Basis. Contribution of Working Group I to the Fourth Assessment Report of the Intergovernmental Panel on Climate Change* [Solomon, S., D. Qin, M. Manning, Z. Chen, M. Marquis, K.B. Averyt, M. Tignor and H.L. Miller (eds.)]. Cambridge University Press, Cambridge, United Kingdom and New York, NY, USA.

Tudhope, A.W., Chilcott, C.P., McCulloch, M.T., Cook, E.R., Chappell, J., Ellam, R.M., Lea, D.W., Lough, J.M., and Shimmield, G.B., (2001), Variability in the El Nino - Southern oscillation through a glacial-interglacial cycle: *Science*, v. 291, p. 1511-1517.

Turner, G. (1861). Nineteen years in Polynesia: missionary life, travels, and researches in the islands of the Pacific, John Snow, London. Digital version available at Google books http://books.google.com/

Ummenhofer, C.C., Sen Gupta, A. and England, M.H., (2009), Causes of late Twentieth-Century trends in New Zealand Precipitation: *Journal of Climate*, v. 22, p. 3-19.

Uppala, S.M., Kallberg, P.W., Simmons, A.J., Andrae, U., Bechtold, V.D., Fiorino, M., Gibson, J.K., Haseler, J., Hernandez, A., Kelly, G.A., Li, X., Onogi, K., Saarinen, S., Sokka, N., Allan, R.P., Andersson, E., Arpe, K., Balmaseda, M.A., Beljaars, A.C.M., Van De Berg, L., Bidlot, J., Bormann, N., Caires, S., Chevallier, F., Dethof, A., Dragosavac, M., Fisher, M., Fuentes, M., Hagemann, S., Holm, E., Hoskins, B.J., Isaksen, L., Janssen, P.A.E.M., Jenne, R., McNally, A.P., Mahfouf, J.F., Morcrette, J.J., Rayner, N.A., Saunders, R.W., Simon, P., Sterl, A., Trenberth, K.E., Untch, A., Vasiljevic, D., Viterbo, P., and Woollen, J., (2005), The ERA-40 re-analysis: *Quarterly Journal of the Royal Meteorological Society*, v. 131, p. 2961-3012.

van Oldenborgh, G. J., S. Philip, and M. Collins, (2005), El Niño in a changing climate: A multi-model study. *Ocean Science*, v. 1, p. 81-95.

Vecchi, G.A., and Soden, B.J., (2007a), Effect of remote sea surface temperature change on tropical cyclone potential intensity: *Nature*, v. 450, p. 1066-1070.

Vecchi, G.A., and Soden, B.J., (2007b), Global warming and the weakening of the tropical circulation: *Journal of Climate*, v. 20, p. 4316-4340.

Vecchi, G.A., Soden, B.J., Wittenberg, A.T., Held, I.M., Leetmaa, A., and Harrison, M.J., (2006), Weakening of tropical Pacific atmospheric circulation due to anthropogenic forcing: *Nature*, v. 441, p. 73-76.

Velicogna, I., (2009), Increasing rates of ice mass loss from the Greenland and Antarctic ice sheets revealed by GRACE: *Geophysical Research Letters*, v. 36.

Vellinga, P., Katsman, C., Sterl, A., Beersma, J., Hazeleger, W., Church, J., Kopp, R., Kroon, D., Oppenheimer, M., Plag, H-P., Rahmstorf, S., Lowe, J., Ridley, J., Storch, H. v., Vaughan, D., van de Wal, R., Weisse, R., Kwadijk, J., Lammersen, R. and Marinova, N., (2009): Exploring high-end climate change scenarios for flood protection of the Netherlands. KNMI Scientific report WR 2009-05, De Bilt, Netherlands.(available from http://www.knmi.nl/bibliotheek/knmipubWR/WR2009-05.pdf).

Verdon, D.C., Wyatt, A.M., Kiem, A.S., and Franks, S.W., (2005), Multi-decadal variability of rainfall and streamflow across eastern Australia: *Regional Hydrological Impacts of Climatic Change - Hydroclimatic Variability*, v. 296, p. 42-52.

Vermeer, M., and Rahmstorf, S., (2009), Global sea level linked to global temperature: *Proceedings of the National Academy of Sciences of the United States of America*, v. 106, p. 21527-21532.

Vincent, D.G., (1994), The South-Pacific Convergence Zone (SPCZ) - a Review: *Monthly Weather Review*, v. 122, p. 1949-1970.

Vincent, E.M., Lengaigne, M., Menkes, C.E., Jourdain, N.C., Marchesiello, P., and Madec, G., (2011), Interannual variability of the South Pacific Convergence Zone and implications for tropical cyclone genesis: *Climate Dynamics*, v. 36, p. 1881-1896.

Wada, Y., van Beek, L.P.H., van Kempen, C.M., Reckman, J.W.T.M., Vasak, S., and Bierkens, M.F.P., (2010), Global depletion of groundwater resources: *Geophysical Research Letters*, v. 37.

Waliser, D.E., and Gautier, C., (1993), A Satellite-Derived Climatology of the ITCZ: *Journal of Climate*, v. 6, p. 2162-2174.

Walsh, K.J.E., Fiorino, M., Landsea, C.W., and McInnes, K.L., (2007), Objectively determined resolution-dependent threshold criteria for the detection of tropical cyclones in climate models and reanalyses: *Journal of Climate*, v. 20, p. 2307-2314.

Walsh, K., and Watterson, I.G., (1997), Tropical cyclone-like vortices in a limited area model: Comparison with observed climatology: *Journal of Climate*, v. 10, p. 2240-2259.

Wang, B., (ed.), (2006): The Asian Monsoon. Springer Praxis Publishing, New York, pp. 797.

Wang, B., Ding, Q.H., Fu, X.H., Kang, I.S., Jin, K., Shukla, J., and Doblas-Reyes, F., (2005), Fundamental challenge in simulation and prediction of summer monsoon rainfall: *Geophysical Research Letters*, v. 32.

Wang, G., and Hendon, H.H., (2007), Sensitivity of Australian rainfall to inter-El Nino variations: *Journal of Climate*, v. 20, p. 4211-4226.

Wang, H.L., Skamarock, W.C., and Feingold, G., (2009), Evaluation of Scalar Advection Schemes in the Advanced Research WRF Model Using Large-Eddy Simulations of Aerosol-Cloud Interactions: *Monthly Weather Review*, v. 137, p. 2547-2558.

Wang, S.S., Trishchenko, A.P., Khlopenkov, K.V., and Davidson, A., (2006), Comparison of International Panel on Climate Change Fourth Assessment Report climate model simulations of surface albedo with satellite products over northern latitudes: Journal *of Geophysical Research-Atmospheres*, v. 111.

Wang, X.L.L., (2008), Accounting for autocorrelation in detecting mean shifts in climate data series using the penalized maximal t or F test: *Journal of Applied Meteorology and Climatology*, v. 47, p. 2423-2444.

Wang, X.L.L., (2008), Penalized maximal F test for detecting undocumented mean shift without trend change: *Journal of Atmospheric and Oceanic Technology*, v. 25, p. 368-384.

Wang, X.L.L., Chen, H.F., Wu, Y.H., Feng, Y., and Pu, Q.A., (2010), New Techniques for the Detection and Adjustment of Shifts in Daily Precipitation Data Series: *Journal of Applied Meteorology and Climatology*, v. 49, p. 2416-2436.

Wang, X.L.L., Wen, Q.H., and Wu, Y.H., (2007), Penalized maximal t test for detecting undocumented mean change in climate data series: *Journal of Applied Meteorology and Climatology*, v. 46, p. 916-931.

Wang, Z., and Chang, C.P., (2008), Mechanism of the asymmetric monsoon transition as simulated in an AGCM: *Journal of Climate*, v. 21, p. 1829-1836.

Webb, D.J., (2000), Evidence for shallow zonal jets in the South Equatorial Current region of the southwest Pacific: *Journal of Physical Oceanography*, v. 30, p. 706-720.

Webster, P.J., Holland, G.J., Curry, J.A., and Chang, H.R., (2005), Changes in tropical cyclone number, duration, and intensity in a warming environment: *Science*, v. 309, p. 1844-1846.

Webster, P.J., Moore, A.M., Loschnigg, J.P., and Leben, R.R., (1999), Coupled ocean-atmosphere dynamics in the Indian Ocean during 1997-98: *Nature*, v. 401, p. 356-360.

Weigel, A.P., Knutti, R., Liniger, M.A., and Appenzeller, C., (2010), Risks of Model Weighting in Multimodel Climate Projections: *Journal of Climate*, v. 23, p. 4175-4191.

Weng, H.Y., Ashok, K., Behera, S.K., Rao, S.A., and Yamagata, T., (2007), Impacts of recent El Nino Modoki on dry/wet conditions in the Pacific rim during boreal summer: *Climate Dynamics*, v. 29, p. 113-129.

Wheeler, M.C. and J.L. McBride, (2005): *Intraseasonal Variability in the Atmosphere-Ocean Climate System*. Lau, W.K.M. and D. E. Waliser (eds), Praxis Publishing, pages 125-173.

Wilby, R.L., Troni, J., Biot, Y., Tedd, L., Hewitson, B.C., Smith, D.M., and Sutton, R.T., (2009), A review of climate risk information for adaptation and development planning: *International Journal of Climatology*, v. 29, p. 1193-1215.

Wongbusarakum, S., (2009): Climate-related socioeconomic assessment in American Samoa. Pacific Regional Integrated Science and Assessment (RISA) Program, East-West Center, Hawaii.

Woodroffe, C.D., Beech, M.R., and Gagan, M.K., (2003), Mid-late Holocene El Nino variability in the equatorial Pacific from coral microatolls: *Geophysical Research Letters*, v. 30.

Woodworth, P.L., (1990), A Search for Accelerations in Records of European Mean Sea-Level: *International Journal of Climatology*, v. 10, p. 129-143.

Woodworth, P. and Blackman, D., (2004), Evidence for systematic changes in extreme high waters since the mid-1970s: *Journal of Climate*, v. 17, p. 1190-1197.

Woodworth, P.L., Menéndez, M. and Gehrels, W.R., (2011), Evidence for century-timescale acceleration in mean sea levels and for recent changes in extreme sea levels: *Surveys in Geophysics*, (in press), doi:10.1007/s10712-011-9112-8

Woodworth, P.L., and Player, R., (2003), The permanent service for mean sea level: An update to the 21st century: *Journal of Coastal Research*, v. 19, p. 287-295.

Woodworth, P.L., White, N.J., Jevrejeva, S., Holgate, S.J., Church, J.A., and Gehrels, W.R., (2009), Evidence for the accelerations of sea level on multi-decade and century timescales: *International Journal of Climatol*ogy, v. 29, p. 777-789.

World Meteorological Organization, (1984): Technical Regulations, Vol. I. WMO Publication No. 49. Geneva, Switzerland.

Wyrtki, K., (1989), Some thoughts about the West Pacific Warm Pool. in: Picaut, J., R. Lucas and T. Delcroix, (eds.), Proceedings of Western Pacific International Meeting and Workshop on TOGA COARE, 99-109.

Wyrwoll, K.H., and Miller, G.H., (2001), Initiation of the Australian summer monsoon 14,000 years ago: *Quaternary International*, v. 83-5, p. 119-128.

Xie, P.P., and Arkin, P.A., (1997), Global precipitation: A 17-year monthly analysis based on gauge observations, satellite estimates, and numerical model outputs: *Bulletin of the American Meteorological Society*, v. 78, p. 2539-2558.

Xie, S.P., Deser, C., Vecchi, G.A., Ma, J., Teng, H.Y., and Wittenberg, A.T., (2010), Global Warming Pattern Formation: Sea Surface Temperature and Rainfall: *Journal of Climate*, v. 23, p. 966-986.

Yeh, S.W., Kug, J.S., Dewitte, B., Kwon, M.H., Kirtman, B.P., and Jin, F.F., (2009), El Nino in a changing climate: *Nature*, v. 462, p. 511.

Yin, J.J., Griffies, S.M., and Stouffer, R.J., (2010), Spatial Variability of Sea Level Rise in Twenty-First Century Projections: *Journal of Climate*, v. 23, p. 4585-4607.

Yu, L.S., and Rienecker, M.M., (1999), Mechanisms for the Indian Ocean warming during the 1997-98 El Nino: *Geophysical Research Letters*, v. 26, p. 735-738.

Zhang, M.H., and Song, H., (2006), Evidence of deceleration of atmospheric vertical overturning circulation over the tropical Pacific: *Geophysical Research Letters*, v. 33.

Zheng, X.T., Xie, S.P., Vecchi, G.A., Liu, Q.Y., and Hafner, J., (2010), Indian Ocean Dipole Response to Global Warming: Analysis of Ocean-Atmospheric Feedbacks in a Coupled Model: *Journal of Climate*, v. 23, p. 1240-1253.

Federated States of Micronesia

Glossary

A

Anthropogenic

Resulting from or produced by human beings.

Anthropogenic emissions

Emissions of greenhouse gases, greenhouse gas precursors, and aerosols associated with human activities, including the burning of fossil fuels, deforestation, land-use changes, livestock, fertilisation, etc.

Anthropogenic forcing – see also **Forcing**

A **forcing** that is caused by human activities including changes in greenhouse gas and aerosol concentrations and land-use changes.

Anomaly

In climate science, a deviation from the normal value of a variable. It is usually the deviation of a variable from the average value at a specific place and time.

Aragonite saturation state – see also **Ocean acidification**

Aragonite is a form of calcium carbonate that makes up the shells and skeletons of key organisms in reef ecosystems, including reef-building corals. The saturation state of aragonite in seawater (known as Ω) is a measure of the potential for the mineral to form or to dissolve. When the $\Omega = 1$, the seawater is in equilibrium with respect to aragonite, so aragonite does not dissolve or precipitate. When $\Omega > 1$ seawater is supersaturated with respect to aragonite and aragonite will precipitate, and when $\Omega < 1$ aragonite will dissolve. Aragonite saturations states above about 4 are considered optimal conditions for healthy coral reef ecosystems, with values below 3.5 becoming increasingly marginal for supporting healthy coral reef growth.

Attribution

Attribution is the process of identifying the most likely causes for the detected changes in the **climate**.

B

Bias – see **Model bias**

C

Carbon cycle

The term used to describe the flow of carbon (in various forms, e.g. as carbon dioxide) through the atmosphere, ocean, terrestrial biosphere and lithosphere.

Climate

Climate in a wider sense is the state, including a statistical description, of the climate system. Climate in a narrow sense is usually defined as the average weather, (or more rigorously, as the statistical description in terms of the mean and variability of relevant quantities), over a period of time ranging from months to thousands or millions of years. The relevant quantities are most often surface variables such as temperature, precipitation and wind. The classical period for averaging these variables is 30 years, as defined by the World Meteorological Organization. In various parts of this publication different averaging periods, such as a period of 20 years, are also used.

Climate change – see also **Climate variability**

Climate change refers to a change in the state of the climate that can be identified (e.g., by using statistical tests) by changes in the mean and/or the variability of its properties, and that persists for an extended period, typically decades or longer. Climate change may be due to natural internal processes or **external forcings**, or to persistent **anthropogenic** changes in the composition of the atmosphere or in land use.

This definition is the same as the one used by the Intergovernmental Panel on Climate Change and differs from that used by the United Nations Framework Convention on Climate Change which makes a distinction between climate change attributable to human activities and **climate variability** attributable to natural causes.

Climate model – see **Global climate model**

Climate model drift – see **Model drift**

Climate projection

A projection of the response of the climate system to emission or concentration scenarios of greenhouse gases and aerosols, or radiative forcing scenarios, often based upon simulations by climate models. Climate projections are distinguished from climate predictions in order to emphasise that climate projections depend upon the emission/concentration/radiative forcing scenario used, which are based on assumptions concerning, for example, future socioeconomic and technological developments that may or may not be realised and are therefore subject to substantial uncertainty.

Climate variability – see also Patterns of variability

Climate variability refers to variations in the mean state and other statistics (such as standard deviations, the occurrence of extremes, etc.) of the climate on all spatial and temporal scales beyond that of individual weather events. Variability may be due to natural internal processes within the climate system (internal variability), or to variations in natural or anthropogenic external forcing (external variability).

Climatology

The description and scientific study of climate.

CMIP3

Coupled Model Intercomparison Project (Phase 3) is a set of climate model experiments from 17 groups in 12 countries with 24 models. Climate model output from simulations of the past, present and future climate was collected by Program for Climate Model Diagnosis and Intercomparison at Lawrence Livermore National Laboratory in the US, during 2005 and 2006. The resulting CMIP3 dataset was used to inform the Fourth Assessment Report of the Intergovernmental Panel on Climate Change.

CMIP5

The fifth phase of the Coupled Model Intercomparison Project (CMIP5). In September 2008, 20 climate modelling groups from around the world, agreed to develop a new set of coordinated climate model experiments which will provide a wider range of emissions scenarios, and improved models and simulations for the 5th Assessment Report of the Intergovernmental Panel on Climate Change.

Cold Tongue – see **Equatorial Cold Tongue**

Convection

Vertical motion driven by buoyancy forces arising from static instability, usually caused by near surface warming in the case of the atmosphere, and by near-surface cooling or increases in salinity in the case of the ocean.

Convergence

In meteorology where winds flow from different directions toward each other, thus meeting at one point or along one line. Similarly, in oceanography, where water currents flow toward each other and meet. Horizontal convergence usually forces vertical motion to occur, such as convection.

Coriolis Effect

Air or water that is in motion is deflected to the right (of the direction of flow) in the Northern Hemisphere and to the left (of the direction of flow) in the Southern Hemisphere as a result of the rotation of the Earth. The Coriolis Effect is largest at the poles and diminishes to zero at the equator.

D

Downscaling

Downscaling refers to techniques that derive small-scale (at a single location or region) information from data on larger spatial scales, such as Global Climate Model output. Two main methods are generally applied: dynamical downscaling (using fine-resolution global or regional climate models) and statistical downscaling (using statistical relationships).

Dynamical downscaling

Dynamical downscaling uses a finer resolution atmospheric climate model, driven by large-scale data from a global climate model to derive local or regional scale information. The fine resolution model provides better representation of topography and land/sea boundaries. This method is computationally intensive and the results are strongly dependent on the choice of both the global climate model and the atmospheric model.

Statistical downscaling

Statistical downscaling techniques develop statistical relationships that link the large-scale climate variables with local-scale or regional climate variables. This technique maintains important information regarding locally observed historical trends and variability, while also introducing important aspects of change from the global climate models.

Driver (of climate change)

Any natural or human-induced factor that directly or indirectly causes a change.

Dynamic response (of ice sheets)

Rapid disintegration of ice sheets through dynamic processes.

E

Ekman Currents

Wind driven currents in the upper few tens of metres of the ocean that flow at 90 degrees to the right of the wind direction in the Northern Hemisphere and to the left in the Southern Hemisphere.

El Niño – see also El Niño-Southern Oscillation, La Niña

This is the warm phase of the El Niño-Southern Oscillation. El Niño events occur on average once every two to seven years. They are associated with basin-wide warming of the tropical Pacific Ocean east of the dateline and a weakening of the Walker Circulation.

Canonical El Niño – see also El Niño, La Niña, El Niño Modoki

This is characterised by warming of waters in the central and eastern Pacific Ocean and cooling in a horse-shoe pattern in the western Pacific Ocean.

El Niño Modoki

El Niño Modoki, also called the Central Pacific El Niño, is a recurring pattern of variability in the tropical Pacific, in which the maximum warming occurs in the central tropical Pacific rather than in the east. This represents a variation on the Canonical El Niño.

ENSO Modoki Index (EMI)

This is the difference between the sea-surface temperature anomalies averaged over the central equatorial Pacific and the out-of-phase variations in the far eastern and far western Pacific.

El Niño-Southern Oscillation (ENSO) – see also El Niño, La Niña

The term El Niño was initially used to describe a warm-water current that periodically flows along the coast of Ecuador and Perú, disrupting the local fishery. It has since become identified with a basin-wide warming of the tropical Pacific Ocean east of the dateline. This oceanic event is associated with a fluctuation of a global-scale tropical and subtropical surface pressure pattern called the Southern Oscillation. This naturally occurring coupled atmosphere-ocean phenomenon, with time scales of approximately two to seven years, is known as the El Niño-Southern Oscillation (ENSO). The state of ENSO is often measured by the Southern Oscillation Index (SOI) and sea-surface temperatures in the central and eastern equatorial Pacific.

During an ENSO event, the prevailing trade winds weaken, reducing upwelling and altering ocean currents such that the sea-surface temperatures warm, further weakening the trade winds. This event has a great impact on the wind, sea-surface temperature and precipitation patterns in the tropical Pacific. It has climatic effects throughout the Pacific region and in many other parts of the world. The cold phase of ENSO is called La Niña.

Ensemble

An ensemble refers to a group of model simulations used for climate projections. It may refer either to a group of simulations from different models; or to a group of simulations run on the same model but using slightly different starting conditions.

Equatorial Cold Tongue

This is a region of relatively cool surface water in the equatorial eastern Pacific Ocean and along the west coast of South America.

Equinox

The times of the year when the Sun crosses the plane of the Earth's equator, occurring around March 21 and September 22 and making the length of night and day approximately equal all over the Earth.

Evapotranspiration – see **Potential evapotranspiration**

External forcing – see **Forcing**

Extreme weather event

An event that is rare at a particular place and time of year. Definitions of rare vary, but an extreme weather event would normally be as rare as or rarer than the 10th or 90th percentile of the observed probability density function.

F

Flux adjustment

In order to prevent drift in climate simulations older climate models and a minority of the CMIP3 models use flux adjustment. Flux adjustment involves making small corrections to heat, freshwater and momentum transfers between ocean and atmosphere models, in order to make sure that the climate remains relatively stable.

Forcing – see also Anthropogenic forcing, Natural forcing

An agent that causes a change in the climate system. External forcing refers to agents outside the climate system, such as changes in greenhouse gases or solar variations. Internal forcing refers to natural climate variations, such as the Interdecadal Pacific Oscillation. Radiative forcing refers specifically to external forcings that change the net radiation at the tropopause.

G

Global Climate Model (GCM)

This is a numerical representation of the climate system based on the physical, chemical and biological properties of its components, their interactions and feedback processes, and accounting for all or some of its known properties. Coupled Atmosphere-Ocean General Circulation Models provide a representation of the climate system that is near the most comprehensive end of the spectrum currently available. There is an evolution towards more complex models with interactive chemistry and biology.

Global surface temperature

The global surface temperature is an estimate of the global mean surface air temperature. However, for changes over time, only anomalies, as departures from a climatology, are used, most commonly based on the area-weighted global average of the sea-surface temperature anomaly and land surface air temperature anomaly.

Gridded data – see also Reanalysis

A set of climate data that are given for the same time or average period on a regular grid in space. Data at each grid point represent the average value over a grid box whose size is determined by the spacing between the grid points (also called the grid resolution). Global climate model and reanalysis data are produced as gridded data.

H

Hadley Circulation

The major vertical movement of heated equatorial air and its north-south transfer into the mid latitudes, first proposed by George Hadley in 1735 as an explanation for the trade winds. It consists of the equatorward movement of the trade winds between about latitude 30° and the equator in each hemisphere, with rising wind components near the equator, poleward flow aloft, and, finally, descending components at about latitude 30° again.

Halosteric – see also Steric

Sea-level changes induced by changes in water density are called steric. Density changes induced by salinity changes are called halosteric.

Holocene

The last 12 000 years of geological time.

Homogenisation

Observed climate variables sometimes show sudden shifts in the average values or variability. Not all of these shifts are caused by real changes in climate. Non-climate related shifts can be due to changes in instrumentation, observation site, surrounding environment and observation practices, or other factors.

Homogenous – see also Homogenisation

Climate data homogenisation aims to adjust data if necessary, so that all variations in the data series are caused by real changes in the climate, and not due to changes in the way the data have been recorded.

Humidity – see **Relative humidity**

I

Ice discharge (dynamical)

Discharge of ice from ice sheets or ice caps caused by the dynamics of the ice sheet or ice cap (e.g. in the form of glacier flow, ice streams and calving icebergs) rather than by melt or runoff.

Ice sheet mass balance – see **Mass balance**

Indian Ocean Dipole (IOD)

The Indian Ocean Dipole (IOD) is a coupled ocean and atmosphere phenomenon in the equatorial Indian Ocean that affects the climate of countries that surround the Indian Ocean basin, particularly rainfall. The IOD is commonly measured by the Indian Ocean Dipole (IOD) Index.

Indian Ocean Dipole (IOD) Index

The IOD index measures the difference in sea-surface temperatures between the western tropical Indian Ocean (50°E to 70°E and 10°S to 10°N) and the eastern tropical Indian Ocean (90°E to 110°E and 10°S to 0°S).

Index

A number representing a measure of a particular feature of the climate system at a given time, varying with time and used as some measure of variability.

Indices – see **Index**

Insolation

The amount of solar radiation reaching the Earth at a given location in a given time.

Interannual

From year to year.

Interdecadal Pacific Oscillation (IPO) – see also Pacific Decadal Oscillation (PDO)

The Interdecadal Pacific Oscillation (IPO) is a natural recurring pattern of variability in tropical Pacific Ocean sea-surface temperatures occurring on periods of about 15 years and longer. While defined differently the IPO and PDO (Pacific Decadal Oscillation) describe essentially the same variability.

Interdecadal Pacific Oscillation (IPO) Index

A measure of the strength and phase of the Interdecadal Pacific Oscillation pattern.

Internal forcing – see **Forcing**

Intertropical Convergence Zone (ITCZ)

An east-west band of low-level wind convergence near the equator where the Southeast trade winds of the Southern Hemisphere meet the Northeast trade winds of the Northern Hemisphere. It is co-located with the ascending branch of the Hadley Circulation and has a associated band of heavy rainfall as the winds converge and moist air is forced upward.

L

La Niña – see also El Niño, El Niño–Southern Oscillation

The most common of several names given to cold phase of the El Niño–Southern Oscillation. La Niña is the counterpart to the El Niño warm event, although La Niña events tend to be somewhat less regular in their behaviour and duration. La Niña is associated with large-scale cooling of the surface waters of the eastern tropical Pacific Ocean and a strengthening of the Walker Circulation.

M

Madden Julian Oscillation

The Madden Julian Oscillation (MJO) is a global-scale feature of the tropical atmosphere that is characterized as an eastward moving pulse of cloud and rainfall near the equator that typically recurs every 30 to 60 days, but it is not always present.

Maritime Continent

The Maritime Continent consists of parts of Southeast Asia and the islands of Indonesia and the Philippines on the western equatorial edge of the Pacific, and includes large areas of ocean as well as the islands.

Mass balance (of ice sheets)

The mass balance is the net gain or loss of ice and snow for an ice sheet. It is related to difference between snow accumulation versus melt, runoff and iceberg calving.

Mean High Water (MHW)

The average of all high waters observed over a sufficiently long period.

Mean Higher High Water (MHHW)

The mean of the higher of the two daily high waters over a period of time.

Mean sea level – see also **Relative sea level, Sea level change/rise**

Mean sea level is normally defined as the average relative sea level over a period, such as a month or a year, long enough to average out transients such as waves and tides.

Meridional – see also **Zonal**

In meteorology, a flow in a direction that is parallel to a line of longitude; along a meridian; northerly or southerly; as opposed to **zonal**.

Model bias

Model biases are spurious differences between climate model simulations and observations. These may be caused by a number of factors including a lack of model resolution or an insufficiently realistic representation of certain physical processes. Systematic biases are errors that are common to a majority the climate models.

Model drift

Model drift refers to spurious trends in climate simulations that are not caused by changing external **drivers** (such as increased greenhouse gases or changes in solar radiation). Instead these spurious trends arise as a result of the way that models are initialised or imperfections in the representation of physical processes. Under many circumstances drift only introduces a small error in the estimation of climate trends however it must be accounted for where it is large.

Model skill

Model skill is a measure of how well a climate model can realistically represent the climate system.

Multivariate ENSO Index (MEI)

A measure used to describe ENSO combining six observed variables over the tropical Pacific. These six variables are: sea-level pressure, zonal and meridional components of the surface wind, sea-surface temperature, surface-air temperature, and total cloudiness fraction of the sky.

N

Natural forcing – see also **Forcing**

A **forcing** in the climate system due to natural causes as opposed to **anthropogenic forcing**, Natural forcing includes changes in solar output, the Earth's orbit and volcanic eruptions.

NINO3 index

An average of sea-surface temperature anomalies in the Pacific Ocean over the area 5°N to 5°S, 150°W to 90°W.

NINO3.4 index

An average sea-surface temperature **anomaly** in the central Pacific (latitude 5°N to 5°S; longitude 170°W to 120°W).

NINO4 index

An average of sea-surface temperature anomalies in the Pacific Ocean over the area 5°N to 5°S, 160°E to 150°W.

O

Ocean acidification – see also **Aragonite saturation state**

Ocean acidification is the name given to the ongoing decrease in the **pH** of the Earth's oceans, caused by their uptake of **anthropogenic** carbon dioxide from the atmosphere. When carbon dioxide dissolves in the ocean it lowers the **pH**, making the ocean more acidic.

Oceanic NINO3.4 Index (ONI)

An average of sea-surface temperatures anomalies in the Niño 3.4 region (latitude 5°N to 5°S; longitude 120° to 170°W).

P

Pacific Climate Change Science Program (PCCSP)

A collaborative research partnership between Australian Government agencies, 14 Pacific island countries and East Timor, and regional and international organisations.

Pacific Climate Change Science Program (PCCSP) Region

The region defined by the coordinates: 25°S–20°N and 120°E–150°W (excluding the Australian region south of 10°S and west of 155°E).

Pacific Decadal Oscillation (PDO)

A naturally recurring pattern of variability in the tropical and northern Pacific characterised by warming and cooling sea-surface temperature, similar to that of ENSO, although broader in a north-south direction. Oscillations in the PDO take multiple decades usually 20–30 years.

Parameterisation

Representing in an approximate form processes that cannot be explicitly resolved at the spatial or temporal resolution of the model (e.g. cloud formation, ocean eddies).

Patterns of variability – see also **Climate variability**

Natural variability of the climate system, in particular on seasonal and longer time scales, predominantly occurs with preferred spatial patterns and time scales, through the dynamical characteristics of the atmospheric circulation and through interactions with the land and sea surfaces. Examples include the **El Niño-Southern Oscillation**.

pH

A measure of the acidity or alkalinity of a solution, numerically equal to 7 for neutral solutions, increasing with increasing alkalinity and decreasing with increasing acidity. The pH scale ranges from 0 to 14.

Potential evapotranspiration

Evapotranspiration is the sum of evaporation from the land surface (e.g. from the soil and bodies of water such as lakes and rivers) and transpiration from vegetation. Potential evapotranspiration is defined as the evapotranspiration that would take place if there was an unlimited water supply. It is a representation of the environmental demand for evapotranspiration.

Probability Distribution Function (PDF)

A PDF describes the likelihood that a certain event or outcome will occur based on prior experience. For example a PDF of daily temperatures would provide information on how likely it is to have an extremely hot or cold temperature.

Pycnocline

Moving downward through the ocean, the pycnocline is the region where there is a rapid increase in density with depth. It acts as a barrier to mixing between deep and surface waters.

R

Radiative forcing – see **Forcing**

Reanalysis – see also **Gridded data**

An analysis combining many irregular meteorological or oceanographic observations from close to the same time into a physically consistent, complete **gridded data** set for a given time and usually for the whole globe.

Relative humidity

Relative humidity is defined as the amount of water vapour in the air, relative to the maximum amount of water vapour that the air is able to hold, without it condensing (expressed as a percentage).

Relative sea level is sea level measured by a tide gauge with respect to the land upon which it is situated.

Relative sea-level rise – see also **Mean sea level, Sea level change/rise**

Relative sea level rise occurs where there is a local increase in the level of the ocean relative to the land, which might be due to ocean rise and/or land level subsidence.

Rossby wave

Also known as a planetary wave, it is a large, slow-moving, planetary-scale wave generated in the troposphere by ocean-land temperature contrasts and topographic forcing (winds flowing over mountains), and affected by the **Coriolis Effect** due to the earth's rotation. Rossby waves are also observed in the ocean.

S

Sea level change/rise – see also **Mean sea level, Relative sea-level rise, Thermal expansion**

Sea level can change, both globally and locally, due to; (1) changes in the shape of the ocean basins; (2) changes in the total mass of water and, (3) changes in water density.

Factors leading to sea level rise under global warming include both increases in the total mass of water from the melting of land-based snow and ice, and changes in water density from an increase in ocean water temperatures and salinity changes.

Sea-surface temperature

The temperature of the ocean surface. The term sea-surface temperature is generally representative of the upper few metres of the ocean as opposed to the skin temperature, which is the temperature of the upper few centimetres.

Solstice

The times of the year when the Sun is at its greatest distance from the equator, occurring around June 21, when the Sun reaches its northernmost point on the celestial sphere, or around December 22, when it reaches its southernmost point.

Southern Annular Mode (SAM)

The Southern Annular Mode (SAM) is the most important recurring pattern of natural variability in the Southern Hemisphere outside of the tropics. Oscillations in the SAM are associated with shifts in the position and strength of the mid-latitude westerly winds.

Southern Annual Mode (SAM) Index

Index measuring the difference in surface pressure between latitudes 40ºS and 65ºS. A positive SAM index corresponds to a southward movement and intensification of the sub-tropical westerly winds.

Southern Oscillation – see also **El Niño-Southern Oscillation**

Fluctuation of a global-scale tropical and subtropical surface pressure pattern.

Southern Oscillation Index (SOI)

The Southern Oscillation Index (SOI) is calculated from the monthly or seasonal fluctuations in the air pressure difference between Tahiti and Darwin.

South Pacific Convergence Zone (SPCZ)

A persistent and greatly elongated zone of low-level **convergence** extending from approximately 140°E near the equator to approximately 120°W at 30°S. The zone is not quite linear, but is oriented more west to east near the equator and has a more diagonal orientation (northwest to southeast) at higher latitudes.

SPCZ Position Index

The SPCZ Position Index is a measure of SPCZ location and is calculated as the normalised November-April difference in 9am (local time) in mean sea-level pressure between Suva and Apia. The SPCZ Position Index defines the latitude of the SPCZ between longitudes 180°W and 170°W.

Standardised Precipitation Index (SPI)

The Standardised Precipitation Index (SPI) is an **index** based on the probability of recording a given amount of precipitation. The probabilities are standardized so that an index of zero indicates the median precipitation amount. The index is negative for drought, and positive for wet conditions.

Statistical downscaling – see **Downscaling**

Steric – see also **Halosteric, Thermosteric**

Steric effects refer to the expansion and contraction of sea water.

Storm surge

The temporary increased height of the sea above the level expected from tidal variation alone at that time and place due to extreme meteorological conditions.

Stratosphere

The region of the atmosphere extending from the top of the troposphere at heights of roughly 10–17 km, to the base of the mesosphere at a height of roughly 50 km.

Sub-tropical High Pressure System

Areas of raised surface pressure between latitudes 20° and 40°.

T

Thermal Expansion – see also **Sea level change/rise, Mean sea level**

The increase in volume (and decrease in density) that results from warming water.

Thermocline

Moving downward through the ocean, the region where there is a rapid reduction in temperature with depth. The thermocline separates warm surface waters from cold deep waters.

Thermosteric – see also **Steric**

The expansion or contraction of sea water due to heating or cooling.

Time-series

The values of a variable generated successively in time. Graphically, a time series is usually plotted with time on the horizontal axis (x-axis), and the values of the variable on the vertical axis (y-axis).

Trade winds

The wind system, occupying most of the tropics that blow from the subtropical high pressure areas toward the equator.

Tropical cyclone

A tropical cyclone is a tropical depression of sufficient intensity to produce sustained gale force winds (at least 63 km per hour). A severe tropical cyclone produces sustained hurricane force winds (at least 118 km per hour). Severe tropical cyclones correspond to the hurricanes or typhoons of other parts of the world.

Troposphere

The lowest part of the atmosphere from the surface to about 10 km in altitude in mid-latitudes (ranging from 9 km in high latitudes to 16 km in the tropics on average), where clouds and weather phenomena occur.

Trough

An elongated region of low atmospheric pressure.

W

Walker Circulation

The Walker Circulation is the east-west circulation of air, oriented along the Equator, across the Pacific region.

Warm Pool (also known as **West Pacific Warm Pool** and **Indo-Pacific Warm Pool**)

An extensive pool of the world's warmest water, with temperatures exceeding 28–29°C extending from the central Pacific to the far eastern Indian Ocean. The PCCSP focuses on the region of the Warm Pool to the east of 120°E.

West Pacific Monsoon

A monsoon is a tropical and subtropical seasonal reversal of both surface winds and associated rainfall, caused by differential heating between a continental scale land mass and the adjacent ocean. The Western Pacific Monsoon is the eastern edge of the Indonesian or Maritime Continent Monsoon, and the southern extension of the larger Asian-Australian Monsoon system.

Z

Zonal – see also **Meridional**

In meteorology, latitudinal, that is, easterly or westerly; opposed to **meridional**.

Market, Vanuatu

Index

www.pacificclimatechangescience.org

Australian Government
AusAID

Australian Government
Bureau of Meteorology

Australian Government
Department of Climate Change
and Energy Efficiency

CSIRO